Springer Series in Biophysics 20

Amitabha Chattopadhyay *Editor*

Membrane Organization and Dynamics

Springer

Springer Series in Biophysics 20

Series editor
Boris Martinac

More information about this series at http://www.springer.com/series/835

Amitabha Chattopadhyay
Editor

Membrane Organization and Dynamics

Springer

Editor
Amitabha Chattopadhyay
Centre for Cellular & Molecular Biology
Hyderabad, India

Series editor
Boris Martinac
University of New South Wales
Victor Chang Cardiac Research Inst.
Darlinghurst, New South Wales
Australia

ISSN 0932-2353 ISSN 1868-2561 (electronic)
Springer Series in Biophysics
ISBN 978-3-319-66600-6 ISBN 978-3-319-66601-3 (eBook)
DOI 10.1007/978-3-319-66601-3

Library of Congress Control Number: 2017956743

Printed on acid-free paper

This Springer imprint is published by Springer Nature
The registered company is Springer International Publishing AG
The registered company address is: Gewerbestrasse 11, 6330 Cham, Switzerland

Preface

Biological membranes are soft matter-like complex nanofluids that separate cells from each other in living matter. Besides providing the much-needed identity to cells, they facilitate cell–cell communication. A major role of cell membranes is to provide an ideal environment to the constituent proteins for their function. This is because membrane proteins are dynamic and they work best when the immediate environment around them offers enough flexibility for conformational plasticity, necessary for their function. Almost 50% of all proteins encoded by a eukaryotic genome are membrane proteins. As a result, a majority of biological processes take place on the cell membrane. In the last few years, crystal structures of an impressive number of membrane proteins have been reported, thanks to tremendous advances in membrane protein crystallization techniques. Some of these recently solved structures belong to the G protein-coupled receptor (GPCR) family, which are particularly difficult to crystallize due to their intrinsic flexibility. Nonetheless, these static structures do not provide the necessary information to understand the function of membrane proteins in the complex membrane milieu. This is due to two reasons: (i) most of these structures are not in the natural membrane bilayer, thereby raising the concern of physiological relevance; and (ii) more importantly, these structures do not provide any dynamic information, crucial for understanding membrane function.

It is against this general backdrop that this monograph on membrane organization and dynamics is being organized. This monograph brings together information on membrane organization and dynamics from a variety of spectroscopic, microscopic, and simulation approaches, spanning a broad range of timescales. The implications of such dynamic information on membrane function in health and disease are a topic of contemporary interest. The articles in this volume cover various aspects of membrane lipid and protein dynamics, explored using a battery of experimental and theoretical approaches. It is hoped that the synthesis of information and knowledge gained by utilizing multiple approaches would provide a comprehensive understanding of the underlying membrane organization, dynamics, and function.

This would help to develop robust models for understanding membrane function in healthy and diseased states.

I believe that this book will help the prospective reader to gain an overall understanding of membrane organization and dynamics in terms of currently emerging themes and approaches. I would like to make use of this opportunity to thank all the contributors who are leaders in their respective areas of research. Special thanks are due to Boris Martinac (Series Editor), Sabine Schwarz, Martina Himberger, Madona Samuel, and Parijat Sarkar for their cooperation and support in organizing this monograph.

Hyderabad, India Amitabha Chattopadhyay

Contents

About the Editor

Amitabha Chattopadhyay is a J.C. Bose Fellow at the Centre for Cellular and Molecular Biology in Hyderabad, India. He received B.Sc. with Honors in Chemistry from St. Xavier's College (Calcutta) and M.Sc. from the Indian Institute of Technology at Kanpur. He received his Ph.D. from the State University of New York at Stony Brook and worked as a Postdoctoral Fellow at the University of California, Davis. He subsequently joined the Centre for Cellular and Molecular Biology in Hyderabad and became a Group Leader. He is an Adjunct Professor in a number of institutions in India and abroad. He served as the first Dean of Biological Sciences of the Academy of Scientific and Innovative Research.

Prof. Chattopadhyay's research interest is in the area of membrane and receptor biology. His group has developed and applied novel, innovative, and sensitive techniques using fluorescence spectroscopy for monitoring solvent relaxation in membranes and related assemblies. A seminal contribution of Prof. Chattopadhyay is the role of membrane cholesterol in regulating the organization, dynamics, and function of G protein-coupled receptors (GPCRs). His work has provided novel insight into the role of membrane cholesterol in the entry of pathogens into host cells.

Prof. Chattopadhyay's scientific contributions have been recognized by the prestigious TWAS Prize, Shanti Swarup Bhatnagar Award, Ranbaxy Research Award, Prof. G.N. Ramachandran 60th Birthday Medal, and Dozor Visiting Fellowship. He is an elected Fellow of the Royal Society of Biology, the Royal Society of Chemistry and all the Indian Academies of Science. He serves as a member of the editorial board of a large number of reputed journals. He has contributed close to 250 research publications and invited reviews and has guest edited special issues of a number of journals.

Chapter 1
What Is So Unique About Biomembrane Organization and Dynamics?

Sreetama Pal and Amitabha Chattopadhyay

Abstract Biological membranes are complex *quasi* two-dimensional, supramolecular assemblies of a diverse variety of lipids, proteins and carbohydrates, that compartmentalize living matter into cells and subcellular structures. Membranes are held together by the hydrophobic effect, which is an entropy-driven process originating from strong attractive forces between water molecules. Membrane organization and dynamics are characterized by the absence of intermolecular connectivity among its constituent units, thermodynamically controlled (spontaneous) self assembly, and inherent dynamics characterized by a gradient. Membrane phenomena display a wide range of spatiotemporal scales, thereby making it challenging for experiments and simulations alike. We envision that unraveling the spatiotemporal complexity of biological membranes would enable us to build a more robust membrane model, which would help in addressing unresolved issues in human health and disease.

1.1 Cellular Membranes as Identity Markers

A long time back, biochemists used to think that a living cell is a bag full of enzymes. In reality, eukaryotic cells are characterized by a number of compartments separated from each other and the cytoplasm by thin membranes (see Fig. 1.1). The composition, organization and physical dimension of the intracellular organelle membranes exhibit a lot of variation. The outermost membrane in eukaryotic cells is termed the plasma membrane, which separates the interior of the cell from the outer milieu and provides the cell its unique identity. Cellular organization is therefore characterized by morphological compartmentalization

S. Pal
Academy of Scientific and Innovative Research, New Delhi, India

CSIR-Indian Institute of Chemical Technology, Uppal Road, Hyderabad 500 007, India

A. Chattopadhyay (✉)
Academy of Scientific and Innovative Research, New Delhi, India

CSIR-Centre for Cellular and Molecular Biology, Uppal Road, Hyderabad 500 007, India
e-mail: amit@ccmb.res.in

A. Chattopadhyay (ed.), *Membrane Organization and Dynamics*, Springer Series in Biophysics 20, DOI 10.1007/978-3-319-66601-3_1

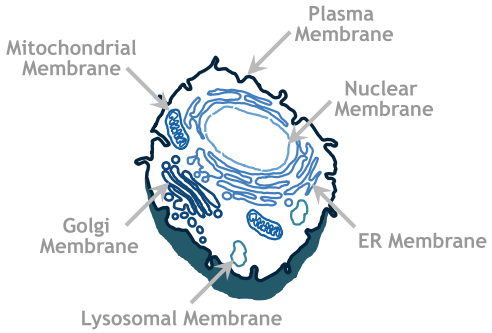

Fig. 1.1 A schematic representation of a eukaryotic cell showing the plasma membrane and membrane bound organelles

offered by the membrane. Membranes compartmentalize living matter into cells and subcellular structures. Cells require some mechanism to prevent dissipation (diffusing away) of their genetic information (contained mainly in the nucleus) and therefore "*compartmentalization has long been recognized as a physical prerequisite for Darwinian evolution*" [1]. Importantly, the membrane is the first organelle in a cell to sense any stress or stimuli [2].

In physical terms, membranes can be described as a complex anisotropic fluid that are deformable and can therefore be treated as soft matter [3, 4]. In molecular terms, this means membranes are optimally fluid to be able to carry out their function while maintaining their characteristic selective barrier properties. Membranes present themselves to macromolecules as highly structured interfaces on which important biochemical processes are carried out and catalyzed. For this reason, the structure and molecular organization of membranes are crucial for membrane function.

Biological membranes are complex *quasi* two-dimensional, supramolecular assemblies of a diverse variety of lipids, proteins and carbohydrates (see Fig. 1.2a). Membranes of eukaryotic cells contain thousands of diverse lipid types [6, 7]. Membranes provide an identity to the cell and its organelles, and represent an ideal milieu for the proper function of membrane proteins. Cells are densely packed with membranes. In fact, ~35% of the dry weight of a cell is that of its membranes. The human body is composed of $\sim 10^{14}$ cells which correspond to a total membrane surface area of ~3 km^2. Contrary to textbook descriptions [8], cellular membranes are often crowded [9, 10] with a high protein density (typically ~25,000 proteins/μm^2; [11]). Even a number of years back it was postulated that there could be only a few lipid molecules separating two protein molecules in a biological membrane [12]. Taken together, the model of biological membranes is evolving into one where "*the membrane resembles a cobble-stone pavement, with the proteins organized in patches that are surrounded by lipidic rims, rather than icebergs floating in a sea of lipids*" [10].

The actin cytoskeletal network underlying the membrane was initially not considered to be an active part of the membrane. However, this has changed in recent years. A number of observations using sophisticated microscopic techniques have established the notion of actin cytoskeleton dependent dynamics of molecules

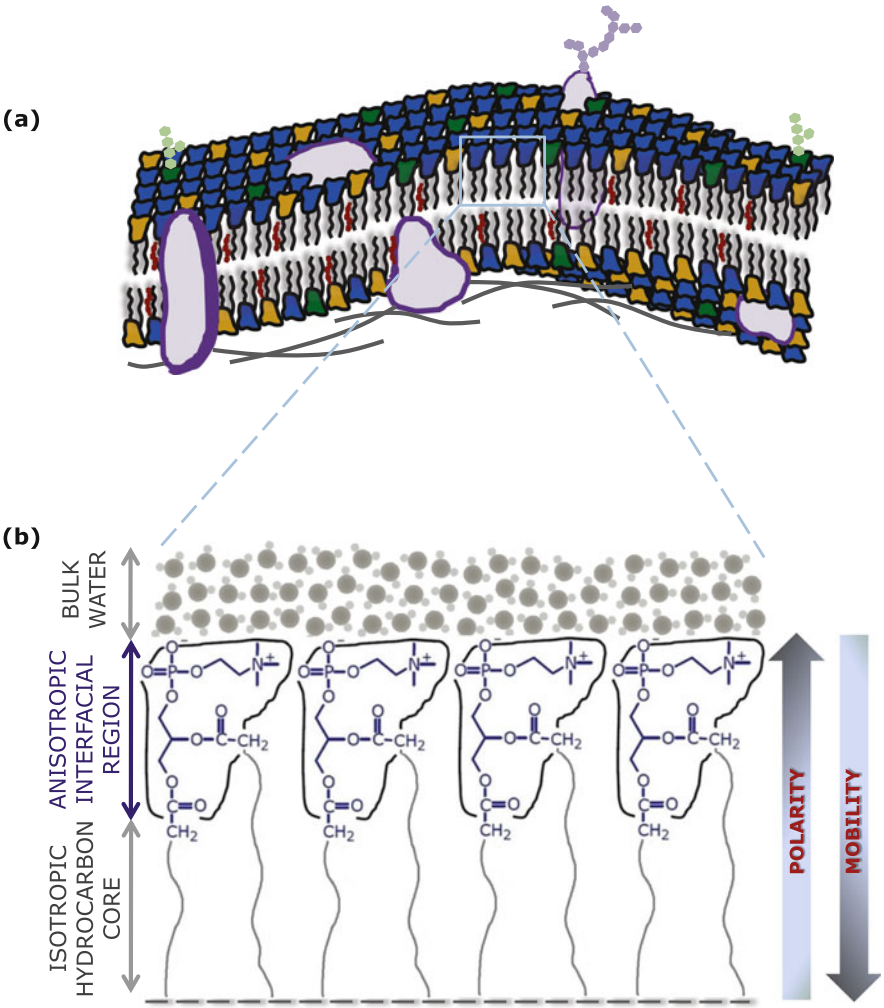

Fig. 1.2 (**a**) A schematic representation of a membrane bilayer showing the major components of biological membranes: lipids, proteins and carbohydrates. The actin cytoskeleton is also shown since emerging evidence suggests that it is coupled to the membrane (see Sect. 1.1). Eukaryotic membranes consist of phospholipids, sterols and sphingolipids. The predominant phospholipids are zwitterionic (shown in *blue*) phosphatidylcholine and phosphatidylethanolamine; and negatively charged (shown in *mustard*) phosphatidylglycerol and phosphatidylserine. Negatively charged lipids are key players in lipid-protein interactions and are known to modulate membrane insertion, translocation and subsequent function of membrane proteins. Cholesterol, the predominant sterol in eukaryotic membranes, is shown in *maroon* and sphingolipids in *green*. Cholesterol is a functionally relevant lipid in terms of its role in the organization, dynamics and function of biological membranes. Integral and peripheral membrane proteins are shown in *purple*. The underlying actin cytoskeleton, depicted in *gray*, imparts structural integrity and induces dynamic compartmentalization with its meshwork underneath the membrane, thereby leading to membrane domains. (**b**) An enlarged representation of one-half of the bilayer (highlighted by a *light blue box*) shows the intrinsically anisotropic nature of biological membranes. The *dotted line* at the bottom indicates the center of the bilayer. The anisotropy along the membrane z-axis compartmentalizes the membrane leaflet into two regions characterized by differential dynamics, as reported by

in cell membranes [13–15], and have led to the 'anchored protein picket model' of membranes [16]. In addition, a model involving cross-talk between membrane cholesterol and actin cytoskeleton is emerging based on observations such as destabilization of the cortical actin cytoskeleton due to depletion of plasma membrane cholesterol ([17, 18]; Sarkar P, Kumar GA, Shrivastava S, Chattopadhyay A, unpublished observations). This implies that the membrane components (lipids, proteins, carbohydrates and the underlying cytoskeleton) must interact with each other in order to provide much needed functionality to the membrane.

1.2 What Holds the Membrane Together?

The physical principle underlying the formation of membranes is the hydrophobic effect [19–21]. The hydrophobic effect describes how an aqueous medium deals with non-polar substances. The driving force behind the hydrophobic effect is essentially entropic in nature and has its genesis in the strong attractive forces between water molecules that must be disrupted to accommodate hydrophobic moieties in it and the entropic cost of incorporating a non-polar molecule in water. This effect should not be confused with the force of interaction among two non-polar (hydrophobic) molecules which plays a very minor role in hydrophobic effect. The hydrophobic effect serves as a common mechanism responsible for formation of other organized membrane-mimetic molecular assemblies, such as micelles and reverse micelles, and folding of globular proteins.

1.3 Unique Features of Biomembrane Organization and Dynamics

A unique feature of membrane organization, different from other macromolecular assemblies prevalent in biology, is that there is no intermolecular connectivity (and the implied information content) among membrane constituents (lack of a sequence). The fundamental paradigm in the protein world, a specific sequential

Fig. 1.2 (continued) spectroscopic techniques (such as ESR, NMR, fluorescence) and molecular dynamics simulations. The anisotropic membrane interface (shown in *blue*) ensures a dynamic segregation between the bulk aqueous phase and the isotropic hydrocarbon-like core of the membrane (shown in *gray*). Both the bulk aqueous phase and the hydrocarbon-like core of the membrane are characterized by fast and isotropic solvent relaxation. The membrane interface is uniquely characterized by a functionally relevant chemically heterogeneous environment, slow solvent relaxation, and limited water penetration (interfacial water). This inherent membrane anisotropy is reflected in polarity and mobility gradients (shown as *shaded gray arrows*) along the membrane normal (perpendicular to the plane of the membrane). See text for more details. Adapted and modified with permission from [5]. Copyright (2011) American Chemical Society

arrangement of the constituent units (amino acids), is therefore not a deciding factor in self assembly of lipids in biological membranes. Instead, self assembly of lipids into membranes is a consequence of the amphipathic nature of lipid molecules. The prominent dogma of molecular biology, *i.e.*, sequence dictating function, is therefore absent in biological membranes. Viewed from another perspective, the lack of intermolecular connectivity (sequence) provides the membrane its inherent dynamic nature. This makes the study of biological membranes unique and challenging.

The interfacial region (see Fig. 1.2b) is the most important part of the membrane, in terms of physicochemical characteristics and function [5, 22]. The membrane interface exhibits distinct motional and dielectric characteristics [23] different from the bulk aqueous phase and the more isotropic hydrocarbon-like deeper regions of the membrane. In a chemical sense, the membrane interface plays a crucial role in substrate recognition and activity of membrane-active enzymes [24]. The reduced probability (due to geometrical constraints) of energetically favorable hydrogen bonding induces dynamic confinement of water molecules at the membrane interface [25]. The membrane interface displays slow rates of solvent relaxation [5, 22, 26–29], participates in intermolecular charge interactions [30] and hydrogen bonding mediated by the polar lipid headgroup [31, 32].

As mentioned above, a unique feature of membranes is their inherent dynamics, characterized by a gradient along the bilayer normal (z-axis) (see Fig. 1.2b) [5, 33]. While the center of the membrane bilayer is nearly isotropic, the upper portion, only a few angstroms away toward the membrane surface, is highly ordered [5, 22]. As a consequence of this organization, properties such as polarity, segmental mobility (collectively termed as membrane fluidity), ability to form hydrogen bonds, and extent of solvent penetration vary in a depth-dependent manner in the membrane [34]. In addition, biological membranes display a gradient of environmental heterogeneity along the bilayer normal [33]. Taken together, absence of intermolecular connectivity (sequence), thermodynamically controlled (spontaneous) self assembly, and inherent dynamics characterized by a gradient, represent the essential aspects of membrane organization and dynamics.

1.4 Spatiotemporal Scales of Membrane Phenomena

Cellular events at the membrane span a wide range of spatiotemporal scales (see Fig. 1.3) [35–37]. An important aspect of the cell membrane is its dynamics that span a very large range of time scales, which supports a wide variety of biological processes, necessary for cellular function. The corresponding length scales also cover several orders of magnitude. Monitoring membrane dynamics with all its complexities continues to be challenging in contemporary membrane biophysics. Membrane probes offer the possibility of measuring membrane dynamics at various spatiotemporal resolutions, depending on the experimental approach chosen [38]. However, it is not possible to address problems in these spatiotemporal scales using any single technique and phenomena-dependent approaches are necessary.

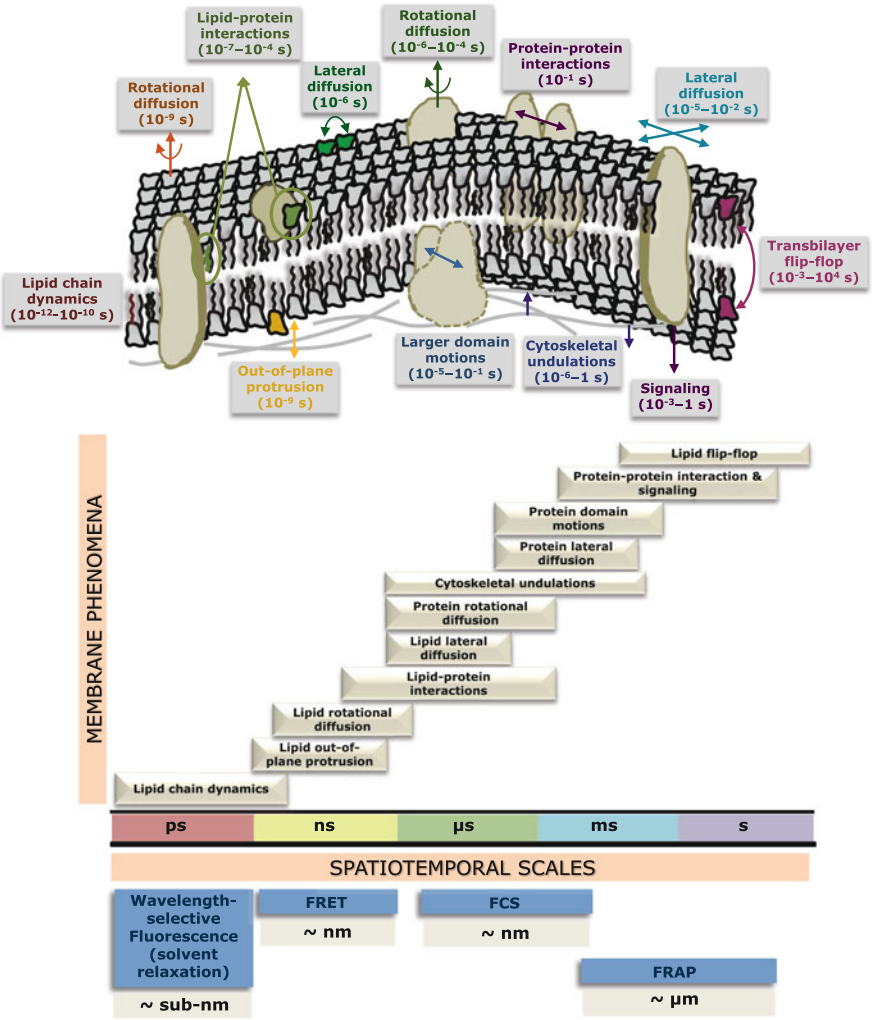

Fig. 1.3 Range of spatiotemporal scales relevant in biological membrane phenomena. Predominant membrane-associated processes are shown, with the corresponding time scales increasing *from left to right*. As shown in the figure, the range of time scales for membrane phenomena could span more than ten orders of magnitude, whereas the spatial scale ranges cover over three orders of magnitude. It is not possible to resolve these spatiotemporal scales simultaneously using any single technique. It is therefore crucial to select techniques with spatiotemporal scales comparable to that of the specific phenomenon probed. In this respect, fluorescence-based approaches (shown at the *bottom of the figure*) appear suitable since many membrane-associated processes can be addressed by fluorescence spectroscopic and microscopic techniques. Adapted and modified from [35]

Among various techniques used, fluorescence-based approaches offer certain advantages due to their enhanced sensitivity, minimal perturbation, multiplicity of measurable parameters, and suitable time scales that allow the analysis of several

membrane phenomena [39]. With the advent of confocal microscopy and organelle-specific probes, it has now become possible to explore lateral [40] and rotational [41] dynamics of specific organelle membranes such as Golgi membranes.

1.5 Future Perspectives: What Lies Ahead

Unraveling the spatiotemporal complexity of biological membranes appears to hold the key to understanding the molecular basis of diseases that pose a threat to mankind. This constitutes a major challenging area of research in the post-genomic era, particularly keeping in mind the fact that more than 50% of current drug targets in all clinical areas are membrane proteins [42]. In addition, the biological membrane plays a crucial role in amyloidogenic diseases that are associated with protein aggregation [43]. Membrane lipid mediated pathogen entry into host cells offers another potential avenue for developing novel therapeutic strategies to effectively tackle intracellular pathogenesis [44]. Tissue-specific and age-dependent drug efficacy represents another promising development in human health [45]. The articles that follow in this monograph will address several important topics in membrane biology with focus on membrane lipids and proteins using experimental and simulation approaches.

Acknowledgments A.C. gratefully acknowledges J.C. Bose Fellowship from the Department of Science and Technology, Govt. of India. S.P. thanks the University Grants Commission for the award of a Senior Research Fellowship. A.C. is an Adjunct Professor of Tata Institute of Fundamental Research (Mumbai), RMIT University (Melbourne, Australia), Indian Institute of Technology (Kanpur), and Indian Institute of Science Education and Research (Mohali). We thank G. Aditya Kumar for help with making figures and members of the Chattopadhyay laboratory for their comments and discussions.

References

1. Budin I, Szostak JW. Expanding roles for diverse physical phenomena during the origin of life. Annu Rev Biophys. 2010;39:245–63.
2. Revathi CJ, Chattopadhyay A, Srinivas UK. Change in membrane organization induced by heat shock. Biochem Mol Biol Int. 1994;32:941–50.
3. Bao G, Suresh S. Cell and molecular mechanics of biological materials. Nat Mater. 2003;2:715–25.
4. Mouritsen OG. A matter of softness. In: Mouritsen OG, editor. Life – as a matter of fat. Heidelberg: Springer; 2005. p. 53–62.
5. Haldar S, Chaudhuri A, Chattopadhyay A. Organization and dynamics of membrane probes and proteins utilizing the red edge excitation shift. J Phys Chem B. 2011;115:5693–706.
6. Sud M, Fahy E, Cotter D, et al. LMSD: LIPID MAPS structure database. Nucleic Acids Res. 2007;35:D527–32.
7. van Meer G, de Kroon AIPM. Lipid map of the mammalian cell. J Cell Sci. 2011;124:5–8.

8. Singer SJ, Nicolson GL. The fluid mosaic model of the structure of cell membranes. Science. 1972;175:720–31.
9. Goose JE, Sansom MSP. Reduced lateral mobility of lipids and proteins in crowded membranes. PLoS Comput Biol. 2013;9:e1003033.
10. Takamori S, Holt M, Stenius K, et al. Molecular anatomy of a trafficking organelle. Cell. 2006;127:831–46.
11. Ramadurai S, Holt A, Krasnikov V, et al. Lateral diffusion of membrane proteins. J Am Chem Soc. 2009;131:12650–6.
12. Yeagle PL. Lipid regulation of cell membrane structure and function. FASEB J. 1989;3:1833–42.
13. Fujiwara T, Ritchie K, Murakoshi H, et al. Phospholipids undergo hop diffusion in compartmentalized cell membrane. J Cell Biol. 2002;157:1071–81.
14. Ganguly S, Chattopadhyay A. Cholesterol depletion mimics the effect of cytoskeletal destabilization on membrane dynamics of the serotonin$_{1A}$ receptor: a zFCS study. Biophys J. 2010;99:1397–407.
15. Ganguly S, Pucadyil TJ, Chattopadhyay A. Actin cytoskeleton-dependent dynamics of the human serotonin$_{1A}$ receptor correlates with receptor signaling. Biophys J. 2008;95:451–63.
16. Kusumi A, Murakoshi H, Murase K, et al. Single-molecule imaging of diffusion, recruitment, and activation of signaling molecules in living cells. In: Damjanovich S, editor. Biophysical aspects of transmembrane signaling, Springer series in biophysics, vol. 8. Berlin: Springer; 2005. p. 123–52.
17. Kwik J, Boyle S, Fooksman D, et al. Membrane cholesterol, lateral mobility, and the phosphatidylinositol 4,5-bisphosphate-dependent organization of cell actin. Proc Natl Acad Sci U S A. 2003;100:13964–9.
18. Tsai H-I, Tsai L-H, Chen M-Y, et al. Cholesterol deficiency perturbs actin signaling and glutamate homeostasis in hippocampal astrocytes. Brain Res. 2006;1104:27–38.
19. Galli G. Dissecting hydrophobicity. Proc Natl Acad Sci U S A. 2007;104:2557–8.
20. Israelachvili JN, Marčelja S, Horn RG. Physical principles of membrane organization. Q Rev Biophys. 1980;13:121–200.
21. Tanford C. The hydrophobic effect and the organization of living matter. Science. 1978;200:1012–8.
22. Chattopadhyay A. Exploring membrane organization and dynamics by the wavelength-selective fluorescence approach. Chem Phys Lipids. 2003;122:3–17.
23. Ashcroft RG, Coster HGL, Smith JR. The molecular organization of bimolecular lipid membranes: the dielectric structure of the hydrophilic/hydrophobic interface. Biochim Biophys Acta. 1981;643:191–204.
24. El-Sayed MY, DeBose CD, Coury LA, et al. Sensitivity of phospholipase C (*Bacillus cereus*) activity to phosphatidylcholine structural modifications. Biochim Biophys Acta. 1985;837:325–35.
25. Marrink S-J, Tieleman DP, van Buuren AR, et al. Membranes and water: an interesting relationship. Faraday Discuss. 1996;103:191–201.
26. Chattopadhyay A. Application of the wavelength-selective fluorescence approach to monitor membrane organization and dynamics. In: Kraayenhof R, Visser AJWG, Gerritsen HC, Wolfbeis O, editors. Fluorescence spectroscopy, imaging and probes. Heidelberg: Springer; 2002. p. 211–24.
27. Chattopadhyay A, Mukherjee S. Fluorophore environments in membrane-bound probes: a red edge excitation shift study. Biochemistry. 1993;32:3804–11.
28. Demchenko AP. The red-edge effects: 30 years of exploration. Luminescence. 2002;17:19–42.
29. Hof M. Solvent relaxation in biomembranes. In: Retting W, Strehmel B, Schrader S, Seifert H, editors. Applied fluorescence in chemistry, biology and medicine. New York: Springer; 1999. p. 439–56.
30. Yeagle P. The membranes of cells. Orlando, FL: Academic Press; 1987. p. 89–90.

31. Boggs JM. Lipid intermolecular hydrogen bonding: influence on structural organization and membrane function. Biochim Biophys Acta. 1987;906:353–404.
32. Shin T-B, Leventis R, Silvius JR. Partitioning of fluorescent phospholipid probes between different bilayer environments: estimation of the free energy of interlipid hydrogen bonding. Biochemistry. 1991;30:7491–7.
33. Haldar S, Kombrabail M, Krishnamoorthy G, et al. Depth-dependent heterogeneity in membranes by fluorescence lifetime distribution analysis. J Phys Chem Lett. 2012;3:2676–81.
34. Chattopadhyay A, Mukherjee S. Depth-dependent solvent relaxation in membranes: wavelength-selective fluorescence as a membrane dipstick. Langmuir. 1999;15:2142–8.
35. Sengupta D, Kumar GA, Prasanna X, et al. Experimental and computational approaches to study membranes and lipid-protein interactions. In: Domene C, editor. Computational biophysics of membrane proteins, RSC theoretical and computational chemistry series, vol. 10. London: Royal Society of Chemistry; 2017. p. 137–60.
36. Jacobson K, Mouritsen OG, Anderson RGW. Lipid rafts: at a crossroad between cell biology and physics. Nat Cell Biol. 2007;9:7–14.
37. Marguet D, Lenne P-F, Rigneault H, et al. Dynamics in the plasma membrane: how to combine fluidity and order. EMBO J. 2006;25:3446–57.
38. Chattopadhyay A, editor. Lipid probes in membrane biology. Chem Phys Lipids. 2002;116:1–193.
39. Jafurulla M, Chattopadhyay A. Application of quantitative fluorescence microscopic approaches to monitor organization and dynamics of the serotonin$_{1A}$ receptor. In: Mély Y, Duportail G, editors. Springer series on fluorescence, vol. 13. Heidelberg: Springer; 2013. p. 417–37.
40. Cole NB, Smith CL, Sciaky N, et al. Diffusional mobility of Golgi proteins in membranes of living cells. Science. 1996;273:797–801.
41. Lajevardipour A, Chon JWM, Chattopadhyay A, et al. Imaging cellular dynamics with spectral relaxation imaging microscopy: distinct spectral dynamics in Golgi membranes of living cells. Sci Rep. 2016;6:37038.
42. Jacobson KA. New paradigms in GPCR drug discovery. Biochem Pharmacol. 2015;98:541–55.
43. Aisenbrey C, Borowik T, Byström R, et al. How is protein aggregation in amyloidogenic diseases modulated by biological membranes? Eur Biophys J. 2008;37:247–55.
44. Kumar GA, Jafurulla M, Chattopadhyay A. The membrane as the gatekeeper of infection: cholesterol in host-pathogen interaction. Chem Phys Lipids. 2016;199:179–85.
45. Prasanna X, Sengupta D, Chattopadhyay A. Cholesterol-dependent conformational plasticity in GPCR dimers. Sci Rep. 2016;6:31858.

Chapter 2
Dynamics and Organization of Archaeal Tetraether Lipid Membranes

Parkson Lee-Gau Chong, Alexander Bonanno, and Umme Ayesa

Abstract Archaeal bipolar tetraether lipids (BTLs) have distinct structural differences from the lipids isolated from bacteria and eukaryotes. Because of the presence of the unusual structural features, such as macrocyclic structures, cyclopentane rings, isoprenoid units, tetraether linkages, and a variety of polar head groups, archaeal BTL membranes possess physical properties distinctly different from those found in conventional diester lipid membranes. This chapter reviews the salient physical properties of archaeal BTL membranes as well as the membranes formed by synthetic BTLs, with the emphasis focused on membrane dynamics, stability, phase behaviors, and organization.

2.1 Chemical Structures of Bipolar Tetraether Lipids

2.1.1 Bipolar Tetraether Lipids Isolated from Archaea

Bipolar tetraether lipids (BTLs) are present in all three major archaeal kingdoms: euryarchaeota, crenarchaeota and thaumarchaeota [1]. BTLs are the dominating lipid species in crenarchaeota (~90–95% of the total lipid extract), which thrive under high temperature and low pH conditions. Euryarchaeota include methanogens and halophiles. BTLs are present in methanogens (0–50%), but virtually absent in halophiles. BTLs are also abundant in thaumarchaeota, which are mesophilic, found in ambient environments such as soil and lakes [1]. Archaeal BTLs have distinct structural differences from the lipids isolated from bacteria and eukaryotes [2]. The structures of archaeal BTLs are either macrocyclic or hemi-macrocyclic (also called semi-macrocyclic) as illustrated below.

P.L.-G. Chong (✉) • A. Bonanno • U. Ayesa
Department of Medical Genetics and Molecular Biochemistry, Lewis Katz School of Medicine at Temple University, Philadelphia, PA 19140, USA
e-mail: pchong02@temple.edu; tuf20683@temple.edu; tua46021@temple.edu

A. Chattopadhyay (ed.), *Membrane Organization and Dynamics*, Springer Series in Biophysics 20, DOI 10.1007/978-3-319-66601-3_2

Archaeal Macrocyclic BTLs In an archaeal macrocyclic BTL molecule, the hydrophobic core contains two biphytanyl chains (i.e., one dibiphytanyl chain), which consist of branched methyl groups and cyclopentane or cyclohexane rings. BTLs containing cyclohexane rings occur only in thaumarchaeota [3]. The hydrophobic core is connected to either glycerol or calditol via ether linkages with a *sn*-2,3 configuration, forming a macrocyclic structure. An ether linkage is more resistant against acidic or alkaline hydrolysis than an ester linkage. Archaeal BTLs have an L-glycerol backbone, in contrast to D-glycerol in eukaryotic and bacterial phosphoacylglycerols. Various polar moieties, such as sugars and phosphate, are linked to the glycerol or calditol backbones. The number of cyclopentane rings in biphytanyl chains increases with increasing growth temperature [4–6] and decreases with decreasing growth pH [7].

The structural features of archaeal macrocyclic BTLs are illustrated in Fig. 2.1, where the chemical structures of the polar lipid fraction E (PLFE) isolated from the thermoacidophilic crenarchaeon *Sulfolobus acidocaldarius* (optimum growth conditions: 75–80 °C and pH 2.5–3.0) [10] are presented. PLFE contains a mixture of either a calditolglycerocaldarchaeol (also termed glycerol dialkylcalditol tetraether, abbreviated as GDNT) or a caldarchaeol (also termed glycerol dialkylglycerol tetraether, GDGT) skeleton [10–13] (Fig. 2.1A). The GDNT component of PLFE (~90% of total PLFE) contains phospho-*myo*-inositol on the glycerol end and β-glucose on the calditol end, whereas the GDGT component (~10% of total PLFE) has phospho-*myo*-inositol attached to one glycerol and β-D-galactosyl-D-glucose to the other glycerol skeleton. In PLFE, the non-polar regions of these lipids consist of a pair of 40-carbon biphytanyl chains, each of which contains up to four cyclopentane rings (Fig. 2.1A), dependent upon the growth temperature and pH. The distribution of the number of cyclopentane rings for a given growth temperature is broad, ranging from 0–8 rings per BTL molecule [14, 15]. The maximum of the distribution curve shifts to a larger number of cyclopentane rings at a higher cell growth temperature [14, 15].

Not all archaeal macrocyclic BTLs are of the same structure. Like PLFE, the main phospholipid fraction (MPL) isolated from the crenarchaeota *Thermoplasma acidophilum* (optimum growth: 55–59 °C and pH 1–2) contains biphytanyl chains forming macrocyclic tetraether structures (Fig. 2.1B). However, MPL has up to three cyclopentane rings in the dibiphytanyl area per molecule (Fig. 2.1B) while PLFE contains up to eight cyclopentane rings per molecule [9, 15]. There are also structural differences in the polar head group regions. As discussed earlier, PLFE lipids contain phospho-*myo*-inositol, β-glucose, and β-D-galactosyl-D-glucose in the polar head groups (Fig. 2.1A). In comparison, MPL lipids have β-L-gulose (Gul) attached to one glycerol end and a phosphoglycerol moiety to another glycerol end (Fig. 2.1B) [9].

Several rather unusual structural variations can occur in the hydrophobic core of macrocyclic BTLs. One variation is the direct cross-linking between the two biphytanyl chains, forming H-shaped BTLs (Fig. 2.2B). Furthermore, additional $–CH_3$ (Fig. 2.2B) or –OH groups may appear in the biphytanyl chains [3, 16].

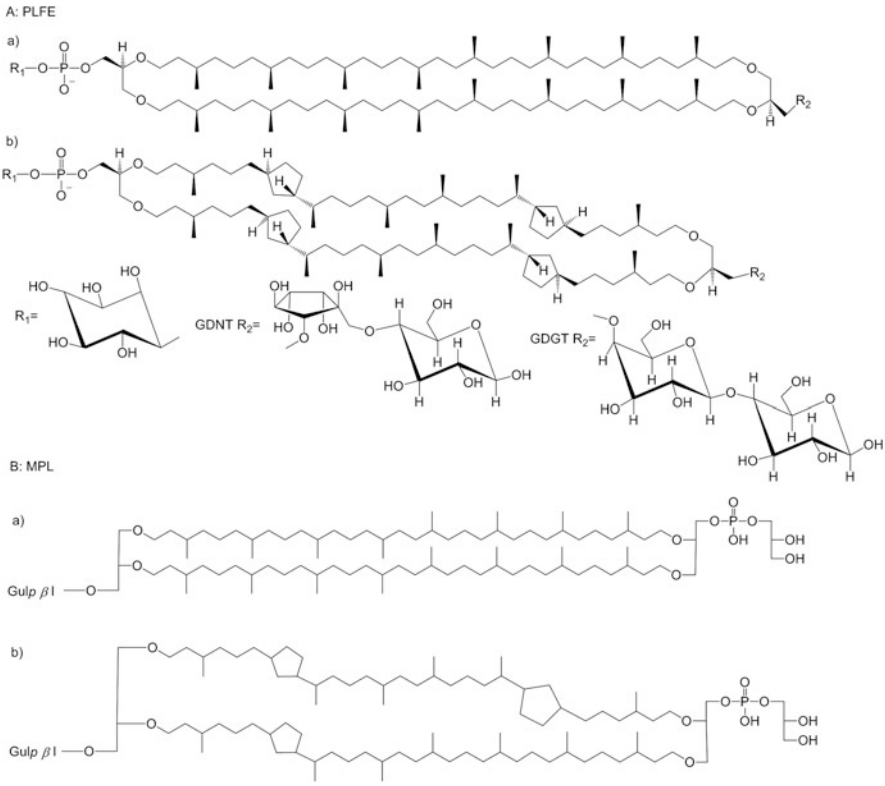

Fig. 2.1 Illustrations of the molecular structures of the macrocyclic bipolar tetraether lipids found in crenarchaeota. (**A**) Molecular structures of PLFE isolated from *S. acidocaldarius*. PLFE contains (**a**) GDGT (or caldarchaeol, ~10%) and (**b**) GDNT (or calditolglycerocaldarchaeol, ~90%). The number of cyclopentane rings in each biphytanyl chain can vary from 0 to 4. *R1* *myo*-inositol, *GDGT R2* β-D-galactosyl-D-glucose, and *GDNT R2* β-D-glucose linked to calditol. GDG(N)T-0 and GDG(N)T-4 contain 0 and 4 cyclopentane rings per molecule, respectively (Reprinted from [8] with permission). (**B**) Illustrations of the molecular structures of the lipids found in the main phospholipid fraction (MPL) isolated from *Thermoplasma acidophilum* HO-62 [9]: (**a**) with no cyclopentane rings; (**b**) with three cyclopentane rings per molecule, which is the maximum in MPL

Archaeal Hemi-Macrocyclic BTLs Archaeal BTLs also exist in a hemi-macrocyclic form containing one biphytanyl chain with both ends linking to a different glycerol moiety (thus, having no mid-plane space) and two phytanyl chains, each of which is ether-linked to a glycerol backbone [6]. Figure 2.2a shows the structure of such a glycerol trialkyl glycerol tetraether (GTGT) isolated from *Sulfolobus solfataricus*. However, hemi-macrocyclic BTLs are present only in a small amount (~3.2 wt% in the case of *S. solfataricus* [6]) compared to the total lipid extract from the archaea.

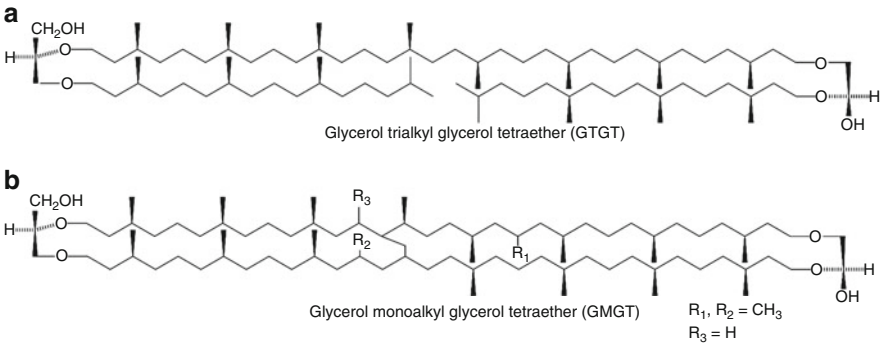

Fig. 2.2 Illustrations of the hydrophobic core structures of (**a**) the hemi-macrocyclic bipolar tetraether lipids (or called glycerol trialkyl glycerol tetraether, GTGT) and (**b**) the H-shaped and dimethylated isoprenoid macrocyclic bipolar tetraether lipids (glycerol monoalkyl glycerol tetraether, GMGT) found in archaea [3]

2.1.2 Synthetic Bipolar Tetraether Lipid Analogues

Highly purified archaeal BTLs are hard to obtain in large quantities. To circumvent this problem, chemical synthesis has been employed to generate BTLs with structure features similar to archaeal BTLs. Total synthesis of macrocyclic archaeal BTL analogues involves many steps [17, 18]. Very few synthetic macrocyclic BTLs include both rings and sugar moieties. Compared to the synthesis of macrocyclic BTLs, hemi-macrocyclic structures are easier to make and thus more popular in the field of synthetic archaeal lipid analogues [19], despite that hemi-macrocyclic BTLs occur in a relatively small amount in archaea. Examples of different chemically synthesized hemi-macrocyclic BTLs can be seen in Fig. 2.3. By adding particular polar head groups to the macrocyclic or hemi-macrocyclic tetraether core, one can synthesize BTL analogues for specific applications such as target delivery of drugs and genes [22].

2.2 BTL Membranes

Both archaeal and synthetic BTLs can form vesicular and supported planar membranes (e.g., [8, 10, 23, 24]). Archaeal BTLs have also been used to make free-standing planar membranes (black lipid membranes) on micro pores in solid support [25–27]. Because of the presence of the unusual structural features such as macrocyclic structures, cyclopentane rings, isoprenoid units, tetraether linkages, and a variety of polar head groups, BTL membranes possess physical properties (e.g., stability, permeation, dynamics, phase behavior, and lateral organization) distinctly different from those found in diester lipid membranes.

BTLs can adopt a U-shaped configuration or an upright configuration in the membrane (reviewed in [14]). In most cases, BTLs in membranes span the entire

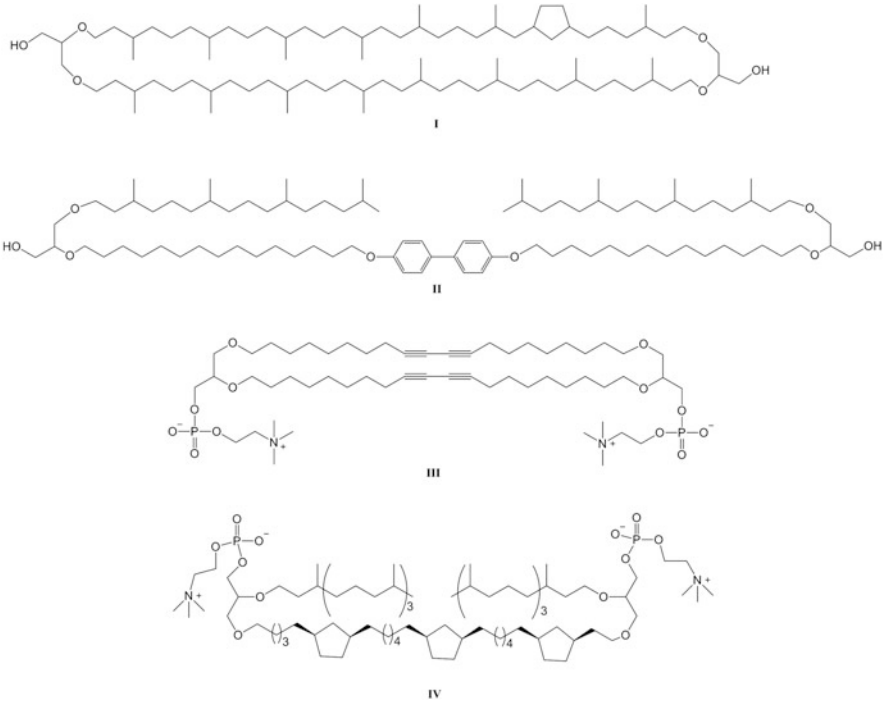

Fig. 2.3 Examples of synthetic macrocyclic (I [20]) and hemi-macrocyclic (II [20]; III [21]; and IV [19]) BTLs

lamellar structure, forming a monomolecular thick membrane [28], which contrasts to the bilayer structure formed by diester (or diether) lipids. The lamellar repeat distance (*d*-spacing) of PLFE liposomes has been measured over a wide range of temperatures using small angle X-ray scattering (SAXS) [29]. The *d*-spacing values (e.g., 4.9–5.0 nm at 5–50 °C, [29]; *d*-spacing = membrane thickness + thickness of water layer) indicate that PLFE lipid molecules span the entire membrane and have an upright configuration. Black lipid membrane studies determined the specific membrane capacitance of main phospholipid fraction (MPL), one BTL component from the archaeon *Th. acidophilum*, to be 0.744 mF/cm^2. This number was converted to a membrane thickness of 2.5–3.0 nm, which suggests that MPL membranes are monolayers and that the tetraether lipids in MPL membranes are also oriented vertically spanning the entire membrane [26].

2.3 Stability of BTL Membranes

Irrespective of the membrane types and lipid sources, BTL liposomal membranes exhibit remarkable chemical, physical, and mechanical stability (reviewed in [14]). For example, in the pH range 4–10, PLFE-based liposomes are able to retain vesicle size and morphology through at least six autoclaving cycles, whereas liposomes made

of diester lipids cannot maintain their integrity with just one autoclaving cycle [30]. Light scattering data showed that PLFE liposomes do not aggregate or fuse spontaneously for at least 6 months [31]. In the presence of fusogenic compounds such as Ca^{2+}, BTL vesicle aggregation may occur but with little membrane fusion [31–33]. Zeta potential of PLFE liposomes is <-30 mV [34], indicating that those BTL liposomes do not coalesce. PLFE liposomes are stable at shear stress rates 0–7600 s^{-1} [35]. BTL liposomes are also highly resistant to surfactants [36] and bile salts [37]. Furthermore, addition of BTLs to liposomal drugs increases their stability, even in the gastrointestinal tract [38, 39]. Molecular dynamics (MD) studies suggested that, compared to their diester and hemi-macrocyclic counterparts, macrocyclic BTL membranes have highest stability against external mechanical forces [40].

Like BTL liposomes, BTL free-standing planar membranes (also called black lipid membranes or suspended planar membranes) over micro pores in solid support are also extraordinarily stable compared to their diester counterparts. Membrane electrical resistance in traditional black lipid membranes made of diester lipids drops abruptly in 2–4 h. In contrast, the dielectric properties of PLFE free-standing planar membranes remain almost unchanged over a period of at least 50 h at 13–40 °C [41]. This remarkable stability of PLFE membranes, which is on the order of days and achieved without having lipid polymerization nor using nanopores, makes BTLs particularly appealing for developing durable and efficient planar membrane-based biotechnologies [41].

The great stability of BTL lipid membranes can be attributed to the strong electrostatic, van der Waals, and hydrogen bonding interactions among BTL molecules due to the presence of sugar/phosphate moieties in the polar head groups and the macrocyclic and dibiphytanyl structures in the hydrophobic core [42, 43]. Although PLFE liposomes are extraordinarily stable, they become completely disintegrated in the presence of two archaeal proteins: ESCRT-III and CdvA [44, 45]. The underlying mechanism is not known.

2.4 Phase Behaviors of BTL Membranes

PLFE liposomes are one of a handful of archaeal BTL membrane systems that have been studied extensively for their phase behaviors. PLFE liposomes have been characterized by SAXS, infrared and fluorescence spectroscopy, and differential scanning calorimetry (DSC). PLFE liposomes exhibit two thermally-induced lamellar-to-lamellar phase transitions at ~47–50 °C and ~60 °C [2, 23, 29, 46] and a lamellar-to-cubic phase transition at ~74–78 °C [29, 46], all of which involve low enthalpy and volume changes as revealed by DSC and pressure perturbation calorimetry (PPC) [46]. Another archaeal BTL membrane that has been rigorously studied for phase behaviors is the P2 fraction of the polar lipid extract of *Sulfolobus solfataricus* [47, 48].

The number of cyclopentane rings in the biphytanyl chains is a major factor governing the phase behaviors of BTL membranes. An increase in the number of cyclopentane rings resulted in a higher thermal phase transition temperature in

membranes made of GDGT derived from *S. solfataricus* [49, 50]. A study of BTL liposomes derived from *S. acidocaldarius* showed that an increase of cell growth temperature from 68 to 81 °C, which could lead to an increase of the number of cyclopentane rings per tetraether molecule from 3.4 to 4.8 [51], increased the phase transition temperature of PLFE liposomes from 39.1 to 56.5 °C [52].

The stereochemistry of the cyclopentane ring also plays an important role in phase behaviors. The cyclopentane ring in native archaeal BTLs is in a *trans*-1,3-dialkyl configuration. A SAXS study on a synthetic hemi-macrocyclic BTL with one central cyclopentane ring in the membrane spanning chain reveals that a *cis*-1,3-dialkyl cyclopentane ring led to the $L_c-L_\alpha-Q_{II}$ phase transitions whereas the *trans* isomer retained an L_α phase from 20 to 100 °C [53]. (Note: L_c: lamellar crystalline phase; L_α: lamellar liquid-crystalline phase; Q_{II}: a diamond-type bi-continuous cubic phase with the symmetry Pn3m).

How the branched methyl groups contribute to the phase behaviors of BTL membranes remains elusive. A recent MD simulation study showed that the branched methyl groups increase the BTL inter-chain distance from ~0.6 to ~0.85 nm and reduces the hydrocarbon chain tilt angle from ~35° to ~10° [54]. Without the branched methyl groups, BTLs form a gel-like rigid phase (Fig. 2.4, top) [54]. This simulation study suggested that the branched methyl groups play an important role in keeping BTL membranes densely packed and stable, and, at the same time, maintaining the membrane in a "liquid-crystalline" state with fast-fluctuating hydrocarbon chains (Fig. 2.4, bottom) [54]. However, the polar head groups used in this simulation were exclusively phosphatidylcholine, which has very limited hydrogen bonding capabilities. As mentioned earlier, hydrogen bonding among sugar and phosphate moieties in the polar head group regions is one of the major stabilizing forces of native archaeal BTL membranes. In light of this, it is of interest to extend the MD study to interrogate if the branched methyl groups still lead to fast fluctuations in hydrocarbon chains when the sugar moieties are present. In addition, calorimetric and spectroscopic experiments on membranes made by synthetic BTLs with systematic changes in hydrocarbon chain branching are in demand in order to advance our understanding of the role of branched methyl groups in BTL phase behaviors and membrane packing.

2.5 Membrane Lateral Diffusion

Lateral diffusion constant D in BTL liposomes made of total polar lipids from *Thermoplasma acidophilum* was determined by ^{31}P–NMR to be 2×10^{-8} cm^2/s near the cell growth temperature 55 °C. The D value dropped to 6–8 $\times 10^{-9}$ cm^2/s when the temperature was lowered to 30 °C [55]. MD calculations revealed nearly one order of magnitude difference in D between a macrocyclic BTL membrane (0.53×10^{-8} cm^2/s) and the membrane made of diphytanyl phosphatidylcholine (DPhPC) (4.82×10^{-8} cm^2/s) [40].

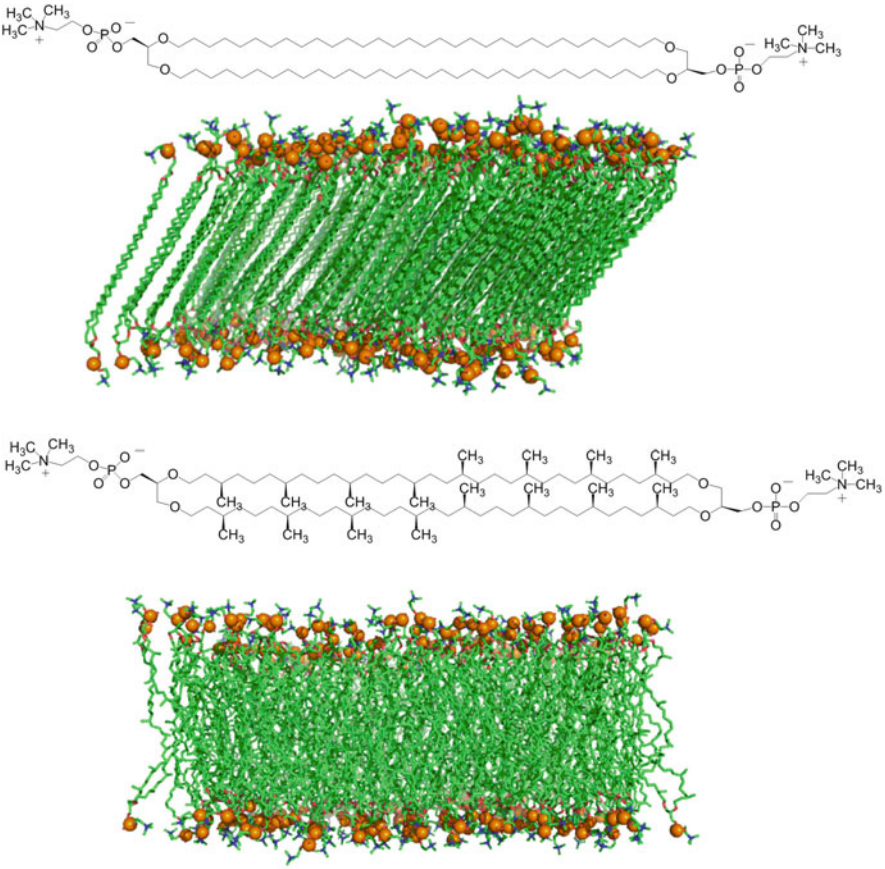

Fig. 2.4 Effects of branched methyl groups on membrane packing as revealed by MD simulations [54]. (*top*) Model membranes of the synthetic BTL with no branched methyl groups (chemical structure shown *above*). This membrane is packed like a gel state, with the hydrocarbon chains remained straight. (*bottom*) Model membranes of the synthetic BTL with branched methyl groups (chemical structure shown *above*). In this case, the membrane is more fluid, resembling liquid-crystalline state (modified from [54] and used with permission)

Using pyrene fluorescence excimer formation to reflect membrane lateral mobility, it was found that BTL membrane lateral mobility was more limited, especially at low temperatures [56], compared to diester liposomes. Larudan fluorescence intensity images showed that the lipid domains were virtually immobile in the membrane surface when the temperature of giant unilamellar vesicles of PLFE membranes was <26 °C [23]. The overall low lateral mobility in BTL membranes can be understood in terms of the low membrane free volume in PLFE liposomes [52, 57]. It has been suggested that membrane free volume is required for membrane lateral diffusion [58].

To date, the studies of lateral diffusion in BTL membranes are still in the primitive stage. More advanced techniques should be employed in order to gain a better mechanistic understanding.

2.6 Probe Rotations and Insertion in BTL Membranes

Fluorescent probe studies on BTL membranes yielded a few surprising results, which are the consequence of the unique structures of BTLs.

Laurdan It is well known that 6-lauroyl-2-(dimethylamino)naphthalene (Laurdan) can insert into conventional diester liposomes with its chromophore located near the polar head group regions and with its chromophore's dipole moment aligned in parallel with the membrane normal [59]. In addition, when the membrane packing is tight, the generalized polarization ($GP = (I_{blue} - I_{red})/(I_{blue} + I_{red})$) value of Laurdan fluorescence is high, and vice versa [59]. However, in a fluorescence microscopy study, it was found that the GP values of Laurdan fluorescence in PLFE giant unilamellar vesicles (GUVs) were surprisingly low (near zero) at all of the temperatures and pHs examined, despite that the overall membrane packing is tight [23]. The second surprise is that, when excited with light polarized in the *y* direction, Laurdan fluorescence in the center cross section of the PLFE GUVs exhibited a photoselection effect showing much higher intensities in the *x* direction of the vesicles, a result opposite to that observed on diester liposomes (e.g., DPPC). This result indicates that the dipole moment of Laurdan's chromophore in PLFE GUVs is aligned parallel to the membrane surface, in sharp contrast to the results obtained using diester liposomes. This photoselection effect and the low GP values together suggest that the Laurdan's chromophore resides in the polar head group region of the PLFE liposomes but its long axis is aligned in parallel with the membrane surface, while the lauroyl tail inserts into the hydrocarbon core of the membrane. This unusual L-shape disposition is presumably caused by the rigid/tight packing in PLFE liposomes and by the steric hindrance of the branched methyl group.

It was found in a separate study that the values of red edge excitation shift (REES) [60, 61] for Laurdan in PLFE liposomes are much greater than those in diester liposomes [62]. For example, the REES value for PLFE liposomes is 22.8 nm at pH 3 and 37 °C whereas that for dilauroylphosphatidylcholine (DLPC) is 8.3 nm and for distearoylphosphatidylglycerol (DSPG) is 4.7 nm under the same experimental conditions [62]. These data indicate that Laurdan's chromophore is localized in an environment of highly restricted mobility and that the membrane regions near Laurdan's chromophore have extraordinary restriction to the reorientational motion of water or lipid polar residues around Laurdan's excited state. This interpretation is consistent with the assertion that there is a strong hydrogen bond network in the polar head group regions of PLFE lipid membranes [14, 63].

Perylene Perylene is a flat and disk-like fluorescent probe. This probe appears to be able to penetrate into BTL membranes with its molecular axis in parallel to the membrane normal [64]. The average (R) and in-plane (R_{ip}) rotational rate of perylene in PLFE liposomes underwent an abrupt increase when the temperature was raised to ~48 °C [64], which is near one of the phase transition temperatures of PLFE (discussed earlier). A plausible explanation is that the cyclopentane rings and the branched methyl groups of PLFE provide a steric hindrance for the in-plane rotation of perylene at low temperatures. For some reason, this hindrance is reduced at temperatures >48 °C. It was also observed that, at 20–35 °C, the R_{ip} values of perylene in PLFE liposomes are 0.06–0.12 ns^{-1} [64], which are significantly lower than the R_{ip} values of perylene 0.41 ns^{-1} found in 50 mol% cholesterol/POPC liposomes [65] at 10 °C. These results suggested that PLFE liposomes are rigid and tightly packed at low temperatures [64].

DPH Diphenyl-1,3,5-hexatriene (DPH) is a commonly used membrane probe, with its long molecular axis preferentially aligned in parallel with the membrane normal of diester liposomes [66]. In addition, the fluorescence lifetime of DPH is known to increase when the probe is exposed to more hydrophobic environment and decrease when the water content near the probe increases [66].

DPH fluorescence in PLFE liposomes generates interesting yet surprising results. For example, as illustrated in Table 2.1, the average fluorescence lifetime of DPH in PLFE remains low (~7.5–7.7 ns) over a wide range of temperatures (20–50 °C) [67]. The lack of an abrupt change in DPH fluorescence lifetime with temperature is consistent with the phase behavior of PLFE liposomes mentioned earlier. More interestingly, this lifetime value (~7.5–7.7 ns) is even lower than the DPH fluorescence lifetime in DPPC liquid-crystalline (fluid) state (e.g., at 46.1 °C, Table 2.1 and [67]). According to the conventional interpretation of DPH fluorescence lifetime data, this would indicate that, at all the temperatures examined (20–50 °C), PLFE liposomes would be even more loosely packed than DPPC fluid state, which apparently is not true and would contradict the limiting anisotropy data (Table 2.1 and [67]). One plausible explanation of the low lifetime is that DPH in PLFE liposomes does not insert into the membrane as deep as that in diester liposomes, due to the steric hindrance provided by the branched methyl groups and the cyclopentane rings. Both Laurdan and DPH data indicate that probe location in BTL membranes could be very different from that in diester membranes and that the interpretation of the fluorescence data should take probe location into consideration.

DPH fluorescence correlation times in PLFE liposomes are higher than those in DPPC liposomes (Table 2.1 and [67]), which indicates that the average rotational rate of DPH is slower in PLFE than in DPPC liposomes, probably due to tight packing and steric hindrance in PLFE liposomes. In addition, the limiting anisotropy of DPH fluorescence remains high over a wide range of temperatures (Table 2.1 and [67]). This parameter clearly indicates that PLFE membranes provide a restricted environment for the rotation of DPH.

Table 2.1 Comparison of membrane physical parameters between tetraether (BTL) and diester or diether liposomes

Physical parameters	Tetraether liposomes	Conventional diester or diether liposomes	References
DPH fluorescence average lifetime	PLFE 7.57 ns (24.9 °C) 7.61 ns (35.4 °C) 7.67 ns (47.2 °C)	DPPC 9.91 ns (25.2 °C) 9.92 ns (35.0 °C) 8.17 ns (46.1 °C)	[67]
DPH apparent rotational correlation time	2.73 ns (24.9 °C) 2.72 ns (35.4 °C) 2.89 ns (47.2 °C)	2.26 ns (25.2 °C) 2.17 ns (35.0 °C) 1.43 ns (46.1 °C)	[67]
DPH fluorescence limiting anisotropy, r_∞	0.302 (24.9 °C) 0.279 (35.4 °C) 0.217 (47.2 °C)	0.340 (25.2 °C) 0.304 (35.0 °C) 0.072 (46.1 °C)	[67]
Perylene in-plane rotational rate, R_{ip}	PLFE 0.06–0.12 ns^{-1} (20–35 °C)	50 mol% Chol/POPC 0.41 ns^{-1} (10 °C)	[64, 65]
Laurdan GP	PLFE below or near zero (12–66 °C)	DPPC ~0.6 (<40 °C)	[23, 68]
Laurdan REES	PLFE 22.8 nm (pH 3; 37 °C)	DSPG 4.7 nm (pH 3; 37 °C) DLPC 8.3 nm (pH 3; 37 °C)	[62]
n-AS REES	PLFE 7 nm (pH 5; 67 °C)	DHPC 3 nm (pH 5; 67 °C)	[69]
n-AS apparent rotational correlation time	PLFE 4.0 ns (2-AS) 4.3 ns (12 AS)	DHPC 1.2 ns (2-AS) 0.6 ns (12 AS)	[69]
Zeta potential	PLFE −34.3 mV	Egg-PC −7.5 mV	[34]
Lamellar repeat distance (*d*-spacing)	PLFE 5 nm (50 °C)	DPPC 6.72 nm (50 °C)	[29, 70]
Lateral diffusion coefficient	Synthetic macrocyclic BTL membrane 0.53 x 10^{-8} cm^2/s	DPhPC 4.82 x 10^{-8} cm^2/s	[40]
Relative volume change (ΔV/V) of the phase transition	PLFE (T_{growth} = 68 °C) 0.18% ($T_{transition}$ = 39 °C)	DPPC 3.1% (main transition)	[52]
Enthalpy change of the phase transition	PLFE 3.5 kJ/mol (T_{trans} = 46.7 °C)	DPPC 35 kJ/mol (main transition)	[46]
Relative volume fluctuations	PLFE 2.2% (40 °C) 2.3% (60 °C)	DPPC 4.0% (40 °C) 4.7% (60 °C)	[57]

2.7 Gradient of Membrane Dynamics Along the Membrane Normal

The biphytanyl chains in archaeal BTLs contain branched methyl groups and cyclopentane rings. They are covalently linked to either glycerol or calditol backbone moieties located on the opposite side of the membrane. When such lipids form membranes, the lipid hydrocarbon chains do not have the same type of *gauche*-to-*trans* conformational transitions nor the mid-plane spacing that normally encountered in diester lipid membranes. How this structural difference affects membrane dynamics and heterogeneity along the membrane normal has been investigated by probe techniques.

Using a series of membrane depth-dependent fluorescent probes, namely, 2-, 6-, 9-, and 12-(9-anthroyloxy)stearic acid (2-AS, 6-AS, 9-AS, and 12-AS, respectively), Chakraborty et al. found that the dynamic anisotropy gradient along the membrane normal is greatly attenuated in PLFE liposomes, but clearly discernible in diether liposomes made of 1,2-dihexadecyl-*sn*-glycerol-3-phosphocholine (DHPC) [69]. For example, in PLFE liposomes, the rotational correlation time of n-AS increases only slightly with increasing the membrane depth of probe's chromophore location. In comparison, the rotational correlation time of n-AS in DHPC decreases dramatically with increasing the membrane depth of the probe's chromophore. The rotational correlation times are inversely proportional to the rotational rates. Thus, these data indicate that, in diether (DHPC) liposomes, when the chromophore of the probe is embedded more deeply into the center of the membrane bilayer, the chromophore rotates faster, whereas, in PLFE liposomes, when the probe's chromophore penetrates deeper into the membrane core, the probe's rotational rate becomes slightly lower [69]. All these differences can be understood in terms of the structural differences between BTL liposomes and conventional diester or diether liposomes. In the diester liposomal bilayers, the existence of mid-plane space and the great flexibility near the end of the acyl chain tail would allow for more probe rotations when the probe's chromophore reaches that area. Such a mid-plane advantage for probe rotation is not existent in PLFE liposomes.

As another example, the wobbling-in-cone angle of n-AS probes in PLFE liposomes decreases only slightly with the membrane depth of the chromophore in n-AS probes [69]. In sharp contrast, in DHPC liposomes, the cone angle of n-AS probes increases abruptly with increasing the probe depth due to the presence of the mid-plane space and the increased chain flexibility near the end of DHPC fatty acyl chains [69].

The n-AS fluorescence data obtained from PLFE liposomes are in good agreement with the electron spin resonance (ESR) data obtained from liposomes made of the P2 fraction of the total lipid extract from *S. solfataricus* [71]. The spectral anisotropy and isotropic hyperfine couplings from ESR measurements indicated that the chain flexibility and polarity gradients in P2 liposomes are more ordered and less flexible than in diester liposomes [71].

2.8 Solute Permeation in BTL Membranes

Linking Low Volume Fluctuations to Low BTL Solute Permeability Compared to liposomes made of diester lipids, archaeal BTL liposomes exhibit unusually low solute permeability [34, 72, 73], which can be attributed to tight and rigid membrane packing as revealed by probe spectroscopy mentioned above and by the values of relative volume fluctuations determined by the combination of calorimetry and molecular acoustics [52, 57]. Volume fluctuations are required in order to have solute permeation across lipid membranes [74]. The relative volume fluctuation values of PLFE liposomes are substantially less than those detected from diester lipid membranes (e.g., DPPC) [52, 57], due to the rigid and tightly packed membrane matrix.

Effect of Cyclopentane Rings on Solute Permeation The number of cyclopentane rings in BTLs has a significant effect on BTL membrane properties such as membrane packing, phase behavior, membrane permeation, and volume fluctuations. An earlier molecular modeling study showed that an increase in the number of cyclopentane rings from zero per GDNT molecule to eight rings per molecule increases membrane packing tightness [42]. The effect of the number of cyclopentane rings on solute permeability across archaeal BTL membranes has not been investigated directly because naturally occurring BTLs with purity of a single number of cyclopentane rings are hard to obtain. Nevertheless, membrane volume fluctuation measurements using PLFE obtained from cells grown at different temperatures have shed some light on this subject. Volume fluctuations of PLFE liposomes exhibited small but significant differences with the growth temperature of the cells [52]. Since the number of cyclopentane rings increases with cell growth temperature and the volume fluctuation is related to solute permeation, the volume fluctuation data suggested that membrane permeability in PLFE liposomes vary with the number of cyclopentane rings in a non-linear manner, reaching a minimum when using PLFE isolated from cells grown at optimal growth temperatures [52].

Using a series of synthetic hemi-macrocyclic BTLs containing varying numbers of cyclopentane rings in the tethered hydrocarbon chain (for example, see the structure of Compound IV in Fig. 2.3), Koyanagi et al. reported that the number of cyclopentane rings had no effect on the rate of proton permeation [19]. However, all the cyclopentane rings in the hemi-macrocyclic BTLs used in that study were placed exclusively in the singly tethered chain, not in both the tethered and un-tethered. This will lead to a biased conclusion because the regions with an un-tethered chain remain flexible and leaky. This raises the concern that the permeability result obtained from synthetic BTLs, many of which are singly tethered [75], may not be comparable with that obtained from naturally occurring archaeal BTLs, where the cyclopentane rings (and the branched methyl groups) are distributed into both biphytanyl chains.

2.9 Role of Sugar Moieties in BTL Membrane Physical Properties

Shimada et al. [7] reported that the archaeon *T. acidophilum* adapts to low pHs and high temperatures by extending sugar chains on their cell surface BTLs. The proton permeability of liposomes made of *T. acidophilum* BTLs that contained two or more sugar units was lower than that of liposomes made of *T. acidophilum* BTLs that contained one sugar unit [7]. Many studies on tetraether lipid membranes have used lipids with the polar head groups truncated to either glycerol or calditol (i.e., removing the phosphate and sugar moieties). In membranes made of truncated tetraether lipids, the end of the lipid molecules can move almost freely within and across the membrane [76]. The liposomes made of truncated GDNT failed to sustain autoclaving, while liposomes made of intact PLFE can tolerate at least six autoclaving cycles [30]. These studies clearly suggest that the hydrogen bond network among the phosphate and sugar moieties in the polar head group regions is critical for BTL membrane stability. DSC on the hydrolytic fractions GDGT and GDNT indicates the presence of a gel-to-liquid-crystalline transition that occurs at lower temperatures as the number of cyclopentane rings decreases [49]. A systematic study of the role of sugar moiety in BTL membrane dynamics and organization is in demand.

2.10 Lateral Organization in BTL Membranes

It is well known in modern membrane biophysics that membrane lateral organization is a key issue in governing membrane properties. Numerous studies have been devoted to study how lipids and proteins are laterally organized in eukaryotic or bacterial cell membranes or model membranes (see other chapters in this book volume). In comparison, little has been done to address this important membrane issue in archaea. Most, if not all, crenarchaeota contain a small amount of diether lipids, in addition to BTLs. The ratio of diethers to tetraethers in archaea varies with the temperature, pH and pressure of the growth environment. For example, increasing pressure and decreasing temperature led to an increase of the proportion of diethers in the piezo-hyperthermic archaeon *Thermococcus barophilus* [77]. Thus, it is important to ask the questions [77]: How are diethers and tetraethers distributed in the archaea plasma membranes? Are diethers domain-segregated from tetraethers? How does the lipid lateral organization change in response to environmental adaptation? It is conceivable that these subjects will be rigorously studied in the near future.

PLFE membranes have been extensively studied. However, PLFE is not a single lipid species; PLFE contains two components, GDGT (minor) and GDNT (major) (Fig. 2.1). In PLFE liposomes, how these two components are laterally organized in the plane of the membrane is little known. To our knowledge, the only information about membrane lateral organization in BTL liposomes came from PLFE GUV studies [23]. When the temperature was above 26 °C, the entire membrane surface of PLFE

GUVs was covered by Laurdan fluorescence. When the temperature was lowered to 26 °C or below, the Laurdan intensity images on PLFE GUVs revealed snowflake-like domains. In those domains, no Laurdan fluorescence was detected, which implies that the snowflake domains were extremely tightly packed so Laurdan molecules were excluded completely from those domains. In fact, those snowflake domains were virtually immobile in the membrane during the experiment time employed (many hours). When the temperature was raised to above 26 °C, the domains disappeared and the entire membrane was uniformly covered by Laurdan fluorescence again.

2.11 Concluding Remarks

To date, there are many pieces of evidence (as illustrated in Table 2.1) showing that the physical behaviors of archaeal or synthetic tetraether membranes are very different from those seen in diester or diether liposomes. These differences are important to know for two main reasons. First, BTL membranes are appealing biomaterials that hold great promise for technological applications [78–81]. Second, BTL membranes also serve as excellent model systems to promote our understanding of archaeal membrane biology. Therefore, more rigorous biophysical studies of BTL membranes using more advanced technologies and methodologies are needed.

In most, if not all, biophysical experimental works of archaeal BTL membranes, crude lipid extracts or partially purified lipid fractions were used. Crude extracts contain at least several polar lipid fractions. In each lipid fraction, there may exist both GDNT and GDGT components. In each component, there is a wide distribution of the number of cyclopentane rings. It will be useful if, in the future studies, archaeal BTL membranes are studied using highly purified intact (not hydrolyzed) BTLs with single cyclopentane ring resolutions in the hydrophobic core and single types of polar head groups, so that the physicochemical data can be interpreted in a more straightforward manner. Synthetic BTLs are useful for systematic studies of BTL membranes; however, synthesing the same stereochemistry as that found in archaeal BTLs is a big challenge. Hydrolyzed BTLs (with the removal of the sugar and phosphate moieties in the polar head group regions) have been separated by HPLC to single cyclopentane ring resolutions. Worth noting is that the behaviors of liposomal or planar membranes made of hydrolyzed BTLs are quite different from those made of unhydrolyzed BTLs, as discussed earlier.

The biophysical studies of BTL membranes could also be extended to membrane proteins. A number of proteins or peptides such as cytochrome-c oxidase, quinol oxidase, primary proton pumps, a leucine transport system, and isoprenylcysteine carboxyl methyltransferase that are known to be naturally membrane bound have been shown to remain active in BTL membranes [25, 26, 28, 82–87]. Detailed studies on the interactions of proteins/peptides and BTLs in well-defined BTL model membranes would be very beneficial.

Acknowledgment We thank the support from NSF and ARO.

References

1. Brochier-Armanet C, Boussau B, Gribaldo S, Forterre P. Mesophilic crenarchaeota: proposal for a third archaeal phylum, the thaumarchaeota. Nat Rev Microbiol. 2008;6:245–52.
2. Gliozzi A, Relini A, Chong PLG. Structure and permeability properties of biomimetic membranes of bolaform archaeal tetraether lipids. J Membr Sci. 2002;206:131–47.
3. Knappy C, Barilla D, Chong J, Hodgson D, Morgan H, Suleman M, Tan C, Yao P, Keely B. Mono-, di- and tri-methylated homologues of isoprenoid tetraether lipid cores in archaea and environmental samples: mass spectrometric identification and significance. J Mass Spectrom. 2015;50:1420–32.
4. Lai D, Springstead JR, Monbouquette HG. Effect of growth temperature on ether lipid biochemistry in *Archaeoglobus fulgidus*. Extremophiles. 2008;12:271–8.
5. De Rosa M, Gambacorta A, Nicolaus B. A new type of cell membrane in thermophilic archaebacteria based on bipolar ether lipids. J Membr Sci. 1983;16:287–94.
6. De Rosa M, Gambacorta A, Nicolaus B, Chappe B, Albrecht P. Isoprenoid ethers: backbone of complex lipids of the archaebacterium *Sulfolobus solfataricus*. Biochim Biophys Acta. 1983;753:249–56.
7. Shimada H, Nemoto N, Shida Y, Oshima T, Yamagishi A. Effects of pH and temperature on the composition of polar lipids in *Thermoplasma acidophilum* HO-62. J Bacteriol. 2008;190:5404–11.
8. Jeworrek C, Evers F, Erlkamp M, Grobelny S, Tolan M, Chong PLG, Winter R. Structure and phase behavior of archaeal lipid monolayers. Langmuir. 2011;27:13113–21.
9. Shimada H, Shida Y, Nemoto N, Oshima T, Yamagishi A. Complete polar lipid composition of *Thermoplasma acidophilum* HO-62 determined by high-performance liquid chromatography with evaporative light-scattering detection. J Bacteriol. 2002;184:556–63.
10. Lo SL, Chang EL. Purification and characterization of a liposomal-forming tetraether lipid fraction. Biochem Biophys Res Commun. 1990;167:238–43.
11. Kates M. Archaebacterial lipids: structure, biosynthesis and function. In: Danson MJ, Hough DW, Lunt GG, editors. The archaebacteria: biochemistry and biotechnology. London: Portland Press; 1992. p. 51–72.
12. Sugai A, Sakuma R, Fukuda I, Kurosawa N, Itoh YH, Kon K, Ando S, Itoh T. The structure of the core polyol of the ether lipids from *Sulfolobus acidocaldarius*. Lipids. 1995;30:339–44.
13. Koga Y, Morii H. Recent advances in structural research on ether lipids from archaea including comparative and physiological aspects. Biosci Biotechnol Biochem. 2005;69:2019–34.
14. Chong PLG. Archaebacterial bipolar tetraether lipids: physico-chemical and membrane properties. Chem Phys Lipids. 2010;163:253–65.
15. Chong PLG, Ayesa U, Daswani VP, Hur EC. On physical properties of tetraether lipid membranes: effects of cyclopentane rings. Archaea. 2012;2012:138439.
16. Schouten S, Hopmans EC, Sinninghe-Damste JS. The organic geochemistry of glycerol dialkyl glycerol tetraether lipids: a review. Org Geochem. 2013;54:19–61.
17. Arakawa K, Eguchi T, Kakinuma K. An olefin metathesis approach to 36- and 72-membered archaeal macrocyclic membrane lipids. J Org Chem. 1998;63:4741–5.
18. Eguchi T, Ibaragi K, Kakinuma K. Total synthesis of archaeal 72-membered macrocyclic tetraether lipids. J Org Chem. 1998;63:2689–98.
19. Koyanagi T, Leriche G, Onofrei D, Holland GP, Mayer M, Yang J. Cyclohexane rings reduce membrane permeability to small ions in archaea-inspired tetraether lipids. Angew Chem Int Ed. 2016;55:1890–3.
20. Raguse B, Culshaw PN, Prashar JK, Raval K. The synthesis of archaebacterial lipid analogues. Tetrahedron Lett. 2000;41:2971–4.
21. Patwardhan AP, Thompson DH. Efficient synthesis of 40- and 48-membered tetraether macrocyclic bisphosphocholines. Org Lett. 1999;1:241–4.

22. Brard M, Laine C, Rethore G, Laurent I, Neveu C, Lemiegre L, Benvegnu T. Synthesis of archaeal bipolar lipid analogues: a way to versatile drug/gene delivery systems. J Org Chem. 2007;72:8267–79.
23. Bagatolli LA, Gratton E, Khan TK, Chong PLG. Two-photon fluorescence microscopy studies of bipolar tetraether giant liposomes from thermoacidophilic archaebacteria *Sulfolobus acidocaldarius*. Biophys J. 2000;79:416–25.
24. Schuster B, Weigert S, Pum D, Sara M, Sleytr UB. New method for generating tetraether lipid membranes on porous supports. Langmuir. 2003;19:2392–7.
25. Gliozzi A, Paoli G, Rolandi R, De Rosa M, Gambacorta A. Structure and transport properties of artificial bipolar lipid membranes. Bioelectrochem Bioenerg. 1982;9:591–601.
26. Stern J, Freisleben H, Janku S, Ring K. Black lipid membranes of tetraether lipids from *Thermoplasma acidophilum*. Biochim Biophys Acta. 1992;1128:227–36.
27. Ren X, Liu K, Zhang Q, Noh HM, Kumbur EC, Yuan WW, Zhou JG, Chong PLG. Design, fabrication and characterization of archaeal tetraether free-standing planar membranes in a PDMS- and PCB-based fluidic platform. ACS Appl Mater Interfaces. 2014;6:12618–28.
28. Elferink MG, de Wit JG, Demel R, Driessen AJ, Konings WN. Functional reconstitution of membrane proteins in monolayer liposomes from bipolar lipids of *Sulfolobus acidocaldarius*. J Biol Chem. 1992;267:1375–81.
29. Chong PLG, Zein M, Khan TK, Winter R. Structure and conformation of bipolar tetraether lipid membranes derived from thermoacidophilic archaeon *Sulfolobus acidocaldarius* as revealed by small-angle X-ray scattering and high pressure FT-IR spectroscopy. J Phys Chem. 2003;107:8694–700.
30. Brown DA, Venegas B, Cooke PH, English V, Chong PLG. Bipolar tetraether archaeosomes exhibit unusual stability against autoclaving as studied by dynamic light scattering and electron microscopy. Chem Phys Lipids. 2009;159:95–103.
31. Kanichay R, Boni LT, Cooke PH, Khan TK, Chong PLG. Calcium-induced aggregation of archaeal bipolar tetraether liposomes derived from thermoacidophilic archaeon *Sulfolobus acidocaldarius*. Archaea. 2003;1:175–83.
32. Relini A, Cassinadri D, Fan Q, Gulik A, Mirghani Z, De Rosa M, Gliozzi A. Effect of physical constraints on the mechanisms of membrane fusion: bolaform lipid vesicles as model systems. Biophys J. 1996;71:1789–95.
33. Relini A, Cassinadri D, Mirghani Z, Brandt O, Gambacorta A, Trincone A, De Rosa M, Gliozzi A. Calcium-induced interaction and fusion of archaeobacterial lipid vesicles: a fluorescence study. Biochim Biophys Acta. 1994;1194:17–24.
34. Komatsu H, Chong PLG. Low permeability of liposomal membranes composed of bipolar tetraether lipids from thermoacidophilic archaebacterium *Sulfolobus acidocaldarius*. Biochemistry. 1998;37:107–15.
35. Bonanno A, Andrews A, Ayesa U, Ramirez S, Chong PLG. PLFE as a liposomal stabilizing agent: a shear stress study. Biophys J. 2016;110:242a.
36. Fafaj A, Lam J, Taylor L, Chong PLG. Unusual stability of archaeal tetraether liposomes against surfactants. Biophys J. 2011;100:329a.
37. Jensen SM, Christensen CJ, Petersen JM, Treusch AH, Brandl M. Liposomes containing lipids from *Sulfolobus islandicus* withstand intestinal bile salts: an approach for oral drug delivery? Int J Pharm. 2015;493:63–9.
38. Mahmoud G, Jedelska J, Strehlow B, Bakowsky U. Bipolar tetraether lipids derived from thermoacidophilic archaeon *Sulfolobus acidocaldarius* for membrane stabilization of chlorin e6 based liposomes for photodynamic therapy. Eur J Pharm Biopharm. 2015;95:88–98.
39. Parmentier J, Thewes B, Gropp F, Fricker G. Oral peptide delivery by tetraether lipid liposomes. Int J Pharm. 2011;415:150–7.
40. Shinoda W, Shinoda K, Baba T, Mikami M. Molecular dynamics study of bipolar tetraether lipid membranes. Biophys J. 2005;89:3195–202.
41. Ren X, Kumbur EC, Zhou JG, Noh HM, Chong PLG. Stability of free-standing tetraether planar membranes in microchips. J Membr Sci. 2017;540:27–34.

42. Gabriel JL, Chong PLG. Molecular modeling of archaebacterial bipolar tetraether lipid membranes. Chem Phys Lipids. 2000;105:193–200.
43. Arakawa K, Eguchi T, Kakinuma K. 36-membered macrocyclic diether lipid is advantageous for archaea to thrive under the extreme thermal environments. Bull Chem Soc Jpn. 2001;74:347–56.
44. Dobro MJ, Samson RY, Yu Z, McCullough J, Ding HJ, Chong PLG, Bell SD, Jensen GJ. Electron cryotomography of ESCRT assemblies and dividing *Sulfolobus* cells suggests that spiraling filaments are involved in membrane scission. Mol Biol Cell. 2013;24:2319–27.
45. Samson RY, Obita T, Hodgson B, Shaw MK, Chong PLG, Williams RL, Bell SD. Molecular and structural basis of ESCRT-III recruitment to membranes during archaeal cell division. Mol Cell. 2011;41:186–96.
46. Chong PLG, Ravindra R, Khurana M, English V, Winter R. Pressure perturbation and differential scanning calorimetric studies of bipolar tetraether liposomes derived from the thermoacidophilic archaeon *Sulfolobus acidocaldarius*. Biophys J. 2005;89:1841–9.
47. Gulik A, Luzzati V, De Rosa M, Gambacorta A. Structure and polymorphism of bipolar isopranyl ether lipids from archaebacterial. J Mol Biol. 1985;182:131–49.
48. Gulik A, Luzzati V, De Rosa M, Gambacorta A. Tetraether lipid components from a thermoacidophilic archaebacterium. Chemical structure and physical polymorphism. J Mol Biol. 1988;201:429–35.
49. Gliozzi A, Paoli G, DeRosa M, Gambacorta A. Effect of isoprenoid cyclization on the transition temperature of lipids in thermophilic archaebacteria. Biochim Biophys Acta. 1983;735:234–42.
50. Uda I, Sugai A, Itoh YH, Itoh T. Variation in molecular species of polar lipids from *Thermoplasma acidophilum* depends on growth temperature. Lipids. 2001;36:103–5.
51. De Rosa M, Esposito E, Gambacorta A, Nicholaus B, Bu'lock JD. Effects of temperature on ether lipid composition of *Caldariella acidophila*. Phytochemistry. 1980;19:827–31.
52. Zhai Y, Chong PLG, Taylor LJ, Erlkamp M, Grobelny S, Czeslik C, Watkins E, Winter R. Physical properties of archaeal tetraether lipid membranes as revealed by differential scanning and pressure perturbation calorimetry, molecular acoustics, and neutron reflectometry: effects of pressure and cell growth temperature. Langmuir. 2012;28:5211–7.
53. Jacquemet A, Meriadec C, Lemiegre L, Artzner F, Benvegnu T. Stereochemical effect revealed in self-assemblies based on archaeal lipid analogues bearing a central five-membered carbocycle: a SAXS study. Langmuir. 2012;28:7591–7.
54. Chugunov AO, Volynsky PE, Krylov NA, Boldyrev IA, Efremov RG. Liquid but durable: molecular dynamics simulations explain the unique properties of archaeal-like membranes. Sci Rep. 2014;4:7462. https://doi.org/10.1038/srep07462.
55. Jarrell HC, Zukotynski KA, Sprott GD. Lateral diffusion of the total polar lipids from *Thermoplasma acidophilum* in multilamellar liposomes. Biochim Biophys Acta. 1998;1369:259–66.
56. Kao YL, Chang EL, Chong PLG. Unusual pressure dependence of the lateral motion of pyrene-labeled phosphatidylcholine in bipolar lipid vesicles. Biochem Biophys Res Commun. 1992;188:1241–6.
57. Chong PLG, Sulc M, Winter R. Compressibilities and volume fluctuations of archaeal tetraether liposomes. Biophys J. 2010;99:3319–26.
58. Almeida PF, Vaz WL, Thompson TE. Lateral diffusion and percolation in two-phase, two-component lipid bilayers. Topology of the solid-phase domains in-plane and across the lipid bilayer. Biochemistry. 1992;31:7198–210.
59. Bagatolli LA. LAURDAN fluorescence properties in membranes: a journey from the fluorometer to the microscope, in Fluorescent methods to study biological membranes, book editors: Y. Mely and G. Duportail; series editor: M. Hof, Springer series on fluorescence, 13th ed., New York, NY: Springer; 2013, p. 3–36.

60. Chattopadhyay A, Rawat SS, Kelkar DA, Ray S, Chakrabarti B. Organization and dynamics of tryptophan residues in erythroid spectrin: novel structural features of denatured spectrin revealed by the wavelength selective fluorescence approach. Protein Sci. 2003;12:2389–403.
61. Demchenko AP. Site-selective red-edge effects. Methods Enzymol. 2008;450:59–78.
62. Laney A. Spectroscopic characterization of bipolar tetraether lipids derived from thermoacidophilic archaeal membranes. PhD Thesis, Temple University-Philadelphia, PA; 2002.
63. Vilalta I, Gliozzi A, Prats M. Interfacial air/water proton conduction from long distances by *sulfolobus solfataricus* archaeal bolaform lipids. Eur J Biochem. 1996;240:181–5.
64. Khan TK, Chong PLG. Studies of archaebacterial bipolar tetraether liposomes by perylene fluorescence. Biophys J. 2000;78:1390–9.
65. Chong PLG, Van der Meer BW, Thompson TE. The effects of pressure and cholesterol on rotational motions of perylene in lipid bilayers. Biochim Biophys Acta. 1985;813:253–65.
66. Bernsdorff C, Wolf A, Winter R, Gratton E. Effect of hydrostatic pressure on water penetration and rotational dynamics in phospholipid-cholesterol bilayers. Biophys J. 1997;72:1264–77.
67. Ayesa U. Characterization of thermosensitive hybrid archaeosomes, and DPA-Cy3[22,22]/POPC liposomes and *in vitro* evaluation of their potential usefulness in targeted delivery and controlled release. PhD Thesis-Temple University School of Medicine, Philadelphia, PA; 2016.
68. Parasassi T, De Stasio G, Ravagnan G, Rusch RM, Gratton E. Quantitation of lipid phases in phospholipid vesicles by the generalized polarization of Laurdan fluorescence. Biophys J. 1991;60:179–89.
69. Chakraborty H, Haldar S, Chong PLG, Kombrabail M, Krishnamoorthy G, Chattopadhyay A. Depth-dependent organization and dynamics of archaeal and eukaryotic membranes: development of membrane anisotropy gradient with natural evolution. Langmuir. 2015;31:11591–7.
70. Nagle JF, Zhang R, Tristram-Nagle S, Sun WS, Petrache HI, Suter RM. X-ray structure determination of fully hydrated L_a phase dipalmitoylphosphatidylcholine bilayers. Biophys J. 1996;70:1419–31.
71. Bartucci R, Gambacorta A, Gliozzi A, Marsh D, Sportelli L. Bipolar tetraether lipids: chain flexibility and membrane polarity gradients from spin-label electron spin resonance. Biochemistry. 2005;44:15017–23.
72. Chang EL. Unusual thermal stability of liposomes made from bipolar tetraether lipids. Biochem Biophys Res Commun. 1994;202:673–9.
73. Mathai JC, Sprott GD, Zeidel ML. Molecular mechanisms of water and solute transport across archaebacterial lipid membranes. J Biol Chem. 2001;276:27266–71.
74. Falck E, Patra M, Karttunen M, Hyvonen MT, Vattulainen I. Impact of cholesterol on voids in phospholipid membranes. J Chem Phys. 2004;121:12676–89.
75. Schroeder TBH, Leriche G, Koyanagi T, Johnson MA, Haengel KN, Eggenberger OM, Wang CL, Kim YH, Diraviyam K, Sept D, Yang J, Mayer M. Effects of lipid tethering in extremophile-inspired membranes on H^+/OH^- flux at room temperature. Biophys J. 2016;110:2430–40.
76. Luzatti V, Gulik A. Structure and polymorphism of tetraether lipids from *Sulfolobus solfataricus*: II. Conjectures regarding biological significance. Syst Appl Microbiol. 1986;7:262–5.
77. Cario A, Grossi V, Schaeffer P, Oger PM. Membrane homeoviscous adaptation in the piezohyperthermophilic archaeon *Thermococcus barophilus*. Front Microbiol. 2015;6:1152. https://doi.org/10.3389/fmicb.2015.01152.
78. Patel GB, Sprott GD. Archaeobacterial ether lipid liposomes (archaeosomes) as novel vaccine and drug delivery systems. Crit Rev Biotechnol. 1999;19:317–57.
79. Whitfield DM, Eichler EE, Sprott GD. Synthesis of archaeal glycolipid adjuvants-what is the optimum number of sugars? Carbohydr Res. 2008;343:2349–60.
80. Benvegnu T, Rethore G, Brard M, Richter W, Plusquellec D. Archaeosomes based on novel synthetic tetraether-type lipids for the development of oral delivery systems. Chem Commun (Camb). 2005;44:5536–8.

81. Patel GB, Agnew BJ, Deschatelets L, Fleming LP, Sprott GD. *In vitro* assessment of archaeosome stability for developing oral delivery systems. Int J Pharm. 2000;194:39–49.
82. Febo-Ayala W, Morera-Felix SL, Hrycyna CA, Thompson DH. Functional reconstitution of the integral membrane enzyme, isoprenylcysteine carboxyl methyltransferase, in synthetic bolalipid membrane vesicles. Biochemistry. 2006;45:14683–94.
83. Elferink MGL, Bosma T, Lolkema JS, Gleiszner M, Driessen AJM, Konings WN. Thermostability of respiratory terminal oxidases in the lipid environment. Biochim Biophys Acta. 1995;1230:31–7.
84. Elferink MGL, De Wit JG, Driessen AJ, Konings WN. Energy-transducing properties of primary proton pumps reconstituted into archaeal bipolar lipid vesicles. Eur J Biochem. 1993;214:917–25.
85. Freisleben HJ, Zwicker K, Jezek P, John G, Bettin-Bogutzki A, Ring K, Nawroth T. Reconstitution of bacteriorhodopsin and ATP synthase from *Micrococcus luteus* into liposomes of the purified main tetraether lipid from *Thermoplasma acidophilum*: proton conductance and light-driven ATP synthesis. Chem Phys Lipids. 1995;78:137–47.
86. In't Veld G, Elferink MGL, Driessen AJ, Konings WN. Reconstitution of the leucine transport system of *Lactococcus lactis* into liposomes composed of membrane-spanning lipids from *Sulfolobus acidocaldarius*. Biochemistry. 1992;31:12493–9.
87. Jacquemet A, Barbeau J, Lemiègre L, Benvegnu T. Archaeal tetraether bipolar lipids: structures, functions and applications. Biochimie. 2009;91:711–7.

Chapter 3
Effects of Oxidative Stress, Hyperglycemia, and Hypercholesterolemia on Membrane Structural Organization and the Interactions of Omega-3 Fatty Acids

R. Preston Mason and Robert F. Jacob

Abstract Cellular membranes are dynamic structures that play a critical role in facilitating and maintaining cell function. Membrane structure and fluidity are dependent on relative lipid (including cholesterol) and protein levels, which are known to change with aging and in different disease processes. The plasma membrane is organized into microdomains that have distinct biophysical and biochemical characteristics that mediate specific cellular activities. Lipid rafts, for example, sequester a variety of important intracellular signaling proteins and directly regulate their activity. In response to changes in membrane structure, some proteins can migrate between lipid-disordered, cholesterol-poor membrane regions and lipid-ordered, cholesterol-rich domains to differentially affect intracellular signaling. Cholesterol crystalline domains have been observed to form in vascular cells and in various membrane model systems when exposed to disease-like perturbations, including oxidative stress, hyperglycemia, and hypercholesterolemia. Membrane cholesterol enrichment and domain formation is believed to precipitate extracellular changes, such as crystal deposition in the atheroma with subsequent plaque destabilization and thrombus formation. Marine-derived long chain polyunsaturated omega-3 fatty acids have been shown to affect membrane lipid structure and fluidity. Both eicosapentaenoic acid (EPA) and docosahexaenoic acid (DHA) have potent antioxidant effects in model membranes and human lipoproteins, but the sustainability of these effects appear to vary under certain conditions, and EPA and DHA seem to differentially affect membrane fluidity, cholesterol domain formation, and membrane function. In this chapter, we will discuss how disease-like conditions induce structural changes to the cell membrane

R.P. Mason (✉)
Cardiovascular Division, Department of Medicine, Brigham and Women's Hospital, Harvard Medical School, Boston, MA 02115, USA

Elucida Research LLC, Beverly, MA 01915, USA
e-mail: rpmason@elucidaresearch.com

R.F. Jacob
Elucida Research LLC, Beverly, MA 01915, USA

A. Chattopadhyay (ed.), *Membrane Organization and Dynamics*, Springer Series in Biophysics 20, DOI 10.1007/978-3-319-66601-3_3

that negatively affect cellular function and potentiate the atherogenic process, as well as how lipid components within the membrane may alter these effects.

3.1 Cholesterol Is an Important Component of Cellular Membranes

When placed into an aqueous environment, phospholipids spontaneously form spherical micelles or bimolecular lipid sheets (bilayers) by orienting their polar head groups outward, into the water space, and their hydrophobic fatty acid chain segments inward, forming the hydrocarbon core region. The lipid bilayer is fundamental to the basic design of the cellular membrane, which provides both a structural and functional barrier between the cell and its external environment as well as between intracellular compartments or organelles. Early models of the cell membrane suggested that it was highly fluid with component lipids distributed in random fashion. However, we now understand that the plasma membrane is inherently asymmetrical, where phospholipids rarely "flip-flop" from one side of the membrane to the other and lipids aggregate in more- or less-fluid domains within the same side of the membrane. Membrane lipid fluidity is largely dependent on temperature as well as relative lipid and protein composition. For example, decreasing temperature or increasing the saturated fatty acid content of the bilayer leads to reductions in membrane fluidity. Similarly, the addition of free (i.e. unesterified) cholesterol significantly orders the lipid bilayer and decreases membrane fluidity.

The unique physicochemical properties of each membrane constituent are thought to provide the basis for their separation into distinct membrane domains, which play important roles in cellular activity. Membrane domains have been increasingly studied through their roles in ligand-receptor interactions, such as the lymphocyte T-cell receptor (TCR) with the major histocompatibility complex (MHC) or cholera toxin with the ganglioside GM_1 receptor [1]. In these models, efficient signal transduction was dependent on the formation of membrane domains, commonly referred to as "lipid rafts," that are significantly more ordered than the surrounding membrane and contain higher concentrations of cholesterol, glycosphingolipids, and signaling proteins [2]. These cholesterol-rich domains act as molecular scaffolds for the assembly and regulation of membrane-associated signaling proteins, and cholesterol is required for efficient receptor activation and downstream signaling. Lipid rafts are thought to "float" as a structural unit within the lipid bilayer and can combine to form larger domains in response to increases in cholesterol, lipid modification, or expression of lipid raft-associated protein.

Cholesterol-rich domains are important for a variety of cellular processes. For example, T-cell activation and leukocyte adhesion are regulated by cholesterol domains [1, 3]. Caveolae are a type of lipid raft that contain caveolin and a variety of proteins that are important mediators of endothelial function and signal

transduction [4, 5]. T-cell activation, leukocyte adhesion, and signal transduction through caveolae are all dependent on the presence of membrane cholesterol. This suggests that membrane cholesterol content is critical in maintaining normal cellular function and any modification to normal membrane cholesterol homeostasis may have significant effects on cellular function and signal transduction.

3.2 Effects of Oxidation, Hyperglycemia, and Hypercholesterolemia on Cellular Membranes

While cholesterol-rich domains are vital to normal cell function, cellular function is altered through changes to membrane signaling systems that rely on normal membrane organization. Oxidative stress, in particular, modifies membrane lipids which has a negative effect on membrane function. Atherosclerosis is characterized by excessive accumulation of cholesterol and oxidative damage in endothelial cells, smooth muscle cells, and eventually macrophages in the arterial cell wall. Oxidative damage and excessive cholesterol accumulation induce the formation of distinct immiscible cholesterol crystalline domains in cellular membranes [6, 7]. Over time, these cholesterol domains can precipitate the formation of insoluble, extracellular cholesterol crystals, a hallmark feature of the atherosclerotic plaque [8]. Cholesterol crystals have been observed using scanning electron microscopy and have been shown to have sharp, jagged edges [9] that can eventually expand to puncture the fibrous caps of atherogenic plaque [10] and activate local inflammatory and thrombotic processes [11]. The association of cholesterol crystals with vulnerable plaque features can be seen with advanced imaging in patients who have had a myocardial infarction [12].

Under disease-like conditions, sources of oxidative damage to membrane lipids include autoxidation of sugars (glucose) and membrane components, as well as external factors, such as circulating oxidized low-density lipoprotein (oxLDL). Phospholipids, glycolipids, and cholesterol are all targets of oxidative damage. In aging and disease, oxidative stress at the membrane level is enhanced by free radical propagation and increasingly dysfunctional cellular free-radical scavenging mechanisms [13]. Glucose contributes to oxidative stress mechanisms and is itself responsible for the non-enzymatic modification of phospholipids and membrane proteins, resulting in the formation of advanced glycation end products, increased lipid peroxidation, and cell injury [14]. In patients with type II diabetes mellitus, oxidative stress to endothelial cell membranes is amplified under hyperglycemic conditions, leading to increased propagation of free radicals [14, 15].

Oxidative stress and the resultant lipid and protein modifications can lead to numerous downstream effects. For example, glucose-enhanced oxidative stress initiates inflammatory processes including the activation of various transcription factors, such as NF-kB, which results in the overproduction of NADPH, a

significant source of superoxide. Oxidative stress also impairs insulin endocytosis, potentially through impaired insulin receptor activation [15]. The insulin receptor is located primarily in caveolae and sterol binding agents inhibit caveolae-mediated insulin transport [15]. Oxidative stress also leads to a reduction of nitric oxide (NO) bioavailability, which disrupts the balance between this potent vasodilator and systemic vasoconstrictors such as angiotensin II and endothelin, resulting in increased vascular resistance. Endothelial nitric oxide synthase (eNOS) produces NO by converting L-arginine to L-citrulline, a process that involves multiple cofactors. One oxidative mechanism associated with the loss of NO secretion is the overproduction of superoxide (O_2^-) by uncoupled eNOS and other oxidases. In particular, NADPH oxidases represent major sources of O_2^- in animal models of hypertension and other models of cardiovascular risk [16].

One mechanism through which membrane peroxidation can induce cellular dysfunction is by inducing cholesterol crystalline domain formation. Cholesterol crystalline domain formation has been characterized in model lipid vesicles using small-angle X-ray diffraction approaches, which yield diffraction patterns with a characteristic repeat of 34 Å associated with membrane-restricted cholesterol domains and consistent with the tail-to-tail orientation of two cholesterol molecules, each with a long-axis length of 17 Å (Fig. 3.1) [4, 7]. In model membranes prepared at cholesterol levels that mimic non-atherosclerotic conditions (cholesterol-to-phospholipid ratio of 0.6:1, for example), treatment with glucose results in a decrease in overall membrane width and a dose-dependent increase in the formation of lipid hydroperoxide (LOOH), an intermediate product of oxidative

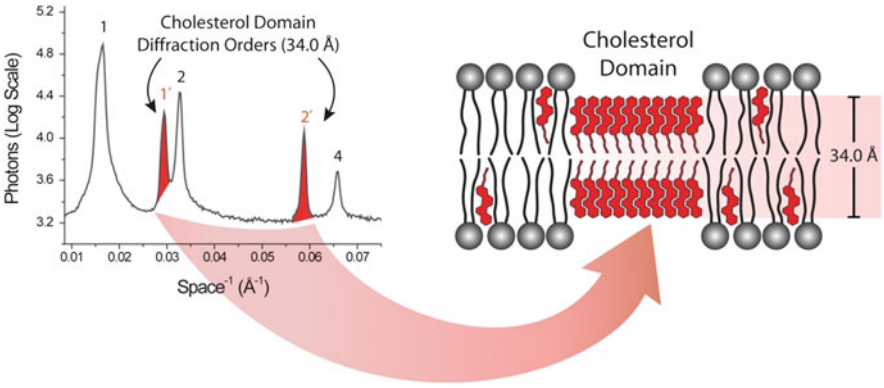

Fig. 3.1 Schematic illustration of a typical diffraction pattern collected from a biphasic membrane sample, exhibiting sterol-poor, phospholipid bilayer domains (peaks 1, 2, and 4) and cholesterol crystalline domains (peaks 1′ and 2′), and its relationship to the spatial arrangement of these domains in a representative membrane bilayer. This research was originally published in The Journal of Biological Chemistry. Mason RP, Walter MF, Day CA, Jacob RF. Active metabolite of atorvastatin inhibits membrane cholesterol domain formation by an antioxidant mechanism. J Biol Chem. 2006;281(14):9337–45. © The American Society for Biochemistry and Molecular Biology [6]

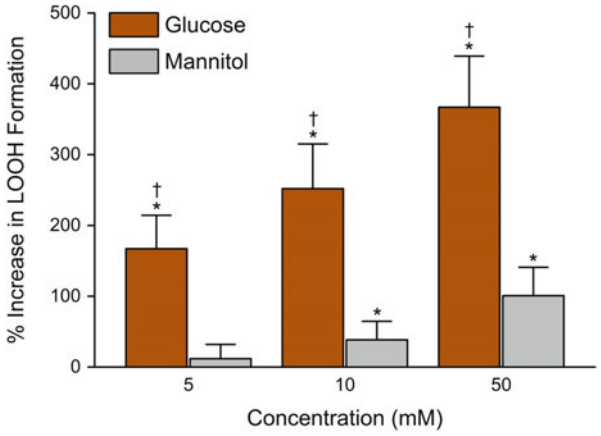

Fig. 3.2 Glucose promoted a dose-dependent increase in LOOH formation over mannitol in membranes enriched in dilinoleoylphosphatidylcholine (DLPC). Membranes underwent autoxidation while incubated for 48 h at 37 °C in a phosphate buffer solution containing glucose or mannitol (each at 5, 10, or 50 mM). Total levels of LOOH were measured iodometrically and expressed as percent increase normalized to vehicle-treated controls. Values are mean ± SD (N = 5). *$p < 0.01$ versus vehicle-treated control (Dunnett multiple comparisons test; overall ANOVA: $p < 0.0001$; F = 183.86); †$p < 0.0001$ versus cognate mannitol treatment (unpaired, two-tailed Student's t-test). Reprinted with permission from Elsevier B.V. [17]

damage (Fig. 3.2) [17]. In these membranes, the formation of LOOH was also associated with increased formation of cholesterol crystalline domains (Fig. 3.3), suggesting that lipid peroxidation induces the formation of these domains without otherwise altering membrane cholesterol levels. These results are consistent with experiments conducted under other conditions of oxidative stress, such as autoxidative conditions, where distinct cholesterol crystalline domains are formed even in membranes prepared at relatively low cholesterol levels (Fig. 3.4) [18]. Treatment with free radical-scavenging agents has been shown to inhibit both oxidative damage and structural changes to model membranes, confirming the role of lipid peroxidation in changes to membrane structure. For example, atorvastatin *o*-hydroxy metabolite (ATM), a potent antioxidant metabolite of atorvastatin, was able to inhibit lipid peroxidation in a dose-dependent manner [19, 20] as well as cholesterol domain formation in model membranes. This suggests that ATM inhibits peroxidation and cholesterol domain formation through a direct antioxidant mechanism [6].

Hypercholesterolemic conditions are associated with an increase in membrane cholesterol [7] and increased expression of caveolin, the main structural component of caveolae [21]. Because caveolin is a potent inhibitor of eNOS, an increase in cholesterol may contribute to endothelial dysfunction and atherogenesis. In model membranes, the addition of cholesterol enhances membrane LOOH formation and the formation of cholesterol crystalline domains (Fig. 3.4) [18]. As may be expected, treatment of cells with 3-hydroxy-3-methylglutaryl coenzyme A

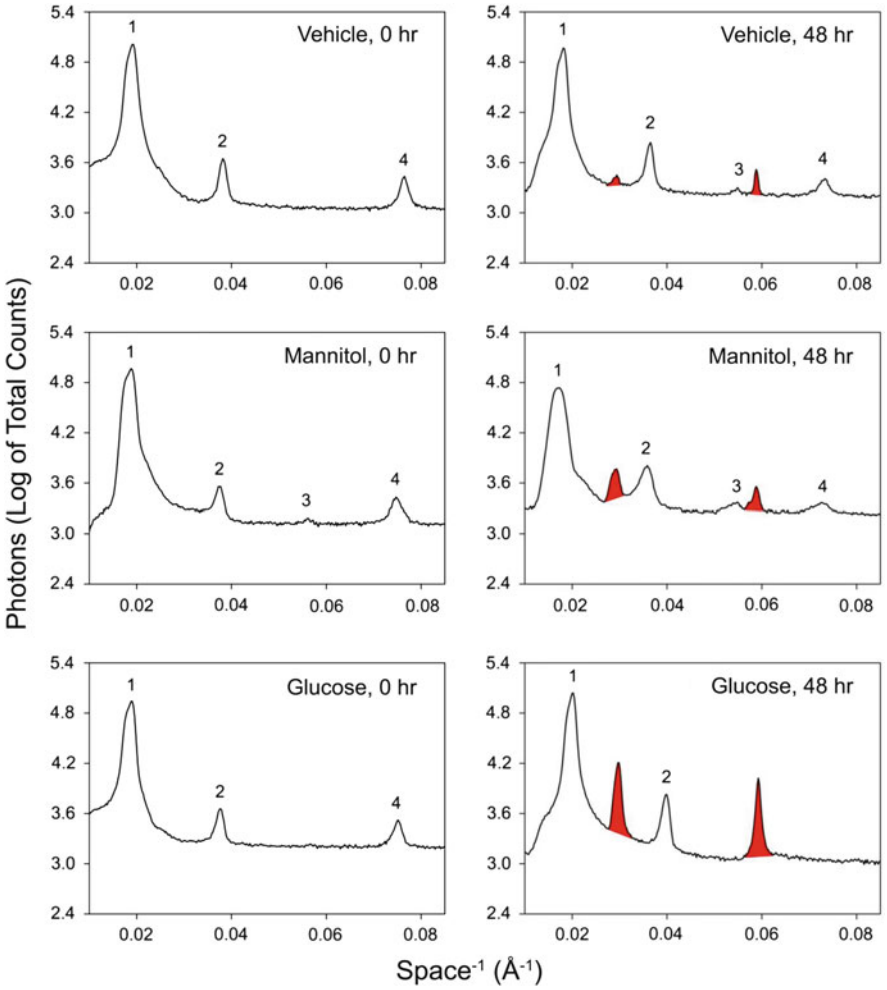

Fig. 3.3 Membrane lipid peroxidation and cholesterol domain formation increased with glucose treatment following exposure to oxidative conditions for 48 h. Small angle X-ray diffraction patterns were obtained from oriented DLPC membranes (prepared at 0.6:1 C/P) in the absence or presence of mannitol or glucose (each at 10.0 mM) before and after autoxidation for 48 h. At 0 h, all three treatments resulted in a single lipid bilayer phase with a *d*-space value of 53 Å. After 48 h exposure to lipid peroxidation, small cholesterol domain peaks (shown in *red fill*) were observed in control and mannitol-treated samples. In contrast, large cholesterol domain peaks and a decrease in bilayer *d*-space (49 Å) were observed for membrane samples treated with glucose and exposed to oxidation for 48 h. Reprinted with permission from Elsevier B.V. [17]

(HMG-CoA) reductase inhibitors (statins) reduces caveolin expression, thereby restoring active eNOS and the production of NO further supporting the cardioprotective role statins play in cardiovascular disease [22]. Taken together, these data suggest that lipid peroxidation and hypercholesterolemia negatively

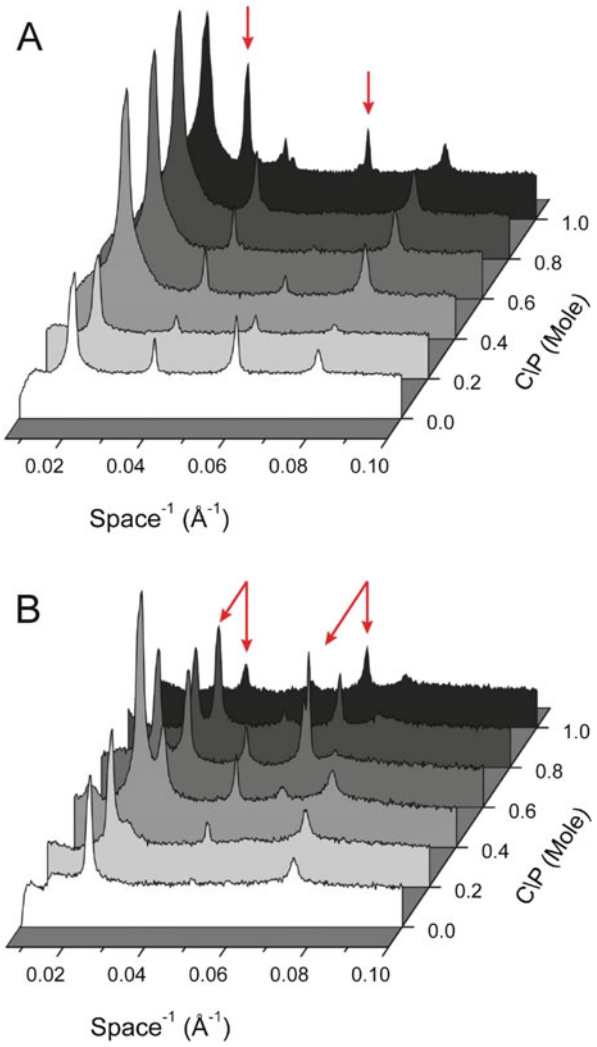

Fig. 3.4 Characterization of cholesterol domain formation in model membranes as a function of increasing cholesterol content and lipid peroxidation state. Diffraction profiles were generated from membrane prepared as binary mixtures of DLPC and cholesterol (over a range of C/P mole ratios) and examined prior to (**a**) and after (**b**) exposure to oxidative conditions for 72 h. Diffraction peaks corresponding to cholesterol domains were obtained only at a C/P mole ratio of 1.0 in the absence of peroxidation (panel **a**). After extensive peroxidation, well defined cholesterol domain peaks were observed at all C/P mole ratios greater than 0.4 (panel **b**). Bragg peaks associated with cholesterol domains are marked by *red arrows* in each *panel*. This research was originally published in The Journal of Biological Chemistry. Jacob RF, Mason RP. Lipid peroxidation reduces cholesterol domain formation in model membranes. J Biol Chem. 2005;280 (47): 39380–7. © The American Society for Biochemistry and Molecular Biology [18]

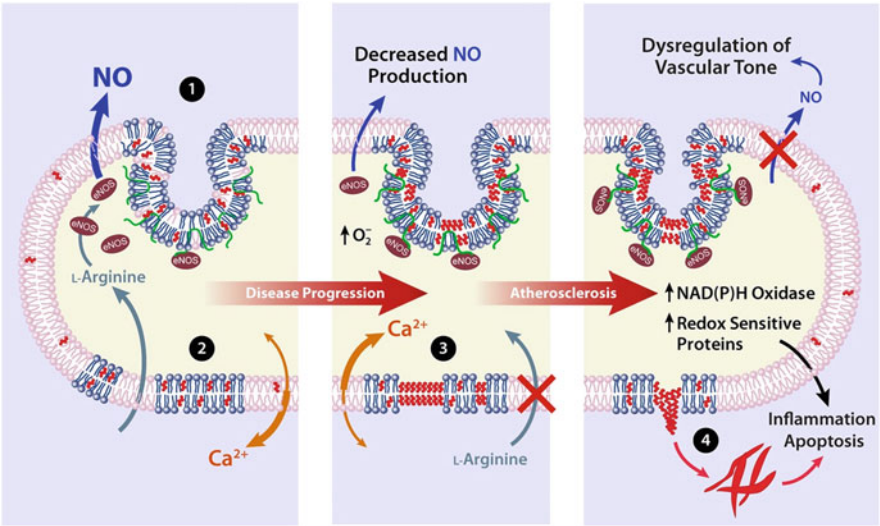

Fig. 3.5 Schematic diagram of changes in lipid raft structure and cell function during cholesterol enrichment and atherosclerosis. Subtypes of lipid rafts enriched with sphingolipid (*blue*) and cholesterol (*red*) include caveolae (1) that contain caveolin protein (*green*) and detergent-resistant membrane domains (2). With progressive cholesterol accumulation, separate cholesterol crystalline membrane domains (3) form and precede the development of extracellular cholesterol crystals (4), which contribute to mechanisms of cell injury and death, including apoptosis. Cholesterol enrichment also increases the number of membrane caveolae, leading to inhibition of endothelial nitric oxide (eNOS) following by a reduction in nitric oxide (NO) production and associated vascular benefits. Loss of normal membrane structure and function with cholesterol enrichment is also associated with disruptions in calcium regulation and redox potential [4]

affect membrane structure and induce the formation of cholesterol crystalline domains, all of which have detrimental downstream effects on vascular cell function (Fig. 3.5) [4].

3.3 Effects of Omega-3 Long Chain Polyunsaturated Acids on Membranes

The marine-derived long chain polyunsaturated omega-3 fatty acids, eicosapentaenoic acid (EPA) and docosahexaenoic acid (DHA), are important constituents of the plasma membrane and have been increasingly studied due to their putative cardioprotective benefits (Fig. 3.6). Prescription forms of omega-3 fatty acids are indicated for use as adjuncts to diet to reduce very high triglyceride levels ($\geq$500 mg/dL) in adult patients; however, other mechanisms by which EPA

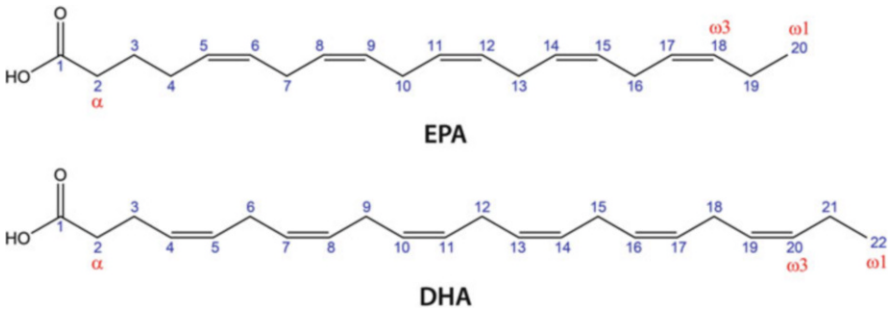

Fig. 3.6 Chemical structures of eicosapentaenoic acid (EPA) and docosahexaenoic acid (DHA)

and DHA may offer cardioprotection are derived from their ability to intercalate directly into lipid bilayers. Accumulating evidence suggests that omega-3 fatty acids provide both potent antioxidant and functional benefits to the endothelium [23, 24]. For example, under oxidative conditions, treatment of apolipoprotein B (ApoB)-containing small dense low-density lipoprotein (sdLDL), very-low-density lipoprotein (VLDL), and oxidized low-density lipoprotein (oxLDL) with EPA or DHA results in significant reductions in lipid peroxidation relative to untreated controls (Fig. 3.7) [25].

The antioxidant effects of omega-3 fatty acids appear to be dose-dependent. When model membranes are treated with various concentrations of EPA and exposed to oxidative conditions, a dose-response curve is observed whereby increasing concentrations of EPA result in decreasing lipid hydroperoxide generation (Fig. 3.8). Interestingly, the addition of ATM was shown to have a potentially synergistic antioxidant effect on lipid peroxidation, but reductions in lipid oxidation were not observed when membranes were treated with vitamin E [23]. Finally, treatment of model membranes with EPA, but not vitamin E, at pharmacologic levels significantly inhibited glucose-induced cholesterol crystalline domain formation (Fig. 3.9) [23]. These data suggest that, like ATM, long chain omega-3 fatty acids inhibit lipid oxidation and cholesterol crystalline domain formation through a direct antioxidant effect within the lipid bilayer.

Omega-3 fatty acids may also affect normal cellular function through direct structural effects on the plasma membrane and regulation of cholesterol domain formation in the absence of lipid peroxidation. The unsaturated double bonds contained within omega-3 fatty acids are highly flexible; thus incorporation of omega-3 into resident phospholipids may change the overall structure and fluidity of the membrane lipid bilayer [26]. For example, the increased flexibility of EPA and DHA may "push" cholesterol away in lipid bilayers, causing EPA and DHA to be separated from cholesterol (and cholesterol domains) in the plasma membrane, and these effects can be further modulated by the head group to which the fatty acids are attached [27].

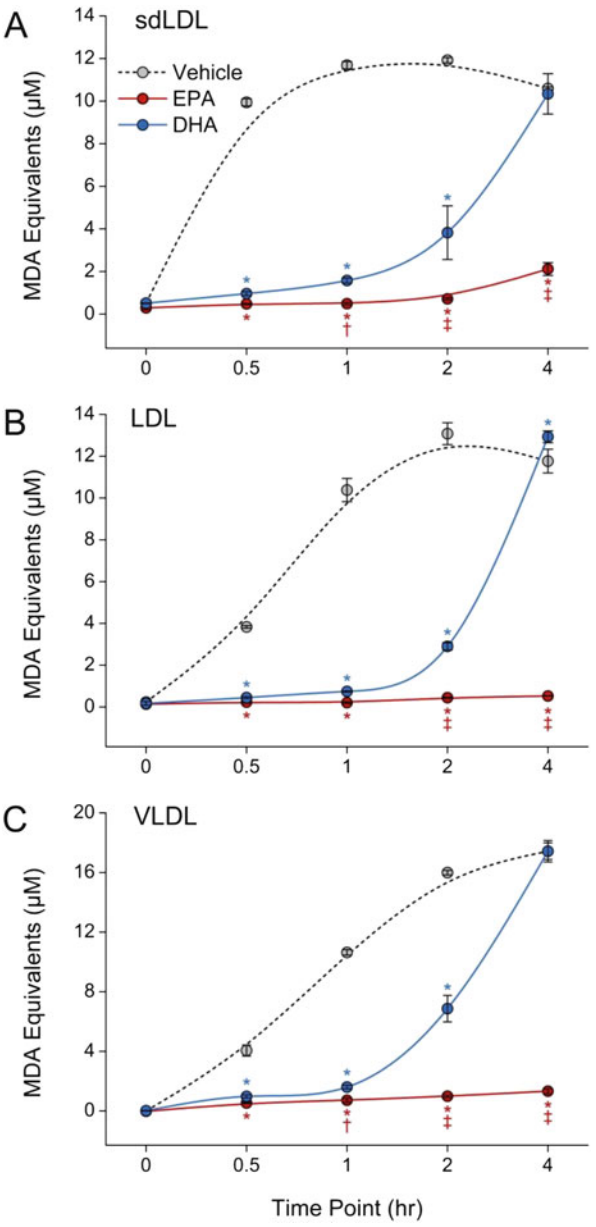

Fig. 3.7 Comparative effects of EPA and DHA on human sdLDL (**a**) LDL (**b**) and VLDL (**c**) oxidation. EPA and DHA were tested at 10 μM (sdLDL) and 2.5 μM (LDL and VLDL). Data were collected at various time points up to 4 h following initial exposure to oxidative conditions. Values are mean ± SD (N = 3). *$p < 0.001$ versus vehicle-treated control; $^{\dagger}p < 0.05$ and $^{\ddagger}p < 0.001$ versus DHA (Student-Newman-Keuls multiple comparisons test; overall ANOVA—sdLDL data: $p < 0.0001$, F = 391.88; LDL data: $p < 0.0001$, F = 1191.3; VLDL data: $p < 0.0001$, F = 1074.8). Abbreviations are: *DHA* docosahexaenoic acid, *EPA* eicosapentaenoic acid, *LDL* low-density lipoprotein, *MDA* malondialdehyde; *sdLDL* small dense low-density lipoprotein, *VLDL* very-low-density lipoprotein. Reprinted with permission from Wolters Kluwer Health, Inc. [25]

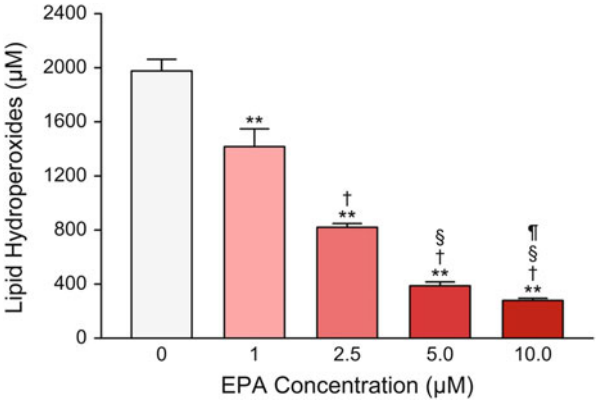

Fig. 3.8 Dose-dependent effects of EPA on glucose-induced membrane lipid peroxidation. Model membrane samples were reconstituted from DLPC and cholesterol at a C/P mole ratio of 0.6:1, treated with glucose (200 mg/dL), and tested for LOOH formation following exposure to oxidative conditions for 48 h. Values are mean ± SD (N = 6). $^{**}p < 0.001$ versus vehicle-treated control; $^{\dagger}p < 0.001$ versus 1.0 μM EPA; $^{\S}p < 0.001$ versus 2.5 μM EPA; $^{\P}p < 0.05$ versus 5.0 μM EPA (Student-Newman-Keuls multiple comparisons test; overall ANOVA: $p < 0.0001$, F = 561.62). Reprinted with permission from Elsevier B.V. [23]

3.4 Differential Effects of Fatty Acids: EPA and DHA

Although EPA and DHA are both long chain omega-3 fatty acids, increasing evidence suggests that EPA and DHA may have different effects on biological systems [28]. Differences in chain length and the number of double bonds between EPA and DHA may differentially affect how these individual fatty acids intercalate into and interact with lipid monolayers and bilayers, perhaps by altering their own precise orientation and location in the outer lipid layer of lipoproteins and thereby leading to differences in antioxidant properties. For example, the antioxidant effects of DHA, as shown in Fig. 3.7, are time dependent, decreasing significantly within the first 2 h, whereas EPA stably prevented lipoprotein oxidation through at least 4 h.

Additionally, EPA and DHA may incorporate into separate domains within the lipid bilayer [29], with distinct effects on membrane stability or the formation of cholesterol domains [30, 31]. In model membranes that contain normal levels of cholesterol, treatment with DHA, but not EPA, had no effect on membrane width, increased membrane fluidity, and simultaneously induced the formation of cholesterol domains relative to untreated controls [32]. In atherosclerotic-like membranes (model membranes enriched in cholesterol at levels that predispose to cholesterol crystalline domain formation) that were formed in the absence of oxidative stress, treatment with EPA resulted in a significant, dose-dependent reduction in cholesterol domain formation relative to untreated controls, while DHA induced cholesterol domain formation in cholesterol-enriched membranes. In addition, treatment with EPA stabilized membrane width across increasing temperatures, while no effect was observed with DHA, suggesting that EPA has a direct stabilizing effect on lipid bilayers even in the absence of lipid peroxidation [32].

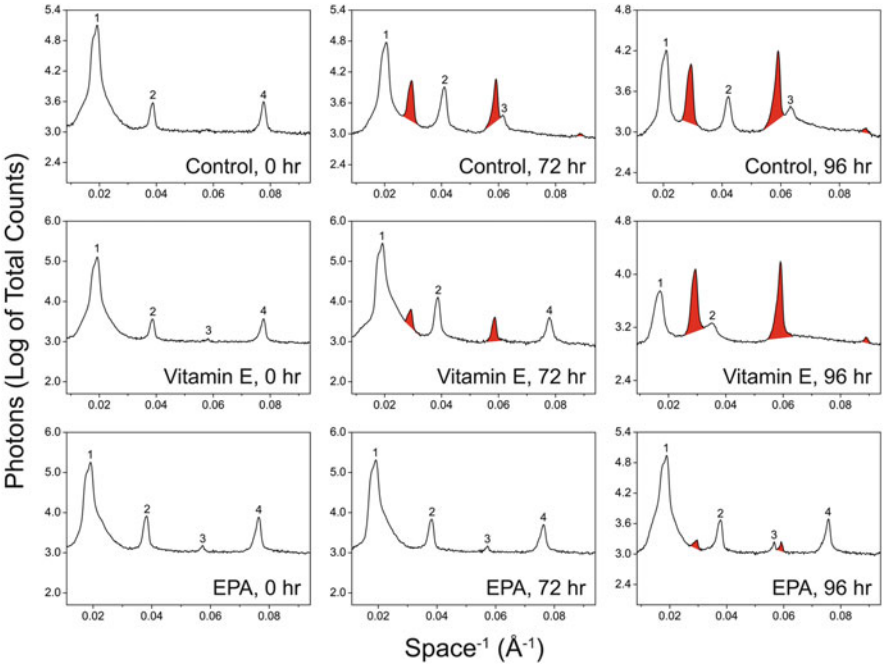

Fig. 3.9 Representative X-ray diffraction patterns collected from model membranes prepared in the presence of glucose, treated with vehicle (control), vitamin E, or EPA and subjected to oxidative conditions for 96 h. Membranes were reconstituted from DLPC and cholesterol at a C/P mole ratio of 0.6:1 and treated with each of the various agents to achieve a total drug-to-phospholipid mole ratio of 1:30. At 0 h, each sample exhibited a single lipid bilayer phase with an average periodicity (*d*-space value) of 51.5 Å, represented by diffraction peaks 1 through 4. At 72 h, cholesterol crystalline domains, having a characteristic *d*-space value of 34 Å and represented by a set of distinct diffraction peaks (shown in *red fill*),were also observed in membrane samples treated with vehicle (control) and vitamin E. At 96 h, cholesterol domains peaks were observed in all experimental samples; however, these peaks were disproportionately greater in samples treated with vehicle (control) and vitamin E as compared to EPA. Reprinted with permission from Elsevier B.V. [23]

Overall, it appears that EPA and DHA have complementary antioxidant characteristics but that the antioxidant effects of DHA may be lost with time under certain conditions. Furthermore, EPA and DHA may have potentially differential structural effects on the formation of cholesterol crystalline domains in lipid bilayers (Fig. 3.10). Additionally, plasma EPA levels may have beneficial effects on plaque characteristics and stabilization as compared with DHA levels [34]. Further research is needed to elucidate the antioxidant, structural, and functional effects of EPA versus DHA on endothelial membranes and plaque characteristics.

Interestingly, several [35–43], but not all [44–50], long-term cardiovascular outcomes studies and related subgroup or meta-analyses have suggested a benefit from omega-3 fatty acid supplementation. Potential confounders to providing

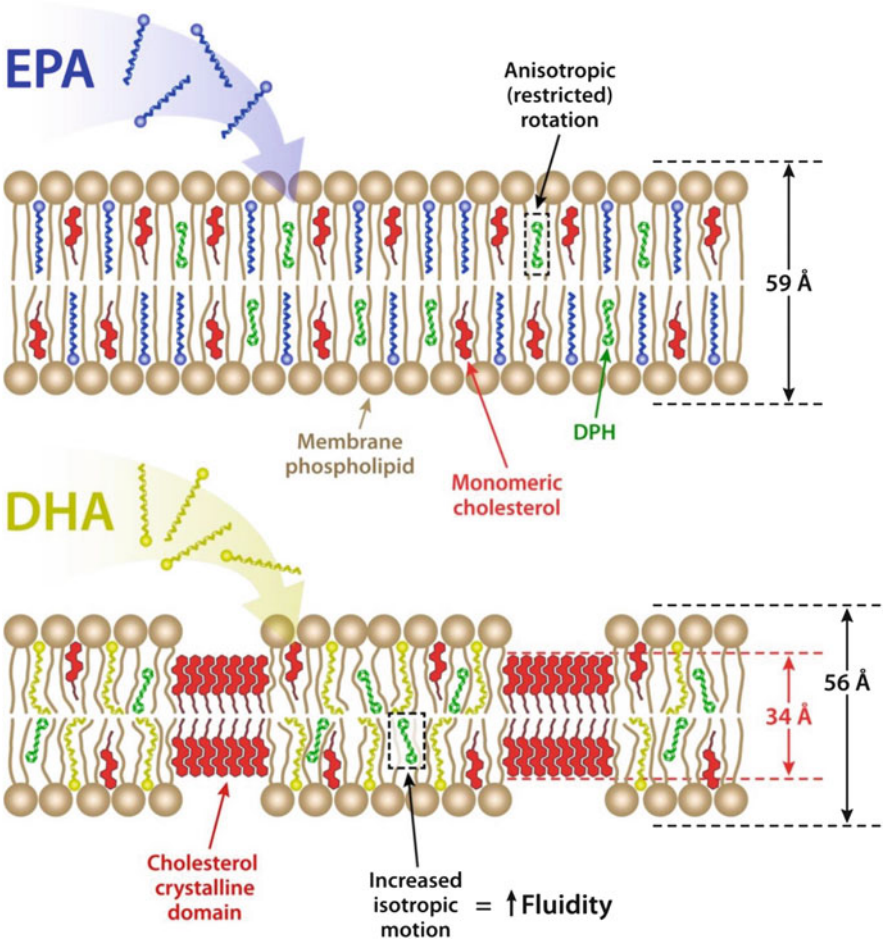

Fig. 3.10 Schematic illustration of the proposed effects of EPA and DHA on membrane structural and dynamic properties. EPA intercalates into the hydrocarbon core region of the membrane lipid bilayer where it provides important antioxidant benefits, as previously reported, but without inducing any significant changes in membrane lipid fluidity, bilayer width, and cholesterol distribution. In contrast, DHA increases membrane lipid fluidity, promotes the formation of discrete, cholesterol crystalline domains, and reduces the overall width of the membrane bilayer. The distinct effects of DHA as measured in this study are attributed to its greater molecular length and reduced saturation level, which alters membrane phospholipid packing constraints, effectively increasing molecular space in the hydrocarbon core, with subsequent effects on cholesterol redistribution and bilayer width. Reprinted from Elsevier B.V. [33]

conclusive evidence as to whether omega-3 fatty acids are cardioprotective are the heterogeneity of the omega-3 formulations and of the patient populations studied. Studies have utilized various therapies ranging from dietary fish supplementation to treatment with prescription strength purified marine-derived omega-3 fatty acids at various doses and with various ratios of EPA and DHA (some with EPA only), and

patient populations have varied across studies. Cardiovascular outcomes studies are currently ongoing with high dose prescription omega-3 formulations as statin adjuncts in patients with high triglyceride levels (median of 200–499 mg/dL) to determine the CV benefit of adding 4 g/day of a highly purified EPA formulation [51] as well as a 4 g/day EPA+DHA formulation [52].

3.5 Summary

Cellular membranes play an important role in the maintenance and regulation of cellular function. Interactions between lipids and proteins induce the formation of distinct cholesterol domains on the plasma membrane of cells that are important regulators of cellular activity and signal transduction. Under conditions of oxidative stress, such as hyperglycemia or hypercholesterolemia, membrane lipids undergo extensive peroxidation which leads to cellular dysfunction and the formation of cholesterol crystalline domains. In model membranes, treatment with ATM and EPA inhibits membrane peroxidation and the formation of cholesterol crystalline domains, providing additional insight into the mechanisms associated with the known and proposed cardioprotective effects of statins and marine-derived omega-3 fatty acids. While EPA and DHA both provide antioxidant benefits, the sustainability of these effects appear to vary under certain conditions, and EPA and DHA may differentially affect membrane fluidity, membrane width, and the formation of cholesterol crystalline domains. There may also be a differential effect on plaque characteristics between EPA and DHA plasma levels. Both in vitro and clinical research is ongoing to further elucidate the potential cardioprotective effects of EPA and DHA on endothelial cell membranes and plaque.

References

1. Jury EC, Flores-Borja F, Kabouridis PS. Lipid rafts in T cell signalling and disease. Semin Cell Dev Biol. 2007;18(5):608–15.
2. Lingwood D, Simons K. Lipid rafts as a membrane-organizing principle. Science. 2010;327 (5961):46–50.
3. Fu C, He J, Li C, Shyy JY, Zhu Y. Cholesterol increases adhesion of monocytes to endothelium by moving adhesion molecules out of caveolae. Biochim Biophys Acta. 2010;1801(7):702–10.
4. Mason RP, Jacob RF. Membrane microdomains and vascular biology: emerging role in atherogenesis. Circulation. 2003;107(17):2270–3.
5. Michel T, Vanhoutte PM. Cellular signaling and NO production. Pflugers Arch. 2010;459 (6):807–16.
6. Mason RP, Walter MF, Day CA, Jacob RF. Active metabolite of atorvastatin inhibits membrane cholesterol domain formation by an antioxidant mechanism. J Biol Chem. 2006;281 (14):9337–45.

7. Tulenko TN, Chen M, Mason PE, Mason RP. Physical effects of cholesterol on arterial smooth muscle membranes: evidence of immiscible cholesterol domains and alterations in bilayer width during atherogenesis. J Lipid Res. 1998;39(5):947–56.
8. Grebe A, Latz E. Cholesterol crystals and inflammation. Curr Rheumatol Rep. 2013;15(3):313.
9. Kellner-Weibel G, Yancey PG, Jerome WG, Walser T, Mason RP, Phillips MC, et al. Crystallization of free cholesterol in model macrophage foam cells. Arterioscler Thromb Vasc Biol. 1999;19(8):1891–8.
10. Abela GS, Aziz K. Cholesterol crystals rupture biological membranes and human plaques during acute cardiovascular events – a novel insight into plaque rupture by scanning electron microscopy. Scanning. 2006;28(1):1–10.
11. Rajamaki K, Lappalainen J, Oorni K, Valimaki E, Matikainen S, Kovanen PT, et al. Cholesterol crystals activate the NLRP3 inflammasome in human macrophages: a novel link between cholesterol metabolism and inflammation. PLoS One. 2010;5(7):e11765.
12. Dai J, Tian J, Hou J, Xing L, Liu S, Ma L, et al. Association between cholesterol crystals and culprit lesion vulnerability in patients with acute coronary syndrome: an optical coherence tomography study. Atherosclerosis. 2016;247:111–7.
13. Girotti AW. Lipid hydroperoxide generation, turnover, and effector action in biological systems. J Lipid Res. 1998;39(8):1529–42.
14. Baynes JW. Role of oxidative stress in development of complications in diabetes. Diabetes. 1991;40(4):405–12.
15. Bertelsen M, Anggard EE, Carrier MJ. Oxidative stress impairs insulin internalization in endothelial cells *in vitro*. Diabetologia. 2001;44(5):605–13.
16. Forstermann U, Munzel T. Endothelial nitric oxide synthase in vascular disease: from marvel to menace. Circulation. 2006;113(13):1708–14.
17. Self-Medlin Y, Byun J, Jacob RF, Mizuno Y, Mason RP. Glucose promotes membrane cholesterol crystalline domain formation by lipid peroxidation. Biochim Biophys Acta. 2009;1788(6):1398–403.
18. Jacob RF, Mason RP. Lipid peroxidation induces cholesterol domain formation in model membranes. J Biol Chem. 2005;280(47):39380–7.
19. Mason RP, Walter MF, Jacob RF. Effects of HMG-CoA reductase inhibitors on endothelial function: role of microdomains and oxidative stress. Circulation. 2004;109(21 Suppl 1): II34–41.
20. Aviram M, Rosenblat M, Bisgaier CL, Newton RS. Atorvastatin and gemfibrozil metabolites, but not the parent drugs, are potent antioxidants against lipoprotein oxidation. Atherosclerosis. 1998;138(2):271–80.
21. Feron O, Dessy C, Moniotte S, Desager JP, Balligand JL. Hypercholesterolemia decreases nitric oxide production by promoting the interaction of caveolin and endothelial nitric oxide synthase. J Clin Invest. 1999;103(6):897–905.
22. Feron O, Dessy C, Desager JP, Balligand JL. Hydroxy-methylglutaryl-coenzyme a reductase inhibition promotes endothelial nitric oxide synthase activation through a decrease in caveolin abundance. Circulation. 2001;103(1):113–8.
23. Mason RP, Jacob RF. Eicosapentaenoic acid inhibits glucose-induced membrane cholesterol crystalline domain formation through a potent antioxidant mechanism. Biochim Biophys Acta. 2015;1848(2):502–9.
24. Johansen O, Seljeflot I, Hostmark AT, Arnesen H. The effect of supplementation with omega-3 fatty acids on soluble markers of endothelial function in patients with coronary heart disease. Arterioscler Thromb Vasc Biol. 1999;19(7):1681–6.
25. Mason RP, Sherratt SC, Jacob RF. Eicosapentaenoic acid inhibits oxidation of ApoB-containing lipoprotein particles of different size in vitro when administered alone or in combination with atorvastatin active metabolite compared with other triglyceride-lowering agents. J Cardiovasc Pharmacol. 2016;68(1):33–40.
26. Shaikh SR, Teague H. N-3 fatty acids and membrane microdomains: from model membranes to lymphocyte function. Prostaglandins Leukot Essent Fatty Acids. 2012;87(6):205–8.

27. Shaikh SR, Kinnun JJ, Leng X, Williams JA, Wassall SR. How polyunsaturated fatty acids modify molecular organization in membranes: insight from NMR studies of model systems. Biochim Biophys Acta. 2015;1848(1 Pt B):211–9.
28. Mozaffarian D, Wu JH. (n-3) Fatty acids and cardiovascular health: are effects of EPA and DHA shared or complementary? J Nutr. 2012;142(3):614S–25S.
29. Williams JA, Batten SE, Harris M, Rockett BD, Shaikh SR, Stillwell W, et al. Docosahexaenoic and eicosapentaenoic acids segregate differently between raft and nonraft domains. Biophys J. 2012;103(2):228–37.
30. Hashimoto M, Hossain S, Yamasaki H, Yazawa K, Masumura S. Effects of eicosapentaenoic acid and docosahexaenoic acid on plasma membrane fluidity of aortic endothelial cells. Lipids. 1999;34(12):1297–304.
31. Shaikh SR, Rockett BD, Salameh M, Carraway K. Docosahexaenoic acid modifies the clustering and size of lipid rafts and the lateral organization and surface expression of MHC class I of EL4 cells. J Nutr. 2009;139(9):1632–9.
32. Mason RP, Sherratt SCR, Jacob RF. Eicosapentaenoic acid (EPA) inhibited cholesterol domain formation and lipid oxidation while preserving bilayer width in model membranes exposed to oxidative stress or cholesterol levels. In: Poster presentation at the 2016 DEUEL Conference on Lipids March 1–4, 2016, Napa, CA. 2016.
33. Mason RP, Jacob RF, Shrivastava S, Sherratt SC, Chattopadhyay A. Eicosapentaenoic acid reduces membrane fluidity, inhibits cholesterol domain formation, and normalizes bilayer width in atherosclerotic-like model membranes. Biochim Biophys Acta. 2016;1858 (12):3131–40.
34. Iwamatsu K, Abe S, Nishida H, Kageyama M, Nasuno T, Sakuma M, et al. Which has the stronger impact on coronary artery disease, eicosapentaenoic acid or docosahexaenoic acid? Hypertens Res. 2016;39(4):272–5.
35. GISSI-Prevenzione Investigators. Dietary supplementation with n-3 polyunsaturated fatty acids and vitamin E after myocardial infarction: results of the GISSI-Prevenzione trial. Lancet. 1999;354(9177):447–55.
36. Heart Failure Investigators GISSI, Tavazzi L, Maggioni AP, Marchioli R, Barlera S, Franzosi MG, et al. Effect of n-3 polyunsaturated fatty acids in patients with chronic heart failure (the GISSI-HF trial): a randomised, double-blind, placebo-controlled trial. Lancet. 2008;372 (9645):1223–30.
37. Marchioli R, Barzi F, Bomba E, Chieffo C, Di Gregorio D, Di Mascio R, et al. Early protection against sudden death by n-3 polyunsaturated fatty acids after myocardial infarction: time-course analysis of the results of the Gruppo Italiano per lo Studio della Sopravvivenza nell'Infarto Miocardico (GISSI)-Prevenzione. Circulation. 2002;105(16):1897–903.
38. Yokoyama M, Origasa H, Matsuzaki M, Matsuzawa Y, Saito Y, Ishikawa Y, et al. Effects of eicosapentaenoic acid on major coronary events in hypercholesterolaemic patients (JELIS): a randomised open-label, blinded endpoint analysis. Lancet. 2007;369(9567):1090–8.
39. Saito Y, Yokoyama M, Origasa H, Matsuzaki M, Matsuzawa Y, Ishikawa Y, et al. Effects of EPA on coronary artery disease in hypercholesterolemic patients with multiple risk factors: sub-analysis of primary prevention cases from the Japan EPA lipid intervention study (JELIS). Atherosclerosis. 2008;200(1):135–40.
40. Tanaka K, Ishikawa Y, Yokoyama M, Origasa H, Matsuzaki M, Saito Y, et al. Reduction in the recurrence of stroke by eicosapentaenoic acid for hypercholesterolemic patients: subanalysis of the JELIS trial. Stroke. 2008;39(7):2052–8.
41. Matsuzaki M, Yokoyama M, Saito Y, Origasa H, Ishikawa Y, Oikawa S, et al. Incremental effects of eicosapentaenoic acid on cardiovascular events in statin-treated patients with coronary artery disease. Circ J. 2009;73(7):1283–90.
42. Casula M, Soranna D, Catapano AL, Corrao G. Long-term effect of high dose omega-3 fatty acid supplementation for secondary prevention of cardiovascular outcomes: a meta-analysis of randomized, placebo controlled trials [corrected]. Atheroscler Suppl. 2013;14(2):243–51.

43. Einvik G, Klemsdal TO, Sandvik L, Hjerkinn EM. A randomized clinical trial on n-3 polyunsaturated fatty acids supplementation and all-cause mortality in elderly men at high cardiovascular risk. Eur J Cardiovasc Prev Rehabil. 2010;17(5):588–92.
44. Galan P, Kesse-Guyot E, Czernichow S, Briancon S, Blacher J, Hercberg S, et al. Effects of B vitamins and omega 3 fatty acids on cardiovascular diseases: a randomised placebo controlled trial. BMJ. 2010;341:c6273.
45. Geleijnse JM, Giltay EJ, Schouten EG, de Goede J, Oude Griep LM, Teitsma-Jansen AM, et al. Effect of low doses of n-3 fatty acids on cardiovascular diseases in 4837 post-myocardial infarction patients: design and baseline characteristics of the Alpha Omega Trial. Am Heart J. 2010;159(4):539–46. e2
46. Kromhout D, Giltay EJ, Geleijnse JM. Alpha Omega Trial G. n-3 fatty acids and cardiovascular events after myocardial infarction. N Engl J Med. 2010;363(21):2015–26.
47. Origin Trial Investigators, Bosch J, Gerstein HC, Dagenais GR, Diaz R, Dyal L, et al. n-3 fatty acids and cardiovascular outcomes in patients with dysglycemia. N Engl J Med. 2012;367 (4):309–18.
48. Rauch B, Schiele R, Schneider S, Diller F, Victor N, Gohlke H, et al. OMEGA, a randomized, placebo-controlled trial to test the effect of highly purified omega-3 fatty acids on top of modern guideline-adjusted therapy after myocardial infarction. Circulation. 2010;122 (21):2152–9.
49. Risk Prevention Study Collaborative Group, Roncaglioni MC, Tombesi M, Avanzini F, Barlera S, Caimi V, et al. n-3 fatty acids in patients with multiple cardiovascular risk factors. N Engl J Med. 2013;368(19):1800–8.
50. Rizos EC, Ntzani EE, Bika E, Kostapanos MS, Elisaf MS. Association between omega-3 fatty acid supplementation and risk of major cardiovascular disease events: a systematic review and meta-analysis. JAMA. 2012;308(10):1024–33.
51. Clinicaltrials.gov. A study of AMR101 to evaluate its ability to reduce cardiovascular events in high risk patients with hypertriglyceridemia and on statin. The primary objective is to evaluate the effect of 4 g/Day AMR101 for preventing the occurrence of a first major cardiovascular event (REDUCE-IT). Clinicaltrials.gov Identifier: NCT01426361. 2015.
52. Clinicaltrials.gov. Outcomes study to assess STatin Residual risk reduction with EpaNova in HiGh CV risk PatienTs with Hypertriglyceridemia (STRENGTH). Clinicaltrials.gov Identifer: NCT02104817. 2015.

Chapter 4
Interaction of Amphiphilic Molecules with Lipid Bilayers: Kinetics of Insertion, Desorption and Translocation

Hugo A.L. Filipe, Renato M.S. Cardoso, Luís M.S. Loura, and Maria João Moreno

Abstract Passive transport across lipid bilayers is a significant, if not dominant, route for the permeation of biologically active amphiphiles through cell membranes. Often, the quantitative description of the rate of permeation is based on a single kinetic parameter, the permeability coefficient. However, the nature of the interactions between amphiphilic molecules and lipid bilayers is complex and involves different steps (insertion, translocation and desorption), which affect both the extent of partition and the rate of permeation. Quantitative knowledge of the rate constants associated with each individual step is required for proper understanding of the whole process, and certainly useful in prediction of the ability of new drug compounds to access the interior of their cell targets. This chapter reviews the formalisms applicable to the kinetics of interaction of small solutes with lipid bilayers. Several important limiting cases, corresponding to different

H.A.L. Filipe • M.J. Moreno (✉)
Centro de Química de Coimbra, Largo D. Dinis, Rua Larga, 3004-535 Coimbra, Portugal

Departamento de Química, Faculdade de Ciências e Tecnologia, Universidade de Coimbra, Largo D. Dinis, Rua Larga, 3004-535 Coimbra, Portugal

Centro de Neurociências e Biologia Celular, Universidade de Coimbra, 3004-504 Coimbra, Portugal
e-mail: mmoreno@ci.uc.pt

R.M.S. Cardoso
Centro de Química de Coimbra, Largo D. Dinis, Rua Larga, 3004-535 Coimbra, Portugal

Departamento de Química, Faculdade de Ciências e Tecnologia, Universidade de Coimbra, Largo D. Dinis, Rua Larga, 3004-535 Coimbra, Portugal

L.M.S. Loura (✉)
Centro de Química de Coimbra, Largo D. Dinis, Rua Larga, 3004-535 Coimbra, Portugal

Centro de Neurociências e Biologia Celular, Universidade de Coimbra, 3004-504 Coimbra, Portugal

Faculdade de Farmácia, Universidade de Coimbra, Pólo das Ciências da Saúde, Azinhaga de Santa Comba, 3000-548 Coimbra, Portugal
e-mail: lloura@ff.uc.pt

A. Chattopadhyay (ed.), *Membrane Organization and Dynamics*, Springer Series in Biophysics 20, DOI 10.1007/978-3-319-66601-3_4

ranges of aqueous solubility and membrane partition, are considered, and selected examples of applications of fluorescence spectroscopy to quantitative description of solute/bilayer interaction are presented. We also address the state of the art regarding methods for calculation of rate constants of solute/lipid interaction and permeability coefficients from molecular dynamics simulations. These methods rely on accurate computation of free energy profiles of solutes across lipid bilayers, and strategies to this purpose, namely employing enhanced sampling of improbable states with the so-called umbrella sampling method, are discussed.

The interaction of small molecules with biological membranes is of fundamental importance in organelle, cell and whole organism homeostasis. Most biologically active small molecules such as metabolites and pharmaceuticals are amphiphilic and as a consequence they interact to some extent with hydrophobic assemblies such as lipid bilayers. This is actually a requirement for their efficient distribution between the distinct aqueous compartments in the living being, all delimited by biomembranes. Most biologically active amphiphiles are not recognized by transporters in the biological membrane and they cross those barriers by passive mechanisms. The rate of equilibration between the distinct compartments depends on the permeability coefficient through the lipid bilayer of biomembranes, which in turn is a function of the rate of translocation between the bilayer leaflets, as well as on the rates of insertion and desorption into/from each leaflet. In addition, a large fraction of cellular enzymes are associated with membranes (either permanently or transiently due to electrostatic interactions and/or regulated acylation), and the effective concentration of the bioactive compound depends on its partition between the aqueous medium and the membrane as well as on the rates of interaction with the membrane.

Given its importance, it is to some extent surprising that so little information is available on the rates of interaction of small amphiphilic molecules with lipid bilayers and biological membranes. This is justified by the extreme difficulty on obtaining experimental data of high quality due to the limited availability of techniques with the required sensitivity and time resolution. An example that illustrates well this difficulty may be found in the effort dedicated by several authors to characterize the rates of interaction of fatty acids with lipid bilayers. The kinetics of the interaction is somewhat easier to characterize for the case of fluorescent molecules, but nevertheless the available information is still quite limited. Molecular Dynamics (MD) simulations is a well-established methodology to obtain molecular details on the interaction between amphiphilic molecules and lipid bilayers. More recently, this methodology has been applied to obtain information regarding the kinetics of the interaction.

In this chapter we will review the methodologies available to characterize the kinetics of interaction between small molecules and lipid bilayers. The distinct methodologies commonly used, and the required mathematical formalisms, will be presented with a critical evaluation of their strengths and limitations. The list of

references given is by no mean extensive, the objective being simply to illustrate the distinct methodologies available.

4.1 Experimental Approaches to Characterize the Interaction Between Small Molecules and Lipid Bilayers

To characterize quantitatively the kinetics of interaction between a solute and lipid bilayers it is necessary to quantify the concentration of solute associated with the bilayer. Fluorescence based methodologies are by far the most convenient because the fluorescence properties of the solute (quantum yield, lifetime and/or anisotropy) are strongly dependent on the environment. This permits following the transfer of a fluorescent molecule between media with distinct properties without the need to physically separate them. In addition, fluorimeters are inexpensive and easy to work with, display a high sensitivity (allowing the use of small concentrations that do not perturb the lipid bilayer), and little interference from other molecules present in the system as most molecules do not fluoresce.

The kinetic models required to characterize the kinetics of interaction of small molecules with liposomes will be presented and discussed in the first part of this section. A focus on fluorescent molecules will be given, with the discussion of common difficulties and possible artifacts. The models presented are also valid for the case of non-fluorescent molecules, provided that their concentration in the distinct compartments may be quantified. Some common methods to follow non-fluorescent molecules, both directly and using fluorescent probes, will also be described.

We have opted to present the kinetic models organized according to solute solubility in the aqueous media, considering separately very high, moderate and low aqueous solubility, because the experimental approaches and the mathematical formalisms depend strongly on this solute property.

4.1.1 Solutes with High Solubility in the Aqueous Media and Insoluble in the Lipid Bilayer

Usually, when the solubility of the molecule of interest in the aqueous media is very high it does not associate significantly with the lipid bilayer. The solute molecules in the vicinity of the lipid bilayer on one side, will permeate directly into the other side of the bilayer with a given rate constant κ, scheme (4.1):

$$S_{\mathrm{w}}^{\mathrm{o}} \underset{\kappa}{\overset{\kappa}{\rightleftarrows}} S_{\mathrm{w}}^{\mathrm{i}}, \tag{4.1}$$

where $S_{\mathrm{W}}^{\mathrm{o}}$ and $S_{\mathrm{W}}^{\mathrm{i}}$ represent the solute in the aqueous media outside and inside the liposomes, respectively. It is assumed that the rate constant for crossing the bilayer in both directions is the same, which should hold for symmetric bilayers.

The differential equations that relate the time dependence of the amount of solute on both sides of the bilayer with the rate constants for crossing the bilayer are given below.

$$\begin{cases} \dfrac{dnS_{\mathrm{w}}^{\mathrm{o}}}{dt} = -\kappa\left(ns_{\mathrm{w}}^{\mathrm{o}} - ns_{\mathrm{w}}^{\mathrm{i}}\right) \\ \dfrac{dnS_{\mathrm{w}}^{\mathrm{i}}}{dt} = -\dfrac{dnS_{\mathrm{w}}^{\mathrm{o}}}{dt} \end{cases} \tag{4.2}$$

Note that the total amount of solute in a given aqueous compartment is represented by an uppercase S, whereas a lowercase s represents the solute in the immediate vicinity of the bilayer. The rate for crossing the bilayer is proportional to the difference in the amount of solute in the immediate vicinity of the bilayer (and not to the difference in the total amount of solute in the two aqueous compartments), because only those solute molecules are able to cross the bilayer with the rate constant κ. Solute molecules further away have first to diffuse into the region near the bilayer, and after crossing the barrier the solutes will equilibrate with the respective aqueous compartment by diffusion.

For small and polar molecules the diffusion in the aqueous media is much faster than crossing the lipid bilayer barrier. Therefore, the solute molecules in the immediate vicinity of the bilayer are in equilibrium with the solute in the bulk aqueous phase. If the solute does not interact with the surface of the lipid bilayer, the concentration in the volume of aqueous phase in the immediate vicinity of the lipid bilayer is the same as the concentration in the respective bulk aqueous phase. In this case, the fraction of solute in the immediate vicinity of the lipid bilayer is equal to the ratio between the volume of the aqueous phase with a thickness that depends on the solute dimensions, and the area of the bilayer in direct contact with it, $K = 1$ in Eq. (4.3). For the case of ions and charged membranes, the solute may be enriched or depleted at the surface of the bilayer due to electrostatic attraction or repulsion; in this case the distribution coefficient between the bulk aqueous phase and the aqueous layer in the immediate vicinity of the bilayer (K) will be larger or smaller than 1, respectively. The product of the distribution coefficient (K) and the characteristic length (λ) converts the solute concentration in bulk aqueous phase (in units of mol dm^{-3}) into the surface concentration of solute near the permeation barrier (in units of mol dm^{-2}).

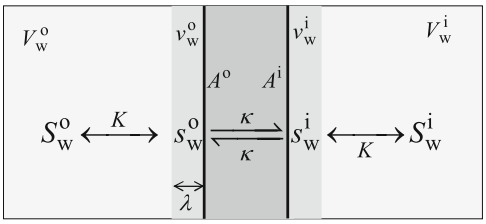

Fig. 4.1 Schematic drawing with the kinetic scheme considered for the transport of very polar solutes across a lipid membrane. The lipid bilayer is represented by the *medium intensity gray bar* (▮), the aqueous layer in the immediate vicinity of the bilayer by the *light gray bar* (▮), and the bulk aqueous phase by *very light grey* (▮). The volumes of the aqueous phases outside and inside the liposomes are represented by V_w^o and V_w^i, respectively; the volumes of aqueous phase immediately in the vicinity of the bilayer are represented by v_w^o and v_w^i; and the total area of the bilayer surface in direct contact with the aqueous media is represented by A^o and A^i (—). The solute in the bulk aqueous phase (S_w^o and S_w^i) equilibrates rapidly with the solute in the immediate vicinity of the lipid bilayer (s_w^o and s_w^i) and slowly permeates the bilayer with the rate constant κ

$$\begin{aligned} ns_w^o &= K\ nS_w^o \frac{v_w^o}{V_w^o} = K\ nS_w^o \frac{A^o}{V_w^o}\lambda \\ ns_w^i &= K\ nS_w^i \frac{v_w^i}{V_w^i} = K\ nS_w^i \frac{A^i}{V_w^i}\lambda \end{aligned} \tag{4.3}$$

See Fig. 4.1 for the definition of the distinct variables and parameters in Eq. (4.3).

Using the relations given in Eq. (4.3), the differential equations for the total amount of solute in each aqueous compartment as a function of the total amount of solute in that compartment may be found, Eq. (4.4). Note that for large unilamelar vesicles (LUVs) and giant unilamelar vesicles (GUVs), the area of the bilayer in contact with the aqueous media outside and inside the liposomes is the same, that means $A^o = A^i = A$.

$$\begin{cases} \dfrac{dnS_w^o}{dt} = -\kappa K A \lambda \left(\dfrac{nS_w^o}{V_w^o} - \dfrac{nS_w^i}{V_w^i} \right) \\ \dfrac{dnS_w^i}{dt} = -\dfrac{dnS_w^o}{dt} \end{cases} \tag{4.4}$$

When the concentration of solute in a given aqueous compartment with respect to the volume of that aqueous compartment is the property being followed (as is the case for permeation through cell monolayers), it is convenient to describe the time evolution of the solute in terms of its concentration with respect to the volume of the aqueous compartment where it is dissolved $\left(\left[S_w^x \right]_{V_w^x} = nS_w^x / V_w^x \right)$, Eq. (4.5).

$$\begin{cases} \dfrac{d\left[S_{\mathrm{w}}^{\mathrm{o}}\right]_{V_{\mathrm{w}}^{\mathrm{o}}}}{dt} = -\kappa K \dfrac{A\lambda}{V_{\mathrm{w}}^{\mathrm{o}}}\left(\left[S_{\mathrm{w}}^{\mathrm{o}}\right]_{V_{\mathrm{w}}^{\mathrm{o}}} - \left[S_{\mathrm{w}}^{\mathrm{i}}\right]_{V_{\mathrm{w}}^{\mathrm{i}}}\right) \\ \dfrac{d\left[S_{\mathrm{w}}^{\mathrm{i}}\right]_{V_{\mathrm{w}}^{\mathrm{i}}}}{dt} = -\kappa K \dfrac{A\lambda}{V_{\mathrm{w}}^{\mathrm{i}}}\left(\left[S_{\mathrm{w}}^{\mathrm{o}}\right]_{V_{\mathrm{w}}^{\mathrm{o}}} - \left[S_{\mathrm{w}}^{\mathrm{i}}\right]_{V_{\mathrm{w}}^{\mathrm{i}}}\right) \end{cases} \tag{4.5}$$

The differential equations that describe the time evolution of the concentration of solute in the two aqueous compartments with respect to the volume of the specific compartment are no longer symmetric. This is because the incremental concentration in each aqueous compartment due to the transfer of a given amount of solute depends on the volume of the respective compartment.

When using the fluorescence of the whole solution to follow the permeation of a solute through the lipid bilayer, it is not usually possible to quantify the concentration of solute in a given compartment with respect to the volume of that compartment, but rather the corresponding concentration with regard to the total volume of the solution, $\left[S_{\mathrm{w}}^{\mathrm{x}}\right]_{V_{\mathrm{T}}} = nS_{\mathrm{w}}^{\mathrm{x}}/V_{\mathrm{T}}$. The differential equations obtained for the time variation in the concentration of solute in each aqueous compartment, with respect to the total volume of the system, are given by:

$$\begin{cases} \dfrac{d\left[S_{\mathrm{w}}^{\mathrm{o}}\right]_{V_{\mathrm{T}}}}{dt} = -\kappa K A\lambda\left(\dfrac{\left[S_{\mathrm{w}}^{\mathrm{o}}\right]_{V_{\mathrm{T}}}}{V_{\mathrm{w}}^{\mathrm{o}}} - \dfrac{\left[S_{\mathrm{w}}^{\mathrm{i}}\right]_{V_{\mathrm{T}}}}{V_{\mathrm{w}}^{\mathrm{i}}}\right) \\ \dfrac{d\left[S_{\mathrm{w}}^{\mathrm{i}}\right]_{V_{\mathrm{T}}}}{dt} = -\dfrac{d\left[S_{\mathrm{w}}^{\mathrm{o}}\right]_{V_{\mathrm{T}}}}{dt} \end{cases}. \tag{4.6}$$

Using the molar conservation equation for the total amount of solute $\left(nS^{\mathrm{T}} = nS_{\mathrm{w}}^{\mathrm{o}} + nS_{\mathrm{w}}^{\mathrm{i}}\right)$, one can obtain the differential equation for each of the species (namely $S_{\mathrm{w}}^{\mathrm{o}}$) where its own concentration is the only time dependent variable:

$$\begin{aligned} \frac{d\left[S_{\mathrm{w}}^{\mathrm{o}}\right]_{V_{\mathrm{T}}}}{dt} &= -\kappa K A\lambda\left(\left[S_{\mathrm{w}}^{\mathrm{o}}\right]_{V_{\mathrm{T}}}\frac{V_{\mathrm{w}}^{\mathrm{o}} + V_{\mathrm{w}}^{\mathrm{i}}}{V_{\mathrm{w}}^{\mathrm{o}}\ V_{\mathrm{w}}^{\mathrm{i}}} - \frac{\left[S_{\mathrm{w}}^{\mathrm{T}}\right]_{V_{\mathrm{T}}}}{V_{\mathrm{w}}^{\mathrm{i}}}\right) \\ &= -\kappa K A\lambda\frac{V_{\mathrm{w}}^{\mathrm{o}} + V_{\mathrm{w}}^{\mathrm{i}}}{V_{\mathrm{w}}^{\mathrm{o}}\ V_{\mathrm{w}}^{\mathrm{i}}}\left(\left[S_{\mathrm{w}}^{\mathrm{o}}\right]_{V_{\mathrm{T}}} - \frac{V_{\mathrm{w}}^{\mathrm{o}}}{V_{\mathrm{w}}^{\mathrm{o}} + V_{\mathrm{w}}^{\mathrm{i}}}\left[S_{\mathrm{w}}^{\mathrm{T}}\right]_{V_{\mathrm{T}}}\right) \end{aligned} \tag{4.7}$$

Equation (4.7) has the form:

$$\frac{dx}{dt} = -k(x + a), \tag{4.8}$$

and its integration gives:

$$x = x_{\infty} + (x_0 - x_{\infty})e^{-kt}, \tag{4.9}$$

where x_0 is the value of variable x at time equal to zero and x_∞ is its value at the end of the time window considered in the experiment.

The rate constant for transfer of solute from the aqueous media outside the liposomes to the aqueous media inside the liposomes (k) is therefore given by:

$$k = \kappa K A \ \lambda \ \frac{V_{\mathrm{w}}^{\mathrm{i}} + V_{\mathrm{w}}^{\mathrm{o}}}{V_{\mathrm{w}}^{\mathrm{i}} \ V_{\mathrm{w}}^{\mathrm{o}}} \tag{4.10}$$

The above expression may be simplified because several of the variables depend on common parameters. The total area of lipid bilayer in contact with each aqueous compartment is given by:

$$A = N_{\mathrm{Lv}} 4\pi r^2, \tag{4.11}$$

where N_{Lv} is the number of liposomes in the total volume of solution considered, and r the radius of the liposomes. On the other hand, the total volume of aqueous media inside the liposomes is given by:

$$V_{\mathrm{w}}^{\mathrm{i}} = N_{\mathrm{Lv}} \frac{4}{3} \pi r^3. \tag{4.12}$$

If the aqueous volume inside the liposomes is much smaller than the total volume of the solution, and because the volume of the lipid bilayer is negligible, the aqueous volume outside the liposomes may be considered equal to the total volume of solution. In that case, the rate constant for transfer of solute through the lipid bilayer of the liposomes depends on the size of the liposomes, being given by:

$$k = \kappa K \frac{3\lambda}{r}. \tag{4.13}$$

The rate constant of transfer of solute is therefore inversely proportional to the size of the liposomes. Due to this dependence, the kinetic parameter that is usually reported is the permeability coefficient (P). This parameter may be calculated from the rate of accumulation of solute in the acceptor compartment, which is described by Eq. (4.14) for the case where no significant back transfer of solute occurs:

$$P = \frac{\frac{dnS_{\mathrm{w}}^{\mathrm{A}}}{dt} V_{\mathrm{w}}^{\mathrm{D}}}{A \ nS_{\mathrm{w}(0)}^{\mathrm{D}}}, \tag{4.14}$$

where the superscripts D and A denote the donor and acceptor compartments, and $nS_{\mathrm{w}(0)}^{\mathrm{D}}$ is the amount of solute in the donor compartment at $t = 0$. The differential equation for the amount of S in the acceptor compartment is given by,

$$\frac{dnS_{\mathrm{w}}^{\mathrm{A}}}{dt} = -k\left(nS_{\mathrm{w}}^{\mathrm{A}} - nS^{\mathrm{T}}\frac{V_{\mathrm{w}}^{\mathrm{A}}}{V_{\mathrm{w}}^{\mathrm{A}} + V_{\mathrm{w}}^{\mathrm{D}}}\right). \tag{4.15}$$

At the beginning of transfer from D to A, when $nS_{\mathrm{w}}^{\mathrm{A}} = 0$ and $nS_{\mathrm{w}}^{\mathrm{D}} = nS^{\mathrm{T}}$, the above equation simplifies to:

$$\begin{aligned}\frac{dnS_{\mathrm{w}}^{\mathrm{A}}}{dt} &= k\ nS^{\mathrm{T}}\frac{V_{\mathrm{w}}^{\mathrm{A}}}{V_{\mathrm{w}}^{\mathrm{A}} + V_{\mathrm{w}}^{\mathrm{D}}} \\ &= k\ nS_{\mathrm{w}(\infty)}^{\mathrm{A}}.\end{aligned} \tag{4.16}$$

Substituting Eq. (4.16) in Eq. (4.14) leads to the relation between the permeability coefficient and the transfer rate constant:

$$P = k\ \frac{1}{A}\ \frac{V_{\mathrm{w}}^{\mathrm{A}}\ V_{\mathrm{w}}^{\mathrm{D}}}{V_{\mathrm{w}}^{\mathrm{A}} + V_{\mathrm{w}}^{\mathrm{D}}}. \tag{4.17}$$

If the donor compartment is the aqueous medium inside the liposomes, $V_{\mathrm{w}}^{\mathrm{A}} \gg V_{\mathrm{w}}^{\mathrm{D}}$ and the above equation simplifies to:

$$P = k\ \frac{V_{\mathrm{w}}^{\mathrm{D}}}{A}\ . \tag{4.18}$$

Substituting in the expression the Eqs. (4.11), (4.12) and (4.13), for A, $V_{\mathrm{w}}^{\mathrm{D}}$ and k, respectively, one obtains the following equation:

$$P = \kappa K \lambda, \tag{4.19}$$

which relates the permeability coefficient with the parameters initially considered in the kinetic model, κ and λ.

In this mechanism of permeation it is assumed that the solutes do not interact with the bilayer (except for some eventual electrostatic interaction). Therefore, the intrinsic rate constant for crossing the barrier (κ) is related with the formation of transient hydrated defects due to thermal fluctuations, which depend on the bilayer thickness and lipid-lipid interactions. The rate constant is also affected by the size of the solute which will have to diffuse through the transient pores. For a given ion, the rate of permeation is expected to decrease exponentially with the increase in the thickness of the bilayer. This has been observed for the permeation of small ions through thin lipid bilayers [1].

The mathematical formalism above has been used to characterize the rate of permeation of the anion dithionite through LUVs of distinct lipid composition [2]. Dithionite is not fluorescent but its concentration in the aqueous media inside the LUVs was quantitatively followed via its reaction with the fluorescent group nitrobenzoxadiazole (NBD) covalently linked to the head group of 1,2-dimiristoyl-*sn*-glycero-3-phosphoethanolamine (DMPE). The same formalism has been used to

calculate the permeability coefficient of several non-fluorescent small molecules (water, urea and glycerol) [1, 3] and ions (such as amino acids, peptides, thyroid hormones, phosphate and H^+/OH^-) [1, 4–6]. The time evolution of the concentration of the relevant solute in the inner or outer aqueous media was followed by changes in the liposome volume (therefore leading to the permeability coefficient under an osmotic gradient) [1, 3, 4], using specific electrodes [1], through the selective reaction of the solute in the inner or outer aqueous phase [4, 5], or by solute quantification after physical separation of the two aqueous compartments [6].

To characterize the rate of permeation of fluorescent molecules through lipid bilayers, the most common approach is to encapsulate the fluorescent molecule at high concentrations (leading to efficient fluorescence quenching) inside liposomes. The fluorescent molecules outside the liposomes are then removed (usually by size exclusion chromatography), and the permeation through the lipid bilayer is followed through the time dependent fluorescent increase due to dilution of the fluorophore when going from the inner to the outer aqueous media [7]. This approach can only be used for molecules with low and very low permeability, because it requires previous removal of the probe located in the aqueous media outside the liposomes. Additionally, the fluorescent molecules must have a very high solubility in the aqueous phase to achieve self-quenching concentrations, and they cannot interact efficiently with the membranes to ensure slow permeability. The method cannot therefore be used to characterize amphiphilic molecules. It has been used mostly to characterize the effect of several membrane perturbing molecules, such as peptides and surfactants, on the barrier properties of liposomes [7–12]. The fluorescent probe used to report on the bilayer properties is most commonly carboxyfluorescein (CBF), but calcein has also been employed [8]. To follow quantitatively the permeation, attention should be given to the fact that fluorescence intensity may have a non-linear relation with the extent of transfer [7, 13].

4.1.2 Solutes with a Moderate Solubility in the Aqueous Media and in the Lipid Bilayer

The overall permeation of solutes with moderate solubility in both the aqueous and the lipidic phases is usually described by the partition-diffusion mechanism. Early descriptions of permeation following this mechanism considered the presence of several diffusion barriers in the system water/bilayer/water [14]. However, the approximation of a single rate limiting step, the diffusion through the bilayer non-polar core, became the prevailing model. According to this formalism, the overall permeability coefficient (P) is related with the microscopic parameters: partition coefficient between the water and the bilayer (K_P), diffusion coefficient of the solute through the bilayer (D), and thickness of the barrier (h), by:

$$P = K_P \frac{D}{h}. \tag{4.20}$$

This model for permeation through membranes is based on the work done by Overton more than a century ago [15], and Eq. (4.20) is commonly referred to as Overton's rule [16, 17].

Equation (4.20) is formally equivalent to the equation derived in the previous section for solutes that do not partition into the lipid bilayer, Eq. (4.19), with the equilibrium distribution between the bulk aqueous phase and the immediate vicinity of the lipid bilayer (K) replaced by the partition coefficient between the aqueous and lipidic phases (K_P). The first order rate constant associated with transport with the diffusion coefficient D is D/ℓ^2, where ℓ is the distance between the two equilibrium positions that is being crossed by diffusion [14]. Therefore, Eq. (4.20) is equivalent to Eq. (4.19) with the solute characteristic length (λ) equal to the thickness of the diffusion barrier. The length parameter in Eq. (4.20), h, is usually considered as the thickness of the bilayer, although it is in fact the distance between the equilibrium positions of the solute center of mass on both sides of the bilayer. The assumptions in the derivation of Eq. (4.20) are very similar to those considered in the previous section: (1) negligible accumulation of solute in the bilayer; (2) rapid transport of solute from the bulk aqueous media to the bilayer; and (3) transport through the lipid bilayer as a single step.

The major difference between the partition/diffusion model and the model presented in the last section is the nature of the intrinsic rate constant for transport through the barrier; diffusion of solute dissolved in the nonpolar portion of the lipid bilayer, and diffusion through transient hydrated defects, respectively. The distinction between the two permeation mechanisms may be done through the dependence of the overall permeability coefficient on the thickness of the bilayer. Assuming an invariant partition coefficient and diffusion coefficient; P is predicted to depend inversely on the thickness of the bilayer for the partition/diffusion mechanism of permeation, while an exponential dependence is predicted for the pore mechanism [1]. The permeation of small neutral molecules such as water, urea and glycerol, has been shown to follow the predictions from the partition/diffusion mechanism of permeation through lipid bilayers. This same mechanism is observed for the permeation of large ions, due to their significant solubility in the lipid bilayer, the small probability of pore formation with the appropriate size and the slow diffusion of the large ion through the transient pore.

There are several reports on the overall permeability coefficient of small molecules through liposomes considering the partition/diffusion mechanism. The methods used are essentially equal to those described in the previous section for solutes very soluble in the aqueous phase, except that permeation may be too fast to allow the physical separation of the inner and outer aqueous compartments. The permeation of fluorescent amphiphiles into GUVs has also been followed directly using fluorescence microscopy [18], and the permeation of weak acids and bases has been characterized through the pH variation in the aqueous compartment inside

the LUVs, as measured by the fluorescence probes carboxyfluorescein or pyranin [19].

When comparing distinct solutes along a homologous series, Eq. (4.20) provides a good description for the dependence of the rate of overall permeation coefficient with the solute hydrophobicity. However, for structurally unrelated solutes the correlation between P and K_P is poor and no clear relation is obtained with the diffusion coefficient as predicted by the size of the solutes. This is due to the assumptions considered in the development of the partition/diffusion mechanism which are not valid for the case of medium size and amphiphilic molecules.

In the partition/diffusion mechanism of permeation, the barrier region of the lipid bilayer is treated as a homogeneous medium through which the solute diffuses due to the concentration gradient on both sides of the barrier. There are several difficulties associated with this assumption, namely the high transversal heterogeneity of the lipid bilayer (with density, viscosity and polarity gradients), which is not compatible with the assumption of a smooth continuous resistance offered by the media on the diffusing molecules required to treat transport as diffusion [14]. It is therefore challenging, if not impossible, to know what would be the diffusion coefficient to use in Eq. (4.20) in order to predict the permeability coefficient from the structure of a given molecule; the more general inhomogeneous solubility-diffusion model, which can accommodate this heterogeneity, will be described below in the context of MD simulations. Also, for amphiphilic molecules (with well-defined polar and non-polar regions) the transport through the bilayer center cannot be considered as random diffusion because the energy of the solute in the bilayer does not depend only on the position of its center of mass, but also on the orientation of the polar and non-polar regions. The high Gibbs energy state in the transport of amphiphilic molecules through the bilayer usually corresponds to the solubilization of the polar region in the non-polar center of the bilayer (transition state) and is more conveniently treated as a single step corresponding to translocation from the equilibrium position in one side of the bilayer to the other. The rate constant of translocation depends on the activation energy barrier, which is a function of the interactions that the solute establishes with the lipids and the hydration shell at the equilibrium positions and with the non-polar portion of the lipids when in the transition state. The prediction of this activation energy, and therefore the rate constant for translocation, from the structure of the amphiphile and the properties of the bilayer is a feasible task, allowing the prediction of the overall permeation from the structure of the permeating solute.

Another important limitation of the partition/diffusion model is the assumption that transport through the non-polar region of the bilayer is the rate limiting step. In the overall process of entering an aqueous compartment delimited by a lipid membrane (cell, organelle or liposome) the amphiphile first interacts with the outer leaflet (rate of insertion), followed by equilibration with the inner leaflet (rate of translocation, or diffusion, through the non-polar part of the bilayer), and then it equilibrates with the inner aqueous compartment (rate of desorption). For amphiphiles with a high Hydrophilic/Lipophilic Balance (HLB), the rate limiting step in the overall process is usually translocation through the non-polar center of

the bilayer. In this case, the permeability coefficient is directly proportional to the rate of translocation and to the partition coefficient between the aqueous media and the lipid bilayer as predicted by Eq. (4.20). However, in the last years several exceptions to this behavior have been observed, and it is now well established that for amphiphiles with intermediate and low HLB, Eq. (4.20) does not adequately predict the rate of overall permeation through lipid bilayers [20–23], as the rate limiting step is the desorption from the bilayer (and not translocation) [20].

The overall rate of permeation is the relevant parameter to evaluate how fast the amphiphile crosses the biological membranes. However, a rational interpretation of the dependence of this parameter on the structure and properties of the permeating amphiphile is not straightforward, because it depends on several steps, each being affected differently by the amphiphile properties [20]. To rationalize and gain predictive value on the dependence of the overall permeation with the molecular properties of the amphiphile, it is necessary to obtain all the relevant rate constants (insertion, desorption and translocation) for a large set of structurally unrelated molecules.

To obtain the rate constants of insertion and desorption from the lipid bilayer it is necessary to consider those steps explicitly in the kinetic scheme. Therefore, the association between the amphiphile and the lipid bilayer is not assumed to be in fast equilibrium. The resulting kinetic scheme is given below.

$$S_W^o + L_V \underset{k_-}{\overset{k_+^{L_V}}{\rightleftarrows}} S_L^o \overset{k_f}{\leftrightarrow} S_L^i \tag{4.21}$$

where S_W^o represents the amphiphile (solute) in the aqueous media outside the liposomes; L_V the liposomes; S_L^o and S_L^i represent the amphiphile in the outer and inner leaflet of the liposomes, respectively; k_f is the rate constant for translocation between the leaflets; $k_+^{L_V}$ is the rate constant for insertion of the amphiphile in the lipid bilayer of the liposomes; and k_- is the rate constant for desorption from the lipid bilayer into the aqueous media.

We call the reader's attention to the fact that the notation used for the rate constants of desorption and translocation does not include reference to the topology of the lipid phase, while this is included in the notation used for the rate constant of insertion. This is because the rate of insertion requires the encounter between the amphiphile in the aqueous media and the lipid phase, which depends on the size of the lipid assemblies for the case of processes near or at the diffusion limit. In accordance, the lipid phase is represented with the topology present in the solution (liposomes, L_V). This allows the comparison between the obtained rate constant of insertion and the diffusion limited rate constant. Additionally, this formalism permits the comparison between the rates of insertion in lipid aggregates of distinct sizes with the uncoupling between the contributions from size and other properties [24]. It should however be noted that the usual equations to calculate the diffusion limited rate constants are only valid in the absence of electrostatic interaction between the reactants [25]. Also, the model considers that all the volume occupied by the reactants is active, which is only an approximation for the case of liposomes

and leads to significant deviations for the case of very large liposomes and cells [26].

Although the interaction is considered to take place with the individual liposomes, equilibration of the amphiphile between the aqueous phase and the lipid leaflet in direct contact is considered to occur via partition and not binding to well defined binding sites. In addition, the capacity of the liposomes to interact with the amphiphile is considered as independent of the presence of amphiphile already associated with the liposomes; this being valid only for small local concentrations of solute. As a consequence, the concentration of liposomes (binding agent available for the interaction) remains constant throughout the equilibration process, which significantly simplifies the mathematical description of the interaction between small molecules and liposomes.

In kinetic scheme (4.21), the equilibration of the amphiphile with the aqueous media inside the liposomes is not considered. Although this approximation is valid for LUVs because the volume of the encapsulated aqueous media is negligible, it does not hold for GUVs. Another simplification considered is that the rate constant for translocation is the same in both directions. This is valid for liposomes with a small curvature (diameter equal to or larger than 100 nm) with the same lipid composition in both leaflets.

The rate constant for equilibration between the aqueous media and the liposome leaflet in direct contact is given by,[1]

$$k = k_- + k_+^{\mathrm{L_V}}[\mathrm{L_V}]. \tag{4.22}$$

If this process occurs at least one order of magnitude faster than translocation into the inner leaflet, the two processes are uncoupled and the fluorescence variation that follows the addition of liposomes to the fluorescent amphiphile is a single-exponential function, from which the rate constant k is directly obtained. Performing the experiment at different liposome concentrations permits obtaining the rate constant of insertion and the rate constant of desorption, [27] Eq. (4.22).

When the rate of translocation is much faster than the rate of equilibration between the aqueous phase and the exposed liposome leaflet, the fluorescence variation observed is also a single-exponential function but the relation between the transfer rate constant with the intrinsic rate constants for insertion and desorption is given by,

$$k = \frac{k_-}{2} + k_+^{\mathrm{L_V}}[\mathrm{L_V}]. \tag{4.23}$$

[1] In this and in the next equations, the concentrations are calculated with respect to the total volume of the solution except when explicitly indicated.

The rate of desorption is proportional to half the value of the respective rate constant because only the amphiphile in the outer leaflet of the bilayer (half of the total amphiphile) is able to desorb into the aqueous phase outside the liposomes.

Both situations described above allow the characterization of the rate constants of insertion and desorption, but not the rate constant of translocation. An important difficulty is whether Eqs. (4.22) or (4.23) should be used if no independent information is available regarding the relative rate of translocation.

For some amphiphiles, the two distinct processes occur on similar time scales and the fluorescence variation observed does not follow a single-exponential function. In this situation the time dependence of the fluorescence variation must be described by the integration of the full set of differential equations obtained from the kinetic scheme, Eq. (4.24), and all the rate constants may in principle be obtained.

$$\begin{cases} \dfrac{d\left[S_{\mathrm{W}}^{\mathrm{o}}\right]}{dt} = k_{-}\left[S_{\mathrm{L}}^{\mathrm{o}}\right] - k_{+}^{\mathrm{Lv}}[L_{\mathrm{V}}]\left[S_{\mathrm{W}}^{\mathrm{o}}\right] \\ \dfrac{d\left[S_{\mathrm{L}}^{\mathrm{o}}\right]}{dt} = k_{+}^{\mathrm{Lv}}[L_{\mathrm{V}}]\left[S_{\mathrm{W}}^{\mathrm{o}}\right] - k_{-}\left[S_{\mathrm{L}}^{\mathrm{o}}\right] - k_{\mathrm{f}}\left(\left[S_{\mathrm{L}}^{\mathrm{o}}\right] - \left[S_{\mathrm{L}}^{\mathrm{i}}\right]\right) \\ \dfrac{d\left[S_{\mathrm{L}}^{\mathrm{i}}\right]}{dt} = +k_{\mathrm{f}}\left(\left[S_{\mathrm{L}}^{\mathrm{o}}\right] - \left[S_{\mathrm{L}}^{\mathrm{i}}\right]\right) \end{cases} \tag{4.24}$$

The relative weights of the fast and slow steps reflect the equilibrium association of the amphiphile with the lipid in the outer leaflet and with the total lipid (outer and inner leaflet). For very small lipid concentrations, doubling the amount of lipid leads to a proportional increase in the amount of amphiphile associated with the membrane. In this case equal weight is expected for the fluorescence increase in the fast and slow processes of interaction with the LUVs. On the other hand, for very large concentrations of lipid all the amphiphile associates with the outer leaflet of the liposomes and the equilibration with the inner leaflet does not lead to any further fluorescence variation. The optimal range of lipid concentrations to characterize the rate constants for interaction with the outer leaflet and the rate constant for translocation, depends on the fraction of amphiphile associated with the lipid bilayer at equilibrium, which in turn depends on the liposome concentration and equilibrium constant for association with the liposome:

$$\begin{aligned} &[S_{\mathrm{L}}]_{(\mathrm{fast})} = [S_{\mathrm{T}}]\frac{K_{\mathrm{Lv}}[L_{\mathrm{V}}]}{1 + K_{\mathrm{Lv}}[L_{\mathrm{V}}]}; \quad [S_{\mathrm{L}}]_{(\infty)} = [S_{\mathrm{T}}]\frac{2K_{\mathrm{Lv}}[L_{\mathrm{V}}]}{1 + 2K_{\mathrm{Lv}}[L_{\mathrm{V}}]} \\ &\Delta_{(\mathrm{slow})} = \frac{[S_{\mathrm{L}}]_{(\infty)} - [S_{\mathrm{L}}]_{(\mathrm{fast})}}{[S_{\mathrm{L}}]_{(\infty)}} = \frac{1}{2}\,\frac{1}{1 + K_{\mathrm{Lv}}[L_{\mathrm{V}}]}, \end{aligned} \tag{4.25}$$

where $[S_{\mathrm{L}}]_{(\mathrm{fast})}$ is the concentration of amphiphile associated with the outer leaflet of the liposomes before equilibration with the inner leaflet, and $[S_{\mathrm{L}}]_{(\infty)}$ is the concentration of amphiphile associated with the liposomes after equilibration with both the outer and inner leaflet; K_{Lv} is the equilibrium association constant

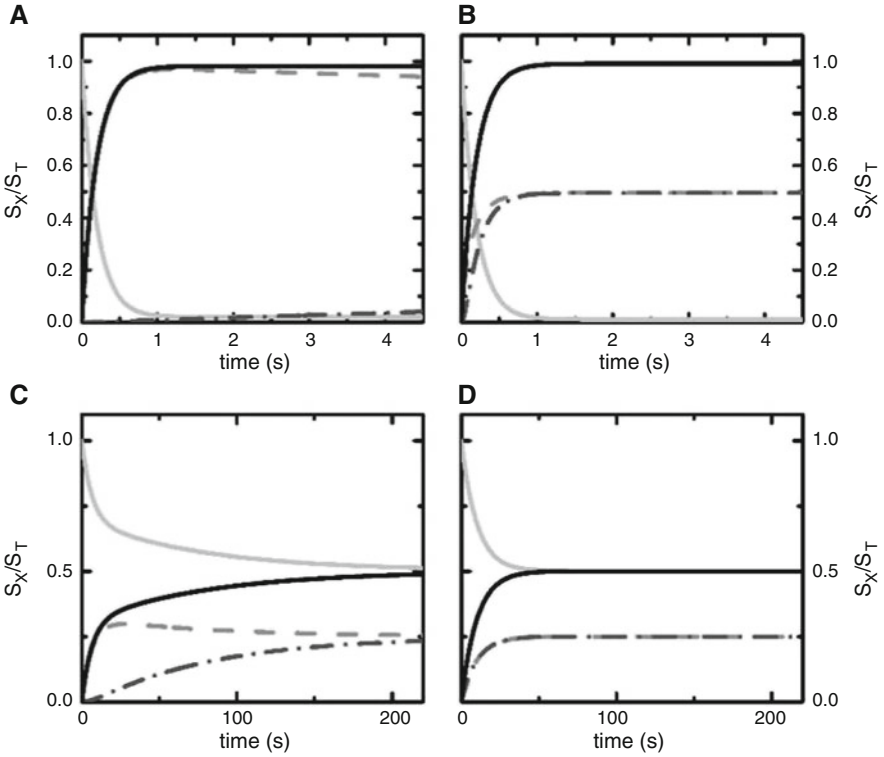

Fig. 4.2 Kinetics of equilibration of an amphiphile from the aqueous phase to liposomes. The rate constants for insertion and desorption are the same in all panels $\left(k_+^{\mathrm{Lv}} = 5 \times 10^8 \mathrm{M}^{-1}\mathrm{s}^{-1}, k = 10^{-1}\ \mathrm{s}^{-1}\right)$ while translocation is slow in panels A/C ($k_f = 10^{-2}\ \mathrm{s}^{-1}$) and fast in panels B/D ($k_f = 10\ \mathrm{s}^{-1}$). The liposome concentration is 10^{-8} and 10^{-10} M (corresponding to a lipid concentration of 1 mM and 10 μM for 100 nm LUVs) in panels A/B and C/D, respectively. The concentration of solute in the distinct compartments (S_W^o ——, S_L^o – –, S_L^i -·-·-, and the total amphiphile associated with the liposome S_L ——) have been calculated by numerical integration of Eq. (4.24)

with the outer leaflet $\left(K_{\mathrm{Lv}} = k_+^{\mathrm{Lv}}/k_-\right)$, and $\Delta_{(\mathrm{slow})}$ is the amplitude of the slow process relative to the total fluorescence variation.

The effect of the rate of translocation and liposome concentration on the time evolution of the concentration of solute associated with the liposome is shown in Fig. 4.2. When the lipid concentration is high (panels A and B) all the solute interacts with the liposomes, even when the inner leaflet is not accessible (slow translocation, panel A). At long times, the solute in the outer leaflet equilibrates with the inner leaflet but without any effect in the total amount of solute associated with the liposome. The two situations (A and B) cannot be distinguished simply by the analysis of the fluorescence variation (proportional to the total amount of solute associated with the liposome, S_L) because both the time dependence and the

amplitude of the variation are the same. On the other hand, for sufficiently small liposome concentrations (panels C and D), the initial accumulation of solute in the outer leaflet is smaller than the equilibrium value when both the outer and inner leaflets are accessible. In this case, a slow process is observed in the case of slow translocation (panel C), with a relative amplitude $\Delta_{(slow)}$ equal to 0.33 for the parameters considered in this simulation.

When both a fast and a slow process are identified in the fluorescence variation associated with the equilibration of an amphiphile with liposomes, special attention should be given to investigate the possibility of amphiphile aggregation in the aqueous phase, as this may be the origin of the fluorescence variation not following a single-exponential function. This may be done through the dependence of the relative amplitude of the slow process with the liposome concentration, Eq. (4.25), and also through its dependence on the total amphiphile concentration while maintaining the liposome concentration (the rate and weight of the slow step are expected to be independent on the total amphiphile concentration if it reflects translocation). A small local concentration of amphiphile in the lipid bilayer should be used when performing this evaluation because high local concentrations may affect its rate of translocation [28, 29].

The independent evaluation of the rate of translocation would simplify significantly the assignment of the kinetic steps to the distinct rates observed in the fluorescence variation. This is the case for NBD-labelled amphiphiles due to their fast and irreversible reaction with dithionite [2, 27, 30]. The comparison between the rate of fluorescence decrease when dithionite is added to pre-equilibrated liposomes containing the NBD-amphiphile and the fluorescence variation observed when liposomes are added to the amphiphile in the aqueous media, allows the unequivocal identification of the kinetic steps involved [2, 27]. For this goal it is mandatory that dithionite can only react with the NBD-amphiphile located in the outer leaflet. The amount of dithionite that has permeated to the aqueous media inside the liposomes may be evaluated from its rate of permeation [2], leading to less than 1% of the concentration outside the liposomes 1 h after addition to 100 nm LUVs prepared from POPC, 2 h for membranes prepared from POPC/Chol 1:1, and 20 h for the case of liposomes prepared from SM/Chol 6:4, at 35 °C [2]. Whether this small dithionite concentration is negligible or not depends on the rate of its reaction with the NBD amphiphile, because what is important is that the NBD amphiphile does not react with dithionite while it is located in the inner leaflet of the liposomes.

This methodology has been followed to obtain all the rate constants for the interaction of fluorescent amphiphiles with lipid bilayers; namely for NBD-labelled fatty amines with a short alkyl chain [27], lyso-phospholipids [31], short acyl chain phospholipids [32], and deuteroporphyrin [33]. The rate constants for insertion and desorption have also been characterized for the interaction of a quaternary alkyl amine (labelled with 7-hydroxycoumarin) with lipid bilayers with several lipid compositions and in distinct phases [34, 35].

Some of the kinetic parameters for the interaction of non-fluorescent amphiphiles have also been characterized. For this purpose, most approaches are still based on fluorescence [21, 36], although other methodologies such as isothermal titration calorimetry [28] and nuclear magnetic resonance [37] have also been used.

4.1.3 *Solutes with Very Low Solubility in the Aqueous Media and a High Partition into the Lipid Bilayer*

The section above describes methodologies to characterize the kinetics of association of amphiphiles with liposomes where the amphiphile is initially in the aqueous phase in the monomeric state. This requires that the solubility of the amphiphile in the aqueous media is significant. Usually near 1 μM is required although concentrations as small as a few nM have been used for amphiphiles with a high fluorescent quantum yield when associated with the lipid bilayer and a low fluorescence in the aqueous phase, as is the case for NBD-labelled amphiphiles [27]. The kinetic parameters for the interaction of amphiphiles with very low solubility in the aqueous phase must be characterized through their exchange between distinct binding agents. The only requirement for the donor and acceptor binding agents is that at least one fluorescence parameter of the amphiphile (fluorescence intensity, spectrum, lifetime and/or anisotropy) changes when the latter is associated with one or the other binding agents. Countless variations may be encountered on this approach.

The kinetic scheme that describes the equilibration of an amphiphile between donor and acceptor LUVs is given below:

$$\begin{aligned} S_{\mathrm{W}}^{\mathrm{o}} + L_{\mathrm{V}}^{\mathrm{D}} &\underset{k_-^{\mathrm{D}}}{\overset{k_+^{\mathrm{L_V^D}}}{\rightleftarrows}} S_{\mathrm{L}}^{\mathrm{Do}} \overset{k_{\mathrm{f}}^{\mathrm{D}}}{\leftrightarrow} S_{\mathrm{L}}^{\mathrm{Di}} \\ S_{\mathrm{W}}^{\mathrm{o}} + L_{\mathrm{V}}^{\mathrm{A}} &\underset{k_-^{\mathrm{A}}}{\overset{k_+^{\mathrm{L_V^A}}}{\rightleftarrows}} S_{\mathrm{L}}^{\mathrm{Ao}} \overset{k_{\mathrm{f}}^{\mathrm{A}}}{\leftrightarrow} S_{\mathrm{L}}^{\mathrm{Ai}}, \end{aligned} \tag{4.26}$$

where the superscript D/A represents the donor and acceptor vesicles, respectively.

The time variations in the concentration of amphiphile in the distinct compartments may be obtained from the numerical integration of the differential equations obtained from the above kinetic scheme, Eq. (4.27):

$$\begin{cases} \dfrac{d\left[S_{\mathrm{W}}^{\mathrm{o}}\right]}{dt} = k_-^{\mathrm{D}}\left[S_{\mathrm{L}}^{\mathrm{Do}}\right] + k_-^{\mathrm{A}}\left[S_{\mathrm{L}}^{\mathrm{Ao}}\right] - \left(k_+^{\mathrm{L_V^D}}\left[L_{\mathrm{V}}^{\mathrm{D}}\right] + k_+^{\mathrm{L_V^A}}\left[L_{\mathrm{V}}^{\mathrm{A}}\right]\right)\left[S_{\mathrm{W}}^{\mathrm{o}}\right] \\ \dfrac{d\left[S_{\mathrm{L}}^{\mathrm{Do}}\right]}{dt} = k_+^{\mathrm{L_V^D}}\left[L_{\mathrm{V}}^{\mathrm{D}}\right]\left[S_{\mathrm{W}}^{\mathrm{o}}\right] - k_-^{\mathrm{D}}\left[S_{\mathrm{L}}^{\mathrm{Do}}\right] - k_{\mathrm{f}}^{\mathrm{D}}\left(\left[S_{\mathrm{L}}^{\mathrm{Do}}\right] - k_-^{\mathrm{D}}\left[S_{\mathrm{L}}^{\mathrm{Di}}\right]\right) \\ \dfrac{d\left[S_{\mathrm{L}}^{\mathrm{Di}}\right]}{dt} = k_{\mathrm{f}}^{\mathrm{D}}\left(\left[S_{\mathrm{L}}^{\mathrm{Do}}\right] - k_-^{\mathrm{D}}\left[S_{\mathrm{L}}^{\mathrm{Di}}\right]\right) \\ \dfrac{d\left[S_{\mathrm{L}}^{\mathrm{Ao}}\right]}{dt} = k_+^{\mathrm{L_V^A}}\left[L_{\mathrm{V}}^{\mathrm{A}}\right]\left[S_{\mathrm{W}}^{\mathrm{o}}\right] - k_-^{\mathrm{A}}\left[S_{\mathrm{L}}^{\mathrm{Ao}}\right] - k_{\mathrm{f}}^{\mathrm{A}}\left(\left[S_{\mathrm{L}}^{\mathrm{Ao}}\right] - k_-^{\mathrm{A}}\left[S_{\mathrm{L}}^{\mathrm{Ai}}\right]\right) \\ \dfrac{d\left[S_{\mathrm{L}}^{\mathrm{Ai}}\right]}{dt} = k_{\mathrm{f}}^{\mathrm{A}}\left(\left[S_{\mathrm{L}}^{\mathrm{Ao}}\right] - k_-^{\mathrm{A}}\left[S_{\mathrm{L}}^{\mathrm{Ai}}\right]\right) \end{cases} . \tag{4.27}$$

In some situations approximations may be assumed which greatly simplify the set of differential equations and may lead to a simple analytical solution. When the solubility in the aqueous phase is very low, the steady-state approximation for the amphiphile in this compartment may be assumed because it corresponds to a negligible fraction of the total amphiphile.

$$\frac{d\left[S_{\mathrm{W}}^{\mathrm{o}}\right]}{dt} = 0; \quad \left[S_{\mathrm{W}}^{\mathrm{o}}\right] = \frac{k_{-}^{\mathrm{D}}\left[S_{\mathrm{L}}^{\mathrm{Do}}\right] + k_{-}^{\mathrm{A}}\left[S_{\mathrm{L}}^{\mathrm{Ao}}\right]}{k_{+}^{\mathrm{L_V^D}}\left[L_{\mathrm{V}}^{\mathrm{D}}\right] + k_{+}^{\mathrm{L_V^A}}\left[L_{\mathrm{V}}^{\mathrm{A}}\right]} \tag{4.28}$$

If the rate of solute translocation in both the donor and acceptor liposomes is much smaller than the rate of exchange between the liposomes, only the solute in the outer leaflet of the donor liposome is able to equilibrate with the outer leaflet of the acceptor liposome. In this case, the exchange between the donor and acceptor liposomes follows a single-exponential function and the rate constant for exchange (k) is given by:

$$k = \frac{k_{+}^{\mathrm{L_V^A}}\left[L_{\mathrm{V}}^{\mathrm{A}}\right]k_{-}^{\mathrm{D}} + k_{+}^{\mathrm{L_V^D}}\left[L_{\mathrm{V}}^{\mathrm{D}}\right]k_{-}^{\mathrm{A}}}{k_{+}^{\mathrm{L_V^A}}\left[L_{\mathrm{V}}^{\mathrm{A}}\right] + k_{+}^{\mathrm{L_V^D}}\left[L_{\mathrm{V}}^{\mathrm{D}}\right]}. \tag{4.29}$$

It should be recalled that the above derivation assumed a negligible amount of solute in the aqueous phase at all times, that means $K_{\mathrm{L_V}}^{\mathrm{L_V^D}}\left[L_{\mathrm{V}}^{\mathrm{D}}\right] \gg 1$ where $K_{\mathrm{L_V}}^{\mathrm{L_V^D}}$ is the equilibrium constant for the solute between the aqueous phase and the outer leaflet of the donor liposomes, $K_{\mathrm{L_V}}^{\mathrm{L_V^D}} = k_{+}^{\mathrm{L_V^D}}/k_{-}^{\mathrm{D}}$.

When the rate constants for interaction of the amphiphile with the donor and acceptor liposomes are the same, Eq. (4.29) simplifies to $k = k_{-}^{\mathrm{D}} = k_{-}^{\mathrm{A}}$, that is the rate constant for exchange becomes equal to the rate constant of desorption. Therefore, when the lipid composition of the donor and acceptor liposomes is very similar, it is not possible to obtain the rate constant for insertion. Additionally, changing the concentration of acceptor liposomes does not affect the rate constant of exchange. The case of exchange between liposomes with the same properties will be further analyzed and discussed below in relation with Fig. 4.3.

If translocation through both the donor and acceptor liposomes is much faster than the rate of exchange, the expression for the rate constant of exchange is half the value obtained by Eq. (4.29) because only half of the total amphiphile exchanging between the two liposome populations is directly accessible to the aqueous phase that mediates the exchange process (the solute in the outer leaflet). Relevant variations in those exchange experiments may involve lipoproteins or small unilamelar vesicles (SUVs). In this case the fraction of solute directly accessible to the aqueous phase may be different from one half, and the equations derived for the rate constant of exchange will be different [26, 27].

The expression obtained for the rate constant of solute exchange between two populations of LUVs, Eq. (4.29), depends on four unknown parameters: the rate constants for insertion into the outer leaflet of the donor and acceptor liposomes

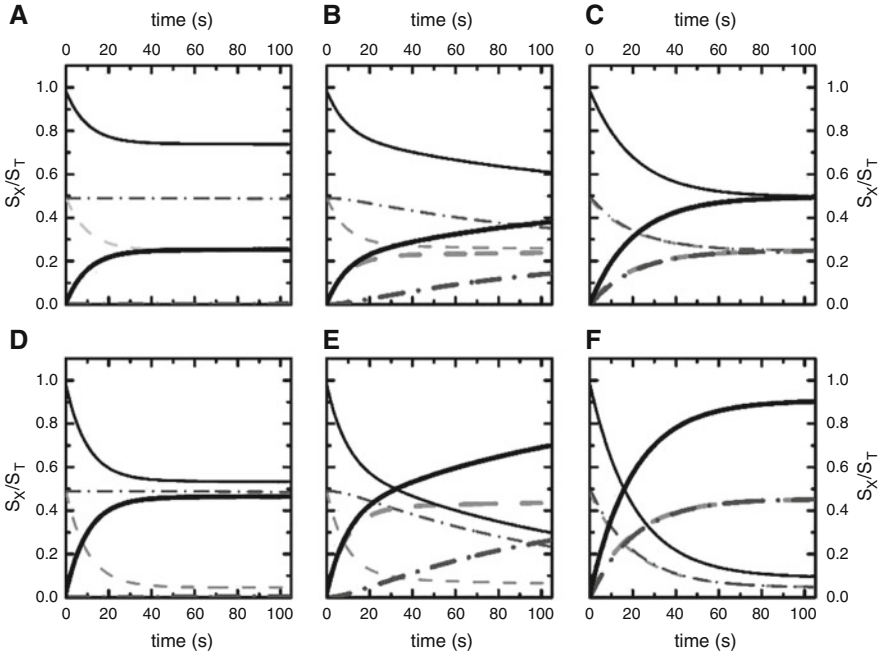

Fig. 4.3 Effect of the rate of translocation and acceptor concentration on the kinetics of solute exchange between LUVs with the same lipid composition. The rate constants of insertion and desorption are the same in all panels, $k_+^{L_V^D} = k_+^{L_V^A} = 5 \times 10^9\ M^{-1}\,s^{-1}$; $k_-^D = k_-^A = 0.1\ s^{-1}$, as well as the concentration of donor liposomes, 5×10^{-10} M (corresponding to 50 μM lipid for 100 nm LUVs) and solute (10^{-6} M). The concentration of acceptor liposomes is the same as that of donor liposomes in panels A, B and C, and is 10 times larger in panels D, E and F. The rate constant for translocation is $10^{-3}\ s^{-1}$ (panel A and D), $10^{-2}\ s^{-1}$ (panel B and E) and $1\ s^{-1}$ (panel C and F). The concentrations of solute in the distinct compartments (S_L^{Xo} – –, S_L^{Xi} -·-·-, S_L^X —; with the concentrations in the donor compartment in thinner lines and those in the acceptor compartment in thicker lines) were calculated through the numerical integration of Eq. (4.27)

$\left(k_+^{L_V^D}\right.$ and $\left.k_+^{L_V^A}\right)$, and the rate constants for desorption from the outer leaflet of the liposomes $\left(k_-^D\right.$ and $\left.k_-^A\right)$. By performing the exchange experiments at distinct concentration ratios of donor and acceptor liposomes it is possible to obtain the rate constants for desorption from the donor and acceptor liposomes (see Fig. 4.4 and discussion below). When the concentration of acceptor liposomes is much larger than that of donors, the rate constant for exchange approaches the rate constant for desorption from the donor liposomes; while at very small concentrations of acceptor liposomes, the rate constant for exchange tends towards the rate constant for desorption from the acceptor liposomes. The total concentration of liposomes should be high enough to guarantee the validity of the steady-state approximation, but at relatively low values to ensure that exchange occurs through the aqueous compartment and not due to collisions between the liposomes

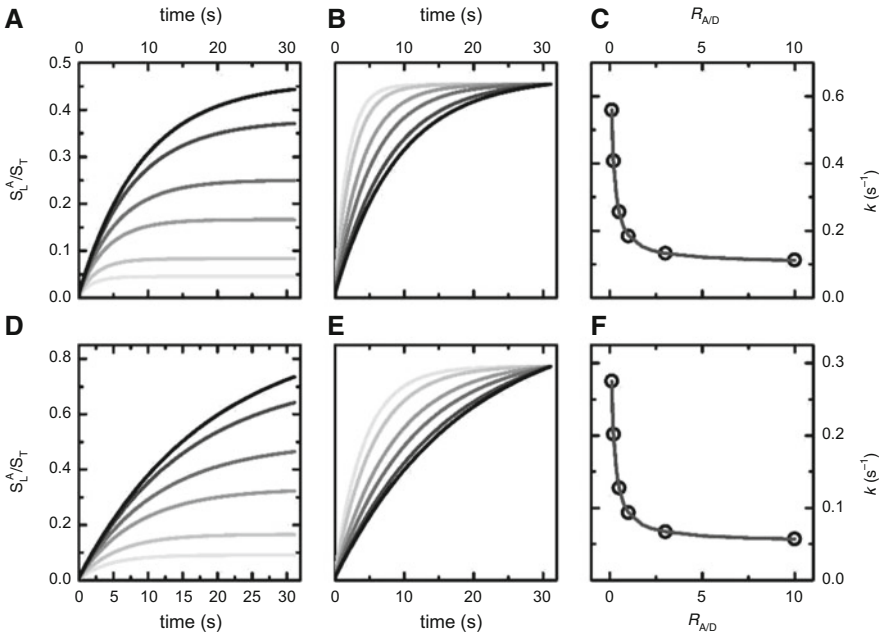

Fig. 4.4 Effect of the concentration of acceptor liposomes in the rate and extent of exchange for donor and acceptor liposomes with distinct properties. The rate constants of insertion and desorption are the same in all panels: $k_+^{L^D_V} = 5 \times 10^9\,M^{-1}s^{-1}$, $k_+^{L^A_V} = 5 \times 10^{10}\,M^{-1}\,s^{-1}$, $k_-^D = 0.1\,s^{-1}$, $k_-^A = 1\,s^{-1}$, as well as the concentration of donor liposomes, 1×10^{-9} M (corresponding to 0.1 mM lipid for 100 nm LUVs) and total solute (10^{-6} M). The top panels (A to C) illustrate the case of slow translocation ($k_f^D = k_f^A = 10^{-4}\,s^{-1}$) while in panels D to F the translocation is faster than exchange ($k_f^D = k_f^A = 10\,s^{-1}$). Note the different scales in the upper and lower panels. The concentration of acceptor LUVs is equal to 1×10^{-10} (—), 2×10^{-10} (—), 5×10^{-10} (—), 1×10^{-9} (—), 3×10^{-9} (—) and 1×10^{-8} M (—). The data in plots A, B, D and E was obtained through the numerical integration of Eq. (4.27), in the central panels the concentration in the acceptor liposomes was normalized to its value at 30 min to highlight the different kinetics. The rate constants of exchange shown in plots C and F were obtained from the best fit of a single-exponential function to the time dependent concentration of solute in the acceptor liposomes (S_L^A) shown in plots A and D respectively; the lines in plots C and F are the best fit of Eq. (4.31) with the parameters: $a_0 = 1.0$, $a_\infty = 0.10$ and $b = 9.9$ for plot C and $a_0 = 0.49$, $a_\infty = 0.052$ and $b = 9.6$ for plot F

[38, 39]. Using this methodology, it is also possible to obtain the ratio between the rate constants for insertion in the donor and acceptor liposomes. To characterize the rate constants for insertion in each liposome, it is necessary to obtain independently the equilibrium constant for association with at least one liposome population.

The above models predict a single-exponential function for the time variation of the signal due to exchange between the donor and the acceptor binding agents, this reflecting a very slow or very fast translocation. To characterize the rate of translocation using exchange experiments, it is necessary to change the conditions in order to alter the relative rates of translocation and insertion/desorption so as to

occur in similar time scales. This may be achieved through variations in the solution pH and/or temperature. If the signal variation due to exchange does not follow a single-exponential, there is no simple analytical expression to allow the calculation of the intrinsic rate constants from the observed rate of exchange. In this case it is advisable to perform the numerical integration of the differential equations, although important information may be obtained from the best fit with a two-exponential function. The case of exchange between liposomes with distinct properties will be further analyzed and discussed below in relation with Fig. 4.4.

The simulation of the time variation in the solute concentration for donor and acceptor liposomes with the same lipid composition is shown in Fig. 4.3 for different rate constants and liposome concentrations. In panels A and D, translocation is much slower than exchange between the liposomes and only the solute in the outer leaflet of the donor liposomes equilibrates with the outer leaflet of the acceptor liposomes. The amount of solute that is transferred to the acceptor liposomes is dependent on the relative concentrations of donor and acceptor liposomes, being larger for higher ratios of acceptor/donor liposomes (in panel A the liposome concentration is 5×10^{-10} M for both donor and acceptor while in panel D there is a tenfold excess of acceptor liposomes). However, the rate constant for the exchange is the same in both situations, and equal to the rate of desorption (which is the same for both donor and acceptor liposomes). The effect of the concentration of acceptor liposomes for the case of fast translocation is shown in panels C and F with a larger fraction of solute exchanged when the concentration of acceptor liposomes is increased, while keeping the same time dependence. The exchange rate constant obtained in panels C and F is half the value of the rate constant for desorption (observed in panels A and D), due to the fact that all solute is exchanging but only that in the outer leaflets is in contact with the aqueous phase that mediates the exchange process. The case of translocation slower than exchange between the outer leaflets, but occurring in similar time scales, is shown in panels B and E. The total amount of solute transferring towards the acceptor vesicles is affected by the relative concentration of donor and acceptor, but the relative amplitudes of the fast and slow processes are unchanged. The correct description of the concentrations time dependence (amplitude and rate constants) requires the numerical integration of the differential equations. However, a good approximation is obtained for the rate constants (desorption and translocation) through the best fit of a bi-exponential equation such as Eq. (4.30) for the concentration of solute in the acceptor liposomes.

$$S_{\mathrm{L}}^{\mathrm{Ao}} \cong a_1\left(1 - e^{-k_1 t}\right) + a_2\left(1 - e^{-k_2 t}\right) \tag{4.30}$$

The main disadvantage of this approach is that the relative amplitudes of the fast and slow steps are not simply the fractions of solute in the outer and inner leaflets, precluding the validation of the slow step as being translocation (and not an artifact such as amphiphile aggregation).

Simulations of the time variation in the concentration of solute in the acceptor liposomes for the case of donor and acceptor liposomes with distinct properties are shown in Fig. 4.4. Transfer is considered at distinct relative concentrations of donor and acceptor liposomes ($R_{A/D}$), for the two limit situations of slow (panels A to C) and fast translocation (panels D to F).

As the concentration of acceptor liposomes increases, the amount of solute that exchanges from the donor to the acceptor liposomes increases (panels A and D). The initial rate of transfer is independent on the concentration of acceptor. However, the rate constant for the exchange process becomes lower as the concentration of acceptor liposomes is increased, because the solute transfer proceeds during a longer time interval (panels B and E) [20]. Both sets of simulations lead to a single-exponential function for the time dependence of the concentration of solute in the acceptor liposomes. The rate constant of exchange may be obtained from the best fit of a single-exponential function to the time variation in the property being observed (fluorescence from the solute or any other property proportional to the concentration of the solute in the acceptor liposomes). The dependence of the exchange rate constant on the ratio between the concentrations of donor and acceptor liposomes is shown in plot C and F, together with the best fit of the general function shown in Eq. (4.31) which has the same dependence on $R_{A/D}$ as Eq. (4.29) but is valid for any fraction of exchangeable solute.

$$k = \frac{b\ a_\infty R_{A/D} + a_0}{1 + b\ R_{A/D}} \tag{4.31}$$

For the case of exchange between LUVs, b gives the ratio between the rate constants for insertion in the acceptor and donor liposomes ($k_+^{L_V^A}/k_+^{L_V^D}$), whereas the parameters a_0 and a_∞ are related with the rate constants of desorption from the acceptor and donor binding agents, respectively. If the approximation of slow translocation is valid, $a_0 = k_-^A$ and $a_\infty = k_-^D$; while if translocation is fast $a_0 = \frac{k_-^A}{2}$ and $a_\infty = \frac{k_-^D}{2}$. The values obtained for the kinetic parameters using this methodology are essentially equal to the values considered in the simulations (see Fig. 4.4).

As was discussed, to characterize the kinetics of interaction of poorly water soluble solutes with lipid membranes, an exchange protocol between two binding agents must necessarily be used. However, the donor and acceptor binding agents do not need to be both liposomes. An approach frequently used is to first equilibrate the solute with an aqueous soluble protein (such as serum albumin) and follow the kinetics of equilibration with the acceptor liposomes. In this case the interaction between the solute and the protein is usually faster than transfer to the liposomes. This situation greatly simplifies the equations that describe the exchange process because the fast equilibration approximation may be used. Additionally, all solute bound to the protein (binding agent, B) is accessible to the aqueous media, kinetic scheme below.

$$
\begin{aligned}
&S_{\mathrm{W}}^{\mathrm{o}} + B \overset{K_{\mathrm{B}}}{\leftrightarrow} S_{\mathrm{B}} \\
&S_{\mathrm{W}}^{\mathrm{o}} + L_{\mathrm{V}}^{\mathrm{A}} \underset{k_{-}^{\mathrm{A}}}{\overset{k_{+}^{L_{\mathrm{V}}^{\mathrm{A}}}}{\rightleftarrows}} S_{\mathrm{L}}^{\mathrm{Ao}} \overset{k_{\mathrm{f}}^{\mathrm{A}}}{\leftrightarrow} S_{\mathrm{L}}^{\mathrm{Ai}}
\end{aligned}
\tag{4.32}
$$

The fast equilibrium approximation for the intermediate (solute in the aqueous phase) is given by:

$$
\left[S_{\mathrm{W}}^{\mathrm{o}}\right] = \left([S_{\mathrm{T}}] - \left[S_{\mathrm{L}}^{\mathrm{A}}\right]\right)\frac{1}{1 + K_{\mathrm{B}}[B]}, \tag{4.33}
$$

and the rate constant for exchange is given by one of the two Eqs. (4.34), depending on whether translocation into the inner leaflet of the acceptor liposome is much slower or much faster than interaction with the outer leaflet:

$$
\begin{aligned}
k &= k_{-}^{L_{\mathrm{V}}^{\mathrm{A}}} + \frac{k_{+}^{L_{\mathrm{V}}^{\mathrm{A}}}[\mathrm{L_V}]}{1 + K_{\mathrm{B}}[\mathrm{B}]_{\mathrm{T}}} \quad \text{slow translocation} \\
k &= \frac{k_{-}^{L_{\mathrm{V}}^{\mathrm{A}}}}{2} + \frac{k_{+}^{L_{\mathrm{V}}^{\mathrm{A}}}[\mathrm{L_V}]}{1 + K_{\mathrm{B}}[\mathrm{B}]_{\mathrm{T}}} \quad \text{fast translocation}
\end{aligned}
\tag{4.34}
$$

As a final remark on those exchange protocols one should note that to obtain the rate constant of transfer the property being followed must be proportional to the concentration of solute in the compartment of interest. Additionally, to avoid the physical separation between the solute associated with the donor and acceptor compartments, the relation between the property and solute concentration must be different for the distinct compartments. Furthermore, the relations must be quantitatively known if the equilibrium constants are to be obtained, and/or, if the identity of the slow step is to be validated from the relative amplitude of signal variation due to this process.

There are several examples in the literature with the characterization of the exchange rate for fluorescent amphiphiles. In some studies, a clear minority, it was possible to obtain all the rate constants involved. It is worth mentioning the early work by Nichols and co-workers with the characterization of the rate constants of insertion and desorption of phospholipids with the fluorescent group NBD attached to the acyl chain of phosphatidylcholines (NBD-PC) [32, 40]. The transfer of NBD-PC was followed through quenching of its fluorescence in one of the compartments due to self-quenching or to fluorescence resonance energy transfer (FRET) to rhodamine labelled phospholipid. All the parameters were characterized for the transfer between bovine serum albumin (BSA) and LUVs, for alkyl amines with different length (labeled with NBD in the amine group, NBD-C_n) [27], phosphatidylethanolamine with NBD in the polar head group (NBD-DMPE) [2, 41] and dehydroergosterol; [42] the exchange being followed via the different fluorescence quantum yield of the fluorescent amphiphiles in the donor and acceptor binding agents. The rate of desorption from LUVs for several pyrene labelled phospholipids has also been characterized [43, 44], as well as the rate of

translocation; [45] transfer being followed via the decrease in the formation of pyrene excimers. The rate constants for desorption and translocation of fatty acids labelled with the fluorescent group 9-anthroyloxy has also been characterized through the exchange between BSA and liposomes (based on the distinct quantum yield of the fluorophore) [46], or exchange between liposomes (with the incorporation of a FRET acceptor in the donor or acceptor liposomes) [47].

Fluorescence based methods have also been used to characterize the exchange of non-fluorescent amphiphiles, such as fluorescence quenching of the protein used as donor or acceptor [48–50], pH and electrostatic potential variations at the surface of the liposomes and/or in the bulk aqueous compartments for the case of exchange of weak acids and bases or charged amphiphiles [49, 50].

4.2 Molecular Dynamics Simulations to Characterize the Interaction and Permeation of Small Molecules Through Lipid Bilayers

Molecular dynamics (MD) simulations are a powerful tool to study the interaction of amphiphiles with lipid membranes, as they can give atomistic insight into processes and phenomena that often cannot be considered experimentally in sufficient detail [51, 52]. Additionally, the field of MD simulations in biological sciences has developed to a level where predictions of new phenomena are frequently being made, thereby generating quite important added value to complement experiments. Indeed, currently there is a variety of software applications and methodologies that makes the MD simulations easily accessed by the scientific community [53]. In the context of the interaction of amphiphilic molecules with lipid membranes, one of the central simulation techniques involves the calculation of free energies [54]. Most commonly, sampling strategies are used, notably the use of biased simulations through the Umbrella Sampling (US) [55, 56] method to calculate the Potential of Mean Force (PMF) profiles for the amphiphiles interacting with a lipid bilayer. Previous work has resulted in PMF profiles for the interaction of a variety of solutes with different bilayer compositions [57–77]. In addition to disclosing mechanistic details, these data are highly useful since they may depict the free energy barriers associated with insertion, translocation and desorption, and hence allow the computation of their rates as well as equilibrium constants [78, 79]. In this context, the systematic comparison and validation between experimental and simulation data is imperative. However, this may not be a straightforward challenge.

4.2.1 General Description on the Generation of the PMF Profile Through Lipid Bilayers

The concept of PMF was originally introduced by Kirkwood [80]. Regarding the interaction of solutes with lipid bilayers, the energy profile across the bilayer normal allows the calculation of the free energy barriers for the processes of insertion, desorption and translocation, which are the individual microscopic steps for membrane permeation. US [55, 56] is probably the most popular technique to compute the PMF along a given reaction coordinate. This technique aims to overcome limited sampling at energetically unfavorable configurations by restraining the simulation system with an additional (typically harmonic) potential [55]. Conjugated with the explicit umbrella potential, stratification strategies are used [81], whereby the reaction pathway is divided into a large number of small overlapping windows.

Generally, to calculate the PMF of the interaction of amphiphiles with lipid bilayers using US, a set of initial structures is first generated along the reaction coordinate. Although the choice of the reaction coordinate is a highly non-trivial matter, especially with complex molecules, the most immediate and simplest choice is usually the distance from the molecule to the membrane's center of mass (COM) along the bilayer normal direction. Then, a set of production runs is carried out, applying a biasing harmonic potential between the molecule and the bilayer, relative to a reference position. From these simulations, distance distributions of the molecule's selected coordinate around the reference position are obtained. Finally, the PMF is generated, correcting for the contribution of the biasing potential [81, 82].

Accordingly, a set of N_w separate umbrella simulations, corresponding to each umbrella window, are carried out, with an umbrella potential,

$$w_i(\zeta) = \frac{K_i}{2}\left(\zeta - \zeta_i^c\right)^2, \tag{4.35}$$

which restrains the system at the position $\zeta_i^c (i = 1, \ldots, N_w)$ with a force constant K_i. From each of the N_w umbrella simulations an umbrella histogram $h_i(\zeta)$ is recorded, representing the probability distribution $P_i^b(\zeta)$ along the reaction coordinate biased by the umbrella potential $w_i(\zeta)$.

After running the simulations, the data of each umbrella window are subsequently pasted together using histogram based algorithms. The most widely used technique to compute the PMF from the umbrella histograms, that is, to unbias the distributions $P_i^b(\zeta)$, is probably the weighted histogram analysis method (WHAM) [83]. The purpose of WHAM is to estimate the smallest statistical uncertainty of the unbiased probability distribution from the umbrella histograms, and compute the PMF [81–83]. The unbiased probability distribution, $P(\zeta)$, is related to the PMF by

$$W(\zeta) = -k_B T \ln\left[\frac{P(\zeta)}{P(\zeta_0)}\right] \tag{4.36}$$

where, k_B is the Boltzmann constant, T is the temperature and ζ_0 is an arbitrary reference point where the PMF $W(\zeta_0)$ is defined to be zero. Following this procedure, an energy profile over a reaction coordinate is obtained, e.g. the energy profile of a molecule through the direction normal to a lipid bilayer.

4.2.2 The General Simulation Protocol

The number of umbrella sampling windows needed to generate a PMF profile makes such kind of procedures computationally demanding. For symmetric lipid bilayers the free energy profile is usually calculated for one leaflet, and the other leaflet is represented symmetrically. For a complete definition of the PMF, adjacent umbrella windows should span the space between the membrane center ($z = 0$) and the bulk water region ($z \approx 4$ nm), usually separated by 1–2 Å. Since the distribution histograms should overlap properly, the harmonic umbrella potential used to restrain the position of the amphiphile should be adapted to the umbrella spacing [81, 82]. For an asymmetric bilayer, sampling of the reaction path must be done through the entire membrane, at least doubling the computational cost. From the performed simulations, the unbiased PMF is then obtained using WHAM [81, 82].

For a given molecule, different choices of variable complexity may be adopted to define the reaction coordinate—the key parameter in free energy profile computations—of a PMF profile. Usually, the distance z of the molecule's COM, or a chemically significant atom/set of atoms (e.g. the most polar group for the case of relatively large and amphiphilic molecules), in respect to the membrane COM along the normal coordinate, is chosen as the reaction coordinate. With this definition, the location $z = 0$ nm represents thus the COM of the lipid molecules [60, 61, 84]. This choice results in the so called 1D-PMF. In order to improve sampling, the position and orientation of the molecules may be simultaneously restrained, resulting in a 2D-PMF. This type of reaction coordinate has been important to differentiate between distinct translocation mechanisms [85–87].

To obtain a PMF profile, the production simulations must start from several system configurations with the molecule at different positions of the reaction coordinate. Different procedures may be used to generate these initial structures [53]. Generation of initial structures from unrestrained simulations would be the most adequate procedure to minimize artifacts [68, 75]. However, this may be not possible for the majority of the systems where an enhanced sampling technique is used. Therefore, the most popular strategy to generate sets of initial structures for US simulations is to artificially pull the amphiphile along the reaction coordinate. In this process, slow pulling rates (e.g., ~0.005 nm/ps) and low force constants (e.g., ~500 kJ/mol/nm^2) are used in order to avoid artificial deformations of the lipid bilayer. Even with such a careful procedure, different directions of pulling (either starting at the water, WC, or at the bilayer center, CW) may not give the same results [84], as shown in Fig. 4.5. Plotting the PMF profiles obtained from the CW and WC initial pulling directions simultaneously and considering different

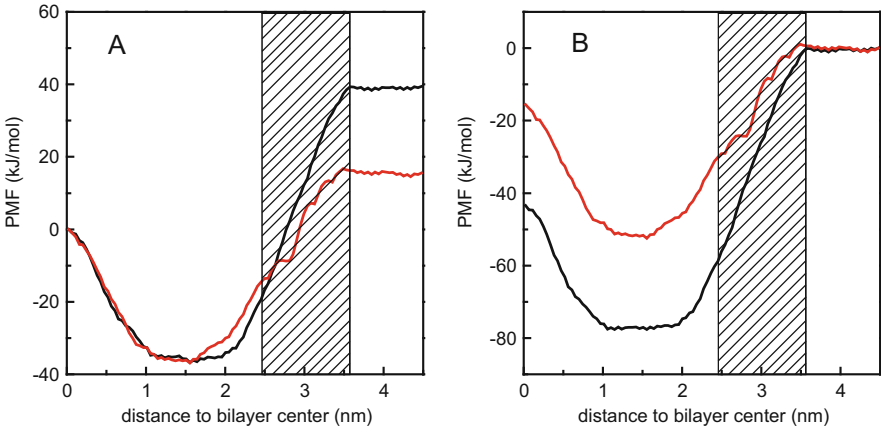

Fig. 4.5 PMF profiles of NBD-C_{16} in a POPC bilayer, calculated with the CW (*black*) and WC (*red*) schemes. In CW, the data used for analysis covered a period from 20 to 110 ns, and in WC a period from 120 ns until the end of the simulation. In (**A**) the PMF is defined to be zero in the center of the bilayer, and in (**B**) the PMF is defined to be zero in the water region. Reprinted with permission from reference [84]. Copyright 2014 American Chemical Society

reference positions (bilayer center used as reference in Fig. 4.5A and the water in Fig. 4.5B) shows that this difference is caused by poor sampling at the lipid/water interface, as highlighted by the dashed boxes in the Fig. 4.5.

4.2.3 Sampling Issues

While US is a seemingly simple technique, there are several potential problems that may compromise the quality of the results. Sampling issues may be critical in the determination of energy profiles from MD simulations. Sampling problems have been addressed by some research groups, being actively discussed in the literature [66–68, 84, 88]. If the sampling is not sufficiently extensive, then the condition of ergodicity is broken and the free energy values found through the analysis are not accurate enough. The sources of sampling problems are several, stemming from solute size, bilayer size, bilayer defects, initial conformations or choice of the reaction coordinate, usually being expressed as orthogonal degrees of freedom separated by hidden energy barriers. Strategies to overcome these problems have been reviewed [88].

Recently, the use of advanced simulation techniques has been proposed to improve sampling in the study of solute permeation through lipid membranes, focusing on the importance of orientation and conformational motions [67, 77, 85, 87, 89, 90]. A related problem regarding sampling issues concerns equilibration. For each simulation window, the system should be properly equilibrated before adequate sampling of the reaction coordinate (for WHAM analysis) can take place

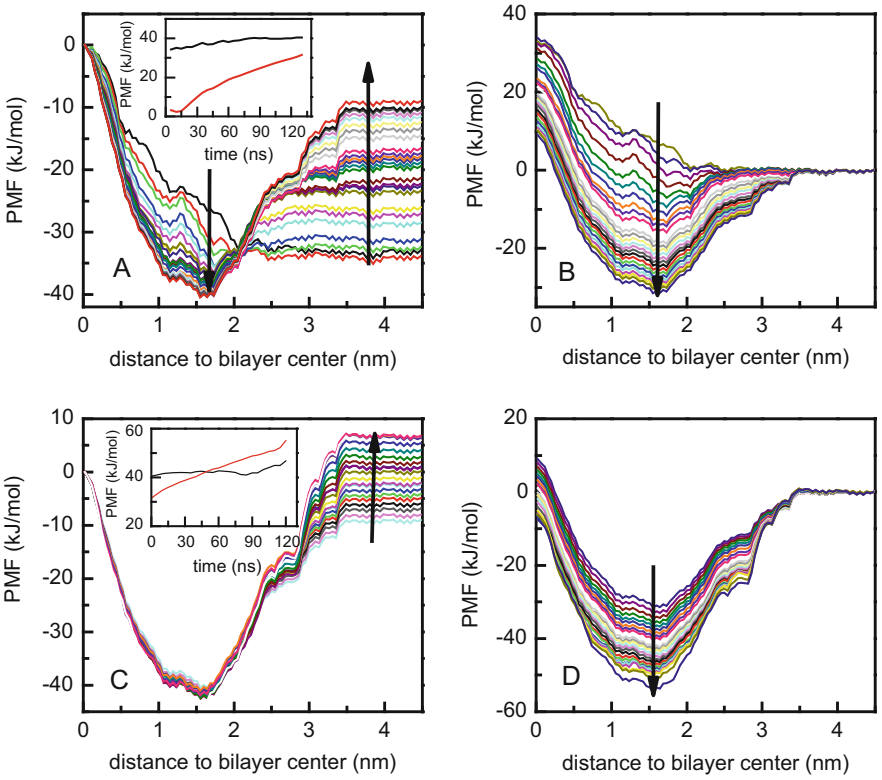

Fig. 4.6 Convergence of the PMF calculated for NBD-C_{16} in a POPC bilayer, with WC: (**A, B**) increasing the total simulation time by 5 ns intervals until the maximum simulation time of 130 ns; (**C, D**) discarding successive 5 ns intervals for equilibration with a maximum simulation time of 130 ns. The profiles shown in panels (**A, C**), and (**B, D**), have the reference position defined to be at the center of the bilayer and in the water region, respectively. The *arrows* show how the PMF profile evolves. The time dependence of the free energy barriers for translocation (*black*) and desorption (*red*) are shown as insets in panels (**A, C**). Reprinted with permission from reference [84]. Copyright 2014 American Chemical Society

[66, 67]. If these issues are not taken care of, the simulation data may include artifacts. For instance, as was shown in Fig. 4.5, when the amphiphile is pulled from the water phase to the interior of the lipid bilayer (WC), different results may be obtained compared to when the amphiphile is pulled in the opposite direction (CW). This is induced by artifacts which were shown to arise from sampling problems at the membrane-water interface, causing the simulation results to not converge despite extensive simulation times [84], as shown in Fig. 4.6. Systematic variation of PMF profiles and energy barriers, when considering different simulation times for analysis, is indicative of non-converged data.

Additionally, an appropriate choice of the reaction coordinate is decisive for finding physically correct results [84]. It has been shown that the definition of the

reaction coordinate may influence the results through generation of membrane deformations during the production runs [66]. Therefore, in each particular case, one must understand how PMF calculations should be performed to avoid any problems that would result in unphysical data. For example, the distance between the solute and a locally defined center of the bilayer (only taking into account the lipid within a cylinder centered at the solute and aligned along the z-axis) may be advantageously employed to minimize membrane deformation artifacts [84]. Alternatively, as mentioned above, in some literature reports, free energy surfaces are computed, characterized by two reaction coordinates. In these works, one of the reaction coordinates is defined as the distance to the bilayer center, and the other is an angular coordinate which accounts for solute orientation [85–87].

Despite the simulation being sampling the true energy minima, the convergence of free energy profiles should be always carefully assessed. The total simulation time for a given umbrella window includes an equilibration of the system, followed by fluctuations around equilibrium. Preferably, the PMF should be computed using only the simulation times after equilibration. The decision on whether or not the system has reached equilibrium after a given simulation time is not trivial. The final PMF (hopefully corresponding to an equilibrated system) may be evaluated in three ways:

1. assume (perhaps incorrectly) that no equilibration is needed, and in each sampling window use simulation data from increasingly long times to generate consecutive PMFs.
2. systematically increase the slice of the simulation time used for equilibration in each sampling window, and use the rest of the simulation data for analysis.
3. systematically increase the amount of data used for equilibration in each sampling window, and analyze the PMF profiles carried out over a fixed time interval (for instance tens of nanoseconds).

In all three analysis schemes, not only the values of the barriers but also the shapes of the profiles should be compared to each other [84], as exemplified in Fig. 4.7. The achievement of small and non-systematic variations of the PMF profiles and energy barriers is indicative of good convergence.

4.2.4 The General Description of the PMF Profile

The PMF profile defines the variation in the Gibbs free energy of the system as a function of the reaction coordinate, solute position relative to the center of the bilayer for the case of permeation through lipid bilayers. The energy minimum gives the equilibrium location of the solute in the hydrated bilayer, and the energy maxima correspond to transition states in the reaction pathway. For amphiphilic molecules, an energy maximum is commonly encountered at the bilayer center due to the energetically unfavorable solvation of the polar portion of the molecule by this nonpolar environment [91, 92]. An energy maximum is also frequently

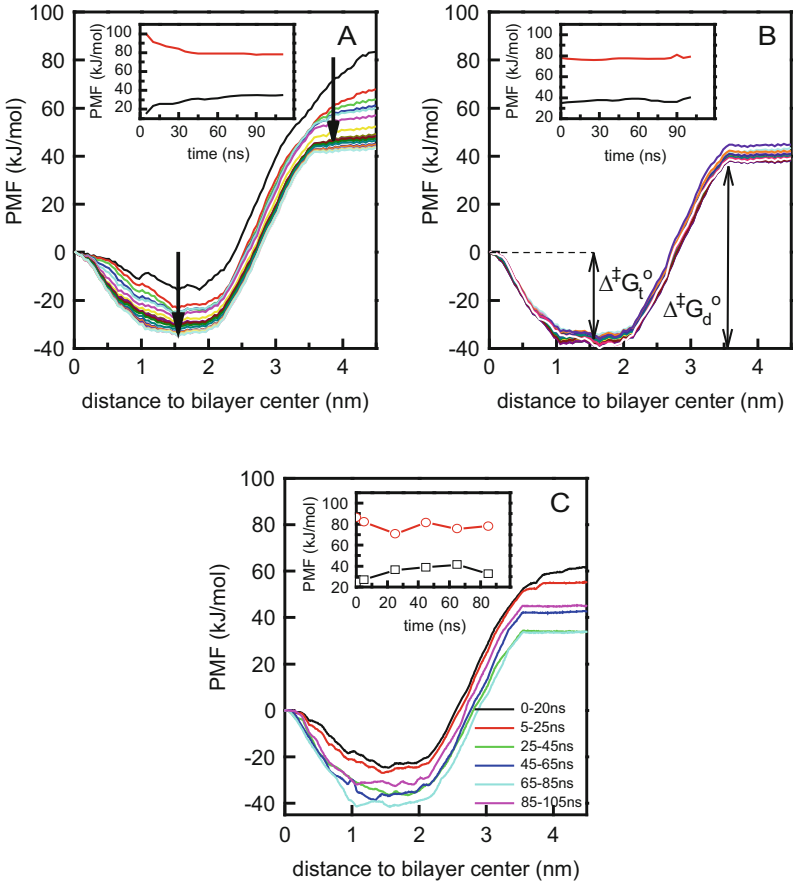

Fig. 4.7 Convergence of the PMF of NBD-C_{16} in a POPC bilayer, calculated in the CW case: (**A**) Increasing the total simulation time by 5 ns intervals until the maximum of 110 ns. The *arrows* indicate the evolution of the PMF profiles (*black line* stands for a 5 ns simulation, *red* being 10 ns, etc.). (**B**) Discarding successive 5 ns intervals from the simulation data (for equilibration) with a maximum simulation time of 110 ns. (**C**) Data analyzed over 20 ns intervals. The time dependence of the free energy barriers for translocation/flip-flop (*black*) and desorption (*red*) are shown as insets in each plot. In the middle panel, $\Delta^{\ddagger}G_t^o$ and $\Delta^{\ddagger}G_d^o$ indicate the free energy barriers for the translocation and desorption processes, respectively. Reprinted with permission from reference [84]. Copyright 2014 American Chemical Society

observed at the bilayer/water interface due to both the hydrophobic effect (as the nonpolar portion of the molecule becomes in contact with water), and to the high density of the system at this region [61, 63, 64, 84]. For amphiphiles with long and/or bulky nonpolar groups, a decrease in the system Gibbs energy when the amphiphile leaves the membrane would be expected. This is because when the nonpolar portion of the amphiphile is partially in the aqueous media and partially inserted in the bilayer, the energetic penalty arising from the hydrophobic effect is

almost complete and an extra energetic penalty is observed due to the formation of a cavity in the lipid bilayer beneath the amphiphile (with the consequent loss of lipid/lipid interactions) [32, 41, 61, 64, 93, 94]. However, for most amphiphiles, the PMF obtained does not show a decrease in energy as the amphiphile moves from its most external position at the bilayer/water interface into the bulk water, see Figs. 4.5, 4.6 and 4.7 for the case of NBD-C_{16} in POPC bilayers. When the PMF profile is analyzed from the amphiphile in bulk water towards its equilibrium position in the bilayer, the absence of an energy barrier at the bilayer/water interface indicates that insertion is a diffusion controlled process. This is in contradiction with the experimental results obtained for this system [27] and may result from poor sampling at this location in the reaction coordinate [66, 84, 88].

The energy barrier obtained from PMF profiles at the bilayer center may also not correspond to the energy required to place the polar portion of the amphiphile in the nonpolar environment of the bilayer center. This is because this configuration is not necessarily involved in the most probable translocation pathway followed by the amphiphile. However, there is not enough information available to evaluate whether this corresponds or not to the pathway observed in the real system.

A review on computational studies of translocation (flip-flop) of phospholipids, sterols and fatty acids has been recently published [95]. While in some systems the results are compatible with the polar portion of the amphiphile in the center of the lipid bilayer as the transition state [2, 84], more complex descriptions have been raised, from different transition paths [85–87, 96–98], to the formation of large pores in the lipid bilayer [61, 64, 99–103]. In the cases without pore formation, three main translocation paths have been proposed [104]. In a "push-in flip-flop", a transverse motion occurs first, followed by the rotation of the molecule; in a "sliding flip-flop", the transverse and rotational motions occur simultaneously; and in a "rotation flip-flop", the rotation motion occurs first followed by the transverse motion of the molecule. The most probable translocation pathway certainly depends on the properties of the amphiphile and lipid bilayer, as well as on the local concentration of amphiphile. The confirmation of several local minima along the translocation path will represent a challenge to the development of new mechanistically meaningful kinetic models for the analysis of experimental data.

The formation of large pores in the lipid bilayer has been implicated in the translocation of phospholipids [61, 64, 99–102]. However, the pore mediated mechanism for the translocation of phospholipid should also not be taken for granted. Lipid translocation has been observed by US simulations [61, 64] or in unrestrained simulations where pores were induced [101, 102]. It should be noted that the formation of a pore implies a considerable change in the structure of the membrane that has not been considered in the kinetic models discussed above in this chapter. It should be worthy to know whether the formation of pores is being induced by the process of restraining the molecules in the membrane, without avoiding the deformation of the latter. For the case of cholesterol (which is not reported to translocate through membrane pores), once initiated, the translocation process occurs on average in 73 ns [97], a time comparable to the duration of each single restricted US simulation in recent studies [63, 66, 84, 105]. Although it may be argued that the

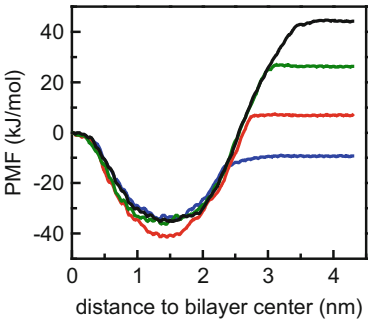

Fig. 4.8 PMF profiles of the NBD-C_n molecules in a POPC bilayer. PMFs of NBD-C_4, -C_8, -C_{12}, and -C_{16} are depicted as *blue*, *red*, *green*, and *black lines*, respectively. Reprinted with permission from reference [84]. Copyright 2014 American Chemical Society

minimum free energy path implies the formation of a pore [100, 104], with too long simulation times the membrane has the opportunity to "over-equilibrate" and deform around the restrained molecule. For solutes with strong electrostatic interactions this may result in the artificial formation of a pore. Spontaneous pore formation in a lipid bilayer has only been observed in long MD simulations for the short acyl chain phospholipid DLPC [100]. The most representative lipids of biological membranes have a longer acyl chain and the spontaneous formation of pores have a much higher energetic cost being an extremely rare event [1, 100].

For the case of the NBD-C_n series, as shown in Fig. 4.8, there is no clear tendency regarding the dependence of the translocation energy barrier on the number of carbons in the alkyl chain [27, 84]. The dependence of the desorption and translocation energy barriers on the number of carbons of the amphiphile's alkyl chain is in qualitative agreement with experimental results for the interaction of these amphiphiles with POPC bilayers [27], and for the transfer of labeled phospholipids between vesicles [45].

4.2.5 How to Obtain Kinetics from the PMF

Clearly, the ultimate goal of calculation of PMF profiles is to be able to estimate rate constants for the lipid/amphiphile interaction processes and permeability coefficients that can be used to calculate the rate of permeation through the bilayer. For this purpose, the Transition State Theory (TST), also known as absolute-rate theory, may be used [106–108]. This theory is usually applied to obtain all thermodynamic parameters for the transition states of each process involved in amphiphile permeation across bilayers from the experimental rate constants [27, 41, 109, 110].

The thermodynamic formulation of the transition state theory describes the rate constant of reaction (k) as

$$k = \kappa \frac{k_B T}{h} e^{-\Delta^{\ddagger} G^{o}/RT}, \tag{4.37}$$

where $k_B T/h$ is a frequency factor, associated to the conversion from the transition state to the products, being k_B, h and R the Boltzmann, Planck and gas constants, respectively; T is the absolute temperature; $\Delta^{\ddagger} G^{o}$ is the Gibbs energy variation from the reactants to the transition state; and κ, the so-called transmission coefficient, is an efficiency parameter.

The value of $\Delta^{\ddagger} G^{o}$ may be directly obtained from the PMF profile. To calculate the rate constant associated with crossing each energy barrier in the PMF, it is also necessary to know the transmission coefficient. A value $\kappa = 1$ is expected for elementary chemical reactions in which every vibration of the mode responsible for converting the activated complex (corresponding to the transition state of the system) to the product is effective. However, in solution, solvent cage effects are present, which delay conversion between the activated complex and the products. Moreover, the processes involved in solute permeation across the membrane are of a physical nature, and such a vibrational mode cannot be identified.

One possible strategy to overcome this problem involves additional (unrestrained) MD simulations. Regarding the translocation step, one may carry out several simulations where the amphiphile is allowed to relax from the transition state (assumed as $z = 0$) towards its equilibrium position. Typical relaxation curves for the NBD-C_n amphiphiles are shown in Fig. 4.9. It should be noted that, in order to achieve a statistically significant value using this strategy, an extreme large number of simulations is implied. This is particularly problematic for highly ordered systems, namely in cholesterol-containing membranes [63]. In a simple analysis, the resulting average of relaxation curves may be analyzed with a single-exponential function. For amphiphilic molecules with the size of a lipid, the characteristic relaxation time is on the order of a few to a few tens of nanoseconds [105]. Therefore, this procedure allows the calculation of the pre-exponential factor, $\left(\kappa \frac{k_B T}{h}\right)$, which is half the value of the relaxation rate constant. This statistical factor stems from the equal probability of going from the transition state back to the reactant (equilibrium position in the initial leaflet) or towards the product (equilibrium position in opposite leaflet) [108]. The pre-exponential factor obtained, in the order of 10^8 s^{-1}, is considerably lower than the value used when applying TST with $\kappa = 1$ (10^{12} s^{-1}). This suggests that the experimentally derived values for the thermodynamic activation functions should be obtained with much lower pre-exponential factors, as already used in several literature works [64, 105, 112]. For the case of the insertion/desorption steps, a similar strategy can in principle be used. Simulations where the amphiphiles are allowed to relax from the insertion/desorption transition state until the equilibrium position may be performed. However, the complexity of this membrane region may require a multi-exponential function fit to the relaxation data. It is expected that these simulations show high variability, with the amphiphile desorbing to water in some cases and inserting towards its membrane equilibrium position in others. In general, the main disadvantages of this method are the large number of unrestrained simulations required to obtain a statistically significant

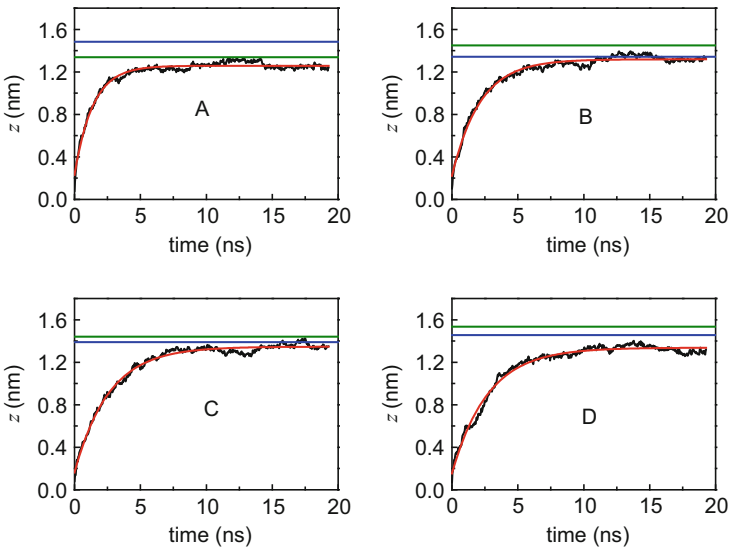

Fig. 4.9 Transfer of the amphiphiles from the center of the bilayer to the equilibrium position evaluated as the z(t) distance from the NBD COM to the bilayer center, in POPC bilayers: (**A**) NBD-C_4, (**B**) NBD-C_8, (**C**) NBD-C_{12}, (**D**) NBD-C_{16}. NBD equilibrium positions determined from unrestrained simulations [111] (*blue*) and from PMF minima [84] (*green*) are shown for comparison. This results are an extension of the work of reference [84]

average relaxation curve; and the possibility of complex relaxation kinetics, of unclear interpretation. In any case, transmission coefficients may be still estimated, and used for improved calculation of the rate constants.

If translocation of the solute occurs through pores, the observed rate constant of translocation depends on both the rate at which the solute translocates through the pore, and on the density of pores in the bilayer. The mathematical formalism that should be used in this situation has been developed by Tieleman and co-workers and applied to predict the rate of translocation of phospholipids and the permeability coefficient of very polar solutes [61].

The conversion between calculated free energy barriers and experimental rate constants for the interaction of amphiphiles with lipid bilayers may also be conducted following the Kramers theory of reaction rates [113], applied to the theoretical description of amphiphile monomer-micelle dissociation developed by Aniansson et al. [93]. Characteristic free energies for the desorption of amphiphiles from lipid bilayers have been obtained from the experimentally observed rate constants following this model [32, 94]. The relation between the rate constant of desorption and the Gibbs energy variation between the equilibrium position in the bilayer and the transition state ($\Delta^{\ddagger}G^{o}$) is:

$$k_{-} = \frac{D_{m}}{{l_{b}}^{2}} \exp\left[-\frac{\Delta^{\ddagger}G^{o}}{RT}\right] \tag{4.38}$$

where D_m is the diffusion constant for the exiting amphiphile, l_b is the width of the barrier that is RT energy units below its maximum. This expression can be understood intuitively, since l_b^2/D_m is the time for diffusional motion over the distance l_b and $\exp[-\Delta^{\ddagger}G^o/(RT)]$ is the relative probability that a monomer resides in the region of length l_b, or within RT energy units of $\Delta^{\ddagger}G^o$. The value of l_b considered in the experimental reports was around 0.1 nm being independent on the length of the alkyl chain in homologous series of amphiphiles [32, 94]. Also, in experiments D_m is assumed to be close to the diffusion constant of the free amphiphile in solution. Considering $l_b = 0.1$ nm and $D_m = 5 \times 10^{-6}$ cm^2/s, a pre-exponential factor of 5×10^{10} s^{-1} is obtained.

The length parameter (l_b) may be easily obtained from the PMF profile. Additionally, the diffusion coefficient at the reaction coordinates near the transition state may be estimated using the force autocorrelation at each sampling window, as will be further addressed in the next section. For example, regarding the above mentioned NBD-C_n series, $l_b \sim$ 0.2–0.3 nm and $D \sim$ 3–4 $\times$ 10^{-7}cm^2/s are obtained for the translocation barrier, leading to pre-exponential factors of the order of $\sim 5 \times 10^8$ s^{-1}. On the other hand, for the desorption barrier, typical values $l_b \sim$ 0.2–0.4 nm and $D \sim 5 \times 10^{-6}$ cm^2/s are found, leading to pre-exponential factors near $\sim 5 \times 10^9$ s^{-1}.

Regarding the example of the NBD labeled amphiphiles described above, the simulated free energy barriers are clearly lower than the values estimated from the experimental rate constants, assuming the absolute rate theory (i.e., a frequency of conversion from the transition to the final states of k_BT/h) [106], for both translocation and desorption processes [27, 84]. In any case, a linear dependence of the desorption free energy barrier on the number of carbons n is observed in both approaches. The slope based on simulations is 4.4 kJ/CH_2, compared to 3.5 kJ/CH_2 based on experiments. The quantitative disagreement between experimental and simulation results is in part a consequence of the direct application of this theory, as the actual reaction frequency is likely much lower than this limiting value [114]. However, the value of this reaction frequency is expected to depend more on the dynamics of the bilayer than on the solute itself, therefore conserving the linear dependence of the energy barriers, and giving good qualitative results.

4.2.6 Calculation of Permeability Coefficients from MD Simulations

The overall permeation through the lipid bilayer and the permeability coefficient P may be calculated from the rate constants of each step in the process [20]. MD simulations also allow calculation of permeability coefficients, which are defined according to Eq. (4.14). In silico estimation of P could provide a means to reduce costs involved in drug design and development.

By keeping track of the motions of all individual molecules in the system, MD simulations have the potential for calculation of solute permeation across membrane systems. However, on the time scales available to atomistic MD, permeation events

are exceedingly rare in unbiased simulations. This precludes direct calculation of permeability coefficients from MD using Eq. (4.14). Despite this setback, there are indirect methods that can be utilized to this purpose [92]. In this section, we focus on the most used approach, the so-called inhomogeneous solubility-diffusion model [115, 116], which leads to the following expression for P:

$$\frac{1}{P} = \int_{z_1}^{z_2} \frac{\exp(\Delta G^{o}(z)/k_B T)}{D_z(z)} dz. \tag{4.39}$$

Here, $\Delta G^{o}(z)$ is the Gibbs free energy across the bilayer (i.e., PMF profile, see above subsections), and D_z is the solute diffusion coefficient along the z-direction. z_1 and z_2 represent locations in the water phase on either side of the membrane, and therefore the integration is carried out across the whole bilayer. $D_z(z)$ may be obtained using the Einstein relation in short time ranges, or, more commonly, using the force autocorrelation method, described below in brief.

For a given z value, a constrained MD run is carried out, in which the solute depth is fixed to the intended value. The local time dependent friction coefficient of the diffusing molecule $\xi(t)$ is related to the time autocorrelation function of the fluctuations of the instantaneous force acting on the solute when located at z, $F(z,t)$, relative to its time average $\langle F(z)\rangle_t$, by:

$$\xi(t) = \frac{\langle \Delta F(z,t) \cdot \Delta F(z,0)\rangle}{RT}, \tag{4.40}$$

where,

$$\Delta F(z,t) = F(z,t) - \langle F(z)\rangle_t. \tag{4.41}$$

Assuming that $\xi(t)$ is large and decays rapidly compared to other time scales in the system, a satisfactory description of the full dynamics is provided by the static friction coefficient ξ:

$$\xi = \int_0^\infty \xi(t)dt = \int_0^\infty \frac{\langle \Delta F(z,t) \cdot \Delta F(z,0)\rangle}{RT} dt. \tag{4.42}$$

When studying diffusion across a free energy barrier, the above condition is met if the slope of the free energy barrier over a distance covered by the particle during the decay time of its friction coefficient is lower than the thermal fluctuation, RT. In this case, ξ is related to the local diffusion coefficient $D_z(z)$ of the permeating solute at depth z by:

$$D_z(z) = \frac{RT}{\xi} = \frac{(RT)^2}{\int_0^\infty \langle \Delta F(z,t) \cdot \Delta F(z,0)\rangle dt}. \tag{4.43}$$

The inhomogeneous solubility-diffusion model has been applied to several small hydrophilic and hydrophobic molecules calculating the local resistance of the membrane to the permeation as the inverse of the local permeability coefficient. It was found that for hydrophilic molecules the main barrier is represented by the hydrocarbon core, while for the hydrophobic molecules the main barrier to permeation is offered by the head group region [91]. More recent applications include a number of studies on the permeation of larger compounds, such as drugs and hormones [117, 118].

A simpler alternative to the integration procedure of Eq. (4.39) may be obtained in the framework of Kramers reaction rate theory, assuming that $\Delta G^{o}(z)$ is characterized by a large barrier value at some value of $z = z^*$, and that $D_z(z)$ is constant ($\cong D$) in that region. Under these hypotheses, one may approximate the permeability coefficient in a transition-state-like approximation according to [119, 120]

$$P = \sqrt{\frac{a}{\pi k_B T}} D \exp\left(\frac{-\Delta\Delta G^{o}(z^*)}{k_B T}\right) \tag{4.44}$$

where

$$a = \frac{1}{2}\left|\frac{\partial^2 \Delta\Delta G^{o}(z^*)}{\partial z^2}\right| \tag{4.45}$$

and $\Delta\Delta G^{o}$ refers to the difference between $\Delta G^{o}(z)$ at the maximum and the bottom of the energy barrier, that means, equal to $\Delta^{\ddagger} G^{o}$.

Although this approach only considers a single energy barrier, an extension to a multibarrier situation could be envisaged in the framework of the inhomogeneous solubility-diffusion model as proposed originally by Diamond and Katz [119]. As derived by these authors, the reciprocal of the permeability coefficient has the significance of a resistance, which consists of three resistances in series, r_i (corresponding to insertion, translocation and desorption, respectively). Each of these terms can be obtained by taking the reciprocal of a hypothetical single-barrier P_i value, obtained from Eq. (4.44), using the pertaining $\Delta\Delta G^{o}$ and D. Finally, they are combined to obtain the global permeation coefficient through

$$\frac{1}{P} = r_1 + r_2 + r_3 = \frac{1}{P_1} + \frac{1}{P_2} + \frac{1}{P_3}. \tag{4.46}$$

Generally, the calculated permeability coefficients are qualitatively consistent with experiments, in that ranking orders are well reproduced. However, P values from simulations are typically several orders of magnitude larger than those from experiments. While several reasons could be invoked to account for this disagreement (including the diversity of experimental approaches and measured values, the much simpler systems used in simulations, unsolved force field and/or sampling issues), it is noteworthy that the ranking order among a set of compounds

constitutes, by itself, valuable information for drug design [121]. Identically to the calculation of rate constants for individual processes, consideration of enhanced sampling strategies and/or multi-dimensional free energy surfaces (including orientational degrees of freedom) to identify hidden energy barriers may lead to improved quantitative accordance with experimental permeability coefficients, especially for relatively large molecules (in which reorientations can take place on the same time scale of displacements along the bilayer normal) [122].

4.3 Concluding Remarks

In this chapter, we address both experimental and simulation-based strategies to obtain kinetic information regarding the processes of interaction (insertion, desorption, translocation) between an amphiphilic solute and lipid membranes. The problem is formulated in general terms, from which limiting cases of practical importance are derived. Different experimental approaches are described, with an emphasis on fluorescence spectroscopy. On the other hand, MD simulations have evolved to the point where, in addition to detailed mechanistic information, free energy profiles and permeability coefficient values across the bilayer can be obtained for small- and medium-sized solutes.

Clearly, there is still plenty of room for improvement regarding quantitative agreement between calculated and experimental energy barriers and corresponding equilibrium and rate constants, due to both MD (important sampling issues), theory (uncertainty in frequency factor for TST) and experiment related (variety of approaches leading to scattered reported values) issues. However, experiment and simulation are most often in good qualitative accordance, and future advances in sampling strategies and identification of hidden energy barriers [77], may lead to an effective utility of MD simulations in prediction of permeation and in rational drug design.

References

1. Paula S, Volkov AG, VanHoek AN, Haines TH, Deamer DW. Biophys J. 1996;70:339.
2. Moreno MJ, Estronca L, Vaz WLC. Biophys J. 2006;91:873.
3. Verkman AS, Dix JA, Seifter JL. Am J Physiol. 1985;248:F650.
4. Chakrabarti AC, Deamer DW. Biochim Biophys Acta. 1992;1111:171.
5. Chehin RN, Isse BG, Rintoul MR, Farias RN. J Membrane Biol. 1999;167:251.
6. Mayer PT, Xiang TX, Niemi R, Anderson BD. Biochemistry. 2003;42:1624.
7. Barbet J, Machy P, Truneh A, Leserman LD. Biochim Biophys Acta. 1984;772:347.
8. Allen TM, Cleland LG. Biochim Biophys Acta. 1980;597:418.
9. Lasch J. Biochim Biophys Acta. 1995;1241:269.
10. Loura LMS, de Almeida RFM, Coutinho A, Prieto M. Chem Phys Lipids. 2003;122:77.
11. Pokorny A, Almeida PFF. Biochemistry. 2004;43:8846.
12. Ahyayauch H, Goni FM, Bennouna M. J Liposome Res. 2003;13:147.

13. Chen RF, Knutson JR. Anal Biochem. 1988;172:61.
14. Zwolinski BJ, Eyring H, Reese CE. J Phys Colloid Chem. 1949;53:1426.
15. Overton E. Vierteljschr d Naturforsch Ges Zurich. 1899;44:88.
16. Deamer DW, Kleinzeller A, Fambrough DM. Membrane permeability: 100 years since Ernest Overton, vol. 48. San Diego: Academic Press; 1999.
17. Missner A, Pohl P. Chemphyschem. 2009;10:1405.
18. Li S, Hu PC, Malmstadt N. Anal Chem. 2010;82:7766.
19. Eyer K, Paech F, Schuler F, Kuhn P, Kissner R, Belli S, Dittrich PS, Kramer SD. J Control Release. 2014;173:102.
20. Filipe HAL, Salvador A, Silvestre JM, Vaz WLC, Moreno M. J Mol Pharm. 2014;11:3696.
21. Thomae AV, Koch T, Panse C, Wunderli-Allenspach H, Kramer SD. Pharm Res. 2007;24:1457.
22. Sawada GA, Barsuhn CL, Lutzke BS, Houghton ME, Padbury GE, Ho NFH, Raub TJ. J Pharmacol Exp Ther. 1999;288:1317.
23. Kramer SD, Lombardi D, Primorac A, Thomae AV, Wunderli-Allenspach H. Chem Biodivers. 2009;6:1900.
24. Estronca LMBB, Moreno MJ, Laranjinha JAN, Almeida LM, Vaz WLC. Biophys J. 2005;88:557.
25. Steinfeld JI, Francisco JS, Hase WL. Chemical kinetics and dynamics. 2nd ed. New Jersey: Prentice-Hall; 1999.
26. Estronca LMBB, Filipe HAL, Salvador A, Moreno MJ, Vaz WLC. J Lipid Res. 2014;55:1033.
27. Cardoso RMS, Martins PAT, Gomes F, Doktorovova S, Vaz WLC, Moreno MJ. J Phys Chem B. 2011;115:10098.
28. Martins PT, Velazquez-Campoy A, Vaz WLC, Cardoso RMS, Valerio J, Moreno MJ. J Am Chem Soc. 2012;134:4184.
29. Donovan JM, Jackson AA. Biochemistry. 1997;36:11444.
30. McIntyre JC, Sleight RG. Biochemistry. 1991;30:11819.
31. Sampaio JL, Moreno MJ, Vaz WLC. Biophys J. 2005;88:4064.
32. Nichols JW. Biochemistry. 1985;24:6390.
33. Kuzelova K, Brault D. Biochemistry. 1994;33:9447.
34. Pokorny A, Almeida PFF, Vaz WLC. Biophys J. 2001;80:1384.
35. Pokorny A, Almeida PFF, Melo ECC, Vaz WLC. Biophys J. 2000;78:267.
36. Luo M, Fadeev EA, Groves JT. J Am Chem Soc. 2005;127:1726.
37. Cabral DJ, Small DM, Lilly HS, Hamilton JA. Biochemistry. 1987;26:1801.
38. Jones JD, Thompson TE. Biochemistry. 1989;28:129.
39. Almeida PF. Biophys J. 1922;1999:76.
40. Nichols JW, Pagano RE. Biochemistry. 1981;20:2783.
41. Abreu MSC, Moreno MJ, Vaz WLC. Biophys J. 2004;87:353.
42. Estronca LMBB, Moreno MJ, Vaz WLC. Biophys J. 2007;93:4244.
43. Roseman MA, Thompson TE. Biochemistry. 1980;19:439.
44. Frank A, Barenholz Y, Lichtenberg D, Thompson TE. Biochemistry. 1983;22:5647.
45. Homan R, Pownall HJ. Biochim Biophys Acta Biomembr. 1988;938:155.
46. Kamp F, Westerhoff HV, Hamilton JA. Biochemistry. 1993;32:11074.
47. Storch J, Kleinfeld AM. Biochemistry. 1986;25:1717.
48. Richieri GV, Anel A, Kleinfeld AM. Biochemistry. 1993;32:7574.
49. Langner M, Isac T, Hui SW. Biochim Biophys Acta Biomembr. 1995;1236:73.
50. Cupp D, Kampf JP, Kleinfeld AM. Biochemistry. 2004;43:4473.
51. Loura LMS, Ramalho JPP. Molecules. 2011;16:5437.
52. Lyubartsev AP, Rabinovich AL. Soft Matter. 2011;7:25.
53. Javanainen M, Martinez-Seara H. Biochim Biophys Acta Biomembr. 2016;1858:2468.
54. Gumbart JC, Roux B, Chipot C. J Chem Theory Comput. 2012;9:794.
55. Torrie GM, Valleau JP. J Comput Phys. 1977;23:187.

56. Kästner J. Wiley Interdiscip Rev: Comput Mol Sci. 2011;1:932.
57. Wennberg CL, van der Spoel D, Hub JS. J Am Chem Soc. 2012;134:5351.
58. MacCallum JL, Bennett WFD, Tieleman DP. Biophys J. 2008;94:3393.
59. Sapay N, Bennett WFD, Tieleman DP. Biochemistry. 2010;49:7665.
60. Hinner MJ, Marrink SJ, de Vries AH. J Phys Chem B. 2009;113:15807.
61. Tieleman DP, Marrink S-J. J Am Chem Soc. 2006;128:12462.
62. Bennett WFD, Tieleman DP. J Lipid Res. 2012;53:421.
63. Bennett WFD, MacCallum JL, Tieleman DP. J Am Chem Soc. 2009;131:1972.
64. Sapay N, Bennett WFD, Tieleman DP. Soft Matter. 2009;5:3295.
65. MacCallum JL, Tieleman DP. J Am Chem Soc. 2006;128:125.
66. Neale C, Bennett WFD, Tieleman DP, Pomès R. J Chem Theory Comput. 2011;7:4175.
67. Neale C, Madill C, Rauscher S, Pomès R. J Chem Theory Comput. 2013;9:3686.
68. Paloncýová M, Berka K, Otyepka M. J Chem Theory Comput. 2012;8:1200.
69. Comer J, Schulten K, Chipot C. J Chem Theory Comput. 2014;10:554.
70. Peters GH, Werge M, Elf-Lind MN, Madsen JJ, Velardez GF, Westh P. Chem Phys Lipids. 2014;184:7.
71. Wang Y, Hu D, Wei D. J Chem Theory Comput. 2014;10:1717.
72. Martin LJ, Chao R, Corry B. Biophys Chem. 2014;185:98.
73. Jakobtorweihen S, Zuniga AC, Ingram T, Gerlach T, Keil FJ, Smirnova I. J Chem Phys. 2014;141:045102.
74. Ma J, Domicevica L, Schnell JR, Biggin PC. Phys Chem Chem Phys. 2015;17:19766.
75. Paloncýová M, Berka K, Otyepka M. J Phys Chem B. 2013;117:2403.
76. Paloncýová M, DeVane R, Murch B, Berka K, Otyepka M. J Phys Chem B. 2014;118:1030.
77. Jämbeck JPM, Lyubartsev AP. J Phys Chem Lett. 2013;4:1781.
78. Awoonor-Williams E, Rowley CN. Biochim Biophys Acta Biomembr. 2016;1858:1672.
79. Dickson CJ, Hornak V, Pearlstein RA, Duca JS. J Am Chem Soc. 2016;139:442–52.
80. Kirkwood JG. J Chem Phys. 1935;3:300.
81. Roux B. Comput Phys Commun. 1995;91:275.
82. Hub JS, de Groot BL, van der Spoel D. J Chem Theory Comput. 2010;6:3713.
83. Kumar S, Rosenberg JM, Bouzida D, Swendsen RH, Kollman PA. J Comput Chem. 1992;13:1011.
84. Filipe HAL, Moreno MJ, Róg T, Vattulainen I, Loura LMS. J Phys Chem B. 2014;118:3572.
85. Jo S, Rui H, Lim JB, Klauda JB, Im W. J Phys Chem B. 2010;114:13342.
86. Wei C, Pohorille A. J Phys Chem B. 2014;118:12919.
87. Parisio G, Sperotto MM, Ferrarini A. J Am Chem Soc. 2012;134:12198.
88. Neale C, Pomès R. Biochim Biophys Acta Biomembr. 2016;1858:2539.
89. Ghaemi Z, Minozzi M, Carloni P, Laio A. J Phys Chem B. 2012;116:8714.
90. Cardenas AE, Elber R. Mol Phys. 2013;111:3565.
91. Bemporad D, Essex JW, Luttmann C. J Phys Chem B. 2004;108:4875.
92. Xiang T-X, Anderson BD. Adv Drug Deliv Rev. 2006;58:1357.
93. Aniansson EAG, Wall SN, Almgren M, Hoffmann H, Kielmann I, Ulbricht W, Zana R, Lang J, Tondre C. J Phys Chem. 1976;80:905.
94. Jones JD, Thompson TE. Biochemistry. 1990;29:1593.
95. Parisio G, Ferrarini A, Sperotto MM. Int J Adv Eng Sci Appl Math. 2016;8:134.
96. Ogushi F, Ishitsuka R, Kobayashi T, Sugita Y. Chem Phys Lett. 2012;522:96.
97. Choubey A, Kalia RK, Malmstadt N, Nakano A, Vashishta P. Biophys J. 2013;104:2429.
98. Róg T, Stimson LM, Pasenkiewicz-Gierula M, Vattulainen I, Karttunen M. J Phys Chem B. 2008;112:1946.
99. Bennett WFD, Tieleman DP. J Chem Theory Comput. 2011;7:2981.
100. Bennett WFD, Sapay N, Tieleman DP. Biophys J. 2014;106:210.
101. Gurtovenko AA, Onike OI, Anwar J. Langmuir. 2008;24:9656.
102. Gurtovenko AA, Vattulainen I. J Phys Chem B. 2007;111:13554.
103. Huang K, García AE. Biophys J. 2013;104:412.

104. Arai N, Akimoto T, Yamamoto E, Yasui M, Yasuoka K. J Chem Phys. 2014;140:064901.
105. Bennett WFD, MacCallum JL, Hinner MJ, Marrink SJ, Tieleman DP. J Am Chem Soc. 2009;131:12714.
106. Eyring H. Chem Rev. 1935;17:65.
107. Wynne-Jones WFK, Eyring H. J Chem Phys. 1935;3:492.
108. Evans MG, Polanyi M. Trans Faraday Soc. 1935;31:0875.
109. McConnell HM, Kornberg RD. Biochemistry. 1971;10:1111.
110. McLean LR, Phillips MC. Biochemistry. 1981;20:2893.
111. Filipe HAL, Moreno MJ, Loura LMS. J Phys Chem B. 2011;115:10109.
112. Neuvonen M, Manna M, Mokkila S, Javanainen M, Rog T, Liu Z, Bittman R, Vattulainen I, Ikonen E. PLos One. 2014;9:e103743.
113. Kramers HA. Physica. 1940;7:284.
114. Roux B. J Gen Physiol. 1999;114:605.
115. Diamond JM, Katz Y. J Membrane Biol. 1974;17:121.
116. Marrink SJ, Berendsen HJC. J Phys Chem. 1994;98:4155.
117. Orsi M, Essex JW. Soft Matter. 2010;6:3797.
118. Carpenter TS, Kirshner DA, Lau EY, Wong SE, Nilmeier JP, Lightstone FC. Biophys J. 2014;107:630.
119. Wilson MA, Pohorille A. J Am Chem Soc. 1996;118:6580.
120. Ulander J, Haymet AD. J Biophys J. 2003;85:3475.
121. Orsi M, Essex JW, editors. Molecular simulations and biomembranes: from biophysics to function. Cambridge: The Royal Society of Chemistry; 2010. p. 76.
122. Parisio G, Stocchero M, Ferrarini A. J Chem Theory Comput. 2013;9:5236.

Chapter 5
Multidimensional Microscopy: Application to Membrane Protein Structure

Andrew H.A. Clayton

Abstract Fluorescence is exquisitely sensitive to environment and thus interactions and dynamics. Fluorescence is also multidimensional in orientation (polarization), energy (wavelength), time (ps-years) and space (nm-m). In the first part of this Chapter we introduce the reader to multidimensional microscopy which we define as the hybridization of fluorescence dimensions with the more orthodox physical dimensions of space and time. In the second part of the Chapter we illustrate how multidimensional microscopy has been employed to examine the quaternary structure, organization and dynamics of an important biomedical cell-surface receptor. We advocate multidimensional microscopy as a general strategy for bridging structural biology with cell biology.

5.1 Introduction

The primary, secondary, tertiary and quaternary structures of biological macromolecules are thought to be major factors that determine protein function in solution [1]. At physiological temperatures (i.e. typically about 300 K above absolute zero) transitions between conformational sub-states of proteins, driven largely by solvent dynamics, provide the motions required for proteins to carry out their functions [2].

Proteins in the cell do not act alone. As enzymes, proteins catalyse reactions involving proteins and other biomolecules. Proteins form transient, non-covalent complexes with other proteins in cell signalling cascades (kiss and run complexes). Proteins can also assemble to form large, stable nano-machines such as the ATPase rotatory motor. A major goal is to image biochemistry in the cell and to map out the biochemical pathways. Another major goal is to determine the stoichiometry of protein complexes and relevance for function. In this regard membrane proteins are

A.H.A. Clayton (✉)
Cell Biophysics Laboratory, Centre for Micro-Photonics, School of Science,
Faculty of Science, Engineering and Technology, Swinburne University of Technology,
Melbourne, Australia
e-mail: aclayton@swin.edu.au

A. Chattopadhyay (ed.), *Membrane Organization and Dynamics*, Springer Series in Biophysics 20, DOI 10.1007/978-3-319-66601-3_5

most challenging because they are usually not soluble in water and methods to determine structure in situ (i.e. at the cell membrane) are therefore highly desirable [3].

The purpose of this chapter is to introduce the reader to approaches to determine the tertiary and quaternary structures of membrane proteins at the cell membrane surface and their associated dynamics. The questions that motivate us are (1) What is the quaternary structure of protein-monomer, dimer, or tetramer? (2) How is the protein assembled on the cell surface- random or clustered? (3) What is the shape or conformation of the protein on the cell surface? (4) How does the protein structure (conformation or assembly) relate to biological function?

Fluorescence is exquisitely sensitive to protein structure and dynamics [4]. This is mainly because of the time a fluorescence probe molecule spends in the excited-state. Judicious choice and placement of a fluorescent molecule(s) within a protein (s) enables the experimentalist to obtain information at a specific site(s) in the protein (complex) of interest.

Fluorescence signals are inherently multidimensional and the information content of these signals is rich. Fluorescence intensity, fluorescence colour (wavelength) [5], fluorescence polarization [6], fluorescence lifetime [7], fluorescence fluctuations (in time) [8, 9] and fluorescence fluctuations (in space) [10] are fluorescence signals that can be acquired. From these fluorescence signals the experimentalist can measure fluorophore concentration, fluorophore rotational and translational motion, interactions between fluorophores, interaction strength and interaction stoichiometry. Fluorescence can be measured from a solution in a cuvette, from the focus of a light microscope, or across an image from a wide-field fluorescence microscope. Because we are dealing with fluorescence from membranes and cells in this Chapter we will mainly focus the discussion to fluorescence microscopy.

Fluorescence or more specifically fluorophores can be perturbed by processes such as photobleaching [11] and quenching [12]. In photobleaching a light source is focused (as in fluorescence microscopy) and either raster-scanned (confocal laser scanning microscopy) or dispersed and imaged onto a 2D array detector such as a CCD camera. Photobleaching by definition is a loss of fluorescence by shining light onto a fluorophore, the loss of fluorescence is due to some photochemical reaction (irreversible, partially reversible or reversible) which renders the fluorophore unable to fluorescence at the excitation wavelength. Although photobleaching is undesirable for normal fluorescence imaging (due to the loss of signal!) it has been used previously to determine dynamics and interactions between molecules, and recently we and others have exploited the phenomenon to determine the quaternary states of proteins on cell surfaces. Quenching is defined as loss of fluorescence intensity by a process normally involving the interaction between a fluorophore and quencher. Quenching is best measured in the microscope by using lifetime measurements. We will discuss quenching in more detail in the latter parts of this chapter.

5.2 Formalism

To provide a systematic view of multidimensional microscopy we have decided to represent physical and fluorescence dimensions as a table or matrix. A selected list of physical dimensions (space and time) and fluorescence dimensions are listed along the first row and first column of Table 5.1. These represent parameters that might be measured by a detector from a solution of fluorophores. For example, intensity, wavelength, polarization, lifetime and fluctuations can be measured alone.

Intensity is a parameter with arbitrary units and is affected by the concentration of fluorophore, the quantum yield of the fluorophore (the quantum yield is defined as the number of photons emitted per photon absorbed), the excitation irradiance, the efficiency of collection and the detector sensitivity. Changes in any one of these factors can affect the fluorescence intensity. If a wavelength sensitive device such as a narrow band filter is used the intensity measured is also affected by shifts in emission spectrum.

Polarization is defined as the normalized signal difference between parallel-polarized and perpendicular-polarized components of the emission. For dilute solutions, the polarization magnitude depends upon the rotational diffusion of a fluorophore during the excited-state lifetime of the fluorophore. The polarization can also be sensitive to interactions between fluorophores in concentration solutions or in complexes [13]. The polarization is a ratio between a difference in intensities to a sum of intensities so is a robust dimensionless parameter. Changes in polarization can occur due to changes in rotation of fluorophores, changes in lifetime of the fluorophore or changes in the interaction between fluorophores.

Lifetime is defined as the mean time a molecule spends in the excited state. Lifetimes can change owing to changes in fluorophore environment (e.g. Polarity, pH etc.) but are also sensitive to quenching caused by interactions between a fluorophore and a quencher. Lifetime is a kinetic parameter so is independent from concentration and signal intensity.

Fluctuations in intensity when not measured as a function of time or space could be considered as a measurement of the standard deviation or variance of the fluorescence intensity.

Intersections between different elements represent hybridization or multiplexing between the different dimensions. In general, we refer to the hybridization of one dimension with another dimension as multidimensional microscopy. These fluorescence dimensions when hybridised with the spatial dimension represent standard forms of fluorescence microscopy. For example, looking at the second column we are essentially measuring fluorescence parameters as a function of space. Fluorescence intensity hybridized with space is simply called fluorescence microscopy. Lifetime with space is called fluorescence lifetime imaging microscopy or FLIM. Polarization with space is called polarization microscopy. Fluctuations with space

Table 5.1 Physical and fluorescence dimensions and multidimensional microscope techniques

Dimension	Space	Time	Wavelength	Lifetime	Polarization	Fluctuation
Space	Space-space	Space-time	Spectral imaging	FLIM	Pol imaging	ICS
Time	Space-time	Time-time	Spectral shift	Time lapse lifetime	Time resolved polarization	FCS
Intensity	Imaging	Time resolved fluorescence	Fluorescence spectrum	Self-quenching/ Static quenching	Conc depol Homo-FRET	Intensity sub ICS
Wavelength	Spectral imaging	Spectral shift	REES	Spectral FLIM	Polarization spectrum	
Lifetime	FLIM	Time lapse lifetime	Spectral FLIM		rFLIM TRAIM	FLIM-ICS, FLICS
Polarization	Anisotropy imaging	Time resolved polarization	Polarization spectrum	rFLIM TRAIM		Pol FCS
Fluctuation	ICS	FCS		FLIM-ICS, FLICS	Pol FCS	Higher-order ICS or FCS
Photobleach	FLIP	FRAP	Photochem	pb FLIM	Pb Pol	Pb ICS

is called image correlation microscopy and so on. The additional of the space variable cannot be overstated. We will attempt to briefly state the advantages of adding an imaging capability to the parameters discussed above.

Fluorescence microscopy [14]. In membrane biophysics and in cell biophysics measurements of fluorescence from a collection of membranes or cells is an average measurement. Fluorescence microscopy opens up the possibility of being able to measure fluorescence from individual cells, individual structures (e.g. organelles, biopolymers) within cells and even individual molecules inside cells.

Spectral imaging enables a fluorescence spectrum or spectral region to be measured at every spatial location in a structure such as a cell [15]. This is useful when multiple fluorophores with different spectra are used. One can then probe multiple structures or molecules in the cell and resolve their spatial locations.

Lifetime imaging [16] measures lifetimes at several spatial locations within a cell or collection of cells. Lifetime imaging enables sensitive measurements of changes in local environment and interactions between molecules to be mapped to spatial location.

Polarization imaging [17] gives the experimentalist the power to measure and spatially map rotational diffusion of molecules inside cells. For example, amongst the first examples of this technique was the measurement of the viscosity of the cytoplasm of cells [18]. Polarization imaging is also sensitive to the orientation of fluorophores in ordered environments such as membranes [19].

Fluctuation imaging is called image correlation spectroscopy [20]. This method utilises the thousands of fluctuations that are present in an image to determine parameters such as fluorophore cluster density and cluster size. Image correlation spectroscopy has grown into a series of methods which are very powerful (i.e. when combined with the time dimension or other fluorescence dimensions).

Photobleaching in a defined subcellular region followed by imaging is called FLIP [21] or fluorescence loss in photobleaching. This method can be used to bleach a region and then watch the redistribution of fluorescence. If the fluorescence moves from unbleached area to bleached area after time then this implies that there is connectivity between the two regions.

Moving to the third column, we can see that intensity, wavelength, lifetime, polarization, fluctuation, polarization is multiplexed with the time dimension.

Intensity versus time is called intensity decay or time-resolved fluorescence. The intensity decay measured using time resolved fluorescence provides information on the excited state decay process leading to deactivation of the excited state [22]. These measurements can determine whether the fluorophore is in a single environment (single exponential decay) or multiple environments (multiple exponential decays).

Time resolved measurements at different wavelengths [23] can be used to determine lifetimes from more complex systems that involve fluorophores in multiple environments or multiple fluorophores. Measurements of spectral shifts as a function of time are used to determine monomer-excimer kinetics [24], energy transfer kinetics [25] and solvent relaxation processes [26].

Time-lapse lifetime measurements can track changes in fluorophore environment or interactions as a function of acquisition time. This can be used to measure

conformational motion, folding-unfolding processes [27], or interactions occurring during a cell signalling event [28].

Time-resolved polarization provides a direct measurement of processes leading to depolarization of the emission [29]. In rotational diffusion measurements time-resolved polarization can resolve individual rotational correlation times leading to an understanding of the amplitudes and time-scales for rotation. For a labelled biomolecule the local motion of the label and the overall rotation of the protein complex can be measured leading to estimates of the extent of internal and global motions. Time-resolved polarization is also used to measure interactions between labelled molecules undergoing homo energy transfer [30].

Fluctuations as a function of time are referred to as FCS or fluorescence correlation spectroscopy [31]. In FCS, fluorescence fluctuations from a tight laser focus are recorded. In general, these fluctuations contain information on the physical processes occurring in the fluorophore ensemble. Translational movement in and outside the laser focus, a change in orientation, time-dependent fluorescence quenching and changes in particle fluorescence due to association/dissociation can all give rise to fluctuations. FCS has grown into a large family of methods. The reader is referred to excellent recent reviews on this area [32, 33].

Photo-bleaching with time is called FRAP or fluorescence recovery after photo-bleaching [34]. In the earlier embodiments of this method, a small region on a cell membrane was photo-bleached with a very fast excitation pulse and then the recovery of fluorescence from that same region was monitored over time (with a less intense monitoring laser). The movement of labelled (i.e. unbleached) molecules into this region is recorded as a recovery of fluorescence. The diffusion coefficient is determined by the rate of recovery and photo-bleach size. The extent of recovery is dictated by the fraction of molecules that are mobile. Continuous measurements of fluorescence over time during constant photo-bleaching (continuous micro-photolysis) can also provide information on translational diffusion of membrane components [35].

So far we have covered the major imaging and time-resolved methods that are in use today. These methods combine one fluorescence dimension with one physical dimension (i.e. space or time). These methods provide insights into interactions and dynamics that underpin tertiary and quaternary structural transitions of membrane proteins. To resolve *more states* or to make *connections* between structure, dynamics and function we need to consider combining fluorescence dimensions.

For example, turning to the fourth column of Table 5.1, by adding excitation wavelength to emission spectroscopy or spectral imaging we have the ability to excite fluorophores at the red-edge of their absorption and to measure shifts in emission that result from this change in excitation wavelength. This technique, called red-edge-excitation-shift, or REES, is a powerful tool to examine fluorophore heterogeneity and environmental relaxation processes in membranes [36]. By adding the wavelength dimension to FLIM we have spectral-FLIM [37]. Spectral FLIM can resolve fluorophores based upon differences in lifetime or spectrum or both. Spectral FLIM can improve the resolution of FRET measurements providing robust determinations of fractions of donors and acceptors in complex, and fractions of donors and acceptors that are free [38]. Spectral FLIM

can also provide spectral relaxation information which in membranes occurs on timescales in the nanosecond regime [39]. Combining wavelength and polarization imaging also provides an increase in image contrast based upon differences in spectral wavelength and/or differences in anisotropy [40]. Polarized FRET in an imaging arrangement with spectral detection is also useful for determining fractions of molecules free and in complex [41]. Photo-bleaching and wavelength represents photo-conversion reactions where excitation with a suitable wavelength photo-converts an emitter with a certain emission spectrum to another emitter with another emission spectrum-this is useful in a range of applications [42]. Photo-conversion can also shift the absorption spectrum. This is particularly useful in photochromic acceptor FRET, where the spectral overlap and therefore FRET efficiency can be switched between two states [43].

Adding the lifetime dimension with other fluorescence dimensions is also very powerful and useful. Because lifetime is a robust measurement of interaction as defined by FRET combining lifetime with an orthogonal fluorescence dimension can increase in the information content further. Polarization with FLIM enables spatial imaging of rotational dynamics (in the absence of homo-FRET) [44]. Adding the FLIM element removes ambiguities associated with interpretation of polarization alone (which is affected by lifetime, correlation time and fluorophore orientation). Because anisotropy is also affected by homo-FRET, polarization with FLIM or rFLIM can also be used to determine average cluster sizes of proteins that are coupled at 1–10 nm separations (assuming rotational motion is known). Rotators with different distinct lifetimes can also be resolved using rFLIM [45]. Combining FLIM with ICS gives us the ability to determine cluster densities of fluorophores with different lifetimes [46]. If a lifetime-based assay is used to establish protein activation, then cluster densities and relative cluster sizes of functional versus non-functional membrane proteins can be determined with this method. In pbFLIM, lifetimes of molecules with different survival probabilities with photobleaching can be determined. This is not yet an established method but we propose that this technique has the potential to resolve more complex FRET situations involving more than one FRET state. FRAP with FLIM has also been combined which enables recovery times of different lifetime species to be determined [47].

Polarization with fluctuation is called polarization FCS and provides information on rotational diffusion of fluorophores [48]. An important advantage of this method is that it is independent of the excited-state lifetime of the fluorophore. Polarization fluctuation with imaging has not yet been realized buy we propose it here to be considered. Nanoscale clustered fluorophores will be brighter in intensity but reduced in polarization compared with unclustered fluorophores which will have a lower intensity but a higher polarization. Polarization with photobleaching is useful for determining homo-FRET [49]. This is because a photobleached fluorophore cannot participate in a FRET interaction with another fluorophore. Estimates of cluster size distributions can be made with this approach [50]. Importantly photobleaching with polarization is more robust than simple polarization imaging or time-resolved polarization for determination of homo-FRET because changes in polarization with continuous bleaching cannot be influenced by rotational diffusion.

Fluctuation (column seven, Table 5.1) can be combined with intensity in the form of intensity-subtraction ICS. In this ICS variant, bright and dim particle fluctuations are isolated by applying a systematic subtraction of intensity from the raw fluorescence image. Subtraction reduces the contribution from the dim particles so that the relative brightness and concentration of the brighter particles can be determined [51]. Complex brightness distributions can be handled using higher-order FCS or ICS. This method uses higher-order moments of the fluctuations present in images or time-series. [52, 53]. Fluctuation with photo-bleaching in an imaging arrangement or pbICS was recently developed [54]. This method can, in principle, determine the cluster size distributions of proteins on membrane surfaces [55]. The method assumes no lateral motion of clusters and so in its present implementation is for fixed cells. To our knowledge, this is the only method that does not require a brightness standard to obtain quantitative estimates of both cluster sizes and cluster densities.

5.3 An Archetypical Membrane Protein: The Epidermal Growth Factor Receptor

Perhaps the best way to show the value of these techniques is to provide an example of where they have been used. Receptors are molecules usually found on the surface of cells that receive chemical signals from outside cells. When a specific extracellular substance, called a ligand, binds to a specific receptor, it ultimately triggers the cell to do something, such a divide, or die, or move. The classic model for receptor activation is ligand-induced dimerisation, wherein single receptor monomers pair-up to form a receptor dimer [56].

The Epidermal Growth Factor receptor (EGFR) is a type 1 membrane protein receptor which is involved in a host of physiological processes and implicated in a range of diseases including neurodegenerative diseases and cancer. Consequently, understanding how the EGFR is activated in physiological and pathological settings is a major goal for the field and has led to a 30 year race to solve the complete structure of the molecule [57].

The receptor consists of extracellular binding domains, a trans-membrane domain, a juxta-membrane domain, a kinase domain and cytoplasmic tail domain. Atomic-resolution structures for all of the major parts of the receptor are now known (since 2002) but at the time of writing (2016) there is no structure of the complete molecule in a living cell membrane. Fortunately, with these partial structures it is possible to design experiments to test how the full length molecule might be assembled and activated on the cell surface.

To begin our journey it is important to understand that already before the first high-resolution structures of the extracellular domain of the EGFR came out in 2002, a substantial body of biochemical and biophysical work from Schlessinger's laboratory established that some form of dimerization was required for EGFR

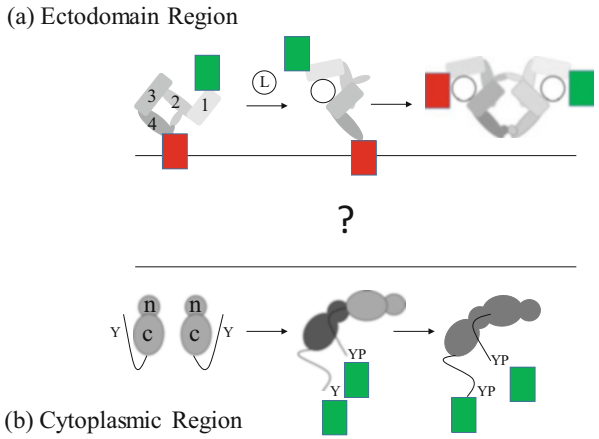

Fig. 5.1 Partial structures of the epidermal growth factor receptor. (**a**) Conformations of the ectodomain region depicting tethered, untethered and dimerized receptor. *Green* and *red rectangles* depict fluorescent label positions at the receptor or at the ligands. (**b**) Conformations of the kinase and cytoplasmic tail of the receptor depicting symmetric inactive, and asymmetric active dimer configurations. *Green rectangle* represents labelling position of green fluorescent protein tag at the C-terminus of the receptor. Note: Transmembrane and juxtamembrane domains are omitted from the figure

activation and biological activity. Biochemical (cross-linking experiments) were interpreted in terms of a ligand-induced monomer to dimer transition model with activation occurring in the dimeric form of the receptor [57]. Cross-linking of EGFR with immunoglobulins of different valence also established a correlation between receptor dimerization and biological activity [58].

The structures of the extra-cellular domain and of the intracellular kinase domain are shown schematically in Fig. 5.1. The structures of the extracellular domain are suggestive of a model for a ligand-induced dimerization process [59]. The extracellular domain consists of four sub-domains 1–4. In the un-liganded compact monomer sub-domains 2 and 4 form a tether that keeps the ligand binding domains 1 and 3 apart. In the structure of a ligand-bound monomer, the tether between domains 2 and 4 is broken and there is a large conformational transition leaving domains 1 and 3 in contact with the ligand. In the ligand-bound extended monomer structure there is a dimerization arm in domain 2 which is left exposed. This dimerization arm appears to facilitate dimerization between ligand-bound EGFR monomers to form a back to back dimer. Thus the extracellular domain structures provide a mechanism for dimerization through a ligand-induced conformational transition leading to dimerization.

Likewise, for the kinase domain, the kinase domain structures [60] provide a very elegant model of EGFR activation. In this model the kinase can exist in an inactive dimer conformation and an active dimer conformation. The active conformation consists of an asymmetric kinase dimer where one kinase acts as the donor and the other kinase acts as the acceptor.

The availability of the atomic resolution structures of the domains is important because it allows the design of fluorescence tag positions that are going to be most sensitive to the changes in structure or the activation being probed. (Figure 5.1 shows potential labelling positions for fluorescent tags). For example, FRET between a donor fluorophore at the ectodomain N terminus and an acceptor fluorophore label at the ectodomain C-terminus or cell surface is expected to be sensitive to ectomain conformation. Likewise FRET between ligands in the back-to-back dimer ectodomain is expected to be very small (less than 2%) but FRET between dimers in a tetramer or higher-order oligomer could be significant. Tags placed at the C-terminus of the full length receptor allow one to probe receptor oligomerisation. In conjunction with probes for receptor activation or complex formation, these receptor probes allow correlations between conformation, oligomerisation and biological activity when appropriate multidimensional microscopy approaches are employed.

5.4 Multidimensional Microscopy of EGFR on Intact Cells

5.4.1 In-Cell Quaternary Structure of EGFR in the Absence of EGF (ICS, Polarization, FCS)

A number of laboratories have used the green fluorescent protein (GFP) and variants to study the assembly of the EGFR. GFP is usually positioned at the C-terminus of the full length EGFR (i.e. after the cytoplasmic tail). We were the first laboratory to measure the oligomerisation state of the EGFR on normal cells expressing physiological levels of receptor and in the absence of secreted ligand or other EGFR members [61]. Image correlation spectroscopy (ICS) on a biologically-active GFP derivative of EGFR expressed at normal levels determined an average oligomeric state of 2 in the absence of ligands or other erbB family members [61]. We determined the cluster density of GFP-tagged EGFR by ICS (from confocal images of the receptor on intact cells) and used estimates of receptor number to extract the number of receptors per cluster.

Wohland's laboratory, using fluorescence cross-correlation spectroscopy (a two color variant of FCS), determined that the majority of EGFRs on CHO cells were in preformed dimers (>50% dimers) by measuring the coincidence of green (GFP) tagged and red (RFP) tagged EGFRs as they diffused through a laser beam focused on the cell surface. Using careful negative and positive control samples, this group determined that EGFRs were pre-dimerized to a large extent in equilibrium with monomers. Interestingly, the degree of dimerisation was found to be independent of receptor expression level over a physiological to pathological range (20,000–260,000 receptors/cell) [62].

Lidke et al. used polarization measurements of EGFR-GFP in CHO cells inferred some degree of predimerization in the absence of added ligand [63]. By

combining photobleaching with anisotropy the authors revealed an enhancement of anisotropy with increases in photobleaching. Since photobleaching is not expected to influence rotation these observations were compatible with a homo-transfer of energy between preassembled EGFR-GFP dimers or oligomers.

Yeow and Clayton developed a theoretical formalism to explain anisotropy as a function of photobleaching for different cluster sizes of oligomers [50]. The Lidke et al. data was interpreted in the context of dimers or oligomers of EGFR in the CHO cells [50]. A dimers-only model was deemed inconsistent with the data and the presence of higher-order oligomers was inferred from the analysis [50].

Saffarian et al. used a moments analysis of intensity fluctuation traces (using an FCS set-up) to determine the fractions of monomer, dimer and oligomer of EGFR in the absence of ligand. Although EGFR-GFP was mostly monomeric (70%) about 20% of EGFR-GFP was in dimers and 10% were in oligomers in the CHO cells [64].

Time-gated polarization was used very successfully by Gerritsen's laboratory to determine cluster sizes of EGFR-GFP in CHO cells. The authors used constructs with an oligomerization domain to create oligomers of defined size (monomers, dimers and oligomers). In this way the authors were able to estimate the long-time polarization of different oligomer sizes. This information was then used for EGFR-GFP in CHO cells. These authors estimated about 40% dimerization of EGFR in the absence of ligand [65].

Nagy et al. used a variant of moments analysis, called number and brightness to determine the average degree of association of EGFR-GFP on CHO cells. In cells expressing low levels of EGFR-GFP, the EGFR-GFP appeared to be 100% monomeric, while in cells expressing high levels, about 30% of EGFR-GFP appeared as dimers. The authors used soluble GFP as a reference [66].

Kozer et al. used photobleaching and polarization to estimate cluster sizes of EGFR-GFP in BaF/3 cells. Using the polarization values of Gerritsen and a linearized version of the Yeow and Clayton model, the authors estimated the proportions of monomer, dimer and oligomer. Photobleaching polarization revealed that the EGFR-GFP was at least 90% dimer and 10% monomer on BaF/3 cells [67].

More recently, Martin-Fernandez and co-workers used photobleaching with super-resolution approaches to observe extended oligomers of EGFR on intact cells [68]. Measurements of distances between immune-labels at the extracellular domain revealed inter-label separations of 11, 22, 33, 44, 55, 66, 77 nm. These separations are compatible with extended oligomers of the EGFR up to octamers. This powerful approach bridges the gap between FRET and the resolution limit of conventional optical microscopy.

To summarize, a number of complementary biophysical techniques have been employed to address the state of association of EGFR in the absence of ligand. Taken together, the studies indicate that EGFR is not 100% monomeric in the absence of ligand but appears to exist in a complex equilibrium with monomeric, dimeric and extended oligomeric forms.

5.4.2 *In-Cell Quaternary Structures of the EGF-EGFR Complex (ICS, FRET-FLIM and Photobleaching, SPIDA)*

ICS measurements on a GFP-tagged receptor as a function of EGF concentration showed that EGF induces a EGFR dimer-to-tetramer transition and kinase activation independently of internalisation [61]. Addition of EGF resulted in a decrease in the density of EGFR by a factor of two consistent with an increased aggregation of EGFR dimers [61]. Independent measurements of the distance between fluorescently-tagged ligands using FLIM detected Förster Resonance Energy Transfer (FRET) [61] and polarization Förster Resonance homotransfer [69] have revealed an unexpectedly close separation between receptor-associated ligands of approximately 5 nm, a distance that is too short to be consistent with the 11 nm separation of ligands in the crystal structure of the ligated EGFR extracellular domain dimer (c/f back to back dimer in Fig. 5.1). Combining the results from the ICS and FRET/homo-FRET measurements the data was consistent with a monomer-dimer-tetramer model, with a major, new species, the liganded EGFR tetramer.

Wiseman's laboratory used the EGFR-GFP CHO system and revealed EGF and EGFR expression-dependent dimerization and clustering. By means of spatial intensity distribution analysis or SpIDA the authors detected monomers and EGF-induced dimers in confocal scanning images [70]. Moments analysis was used to examine the higher-order clustering of EGFR-GFP following EGF treatment [71].

Nagy et al. used number and brightness analysis to examine EGF-induced EGFR-GFP oligomerisation in CHO cells. For cells expressing a physiological level of EGFR-GFP, EGF treatment resulted in detection of mobile monomers, dimers and pentamers [66].

More recently, Kuriyan's laboratory utilised photobleaching and single molecule observations on ooctes expressing an ultra-low density of EGFR-GFP. After addition of EGF, monomers, dimers and tetramers of EGFR-GFP were observed with >50% of EGFR-GFP in tetramers [72]. Using site-directed mutagenesis and molecular modelling, Kuriyan's team identified a tetramer interface.

5.4.3 *Link Between EGFR Quaternary Structure and EGFR Activation (FLIM-ICS)*

While the coincidence of ligand binding, the formation of tetramers and increases in phosphorylation was suggestive that tetramers might be an activated EGFR species, proof that there was a correlation between tetramers and activation on single cells requires an alternative strategy. We made use of an already-developed FLIM-FRET assay for measuring EGFR phosphorylation (activation) and combined this assay with ICS (i.e. FLIM-ICS) to determine the cluster densities and relative sizes of

phosphorylated and unphosphorylated EGFR. From FLIM images containing a GFP-tagged EGFR and an anti-phosphotyrosine conjugated to AlexaFluor555 we were able deconvolute the fluorescence from the activated EGFR from the fluorescence from the inactive EGFR. This is because the lifetimes of the GFP tag are different in the two states and the frequency responses are different. This concept is sketched in Fig. 5.2. From the optically separated images of the active and inactive EGFR we were able to determine the fraction of phosphorylation EGFRs, fraction of unphosphorylated EGFRs, the density of phosphorylated EGFRs, the density of

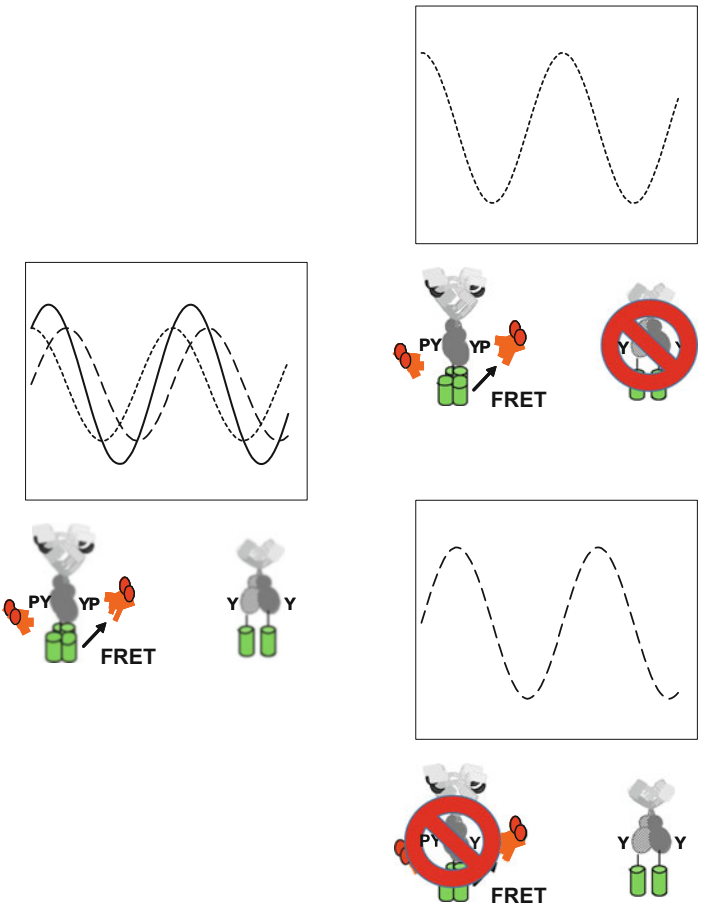

Fig. 5.2 Optical deconvolution of active and inactive epidermal growth factor receptor using frequency-domain FLIM. Activated receptors may be distinguished from un-activated receptors by the different lifetimes and frequency-responses. Un-activated receptors have the characteristic sine wave pattern for GFP while activated receptors have a shorter phase and longer modulation amplitude due to FRET from the GFP to the acceptor-labelled antibody. Phase suppression allows fluorescence from either the active or the inactive receptors to be displayed in an image. Use of ICS methods then gives quantitative information about the cluster densities and relative brightness of active versus inactive receptors

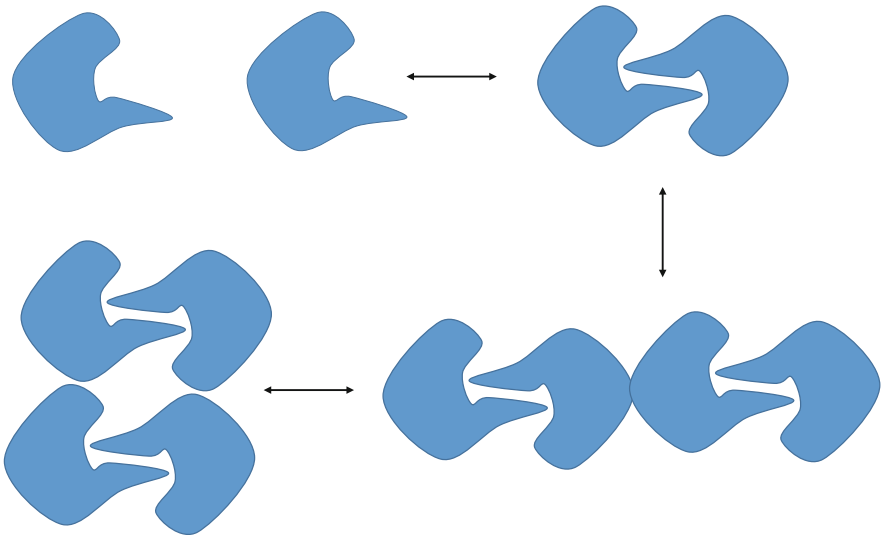

Fig. 5.3 Revised model of EGFR organization as gleaned from a multidimensional microscopy perspective. View of receptor quaternary forms looking down at the membrane from above. Monomer, back-to-back dimer and two tetramer forms are shown. Cis or head-to-head dimer-of-dimers and Trans or side-by-side dimer-of-dimers configurations are shown

unphosphorylated EGFRs, and importantly the relative brightness (or cluster size) of the activated EGFR relative to the unactivated EGFR. These quantitative parameters were compared to different models for the EGFR activation process. For a monomer to dimer transition model the relative brightness of activated EGFR to un-activated EGFR can have a maximum value of 2. For a dimer conformational change model the relative brightness of activated to unactivated EGFR would be 1. Our measurements revealed that the relative brightness was 4 and was more consistent with a monomer-dimer-tetramer model, i.e. involving a pre-equilibrium between monomer-dimer states in the absence of ligand and a ligand-induced dimer to tetramer transition. An alternative model involving dimer-dimer polymerization reaction was also considered and not incompatible with the available data. These results showed that active dimers were not the only active EGFR species and that EGFR tetramers were also phosphorylated as a major species [73] (Fig. 5.3).

5.4.4 EGF Dose and Time-Series ICS Experiments of EGFR Clustering (TICS)

To examine the relationship between EGF binding, EGFR clustering and phosphorylation we measured the clustering of EGFR as a function of EGF concentration and as a function of time and measured EGFR phosphorylation in parallel. To

interpret the data we made use of a rule-based model which included details of ligand binding to receptor (including negative cooperativity), ectodomain dimerization, kinase-mediated dimerization, and the formation of oligomers up to tetramers. Importantly this structure-inspired model included parameters from published biochemical and biophysical studies from other laboratories. This model predicted that cluster size distribution of the EGFR as a function of EGF and time. This model allowed for activation in dimeric EGFR but found that the predominant activated species was the EGFR tetramer under the conditions of our experiments. To the best of our knowledge, this was the first detailed experiment and theory paper describing complex EGFR oligomerization and phosphorylation [74].

5.4.5 *Link Between EGFR Quaternary Structure and the Formation of an EGFR-Adaptor Signalling Complex (FLIM-ICS)*

Growth factor receptor binding protein 2 or Grb2 is an adaptor that links phosphorylated EGFR to downstream intracellular signalling cascades. FRET-FLIM measurements between EGFR-GFP and a co-transfected Grb2-mRFP revealed no interaction between EGFR-GFP and Grb2-mRFP in the absence of EGF. However, EGF addition promoted an interaction between the EGFR-GFP and Grb2-mRFP. Using the FLIM-ICS approach we examined the relative cluster sizes and cluster densities of EGFR-GFP bound to Grb2-mRFP and free EGFR-GFP. The relative brightness was from 4 to 5 indicating that the higher-order EGFR-GFP tetramer bound the Grb2 and thus must be involved in coupling to down-stream signalling cascades. Use of rule-based modelling enabled prediction of the EGFR oligomeric distribution and fraction of Grb2 bound to each type of oligomer. The majority of tetramers was bound to Grb2 with a smaller proportion of dimers bound to Grb2 [75].

5.4.6 *Conformation of the EGFR in Resting and Ligand States (FRET, FLIM and Polarization)*

High resolution structural studies revealed that the extracellular domain of the EGFR was found in two forms-a compact, tethered conformation and an extended, untethered conformation in the complex with EGF (Fig. 5.1). To determine the conformation of the extracellular domain of the full length EGFR on intact cells, two laboratories have placed a fluorescent probe at the N-terminus and used FRET to measure the distance from the probe to the membrane [76, 77].

In our study, distances from YFP probe in YFP-EGFR to rhodamine-labelled lipids in the membranes of BaF/3 cells were determined by flow cytometric FRET. Distances in the range 8–10 nm in the absence of presence of EGF were determined. Homo-transfer between the YFP probes revealed the majority of YFP-EGFRs were pre-dimerized. The results were interpreted in terms of an extended pre-formed dimer which remained extended after ligand binding and activation and further oligomerisation [76].

The Arndt-Jovin study used a different fluorescent reporter and CHO cells and FLIM to measure FRET between the probe and a membrane acceptor. Changes in FRET were observed and interpreted in terms of a tether to untether transition [77].

The discrepancy in the conclusions from the two studies can be understood if the unliganded monomer is tethered (the unliganded EGFR monomer is the prevalent form in CHO cells) and the unliganded dimer (EGFR dimer is prevalent form in BaF/3 cells) is untethered.

5.4.7 EGFR Lateral Dynamics at Cell Surfaces (Image FCS, STICS)

Fluctuations measured in space-time afford even greater information content than either ICS or FCS. Wohland's lab has impressively broken the record for the number of FCS curves measured in parallel by using an image-based approach. Because 2D detectors contain millions of pixels and fast detection allows temporal information, it is now possible to collect many FCS curves using image FCS or iFCS. Wohland utilized his iFCS approach to examine the organization and dynamics of the EGFR-GFP on CHO cells [78].

5.4.8 EGFR Organization on Cancer Cells (ICS, FRET, FLIM-ICS, Super-Resolution)

ICS studies by Peterson and co-workers determined the average cluster density and average number of EGFR proteins per cluster on A431 cancer cells. These cancer cells express the EGFR to a high level of 1–3 million EGFRs per cluster. Consequently, the number of EGFRs per cluster was estimated to be between 10 and 30 receptors per cluster [79].

Gadella and Jovin measured FRET between EGFs on EGFRs on A431 cells. The results were interpreted in terms of monomer-dimer model, with FRET occurring in a dimer. Significantly, the authors revealed pre-dimers of the EGFR in the high affinity ligand-binding population [80].

Clayton et al. [46] used FRET-FLIM-ICS in an attempt to correlate the nanoscale organization of the EGFR revealed by FRET measurements with the sub-micron scale clustering observed by ICS. Using a ligand-blocking antibody

as a probe, FRET clusters containing 10–30 receptors were observed. FRET-FLIM measurements as a function of donor:acceptor ratio were not consistent with FRET between dimers but more consistent with FRET between an oligomer such as a tetramer. The results suggested a nascent hierarchical organization of the EGFR with oligomers assembled into larger clusters. It was proposed that this assembly was responsible for basal activation on the EGFR in this cancer cell line.

Sako utilised a number of single molecule techniques to measure the relationship between EGF binding and EGFR activation. Dynamic clustering was observed after EGF addition in A431 cells and attributed to amplification of activation via interaction of activated EGFR with un-activated EGFR [81].

The Wang group used super-resolution microscopy to directly observe clusters of EGFR from a normal cell line and a cancer cell line. Larger clusters were reported for the cancer cell line. The authors suggested that the EGFR clustering was promoted by receptor-lipid interactions [82].

5.5 Summary and Future Perspectives

Membrane proteins in cells exhibit structural hierarchy over a range of length and time-scales. Fluorescence signals from judiciously-placed probes on membrane proteins are sensitive to interactions on the 5–1000 nm length scales and over the time scales of picoseconds and greater. Using multiple dimensions of fluorescence and combining them with spatial and/or temporal dimensions is an attractive approach to link structure, dynamics and biological activity.

A theme explored in this chapter was how to link information from structural biology with fluorescence experiments on the cell surface. We have explored this theme using the epidermal growth factor receptor as an example. Taken as a whole, the multidimensional microscopy measurements provide data that can be confronted with models derived from structural biology. In the case of the EGFR, it is the author's opinion that the classical ligand-induced monomer-dimer kinase-activation model requires significant revision. First, other oligomeric forms of the receptor can exist in the absence of ligand (i.e. pre dimers and higher-order oligomers). Second, while dimerization is acknowledged as a key initial kinase activation event, higher-order oligomerisation appears to be required for full phosphorylation of the C-terminal tail. Furthermore, adaptor binding, which is important for linking receptor activation to downstream enzyme activation, appears to be enhanced in tetramers, relative to dimers. Membranes and cell-specific factors seem to play some role in dictating EGFR organization as evidenced from experiments on different cell types, and experiments where cell or cytoskeletal components are depleted or denatured.

More work is required to develop new technologies to bridge the gap between the high-resolution structural biology methods and fluorescence methods on the membranes of living cells. Ideally these methods should have an excellent time resolution, an excellent spatial resolution, and inform on the biologically relevant structural dynamics in a living cells and ultimately a living human being.

References

1. Stryer L. Biochemistry. New York: W.H. Freeman and Company; 1988.
2. Frauenfelder H, Chen G, Berendzen J, et al. A unified model of protein dynamics. PNAS. 2009;106:5129–34.
3. Torres J, Stevens TJ, Samsó M. Membrane proteins: the 'Wild West' of structural biology. Trends Biol Sci. 2003;28:137–44.
4. Lakowicz JR. Principles of fluorescence spectroscopy. 3rd ed. New York: Springer; 2007.
5. Weber G. Enumeration of components in complex systems by fluorescence spectrophotometry. Nature. 1961;190:27–9.
6. Weber G. Rotational Brownian motion and polarization of the fluorescence of solutions. Adv Protein Chem. 1953;8:415–59.
7. Millar DP. Time-resolved fluorescence spectroscopy. Curr Opin Struct Biol. 1996;6:637–42.
8. Elson EL, Magde D. Fluorescence correlation spectroscopy I. Conceptual basis and theory. Biopolymers. 1974;13:1–27.
9. Magde D, Elson EL, Webb WW. Fluorescence correlation spectroscopy II. An experimental realization. Biopolymers. 1974;13:29–61.
10. Petersen NO, Wiseman PW, Seger O, Magnusson KE. Quantitation of membrane receptor distributions by image correlation spectroscopy: concept and application. Biophys J. 1993;65:1135–46.
11. Ghauharali RI, Brakenhoff GJ. Fluorescence photobleaching-based image standardization for fluorescence microscopy. J Microsc. 2001;198:88–100.
12. Lakowicz JR, Weber G. Quenching of fluorescence by oxygen. A probe for structural fluctuations in macromolecules. Biochemistry. 1973;12:2161–4170.
13. Weber G. Dependence of the polarization of the fluorescence on the concentration. Trans Faraday Soc. 1954;50:552–5.
14. Lichtman JW, Conchello JA. Fluorescence microscopy. Nat Methods. 2005;2:910–9.
15. Zimmermann T, Rietdorf J, Pepperkok R. Spectral imaging and its applications in live cell microscopy. FEBS Letts. 2003;546:87–92.
16. Berezin MY, Achilefu S. Fluorescence lifetime measurements and biological imaging. Chem Rev. 2011;110:2641–84.
17. Gough AH, Taylor DL. Fluorescence anisotropy imaging microscopy maps calmodulin binding during cellular contraction and locomotion. J Cell Biol. 1993;121:1095–107.
18. Dix JA, Verkman AS. Mapping of fluorescence anisotropy in living cells by ratio imaging-application to cytoplasmic viscosity. Biophys J. 1990;57:231–40.
19. Axelrod D. Carbocyanine dye orientation in red cell membrane studied by microscopic fluorescence polarization. Biophys J. 1979;26:557–74.
20. Rappaz B, Wiseman PW. Image correlation spectroscopy for measurements of particle densities and colocalization. Curr Protoc Cell Biol. 2013;27:1–15.
21. Wüstner D, Solanko LM, Lund FW, Sage D, Schroll HJ, Lomholt MA. Quantitative fluorescence loss in photobleaching for analysis of protein transport and aggregation. BMC Bioinf. 2012;13:296–305.
22. Beechem JM, Brand L. Time-resolved fluorescence of proteins. Annu Rev Biochem. 1985;54:43–71.
23. van Stokkum IHM, Larsen DS, van Grondelle R. Global and target analysis of time-resolved spectra. BBA. 2004;1657:82–104.
24. Martí AA, Li X, Jockusch S, Li Z, Raveendra B, Kalachikov S, Russo JJ, Morozova I, Puthanveettil S, Ju J, Turro NJ. Pyrene binary probes for unambiguous detection of mRNA using time-resolved fluorescence spectroscopy. Nucleic Acids Res. 2006;34:3161–8.
25. Laptenok SP, Borst JW, Mullen KM, van Stokkum IH, Visser AJ, van Amerongen H. Global analysis of Förster resonance energy transfer in live cells measured by fluorescence lifetime imaging microscopy exploiting the rise time of acceptor fluorescence. Phys Chem Chem Phys. 2010;12:7593–602.

26. Gafni A, DeToma RP, Manrow RE, Brand L. Nanosecond decay studies of a fluorescence probe bound to apomyoglobin. Biophys J. 1979;17:155–68.
27. Jones BE, Beechem JM, Matthews CR. Local and global dynamics during the folding of Escherichia coli dihydrofolate reductase by time-resolved fluorescence spectroscopy. Biochemistry. 1995;34:1867–77.
28. Martin-Fernandez ML, Clarke DT, Tobin MJ, Jones GR. Real-time studies of the interactions between epidermal growth factor and its receptor during endocytic trafficking. Cell Mol Biol. 2000;46:1103–12.
29. Cross AJ, Fleming GR. Influence of inhibitor binding on the internal motions of lysozyme. Biophys J. 1986;50:507–12.
30. Tanaka F, Mataga N. Theory of time-dependent photo-selection in interacting fixed systems. Photochem Photobiol. 1979;29:1091–7.
31. Jameson DM, Ross JP, Albanesi JP. Fluorescence fluctuation spectroscopy: ushering in a new age of enlightenment for cellular dynamics. Biophys Rev. 2012;1:105–18.
32. Elson EL. Quick tour of fluorescence correlation spectroscopy from its inception. J Biomed Opt. 2004;9:857–64.
33. Bacia K, Kim SA, Schwille P. Fluorescence cross-correlation spectroscopy in living cells. Nat Methods. 2006;3:83–9.
34. Axelrod D, Koppel D, Schlessinger J, Elson E, Webb W. Mobility measurement by analysis of fluorescence photobleaching recovery kinetics. Biophys J. 1976;16:1055–69.
35. Peters R, Brünger A, Schulten K. Continuous fluorescence microphotolysis: a sensitive method for study of diffusion processes in single cells. Proc Natl Acad Sci U S A. 1981;78:962–6.
36. Chattopadhyay A, Haldar S. Dynamic insight into protein structure utilizing red edge excitation shift. Acc Chem Res. 2014;47:12–29.
37. Hanley QS. Spectrally resolved fluorescent lifetime imaging. J R Soc Interface. 2009;6: S83–92.
38. Chen Y-C, Clegg RM. Spectral resolution in conjunction with polar plots improves the accuracy and reliability of FLIM measurements and estimates of FRET efficiency. J Microsc. 2011;244:21–37.
39. Golfetto O, Hinde E, Gratton E. Laurdan fluorescence lifetime discriminates cholesterol content from changes in fluidity in living cell membranes. Biophys J. 2013;104:1238–47.
40. Urbančič I, Ljubetič A, Arsov Z, Štrancar J. Coexistence of probe conformations in lipid phases—a polarized fluorescence microspectroscopy study. Biophys J. 2013;105:919–27.
41. Mattheyses AL, Hoppe AD, Axelrod D. Polarized fluorescence resonance energy transfer microscopy. Biophys J. 2004;87:2787–97.
42. Ando R, Hama H, Yamamoto-Hino M, Mizuno H, Miyawaki A. An optical marker based on the UV-induced green-to-red photoconversion of a fluorescent protein. Proc Natl Acad Sci U S A. 2002;99:12651–6.
43. Díaz SA, Gillanders F, Jares-Erijman EA, Jovin TM. Photoswitchable semiconductor nanocrystals with self-regulating photochromic Förster resonance energy transfer acceptors. Nat Commun. 2015;6:6036.
44. Clayton AH, Hanley QS, Arndt-Jovin DJ, Subramaniam V, Jovin TM. Dynamic fluorescence anisotropy imaging microscopy in the frequency domain (rFLIM). Biophys J. 2002;83:1631–49.
45. Clayton AH. The polarized AB plot for the frequency-domain analysis and representation of fluorophore rotation and resonance energy homotransfer. J Microsc. 2008;232:306–12.
46. Clayton AH, Tavarnesi ML, Johns TG. Unligated epidermal growth factor receptor forms higher order oligomers within microclusters on A431 cells that are sensitive to tyrosine kinase inhibitor binding. Biochemistry. 2007;46:4589–97.
47. Levitt JA, Morton PE, Fruhwirth GO, Santis G, Chung P-H, Parsons M, Suhling K. Simultaneous FRAP, FLIM and FAIM for measurements of protein mobility and interaction in living cells. Biomed Opt Express. 2015;6:3842–54.

48. Ehrenberg M, Rigler R. Rotational Brownian motion and fluorescence intensify fluctuations. Chem Phys. 1974;4(3):390–401.
49. Sharma P, Varma R, Sarasij RC, Ira GK, Krishnamoorthy G, Rao M, Mayor S. Nanoscale organization of multiple GPI-anchored proteins in living cell membranes. Cell. 2004;116:577–89.
50. Yeow EK, Clayton AH. Enumeration of oligomerization states of membrane proteins in living cells by homo-FRET spectroscopy and microscopy: theory and application. Biophys J. 2007;92:3098–104.
51. Rocheleau JV, Wiseman PW, Petersen NO. Isolation of bright aggregate fluctuations in a multipopulation image correlation spectroscopy system using intensity subtraction. Biophys J. 2003;84:4011–22.
52. Qian H, Elson EL. Distribution of molecular aggregation by analysis of fluctuation moments. Proc Natl Acad Sci U S A. 1990;87:5479–83.
53. Palmer AG 3rd, Thompson NL. Molecular aggregation characterized by high order autocorrelation in fluorescence correlation spectroscopy. Biophys J. 1987;52:257–70.
54. Ciccotosto GD, Kozer N, Chow TT, Chon JW, Clayton AH. Aggregation distributions on cells determined by photobleaching image correlation spectroscopy. Biophys J. 2013;104:1056–64.
55. Lajevardipour A, Chon JWM, Clayton AHA. Determining complex aggregate distributions of macromolecules using photobleaching image correlation microscopy. AIMS Biophys. 2015;2:1–7.
56. Lemmon MA, Schlessinger J. Cell signaling by receptor tyrosine kinases. Cell. 2010;141:1117–34.
57. Yarden Y, Schlessinger J. Epidermal growth factor induces rapid, reversible aggregation of the purified epidermal growth factor receptor. Biochemistry. 1987;26:1443–51.
58. Schreiber AB, Libermann TA, Lax I, Yarden Y, Schlessinger J. Biological role of epidermal growth factor-receptor clustering. Investigation with monoclonal anti-receptor antibodies. J Biol Chem. 1983;258:846–53.
59. Burgess AW, Cho HS, Eigenbrot C, Ferguson KM, Garrett TP, Leahy DJ, Lemmon MA, Sliwkowski MX, Ward CW, Yokoyama S. An open-and-shut case? Recent insights into the activation of EGF/ErbB receptors. Mol Cell. 2003;12:541–52.
60. Zhang X, Gureasko J, Shen K, Cole PA, Kuriyan J. An allosteric mechanism for activation of the kinase domain of epidermal growth factor receptor. Cell. 2006;125:1137–49.
61. Clayton AH, Walker F, Orchard SG, Henderson C, Fuchs D, Rothacker J, Nice EC, Burgess AW. Ligand-induced dimer-tetramer transition during the activation of the cell surface epidermal growth factor receptor-A multidimensional microscopy analysis. J Biol Chem. 2005;280:30392–9.
62. Liu P, Sudhaharan T, Koh RM, Hwang LC, Ahmed S, Maruyama IN, Wohland T. Investigation of the dimerization of proteins from the epidermal growth factor receptor family by single wavelength fluorescence cross-correlation spectroscopy. Biophys J. 2007;93:684–98.
63. Lidke DS, Nagy P, Barisas BG, Heintzmann R, Post JN, Lidke KA, Clayton AH, Arndt-Jovin DJ, Jovin TM. Imaging molecular interactions in cells by dynamic and static fluorescence anisotropy (rFLIM and emFRET). Biochem Soc Trans. 2003;31:1020–7.
64. Saffarian S, Li Y, Elson EL, Pike LJ. Oligomerization of the EGF receptor investigated by live cell fluorescence intensity distribution analysis. Biophys J. 2007;93:1021–31.
65. Hofman EG, Bader AN, Voortman J, van den Heuvel DJ, Sigismund S, Verkleij AJ, Gerritsen HC, van Bergen en Henegouwen PM. Ligand-induced EGF receptor oligomerization is kinase-dependent and enhances internalization. J Biol Chem. 2010;285:39481–9.
66. Nagy P, Claus J, Jovin TM, Arndt-Jovin DJ. Distribution of resting and ligand-bound ErbB1 and ErbB2 receptor tyrosine kinases in living cells using number and brightness analysis. Proc Natl Acad Sci U S A. 2010;107:16524–9.
67. Kozer N, Kelly MP, Orchard S, Burgess AW, Scott AM, Clayton AH. Differential and synergistic effects of epidermal growth factor receptor antibodies on unliganded ErbB dimers and oligomers. Biochemistry. 2011;50:3581–90.

68. Needham SR, Zanetti-Domingues LC, Scherer KM, Hirsch M, Rolfe DJ, Roberts SK, Martin-Fernandez ML, Clarke DT, Tynan CJ. Determining the geometry of oligomers of the human epidermal growth factor family on cells with <10 nm resolution. Biochem Soc Trans. 2015;43:309–14.
69. Whitson KB, Beechem JM, Beth AH, Staros JV. Preparation and characterization of Alexa Fluor 594-labeled epidermal growth factor for fluorescence resonance energy transfer studies: application to the epidermal growth factor receptor. Anal Biochem. 2004;324:227–36.
70. Godin AG, Costantino S, Lorenzo LE, Swift JL, Sergeev M, Ribeiro-da-Silva A, De Koninck Y, Wiseman PW. Revealing protein oligomerization and densities in situ using spatial intensity distribution analysis. Proc Natl Acad Sci U S A. 2011;108:7010–5.
71. Sergeev M, Swift JL, Godin AG, Wiseman PW. Ligand-induced clustering of EGF receptors: a quantitative study by fluorescence image moment analysis. Biophys Chem. 2012;161:50–3.
72. Huang Y, Bharill S, Karandur D, Peterson SM, Marita M, Shi X, Kaliszewski MJ, Smith AW, Isacoff EY, Kuriyan J. Molecular basis for multimerization in the activation of the epidermal growth factor receptor. Elife Mar. 2016;28:5.
73. Clayton AH, Orchard SG, Nice EC, Posner RG, Burgess AW. Predominance of activated EGFR higher-order oligomers on the cell surface. Growth Factors. 2008;26:316–24.
74. Kozer N, Barua D, Orchard S, Nice EC, Burgess AW, Hlavacek WS, Clayton AH. Exploring higher-order EGFR oligomerisation and phosphorylation – a combined experimental and theoretical approach. Mol BioSyst. 2013;9:1849–63.
75. Kozer N, Barua D, Henderson C, Nice EC, Burgess AW, Hlavacek WS, Clayton AH. Recruitment of the adaptor protein Grb2 to EGFR tetramers. Biochemistry. 2014;53:2594–604.
76. Kozer N, Henderson C, Jackson JT, Nice EC, Burgess AW, Clayton AH. Evidence for extended YFP-EGFR dimers in the absence of ligand on the surface of living cells. Phys Biol. 2011;8(6):066002.
77. Ziomkiewicz I, Loman A, Klement R, Fritsch C, Klymchenko AS, Bunt G, Jovin TM, Arndt-Jovin DJ. Dynamic conformational transitions of the EGF receptor in living mammalian cells determined by FRET and fluorescence lifetime imaging microscopy. Cytometry A. 2013;83:794–805.
78. Bag N, Huang S, Wohland T. Plasma membrane organization of epidermal growth factor receptor in resting and ligand-bound states. Biophys J. 2015;109:1925–36.
79. Keating E, Nohe A, Petersen NO. Studies of distribution, location and dynamic properties of EGFR on the cell surface measured by image correlation spectroscopy. Eur Biophys J. 2008;37:469–81.
80. Gadella TW Jr, Jovin TM. Oligomerization of epidermal growth factor receptors on A431 cells studied by time-resolved fluorescence imaging microscopy. A stereochemical model for tyrosine kinase receptor activation. J Cell Biol. 1995;129:1543–58.
81. Ichinose J, Murata M, Yanagida T, Sako Y. EGF signaling amplification by dynamic clustering of EGFR. Biochem Biophys Res Commun. 2004;324:1143–9.
82. Wang Y, Gao J, Guo X, Tong T, Shi X, Li L, Qi M, Wang Y, Cai M, Jiang J, Xu C, Ji H, Wang H. Regulation of EGFR nanocluster formation by ionic protein-lipid interaction. Cell Res. 2014;24:959–76.

Chapter 6
Investigating the Dynamics and Organization of Membrane Proteins and Lipids by Imaging Fluorescence Correlation Spectroscopy

Nirmalya Bag, Shuangru Huang, and Thorsten Wohland

Abstract The dynamics and organization of lipid bilayers, whether they are artificial supported lipid bilayers, lipid vesicles or cell membranes, still pose an enigma. Especially bilayers with multiple lipid components, not to mention peptides and proteins, are difficult to characterize as they often exhibit fast molecular dynamics and structural organization that presumably are on the nanometer scale. Therefore, biophysical techniques are required that measure sufficiently fast to detect molecular movements and interactions but also provide information about structures below the optical diffraction limit. Imaging Fluorescence Correlation Spectroscopy (Imaging FCS) fulfils these conditions and can resolve membrane dynamics with high temporal resolution and provide information even on nanoscopic scales. Compared to conventional confocal FCS, this multiplexed modality can record over hundreds of contiguous points simultaneously on the membrane. In this chapter, we present briefly the theory of Imaging FCS and provide general guidelines for its implementation. This is followed by a description of multiple options to analyse the Imaging FCS data. We discuss the FCS diffusion law to investigate the membrane organization below the optical diffraction limit, the difference in cross-correlation function (ΔCCF) to investigate anisotropies in diffusion, Imaging Fluorescence Cross-correlation (Imaging FCCS) to study interactions, and the recovery of the Arrhenius activation energy of diffusion to determine lipid packing and phases. Lastly, we give a short overview of recent applications of Imaging FCS.

N. Bag • S. Huang
Department of Biological Sciences and Centre for Bioimaging Sciences, National University of Singapore, 14 Science Drive 4, Singapore 117557, Singapore

T. Wohland (✉)
Department of Biological Sciences and Centre for Bioimaging Sciences, National University of Singapore, 14 Science Drive 4, Singapore 117557, Singapore

Department of Chemistry, National University of Singapore, 3 Science Drive 3, Singapore 117543, Singapore
e-mail: twohland@nus.edu.sg

A. Chattopadhyay (ed.), *Membrane Organization and Dynamics*, Springer Series in Biophysics 20, DOI 10.1007/978-3-319-66601-3_6

6.1 Introduction

The plasma membrane defines a semi-permeable barrier between a cell and its exterior and is involved in many cell functions including cell adhesion, signalling and the selective export and import of ions and molecules. Despite the importance of this organelle, we have still a limited understanding of its precise structure, organization and molecular dynamics, which all play important roles in its proper function. This has several reasons originating in the complex spatial organization of the membrane and its fast fluid dynamics. The plasma membrane consists of a complex mixture of proteins inserted in or attached to a lipid bilayer which itself contains hundreds of different lipid species. The different bilayer components interact by homo- and hetero-association [1] and the inner and outer bilayer leaflets couple through transmembrane proteins and specific long chain lipids [2]. This intricate interplay between the membrane components, the transbilayer coupling, and the interaction of the plasma membrane with intracellular and extracellular components yields a complex membrane architecture. These thermodynamically, kinetically, and affinity driven interactions [3–5] have variable strength due to their differential origin and act over a broad range of length and time scales, leading to a unique spatio-temporal organization of the membrane [4, 6]. The present understanding of the membrane organization implies the co-existence of different 'membrane organization principles' that include chemically distinct protein clusters formed by homo- and hetero-association, lipid domains and lipid-protein complexes [1, 7]. The stability and function of these macromolecular entities on the membrane are influenced by the actin cytoskeleton located underneath the plasma membrane at the cytosolic face via passive and/or active (ATP-dependent) mechanisms [3, 8]. The size of these membrane features ranges from a few nanometers to a few micrometers and the time scale of the biochemical processes they are involved in varies from milliseconds to minutes [4, 9]. For simplicity, we refer to a membrane feature as nanoscopic or microscopic depending on whether its size is below or above the optical resolution limit (~200 nm), respectively. A better understanding of the function of the plasma membrane therefore requires techniques that can measure at high temporal resolution and can yield information at nanoscopic and microscopic spatial scales.

A further complicating fact is that the spatial distribution of these nanoscopic features is heterogeneous. For example, certain proteins form clusters along the boundary of the cell [10] while some other proteins form clusters independent of the precise location on the membrane [11]. Likewise, lipid domains create locally ordered but moderately fluid regions on the membrane. This increases the local concentration of the proteins that can facilitate signalling reactions on the cell surface [12]. It is therefore necessary to measure spatially-resolved maps of diffusion coefficients, concentrations and interactions for a better understanding of membrane dynamics and organization and its influence on biological processes.

Ideally, a non-invasive or minimally invasive technique having nanometer spatial resolution and millisecond temporal resolution is necessary to investigate membrane

diffusion and interaction patterns. Methods with single molecule sensitivity are preferred since the interactions could be specific to a single molecule or only few molecules. They should also be readily applicable to living cells or organisms. Unfortunately, the majority of the current fluorescence spectroscopic and microscopic techniques offer either good temporal or spatial resolution but not both simultaneously [13]. Single particle tracking (SPT) fulfils both criteria since it monitors movement of individual particles with a few nanometer precision and at the millisecond time scale [14]. Fitting the time dependence of mean squared displacement (MSD) with an appropriate theoretical model provides the diffusion coefficient. However, SPT requires bright, photostable fluorescent reporters of molecular size for good accuracy and precision of the localization and is constrained to very low labelling densities since high density labelling does not allow the reconstruction of individual trajectories. Both conditions are often not compatible with biological measurements and thus limit the application of SPT [14–18].

Fluorescence correlation spectroscopy (FCS) can at least avoid some of these issues while still preserving single molecule sensitivity and it is routinely used on living systems [19]. Conventionally FCS is performed in a confocal mode. The confocal observation volume is positioned within the sample and the fluorescence intensity originating from this volume is measured over time to provide information on the dynamics of the system. The autocorrelation analysis of the recorded fluorescence time trace yields a characteristic decaying temporal autocorrelation function (ACF) (Fig. 6.1). The width and amplitude of the ACF provide the diffusion coefficient and concentration at the observed point. However, the application of confocal FCS on live cell plasma membranes has also constraints. First, it requires calibration of the confocal volume for the measurement of accurate diffusion coefficients and concentrations. Second, the measurements are conventionally carried out on single diffraction-limited spots at a time, limiting spatial information.

Imaging FCS was developed as an advanced spatio-temporal modality to overcome some of these issues [20]. It requires an illumination scheme that can excite a sample plane instead of a single spot and an array detector to capture the image of the illuminated plane at a fast frame rate. Currently, total internal reflection fluorescence microscopy (TIRFM) and single plane illumination microscopy (SPIM) are used to optically section a single plane of the sample and accordingly the techniques are called Imaging TIR-FCS (ITIR-FCS) and SPIM-FCS. Electron multiplying charge coupled device (EMCCD) and scientific complementary metal oxide semiconductor (sCMOS) cameras are used as detectors. Each pixel on the camera chip acts as an individual detection element. The dimension of the individual pixel in combination with the point spread function (PSF) of the optical system limits the x-y extension, and the thickness of the illumination plane provides the z-dimension of the observation volume. This combination creates an array of small observation volumes. When a time series of images is captured, the autocorrelation analysis of the fluorescence time traces obtained from individual pixels produces images of the diffusion coefficient and concentration with a resolution above the diffraction limit. Although the diffraction-limited quantitative maps of diffusion and concentration significantly improve statistics and provide information about

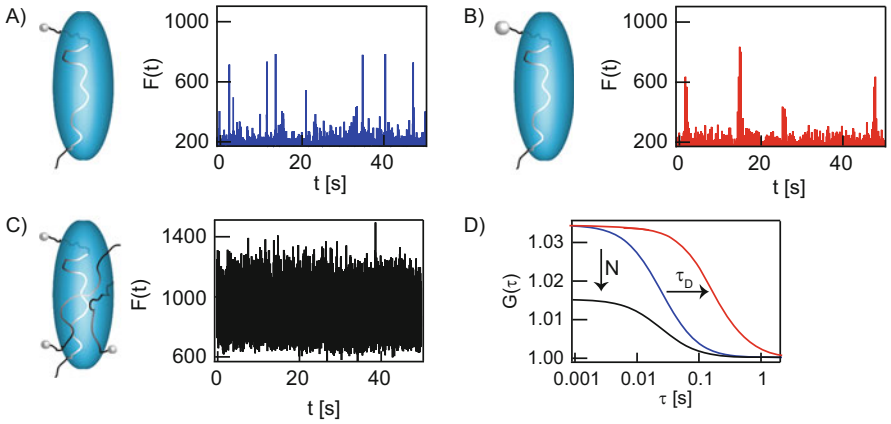

Fig. 6.1 Principles of FCS. (**A**) The *blue ellipsoid* represents the observation volume of the microscope. A particle will not be detected outside the volume but when entering and traversing the observation volume will be excited and emit fluorescence, leading to the fluorescence time trace shown in *blue*. (**B**) A large particle will take longer time to traverse the observation volume leading to fluorescence time trace shown in *red*, where single fluctuations will now be wider. (**C**) If multiple independent particles move simultaneously through the observation volume, as happens in concentrated samples, they will lead to a fluorescence trace that contains contribution from all particles as shown in the trace in *black*. (**D**) This schematic shows how the ACFs for these cases differ. The width of the ACF increases with diffusion time while the amplitude of the ACF decreases with an increasing number of particles in the observation volume

spatial connectivity, they are not sufficient to investigate nanoscale phenomena. Hence several analytical tools were subsequently employed on the diffraction-limited data to characterize the modulation of diffusion behaviour of a given probe in the presence of nanoscale membrane patterns including nanoclusters, nanodomains and the cytoskeleton.

6.2 Theory of Imaging FCS

6.2.1 Principle of FCS

In an FCS measurement, a fluorescence intensity trace, *F(t)*, is acquired from a small observation volume (Fig. 6.1A–C). *F(t)* contains fluctuations due to the movement of particles through the observation volume. Characteristic parameters of the particles and their movement can be obtained by statistical analysis of *F(t)* by an autocorrelation function (ACF, Fig. 6.1D):

$$G(\tau) = \frac{\langle F(t)F(t+\tau)\rangle}{\langle F(t)\rangle\langle F(t+\tau)\rangle} \tag{6.1}$$

The ACF relates the fluorescence of the signal at different lag times τ. It is a unitless function which has its maximum at $\tau = 0$ and converges to 1 for $\tau \to \infty$. This can be seen by the following arguments. For the case of for $\tau \to 0$, the values of $F(t) \approx F(t + \tau)$, and these values are strongly dependent, thus $\langle F(t)F(t+\tau)\rangle$ is at a maximum. For $\tau \to \infty$, i.e. in the case that the lag time is much larger than the characteristic time of diffusion through the observation volume, $F(t)$ and $F(t + \tau)$ are no longer correlated and $\langle F(t)F(t+\tau)\rangle = \langle F(t)\rangle\langle F(t+\tau)\rangle$. Therefore, $G(\tau)$ converges to 1.

Note that the ACF can be written in terms of fluorescence fluctuations $\delta F(t) = F(t) - \langle F(t)\rangle$, i.e.,

$$G'(\tau) = \frac{\langle \delta F(t)\delta F(t+\tau)\rangle}{\langle F(t)\rangle\langle F(t+\tau)\rangle} \tag{6.2}$$

Both definitions are equivalent and differ only in the convergence value. At $\tau \to \infty$, since the particles move in and out, the fluctuations will have an equal probability of being positive or negative, meaning $\langle \delta F(t)\, \delta F(t+\tau)\rangle = 0$, and thus $G(\tau) = G'(\tau) + 1$. Auto-correlation analysis is not limited to only diffusion dynamics. It can be used for any dynamic process which causes fluctuations in the intensity trace [21]. The simultaneous occurrence of multiple dynamic processes gives rise to a correlation function containing multiple decay components. However, in this chapter we will concentrate solely on diffusive processes.

6.2.2 Theoretical Model of Imaging FCS

Here we sketch the derivation of a theoretical model for the autocorrelation function. This model will later be fit to experiments to recover the characteristic parameters of the measured processes. The derivation is based on the mathematical expressions of the detected fluorescence signal and its fluctuations. The temporal fluorescence $F(t)$ and its fluctuation $\delta F(t)$ collected from an observation volume

$$F(t) = Q \int_{-\infty}^{\infty} I(\vec{r})S(\vec{r})CEF(\vec{r})C(\vec{r},t)d\vec{r} \tag{6.3}$$

$$\delta F(t) = Q \int_{-\infty}^{\infty} I(\vec{r})S(\vec{r})CEF(\vec{r})\delta C(\vec{r},t)d\vec{r} \tag{6.4}$$

are given by the following equations: Q is the molecular brightness, which contains the information about the absorption coefficient and quantum yield of the fluorophore and the overall detection efficiency of the microscope. $I(\vec{r})$ is the spatial distribution of the emitter in the image plane which is given by the point spread function (PSF) of the microscope objective. $S(\vec{r})$ describes the extent of the

sample volume. $CEF(\vec{r})$ is the collection efficiency function which describes the collection efficiency of the detection element in dependence on the location of the probe in the sample. Thus the product of $I(\vec{r})$, $S(\vec{r})$ and $CEF(\vec{r})$ defines the observation volume ($W(\vec{r})$) which is also called the molecule detection efficiency function. It determines the final amount of signal from position $\vec{r}$ that is collected by the detection element. $C(\vec{r},t)$ is the concentration of the fluorophore at position $\vec{r}$ and time t.

$$W(\vec{r}) = I(\vec{r})S(\vec{r})CEF(\vec{r}) \tag{6.5}$$

Now, $S(\vec{r})$ can in most cases be assumed to be 1 since the sample volume is much larger than the observation volume and thus (6.5) reduces to:

$$W(\vec{r}) = I(\vec{r})CEF(\vec{r}) \tag{6.6}$$

When (6.3), (6.4), and (6.6) are plugged in (6.1), we obtain

$$G(\tau) = \frac{\iint_{-\infty}^{\infty} W(\vec{r})W(\vec{r}')\langle \delta C(\vec{r},t)\delta C(\vec{r}',t+\tau)\rangle d\vec{r}d\vec{r}'}{\langle C\rangle^2 \left(\int_{-\infty}^{\infty} W(\vec{r})d\vec{r}\right)^2} + 1 \tag{6.7}$$

Here, $\langle \delta C(\vec{r},t)\delta C(\vec{r}',t+\tau)\rangle$ is the concentration correlation function. The expression of this function at any lag time (τ) for a 2D diffusion process [19] is given by:

$$\langle \delta C(\vec{r},t)\delta C(\vec{r}',t+\tau)\rangle = \frac{1}{4\pi D\tau} e^{-\frac{\left(\vec{r}-\vec{r}'\right)^2}{4D\tau}} \tag{6.8}$$

For a rectangular detection element, both concentration correlation function and $CEF(\vec{r})$ are separable in the x- and y- dimension. The distribution of the excitation light along the orthogonal plane of the optical axis ($I(\vec{r})$), i.e., along the sample plane can be approximated by a two-dimensional Gaussian function which is also separable in two dimensions. Therefore, $W(\vec{r})$ is separable in x-and y-dimensions [6]. This allows us to rewrite Eq. (6.7) as:

$$G(\tau) = G_x(\tau)G_y(\tau) + 1 \tag{6.9}$$

where,

$$G_x(\tau) = \frac{\iint_{-\infty}^{\infty} W(\vec{x})W(\vec{x}')\langle \delta C(\vec{x},t)\delta C(\vec{x}',t+\tau)\rangle d\vec{x}d\vec{x}'}{\langle C\rangle^2 \left(\int_{-\infty}^{\infty} W(\vec{x})d\vec{x}\right)^2} + 1 \tag{6.10}$$

$G_y(\tau)$ can be written in a corresponding form. We will only solve the integration for $G_x(\tau)$ as the calculation of $G_y(\tau)$ is analogous. We next find the mathematical

expression of $W(\vec{x})$ using Eq. (6.6). The $CEF(\vec{x})$ for a square pixel, with side length a, is a rectangular function with a value of 1 everywhere inside the pixel and 0 outside the pixel.

$$CEF(\vec{x}) = \begin{bmatrix} 1; -\frac{a}{2} < 0 < \frac{a}{2} \\ 0; \quad otherwise \end{bmatrix} \tag{6.11}$$

However, the image of a molecule is given by the PSF, $I(\vec{x})$, which we approximate by a Gaussian function:

$$I(\vec{x}) = I_0 e^{-\frac{2x^2}{\omega_0^2}} \tag{6.12}$$

The convolution between $CEF(\vec{x})$ and $I(\vec{x})$ can be solved analytically [22] and yields:

$$W(\vec{x}) = \frac{I_0\omega_0}{2}\sqrt{\frac{\pi}{2}}\left(erf\left(\frac{a-2x}{\sqrt{2}\omega_0}\right) + erf\left(\frac{a+2x}{\sqrt{2}\omega_0}\right)\right) \tag{6.13}$$

Incorporating Eqs. (6.13) and (6.8) (for the x-direction) into (6.10), we can solve the intergral:

$$G_x(\tau) = \frac{1}{a\sqrt{\langle C\rangle}}\left(erf\left(\frac{a}{\sqrt{4D\tau+\omega_0^2}}\right) + \frac{\sqrt{4D\tau+\omega_0^2}}{a\sqrt{\pi}}\left(e^{-\frac{a^2}{4D\tau+\omega_0^2}} - 1\right)\right) \tag{6.14}$$

Using Eqs. (6.9, 6.10) (for x and y dimensions) and (6.14), we obtain:

$$G(\tau) = \frac{1}{a^2\langle C\rangle}\left(erf\left(\frac{a}{\sqrt{4D\tau+\omega_0^2}}\right) + \frac{\sqrt{4D\tau+\omega_0^2}}{a\sqrt{\pi}}\left(e^{-\frac{a^2}{4D\tau+\omega_0^2}} - 1\right)\right)^2 + 1 \tag{6.15}$$

Since $N = A_{eff}\langle C\rangle$,

$$G(\tau) = \frac{A_{eff}}{a^2N}\left(erf\left(\frac{a}{\sqrt{4D\tau+\omega_0^2}}\right) + \frac{\sqrt{4D\tau+\omega_0^2}}{a\sqrt{\pi}}\left(e^{-\frac{a^2}{4D\tau+\omega_0^2}} - 1\right)\right)^2 + 1 \tag{6.16}$$

At $\tau = 0$,

$$G(0) = \frac{A_{eff}}{a^2N}\left(erf\left(\frac{a}{\omega_0}\right) + \frac{\omega_0}{a\sqrt{\pi}}\left(e^{-\frac{a^2}{\omega_0^2}} - 1\right)\right)^2 + 1 \tag{6.17}$$

For 2D diffusion, the observation area can be analytically calculated [22] or simply be derived from the fact that

$$G(0) = \frac{1}{N} + 1 \tag{6.18}$$

Comparing Eqs. (6.17) and (6.18), we obtain the functional form of the observation area as:

$$A_{eff} = \frac{a^2}{\left(erf\left(\frac{a}{\omega_0}\right) + \frac{\omega_0}{a\sqrt{\pi}}\left(e^{-\frac{a^2}{\omega_0^2}} - 1\right)\right)^2} \tag{6.19}$$

Note that A_{eff} depends on the pixel size and the dimensions of the PSF. The PSF of a microscope system depends on the numerical aperture of the objective (*NA*) and the emission wavelength of the light (λ_{em}) through the following:

$$\omega_0 = \frac{\omega\lambda_{em}}{NA} \tag{6.20}$$

Theoretical studies showed that the best approximation of a Gaussian to the Airy pattern of an immobile object imaged by a high *NA* fluorescence microscope is provided by an $1/e^2$ radius of $\omega = 0.42$ [23]. In practice, however, ω of an instrumental set up should be determined experimentally [24].

Figure 6.2A shows the dependence of A_{eff} when a is varied for a fixed size of the PSF ($\omega_0 = 320$ nm) (black curve). The influence of the PSF on the observation area can be estimated from the ratio of A_{eff} to a^2 (Fig. 6.2A, red curve). Similarly, ω_0 was also varied while keeping $a = 240$ nm constant (Fig. 6.2B). The observation area increases with increasing pixel or PSF size. When $a \ll \omega_0$, i.e., the PSF is larger than the pixel size, the latter does not influence the size of the observation area significantly (Fig. 6.2C, left). The shape of the observation area is similar to that of the PSF. In this case, the difference between A_{eff} and a^2 is very large. The A_{eff} increases with increasing a while the ratio of A_{eff} to a^2 decreases rapidly. At the other extreme, when $a \gg \omega_0$, the contribution of the PSF is not significant and thus the observation area becomes closer to the spatial distribution of the pixel which is square in shape in this example (Fig. 6.2C, middle). This is more evident when the absolute size of the PSF is smaller than a pixel ($\omega_0 = 320$ nm and $a = 1200$ nm) (Fig. 6.2C, right). For $a \approx \omega_0$, the typical case in most microscope systems, both pixel and the PSF contribute significantly to the resultant observation area.

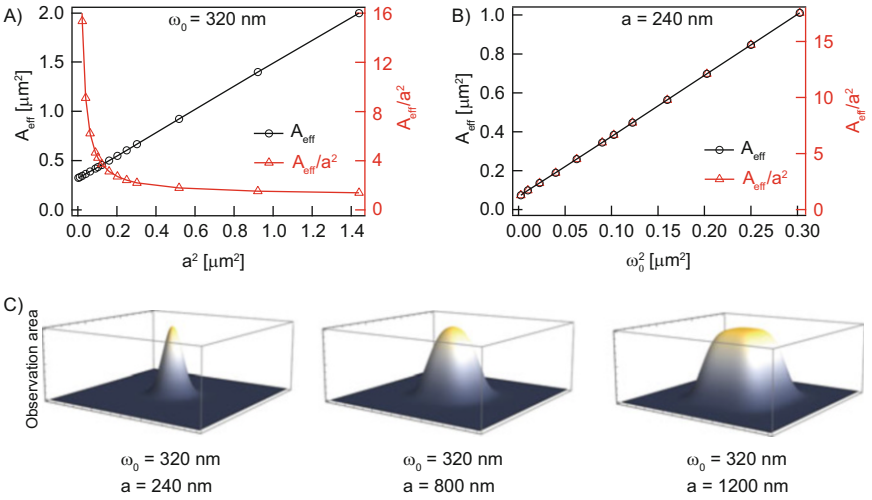

Fig. 6.2 Variation of A_{eff} for ITIR-FCS measurements as a function of the ratio between the pixel size and the PSF size. (**A**) The PSF size is fixed at $\boldsymbol{\omega_0} = 320$ nm while the pixel size is varied. The ratio $A_{eff}/\boldsymbol{a}^2$ gives the effect of PSF on the A_{eff}. This ratio is one if PSF does not influence the observation area. (**B**) The pixel size was fixed at $\boldsymbol{a} = 240$ nm while $\boldsymbol{\omega_0}$ is varied. (**C**) The shape of the observation area is shown for three values with $\boldsymbol{\omega_0}$ equal to 320 nm

6.3 Experimental Realization of Imaging FCS

6.3.1 Set-Up Requirements of Imaging FCS

Imaging FCS requires simultaneous excitation of multiple membrane spots and their recording by an array detector. This can be achieved by SPIM and TIRF illumination schemes that have inherent optical sectioning capability along the z-direction, and thus minimize cross-talk [25, 26]. In case of TIRF illumination (Fig. 6.3A), the excitation beam is focused on the back focal plane of an oil-immersion objective lens after being reflected by a dichroic mirror. The beam is then total internally reflected at the glass-water interface by adjusting the incident angle, which results in an evanescent field in the water medium with a penetration depth of ~100 nm [27]. The fluorescence from the sample is collected by the same objective. In SPIM (Fig. 6.3B), a cylindrical lens creates an excitation light sheet, which is then focused into the sample by an excitation objective. A detection objective placed orthogonally with respect to the illumination objective collects the fluorescence emission. To date, mainly EMCCD and sCMOS cameras are used to record the fluorescence emission due to their high acquisition speed (<2 ms per frame), 100% fill factor and sensitivity (quantum efficiency (QE) > 80%). Imaging FCS can be implemented in any commercial or home-built TIRF and SPIM systems that are coupled with a fast camera [28]. Since the fluorophores diffuse within a ~2–3 nm thick membrane which is much smaller than the thickness of the

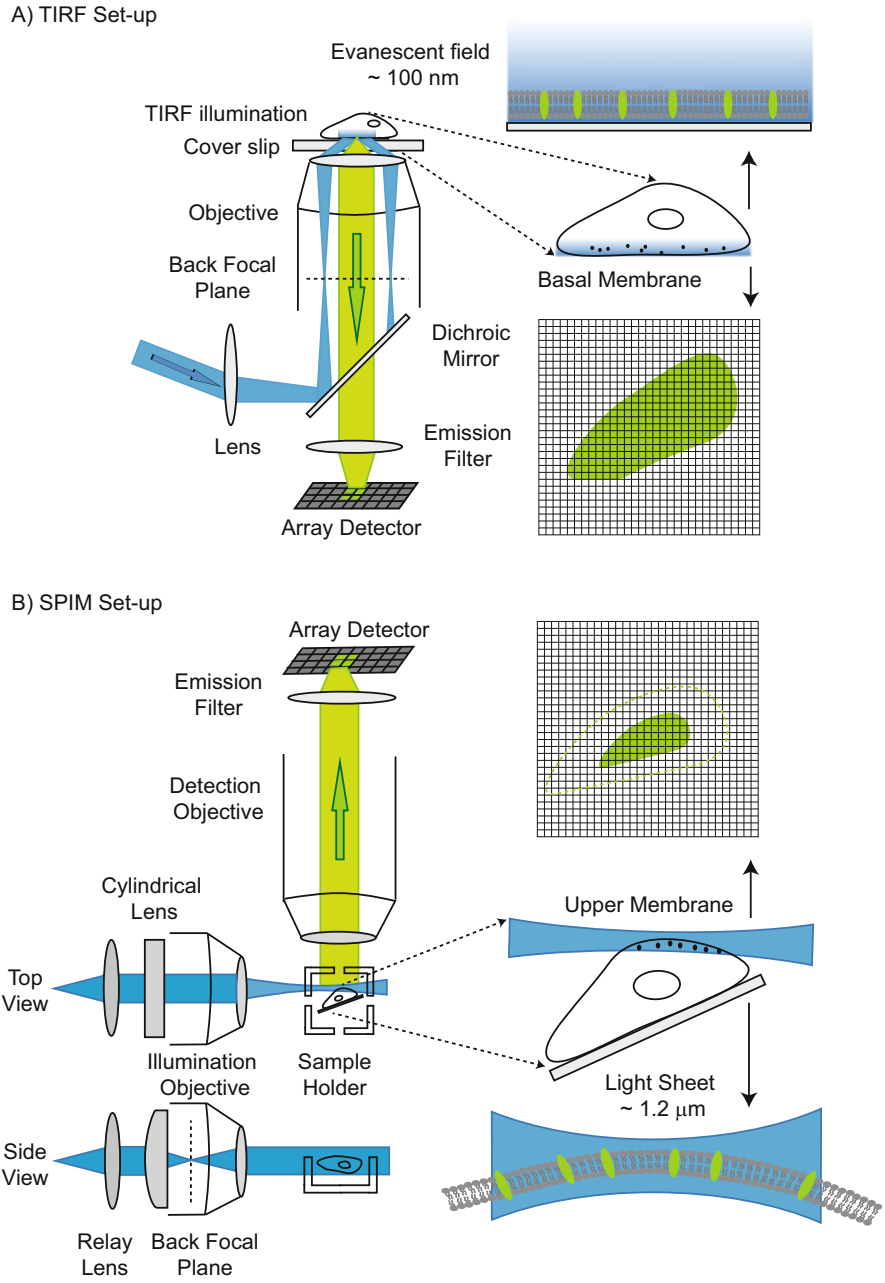

Fig. 6.3 Schematics of (**A**) TIRF and (**B**) SPIM set-ups to illuminate and detect cell membranes. In TIRF, the sample plane close to the cover slip is illuminated while any plane of the sample can be illuminated by SPIM illumination

illuminated plane (∼100 nm for TIRF and ∼1.2 μm for SPIM), we neglect here the contribution of the axial dimension to the observation volume and consider only a 2D effective observation area.

6.3.2 Conditions of Imaging FCS Experiments

The dynamic process under investigation dictates the minimum camera speed for Imaging FCS. Typically, one has to record the data ten times faster than the fastest process to be observed [22]. In the case of diffusion, for instance, the average time for a particle to diffuse through the observation area defined by the pixel, will define this time. On the other hand, a sufficient number of photons have to be captured to achieve a high signal to noise ratio. This becomes especially important for live cell samples expressing fluorescent protein tagged biomolecules due to their weak fluorescence and photostability. These figures of merit of Imaging FCS in relation to various experimental factors have been systematically addressed by simulations and experiments [22, 24, 28–30] and we will summarize their results in the following sections.

Camera Cooling Before experiments, the cameras are cooled to the minimum possible temperature, which the cameras can support at high-speed read-out, to reduce dark current. This is typically −70 to −80 °C for EMCCD cameras, but has to be checked as varying camera temperatures can cause unwanted artefacts in the ACF. In general, air-cooling by a camera-integrated fan is sufficient. Sometimes, vibration due to the fan destabilizes the system leading to periodic oscillation in the experimental ACF. This can be avoided by using external water-cooling. For sCMOS cameras, water-cooling is recommended since it can achieve lower temperatures (typically ∼ −30 °C).

Mode of Acquisition Two modes, namely kinetic and fast kinetic, are available for the acquisition of an image series using an EMCCD camera. Kinetic mode (also known as frame transfer mode) is used for Imaging FCS experiments. The maximum speed attainable for the full frame acquisition is 30–500 frames per second (fps) depending on the camera model. However, one can increase the speed up to 1000–3000 fps by acquiring a sub-region of the chip, e.g., a 25 × 25 pixels region of interest (ROI). Fast kinetic mode can be used for very high frame rates (∼25,000 fps) [31]. Here, only a few lines in the CCD chip are illuminated while the rest of the lines are masked. In this mode, the lines are continuously shifted vertically and read out. Therefore, the speed in this mode is only limited by the time it requires to shift the illuminated lines. This mode sacrifices the imaging aspect to increase the frame rate and thus time resolution. The limitation posed by the frame transfer mode is absent for sCMOS sensor since the signal is read-out within the pixel itself. This allows to image large number of pixels (2048 × 8) with ∼25,000 fps.

Preamplifier Gain Preamplifier gain determines the conversion factor of the electrons that are ejected from the CCD or sCMOS sensor after the incidence of a signal photon to a digital value. It is performed before analog-to-digital converter (ADC) digitization. The dynamic range (full well capacity) of a pixel is generally higher than the ADC dynamic range. For example, the dynamic range of the EMCCD camera used here is 1−160,000 electrons/pixel while that of ADC for a 16-bit image is 0−65,535 (65,536 grey levels or analog-to-digital units (ADU)). Therefore, there will be multiple electrons which are assigned to a grey level (i.e., >1 electrons/ADU). This can pose a problem for low light imaging and FCS since the photon counts are too low and thus the photoelectrons are distributed within very few grey levels. An increase in pre-amplifier gain helps reducing the number of electrons per grey level. This increases camera sensitivity. In our laboratory, the highest pre-amplifier gain was used for each camera resulting in ∼20 electrons per image count [32].

Electron Multiplication (EM) Gain for EMCCD Camera The EM gain determines the amplification of the signal before read-out and is a crucial parameter for FCS measurements. An EMCCD camera operating without EM gain does not have sufficient SNR to perform FCS. EM gain significantly improves both the quality of ACFs and accuracy and precision of D and N. In general, a smaller EM gain (as low as 2% of the maximum) is sufficient for bright organic dyes such as rhodamine labelled phosphatidylethanolamine (RhoPE) and 1,1′-dioctadecyl-3,3,3′,3-′-tetramethylindocarbocyanine (DiI-C_{18}). For less bright dyes such as fluorescent proteins, a higher EM gain is required. We use at least 50% of the maximum EM gain setting provided by the manufacturer. In this context, the experimental protocol to determine real preamplifier gain and EM gain of an EMCCD camera can be found here [33].

6.3.3 Data Acquisition

The performance of Imaging FCS data with an optimum fluorophore brightness strongly depends on the acquisition time per frame ($\Delta\tau$), total acquisition time (T_{acq}), and number of frames (n). T_{acq} is simply the product of $\Delta\tau$ and n ($T_{acq} = \Delta\tau \times n$). $\Delta\tau$ is the sum of the exposure/integration time and the read-out time and constitutes the time resolution of Imaging FCS. The accuracy of the extracted values of D and N depends on the time resolution while the number of frames acquired during the measurements dictates their precision. In general, the following rules of thumb represent minimum requirements for a successful Imaging FCS experiment:

At least 10,000 frames ($n = 10{,}000$) should be recorded while more number of frames is recommended for precise D and N values.

The time resolution ($\Delta\tau$) should be at least ten times smaller than the diffusion time (τ_D) of the sample ($\Delta\tau \leq 0.1\tau_D$). The accuracy deteriorates if $\Delta\tau \leq 0.001\ \tau_D$

for a 10,000 frames acquisition; the accuracy in this condition can be increased by acquiring more frames for a prolonged acquisition time.

$$\frac{\Delta\tau}{\tau_D} < 0.1 \tag{6.21}$$

The precision of the mobility depends on n and T_{acq}. A minimum of 10,000 frames should be recorded and the T_{acq} must be at least 100 times to that of the diffusion time. Since n and T_{acq} are related, the following condition for the optimal T_{acq} should be met:

$$T_{acq} \geq max(100\tau_d, 10000\Delta\tau) \tag{6.22}$$

In general, precision increases with increasing n or T_{acq} or both as long as one obeys the first constraint (Eq. 6.21). So, there are at least two acquisition parameter ranges in which accurate and precise measurements are possible:

$$\begin{aligned} \frac{\Delta\tau}{\tau_D} &\leq 0.01; T_{acq} - controlled \\ \frac{\Delta\tau}{\tau_D} &= 0.01 - 0.1; n - controlled \end{aligned} \tag{6.23}$$

Let us consider a fast diffusion process with $\tau_D = 20$ ms which is recorded with a $\Delta\tau = 1$ ms ($\Delta\tau/\tau_D = 0.05$). The first point of G ($\Delta\tau/\tau_D$) falls in the 'n-controlled' region. This means one needs to collect more than 10,000 frames to get precise D value although 10,000 frames are sufficient for the accuracy of D. Similarly for a slow diffusion process ($\tau_D = 200$ ms) measured with same time resolution ($\Delta\tau/\tau_D = 0.005$), the first point of G ($\Delta\tau/\tau_D$) is positioned in the 'T_{acq}-controlled' region. Here, one can improve the precision by taking the measurement for longer time by increasing $\Delta\tau$ but keeping n constant.

It is also noteworthy that one may not need to choose the highest possible frame rate of the camera since a higher frame rate is achieved in expense of a shorter exposure time, which decreases sample counts per frame. Secondly, the number of frames, total acquisition time and laser power should be optimized based on the photostability of the sample for optimal data acquisition while considering the above rules of thumb (Eqs. 6.26–6.28) as reference. In our experiments, typically, 50,000 images of an ROI consisting of at least 21 × 21 pixels are captured with 1–4 ms time resolution for lipid bilayer and live cell membrane measurements using an EMCCD camera. We recently published a detailed protocol of Imaging FCS measurement elsewhere [28].

6.4 Data Treatment

The raw ACFs obtained from individual pixels are fitted with a modified Eq. (6.16) in which we keep the convergence value of $G(\tau)$ at very large lag time (G_∞) as fitting parameter. In practice, the convergence value is influenced by non-ideal experimental conditions owing to the presence of immobile particles, sample bleaching, finite measurement time and instrumental instability [19].

$$G(\tau) = \frac{1}{N}\left(\frac{erf(p(\tau)) + \frac{\left(e^{-(p(\tau))^2}-1\right)}{\sqrt{\pi}p(\tau)}}{erf\left(\frac{a}{\omega_0}\right) + \frac{\omega_0}{a\sqrt{\pi}}}\left(e^{-\frac{a^2}{\omega_0^2}} - 1\right)\right)^2 + G_\infty; \qquad p(\tau) = \frac{a}{\sqrt{4D\tau + \omega_0^2}} \tag{6.24}$$

The unknown parameters here are D, N, ω_0 and G_∞. ω_0 is given by Eq. (6.20) using the current λ_{em} and NA. The numerical value of ω is 0.61 according to the Rayleigh criteria, although it can take different values for different illumination schemes [34]. It was shown by ITIR-FCS simulation that the ACF cannot be fitted to obtain D, N and ω_0 simultaneously [22]. An iterative method based on the analysis of ACFs at various observation areas was developed to determine ω_0 experimentally [24]. The principle behind the calibration is that for a freely diffusing sample, the diffusion coefficient is a constant that does not change with the area of observation, A_{eff}. Therefore, one can iteratively use different values for ω_0 until D is constant, independent of A_{eff}. The approximate value for the expected D can be deduced from the D recovered from large A_{eff} as in this case the PSF has little influence on the measurement (Fig. 6.2). The calibration of ω_0, and thus the PSF, has to be conducted once for a given experimental set-up. In our experience, it remains the same over the span of the microscope objective lifetime [28]. With the knowledge of ω_0, one can obtain D and N maps after analyzing the ACFs at each pixel (Fig. 6.4A).

6.4.1 Correction of the Intensity Trace

Imaging FCS uses comparatively low excitation intensities. Despite this fact photobleaching can still occur, in particular for fluorescent proteins on the plasma membranes of live cells and organisms. There are two different effects of photobleaching. If the time required to bleach a molecule is faster than it takes a molecule to diffuse through the observation area, then the apparent residence time of the molecule in the observation area decreases and the measured diffusion coefficient is biased to larger values. However, as constantly new fluorophores enter the observation volume from the surrounding, this might not lead to a significant decrease of the overall intensity. This effect has been called ‘cryptic

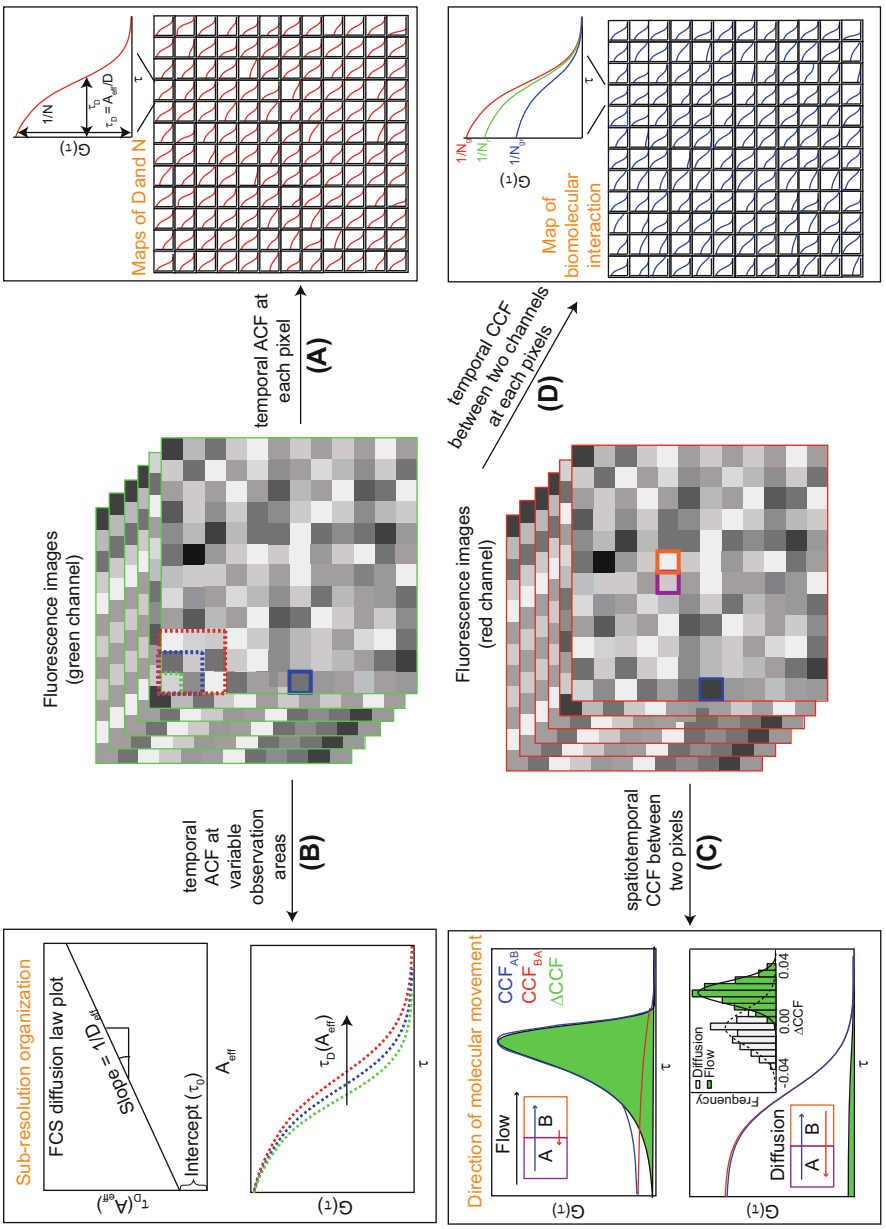

Fig. 6.4 Analytical tools that are applied to Imaging FCS data. Image stacks obtained from spectrally different channels are shown in *red* and *green*. (**A**) Temporal autocorrelation analysis at each pixel to create an array of ACFs. (**B**) Dependence of the ACFs on the size of the observation area. Various

photobleaching' [35]. There is no obvious drop in the average fluorescence over time or distortion of the ACF. This makes it difficult to correct. However, it is easily detected as an increase in laser power will lead to an increase in *D*. The influence of cryptic bleaching can be avoided by using lower laser power. A more commonly encountered scenario is the steady decrease of fluorescence over the time of the measurement. Here fluorophores are depleted from the observation volume continuously and are not sufficiently replenished with new fluorophores from the surrounding areas. This causes a slow decay in the ACF that does not converge at very long lag times. Other artefacts are transient fluorescent signals, e.g. from cell and membrane movement, or from the entry of bright cytosolic components into the observation volume. These transient but often large signals will distort the ACF. Therefore, a proper correction of the intensity trace which corrects for long term bleaching or slow transients, but not for short term fluctuations, needs to be performed before any ACF evaluation. We discuss a variety of correction routines for Imaging FCS data in the following sections.

6.4.1.1 Sliding Window Correction

In this procedure, a raw fluorescence time trace is split into multiple small parts (windows) such that the individual segments show no or very little trends in the intensity trace and ACFs are calculated for each subset. These ACFs are averaged to synthesize the correct ACF. This method does not correct the raw fluorescence trace but divides the trace into parts to minimize the influence of long-term trends on the ACF. While this works well when only bleaching is present, there are some disadvantages. Transient signals are often hard to correct. The length of the sliding window will limit the longest lag time that can be calculated and might lead to problems in data fitting when measuring slow or multiple components. It has to be kept in mind that the limited number of frames used to compute ACFs at each segment increases the variance of the correlation function especially at the longer lag times. Therefore, the length of the segment should be chosen carefully.

Fig. 6.4 (continued) observation area sizes can be created by pixel binning (shown as *dotted squares* of different color in the *green* image stack) and the respective ACFs which are right shifted with increasing observation area sizes. This dependence, as depicted in the FCS diffusion law plot, provides insights about sub-resolution organization. (**C**) The difference between forward and backward CCFs between a pair of pixels (*purple* and *orange*), ΔCCF, is non-zero (given by the *green* area) if there is a directional movement (in this example, the movement is along the forward direction) while for diffusion processes there is no such direction-dependence. The ΔCCF distribution is centred on zero for diffusion and non-zero for directional movement. This analysis gives the directional information for particle movement. (**D**) Temporal ACFs and CCFs at each pixel (for example, the *blue solid square* in both *red* and *green* image stacks) are obtained from a two-colour image stack. From the amplitudes of the ACFs and CCFs one can deduce the amount of interaction between two differently labelled molecules at each pixel

6.4.1.2 Other Intensity Trace Correction Routines

The experimental fluorescence intensity trace ($F(t)$) can be corrected by introducing a scaling function ($f(t)$) to modify the bleached intensity trace to yield a new corrected trace ($F_c(t)$) which retains the variance of the original signal [36].

$$F_c(t) = \frac{F(t)}{\sqrt{f(t)/f(0)}} + f(0)\left(1 - \sqrt{f(t)/f(0)}\right) \tag{6.25}$$

In general, a double exponential as the functional form of $f(t)$ is sufficient to correct a fluorescence trace with bleaching. It fails to account for any secondary artefacts that cause unusual distortion in the temporal fluorescence pattern. The correction of these artefacts can be accomplished using a polynomial function. The order of the polynomial function depends on the exact nature of the artefacts in a given experiment. The lowest order of the polynomial function, which successfully eliminates the influence of the artefacts on the ACF without overcorrecting, should be chosen. One can judge a successful correction by looking at the G_∞ value of the corrected ACF, which should be distributed around the convergence value (1 or 0 for Eqs. (6.1) and (6.2), respectively). Commonly a sixth order polynomial function is sufficient for most intensity traces recorded from bilayers or fluorescent proteins on live cell membranes [37].

In general, the sliding window correction should only be used on large data sets (at least 50,000 frames) with weak trends in the intensity trace caused by bleaching or other artefacts. If only photobleaching is present, then the exponential correction yields satisfactory results. Polynomial corrections are better suited for all cases where bleaching and strong transient artefacts distort the intensity trace.

6.4.2 Fitting Models

In general, all dynamic processes that result in fluorescence fluctuations can be incorporated in the theoretical model of the ACF in Imaging FCS. These processes include diffusion and flow of multiple dynamic species (typically 1–3 components) through the observation area [29]. At the moment, Imaging FCS fitting models do not include contributions from fast processes in the microsecond time scale such as triplet kinetics since the time resolution of currently available cameras is too slow to capture these processes.

The data analysis in FCS is traditionally performed by fitting the experimental ACF (or, bleach corrected ACF where necessary) with a pre-determined model of a dynamical process using a local non-linear minimization algorithms, for instance, the Levenberg-Marquardt algorithm. However, the selection of the model is sometimes equivocal. For example, one-particle and two-particle fitting models are often difficult to distinguish and supporting experiments are needed to confirm the

existence of the second particle. Therefore, the robust evaluation of fitting parameters is very important to reach an unambiguous interpretation of FCS data. In practice, more complex models are tested and accepted if they significantly improve the fit compared to the simpler models as determined by hypothesis tests, e.g. the F-test, or by judging the residuals [38]. However, a proper hypothesis test for FCS data has to rely also on the precise knowledge of the noise at each point of the ACF. A number of methods were developed to characterize the standard deviation in improving FCS data fitting and avoiding over-interpretation of results [39, 40]. Moreover, the fitting of raw ACFs without accounting for the noise characteristics leads to biased fit parameters [41].

A number of fitting routines to choose the correct theoretical model for a given experimental data set are available for single spot FCS to reach unambiguous outcomes. For example, the maximum entropy method (MEM) considers that an experimental physical process arises from a heterogeneous mixture of independently diffusing species with an unknown population distribution. The maximization of the posterior probability of the population distribution given an experimental data constitutes the basis of data analysis by MEM-FCS [42, 43]. Recently, the Bathe group introduced model selection for a given experimental FCS data by Bayesian inference testing. In this approach, the posterior probability of a particular fitting model given the raw data is calculated from the prior probability of that model function and the conditional probability of observing the raw data (likelihood) given the fitting model [44]. The likelihood is obtained from the noise distribution of each point in the raw data. For this purpose, it was necessary to improve the estimation of the noise of the ACF. While in the past it was assumed that the noise of the points in the ACF are independent from each other, the Bayesian approach took into account the correlations in the noise to arrive at better fitting outcomes [45].

6.5 Spatio-Temporal Analytical Tools Using Imaging FCS

The wealth of information embedded in the image stacks recorded is not limited to diffusion and concentration at each pixel of the image (Figs. 6.4A, 6.5B, C, and 6.6B, C). The data contains spatio-temporal information that permits the analysis of a variety of spatiotemporal correlation functions on the same data set. Here we describe some of their principles and how they can be integrated into the Imaging FCS format.

6.5.1 FCS Diffusion Law

The diffusion time (τ_D) of a probe undergoing free diffusion (i.e., Brownian diffusion) increases linearly with the observation area (A_{eff}). The plot of diffusion time

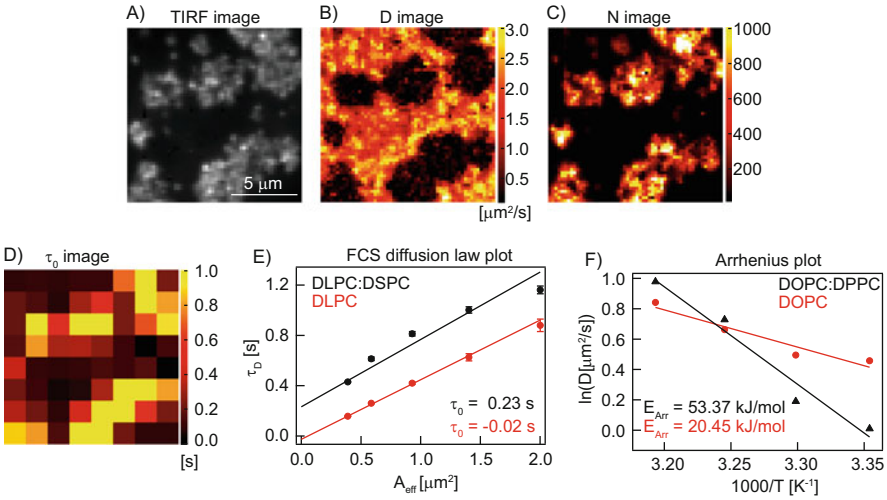

Fig. 6.5 Demonstration of Imaging FCS on RhoPE labelled DLPC:DSPC SLB. (**A**) TIRF image, (**B**) Diffusion coefficient (*D*) image, (**C**) number of particles (*N*) image, (**D**) FCS diffusion law intercept (τ_0) image calculated for 7 × 7 pixel sub-regions, (**E**) The FCS diffusion law plot (*black*) obtained from the entire image shown in figure (**A**), which shows a positive intercept. For comparison, the FCS diffusion law plot of a DLPC bilayer is shown in *red*. (**F**) Comparison of Arrhenius plots of DOPC (*red*) and DOPC:DPPC (*black*) bilayers

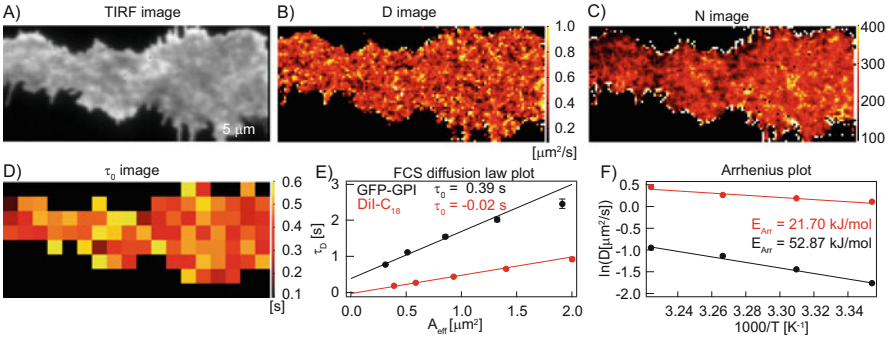

Fig. 6.6 Demonstration of Imaging FCS on GFP-GPI expressing SH-SY5Y cells. (**A**) TIRF image, (**B**) Diffusion coefficient (*D*) image, (**C**) number of particles (*N*) image, (**D**) FCS diffusion law intercept (τ_0) image, (**E**) The FCS diffusion law plot (*black*) obtained from the entire image shown in figure (**A**), which shows positive intercept. For comparison, FCS diffusion law plot of DiI-C_{18} labelled cell is shown in *red*. (**F**) Comparison of Arrhenius plots of GFP-GPI and DiI-C_{18} labelled HeLa cells

against observation area, i.e., the so-called FCS diffusion law plot [46], will therefore have zero intercept and a slope that is inversely proportional to the effective diffusion coefficient (D_{eff}) (Fig. 6.4B). A deviation from linearity signifies the existence of obstructed diffusion. In the context of plasma membranes, such hindered diffusion

could originate mainly from two sources: (a) lateral compartmentalization of the membrane by a meshwork, e.g. the cytoskeleton, and (b) transient trapping of molecules in domains. In the first scenario, molecules move freely inside one mesh but are not allowed to freely cross the mesh boundary to the neighbouring compartment. Inter-mesh communication is only possible via hop diffusion over the mesh boundary. The meshwork therefore behaves like a diffusion barrier. The FCS diffusion law plot will be linear as long as A_{eff} is smaller than the mesh-size and the slope will correspond to the inverse of the diffusion coefficient inside a mesh (short-range diffusion, D_{short}). If A_{eff} is increased further, i.e., it contains one or more meshes, the diffusion coefficient (long-range diffusion, D_{long}) will be smaller than D_{short} due to the presence of the diffusion barriers leading to a larger slope of the τ_{D} versus A_{eff} plot. Therefore, corralled diffusion leads to non-linear FCS diffusion law plot in which the inflection point indicates the spatial scale of switching of diffusion modes (short-range to long-range), i.e., the average mesh size. The mechanism is complex in the second type of hindered diffusion. Molecules diffuse inside domains and remain trapped for a finite amount of time before diffusing again out of the domains into the more fluid membrane matrix. The domains, by definition, are more ordered and viscous. They are isolated from each other unlike the meshwork where the meshes are spatially connected. This transient trapping is perceived as an increased diffusion time of the probe molecules and thus an otherwise smooth and linear FCS diffusion law plot takes a sudden jump along the diffusion time axis at an A_{eff} size that contains a domain. Diffraction-limited observation areas created in conventional experimental set-ups are usually much larger than domain or mesh size and only the linear regimes above the characteristic spatial scales of meshwork and domains can be measured. However, extrapolation of the experimentally obtained FCS diffusion law plot to zero area give strictly negative and positive intercepts for corralled diffusion in a meshwork and hindered diffusion due to transient trapping, respectively. The diffusion law plot for A_{eff} above the characteristic mesh size or the size where it contains domains can be written as [24, 46, 47]:

$$\tau_D\left(A_{eff}\right) = \tau_0 + \frac{A_{eff}}{D_{eff}} \tag{6.26}$$

In the above equation, τ_0 is zero, positive and negative for free diffusion, transient trapping and meshwork diffusion, respectively. It is worth noting that any process that transiently arrests diffusion of a probe results in a positive τ_0 value, for example, trapping of proteins in lipid rafts and dynamic formation/deformation of protein clusters. The magnitude of τ_0 depends on the partition efficiency/binding affinity of the molecules and domain/meshwork density. The slope of the FCS diffusion law plot is inversely proportional to the effective diffusion coefficient (D_{eff}). The D_{eff} describes the length-scale dependence of the diffusion coefficient. In the case of free diffusion, D_{eff} is equal to D obtained by fitting the ACFs of individual pixels (D_{ACF}). For non-Brownian diffusion, D_{ACF} deviates from D_{eff}. Therefore, a ratio of D_{eff} to D_{ACF} provides a good way to distinguish Brownian and non-Brownian diffusion processes [48].

Implementation of the FCS diffusion law in Imaging FCS is straightforward since a stack of a large membrane area is measured in a single experiment. This can be utilized to create various observation areas by pixel-binning to compute the FCS diffusion law plot for the whole image or even for small regions within the image, thus providing a spatially resolved diffusion law map (Figs. 6.5D, E, 6.6D, E). The minimum size of a ROI to calculate a diffusion law plot spans typically 6×6 pixels, which corresponds to an area of about 1–2 µm, depending on the particular camera pixel size and the magnification used [48]. This is comparable to imaging Mean Squared Displacement (iMSD) analysis in which the temporal evolution of spatial correlation functions is determined [49, 50]. Recently, Moens et al. applied iMSD to characterize the spatial dependence of diffusion modes of cholera toxin B (CTxB) on live cell membranes with 6 µm spatial resolution [51].

Importantly, Imaging FCS requires only a single measurement to compute the FCS diffusion law plot and thus avoids potential sample damage due to prolonged illumination, which is required for the multiple measurements when using confocal FCS modalities. This increases the time resolution and allows the measurement of time dependent processes on a minute scale or faster [52–54].

6.5.2 *Difference in Cross Correlation Function (ΔCCF)*

The second analysis tool in this category investigates any dynamic exchange between two regions of an image. In principle, spatiotemporal cross-correlations between pairs of pixels at any distance and direction can be computed to establish the spatial connectivity across different membrane regions along with vectorial mobility information. A particular realization is the concept of differences in spatial cross-correlation functions (ΔCCF) [29]. It is calculated by subtracting the forward and backward CCFs between two adjacent pixels A and B followed by integration over the entire measurement time.

$$\Delta CCF = \int_0^{\tau_{max}} (CCF_{AB}(\tau) - CCF_{BA}(\tau))d\tau \tag{6.27}$$

In the above, $CCF_{AB}(\tau)$ is the forward spatio-temporal correlation function between pixels A and B while $CCF_{BA}(\tau)$ is the backward spatio-temporal correlation function in the reverse direction, i.e., between pixels B and A. The ΔCCF function is the difference between these two functions. The magnitude of ΔCCF between the pixels A and B is given be the area under the ΔCCF function, which is calculated by integrating the function from zero to the maximum lag time (τ_{max}). This is demonstrated in Fig. 6.4C. The green area corresponds to the area under the curve of the ΔCCF function. Repetition of the process of all possible pairs of neighbouring pixels generates a distribution of ΔCCF values. This distribution is

centred at zero for free diffusion since the particles have, on an average, an equal probability of movement in all directions, meaning that the forward and backward CCFs will be similar (Fig. 6.4C, inset, white). The centre of the ΔCCF distribution shifts to a non-zero value in case of directed motion, e.g. flow, or anisotropic diffusion (Fig. 6.4C, inset, green). Any broadening of this distribution indicates spatial inhomogeneities such as transient trapping. In this case, the mismatch between forward and backward CCFs between a pair of pixels becomes more probable resulting in a larger fraction of non-zero ΔCCF values. Since there is no net direction of the molecular movements in transient trapping the ΔCCF distribution is still centred at zero. The position and width of the ΔCCF distribution provides a means of studying modes of membrane dynamics and heterogeneity.

6.5.3 *Imaging FCCS*

In Imaging FCCS, the sample contains two spectrally distinct fluorophores which are excited with two laser beams. The sample fluorescence is first spectrally separated by a dichroic mirror into two channels followed by imaging on two separate cameras or onto one camera using an image splitter. The spectrally separated pixels belonging to the same spatial position are then cross-correlated [28]. For example, the blue pixels on the red and green channels in Fig. 6.4D correspond to the same position of the sample but are spectrally and/or temporally separated. ACFs obtained from the fluctuations of this pair of pixels gives diffusion coefficients of spectrally different fluorohores (D_{green} and D_{red}). The amplitude of the green (or red) ACF ($G_{green}(0)$ or $G_{red}(0)$) is inversely proportional to the total number of green (or red) particles within the observation area, i.e., the sum of unbound green (or red) particles and bound particles that have at least one green (or red) label (Fig. 6.4D, red and green and (6.28) and (6.29) assuming equal brightness of both particles). The amplitude of the cross-correlation function (CCF), $G_{rg}(0)$, between the fluorescence traces reflects the number of molecules that contain both colors (N_{rg}) revealing the extent of association and co-diffusion of the molecules under investigation (Fig. 6.4D, blue) and is given by Eq. (6.30).

$$G_{green}(0) = \frac{1}{N_{green} + N_{rg}} \tag{6.28}$$

$$G_{red}(0) = \frac{1}{N_{red} + N_{rg}} \tag{6.29}$$

$$G_{rg}(0) = \frac{N_{rg}}{\left(N_{green} + N_{rg}\right)\left(N_{red} + N_{rg}\right)} \tag{6.30}$$

Using the above three equations, the number of bound particles (N_{rg}) can be obtained:

$$N_{rg} = \frac{G_{rg}(0)}{G_{green}(0)G_{red}(0)} \tag{6.31}$$

However, the amplitude of green and red ACFs depends on the maturation, brightness and concentration of the fluorophores, which vary across samples. A more general procedure to estimate the bound fraction is to calculate the relative cross-correlation value (q) which is defined as the ratio of the CCF amplitude to the ACF amplitude of the less abundant particles (Eq. 6.32) [55]. This q value can be used to represent interaction maps in Imaging FCCS:

$$q = \frac{G_{rg}(0)}{\max\left(G_{green}(0), G_{red}(0)\right)} \tag{6.32}$$

6.5.4 Temperature Dependence of Membrane Diffusion

The existence of nanodomains on the plasma membrane gives rise to membrane regions of distinct physical properties. The ordered domains are characterized by strong molecular packing that leads to a reduction of the free area for diffusion and also poses a stronger barrier for the hopping of the diffusants to an available free space. Thus the membrane molecules residing in the ordered domains require a higher activation energy for diffusion compared to those diffusing in the disordered region of the bilayer. An increase in temperature results in a larger fraction of molecules having sufficient energy to overcome the activation energy barrier. In other words, a larger fraction of membrane molecules in the less viscous region at a given temperature will be able to cross the activation energy barrier in comparison to those located in the high viscous region. Therefore, the temperature dependence of probe diffusion, which is shown to follow the Arrhenius equation [33], can be used to investigate sub-resolution domains.

$$D = D_0 e^{-\frac{E_{Arr}}{RT}} \tag{6.33}$$

$$lnD = lnD_0 - \frac{E_{Arr}}{RT}$$

In the above equation, D is the diffusion coefficient at a given temperature, D_0 is the pre-exponential factor and E_{Arr} is the activation energy of diffusion. The E_{Arr} value for a given system compliments the outcomes of the FCS diffusion law and ΔCCF analyses since they provide information about sub-resolution spatial variation of membrane heterogeneity independently. Examples for the use of the Arrhenius plot are discussed in the applications.

6.6 Current Limitations of Imaging FCS and Possible Solutions

The main limitation of Imaging FCS is the time resolution of the cameras. Currently, EMCCD cameras deliver a maximum of 3000 frames per second for a 128 × 2 ROI acquisition. However, imaging of two horizontal lines is not sufficient for most practical purposes. A slower speed of 1800 frames per second, which is sufficient to measure membrane diffusion, is achieved for a 21 × 21 ROI. Additional processes that have a cytosolic component, where the dynamics is faster, can often not be accessed by EMCCD based detection. A few solutions were proposed to address the limitation of time resolution. First, the current generation sCMOS cameras offer frame rates as high as 25,000 frames per second. The small pixel size of sCMOS camera along with short exposure time when run at high frame rates compromises the SNR, which, however, can be improved by pixel binning. Recently introduced organic labelling methods such as SNAP-tag, CLIP-tag and ACP-tag allow labelling with more photostable probes. Their higher brightness and better photostability improve data quality in Imaging FCS and can provide sufficient counts even at short exposure times. A second replacement of the EMCCD camera are single molecule sensitive APD (SPAD) arrays, which have microsecond time resolution [30]. However, because of their structure they have relatively low fill factors, which can be partly improved by microlens arrays. But most importantly at the time of writing they were not yet commercially available. However, in the future they could serve as very good detectors for Imaging FCS.

Another limitation is that Imaging FCS does not provide absolute numbers of particles [30]. However, relative changes are correct; so when changing a concentration by a factor 2, N will change accordingly. This is due to the complicated noise of EMCCD cameras since they are not true photon detectors [56]. Singh et al. suggested to create a calibration plot by measuring samples of known concentration [30]. However, one needs to have a good calibration standard for an experimental sample.

6.7 Applications of Imaging FCS

Since its inception [20] and subsequent development [29], Imaging FCS was applied to various biological systems in vitro and in vivo elucidating a range of physico-chemical and biophysical questions. Examples include, but are not limited to, the interaction mode of membrane-active peptides and the influence of membrane domains and cytoskeleton on the dynamics and interactions of signalling proteins. In this section, we summarize a collection of applications on model membranes, cultured cell membranes and live cell membranes of organisms to highlight the capabilities of Imaging FCS.

6.7.1 Diffusion Properties of Model Membranes

Supported or free-standing lipid bilayers are ideal systems for the measurements of lipid dynamics and the testing of Imaging FCS as they are simple in their composition, have known diffusion coefficients and are easy to prepare. Therefore, the first measurements of Imaging FCS were performed on supported lipid bilayers (SLBs) containing a single component. Guo et al. compared *D* of RhoPE labeled zwitterionic POPC SLBs on glass between various methods, including confocal FCS, z-scan FCS, SPT and ITIR-FCS [57]. A fair agreement of the *D* values obtained from these methods demonstrated that ITIR-FCS provides an absolute measure of diffusion coefficients without the requirement of constant calibrations. It was recently demonstrated that Imaging FCS provides comparable results to Fluorescence Recovery After Photobleaching (FRAP) on SLBs and live cells [37]. Interestingly, despite the strong time-dependent changes in the intensity trace during FRAP acquisition, the data could easily be corrected and Imaging FCS demonstrated that the diffusion coefficients before bleaching, during and after recovery are the same. This, therefore, demonstrated that the bleaching during FRAP does not change the diffusion coefficient (although this does not exclude other long term changes and phototoxic effects) but that FRAP had a much higher volatility in data fitting leading to a larger uncertainty in FRAP compared to Imaging FCS.

We assessed the influence of intermolecular interaction on membrane diffusion. The degree of hydrogen bonding among the lipid head groups in a mixed lipid bilayer regulates the lateral diffusion [24]. The *D* of POPC:POPG lipid bilayer decreases with increasing mole fraction of POPG, a negatively charged lipid. The FCS diffusion law and ΔCCF analyses on these systems confirm the absence of any phase separation. Therefore, the reduction of membrane diffusivity with increasing POPG content is due to the presence of a PG-PG hydrogen bonding network which results in stronger molecular packing.

6.7.2 Fluorescent Probe Partitioning on Phase-Separated Model Membranes

DLPC:DSPC SLBs on glass exhibit microscopic phase separation into co-existing solid ordered or gel (S_o) and liquid disordered or fluid (L_d) phases at room temperature which can be readily identified by ITIR-FCS. The fluorescent probe, RhoPE, partitions into the S_o phase of DLPC:DSPC bilayers since a slower *D* and higher *N* were associated with the brighter regions of the bilayers [24, 28]. Domain partitioning of RhoPE was also confirmed by the FCS diffusion law and ΔCCF analyses [24, 53]. In contrast, SPIM-FCS experiments showed that RhoPE diffuses at a rate of ~2.3 times slower in the dark region of microscopically phase-separated giant plasma membrane vesicles (GUVs) containing DOPC:DPPC:Cholesterol [58]. This suggests that the dark region is the liquid ordered phase (L_o) and the bright region is L_d phase into which RhoPE

partitions preferentially. Note that the L_o phase does not exist in the phase diagram of a single component lipid. It only appears when cholesterol is mixed with a gel lipid or a gel-fluid lipid mixture as was shown by the temperature dependence of lipid diffusion on model membranes by ITIR-FCS [59]. These results demonstrate the capability of Imaging FCS to measure diffusion coefficients in low intensity regions and the importance of diffusion measurements in addition to fluorescence imaging to characterize partitioning behaviour of a probe in different membrane phases.

Bayesian analysis of the ITIR-FCS data on the phase separated DLPC:DSPC SLB identified the existence of a single diffusing species outside domains and a major fraction of the pixels inside domains but two particles at the domain borders [32]. The pixels that can be fitted with a single component model exhibit fast (D~1.2 μm^2/s) or slow (D~0.3 μm^2/s) diffusion depending on their location in the fluid or gel phase, respectively. The pixels along borders between these phases shows two-component diffusion since a pixel on which the border falls contain both phases. Interestingly, some of the pixels (~5%) inside the domains are also best fitted with a two-particle model. The resolved D values of these two species correspond well with the D of fluid and gel phase. This suggests that the microdomains observed by TIRF imaging are comprised of small nanodomains. This supports the recent inference made from the ratio of D_{eff} to D_{ACF} obtained from the FCS diffusion law analysis on the same bilayer [48] and heterogeneous ΔCCF distribution inside the domains [24].

The FCS diffusion law analysis shows that the diffusion of DOPC:DPPC and DOPC:DPPC:Cholesterol SLBs deviates from free diffusion at 25 °C [59]. The dynamics becomes closer to free diffusion when temperature is raised to 40 °C. This is attributed to the disappearance of the S_o or L_o phase nanodomains at higher temperature. Moreover, our results point towards a cholesterol-dependent change of line tension at the domain boundary, which plays a significant role in determining domain size and stability. However, stronger and more direct evidence is needed to establish the link between line tension and domain morphology.

6.7.3 *Arrhenius Activation Energy of Diffusion in Model and Live Cell Membranes*

The E_{Arr} was determined for model membranes of a range of chemical composition [59]. Membranes that are more compact show stronger temperature dependence and thus are associated with higher E_{Arr}. The E_{Arr} for the S_o-L_d co-existing phase (~50 kJ/mol) was ~2.5 times larger than that of the L_d phase (~20 kJ/mol). A representative example is shown in Fig. 6.5F. It was shown that cholesterol plays a crucial role in membrane organization. It progressively reduces the membrane diffusivity but does not induce a new phase when it is incorporated in the L_d phase as the E_{Arr} did not change. In contrast, addition of 17 mol% of cholesterol in a S_o-L_d SLB results in the formation of an L_o-L_d phase as shown by a reduced E_{Arr} value (~30 kJ/mol) which is still ~1.5 times larger than that of the L_d phase. Removal of cholesterol from the

L_o-L_d SLB spontaneously changes the bilayer into an S_o-L_d phase. Overall, distinct ranges of E_{Arr} are associated with commonly observed phase-separated lipid bilayers enabling the investigation of sub-resolution phase separation with diffraction-limited measurements.

It should be noted that E_{Arr} distinguishes membrane systems based on their molecular packing. Therefore, stronger molecular packing other than the one caused by rigid lipid domains also increases the E_{Arr} value. This could complicate the temperature-dependence diffusion behaviour in live cell membranes [59]. For example, the E_{Arr} values of DiI-C_{18} diffusion were shown to vary across cell lines although the FCS diffusion law analyses revealed that the probe exhibits free diffusion at all temperatures. However, the E_{Arr} values were significantly smaller than that of GFP-GPI which is shown to undergo confined diffusion. This suggests that change in membrane composition does not change the partitioning behaviour of DiI-C_{18} but influences the diffusion properties. Representative Arrhenius plots for DiI-C_{18} and GFP-GPI on HeLa cells are shown in Fig. 6.6F.

6.7.4 Interactions of Membrane-Active Peptides with Cell Membranes

The interactions of peptides with lipid membranes can often be detected by the change of the membrane physical properties. ITIR-FCS was applied to establish the mechanism of the interaction between SLBs and monomeric human islet amyloid polypeptide (hIAPP) [52]. At lower concentration, the peptide forms a 'dynamic carpet' on top of the membrane. At high concentration, hIAPP instantaneously extracts lipids from the membrane leading to an increase of membrane diffusion. The extent of change of membrane diffusion is also dependent on the membrane composition; in general, the change was more noticeable for more ordered membranes. Taken together, monomeric hIAPP was shown to interact with model membranes in a two-step concentration-dependent manner: (i) formation of 'dynamic carpet' at low concentration and (ii) extraction of lipids resulting in an elevation of membrane diffusion at high concentration.

The scenario becomes more complex on live cell membranes in which monomeric hIAPP increases membrane diffusion up to 10 min after addition [52]. This is followed by the formation of diffusion-restricted microdomains around 15 min, which encompasses the entire membrane with time. The D inside these domains was ~5 times slower than outside, leading to a time-dependent decrease of average membrane diffusion. This temporal change of heterogeneous diffusion because of domain nucleation and growth was presented as an 'FCS video', which allows directly visualizing concerted changes of DiI-C_{18} diffusion over large membrane areas. Bayesian analysis on this data set revealed an interesting pattern that is in sharp contrast with the commonly observed domains on model membranes arising from phase separation of lipid mixture [32]. Whereas the pixels at the domain boundary majorly showed two-component diffusion in phase-separated lipid bilayers, almost

all pixels containing hIAPP-induced domains are best described with a two-particle model having two diffusion coefficients with a ratio of ~50–100. The fraction of the slow component increases with time resulting in a decrease of average membrane diffusion. Based on these results, the temporal behaviour of hIAPP-induced domain formation can be segregated into three phases- (i) Pre-nucleation phase (1–10 min) where single component diffusion was observed in almost all pixels with increasing D with time. (ii) Propagation phase (15–40 min) where the two-component model fits better for the pixels within the domains while the fraction of the slow diffusing species increases with time. The D of the fast diffusing species decreases to a value similar to the untreated cell membrane while that of the slow particles remains constant. (iii) Saturation phase (40–60 min) where pixels within the domain fit better with a single-component model. In essence, Bayesian analysis uncovered the time-dependent phases of hIAPP-membrane interactions.

6.7.5 Diffusion and Organization of Proteins and Lipids on Live Cell Membranes

In the first demonstration of ITIR-FCS, Kannan et al. produced diffraction-limited images of D and N of epidermal growth factor receptor labelled with monomeric red fluorescence protein (EGFR-mRFP) on live CHO-K1 cells and compared this with the lipid probe, R18 [20]. Their results demonstrated a very heterogeneous distribution of EGFR-mRFP diffusion compared to that of R18 indicting distinct spatial organization of these two probes. Next, ITIR-FCS investigated the diffusion and heterogeneity of sphingolipid binding domain (SBD), a 25 amino acid fragment of amyloid beta (Aβ) peptide, in relation to cholesterol and the actin cytoskeleton on live SH-SY5Y cells [60]. Over the next years, with better camera technology and improved understanding of Imaging FCS theory, the technique was applied to illuminate the physico-chemical origin of unique organization of plasma membrane and how these organizational features influence the behaviour of signalling proteins.

6.7.5.1 Glycosylphosphatidylinositol Anchored Proteins (GPI-APs)

In a recent study, Huang et al. investigated the localization of GPI-APs on live PtK2 cells using a slightly modified FCS diffusion law analysis [54]. They used a single, averaged ACF for each of the observation areas to compute the dependence of τ_D on A_{eff} and named the method binned Imaging FCS (bimFCS). The authors observed that Glycosylphosphatidylinositol-anchored monomeric green fluorescence protein (mGFP-GPI), a model GPI-AP, is transiently trapped in cholesterol-sensitive domains. Such domain trapping increases with the dimerization of the protein. Interestingly, they found that the dimerization of mGFP-GPI does not induce dimerization of other GPI-anchored proteins but increases their domain trapping. These observations led to the conclusion that dimerization of GPI-AP not only facilitates its

domain confinement but also modifies the physical properties of the domains, which allow other GPI-APs to spend longer time inside the domains. They also found weak effects of the cortical actin cytoskeleton on mGFP-GPI domain trapping and suggested that the cytoskeleton pinning might play a secondary role in the domain localization of the proteins.

6.7.5.2 Epidermal Growth Factor Receptor (EGFR)

EGFR is an extensively studied membrane signalling protein due to its important role in aberrant cancer cell signalling [61]. The dynamics and organization of EGFR on live CHO-K1 cell membrane were investigated with Imaging FCS both at its resting and ligand-bound states in a recent study [53]. This study revealed that EGFR is partly trapped in cholesterol-dependent domains and at the same time hindered by the actin cytoskeleton in its resting state. Furthermore, a significant fraction of EGFR showed cholesterol-independent confinement which could be due to formation of receptor nanocluster or localization in cholesterol-insensitive domains. With stimulation by its cognate ligand epidermal growth factor (EGF), EGFR diffused faster and endocytosed in a dose-dependent manner. At low dose stimulation, presumably EGFR internalization relied on clathrin mediated endocytosis [62] and the receptor recycled back to the plasma membrane. At high dose, EGFR formed clusters on the membrane which were subsequently internalized. The faster diffusion of EGFR after stimulation is a direct consequence of endocytosis which removes the more viscous cholesterol-dependent domains from the membrane. However, the remaining EGFR on the membrane had an overall unchanged confinement strength. Both, cholesterol removal or cytoskeleton disruption inhibited receptor endocytosis. Ligand stimulation after cholesterol depletion or cytoskeleton disruption induced microscopic receptor clusters on the membrane. These results indicate that a dynamic equilibrium is established between receptor clustering and endocytosis after ligand stimulation. Upon inhibition of endocytosis, receptor clusters, which are presumably present in a variety of sizes, are no longer internalized and can grow to larger sizes. Therefore, impairment of one process (endocytosis) allowed the other process (clustering) to be more prevalent.

6.7.6 Protein Organization in the Cell Membranes of Live Organisms

The applications of SPIM-FCS were recently extended to study the dynamics of membrane proteins in living organisms. Struntz and Weiss used SPIM-FCS to investigate the dynamical properties of peripheral membrane protein PLC1δ1 in the cytosol and on the plasma membrane of early *C. elegans* embryos [63]. PLC1δ1 diffuses on average ~10 times faster in the cytosol (~10 $\mu m^2/s$) compared to the plasma membrane (~1 $\mu m^2/s$). The diffusion map of the membrane bound pool of

PLC1δ1 showed a slightly broader distribution than that of the cytosol, possibly due to a more heterogeneous membrane environment.

The capability of SPIM illumination to penetrate deep inside tissue and the power of the FCS diffusion law was utilized to investigate the sub-resolution spatial organization of Wnt3, a secreted morphogen, in live zebrafish embryos [58]. It was shown that Wnt3 is transiently trapped in cholesterol-dependent domains in the plasma membrane. This trapping was dependent on the state of palmitoylation of Wnt3. This is, to the best of our knowledge, the first implementation of FCS diffusion law in a live organism.

6.8 Summary

Imaging FCS couples advanced microscopic illumination schemes with fast camera-based fluorescence detection to provide spatiotemporal information about the sample with high temporal resolution at the optical diffraction limit. The dynamic information collected in Imaging FCS can be further used to gain insights into sample properties even beyond the diffraction limit by the so-called FCS diffusion law. It provides contiguous maps of diffusion coefficients, concentrations, and if used in a multi-colour mode also interactions, significantly improving statistics. An especially attractive feature of the technique is that it can be easily incorporated into existing TIRF or Light Sheet microscopes without any modifications, it is essentially calibration free and provides absolute diffusion coefficients, and can be easily combined with various techniques as it can often work with exactly the same data acquired by the cameras. At the time of writing, Imaging FCS was applied to 2D and 3D systems in vitro and in vivo. It was used to characterize supported lipid bilayers of different composition, to investigate the interaction of membrane active peptides with these bilayers, and to observe lipid and protein organization in the plasma membrane of live cells. Recently, SPIM-FCS was applied in live zebrafish embryos to determine the membrane partitioning of a secreted morphogen [58]. Overall, easy implementation along with an arsenal of analytical tools makes Imaging FCS an excellent quantitative bio-imaging platform in which image contrast is given by quantitative measurement parameters, including diffusion coefficient, concentration or any other measurable parameter within this framework, instead of simple fluorescence intensity. In the future, Imaging FCS could play important roles in further characterizing membrane dynamics and organization, especially the presence, size and density of domains or trapping sites in membranes, and if combined with super-resolution techniques [64, 65] could establish new imaging capabilities that provide not only excellent spatial resolution but give simultaneously access to very fast dynamical processes.

Acknowledgements The authors would like to thank Xue Wen Ng for help with graphics and Jagadish Sankaran for critical comments on the manuscript. T.W. gratefully acknowledges the funding by the Ministry of Education Singapore (MOE2012-T3-1-008). N.B. was the recipient of a

postdoctoral fellowship from the same grant. S.H. is the recipient of a graduate scholarship of the National University of Singapore.

References

1. Garcia-Parajo MF, Cambi A, Torreno-Pina JA, Thompson N, Jacobson K. Nanoclustering as a dominant feature of plasma membrane organization. J Cell Sci. 2014;127:4995–5005.
2. Raghupathy R, Anilkumar AA, Polley A, Singh PP, Yadav M, Johnson C, Suryawanshi S, Saikam V, Sawant SD, Panda A, Guo Z, Vishwakarma RA, Rao M, Mayor S. Transbilayer lipid interactions mediate nanoclustering of lipid-anchored proteins. Cell. 2015;161:581–94.
3. Rao M, Mayor S. Active organization of membrane constituents in living cells. Curr Opin Cell Biol. 2014;29:126–32.
4. Lingwood D, Simons K. Lipid rafts as a membrane-organizing principle. Science. 2010;327:46–50.
5. Nicolson GL. Fluid-mosaic membrane structure: from cellular control and domains to extracellular vesicles. In: Membrane organization and lipid rafts in cells and artificial membranes. New York: Nova Science Publishers; 2016. p. 1–23.
6. Kusumi A, Fujiwara TK, Chadda R, Xie M, Tsunoyama TA, Kalay Z, Kasai RS, Suzuki KG. Dynamic organizing principles of the plasma membrane that regulate signal transduction: commemorating the fortieth anniversary of Singer and Nicolson's fluid-mosaic model. Annu Rev Cell Dev Biol. 2012;28:215–50.
7. Kraft ML. Plasma membrane organization and function: moving past lipid rafts. Mol Biol Cell. 2013;24:2765–8.
8. Kusumi A, Suzuki KG, Kasai RS, Ritchie K, Fujiwara TK. Hierarchical mesoscale domain organization of the plasma membrane. Trends Biochem Sci. 2011;36:604–15.
9. Truong-Quang BA, Lenne PF. Membrane microdomains: from seeing to understanding. Front Plant Sci. 2014;5:18.
10. Yap AS, Gomez GA, Parton RG. Adherens junctions revisualized: organizing cadherins as nanoassemblies. Dev Cell. 2015;35:12–20.
11. Suzuki KG, Kasai RS, Hirosawa KM, Nemoto YL, Ishibashi M, Miwa Y, Fujiwara TK, Kusumi A. Transient GPI-anchored protein homodimers are units for raft organization and function. Nat Chem Biol. 2012;8:774–83.
12. Simons K, Toomre D. Lipid rafts and signal transduction. Nat Rev Mol Cell Biol. 2000;1:31–9.
13. van Zanten TS, Mayor S. Current approaches to studying membrane organization. F1000Research; 2015.
14. Manzo C, Garcia-Parajo MF. A review of progress in single particle tracking: from methods to biophysical insights. Rep Prog Phys. 2015;78:124601.
15. Manley S, Gillette JM, Patterson GH, Shroff H, Hess HF, Betzig E, Lippincott-Schwartz J. High-density mapping of single-molecule trajectories with photoactivated localization microscopy. Nat Methods. 2008;5:155–7.
16. Serge A, Bertaux N, Rigneault H, Marguet D. Dynamic multiple-target tracing to probe spatiotemporal cartography of cell membranes. Nat Methods. 2008;5:687–94.
17. Giannone G, Hosy E, Levet F, Constals A, Schulze K, Sobolevsky AI, Rosconi MP, Gouaux E, Tampe R, Choquet D, Cognet L. Dynamic superresolution imaging of endogenous proteins on living cells at ultra-high density. Biophys J. 2010;99:1303–10.
18. Moertelmaier M, Brameshuber M, Linimeier M, Schütz GJ, Stockinger H. Thinning out clusters while conserving stoichiometry of labeling. Appl Phys Lett. 2005;87:263903.
19. Ries J, Weidemann T, Schwille P. Fluorescence correlation spectroscopy. In: Egelman EH, editor. Comprehensive biophysics. Amsterdam: Elsevier; 2012. p. 210–45.
20. Kannan B, Guo L, Sudhaharan T, Ahmed S, Maruyama I, Wohland T. Spatially resolved total internal reflection fluorescence correlation microscopy using an electron multiplying charge-coupled device camera. Anal Chem. 2007;79:4463–70.

21. Petrov EP, Schwille P. State of the art and novel trends in fluorescence correlation spectroscopy. Springer Ser Fluoresc. 2008;6:145–97.
22. Sankaran J, Bag N, Kraut RS, Wohland T. Accuracy and precision in camera-based fluorescence correlation spectroscopy measurements. Anal Chem. 2013;85:3948–54.
23. Zhang B, Zerubia J, Olivo-Marin JC. A study of Gaussian approximations of fluorescence microscopy PSF models. Proceedings of SPIE 6090, Three-dimensional and multidimensional microscopy: image acquisition and processing XIII 6090:60900K-60900K-60911; 2006.
24. Bag N, Sankaran J, Paul A, Kraut RS, Wohland T. Calibration and limits of camera-based fluorescence correlation spectroscopy: a supported lipid bilayer study. Chem Phys Chem. 2012;13:2784–94.
25. Bag N, Wohland T. Imaging fluorescence fluctuation spectroscopy: new tools for quantitative bioimaging. Annu Rev Phys Chem. 2014;65:225–48.
26. Singh AP, Wohland T. Applications of imaging fluorescence correlation spectroscopy. Curr Opin Chem Biol. 2014;20:29–35.
27. Axelrod D. Total internal reflection fluorescence microscopy in cell biology. Traffic. 2001;2:764–74.
28. Krieger JW, Singh AP, Bag N, Garbe CS, Saunders TE, Langowski J, Wohland T. Imaging fluorescence (cross-) correlation spectroscopy in live cells and organisms. Nat Protoc. 2015;10:1948–74.
29. Sankaran J, Manna M, Guo L, Kraut R, Wohland T. Diffusion, transport, and cell membrane organization investigated by imaging fluorescence cross-correlation spectroscopy. Biophys J. 2009;97:2630–9.
30. Singh AP, Krieger JW, Buchholz J, Charbon E, Langowski J, Wohland T. The performance of 2D array detectors for light sheet based fluorescence correlation spectroscopy. Opt Express. 2013;21:8652–68.
31. Burkhardt M, Schwille P. Electron multiplying CCD based detection for spatially resolved fluorescence correlation spectroscopy. Opt Express. 2006;14:5013–20.
32. Guo SM, Bag N, Mishra A, Wohland T, Bathe M. Bayesian total internal reflection fluorescence correlation spectroscopy reveals hIAPP-induced plasma membrane domain organization in live cells. Biophys J. 2014;106:190–200.
33. Hirsch M, Wareham RJ, Martin-Fernandez ML, Hobson MP, Rolfe DJ. A stochastic model for electron multiplication charge-coupled devices—from theory to practice. PLoS One. 2013;8:e53671.
34. Zhang B, Zerubia J, Olivo-Marin JC. Gaussian approximations of fluorescence microscope point-spread function models. Appl Opt. 2007;46:1819–29.
35. Petrasek Z, Schwille P. Photobleaching in two-photon scanning fluorescence correlation spectroscopy. Chemphyschem Eur J Chem Phys Phys Chem. 2008;9:147–58.
36. Ries J, Chiantia S, Schwille P. Accurate determination of membrane dynamics with line-scan FCS. Biophys J. 2009;96:1999–2008.
37. Macháň R, Foo YH, Wohland T. On the equivalence of FCS and FRAP: simultaneous lipid membrane measurements. Biophys J. 2016;111(1):152–61.
38. Meseth U, Wohland T, Rigler R, Vogel H. Resolution of fluorescence correlation measurements. Biophys J. 1999;76:1619–31.
39. Wohland T, Rigler R, Vogel H. The standard deviation in fluorescence correlation spectroscopy. Biophys J. 2001;80:2987–99.
40. Saffarian S, Elson EL. Statistical analysis of fl uorescence correlation spectroscopy: the standard Deviation and bias. Biophys J. 2003;84:2030–42.
41. Schatzel K, Peters R. Noise on multiple-tau photon-correlation data. Proc SPIE Photon Correl Spectrosc Multicomponent Syst. 1991;1430:109–15.
42. Sengupta P, Garai K, Balaji J, Periasamy N, Maiti S. Measuring size distribution in highly heterogeneous systems with fluorescence correlation spectroscopy. Biophys J. 2003;84:1977–84.
43. Modos K, Galantai R, Bardos-Nagy I, Wachsmuth M, Toth K, Fidy J, Langowski J. Maximum-entropy decomposition of fluorescence correlation spectroscopy data: application to liposome-human serum albumin association. Eur Biophys J. 2004;33:59–67.

44. He J, Guo SM, Bathe M. Bayesian approach to the analysis of fluorescence correlation spectroscopy data I: theory. Anal Chem. 2012;84:3871–9.
45. Guo SM, He J, Monnier N, Sun G, Wohland T, Bathe M. Bayesian approach to the analysis of fluorescence correlation spectroscopy data II: application to simulated and in vitro data. Anal Chem. 2012;84:3880–8.
46. Wawrezinieck L, Rigneault H, Marguet D, Lenne P. Fluorescence correlation spectroscopy diffusion laws to probe the submicron cell membrane organization. Biophys J. 2005;89:4029–42.
47. Ng XW, Bag N, Wohland T. Characterization of lipid and cell membrane organization by the fluorescence correlation spectroscopy diffusion law. CHIMIA Int J Chem. 2015;69:112–9.
48. Bag N, Ng XW, Sankaran J, and Wohland T. Spatiotemporal mapping of diffusion dynamics and organization in plasma membranes. Methods Appl. in Fluoresc. 2016;4(3):034003.
49. Di Rienzo C, Gratton E, Beltram F, Cardarelli F. Fast spatiotemporal correlation spectroscopy to determine protein lateral diffusion laws in live cell membranes. Proc Natl Acad Sci U S A. 2013;110:12307–12.
50. Cardarelli F, Gratton E. Spatiotemporal fluorescence correlation spectroscopy of inert tracers: a journey within cells, one molecule at a time. Berlin: Springer; 2016. p. 1–23.
51. Moens PD, Digman MA, Gratton E. Modes of diffusion of cholera toxin bound to GM1 on live cell membrane by image mean square displacement analysis. Biophys J. 2015;108:1448–58.
52. Bag N, Ali A, Chauhan VS, Wohland T, Mishra A. Membrane destabilization by monomeric hIAPP observed by imaging fluorescence correlation spectroscopy. Chem Commun (Camb). 2013;49:9155–7.
53. Bag N, Huang S, Wohland T. Plasma membrane organization of epidermal growth factor receptor in resting and ligand-bound states. Biophys J. 2015;109:1925–36.
54. Huang H, Simsek MF, Jin W, Pralle A. Effect of receptor dimerization on membrane lipid raft structure continuously quantified on single cells by camera based fluorescence correlation spectroscopy. PLoS One. 2015;10:e0121777.
55. Kohl T, Haustein E, Schwille P. Determining protease activity in vivo by fluorescence cross-correlation analysis. Biophys J. 2005;89:2770–82.
56. Unruh JR, Gratton E. Analysis of molecular concentration and brightness from fluorescence fluctuation data with an electron multiplied CCD camera. Biophys J. 2008;95:5385–98.
57. Guo L, Har JY, Sankaran J, Hong Y, Kannan B, Wohland T. Molecular diffusion measurement in lipid bilayers over wide concentration ranges: a comparative study. Chemphyschem Eur J Chem Phys Phys Chem. 2008;9:721–8.
58. Ng XW, Teh C, Korzh V, Wohland T. The secreted signaling protein wnt3 is associated with membrane domains in vivo: a SPIM-FCS study. Biophys J. 2016;111(2):418–29.
59. Bag N, Yap DHX, Wohland T. Temperature dependence of diffusion in model and live cell membranes characterized by imaging fluorescence correlation spectroscopy. Biochim Biophys Acta Biomembr. 2014;1838:802–13.
60. Sankaran J, Shi X, Ho LY, Stelzer EH, Wohland T. ImFCS: a software for imaging FCS data analysis and visualization. Opt Express. 2010;18:25468–81.
61. Arndt-Jovin DJ, Botelho MG, Jovin TM. Structure-function relationships of ErbB RTKs in the plasma membrane of living cells. Cold Spring Harb Perspect Biol. 2014;6:a008961.
62. Sigismund S, Argenzio E, Tosoni D, Cavallaro E, Polo S, Di Fiore PP. Clathrin-mediated internalization is essential for sustained EGFR signaling but dispensable for degradation. Dev Cell. 2008;15:209–19.
63. Struntz P, Weiss M. Multiplexed measurement of protein diffusion in Caenorhabditis elegans embryos with SPIM-FCS. J Phys D Appl Phys. 2016;49:044002.
64. Kisley L, Brunetti R, Tauzin LJ, Shuang B, Yi X, Kirkeminde AW, Higgins DA, Weiss S, Landes CF. Characterization of porous materials by fluorescence correlation spectroscopy super-resolution optical fluctuation imaging. ACS Nano. 2015;9:9158–66.
65. Ashdown GW, Cope A, Wiseman PW, Owen DM. Molecular flow quantified beyond the diffraction limit by spatiotemporal image correlation of structured illumination microscopy data. Biophys J. 2014;107:L21–3.

Chapter 7
Probing Membrane Heterogeneity with k-space Image Correlation Spectroscopy

Elvis Pandzic and Paul W. Wiseman

Absract Understanding and quantifying the plasma membrane complexity, with its myriad of structures and intricate interactions within and with components inside and outside of the cell boundary is one of paramount importance in the field of medical sciences. Indeed, when it comes to design and development of novel drug therapies targeting of G-protein coupled receptors (GPCR) and similar protein complexes, seeing the interaction of these proteins in situ with major players involved in drug uptake requires novel tools that can follow these process in live cells by fluorescence microscopy. In past 10 years, k-space Image Correlation Spectroscopy (kICS) was demonstrated to be a simple to implement and reliable approach for such studies. In this chapter we introduce the kICS methodology, followed by series of examples of its adaptations used in different case studies of membrane protein dynamics and kinetics in live cell membrane environment.

7.1 Introduction

Several different variants of image correlation spectroscopy have been applied to study the transport and aggregation of membrane protein complexes before the development of k-space image correlation spectroscopy (kICS). For example, ICS was used to study aggregation of PDGF-β receptors on the plasma membrane of human skin fibroblasts [1, 2], and ICS analysis of photo-bleached image series was used for quantification of the aggregation state of Aβ on nerve cells [3]. Another related imaging based fluorescence fluctuation analysis technique called spatial intensity distribution analysis (spIDA) was used to measure epidermal growth factor receptor (EGFR) dimerization and its trans-activation by stimulation of GPCRs [4, 5]. Time domain measurements in two detection channels with single

E. Pandzic
Biomedical Imaging Facility—Mark Wainwright Analytical Centre, University of New South Wales, Sydney, Australia
e-mail: e.pandzic@unsw.edu.au

P.W. Wiseman (✉)
Departments of Physics and Chemistry, McGill University, Montreal, Canada
e-mail: paul.wiseman@mcgill.ca

A. Chattopadhyay (ed.), *Membrane Organization and Dynamics*, Springer Series in Biophysics 20, DOI 10.1007/978-3-319-66601-3_7

wavelength excitation fluorescence cross-correlation spectroscopy (sw-FCCS) allowed for quantification of fractions of hetero-dimers of EGFR and the ErbB2 receptor family [6]. Temperature dependent dynamics of EGFR clusters were assessed with a temporal pixel fluctuation correlation analysis [7] and an adaptation of ICS exploiting the hidden time structure of laser scanning confocal microscopes (raster-scan-ICS) was used to measure the phospholipase Cγ, protein kinase C, and protein kinase D (PKD) dependent oscillations between the monomer-dimer states of EGFR in living CHO cells [8]. The kICS implementation for imaging based fluorescence fluctuation analysis was introduced to tackle measurements in systems with complex probe photophysics.

In the original development [9], kICS was used to separate, in Fourier space, the time dependent photo-physics of fluorophores (blinking, photo-bleaching) from the space-time dependent transport dynamics (diffusion, flow) of molecular species. Data treatment in Fourier space provided more accurate measurement of molecular dynamics for blinking fluorophore labels, such as quantum dots (QD) [10]. Later it was discovered that the photo-physics correlation function obtained by kICS proved to be useful in assessing the nano-scale aggregation of T-cell receptors in naive or active T-cells [11, 12]. Subsequent extensions of kICS allowed for quantification of ligand-receptor binding kinetics as well as in membrane receptor docking to an immobile receptor complex [13]. This extension was also used to quantify membrane domain confinement and cholesterol modulation of Cystic Fibrosis Transmembrane Conductance Regulator (CFTR) where the kICS correlation function was quantified by fitting for two different CFTR dynamic populations [14]. Finally, a recent adaptation [15] of kICS develops a model for intermittent dynamics of gold nanostars between diffusive and active transport states inside live cells. This flexibility of adaptability and simplicity of kICS is what makes it one of the ideal approaches to study complex transport and kinetics processes of molecules inside and across plasma membrane of live cells.

7.2 kICS Theory and Development

Here we derive the basic theory of kICS for the case of single population of molecules freely diffusing in a 2D environment (membrane like) with a simple photophysics model blinking and/or bleaching. For a more in depth treatment of kICS theory for cases of multiple populations and dynamics please consult references [9, 16].

We start our derivation considering the expression for intensity in a pixel from an image time series, $i(\vec{r},t)$ which we model as a convolution of the microscope point spread function (PSF), $I(\vec{r})$, and the molecules concentration at their space-time dependent locations, $\varrho(\vec{r},t)$:

$$i(\vec{r},t) = qI(\vec{r}) \times \varrho(\vec{r},t) \tag{7.1}$$

where q is a constant incorporating the quantum yield of the fluorophore, the collection efficiency and the detector gain. Writing the number density of molecules as:

$$\varrho(\vec{r},t) = \sum_{i=1}^{N} \theta_i(t)\delta(\vec{r} - \vec{r}_i(t)) \tag{7.2}$$

where the sum is over all N molecules and δ is again the Dirac δ-function. The molecules' bleaching and blinking are described by the time dependent function:

$$\theta_i = \begin{cases} 1 & \text{if } i \text{ is fluorescing at time t;} \\ 0 & \text{otherwise.} \end{cases} \tag{7.3}$$

while the PSF of the fluorescence microscope is approximated by a 2D Gaussian:

$$I(\vec{r}) = I_0 exp\left[-2\left(\frac{x^2+y^2}{\omega_0^2}\right)\right], \tag{7.4}$$

where I_0 denotes the laser intensity at the center of the focal spot, and ω_0 is the e^{-2} beam radius of the laser beam in the lateral direction. For the theory development accounting for motion in 2D (flat cellular membrane), and considering that data are collected in an image on an area sensor or sequential point detection (CCD camera or raster scanned confocal point detection), we will ignore the third dimension. Other theoretical developments presented in further sections of this chapter, might not explicitly ignore the third dimension.

Considering that the convolution becomes a product in Fourier space, and expressions (7.2)–(7.4), Eq. (7.1) transforms to k-space after spatial Fourier transform as:

$$\tilde{i}(\vec{k},t) = \frac{qI_0\omega_0^2\pi}{2} \sum_{i=1}^{N} \theta_i exp\left[i\vec{k}\cdot\vec{r}_i(t) - \frac{\omega_0^2\left|\vec{k}\right|^2}{8}\right]. \tag{7.5}$$

Using Eq. (7.5) we define the intensity-intensity fluctuation time correlation function in k-space:

$$G(\vec{k};\tau) = \left\langle \tilde{i}(\vec{k},t)\tilde{i}^*(\vec{k},t+\tau) \right\rangle \tag{7.6}$$

Inserting Eq. (7.5) into (7.6) gives:

$$G(\vec{k};\tau) = \frac{q^2 I_0^2 \omega_0^4 \pi^2}{4} \times \left\langle \sum_{i=1}^{N} \theta_i(t) e^{i\vec{k}\cdot\vec{r}_i(t) - \frac{\omega_0^2|\vec{k}|^2}{8}} \sum_{j=1}^{N} \theta_j(t+\tau) e^{i\vec{k}\cdot\vec{r}_j(t+\tau) - \frac{\omega_0^2|\vec{k}|^2}{8}} \right\rangle \quad (7.7)$$

For the purpose of demonstration, we assume that the system is sufficiently dilute the cross-product terms will be vanishing and since the $\theta(t)$ is only function of time, we can pull it out of the spatial integral. Moreover, assuming only single population of molecules diffusing in 2D with diffusion coefficient D Eq. (7.7) reduces to:

$$G(\vec{k};\tau) = N \frac{q^2 I_0^2 \omega_0^4 \pi^2}{4} \times \langle \theta(t)\theta(t+\tau) \rangle \times e^{\frac{-|\vec{k}|^2 \omega_0^2}{4}} \times e^{-|\vec{k}|^2 D\tau} \quad (7.8)$$

Equation (7.8) has four multiplicative parts. The first part groups all the constants in the imaging system, the second factor is the time varying photophysics correlation function, the third is time independent PSF function and the fourth models the space-time dependent molecular dynamics in the correlation function. Since first and third terms are time independent, it is practical to normalize them out using the $\tau = 0$ function as previously demonstrated [9, 10]:

$$\frac{G(\vec{k};\tau)}{G(\vec{k};0)} = \langle \theta(t)\theta(t+\tau) \rangle \times e^{-|\vec{k}|^2 D\tau} \quad (7.9)$$

This implies that kICS analysis does not depend on the shape and size of microscope's PSF (assuming that it does not change in time), which makes it very practical as measurements of PSF is not required to apply the analysis.

In practice, the kICS correlation functions are obtained by first calculating 2D fast Fourier transforms for each image in time series set (Fig. 7.1a, b). Then the frequency space images are correlated temporally (Fig. 7.1c) producing for a freely diffusing molecules in 2D a series of Gaussian functions collapsing in k-space with increasing temporal lag τ (as described by Eq. 7.9).

These correlation functions could be fit by symmetric 2D Gaussians, but considering the isotropic diffusion in 2D, a reduction in number of fitting parameters can be made by azimuthal (circular) averaging of correlation function at a given τ (Fig. 7.1d). This operation produces a carpet like correlation function (Fig. 7.1e) which is a function of temporal lag between images τ and spatial frequencies k^2 which are linked to spatial distance through reciprocal relationship, $k^2 = \frac{2\pi}{r^2}$. Figure 7.1f shows the correlation function plotted in symbols blue to red for increasing temporal lag τ, as a function of k^2. Dashed black lines are fits to single exponential equation $f(k^2) = Ae^{-k^2 B}$, where A incorporates the photophysics correlation function while B is a parameter that has units of μm^2 and is extracted for every temporal lag τ. Plotting B vs temporal lag τ gives a linear trend for diffusion transport (blue symbols in Fig. 7.1g) which can be fit by linearly regression (red line in Fig. 7.1g) and its slope equal to the diffusion coefficient D of

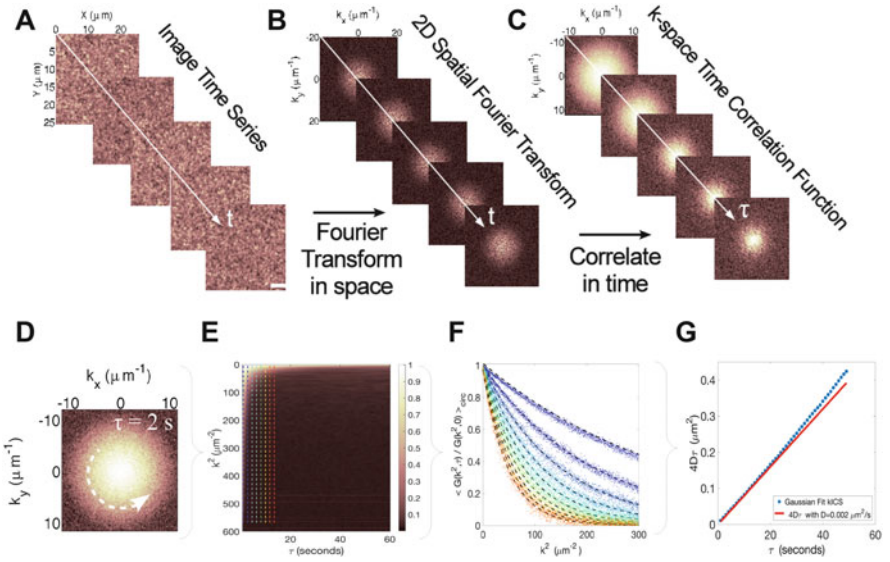

Fig. 7.1 Principles of kICS correlation function (CF) calculation and characterization. (**a**, **b**) Images in time series from fluorescence microscope are fast Fourier transformed in 2D then temporally correlated (**c**) giving the spatio-temporally varying CF. Simulated case of 2D freely diffusing molecules with $D = 0.002\,\mu m^2 s^{-1}$. (**d**) Circular averaging of CF at a given time lag τ, leads to CF represented in 2D (**e**) which is function of spatial frequency, k^2 and temporal lag τ. *Blue to red dashed line* (**e**) and symbols (**f**) are representing CF contribution for increasing temporal lag. Fitting the correlation with an exponential, at every τ, (**f**) gives the trend of $D\tau$ vs. τ (*blue symbols* in g) that by linear fit recovers the diffusion coefficient D (*red line*)

labelled molecules in the system. The original kICS development calculated the logarithm of Eq. (7.9), which transform the expression into a sum of two components: logA and $-k^2B$ which can be fit with a linear function instead of exponential decay. This is only practical for the system of single component freely diffusing molecules, while more complicated dynamic and kinetic scenarios, as shown in next sections, will lead more complex forms of the correlation functions.

Importantly, we note that if the probe photophysics dynamics are only time dependent, the dynamical part of correlation function, $e^{-k^2 D\tau}$, will not be affected and hence the recovered parameters. This is true provided that rates of photobleaching are not extremely high or blinking rates are not on the same temporal scale as imaging. In those cases, molecules would disappear at rate faster than any spatio-temporal fluctuations, from same particles, and would impact the kICS correlation function.

7.2.1 *Photo-Physics of QDs Change with Nearest Neighbour Distance*

The photophysics component of the Eq. (7.9) can often be perceived as a problematic bias, that is undesirable when measuring the molecular dynamics. Nevertheless, it was shown to indirectly provide insight in nano-scale organization of T-cell receptors (TCR) labeled with quantum dots (QDs) [11, 12]. In fact, the QDs blinking statistics depend on the nearest neighbour distance in a way similar to the Forster resonance energy transfer. It was found that calculating the ratio of $\langle \theta(t)\theta(t+\tau) \rangle$ at later temporal lags vs the value at $\tau = 1$, permitted a qualitative assessment, that was useful to provide comparison in clustering of TCR in naive and time evolution of activated T-cells. For more info on basic kICS developments we suggest further reading following references [9, 10, 16]. Detailed information about the sampling requirements, accuracy, precision, signal-to-noise effects and limitations can be found in following manuscripts [17, 18]. The standard methodology and protocol for measurement of diffusion coefficient of membrane proteins using kICS can be found in [19].

7.3 kICS Applied to Study of Reactions Kinetics

Most membrane proteins have complex transport properties that are not simply represented by a single dynamical component, but rather they partition into several dynamical states in a steady state equilibrium. Moreover, it is unlikely that any model can fully account for all of those states. Nevertheless, for typical measurement sampling timescales, e.g. for image times series measurement, some models approximate well the states of membrane receptors in steady state equilibrium. Two models that were explored using kICS analysis [13]. First, deals with ligand-receptor binding kinetics (Lower diagram in Fig. 7.2a) where a ligand can rapidly diffuse in extracellular 3D environment and bind to the membrane embedded receptor. The second model explored kinetics of membrane receptor diffusing and intermittently converting between two diffusive states, one with a higher diffusion coefficient D_1 and one with a lower coefficient D_2 (Upper diagram in Fig. 7.2a). This latter model describes situations when receptors form higher order oligomers or interact with another macromolecular complex.

7.3.1 *Ligand-Receptor Kinetics by kICS*

When the ligand is fluorescently tagged but the receptor is not, the latter can be represented in a two state model: unoccupied invisible (dark) state or occupied fluorescently labelled state depending on ligand binding/unbinding the receptor. At

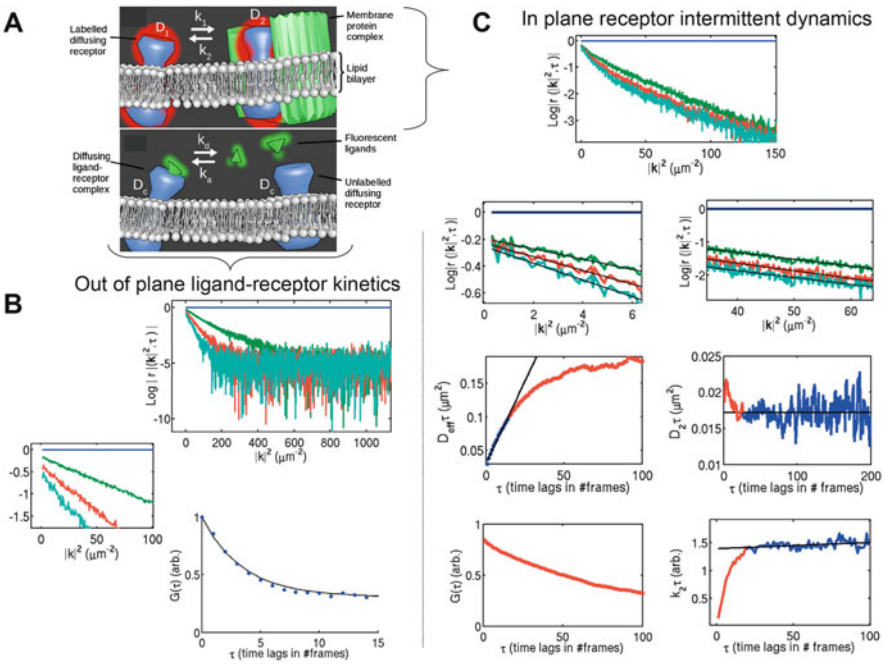

Fig. 7.2 Figure adapted with permission from the [13]. (**a**) Schematics representation of two kinetic models explored by kICS. *Upper diagram* depicts in plane intermittent dynamics of membrane embedded protein, while *lower* depicts the ligand-receptor binding kinetics. (**b**) Characterization of temporally varying amplitude of the circularly averaged k-space correlation function leads to the quantification of ligand-receptor binding kinetics. (**c**) Logged circularly average k-space correlation function exhibits two linear regimes as function of spatial frequency, k^2. Lower k^2 range linear fit (*left column sub-figures*) extracts the effective diffusion coefficient, D_{eff}, that receptor explores as it diffuses through 2D environment and intermittently switches between two dynamics states. From the higher k^2 regime linear fit (*right column sub-figures*) molecular movement in the slow molecular regime, D_2 and conversion from slow to fast regime, k_2 are extracted from the measurement and fits

the imaging frame rate typically employed, we do not resolve the fluctuations of the unbound 3D diffusing ligand and hence it is only resolved in the image when bound to slowly diffusing or immobile membrane embedded receptor. With these assumptions and that of equilibrium for short time periods, [13] explored the solution to the two state model, time-dependent partial differential equation for following reaction:

$$[L]^{free}_{fluo} + [R]^{free}_{dark} \underset{k_{unbind}}{\overset{k_{bind}}{\rightleftharpoons}} [C]^{bound}_{fluo} \tag{7.10}$$

One of the assumption made in [13] is that receptor is very slow diffusing or immobile on the time scale of the imaging frame rate, such that temporal intensity

fluctuation correlation, in any of the pixels of the image series, is purely due to either ligand-receptor binding kinetics or some other photophysics effect. In that scenario, the reaction system described by Eq. (7.10) is described by a set of purely temporal coupled differential equations which can be solved to get expressions for time dependent concentrations of ligand, receptor and ligand-receptor complexes. Since the ligand-receptor complexes, C, are the visible objects, on the frame rate time scale, we expect that kICS temporal correlation function will reflect this. Indeed, the theta function of the Eq. (7.9) can be expressed as product of two terms:

$$\langle \theta(0)\theta(\tau)\rangle = \langle \psi_{bind}(0)\psi_{bind}(\tau)\rangle\langle \varphi_{photo}(0)\varphi_{photo}(\tau)\rangle \tag{7.11}$$

The second term on the right hand side of Eq. (7.11), $\langle \varphi_{photo}(0)\varphi_{photo}(\tau)\rangle$ incorporates the photo-physics events, such as photo-bleaching or blinking, which can be determined by proper control experiment and corrected from the total temporal correlation function. The first term on the right hand side of Eq. (7.11) represents the binding kinetics correlation function and is proportional to the ligand-receptor complexes density-density correlation function:

$$\langle \psi_{bind}(0)\psi_{bind}(\tau)\rangle \propto \langle C(0)C(\tau)\rangle \tag{7.12}$$

Therefore, with the derived expression for the time varying ligand-receptor complexes and with the measured temporal correlation function from kICS, the equilibrium binding and unbinding rates of ligand can be extracted.

7.3.2 *In Plane Receptor Intermittent Dynamics by kICS*

Another scenario explored in [13] is that of diffusing membrane receptor and randomly converting between a fast and slow diffusion states. The model assumed stochastic conversion between the fast and slow diffusion regimes with average rates k_1 and k_2, respectively. The system of equations involved is similar to the one from previous example, except that here the spatial part of the partial differential equations, namely $D\nabla^2\rho(x,t)$, cannot be ignored as receptors are allowed to diffuse with finite diffusion coefficients, D_1 and D_2. Even if analytical solutions to this coupled system of partial differential equations exist as concentrations of receptors in either fast or slow diffusion states, they are too complex to be used trivially to express the density-density correlation functions and link them to the kICS correlation functions. Fortunately, there are two limiting scenarios in which the expressions for the fitting correlation functions can be simplified. First is the scenario, also known as fast-exchange regime, which holds for very small values of spatial frequencies k^2 and small temporal lag τ. In this regime $(k_1 + k_2) \gg D_1 k^2$ and zeroth time-lag normalized kICS correlation function has simple form:

$$G_{fast}\left(k^2,\tau\right) = C_1 G(\tau) e^{-k^2 D_{eff}\tau} \tag{7.13}$$

where,

$$D_{eff} = \frac{k_2 D_1 + k_1 D_2}{k_1 + k_2} \tag{7.14}$$

where C_1 is a constant, $G(\tau)$ is a temporal photophysics function. The emerging effective diffusion coefficient, D_{eff} is a value between D_1 and D_2 if the conversion rate k_1 is higher than rate k_2. Practically, $D_{eff}\tau$ vs. τ trend (Fig. 7.2c left column, second sub-figure) is recovered from the fit of the semi-logged correlation function at every temporal lag τ for small range of spatial frequencies k^2 (Fig. 7.2c left column, first sub-figure). The extra information that is extracted from this regime is the photophysics function, $G(\tau)$, (Fig. 7.2c left column, third sub-figure) which can be used in the slow-exchange regime (below) to accurately correct the correlation function at high k^2 and τ and hence better estimate the rate constant k_2.

In the second regime considered for the simplification of the solution to the partial differential equations, we look at the case when $(k_1 + k_2) \ll D_1 k^2$ and at very large temporal lags τ. This slow-exchange regime, approximates the correlation function fitted at large spatial frequencies and temporal lags:

$$G_{slow}\left(k^2,\tau\right) = C_2 G(\tau) e^{-k^2 D_2 \tau - k_2 \tau} \tag{7.15}$$

where C_2 is a constant. In this case, the fitting recovers the diffusion coefficient in slow regime and rate constant for the conversion from slow to fast diffusing regime, k_2. An example of practical implementation is shown in the example shown in the right sub-figures in Fig. 7.2c.

So far, all the solutions to the differential equations were kept in Fourier space as it is convenient to solve differential equations in Fourier space, but also because convolutions, such as the one of PSF or temporal correlation functions, becomes multiplications in Fourier space which can be simply normalized out as seen in Eq. (7.9). Inverse Fourier transforming would make the already complex expressions for the solution of differential equations, even more prohibitively complicated by introducing extra spatial convolutions. This will be seen in the next sections.

7.4 Membrane Receptor Confinement Analysis by kICS

In this section, we will explore the model by which membrane embedded proteins can get trapped inside small sub diffraction limit size membrane domains. It is similar to the previous described model of the membrane receptor intermittent dynamics, except that the receptor not only diffuses at a lower diffusion coefficient but also does not wander outside of the physical boundary of confining domains,

except if it exceed the probability threshold for escape. Therefore, the domains size, viscosity, composition and nature of its physical barrier will all influence the receptors escape probability and indirectly the rate at which it leaves or enters the small domain. Moreover, in the previous intermittent dynamics model, kinetics rates did not influence the diffusion rates and or vice verse. In the current model, the diffusion coefficient inside the domain, influences how often receptor encounters the domain boundary, and effectively the rate at which it exits the region. Similarly, besides the actual domain surface density, the rate of diffusion outside the domains, determines how often the receptor collides with a domain, and by the same token what is the likelihood of it entering it. Therefore, this model is more complex as several physical parameters can influence the observable receptor dynamical behaviour. A thorough study on the effects of domain sizes, diffusion coefficients inside and outside of domain, probability of entering and exiting domains and domains surface coverage density, on the kICS correlation function, have been subject of a previous thesis [20].

In order to provide you an example of the effect receptor confinement in 2D has on the kICS correlation function, let us consider for the moment a simple case of receptor diffusing freely in 2D at a rate of 0.01 $\mu m^2 s^{-1}$ (Fig. 7.3a). Then the kICS correlation function will collapse with temporal lag, τ until it completely vanishes (de-correlates) at large temporal lags (Fig. 7.3b). On the other hand, if we introduce randomly distributed domains having a radius of 0.2 μm, at 5% surface density coverage, the receptor will have periods of free diffusion (Fig. 7.3c magenta parts of trajectory) and of confinement (Fig. 7.3c blue parts of trajectory). This results in the kICS correlation function collapsing with effectively two decay components (Fig. 7.3d), one fast decay component that we label Macro as it reflects receptors' exploring large spatial scales, and the second component labelled Micro which collapses at later temporal lags, τ and at large spatial frequencies, k^2. The Micro component reflects the events happening at the interface of domains and receptors mobility in and around domains. Figure 7.3e–h shows how changes in ratio of receptors' probability of entering to the probability of exiting domains, $\frac{P_{in}}{P_{out}}$, dramatically affects the amplitude of the PSF-normalized and circularly averaged kICS correlation function. This simulated dynamics of confinement shows that as we increase the ratio, the receptors practically populate more and more domains, as shown by the non-zero amplitudes of correlation function at large k^2 at late temporal lags τ.

From the examples given by the simulated cases shown in Fig. 7.3, it becomes clear that presence of membrane domains leads to more complex pattern in kICS correlation functions. Several parameters describing the physical property of confining domains can be varied to produce similar kICS CF, and hence make this a degenerate problem. Nevertheless, in order to phenomenologically describe the experimentally obtained kICS CF, a strategy of effectively fitting two dynamical components can be employed while some physical parameters of the domains such as lipidic composition and viscosity are changed by employing the drugs and

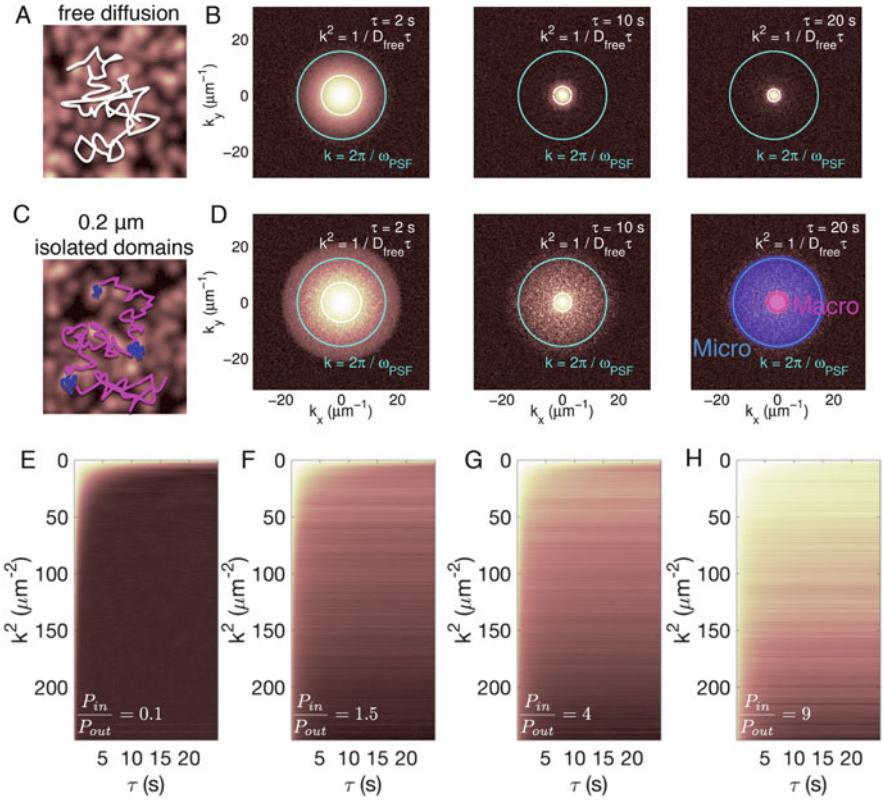

Fig. 7.3 Receptor confinement by membrane domains detected by kICS analysis. (**a**) Simulated case of freely diffusing receptor in 2D environment at $D = 0.01\ \mu m^2 s^{-1}$. (**b**) kICS correlation function at temporal lags $\tau = 2$, 10 and 20 s for image series shown in (**a**). The *cyan circle* denotes boundary of e^{-2} simulated PSF radius, which was set to 0.28 μm. The *yellow circle* denotes the boundary of the de-correlation that particle would have explored if they purely diffused, $k^2 = \frac{1}{D_{free}\tau}$, at a given τ. (**c** and **d**) same as (**a** and **b**) but for the case of receptor diffusion in presence of randomly distributed circular domains. Note: radius of the domain (0.2 μm) was set to be smaller than PSF radius. At $\tau = 20$ s, blue semi-transparent disk denotes the k^2 value regime over which the receptors explore the domains and their surrounding. Magenta disk outlines the Macro dynamical component, which receptors contribute to when diffusing outside of domains. (**d**-**h**) display the circularly averaged PSF-normalized kICS correlation function for simulated cases where receptors were encountering domains of 0.2 μm radius, dispersed uniformly at 5% surface area density and diffusing at rates of 0.01 and $0.005\ \mu m^2 s^{-1}$ outside and inside domains, respectively. The only factor changing was the ratio of probabilities for receptors entering to that of exiting surface domains

enzymes, and effectively shifting the system's equilibrium to systematically study the effects.

This is equivalent to the work done by single spot beam size varying FCS [21, 22], where by simultaneous variation of several domain physical parameters authors were obtaining indistinguishable diffusion laws. This in turn made it

impossible to determine which of the parameters (domain size, probabilities of receptor partitioning, density of domains and diffusion coefficients) were responsible for the change in the characteristic decay time of FCS autocorrelation function and effectively the observed diffusion law. The best that authors were able to determine from such studies [21, 22] were the effective diffusion coefficient receptors explore as they diffuse through 2D environment populated with domains, the confinement strength (which depended on simulated domains physical parameters) and by the trend in the diffusion law were able to define the nature of confinement (i.e. isolated membrane domains vs. an underlying cytoskeleton meshwork). In our work [20] with kICS employed to study receptor confinement in heterogeneous membranes, we employ the fitting kICS' CF with 2 components that phenomenologically account for the two emerging dynamic populations, micro and macro respectively (Fig. 7.3d):

$$\frac{G(\vec{k};\tau)}{G(\vec{k};0)} = A_{\mu} e^{-|\vec{k}|^2 D_{\mu}\tau} + A_M e^{-|\vec{k}|^2 D_M \tau} \tag{7.16}$$

From bi-exponential fit of kICS CF at every temporal lag τ we obtain the temporally varying amplitudes, $A_{\mu}(\tau)$ and $A_M(\tau)$, and decay rates $D_{\mu}(\tau)$ and $D_M(\tau)$, for micro and macro dynamic components, respectively. Fitting the decay rates at early temporal lags, give the diffusion coefficients for receptors at small and large spatial scales. The saturation value of $D_{\mu}\tau$ is directly proportional to the squared radius of domains, but also shifts to the lower values as the ratio $\frac{P_{in}}{P_{out}}$ increases. This is a result of some receptors wandering shorter distances aways from a domain before getting trapped again within the same domain. Other instructive phenomenological parameters are the saturating values of $A_{\mu}(\tau)$ and $A_M(\tau)$ at later τ values. These saturating values are directly proportional to the number density of receptors inside and outside of domains, respectively. This methodology was already applied in the study of cholesterol dependent confinement of CFTR in the plasma membrane of primary epithelial cells, as detailed in [14], which provides the basic principles behind methodology. More detailed publications about the methodology, interpretations and limitations will be subject in a manuscript in preparation [23].

7.5 Intermittent Dynamics of Gold Nano-Stars

Another system to which kICS was applied [15] was transport of gold nanoparticles in cells, imaged by their scattering signal, as they convert from purely diffusive to a biased diffusion dynamic state:

$$D \underset{k_2}{\overset{k_1}{\rightleftharpoons}} D + \vec{v} \tag{7.17}$$

where D represents diffusive state and $D + \vec{v}$ represents particles undergoing combined diffusion and flow (biased diffusion). The constants k_1 and k_2 represent rates at which particle convert back and forth between the two states. This again leads to a system of coupled partial differential equations similar to the ones described in Sect. 7.3.1 and 7.3.2.

Such transport dynamics can occur for vesicles in cells as they diffuse, get tethered to a molecular motor and get transported actively across cell before being released again and resuming diffusive transport. Similarly for cases where membrane bound receptors, mostly existing in diffusive state, occasionally get bound by cytoskeletal elements which can polymerize and depolymerize and hence actively pull the receptor cluster. A specific example is for T-cell receptor clusters during the T-cell activation, as they get intermittently actively pulled toward the central portion of the cell [24]. Therefore, even though authors solved this model for gold nano-stars motion, it is readily applicable to fluorescently labelled membrane receptors with similar dynamic behaviours. Although the authors applied the standard STICS and TICS approaches, they concluded that the system of two partial differential equations cannot lead to an analytically solvable equation for fitting in real space, hence making kICS the analysis tool of choice to yield a tractable analytical solution for this problem.

7.6 Velocity Landscape by k-space Normalization

So far we have demonstrated how kICS is applied to analyze cases of either single species of diffusing membrane receptors, chemical equilibrium of ligand-receptor, confinement of receptor by heterogeneities in membrane and intermittent dynamics of gold nano-particles in cells. In previous sections we described several advantages of analysis in k-space, including separating the time dependent photophysics of fluorophore tags from molecular transport dynamics, normalizing the PSF contribution from the rest of correlation function and solving complex systems of coupled equations describing combined transport scenarios. Another advantage in k-space is that when several dynamic populations of same biological molecule are present, we can normalize out a single dynamical component from the total correlation function. This application is currently being prepared for a publication [25], and applied so far to determine all the flowing populations in an image series.

In order to describe the idea behind the methodology, termed velocity landscape, we start with the equivalent of Eq. (7.9), but consider the case of a biological molecule existing in a one of p molecular flow states, each with N_p molecules and flowing with velocity $\vec{v}_p$, and molecular brightness q_p (monomer will have $q = 1$ and oligomer will be integer multiple):

$$\frac{G(\vec{k};\tau)}{G(\vec{k};0)} = \frac{\Omega_p(\tau)\sum N_p q_p^2 e^{i\vec{k}\cdot\vec{v}_p\tau}}{\Omega_p(0)\sum N_p q_p^2} \tag{7.18}$$

where $\Omega_p(\tau) = \langle \theta_p(t)\theta_p(t+\tau)\rangle$ is temporal correlation function of the photophysics fluctuations of the fluorophores (on or off emission states) in flow state p. Without the loss of generality, in order to obtain Eq. (7.18), we considered that molecules are only flowing in p different flows in absence of diffusive or reactive components. Also, we assume that photophysics will be the same independent of the dynamical transport state of any molecule.

Applying the inverse Fourier transform to this spatio-temporal spectrum function leads to an expression of spatio-temporal image correlation functions as defined previously [26]:

$$G(\vec{r},\tau) = \frac{\sum N_p q_p^2 \delta(\vec{r} - \vec{v}_p\tau)}{\Delta(\tau)\sum N_p q_p^2} \tag{7.19}$$

where $\Delta(\tau) = \frac{\Omega_p(0)}{\Omega_p(\tau)}$ is written for compactness.

The expression in Eq. (7.19) implies that different dynamical populations present flowing each contribute to the spatio-temporal correlation function, $G(\vec{r},\tau)$, as a translating delta function with velocity $\vec{v}_p$ as a function of temporal lags τ.

Now, assuming that one of the existing flow with velocity $\vec{v}_o$ is to be normalized from Eq. (7.19). Then Eq. (7.18) becomes:

$$\frac{G(\vec{k};\tau)}{|\, G(\vec{k};0)\,| \times e^{i\vec{k}\cdot\vec{v}_o\tau}} = \frac{N_o q_o^2 + \sum_{p\neq o} N_p q_p^2 e^{i\vec{k}\cdot(\vec{v}_p - \vec{v}_o)\tau}}{\Delta(\tau)\sum N_p q_p^2} \tag{7.20}$$

which when Fourier inverted leads to:

$$G_{o-norm}(r,\tau) = \frac{N_o q_o^2 \delta(\vec{r}) + \sum_{p\neq o} N_p q_p^2 \delta(\vec{r} - (\vec{v}_p - \vec{v}_o)\tau)}{\Delta(\tau)\sum N_p q_p^2} \tag{7.21}$$

When visualized in space and over time lags τ, the function in Eq. (7.21) will show p-1 flowing peaks at velocities $\vec{v}_p - \vec{v}_o$ and one stationary Delta peak at the origin, due to the normalization of the single dynamic population of velocity $\vec{v}_o$.

If we were to normalize a random velocity, $\vec{v}_{rand}$, that does not sample the observation volume within the sampling time, then we would get an expression similar to the Eq. (7.19) but where $\vec{v}_p$ is replaced by $\vec{v}_p - \vec{v}_{rand}$

$$G_{rand-norm}(r,\tau) = \frac{\sum_p N_p q_p^2 \delta\left(\vec{r} - \left(\vec{v}_p - \vec{v}_{rand}\right)\tau\right)}{\Delta(\tau)\sum N_p q_p^2} \tag{7.22}$$

In other words, normalizing a random velocity (i.e. likely not present) from the correlation function in k-space, still produces p dynamic components. On the other hand, normalizing an existing dynamic component, produces the spatio-temporal correlation function with one stationary delta peak at the origin and p-1 flowing peaks as shown in Eq. (7.21).

Figure 7.4a shows three snapshots (at 1, 10 and 20 s) of simulated image times series containing three dynamic flowing populations, at $(v_{x1}, v_{y1}) = (0.013, -0.015)$, $(v_{x2}, v_{y2}) = (-0.025, -0.03)$ and $(v_{x3}, v_{y3}) = (0.055, -0.06)\,\mu m\,s^{-1}$. Regular STICS approach will produce three peaks, one for each dynamical translational population, that will flow at same rate as existing flows of molecules and change position with the temporal lag τ as shown in Fig. 7.4b. It is standard procedure in STICS to fit a 2D Gaussian to such a data at each τ and extracting the position of the peak in order to obtain the velocity of the underlying flow. Due to peak overlap as a short time lags, this will result in biased and incomplete information about the mixture of dynamic populations. Next, if we apply Eq. (7.22) and normalize out a random flow velocity that does not exist in the data, $(v_{x-rand}, v_{y-rand}) = (-0.077, -0.0377)$ it results in correlation function with three correlation peaks that flow in other directions than the flows present in the data (Fig. 7.4c). Note that for both cases in Fig.7.4b and 7.4c, show the correlation peaks that move off the origin, $r = 0$, as τ increases. On the other hand, if an existing flow, such as flow (v_{x2}, v_{y2}), is normalized out as in Eq. (7.21), then we will be left with two flowing peaks and one immobile delta peak at the origin of the correlation field (Fig. 7.4d). Plotting the amplitude of the correlation functions at the origin (black, red and blue dashed circles in b, c and d, respectively) vs temporal lag shows that in the case of normalization of an existing flowing component, the amplitude never decays to zero (Fig. 7.4e). For every incrementally normalized velocity, one can extract the value of the amplitude at the late temporal lags and build the velocity landscape as shown in Fig. 7.4f. The resulting velocity landscape is characterized by peaks in the velocity coordinate space, which correspond to the existing flows sampled in the original image time series data.

7.7 Conclusion

In this chapter we outlined the early developments and application of k-space Image Correlation Spectroscopy (kICS) for the study of membrane receptors dynamics in situ. Its original implementation [9, 10] was intended to separate the purely temporal bias of fluorophore photophysics from the spatio-temporal part of correlation function, and effectively obtain an accurate measurement of transport

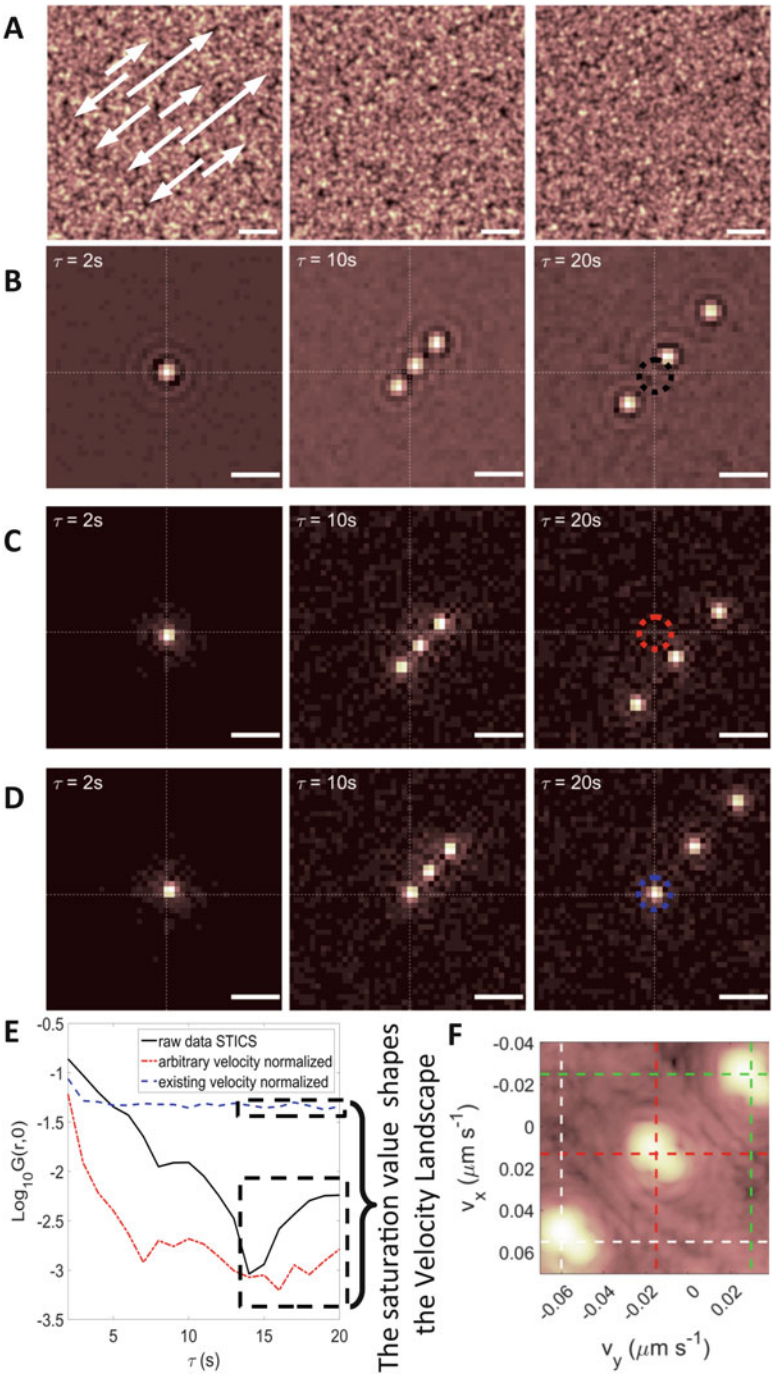

Fig. 7.4 Principle of velocity landscape. (**a**) Simulated images series of 3 flowing particle species (t = 1, 10 and 20 s). *Arrows* indicate the direction of 3 flows and arrow lengths show the relative

properties of molecules. The kICS derived photophysics correlation function was also used in the context of quantum dot labelled T-cell receptors, in order to determine nano-scale clustering properties in naive and activated T-cells [11, 12]. Furthermore, more complex behaviours of membrane receptors, such as ligand binding and intermittent conversion between two different diffusive states, led to extensions in kICS fitting approaches [13]. Similarly, the confinement of membrane receptor in isolated membrane domains was studied by kICS on simulated data and verified experimentally on GPI-anchored receptor in COS-7 cell membrane [20], CFTR in primary epithelial cell membranes [14] and recently on Lck kinase in T-cell membranes [23]. One of advantages of kICS is that spatial convolution of two functions in real space becomes a product in k-space which made it possible to remove the contribution of PSF by normalization of time zero component [9]. Another advantage is that most of the complex systems of coupled equations representing the spatio-temporal evolution of molecular densities, as shown in Sects. 7.3, 7.4 and 7.5, lead to a complex analytical expressions for a spatio-temporal correlation function. Inverting this expression to real space in order to use STICS correlation function for analysis, makes analytical solution intractable for most practical models. Finally, normalization of correlation functions in k-space was demonstrated to be useful to separate contributions from populations with different molecular flows [25].

With the growing number of extensions designed to handle different mechanisms of molecular dynamics, kICS is proving to be a powerful tool to study receptor dynamics in heterogeneous membranes of living cells.

References

1. Wiseman PW, HÃddelius P, Petersen NO, Magnusson KE. Aggregation of PDGF-beta receptors in human skin fibroblasts: characterization by image correlation spectroscopy (ICS). FEBS Lett. 1997;401(1):43–8.
2. Wiseman PW, Petersen NO. Image correlation spectroscopy. II. Optimization for ultrasensitive detection of preexisting platelet-derived growth factor-beta receptor oligomers on intact cells. Biophys J. 1999;76(2):963–77.

Fig. 7.4 (continued) difference in speeds. (**b**) Standard STICS correlation function, at temporal lags 2, 10 and 20 s. (**c**) Correlation function (Eq. 7.21) after a random velocity component is normalized from the k-space correlation function. (**d**) Correlation function (Eq. 7.21) after one of the existing dynamic flows is normalized in k-space. (**e**) The logarithm of the amplitude at $r = 0$ as function of temporal lag. *Black*, *red* and *blue lines* show the trend of the amplitude of CF at the origin, cases depicted in (**b**), (**c** and **d**), respectively. (**f**) Final velocity landscape for this simulated data set. Three peaks in the velocity landscape fall at the crossing of the *dashed lines* (*white*, *red* and *cyan*) outlining the values of flows simulated in this data set

3. Ciccotosto GD, Kozer N, Chow TTY, Chon JWM, Clayton AHA. Aggregation distributions on cells determined by photobleaching image correlation spectroscopy. Biohpys J. 2013;104 (5):1056–64.
4. Godin AG, Costantino S, Lorenzo L-E, Swift JL, Sergeev M, Ribeiro-da-Silva A, De Koninck Y, Wiseman PW. Revealing protein oligomerization and densities in situ using spatial intensity distribution analysis. Proc Natl Acad Sci USA. 2011;107(17):7010–5.
5. Swift JL, Godin AG, Dore K, Freland L, Bouchard N, Nimmo C, Sergeev M, De Koninck Y, Wiseman PW, Beaulieu JM. Quantification of receptor tyrosine kinase transactivation through direct dimerization and surface density measurements in single cells. Proc Natl Acad Sci USA. 2011;108(17):7016–21.
6. Liu P, Sudhaharan T, Koh RML, Hwang LC, Ahmed S, Maruyama IN, Wholand T. Investigation of the dimerization of proteins from the epidermal growth factor receptor family by single wavelength fluorescence cross-correlation spectroscopy. Biophys J. 2007;93 (2):684–98.
7. Keating E, Nohe A, Petersen NO. Studies of distribution, location and dynamic properties of EGFR on the cell surface measured by image correlation spectroscopy. Euro Biophys J. 2008;37(4):469–81.
8. Kluba M, Engelborgs Y, Mizuno H. Inhibition of receptor dimerization as a novel negative feedback mechanism of EGFR signaling. PLoS One. 2015;10(10):e0139971.
9. Kolin DL, Ronis D, Wiseman PW. k-Space image correlation spectroscopy: a method for accurate transport measurements independent of fluorophore photophysics. Biophys J. 2006;91:2061–75.
10. Durisic N, Bachir AI, Kolin DL, Hebert B, Lagerholm C, Grutter P, Wiseman PW. Detection and correction of blinking bias in image correlation transport measurements of quantum dot tagged macromolecules. Biophys J. 2007;93:1338–46.
11. Boyle S, Kolin DL, Bieler JG, Schneck JP, Wiseman PW, Edidin M. Quantum dot fluorescence characterizes the nanoscale organization of T cell receptors for antigen. Biophys J. 2011;101:L57–9.
12. Shaikh SR, Boyle S, Edidin M. A high fat diet containing saturated but not unsaturated fatty acids enhances T cell receptor clustering on the nanoscale. Prostaglandins Leukot Essent Fatty Acids. 2015;100:1–4.
13. Brandao HB, Sangji H, Pandzic E, Brouhard GJ, Wiseman PW. Measuring ligand-receptor binding kinetics and dynamics using k-space image correlation spectroscopy. Methods. 2014;66:273–82.
14. Abu-Arish A, Pandzic E, Goepp J, Matthes E, Hanrahan JW, Wiseman PW. Cholesterol modulates CFTR confinement in the plasma membrane of primary epithelial cells. Biophys J. 2015;109:85–94.
15. Bouzin M, Sironi L, Chirico G, D'Alfonso L, Inverso D, Pallavicini P, Collini M. An intermittent model for intracellular motions of gold nanostars by k-space scattering image correlation. Biophys J. 2015;109:2245–58.
16. Kolin DL. k-Space image correlation spectroscopy: theory, verification, and applications. McGill University, PhD Thesis; 2008.
17. Schwartzentruber JA. k-Space image correlation spectroscopy (kICS): accuracy and precision, capabilities and limitations. McGill University, MSc Thesis; 2010.
18. Brandao HB. Statistical accuracy of image correlation spectroscopy: applications to ligand-receptor binding, flow, and molecular diffusion. McGill University, MSc Thesis; 2014.
19. Arnspag EC, Koffman JS, Marlar S, Wiseman PW, Nejsum LN. Easy measurement of diffusion coefficients of egfp-tagged plasma membrane proteins using k-space image correlation spectroscopy. J Vis Exp. 2014:e51074.
20. Pandzic E. Measurement of protein transport and confinement in heterogeneous membranes by k-space image correlation spectroscopy. McGill University, PhD Thesis; 2013.
21. Wawrezinieck L, Lenne PF, Marguet D, Rigneault H. Fluorescence correlation spectroscopy to determine diffusion laws: application to live cell membranes. Proc SPIE. 2004;5463:92–102.

22. Wawrezinieck L, Rigneault H, Marguet D, Lenne PF. Fluorescence correlation spectroscopy diffusion laws to probe the submicron cell membrane organization. Biophys J. 2005;89:4029–42.
23. Pandzic E, Abu-Arish A, Hanrahan J, Gaus K, Wiseman PW. Measurement of Lck confinement in T-cell membranes by k-space image correlation spectroscopy. TBD; 2017.
24. Varma R, Campi G, Yokosuka T, Saito T, Dustin ML. T cell receptor-proximal signals are sustained in peripheral microclusters and terminated in the central supramolecular activation cluster. Immunity. 2006;25(1):117–27.
25. Pandzic E, Abu-Arish A, Whan R, Hanrahan J, Wiseman PW. Velocity landscapes resolve multiple dynamical populations from fluorescence image time series. TBD; 2017.
26. Toplak T, Pandzic E, Chen L, Vicente-Manzanares M, Horwitz AR, Wiseman PW. STICCS reveals matrix-dependent adhesion slipping and gripping in migrating cells. Biophys J. 2012;103(8):1672–82.

Chapter 8
Determining Oligomerization of Membrane Proteins by Single Molecule Methods

Andreas Anderluh, Anand Kant Das, and Gerhard J. Schütz

Abstract The assembly of proteins to larger oligomeric complexes confers distinct structural, functional, and dynamic properties on the newly formed entity. It is not trivial, however, to experimentally quantify oligomerization of molecules, particularly when different oligomeric states coexist. For this, our group developed a single molecule technique called **T**hinning **O**ut **C**lusters **W**hile **C**onserving **S**toichiometry of **L**abelling (TOCCSL) (Moertelmaier et al., Appl Phys Lett 87:263903, 2005; Brameshuber and Schutz, Methods Enzymol 505:159–186, 2012). The technique allows for the determination of the oligomeric states of fluorescently labeled membrane proteins even at high expression levels. TOCCSL can also be used to determine the kinetics of oligomerization.

Our chapter is divided into two main sections. "Membrane protein oligomerization" presents a brief summary of the concepts of protein oligomerization and kinetics of oligomerization. As a case study, the potential physiological role of Neurotransmitter: Sodium Symporter (NSS) oligomerization is discussed. This is followed by a description of methods to evaluate protein oligomerization, including a detailed description of TOCCSL and the case study of a NSS family member, the Serotonin Transporter (SERT).

8.1 Membrane Protein Oligomerization

It is believed that a large fraction of cellular proteins, between one half and two third, are oligomeric in nature [1]. In contrast to the fluid mosaic model of Singer and Nicolson [2] wherein proteins in the membrane were depicted as sparsely distributed and independent monomeric entities diffusing through a matrix of lipids, most researchers currently understand oligomerization as a more generic phenomenon for many membrane associated proteins [3]. Analysis of the Protein Data Bank of Transmembrane Proteins (PDBTM) suggests that a significant number of membrane proteins (around 65%) form oligomers [4]. Oligomerization is

A. Anderluh • A.K. Das • G.J. Schütz (✉)
Institute of Applied Physics, TU Wien, Wiedner Hauptstrasse 8–10, 1040 Vienna, Austria
e-mail: schuetz@iap.tuwien.ac.at

A. Chattopadhyay (ed.), *Membrane Organization and Dynamics*, Springer Series in Biophysics 20, DOI 10.1007/978-3-319-66601-3_8

very common among ion channels, fusion proteins and membrane-disruptive proteins [5]. Oligomers may be homo-oligomeric or hetero-oligomeric.

A plethora of mechanisms has been proposed to explain what mediates the oligomerization of proteins, e.g. domain swapping, ligand induced dimerization, posttranslational modifications including phosphorylation on dimer interfaces and disulfide bond formation between two subunits [6]. It has been shown that β-barrel membrane proteins can oligomerize through the weakly stable interfacial beta-strands [7], while in case of certain p53 proteins the C-terminal helix might play a crucial role in stabilization of the oligomers [8]. Additionally, for a large number of proteins there exist regions—enabling and disabling loops—that play key roles in enabling or disabling the oligomeric interfaces. These loops mediate interactions or prevent unwanted interactions and are highly conserved in evolution [9]. Lipids have also been found to be important in membrane protein oligomerization [10–12], e.g. phosphatidylglycerol (PG) significantly enhances oligomerization of the voltage-dependent anion channel (VDAC) while cardiolipins have been shown to disrupt VDAC supermolecular assemblies [13].

Oligomerization of proteins may be advantageous as it offers stability, higher order complexity and also leads to compartmentalization of reactions [14]. The reduced surface area of the subunits of the complex further offers protection against denaturation [15]. Next, oligomers may alter the morphological characteristics of the cell, as in case of formation of rings and filaments [3], or may result in allosteric regulation of activity and affinity, both for substrates and interaction partners within the cell. Finally, (hetero-)oligomerization enables proteins to form novel functional entities without changing the genome size by integrating new functions into a complex [14]. G protein-coupled receptors (GPCRs) for example exhibit oligomerization behavior which was first suggested from ligand binding and radiation inactivation studies in the 1970s [16]. It has now been established that GPCRs oligomerize in living cells, that various types of GPCRs can hetero-oligomerize, and that such oligomer formation is crucial for receptor biogenesis and function [17–19].

As a case study, we describe here the oligomerization behavior of Neurotransmitter: Sodium Symporter (NSS) family of membrane proteins.

8.1.1 Oligomerization of Neurotransmitter: Sodium Symporter (NSS)

Transport proteins in the plasma membrane of presynaptic nerve terminals and glial cells aid in removal of specific neurotransmitters from the extracellular space of the synapse, thereby terminating their actions. One major homology class of such transporters, termed Neurotransmitter: Sodium Symporter (NSS) family, derives energy from the co-transport of Na^+ and Cl^-, in order to transport neurotransmitter

molecules into the cell against their concentration gradient. The family has a common structure of 12 presumed transmembrane helices and transports gamma-aminobutyric acid (GABA), serotonin, dopamine, noradrenaline/adrenaline, proline, glycine, betaine, choline or taurine.

It has been suggested that the functional units of NSS are monomers [20]. However, there is increasing evidence that they also form higher oligomeric structures in the cell membrane [21]. The classical biochemical approaches such as co-immunoprecipitation of differently epitope-tagged serotonin transporter (SERT) and dopamine transporter (DAT) constructs [22], oxidative crosslinking of SERT [23] and DAT [24] and optical measurements like Förster resonance energy transfer (FRET) [25] for DAT [26], GABA transporter (GAT) and SERT [27–29] show oligomerization behavior. More recent evidences from our lab using a single molecule approach show co-existence of stable SERT monomers and oligomers in the plasma membrane [30]. What could be the potential physiological role of these oligomers?

8.1.2 Physiological Role of NSS Oligomerization

Based on the available experimental data, two main potential functions of NSS oligomerization can be defined, both of which may contribute to its overall task of controlling the extracellular neurotransmitter concentration.

1. ***Trafficking.*** Post translationally, a protein has to pass the rigid quality control mechanisms at the level of the endoplasmic reticulum (ER) before being trafficked to the plasma membrane. It has been shown that an oligomerization-deficient version of the *gamma*-aminobutyric acid (GABA) transporter (GAT) is retained in the ER but is still capable of GABA transport when integrated into artificial vesicles [20]. This suggests that the oligomerization of correctly folded proteins is necessary to pass the control system for trafficking from the ER [21], which in case of SERT is facilitated by specific interactions with Sec24C-family members [31, 32]. Thus, oligomerization deficiency leads to decreased densities of SERT at the plasma membrane and therefore decreased net uptake rates.
2. ***Reverse transport.*** One of the suggested roles of oligomerization of NSSs relates to the substrate-induced reverse transport of substrate. In this proposed oligomer-based counter-transport model [33], one of the subunits in an oligomer binds the so called releaser (a substrate of the transporter) and induces an electrical current independent from substrate transport, mainly carried out by sodium ions [34, 35]. The energy generated by this current is then used by the neighboring transporter subunit in an unknown way to release the neurotransmitter into the synaptic cleft [33, 36, 37]. Therefore, only NSSs present in an oligomer consisting of at least two transporters would be susceptible for the effect of releasers. The degree of oligomerization could influence the net uptake rate of neurotransmitters.

8.1.3 Kinetics of Protein Oligomerization

Dimerization is well known e.g. for some GPCR family members [38], which show behavior in accordance with a dynamic equilibrium model [39, 40] with continuous formation and dissociation of dimers. The model can be characterized by the rate constant for monomer association k_a, which scales with the surface density of monomers, and the rate constant for dimer dissociation k_d. Hence, the ratio of dimers to monomers depends on the density of GPCRs at the plasma membrane. It appears that the stoichiometry of proteins greatly influence the selectivity for specific ligands which then enables fine tuning of the signaling pathways.

In contrast to the dynamic equilibrium model, a more stable oligomerization behavior occurs when energy barriers make the addition or dissociation of a subunit less favorable. Thus, the monomers/oligomers are kinetically trapped and putative equilibration of the oligomeric distribution is significantly slowed down. For example, corticotropin-releasing factor receptor type 1 (CRF1R), a member of the GPCR family, shows a distinct monomer/dimer ratio; this equilibrium is already established in the ER [41]. It remains constant throughout the life cycle of the receptor regardless of the location at the ER or the plasma membrane and even after ligand binding. These findings strongly indicate kinetic trapping of GPCRs at the plasma membrane.

8.2 Experimental Methods to Evaluate Protein Oligomerization

The biological relevance of protein oligomerization has stimulated the development of a variety of experimental approaches. In the following chapter we will first give the reader an overview about the most common *in vitro* and *in vivo* bulk-based methods to decipher the oligomerization state of membrane-bound proteins, and compare their advantages and disadvantages. In the last part we will give a short introduction into single molecule microscopy and its application for *in vivo* determination of protein oligomerization.

8.2.1 Bulk Measurements: In Vitro Non-fluorescence Methods

8.2.1.1 Chemical Crosslinking

Principle Classical approaches to determine the oligomeric size of proteins are based on chemical crosslinking of the subunits within a complex, followed by isolating the proteins from the membrane [42]. This approach, that has already emerged in the late

1970s [43], makes use of the stable linking of amines or sulfides between different protomers within an oligomer (Fig. 8.1a). To achieve this, cells are treated with chemical crosslinkers, e.g. formaldehyde or bis-(2-methanethiosulfonatoethyl)amine hydrochloride (bis-EA) [24, 44]. Only proteins that are in close proximity (e.g. within an oligomer) are crosslinked during the reaction. Subsequently, plasma membrane bound proteins are extracted from the membrane and the proteins of interest are separated from the mixture by immunoprecipitation or other affinity methods. The size of the isolated oligomers is then evaluated via SDS-PAGE/Western blotting.

Pros Chemical crosslinking is a fast and rather easy method to evaluate the oligomerization behavior of proteins. No sophisticated technical or chemical equipment is needed and the method is well established. Transient interactions of proteins might be captured due to their stabilization during the crosslinking reaction. Moreover, the technique is applicable to both hetero- and homo-oligomerization.

Cons A possible artefact of the technique is the generation of artificial clusters that would not be stable in their native membrane environment. On the other hand, too large distances between reactive sites preclude efficient crosslinking. Furthermore, interpretation of the mixed populations of oligomers from gels is not very sensitive and minority populations might be lost. These factors make it rather difficult to conclude from crosslinking experiments on the actual situation in the living cell.

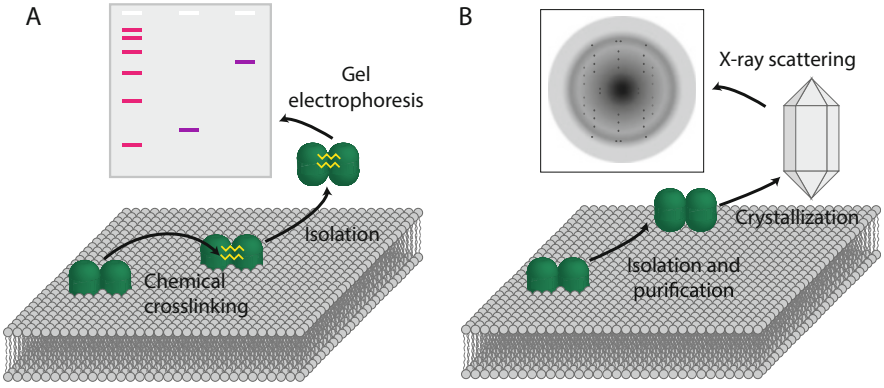

Fig. 8.1 *In vitro* methods to evaluate protein oligomerization. (**a**) *Chemical crosslinking*. Living cells are first treated with crosslinking reagents e.g. formaldehyde or bis-EA. Proteins within an oligomer are stably linked during the reaction and subsequently extracted from the membrane. The size of the isolated protein complexes is then evaluated via gel electrophoresis. (**b**) *Crystallization studies*. Membrane bound proteins are isolated from the membrane and the protein of interest is purified to obtain a highly concentrated protein solution for crystallization. The crystal structure is evaluated using e.g. X-ray scattering

8.2.1.2 Crystallization-Based Approaches

Principle Crystallization studies are not only used to unravel the 3-dimensional structure of a protein, but also to conclude on the oligomeric size. This requires a highly purified protein solution as a starting point in order to crystallize the protein of interest. The analysis is then carried out using X-ray scattering (Fig. 8.1b).

Pros A high-resolution picture of the respective oligomer and its conformation can be obtained with crystallization-based assays. The additional structural information can also yield information about the active state or the protein conformation in conjunction with a bound substrate [45, 46]; in some cases, even stable interactions with lipids were achieved [47, 48].

Cons Highly purified protein solutions are necessary for the approach; the lack of the plasma membrane as a determining factor for oligomerization is prone to produce artefacts in protein crystallization studies. Therefore, the data have to be interpreted with care and are not likely to represent the situation *in vivo*. Particularly, free energy profiles for pure protein crystals may be substantially different from the local minima describing the situation at cell membranes. Finally, the harsh conditions used for isolation of the protein and its crystallization may have a significant impact on the degree of oligomerization and on the protein's conformation; the crystallized protein might not represent the biochemically active conformation.

8.2.2 Bulk Measurements: Live Cell Fluorescence-Based Methods

The above presented *in vitro* approaches have provided important insights into the general concept of protein oligomerization, however, they do not account for the influence of the plasma membrane environment. To assess the situation in the natural environment more directly, several live cell methods based on fluorescence microscopy have been developed in the past years. As we will present in the following section, also with these techniques unambiguous evaluation of the oligomeric state of a given protein remains far from being trivial. A putative pitfall common for all fluorescence based methods is the labelling efficiency: underlabelling of the proteins of interest (e.g. if fluorescent antibodies are used) or incomplete maturation of fluorescent proteins [49, 50] leads to an underestimation of the degree of oligomerization.

8.2.2.1 Förster Resonance Energy Transfer (FRET)

Principle To date, the most common method to show direct interaction of two fluorescently labelled biomolecules is the measurement of FRET between two partner molecules [51, 52] (Fig. 8.2a). This allows for visualizing oligomerization of proteins directly in living cells. The proteins of interest are labelled with two dye molecules, one acting as donor (excitable at a lower wavelength) and the other one as acceptor (excitable at a higher wavelength). After excitation of the donor, non-radiative energy transfer to the acceptor may occur via dipole-dipole coupling. The result is fluorescence emission specific for the acceptor. The efficiency of energy transfer is inversely proportional to the sixth power of the distance, with the Förster radius denoting the donor-acceptor separation at half-maximal transfer efficiency. This depends mainly on the used donor-acceptor pair and lies between 1 nm and 10 nm, a distance that captures many protein oligomers.

Pros The interaction of two players in the plasma membrane can directly be shown with FRET. The strong dependence of the energy transfer on the distance between the two dyes yields a relatively robust readout. At the bulk level, well established

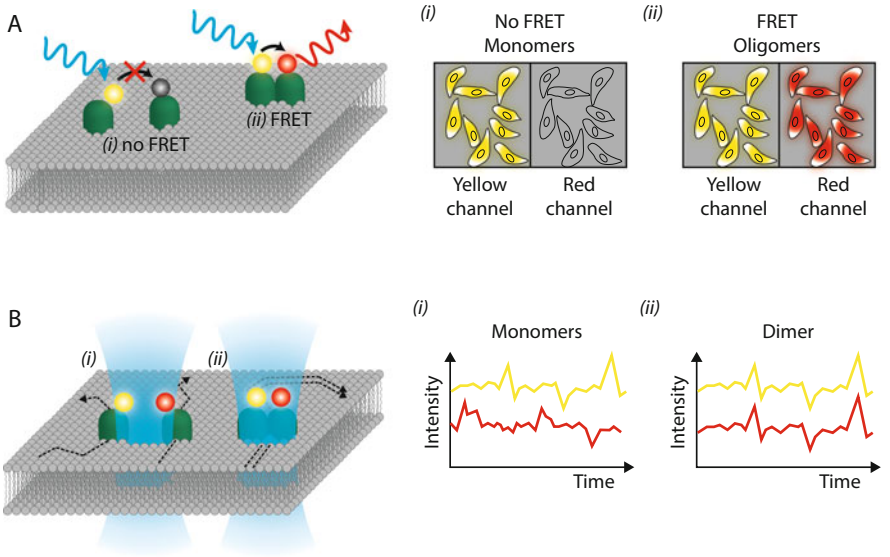

Fig. 8.2 Bulk-based live cell methods. (**a**) *FRET*: Upon excitation of the donor dye molecule, nonradiative energy transfer to the (*red-shifted*) acceptor dye molecule occurs only if the two dyes are in close proximity, e.g. within an oligomer (ii). The rate of the energy transfer depends strongly on the distance between the two dye molecules. (**b**) *FCCS*: also in FCCS, the molecules of interest are labeled with two spectrally different dyes. The recorded fluorescent signal exhibits fluctuations due to particles diffusing through the excitation beam. Whereas independent diffusion of two dye molecules results in independent fluctuations (i), the fluctuations are correlated in co-diffusing (interacting) molecules (ii). The cross-correlation function of the two different dyes increases with the number of molecules within an oligomer

fluorescent proteins can be used for genetic fusion to the protein of interest, e.g. yellow fluorescent protein (YFP) and cyan fluorescent protein (CFP). Furthermore, FRET enables the identification of transient interactions.

Cons Using bulk FRET, it is not possible to decipher the exact number of subunits in the oligomer. A putative drawback of FRET results from the strong correlation of the energy transfer with the distance of the dye molecules; if the separation between the two dye molecules within an oligomer is too large, no FRET will be observable. In addition, if the protein surface density is too high, stochastic proximity of dyes may result in a detectable FRET signal, although no oligomers are actually present.

8.2.2.2 Fluorescence (Cross) Correlation Spectroscopy (FC(C)S)

Principle In FC(C)S the excitation light is focused onto the sample, thereby restricting excitation to a diffraction-limited volume (Fig. 8.2b). The resulting fluorescence signal exhibits fluctuations due to particles diffusing through the excitation volume. The autocorrelation function of these fluctuations can be used as an indicator of particle diffusion. However, the difference in the diffusion coefficient of a monomer and e.g. a dimer is rather small and hence, it is challenging to use FCS for determining oligomeric states. FCCS extends the principle of FCS by using two different fluorescent labels [53]; when the two differently labelled molecules diffuse through the excitation volume, their cross correlation increases with the number of interacting molecules and directly shows oligomerization.

Pros The advantage over e.g. FRET is that FCS/FCCS does not exhibit a distance limit for interacting proteins. Hence, also the detection of larger complexes is possible. In addition, if the interaction time of the subunits in the oligomer is shorter than the time needed to diffuse through the excitation volume, also information about the interaction kinetics of the subunits is encoded in the correlation functions.

Cons Different degrees of oligomerization average out in the analysis and subpopulations might therefore remain hidden. Interaction times cannot be quantified, if complexes remain associated longer than their transit time through the excitation volume.

8.2.2.3 Number and Brightness Analysis

Number and brightness (N&B) analysis is a method that makes use of fluctuations of the fluorescence signals due to varying numbers of particles within single pixels [54–57]. Analysis of the mean and the variance of the fluorescence intensity distributions allow evaluation of the average number of molecules and their brightness at each pixel in a stack of images. In a nutshell, the larger the variance of the fluorescent signal, the fewer molecules contribute to the signal; the ratio of the

square of the average intensity to the variance is proportional to the average number of particles. Also the distribution of oligomers can be obtained: when the brightness of a monomer is known it can be used for a fit to the brightness distribution of the oligomeric mixture.

Pros Being a computational method, no sophisticated technical equipment is necessary. The distribution of oligomeric states of proteins diffusing in the plasma membrane can be calculated if the brightness of a monomer is known.

Cons The determination of the oligomeric distribution using a fit based on the monomeric brightness is rather inexact and gives only approximate values. Hence, usually the average oligomeric size is stated [58].

8.2.3 *Methods Based on Single Molecule Fluorescence Microscopy*

The described bulk-based live cell methods are well suited to measure substantial fractions of oligomers, however, trace amounts are difficult to detect. Bulk methods yield average oligomeric states and hence, variances in the oligomerization average out and subpopulations might remain hidden. Moreover, hardly any further information on the distribution of the oligomeric states and the interaction kinetics can be obtained with these techniques. As a consequence, in the past two decades researchers have looked for ways to measure protein interactions directly at the level of individual molecules.

8.2.3.1 An Introduction into Single Molecule Microscopy

Due to the wave-nature of light, fluorescence microscopy reaches a natural limit in resolution set by the diffraction limit. This means that every point emitter is ideally imaged as an Airy disk. The radius of the Airy disk is given by

$$d = 0.61 \frac{\lambda}{NA}$$

with λ being the emission wavelength and NA the numerical aperture of the objective. In practice, however, aberrations further affect the imaging behavior of the microscope, so that the fluorophore will be imaged according to the empirical point spread function (PSF). The size of the PSF determines the achievable resolution; objects that are closer than d cannot be resolved because their PSFs overlap to an extent that they cannot be distinguished as isolated peaks. In practice, this limit is approximately half the wavelength of the detected light (around 200–300 nm), a distance far above the length scales of a few nm where most oligomerization processes in the cell take place.

In the past years a variety of experimental approaches was introduced to circumvent the diffraction limit [59], with many of them being based on the analysis of single dye molecule positions [60]. The PSF of a fluorescent emitter in a biological sample can be well approximated by a Gaussian intensity distribution [61, 62]. From the fits, the center of the Gaussian function can be determined with an accuracy of a few nm [63] or even below [64]. The localization precision of the emitter depends mainly on the number of photons that can be collected during image acquisition [62, 65, 66] and is approximately given by:

$$\Delta x = \frac{s}{\sqrt{N}}$$

with Δx being the localization error, s the standard deviation of the PSF and N the number of photons collected.

Hence, with this approach, the resolution can potentially be arbitrarily low if the number of photons collected from an emitter is high enough. In addition, the fit also yields the brightness of the molecules, which can be used to determine the oligomeric size of the fluorescent aggregate, as we will show later in this section.

Taken together, the emergence of single molecule microscopy has equipped researchers with a versatile toolbox to overcome the problems of bulk-based methods described above. In this section, we will guide the reader through some strategies to determine the oligomeric state of a protein using single molecule fluorescence microscopy. We will highlight the basic principles, advantages and problems of the respective method.

8.2.3.2 Single Molecule FRET (smFRET)

Principle smFRET has first been shown by Ha and colleagues 20 years ago [67] and is nowadays commonly used to identify conformational changes of biomolecules by attaching the dye pair to different sites of the target molecule. Additionally, the method allows for evaluating molecular oligomerization. The theoretical background for smFRET is the same as for bulk FRET (Fig. 8.2a): a non-radiative energy transfer from a donor molecule to a dye molecule indicates close interaction of the two. However, special precautions are necessary to extend FRET to the single molecule level: the used dye pairs have to be particularly bright and photostable to enable a good signal-to-noise ratio. Hence, instead of using fluorescent proteins, usually organic dyes are used.

Pros Oligomerization and dissociation/association kinetics can be directly visualized. Extension of FRET to the single molecule level thereby also enables the identification and quantification of minor subpopulations in a heterogeneous sample.

Cons The method faces similar problems as bulk FRET: if the dye molecules are much further apart than the Förster radius, the method is not applicable. A missing

smFRET signal can therefore not be interpreted as a missing interaction of the respective biomolecules. In the case of homo-dimerization at least half of the signals are lost because of two proteins carrying the same type of dye molecule. Although smFRET gives reliable qualitative information on oligomerization, determination of the exact complex size is difficult and the outcome depends on the model that is used to interpret the data.

8.2.3.3 Stepwise Photobleaching

Principle The digital decrease of the fluorescence intensity of a protein oligomer is used for determining its stoichiometry [50]. During imaging of a fluorescently labelled sample, the fluorophores get irreversibly photobleached after a number of excitation-emission cycles. This behavior can be used to determine the number of fluorophores present in a diffraction limited spot, e.g. a protein oligomer. Due to its quantal nature photobleaching of a fluorophore occurs in a stepwise manner; each bleaching event of a single dye molecule can be identified by a distinct step in the fluorescence intensity time trace of a complex (Fig. 8.3a). Given that each protomer in a complex carries exactly one dye molecule (e.g. fusion constructs of the protein of interest with green fluorescent protein (GFP)), the number of subunits initially present in the complex is directly encoded by the number of bleaching steps. The method is usually combined with total internal fluorescence reflection (TIRF) microscopy in order to reduce intracellular background.

Pros Stepwise photobleaching represents a powerful and accurate method with an easy and direct readout to determine oligomerization of membrane bound proteins. Since the method works on a single molecule level, rather sensitive and elaborate cameras are used. The analysis of the data, however, is very straightforward, and does not depend on assumed models.

Cons Only immobile complexes can be analyzed. Movement of the fluorescence signal during image acquisition can result in significant brightness fluctuations that might blur the bleaching steps. Mainly, these fluctuations are caused by diffusion along the z-axis in the TIRF field due to partial cell detachment from the glass slide or formation of invaginations and ruffles. Two general strategies are common to prevent this effect: either fixed samples are used, or the protein of interest is expressed in *Xenopus laevis* oocytes. Fixation, however, kills the cell, impeding measurements in the native cellular environment. When expressed in *Xenopus laevis* oocytes, most proteins are immobile after insertion into the plasma membrane, a state that is usually not very abundant for membrane associated proteins [68]. Both strategies thereby prevent dynamic interaction of biomolecules.

Moreover, the requirement of well distinguishable PSFs results in an upper limit of the expression level and high densities of protein at the plasma membrane are thereby not accessible.

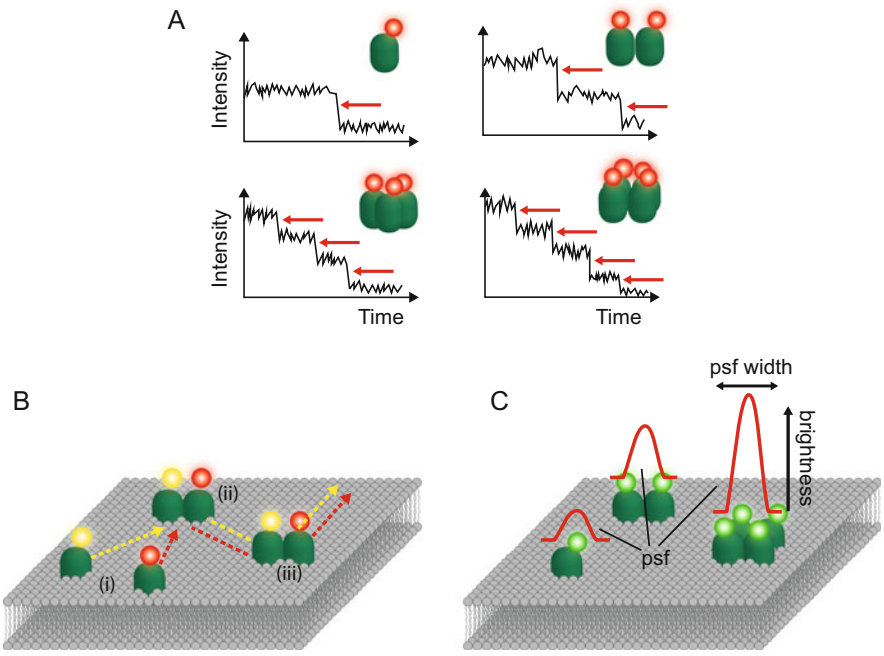

Fig. 8.3 Single molecule methods. (**a**) *Stepwise photobleaching*. *From left top to right bottom*: monomeric, dimeric, trimeric and tetrameric fluorescent intensity traces. Each stepwise decrease in the fluorescence intensity vs. time plot represents one photobleached fluorophore. (**b**) *Single molecule co-tracking*. The proteins of interest are labelled with spectrally different fluorophores and their diffusional path in the membrane is tracked using localization algorithms. Association (i) (or dissociation) and co-diffusion (ii and iii) of molecules can be directly visualized. (**c**) *Single molecule brightness analysis*. Fluorescent molecules are imaged according to their PSF. Larger protein complexes do not yield a broader PSF than monomeric proteins, but its amplitude is larger. Hence, evaluation of the brightness of diffraction limited spots enables deciphering the underlying oligomeric state

8.2.3.4 Single Molecule Co-tracking

Principle Using single molecule fluorescence microscopy, the diffusional path of a protein can be tracked with a localization precision down to the nanometer scale. In each frame recorded, the position of the fluorophores is determined using a localization algorithm. Subsequently, the positions of these localizations are linked between the frames using a tracking algorithm [69–71] (Fig. 8.3b). If two molecules of interest are labelled with spectrally different fluorophores, this strategy can be used to directly visualize co-diffusion and potentially also association and dissociation of the two molecules [72, 73]. The two molecules are characterized as interacting if they move together for several consecutive frames.

Pros The method directly shows interaction of proteins. Besides oligomerization itself, the method can reveal dimerization kinetics if the interaction is shorter than

the time before the complex diffuses out of the field of view or before the fluorophores photobleach.

Cons It is sometimes difficult to distinguish between real oligomers and proteins present in plasma membrane-proximal vesicles. Furthermore, the surface density of the respective protein has to be low enough so that their PSFs do not overlap. Many researchers have overcome this problem by stochastic photobleaching of the cell [74], using sub-saturation labelling conditions [75], or photoactivate only a subfraction of the fluorescent proteins [76]. In all of these strategies, however, the probability of observing interactions gets extremely low [77]. Finally, care has to be taken to rule out stochastic co-diffusion of non-interacting molecules [72].

8.2.3.5 Single Molecule Brightness Analysis

Principle The analytical strategy of fitting a Gaussian intensity distribution to the recorded PSF offers not only information on the position, but also on the brightness of a signal. This information can be used for single molecule brightness analysis (Fig. 8.3c): by counting the number of dyes per fluorescently labelled complex, its oligomeric state can be determined [40, 49, 78]. The brightness distribution of a given fluorophore is characterized by its probability density function (pdf) ρ(B). For larger complexes the resulting pdf exhibits a rather long tail towards higher photon counts in comparison to a monomeric fluorophore. $\rho_1(B)dB$ describes the probability that the number of photons detected from a single dye molecule lies in the interval $(B, B + dB)$. The brightness distribution $\rho_N(B)$ resulting from N colocalized dye molecules is then described by a series of convolution integrals:

$$\rho_N(B) = \int \rho_1\left(B'\right)\rho_{N-1}\left(B - B'\right)dB' \tag{8.1}$$

Hence, a mixed population of monomers, dimers, trimers etc. yields a brightness distribution that is based on a linear combination of the individual distributions:

$$\rho(B) = \sum_{N=1}^{N_{max}} \alpha_N \rho_N(B) \tag{8.2}$$

The weights α_N yield the fractions of the different complex sizes, with

$$\sum_{N=1}^{N_{max}} \alpha_N = 1$$

If the brightness distribution of a single dye molecule is known, the weights α_N of the different oligomers can be calculated by fitting the recorded oligomeric brightness distribution with Eq. 8.2.

Pros Single molecule brightness analysis can be used in combination with well-established fluorescent proteins, e.g. GFP. In contrast to single molecule co-tracking or smFRET, virtually all protein aggregates are encoded by their increased brightness since only one fluorescent dye species is used for labelling. Furthermore, the method is applicable to both immobile and mobile complexes in the native cell membrane. Single molecule brightness analysis can therefore be combined with tracking approaches to gain information on the diffusional behavior of different oligomeric sizes.

Cons There is a limit to the oligomeric size that is accessible with single molecule brightness analysis; the brightness distributions broaden with increasing number of colocalized fluorophores, so the distributions will overlap to an extent that makes an accurate fit difficult. Hence, the obtained distributions may well indicate the presence of large oligomeric structures, but the discrimination between oligomers differing by only one subunit may be no longer possible.

8.3 Thinning Out Clusters While Conserving Stoichiometry of Labelling (TOCCSL)

As described above, single molecule fluorescence microscopy provides researchers with several approaches to decipher the oligomeric state of membrane associated proteins. Despite these technical advances, however, there is a surprisingly low number of reports on direct observations of two interacting biomolecules (e.g. [73, 79, 80]). A general difficulty of current approaches is that they are limited by the density of the fluorescent probes in the sample; if two emitters are closer than the diffraction limit, their PSFs will overlap and their centroids cannot be localized accurately. Hence, an experimental approach is needed to virtually dilute the fluorescent signals while leaving their labelling stoichiometry untouched. In this chapter we demonstrate how to efficiently tackle this issue by using a photobleaching approach termed thinning out clusters while conserving stoichiometry of labelling (TOCCSL).

Considering the normal situation in the cell membrane regarding protein density, it becomes obvious that fluorescence microscopy generally does not allow for imaging individual molecules as separated spots. In a single square micrometer ten thousands of protein molecules are present. Using specific labelling approaches, one can single out individual protein species, but nevertheless they most likely will be expressed at densities that render direct single molecule imaging impossible. This is especially the case when the protein of interest is heterologously overexpressed. A potential strategy might be extreme underlabelling. However, this is not advisable when studying protein oligomerization, since the information on the oligomeric state gets lost. Let us assume as an example a homotretramer, that is fluorescently labeled on every subunit with a labelling probability $p = 0.01$. Assuming binomial labelling conditions, the amount of visible protein oligomers

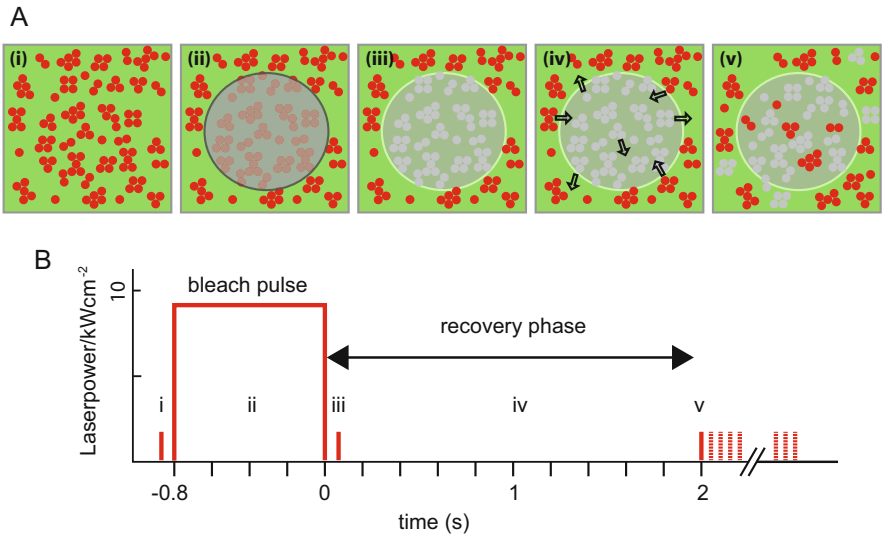

Fig. 8.4 TOCCSL. (**a**) Using a field stop in the laser beam pathway, a small area of the cell membrane (i) is irreversibly photobleached (ii, iii). During a recovery phase (iv) single, well distinguishable fluorescently labelled complexes diffuse back into the bleached area and can be monitored (iv). (**b**) Timing of laser pulses used for imaging and photobleaching

would be reduced to 4%, which is likely sufficient to resolve single copies. However, at the same time only one in four million spots would contain the full load of four active fluorophores.

In order to tackle this problem, we have developed the TOCCSL method to virtually dilute the protein density in a restricted region of the cell membrane while leaving the labelling stoichiometry intact [81]. TOCCSL is based on fluorescence recovery after photobleaching (FRAP), but extends the principle to the level of single molecule fluorescence microscopy. The method is shown in Fig. 8.4 and can be divided into two main parts:

1. *Creating an analysis region:* Fig. 8.4a (i) shows the initial situation at the plasma membrane: fluorescently labelled protein complexes are present at high surface density, so that single molecule signals cannot be separated. After recording a pre-bleach image for control, a distinct small area of the cell membrane is irreversibly photobleached (ii). The photobleached region is confined by imaging an aperture onto the sample. Ideally, the protein complexes are either entirely photobleached (inside the analysis region) or remain entirely fluorescent (outside the analysis region), which can be assessed by a control image recorded right after the bleaching pulse (iii). In practice, this will not be perfectly achievable; especially, complexes that are present at the border of the analysis region will show incomplete bleaching. In addition the bleaching pulse should be as short as possible to minimize movement of proteins during the bleaching pulse.

2. *Recovery of the fluorescent signal and acquisition of the analysis image:* due to Brownian motion unbleached molecules diffuse into the previously bleached analysis region (iv). TOCCSL makes use of the very onset of the recovery process: individual molecules diffuse back into the bleached area and can now be resolved as single, clearly distinguishable fluorescent spots (v). The duration of the recovery phase used for TOCCSL should be adjusted for appropriate surface density of fluorescent spots; typically, it is in the range of 1–20 s.

The recorded image can now be used for single molecule brightness analysis to determine the stoichiometry of the recovering complexes. For membrane-bound proteins, it is advantageous to combine TOCCSL with total internal reflection (TIR) microscopy to restrict the excitation to regions close to the glass coverslip. This (i) improves the signal-to-noise ratio by reducing fluorescent background from the cytosol and (ii) restricts the analysis to proteins that are integrated in the plasma membrane. The recovery pattern of the fluorescent signals indicates if signals originate from plasma membrane bound proteins; for membrane constituents, the surface density of the recovering signals decreases from the edges of the analysis region towards its center. In contrast, signals recovering from the cytosol would homogeneously cover the whole photobleached area. For an extensive manual on the application of TOCCSL, we refer the reader to [77].

Besides for determining the oligomeric state of protein aggregates, the recorded data can further be used for single molecule tracking if several images are recorded after the recovery phase. TOCCSL can also be extended to multiple colors using different fluorophores and hence might be used in combination with single molecule co-tracking. E.g. we have used this approach to detect rare interactions of fluorescent Cholera-Toxin B (CTX-B-Alexa647) to its ligand Bodipy-GM1 in a supported lipid bilayer [72].

A drawback of the method, however, is that immobile complexes are not accessible with TOCCSL. It has been shown that the majority of membrane proteins and protein oligomers are mobile [82–84], but nevertheless, the mobility of the protein of interest should always be evaluated first to determine the compatibility with TOCCSL. In analogy, also different mobility of the respective oligomeric sizes would bias the observed oligomeric distribution in a TOCCSL experiment; e.g. for EGFRs it is known that upon activation and dimerization the diffusion coefficient significantly decreases [85]. Supposedly, this will give a bias towards a monomeric conformation in the analysis region that does not reflect the situation in the remaining part of the plasma membrane. In addition, very short-lived interactions of molecules may be missed with the method; if the interaction time of two molecules is shorter than the duration of the recovery phase, complexes will dissociate on their way into the region of interest and will be ascribed to a smaller oligomeric conformation.

8.3.1 Examples

In the following section, we give the reader a few examples, in which we have used TOCCSL in conjunction with single molecule brightness analysis in order to evaluate the oligomeric state of a membrane bound biomolecule.

8.3.1.1 TOCCSL: Proof of Principle

When introducing the method, we first wanted to demonstrate that TOCCSL indeed correctly assesses the labelling stoichiometry [81]. We used an artificial bilayer consisting of 1-palmitoyl-2-oleoyl-sn-glycero-3-phosphocholin (POPC) and 1,2-dipalmitoyl-snglycero-3-phosphoethanolamine-N-(2,4-dinitrophenyl) (DPPE) carrying the hapten DNP (DNP-DPPE); as a fluorescent probe we added antibodies against DNP carrying in average of 4.5 fluorescein molecules per antibody. In this experimental setting, we could adjust the density of the fluorescent label by titrating DNP-DPPE. At low concentrations of DNP-DPPE (0.15 molecules per μm^2) individual antibody molecules were clearly distinguishable and the recorded images could directly be used for brightness analysis (Fig. 8.5). The resulting pdf therefore represents a fluorescent fingerprint of a dye-cluster diffusing in the membrane. Next, the DNP-DPPE density was increased to ~15 molecules per μm^2. At this density the fluorescent signals significantly overlapped, precluding direct analysis. In this case we used the TOCCSL method and determined again the brightness distributions of the observed fluorescence spots. With TOCCSL, the obtained pdf was virtually identical to the pdf obtained at low DNP-DPPE density, demonstrating that TOCCSL reported the correct brightness distribution. By using the non-linear least squares fitting described in the subsection "Single molecule brightness analysis" we also evaluated the average number of dye molecules attached to the antibody. We found an average of $N = 3.5$ fluorescein molecules per antibody, which is in good agreement with the results from the spectroscopic evaluation.

8.3.1.2 Imaging of Mobile Long-Lived Nanoplatforms in the Live Cell Plasma Membrane

There has been a lively discussion in the past two decades whether proteins and lipids assemble into stable aggregates that travel together in the plasma membrane. The idea is known as the membrane raft or lipid raft hypothesis [86] and was mainly suggested based on the observation of detergent insoluble membrane fractions in biochemical experiments. Rafts are described to recruit proteins such as glycosylphosphatidylinositol (GPI)-anchored proteins. Using TOCCSL, we have evaluated whether and to what extend GPI-anchored mGFP molecules form

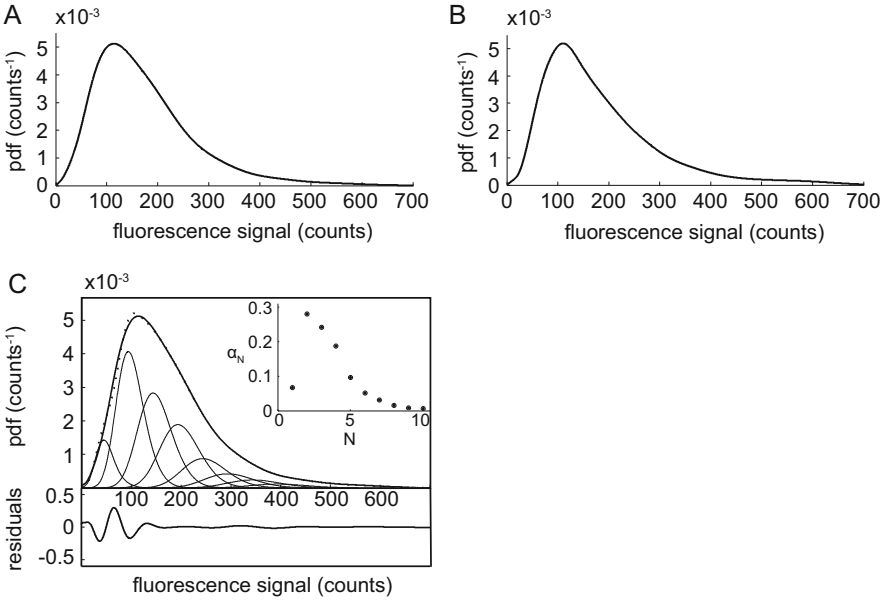

Fig. 8.5 Proof-of-principle experiment on a supported bilayer. To mimic stable fluorescent protein clusters, anti-DNP antibodies labeled with multiple fluorescein molecules were added to a supported lipid bilayer containing different concentrations of DNP-labeled lipid. (**a**) shows the brightness distribution plotted as a probability density function (pdf) at low surface densities (~0.15 molecules per μm^2). In this case, well-separated fluorescent spots could directly be imaged. (**b**) After significantly increasing the surface densities (~15 molecules per μm^2) we applied the TOCCSL protocol. Virtually no difference was found between the two distributions, showing that TOCCSL indeed conserves the stoichiometry of the fluorescent labelling. (**c**) A fit of the pdf obtained from (**b**) (*full line*) using a linear combination of the brightness distributions of fluorescein monomers, dimers, trimers, etc. (*dotted lines*) yielded the distribution of fluorescein load on the antibodies. The *inset* shows the obtained weights representing the fraction of antibodies carrying 1, 2, . . . N fluorescein molecules. Figure adapted with permission from [81]. Copyright 2005, American Institute of Physics

co-diffusing clusters in the live cell plasma membrane [87] (Fig. 8.6). We found that in the native membrane environment GPI-anchored mGFP diffuses both as monomers (~68%) and dimers (~32%). No higher structures were found in this study. In addition, the formation of dimers was shown to strongly depend on the presence of cholesterol. Upon depletion of cholesterol the vast majority of the proteins were found to be monomeric (~98%). This effect was subsequently shown to be reversible by addition of cholesterol. Furthermore, a correlation of monomer/dimer ratio with the surface density was observed: increasing expression levels of mGFP-GPI coincided with increasing fractions of dimeric entities.

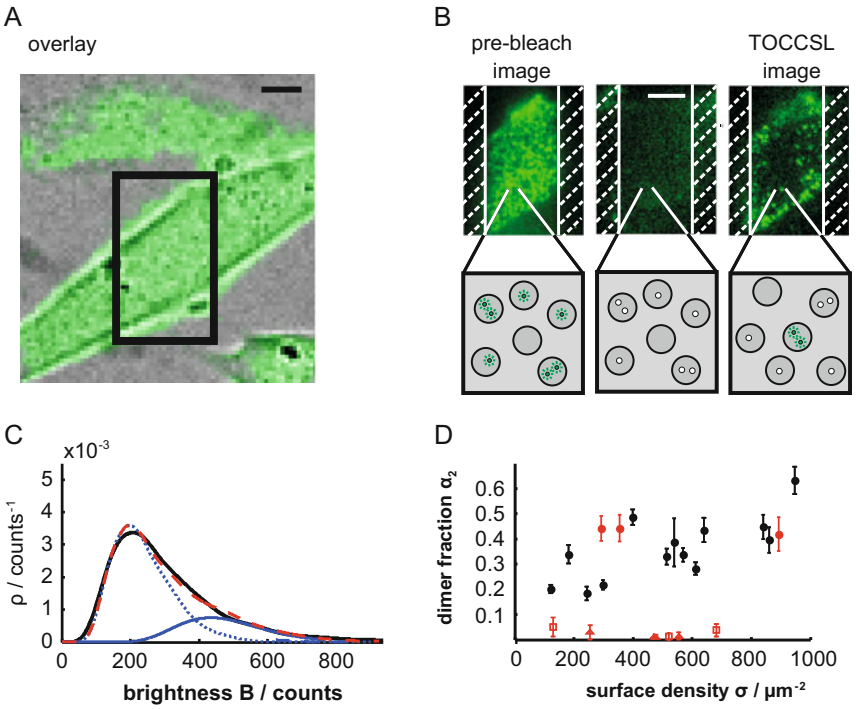

Fig. 8.6 Imaging of long lived mobile nanoplatforms. (**a**) Overlay of a white light image and a fluorescence image of a cell expressing mGFP-GPI. The analysis region for the TOCCSL experiment is indicated by the *black square*. (**b**) *From left to right*: pre-bleach image, post-bleach image and the TOCCSL image used for brightness analysis of the recovered proteins. (**c**) shows the brightness distribution of single mGFP-GPI spots of the TOCCSL image plotted as a pdf (*black full line*). The data were fitted with a linear combination of monomeric (*dotted blue line*) and dimeric (*blue solid line*) contributions, yielding a distribution of ~68% monomers and ~32% dimers. (**d**) A strong dependence of the dimer fraction on the surface density of mGFP-GPI was observed (*black dots*). Furthermore, cholesterol depletion led to monomerization of the complexes (*red squares and red triangles*). This effect could be reversed by the replenishment of cholesterol (*black triangles*). Figure adapted from [87]

8.3.1.3 Resting State Orai1 Diffuses as Homotetramer in the Plasma Membrane of Live Mammalian Cells

Store-operated calcium entry (SOCE) is a pivotal process for many cellular signaling events involved in proliferation, apoptosis, secretion, and gene expression. In conjunction with STIM1, Orai1 is the key protein in SOCE, as it represents the essential pore-forming unit of SOCE channels. The calcium concentration in the endoplasmic reticulum (ER) is sensed by STIM1 and the information is transmitted to Orai1. Although it was shown before that Orai1 forms tetramers in the functioning channel [88], it was not clear if the channels only form after signaling via STIM1 or if the channels are already pre-assembled in the inactive state. We stably transfected a T24 cell line with Orai1-mGFP and determined the oligomeric state of

Orai1 with single molecule brightness analysis [49]. For our experiments high expression levels of Orai1-mGFP in the cells was crucial to avoid underestimation of the stoichiometry, since endogenous subunits were still present in the cell and thereby mix with Orai1-mGFP. Using our TOCCSL method, we recorded brightness distributions of single recovering signals, which could be fitted with a linear combination of GFP oligomers. The fits clearly indicated that Orai1 moves as tetramers in the resting state of HEK cells.

8.3.1.4 The Serotonin Transporter (SERT) Forms Monomers and Oligomers in the Plasma Membrane

The serotonin transporter (SERT) is an integral membrane protein belonging to the closely related family of neurotransmitter: sodium symporters (NSS). SERT is endogenously expressed in serotonergic neurons of the raphe nuclei of the human brain. Here it is responsible for the reuptake of the monoamine neurotransmitter serotonin from the synaptic cleft and it thereby terminates the chemical signaling process between two neighboring neurons. It was known from biochemical as well as FRET experiments that SERT forms at least dimers in the plasma membrane of living cells [22, 23, 28, 29]. The actual size, stability and composition, however, were not known. Although the functional unit in terms of serotonin uptake activity seemed to be a monomer for NSSs [20], there were several indications that oligomerization plays a role in membrane trafficking [20] and reversal transport of serotonin after amphetamine application [33]. We used TOCCSL and single molecule brightness analysis to evaluate the stoichiometry of SERT in the plasma membrane of living cells [30]. In this study, we found that SERT indeed forms higher oligomeric structures in the plasma membrane. The data shows a variety of different configurations ranging from monomers to at least pentamers that coexist in the same cell, in agreement with a linear aggregation model. Interestingly, we found that the oligomeric distribution is independent from SERT density at the plasma membrane (Fig. 8.7).

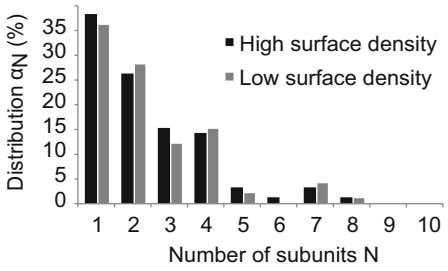

Fig. 8.7 Oligomeric state of SERT at different surface densities. Comparison of different expression levels: high (*black*) and low surface density (*grey*), shows no difference in SERT oligomerization. The mean densities of SERT were ~29 mGFP-SERT/μm^2 (low surface density) and ~840 mGFP-SERT/μm^2 (high surface density). Figure from [30]

8.4 Using TOCCSL to Evaluate Interaction Kinetics

In addition to oligomeric sizes of a specific protein, also interaction kinetics are of importance to describe protein aggregates. It may well be that oligomers only form after activation or inactivation of the protein, but also constitutive oligomers could be present. Hence, knowing the interaction kinetics between protomers may yield indications for the function of oligomerization. In this chapter, we would like to demonstrate how TOCCSL could be used to evaluate both short-term (in the range of the recovery time) as well as long-term (on a minutes time scale) interactions of subunits in a complex.

8.4.1 Short-Term Interactions

After complete photobleaching of the analysis region in the first phase of a TOCCSL experiment, fluorescently labelled protein oligomers diffuse as clusters into the bleached region. On their way, they will collide with bleached protein clusters and (if the clusters are not stable) likely exchange subunits, so that the two populations will mix in the analysis region. This will reduce the brightness of the individual clusters, since oligomers now contain both fluorescent and bleached subunits. If the subunit exchange takes place on a short time-scale (in the range of the recovery time necessary for the experiment), the recovery time can be deliberately varied to obtain information on the stability of the oligomer: extension of the recovery time would in this case increase the fraction of lower oligomeric states, whereas reduction of the recovery time would increase the fraction of higher oligomers.

Another possibility to directly show rearrangement of protomers is the application of 2-color-TOCCSL and single molecule co-tracking; during recovery, dissociation processes may be directly observable if they take place on time scales shorter than the time necessary for full fluorescence recovery of the analysis region. Analysis of the association of proteins, however, is not straightforward, since the vast majority of putative interaction partners in the analysis region are photobleached and hence not visible.

8.4.2 Long-Term Interactions

If the interaction kinetics within an oligomer is rather long, it will be highly unlikely to observe a dissociation process during diffusion into the bleached analysis region. In order to evaluate the stability of protein oligomers that exhibit rather stable interactions between the subunits, we recently designed a TOCCSL protocol based on repetitive TOCCSL runs on the same cell [30]. The principle of the method is depicted in Fig. 8.8: One TOCCSL run per minute is performed over e.g. 10 min on

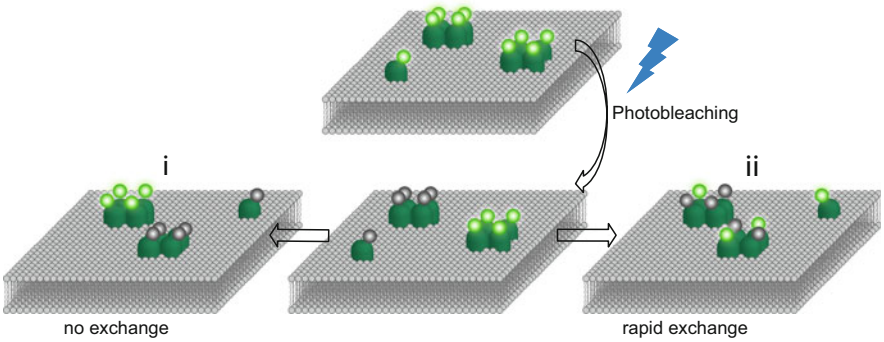

Fig. 8.8 Possible behavior of proteins after stoichiometric photobleaching. Transient interaction of subunits in a complex would lead to rearrangement and hence would result in a mixed population of bleached (*grey*) and unbleached (*green*) molecules. In this case, the number of unbleached dyes per oligomer would be reduced (*right*). In contrast, stable interaction produces either completely bleached or unbleached oligomers, without effecting the distribution of oligomeric states (*left*)

the same cell. After each TOCCSL run, the oligomeric distribution is monitored on the recovery image using single molecule brightness analysis. Pooling the data obtained from multiple cells then provides brightness distributions as a function of time. Two scenarios can be discriminated: If the interaction of subunits within a given complex was stable, repetitive TOCCSL runs would reduce the total number of observed fluorescent spots on the plasma membrane, but would not alter the brightness distribution (Fig. 8.8, scenario i). In contrast, if the exchange rate of subunits between oligomers was high, bleached subunits from the previous TOCCSL experiments would rearrange with unbleached subunits. Over time, this mixing would increase the number of complexes comprised of both dark and fluorescent subunits, thereby shifting the observable oligomeric distribution towards smaller structures (Fig. 8.8, scenario ii).

8.4.2.1 An Example: SERT Forms Stable Oligomers at Plasma Membrane

We applied the method of repetitive TOCCSL to evaluate the oligomer stability of the human serotonin transporter (SERT) at the plasma membrane of chinese hamster ovary (CHO) cells [30]. In order to be able to detect mixing of subunits, bleaching of a sufficient fraction of complexes has to be ensured. To evaluate this, we determined the overall fluorescence intensity of the plasma membrane over time, showing that ~50% of the complexes were bleached at the end of the experiment. We observed no change in the oligomeric state at the plasma membrane with increasing number of TOCCSL runs (Fig. 8.9). This indicates stable association of SERT oligomers at the plasma membrane. We concluded that SERT oligomers are pre-formed at an unknown organelle in the cell before they reach the plasma membrane.

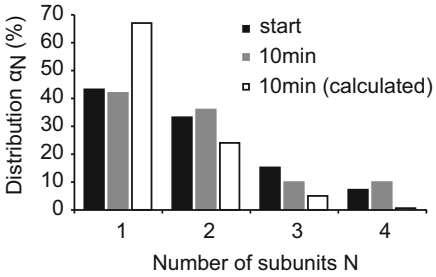

Fig. 8.9 Stability of SERT complexes at the plasma membrane. Using the repetitive TOCCSL strategy, we have evaluated the oligomeric distribution of SERT at the plasma membrane. Oligomeric distributions are shown at the beginning of the experiment (*black bars*) and after 10 min (*grey*). The white bars show the calculated binomial distribution if the interaction kinetics of the subunits would be fast compared with the time of our experiment. No rearrangement of subunits was observed, showing stable interaction of the subunits within an oligomer. Figure from [30]

Acknowledgement This work was supported by the Austrian Science Fund/FWF (F3519-B20).

References

1. Levy ED, Pereira-Leal JB, Chothia C, Teichmann SA. 3D complex: a structural classification of protein complexes. PLoS Comput Biol. 2006;2:1395–406.
2. Singer SJ, Nicolson GL. The fluid mosaic model of the structure of cell membranes. Science. 1972;175:720–31.
3. Goodsell DS, Olson AJ. Structural symmetry and protein function. Annu Rev Biophys Biomol Struct. 2000;29:105–53.
4. Tusnady GE, Dosztanyi Z, Simon I. PDB_TM: selection and membrane localization of transmembrane proteins in the protein data bank. Nucleic Acids Res. 2005;33:D275–8.
5. Hong M. Oligomeric structure, dynamics, and orientation of membrane proteins from solid-state NMR. Structure. 2006;14:1731–40.
6. Hashimoto K, Panchenko AR. Mechanisms of protein oligomerization, the critical role of insertions and deletions in maintaining different oligomeric states. Proc Natl Acad Sci U S A. 2010;107:20352–7.
7. Naveed H, Jackups R Jr, Liang J. Predicting weakly stable regions, oligomerization state, and protein-protein interfaces in transmembrane domains of outer membrane proteins. Proc Natl Acad Sci U S A. 2009;106:12735–40.
8. Joerger AC, Rajagopalan S, Natan E, Veprintsev DB, Robinson CV, Fersht AR. Structural evolution of p53, p63, and p73: implication for heterotetramer formation. Proc Natl Acad Sci U S A. 2009;106:17705–10.
9. Akiva E, Itzhaki Z, Margalit H. Built-in loops allow versatility in domain-domain interactions: lessons from self-interacting domains. Proc Natl Acad Sci U S A. 2008;105:13292–7.
10. Palsdottir H, Hunte C. Lipids in membrane protein structures. Biochim Biophys Acta. 2004;1666:2–18.
11. Barrera NP, Zhou M, Robinson CV. The role of lipids in defining membrane protein interactions: insights from mass spectrometry. Trends Cell Biol. 2013;23:1–8.
12. de Meyer FJ, Venturoli M, Smit B. Molecular simulations of lipid-mediated protein-protein interactions. Biophys J. 2008;95:1851–65.

13. Betaneli V, Petrov EP, Schwille P. The role of lipids in VDAC oligomerization. Biophys J. 2012;102:523–31.
14. Ali MH, Imperiali B. Protein oligomerization: how and why. Bioorg Med Chem. 2005;13:5013–20.
15. Miller S, Lesk AM, Janin J, Chothia C. The accessible surface-area and stability of oligomeric proteins. Nature. 1987;328:834–6.
16. Park PS, Filipek S, Wells JW, Palczewski K. Oligomerization of G protein-coupled receptors: past, present, and future. Biochemistry. 2004;43:15643–56.
17. George SR, O'Dowd BF, Lee SP. G-protein-coupled receptor oligomerization and its potential for drug discovery. Nat Rev Drug Discov. 2002;1:808–20.
18. Gomes I, Jordan BA, Gupta A, Rios C, Trapaidze N, Devi LA. G protein coupled receptor dimerization: implications in modulating receptor function. J Mol Med (Berl). 2001;79:226–42.
19. Parnot C, Kobilka B. Toward understanding GPCR dimers. Nat Struct Mol Biol. 2004;11:691–2.
20. Scholze P, Freissmuth M, Sitte HH. Mutations within an intramembrane leucine heptad repeat disrupt oligomer formation of the rat GABA transporter 1. J Biol Chem. 2002;277:43682–90.
21. Farhan H, Freissmuth M, Sitte HH. Oligomerization of neurotransmitter transporters – a ticket from the endoplasmic reticulum to the plasma membrane. Handb Exp Pharmacol. 2006;175:233–49.
22. Kilic F, Rudnick G. Oligomerization of serotonin transporter and its functional consequences. Proc Natl Acad Sci U S A. 2000;97:3106–11.
23. Jess U, Betz H, Schloss P. The membrane-bound rat serotonin transporter, SERT1, is an oligomeric protein. FEBS Lett. 1996;394:44–6.
24. Hastrup H, Karlin A, Javitch JA. Symmetrical dimer of the human dopamine transporter revealed by cross-linking Cys-306 at the extracellular end of the sixth transmembrane segment. Proc Natl Acad Sci U S A. 2001;98:10055–60.
25. Förster T. Zwischenmolekulare Energiewanderung und Fluoreszenz. Ann Phys. 1948;437:55–75.
26. Sorkina T, Doolen S, Galperin E, Zahniser NR, Sorkin A. Oligomerization of dopamine transporters visualized in living cells by fluorescence resonance energy transfer microscopy. J Biol Chem. 2003;278:28274–83.
27. Schmid JA, Scholze P, Kudlacek O, Freissmuth M, Singer EA, Sitte HH. Oligomerization of the human serotonin transporter and of the rat GABA transporter 1 visualized by fluorescence resonance energy transfer microscopy in living cells. J Biol Chem. 2001;276:3805–10.
28. Fjorback AW, Pla P, Muller HK, Wiborg O, Saudou F, Nyengaard JR. Serotonin transporter oligomerization documented in RN46A cells and neurons by sensitized acceptor emission FRET and fluorescence lifetime imaging microscopy. Biochem Biophys Res Commun. 2009;380:724–8.
29. Just H, Sitte HH, Schmid JA, Freissmuth M, Kudlacek O. Identification of an additional interaction domain in transmembrane domains 11 and 12 that supports oligomer formation in the human serotonin transporter. J Biol Chem. 2004;279:6650–7.
30. Anderluh A, Klotzsch E, Reismann AWAF, Brameshuber M, Kudlacek O, Newman AH, Sitte HH, Schütz GJ. Single molecule analysis reveals coexistence of stable serotonin transporter monomers and oligomers in the live cell plasma membrane. J Biol Chem. 2014;289:4387–94.
31. Farhan H, Reiterer V, Korkhov VM, Schmid JA, Freissmuth M, Sitte HH. Concentrative export from the endoplasmic reticulum of the gamma-aminobutyric acid transporter 1 requires binding to SEC24D. J Biol Chem. 2007;282:7679–89.
32. Sucic S, Koban F, El-Kasaby A, Kudlacek O, Stockner T, Sitte HH, Freissmuth M. Switching the clientele: a lysine residing in the C terminus of the serotonin transporter specifies its preference for the coat protein complex II component SEC24C. J Biol Chem. 2013;288:5330–41.

33. Sitte HH, Freissmuth M. The reverse operation of Na(+)/Cl(−)-coupled neurotransmitter transporters—why amphetamines take two to tango. J Neurochem. 2010;112:340–55.
34. Sitte HH, Huck S, Reither H, Boehm S, Singer EA, Pifl C. Carrier-mediated release, transport rates, and charge transfer induced by amphetamine, tyramine, and dopamine in mammalian cells transfected with the human dopamine transporter. J Neurochem. 1998;71:1289–97.
35. Khoshbouei H, Wang H, Lechleiter JD, Javitch JA, Galli A. Amphetamine-induced dopamine efflux. A voltage-sensitive and intracellular Na+-dependent mechanism. J Biol Chem. 2003;278:12070–7.
36. Seidel S, Singer EA, Just H, Farhan H, Scholze P, Kudlacek O, Holy M, Koppatz K, Krivanek P, Freissmuth M, Sitte HH. Amphetamines take two to tango: an oligomer-based counter-transport model of neurotransmitter transport explores the amphetamine action. Mol Pharmacol. 2005;67:140–51.
37. Sitte HH, Freissmuth M. Amphetamines, new psychoactive drugs and the monoamine transporter cycle. Trends Pharmacol Sci. 2015;36:41–50.
38. Ferre S, Casado V, Devi LA, Filizola M, Jockers R, Lohse MJ, Milligan G, Pin JP, Guitart X. G protein-coupled receptor oligomerization revisited: functional and pharmacological perspectives. Pharmacol Rev. 2014;66:413–34.
39. Kasai RS, Suzuki KG, Prossnitz ER, Koyama-Honda I, Nakada C, Fujiwara TK, Kusumi A. Full characterization of GPCR monomer-dimer dynamic equilibrium by single molecule imaging. J Cell Biol. 2011;192:463–80.
40. Calebiro D, Rieken F, Wagner J, Sungkaworn T, Zabel U, Borzi A, Cocucci E, Zurn A, Lohse MJ. Single-molecule analysis of fluorescently labeled G-protein-coupled receptors reveals complexes with distinct dynamics and organization. Proc Natl Acad Sci U S A. 2013;110:743–8.
41. Teichmann A, Gibert A, Lampe A, Grzesik P, Rutz C, Furkert J, Schmoranzer J, Krause G, Wiesner B, Schulein R. The specific monomer/dimer equilibrium of the corticotropin-releasing factor receptor type 1 is established in the endoplasmic reticulum. J Biol Chem. 2014;289:24250–62.
42. Kluger R, Alagic A. Chemical cross-linking and protein-protein interactions-a review with illustrative protocols. Bioorg Chem. 2004;32:451–72.
43. Peters K, Richards FM. Chemical cross-linking: reagents and problems in studies of membrane structure. Annu Rev Biochem. 1977;46:523–51.
44. Stauffer DA, Karlin A. Electrostatic potential of the acetylcholine binding sites in the nicotinic receptor probed by reactions of binding-site cysteines with charged methanethiosulfonates. Biochemistry. 1994;33:6840–9.
45. Coleman JA, Green EM, Gouaux E. X-ray structures and mechanism of the human serotonin transporter. Nature. 2016;532:334–9.
46. Penmatsa A, Wang KH, Gouaux E. X-ray structure of dopamine transporter elucidates antidepressant mechanism. Nature. 2013;503:85–90.
47. Nogi T, Fathir I, Kobayashi M, Nozawa T, Miki K. Crystal structures of photosynthetic reaction center and high-potential iron-sulfur protein from Thermochromatium tepidum: thermostability and electron transfer. Proc Natl Acad Sci U S A. 2000;97:13561–6.
48. Lee AG. Lipid–protein interactions in biological membranes: a structural perspective. Biochim Biophys Acta Biomembr. 2003;1612:1–40.
49. Madl J, Weghuber J, Fritsch R, Derler I, Fahrner M, Frischauf I, Lackner B, Romanin C, Schutz GJ. Resting state Orai1 diffuses as homotetramer in the plasma membrane of live mammalian cells. J Biol Chem. 2010;285:41135–42.
50. Ulbrich MH, Isacoff EY. Subunit counting in membrane-bound proteins. Nat Methods. 2007;4:319–21.
51. Comps-Agrar L, Maurel D, Rondard P, Pin JP, Trinquet E, Prezeau L. Cell-surface protein-protein interaction analysis with time-resolved FRET and snap-tag technologies: application to G protein-coupled receptor oligomerization. Methods Mol Biol. 2011;756:201–14.

52. Hoppe A, Christensen K, Swanson JA. Fluorescence resonance energy transfer-based stoichiometry in living cells. Biophys J. 2002;83:3652–64.
53. Bacia K, Kim SA, Schwille P. Fluorescence cross-correlation spectroscopy in living cells. Nat Methods. 2006;3:83–9.
54. Digman MA, Dalal R, Horwitz AF, Gratton E. Mapping the number of molecules and brightness in the laser scanning microscope. Biophys J. 2008;94:2320–32.
55. Chen Y, Muller JD, So PT, Gratton E. The photon counting histogram in fluorescence fluctuation spectroscopy. Biophys J. 1999;77:553–67.
56. Digman MA, Wiseman PW, Choi C, Horwitz AR, Gratton E. Stoichiometry of molecular complexes at adhesions in living cells. Proc Natl Acad Sci U S A. 2009;106:2170–5.
57. Kask P, Palo K, Ullmann D, Gall K. Fluorescence-intensity distribution analysis and its application in biomolecular detection technology. Proc Natl Acad Sci U S A. 1999;96:13756–61.
58. Plotegher N, Gratton E, Bubacco L. Number and brightness analysis of alpha-synuclein oligomerization and the associated mitochondrial morphology alterations in live cells. Biochim Biophys Acta. 2014;1840:2014–24.
59. Lakadamyali M. Super-resolution microscopy: going live and going fast. ChemPhysChem. 2014;15:630–6.
60. Patterson G, Davidson M, Manley S, Lippincott-Schwartz J. Superresolution imaging using single-molecule localization. Annu Rev Phys Chem. 2010;61:345–67.
61. Coltharp C, Xiao J. Superresolution microscopy for microbiology. Cell Microbiol. 2012;14:1808–18.
62. Thompson RE, Larson DR, Webb WW. Precise nanometer localization analysis for individual fluorescent probes. Biophys J. 2002;82:2775–83.
63. Yildiz A, Forkey JN, McKinney SA, Ha T, Goldman YE, Selvin PR. Myosin V walks hand-over-hand: single fluorophore imaging with 1.5-nm localization. Science. 2003;300:2061–5.
64. Pertsinidis A, Zhang Y, Chu S. Subnanometre single-molecule localization, registration and distance measurements. Nature. 2010;466:647–51.
65. Henriques R, Griffiths C, Hesper Rego E, Mhlanga MM. PALM and STORM: unlocking live-cell super-resolution. Biopolymers. 2011;95:322–31.
66. Huang B, Bates M, Zhuang X. Super-resolution fluorescence microscopy. Annu Rev Biochem. 2009;78:993–1016.
67. Ha T, Enderle T, Ogletree DF, Chemla DS, Selvin PR, Weiss S. Probing the interaction between two single molecules: fluorescence resonance energy transfer between a single donor and a single acceptor. Proc Natl Acad Sci U S A. 1996;93:6264–8.
68. Ulbrich M. Counting molecules: toward quantitative imaging. Berlin: Springer; 2011. p. 1–29.
69. Wieser S, Schutz GJ. Tracking single molecules in the live cell plasma membrane-do's and don't's. Methods. 2008;46:131–40.
70. Serge A, Bertaux N, Rigneault H, Marguet D. Dynamic multiple-target tracing to probe spatiotemporal cartography of cell membranes. Nat Methods. 2008;5:687–94.
71. Jaqaman K, Loerke D, Mettlen M, Kuwata H, Grinstein S, Schmid SL, Danuser G. Robust single-particle tracking in live-cell time-lapse sequences. Nat Methods. 2008;5:695–702.
72. Ruprecht V, Brameshuber M, Schutz GJ. Two-color single molecule tracking combined with photobleaching for the detection of rare molecular interactions in fluid biomembranes. Soft Matter. 2010;6:568–81.
73. Suzuki KG, Kasai RS, Hirosawa KM, Nemoto YL, Ishibashi M, Miwa Y, Fujiwara TK, Kusumi A. Transient GPI-anchored protein homodimers are units for raft organization and function. Nat Chem Biol. 2012;8:774–83.
74. Douglass AD, Vale RD. Single-molecule microscopy reveals plasma membrane microdomains created by protein-protein networks that exclude or trap signaling molecules in T cells. Cell. 2005;121:937–50.
75. Drbal K, Moertelmaier M, Holzhauser C, Muhammad A, Fuertbauer E, Howorka S, Hinterberger M, Stockinger H, Schutz GJ. Single-molecule microscopy reveals heterogeneous dynamics of lipid raft components upon TCR engagement. Int Immunol. 2007;19:675–84.

76. Manley S, Gillette JM, Patterson GH, Shroff H, Hess HF, Betzig E, Lippincott-Schwartz J. High-density mapping of single-molecule trajectories with photoactivated localization microscopy. Nat Methods. 2008;5:155–7.
77. Brameshuber M, Schutz GJ. Detection and quantification of biomolecular association in living cells using single-molecule microscopy. Methods Enzymol. 2012;505:159–86.
78. Schmidt T, Schütz GJ, Gruber HJ, Schindler H. Local stoichiometries determined by counting individual molecules. Anal Chem. 1996;68:4397–401.
79. Hern JA, Baig AH, Mashanov GI, Birdsall B, Corrie JE, Lazareno S, Molloy JE, Birdsall NJ. Formation and dissociation of M1 muscarinic receptor dimers seen by total internal reflection fluorescence imaging of single molecules. Proc Natl Acad Sci U S A. 2010;107:2693–8.
80. Koyama-Honda I, Ritchie K, Fujiwara T, Iino R, Murakoshi H, Kasai RS, Kusumi A. Fluorescence imaging for monitoring the colocalization of two single molecules in living cells. Biophys J. 2005;88:2126–36.
81. Moertelmaier M, Brameshuber M, Linimeier M, Schutz GJ, Stockinger H. Thinning out clusters while conserving stoichiometry of labeling. Appl Phys Lett. 2005;87:263903.
82. Mittelbrunn M, Yanez-Mo M, Sancho D, Ursa A, Sanchez-Madrid F. Cutting edge: dynamic redistribution of tetraspanin CD81 at the central zone of the immune synapse in both T lymphocytes and APC. J Immunol. 2002;169:6691–5.
83. Kenworthy AK, Nichols BJ, Remmert CL, Hendrix GM, Kumar M, Zimmerberg J, Lippincott-Schwartz J. Dynamics of putative raft-associated proteins at the cell surface. J Cell Biol. 2004;165:735–46.
84. Harms GS, Cognet L, Lommerse PH, Blab GA, Kahr H, Gamsjager R, Spaink HP, Soldatov NM, Romanin C, Schmidt T. Single-molecule imaging of l-type Ca(2+) channels in live cells. Biophys J. 2001;81:2639–46.
85. Low-Nam ST, Lidke KA, Cutler PJ, Roovers RC, van Bergen en Henegouwen PM, Wilson BS, Lidke DS. ErbB1 dimerization is promoted by domain co-confinement and stabilized by ligand binding. Nat Struct Mol Biol. 2011;18:1244–9.
86. Simons K, Ikonen E. Functional rafts in cell membranes. Nature. 1997;387:569–72.
87. Brameshuber M, Weghuber J, Ruprecht V, Gombos I, Horvath I, Vigh L, Eckerstorfer P, Kiss E, Stockinger H, Schutz GJ. Imaging of mobile long-lived nanoplatforms in the live cell plasma membrane. J Biol Chem. 2010;285:41765–71.
88. Mignen O, Thompson JL, Shuttleworth TJ. Orai1 subunit stoichiometry of the mammalian CRAC channel pore. J Physiol. 2008;586:419–25.

Chapter 9
Spatiotemporal Dynamics of Nicotinic Acetylcholine Receptors and Lipid Platforms

Francisco J. Barrantes

Abstract The relationships between neurotransmitter receptors and their membrane environment are complex, mutual (bidirectional) and physiologically important. Some of these relationships are established with subsets of the membrane lipid population, in the form of lipid platforms, lateral heterogeneities of the bilayer lipid having a dynamic chemical composition distinct from that of the bulk membrane. In addition to the equilibrium between the biosynthetic production, exocytic delivery and recycling of receptors on the one hand, and the endocytic internalization on the other, lateral diffusion, clustering and anchorage of receptors at the lipid platforms play key roles in determining the amount of active receptors at the synapse. Mobile receptors traffic between reservoir non-synaptic membranes and the synapse predominantly by thermally driven Brownian motion, and become immobilized at the perisynaptic region or the synapse proper by various mechanisms. These comprise: (a) clustering mediated by homotropic inter-molecular receptor-receptor associations; (b) heterotropic associations with non-receptor scaffolding proteins or the subjacent cytoskeletal meshwork, leading to diffusional "trapping", and (c) protein-lipid interactions, particularly with the neutral lipid cholesterol. Preceded by a brief introduction on the currently used methods to study protein lateral mobility in membranes, this review assesses the contribution of some of these mechanisms to the supramolecular organization and dynamics of the paradigm neurotransmitter receptor of muscle and neuronal cells—the nicotinic acetylcholine receptor (nAChR). The translational mobility of nAChRs at these two cell surfaces differs in terms of diffusion coefficients and residence intervals at the synapse, which cover an ample range of time regimes. Neuronal α7 nAChRs exhibit diffusion coefficients similar to those of other neurotransmitter receptors and spend part of their lifetime confined to the perisynaptic region of glutamatergic (excitatory) and GABAergic (inhibitory) synapses; they may also be involved in the regulation of the dynamic equilibrium between excitation and inhibition in brain.

F.J. Barrantes (✉)
Faculty of Medical Sciences, Laboratory of Molecular Neurobiology, Institute for Biomedical Research (BIOMED), UCA-CONICET, Av. Alicia Moreau de Justo 1600, C1107AFF Buenos Aires, Argentina
e-mail: rtfjb1@gmail.com; francisco_barrantes@uca.edu.ar

A. Chattopadhyay (ed.), *Membrane Organization and Dynamics*, Springer Series in Biophysics 20, DOI 10.1007/978-3-319-66601-3_9

Abbreviations

αBTX	α-Bungarotoxin
FCS	Fluorescence correlation spectroscopy
FRAP	Fluorescence recovery after photobleaching
MSD	Mean-square displacement
nAChR	Nicotinic acetylcholine receptor
SPT	Single particle tracking
TIRF	Total internal reflection fluorescence

9.1 Introduction

The motion of proteins in cell-surface membranes plays a fundamental role in the communication dynamics of the cell with its external and internal milieux. This is dramatically magnified in the synapse, the subcellular structure specialized in (mostly) chemical and electrical communications between cells. Protein motions depend on a multiplicity of factors: the physicochemical properties of the host lipid bilayer, protein-protein homotropic intermolecular associations, heterotropic association with other proteins (e.g. scaffolding, cell-adhesion, cytoskeletal, or motor proteins) and lipid-protein interactions. Physicochemical properties of the lipid bilayer vary from cell to cell and between different membrane compartments and contribute to the heterogeneity of motional regimes experienced by the same protein in different regions of the cell. By far the most important element that influences diffusional motion in the 2-D plane of the membrane is the degree of association with partner molecules (obviously linked with the dynamic phenomena of crowding and clustering), scaffolding proteins or cytoskeletal barriers (e.g. submembrane actin corrals), or tethering to the cytoskeleton [1–5] or lipid platforms [6–8].

In response to acute, mid- (e.g. circadian) and long-term (e.g. denervation supersensitivity) signaling stimuli, and probably in combination with self-regulatory mechanisms, the number and disposition of cell-surface neurotransmitter receptors at the plasma membrane play key roles in determining the functional activity of the synapse, and in particular its strength. This should be envisaged first and foremost in a dynamic perspective: the adaptive changes in the synapse are constantly operative, synaptic receptors being incorporated through active transport, recycling mechanisms, or lateral diffusion, or excluded from the synapse by the latter phenomenon or by various endocytic processes. In the central nervous system (CNS), some of these structural changes may serve for long-term storage of memory. In this review I discuss the idea that the dynamic cross-talk between neurotransmitter receptor molecules and the lipid platforms which serve as their habitats at the cell surface (see recent review in [9]) plays a role in the function of these transient protein-lipid complexes. One can envisage these reciprocal interactions as an orchestrated dialogue with mutual modulatory effects: lipids being selected and sorted in from the bulk bilayer by the receptors' structural features and, reciprocally, lipids tuning and optimizing receptor function, in a process which

probably evolved over the course of millions of years [10, 11]. The nicotinic acetylcholine receptor (nAChR) protein will be used as the paradigm to analyze these phenomena, and the translational dynamics of this receptor protein compared to those of other neurotransmitter receptor proteins in the CNS.

9.2 Experimental Approaches to Investigate the Motion of Proteins and Lipid in Membranes

Various biophysical techniques have been used to address the subject, but three complementary methods have predominated: fluorescence recovery after photobleaching (FRAP) [12, 13], fluorescence correlation spectroscopy (FCS) [14–20], and single-particle (molecule) tracking (SPT) [4, 21–27]. FRAP consists of bleaching an area of the membrane containing the intrinsically (e.g. an incorporated fluorescent protein) or extrinsically labeled proteins or lipids in question with a rapid and relatively intense pulse of light, and then following the time-dependent recovery of the fluorescence signal with a much lower illumination power. The replenishment of the fluorescence signal arises from the diffusion into the photobleached area of fluorescence molecules originally located outside this area. The fluorescence recovery curves are typically characterized by two parameters, a diffusion coefficient (D) and a mobile fraction (M_f). FCS is also an ensemble method enabling one to study the dynamics (diffusion coefficient), concentrations and molecular interactions (molecular aggregation, binding-unbinding, co-diffusion of two molecular entities, etc.) with high temporal and spatial resolution by following the passage of fluorescently-labeled molecules through very small volumes of the cell and analyzing the statistics of fluorescence intensity fluctuations as a function of time (see review in [28]). Recently, the combined application of FCS and superresolution optical microscopy (see section below) has enabled the observation of some of the above phenomena down to the nanometer scale (see recent review in [29]).

SPT can interrogate the motion of membrane proteins in the native membrane milieu of a living cell by following multiple trajectories of a sufficiently large number of single (e.g. fluorescently-labeled) molecules and extracting the apparent average diffusion coefficient from the mean-square displacement (MSD) of the molecules. Some shortcomings of these techniques have been pointed out, such as the invasive nature of FRAP, the essentially "local" interrogation of FCS, and the need to observe isolated particles for relatively long periods of time of SPT [30]. The limited spatial and/or temporal resolution of these techniques is still subject to criticism, since they provide a "global" or "macroscopic" diffusion coefficient which reflects the overall mobility over areas of several square microns [31]. In spite of these criticisms, SPT [1, 24–26, 32] still remains the most common approach for analyzing molecular diffusion in membranes, followed by the FRAP technique (see. e.g. [33–36]). New analytical tools have appeared in recent years to extend the applicability of SPT analysis to more "real life" (e.g. crowding,

anomalous diffusion), complicated membrane environments. One such approach is based on Bayesian and Akaike information criteria in information theory for classifying molecular trajectories [37–40]. The Bayesian method has also been combined with superresolution microscopy techniques such as STED to improve the determination of still positions in sub-diffraction images of GPI-anchored membrane proteins [41]. A recent work [42] reviews the "score" resulting from a competition in which 14 available SPT analytical methods were analyzed on the same, complex data set, offering comparisons among SPT methods to address a given biological question.

9.3 The Nicotinic Acetylcholine Receptor (nAChR) and Its Equilibria at the Synapse

The nAChR is the prototype of the superfamily of pentameric ligand-gated ion channels, a collection of transmembrane receptor proteins with intrinsic anion-selective channels (the γ-amino butyric acid type A ($GABA_A$), γ-amino butyric acid type C ($GABA_C$) and the glycine receptor) and cation-selective channels as is the case with the 5-HT3 (serotonin) receptor and the nAChR [43, 44]. These transmembrane proteins are composed of five polypeptide subunits organized pseudo-symmetrically around a central pore. Each subunit contains an extracellular domain, four hydrophobic transmembrane segments arranged in the form of three concentric rings around the pore [45] and a short extracellular carboxy-terminal domain [46].

In the peripheral nervous system, at the neuromuscular junction in adult myotubes, the nAChR macromolecule is highly concentrated in a relatively small area of the cell, packed at the remarkably high density of 10,000–20,000 particles μm^{-2}. Receptor density drops abruptly in the rest of the plasma membrane (<100 particles μm^{-2} [47, 48]). Despite this abrupt difference in the density of nAChRs, it has been calculated that the pool of extrasynaptic receptors represents ~99% of the total amount of receptors present at the cell surface of muscle fibers [49]. As indicated previously, the functional efficacy of the synapse heavily depends on its strength. This in turn is directly related to the number of receptors present at the synapse, which depends on the equilibrium between two sets of factors: (i) lateral diffusion into and out of the synaptic region from non-synaptic ("extrasynaptic") areas, and (ii) the trafficking and turnover of receptors at the cell surface, determined by the rate and extent of biosynthesis and exocytic delivery to the plasmalemma, plus the contribution of receptor recycling back to the surface, on the one hand, and removal of synaptic receptors by internalization (endocytosis) or two-dimensional diffusion driving them away from the synaptic region, on the other. The first of these two phenomena is usually viewed as the equilibrium between a diffuse pool of extrasynaptic receptors and the clustered receptor pool in the synapse. Recent work in *C. elegans* neuromuscular synapses has shed light

on mechanisms modulating this equilibrium: the leucine-rich repeat protein RSU-1 (Ras suppressor-1) is required for the proper distribution of nAChRs on the muscle surface. RSU-1 mutants form ectopic, "illegitimate" extrasynaptic nAChR clusters at the expense of synaptic clusters [50]. The density of nAChRs is also regulated by a complex cascade involving nerve-secreted agrin, activating the muscle-specific kinase MuSK through the protein Lrp4, in association with binding partners dok-7 and Tid1, various kinases and phosphatases and Rho-family small GTPases (reviewed in [51]). Diffusion into the endplate region is also rare except for accidental or man-tailored conditions such as in denervation hypersensitivity, in which migration of extrasynaptic receptors to the motor endplate occurs in a transient fashion. Several pathological conditions of the neuromuscular junction are associated with an insufficient number of receptor molecules, the disease myasthenia gravis probably being the most prominent example.

In the brain, ACh mediates distant signaling through projection neurons and local signaling via interneurons; the type of message conveyed by ACh depends on a variety of factors, including site of release, the localization of the target neurons, the target receptor subtypes [52] and the status of the target cells at the time of release. Moreover, central cholinergic signaling may be confined to the synapse or involve the de-localized diffusion of the neurotransmitter in the extracellular milieu and binding to non-synaptic sites [53, 54].

In the CNS the dynamics of neurotransmitter receptors at the synapse have been associated with a key physiological phenomenon: synaptic plasticity. Indeed, the rapid lateral exchange of receptors at the synapse with those in non-synaptic areas is thought to underlie the plastic behavior of excitatory glutamatergic synapses (i.e. those operating through AMPA and NMDA receptors, as described below) [55–58]. It has been surmised and supported by a variety of solid experimental approaches that receptors' effective residence time at excitatory synapses directly affects synaptic efficacy and plasticity, that is, long-term potentiation (LTP), long-term depression (LTD) and other biologically important processes which are believed to lie at the root of key cognitive functions such as learning and memory. Furthermore, GABAergic and glycinergic receptors at inhibitory synapses appear to be dynamically regulated through similar processes. Important cognitive functions like learning and memory [59–61] may bear relationship with the ability of α7 nAChRs to reside intermittently in the neighborhood of glutamatergic and GABAergic synapses, and due to their high Ca^{2+} permeability, differentially regulate the excitatory/inhibitory balance and LTP in discrete neuronal locations [62–65].

9.4 Ontogenetic Changes in nAChR Mobility

The pioneer study of Axelrod et al. [66] using the fluorescence recovery after photobleaching (FRAP) technique demonstrated that in developing muscle cells the highly clustered nAChRs present in large (20–60 μm) patches are practically immobile,

with an apparent lateral diffusion coefficient (D) of $<10^{-4}\,\mu m^2\,s^{-1}$ ($<10^{-12}\,cm^2\,s^{-1}$). The translational mobility of diffusely distributed nAChRs in other regions of the same plasma membrane is only slightly faster ($D \sim 0.5 \times 10^{-2}\,\mu m^2\,s^{-1}$). The relative immobility of synaptic nAChRs at the neuromuscular junction is probably due to a multiplicity of factors. The muscle endplate and the electromotor synapse of electric fish are compact "islands" with a huge absolute number of receptor macromolecules densely packed at an extraordinarily high density. It is thus not surprising that receptors hardly diffuse in the plane of the membrane... In order to dissect the contribution of intrinsic (e.g. receptor-receptor interactions, clearly apparent e.g. in early electron micrographs of the *Torpedo* electroplax postsynaptic membrane [67]) and extrinsic (e.g. corralling by the submembrane cytoskeletal meshwork) protein clustering factors it is useful to resort to simpler model systems. Heterologous constitutive expression of receptors in cells is a compromise system offering the possibility to conduct a variety of studies under physiological conditions. The clonal cell line CHO-K1/A5 [68] robustly expresses adult muscle-type nAChR at densities lower than those of the endplate in an adult muscle cell or the motor plate in the electric fish synapses. Recycling of nAChRs is too slow to contribute to the cell-surface pool within the experimentally observed period [69]. Furthermore, since one has the possibility to increase the complexity of the model system one building block at a time, the lack of non-receptor scaffolding proteins like rapsyn or the clustering factor agrin make the CHO-K1/A5 a useful mammalian expression system to explore "intrinsic" factors involved in clustering and 2-D diffusion of the nAChR protein and to interrogate in a systematic manner for possible involvement of additional components.

The 2-D mobility of the adult muscle-type nAChR at the plasma membrane of CHO-K1/A5 cells and its dependence on membrane cholesterol levels were measured using the FRAP technique in the confocal mode (as in [70, 71]). A defined 2-D region was selected from the confocal section of the cell membrane, thus restricting the analysis to a few thousand fluorescent-tagged nAChRs. The region was photobleached by transiently increasing the laser power of the confocal microscope, and the diffusive exchange of bleached proteins with nearby unbleached molecules was then followed using low-intensity laser excitation. Recovery into the bleached region can be described by two parameters, an apparent lateral diffusion coefficient, D, and a mobile fraction, *Mf* [1, 72, 73]. D provides a measure of the kinetics of translational mobility, whereas *Mf* reports on the proportion of fluorescent molecules that are able to diffuse back into the bleached area over the time course of the assay [74]. αBTX-labeled nAChRs exhibited a value of $0.46 \times 10^{-2}\,\mu m^2\,s^{-1}$ [75], a value similar to that of the mobile nAChR fraction in developing rat myotubes ($0.5 \times 10^{-2}\,\mu m^2\,s^{-1}$) [66] and that of diffusely distributed nAChR in adult rat muscle fibers in cell culture ($0.25 \times 10^{-2}\,\mu m^2\,s^{-1}$) [76, 77]. Methyl-β-cyclodextrin-mediated depletion of cholesterol produces a reduction in the fraction of mobile nAChRs from 55 to 20% [75]. Concomitantly, the apparent diffusion coefficient dropped to half the control value. Cholesterol enrichment had the opposite effect.

We subsequently employed the SPT technique in the TIRF model to study nAChR translational diffusion in the same cell model system. Fluorescent-labeled

(AlexaFluor^{488} α-BTX) nAChR particles imaged with TIRF are diffraction-limited, and puncta of about 0.2 μm in diameter could be imaged in wide-field microscopy [78, 79]. The density of these puncta is high, yet there is enough contrast and their separation suffices to track the trajectories with a good signal-to-noise ratio. CHO-K1/A5 cells were labeled with a monovalent ligand (AlexaFluor^{488}α-BTX) or a multivalent ligand (anti-nAChR mAb210 monoclonal antibody followed by AlexaFluor^{488}-conjugated IgG secondary antibody) at 4 °C [80]. The microscopic apparent diffusion coefficient $D_{2\text{–}4}$ [4] of the receptor labeled with α-BTX shifted from a wide distribution spanning from ~$6.7 \times 10^{-4} - 1\ \mu m^2\ s^{-1}$ (~$6.7 \times 10^{-12} - 1 \times 10^{-8}\ cm^2\ s^{-1}$) to a much narrower distribution with an upper limit close to $5.0 \times 10^{-4}\ \mu m^2\ s^{-1}$ upon cholesterol depletion [80]. In the case of antibody-labeled samples, the proportion of slow-moving particles was significantly higher, with a net displacement of particle motion towards the immobile confined regime. $D_{2\text{–}4}$ values as low as ~$3.3 \times 10^{-5}\ \mu m^2\ s^{-1}$ (lower limit) to ~$6.7 \times 10^{-2}\ \mu m^2\ s^{-1}$ (upper limit) were observed. Control samples labeled with mAb210 already exhibited a substantial proportion (19.4%) of immobilized particles. This proportion markedly increased upon cholesterol depletion of the cells, especially during the initial 10 min (83.3%). Simonson and coworkers [81] reported a 2-D diffusion coefficient of $0.1\ \mu m^{-2}\ s^{-1}$ for α7-5HT3 chimeric nAChRs heterologously expressed in HEK cells. The quantitative local point-pattern analysis indicated that nAChR particles were not randomly distributed but organized in clusters, which differed in size, brightness and density between BTX and antibody-treated samples. Interestingly, the density of the nAChR clusters also varied as a function of time of exposure to methyl-β-cyclodextrin, reaching a maximum at ~10 min treatment for BTX- and ~20 min for mAb-labeled samples [80].

The scaffolding protein rapsyn affects nAChR distribution at the cell surface [82–84]. The myristoylated N-terminus of rapsyn molecules anchors nAChRs to the plasma membrane in a 1:1 stoichiometry, playing a major role during myoblast differentiation and neuromuscular junction development. In myoblasts the majority of the receptors were found to be immobile, with 20% of the receptors exhibiting restricted diffusion in small domains of about 50 nm [85]. Before differentiation, only 2% of the nAChRs showed Brownian diffusion, 24% diffused in confined regions, and 74% were immobile. Upon differentiation into multinucleated myoblasts, a strong diminution of the immobile fraction was observed, in conjunction with an increase in the proportion of confined diffusing receptors from 20 to 34%, and Brownian-diffusing receptors from 2 to 10%. In a myoblast cell line devoid of rapsyn, the fraction of mobile nAChRs was higher, and was accompanied by a 3-fold decrease in the immobile population in comparison to rapsyn-expressing cells. About 50% of the mobile receptors were confined to domains of about 120 nm. Irrespective of the presence of the nAChR-anchoring protein rapsyn, nAChR was confined to domains: when rapsyn was present, the size of the domains diminished [85]. This study is in agreement with our findings using direct imaging of nAChR nanoclusters by superresolution microscopy in cells devoid of rapsyn [79].

9.5 Effect of Cholesterol on nAChR Translational Mobility

Several FRAP studies have shown that cholesterol depletion affects the mobility of various proteins at the plasma membrane although the nature, extent and sign of the changes remain a contentious subject. In FRAP experiments performed on cells treated with Mevinolin, a statin that inhibits cholesterol biosynthesis, we found that nAChR mobility was affected in a manner similar to that reported using methyl-β-cyclodextrin mediated acute cholesterol depletion [75]. FCS in the confocal microscopy modality corroborated the results of FRAP microscopy. Whereas values of D of $5.3 \pm 0.4 \times 10^{-2}\,\mu m^2\,s^{-1}$ were observed in control cells, D was reduced to $3.7 \pm 0.3 \times 10^{-2}\ \mu m^2\ s^{-1}$ upon cholesterol depletion [75].

Some authors reported that the mobility of raft- and non-raft resident proteins decreases when cholesterol is removed from the plasma membrane [74, 86]. Restricted diffusion of membrane proteins upon cholesterol depletion is believed to result from the formation of solid-like clusters in the membrane [87, 88]. Sun et al. [89] postulate that cholesterol affects the mechanical properties of plasma membrane through the underlying cytoskeleton. Using SPT methods, another group [90] found that cholesterol depletion produces confinement of the epidermal growth factor receptor and human epidermal growth factor receptor 2 mobility, whereas cholesterol enrichment extended the boundaries of the mobility-restricted areas. In contrast, other authors observed an increase in the lateral mobility of the raft-resident proteins CD44 and wild-type GFP-H-Ras after cholesterol depletion [35, 91]. Removal of cholesterol, particularly with methyl-β-cyclodextrin, not only alters membrane viscosity but can also hinder membrane protein diffusion [92].

9.6 Cholesterol and Scaffolding Proteins Differentially Affect Neuronal α3 and α7 nAChR Mobility

Ciliary ganglion neurons were the first test preparation where α7 nAChRs were reported to occur in liquid-ordered lipid domains (“rafts”) in somatic spines [93]. In their quantum dot SPT study of chick ciliary ganglion neurons, Berg and coworkers [94] found that α7 and α3 nAChRs had similar mobility, but differed in the nature of their synaptic restraints. Furthermore, cholesterol depletion by treatment with cholesterol oxidase increased the mobility of extrasynaptic α3 nAChRs from 0.188 to 0.208 $\mu m^2\ s^{-1}$ without affecting the proportion of immobile α7 nAChRs.

In contrast, cholesterol depletion affected both synaptic and extrasynaptic α7 nAChRs, and the proportion of receptors visiting synaptic territory increased. Cholesterol depletion also raised the proportion of mobile α3 nAChRs from 34 to 54%, without affecting that of α7 nAChRs. Disruption of PDZ-containing scaffolds

or of actin filaments in chick ciliary ganglion neurons increased the mobility of α7 nAChRs but not that of α3, as expected from the wealth of evidence on the role of the actin and PDZ-scaffolds in maintaining synapse, and in particular dendritic spine, architecture [95]. It has been previously reported that in one cell, a single species of protein can have one subset undergoing Brownian diffusion and other subsets undergoing confined or anomalous diffusion [96]. Muscle-type nAChR mobility also displays a strong dependence on cytoskeletal integrity [97–99] in developing myotubes and in the adult neuromuscular junction.

9.7 Diffusional Modulation and Confinement of nAChR Assemblies by Cytoskeletal Components and Scaffolding Proteins

There is evidence of interactions between lipids, lipid domains and the cytoskeleton [100–102]. According to Kwik et al. [103] cholesterol depletion produces general effects on the architecture and function of the membrane, making the sub-membrane cytoskeleton and in particular the cortical actin network more stable. Such a reorganization of the actin meshwork would be associated with reduced receptor mobility. Using FCS and STED it was recently shown that membrane-bound actin networks influence lipid phase separation; a model combining the coupling of membrane composition, membrane curvature, and the actin pinning sites was postulated from this study [100]. More recently, confocal FRAP distinguished two protein populations of membrane proteins, including some classical "synaptic" proteins in PC12 cells, having diffusion coefficients D of 0.22 and 0.01 $\mu m^2 s^{-1}$, respectively [104]. When FCS in the superresolution mode (STED-FCS) was applied, the spatio-temporal resolution afforded the determination of D on fast diffusing molecules (slowly diffusing or immobile molecules do not traverse the observation spot and do not cause intensity fluctuations, thus precluding their detection). D was found to be 0.1–0.6 $\mu m^2 s^{-1}$ for the highly mobile protein fractions, which varied inversely proportional to their density. Interestingly, cholesterol level was found to be the most important factor in determining protein mobility *and* stabilizing protein assemblies (clusters) [104].

Cytoskeletal interactions have been shown to modulate the diffusion and confinement of membrane proteins [3, 5, 105, 106]. Proteins tethered to highly dynamic actin strands may undergo clustering in response to actin aster formation. Another process involving the actin meshwork and affecting receptor mobility is the formation of fences or pickets, as originally postulated by Kusumi and coworkers [3, 5, 105, 107, 108]. The "picket fence" or "hop diffusion" model postulated that the cortical actin cytoskeletal meshwork underneath the plasma membrane hinders the diffusion of membrane proteins (and lipids) in the plane of the membrane and confines their movement within those boundaries. Occasionally, proteins or lipids confined within these "transient confinement zones" hop these barriers, jumping to

a new confined compartment or diffusing more freely in unconfined areas. In the case of the muscle-type nAChR, cholesterol depletion affected the long-range relationship of nAChR nano-clusters of ~55 nm diameter, changing from a random to a non-random distribution (within a radius of 0.5–1.5 μm) upon depletion [79]. Interactions of these nano-clusters with the cytoskeleton were invoked as a possible explanation for these changes since nAChR mobility at the plasma membrane appears to be sensitive to the integrity of the cytoskeleton [76, 97–99]. Furthermore, interaction between nAChR molecules and the cytoskeleton is of physiological and developmental importance: it is a requisite step in the formation and stability of the neuromuscular junction [109]. In subsequent work from our laboratory the effects of cytoskeleton disruption on nAChR dynamics [75] were experimentally explored. Even though cholesterol depletion-induced loss of nAChR mobility was partially restored in cells incubated with Latrunculin A [75], the percentage of mobile nAChRs in these cells did not reach control levels. From this we concluded that although the cortical actin meshwork is likely involved in receptor mobility at the cell surface in cholesterol-depleted cells, it is not necessarily the only factor influencing nAChR translational diffusion. Other cortical cytoskeletal proteins and/or actin-binding proteins may be involved, and direct interactions of cholesterol with the nAChR may also be implicated. Furthermore, inhibition of actin polymerization by cytochalasin D, which binds to the barbed end of the actin filament and blocks monomer addition, resulted in inhibition of nAChR internalization [69]. However, direct effects of cholesterol on the nAChR cannot be discarded when considering the profound influence of this lipid on the macromolecule's cell surface mobility.

Disruption of the cytoskeleton or the microtubule networks with Latrunculin A or nocodazole, respectively, affected the mobility of the neuronal α7 nAChR but not its ability to form clusters, as we have observed in muscle-type nAChRs using superresolution microscopy [110]. The exact mechanisms of nAChR immobilization in CNS synapses and in particular the role of the cytoskeleton or other diffusional traps merit further investigation.

Which other factors might contribute to nAChR mobility, trafficking and clustering? Various post-translational modifications are known to occur in nAChRs: the macromolecule is the target of disulphide bond formation, glycosylation, phosphorylation, palmitoylation and other modifications which might affect nAChR dynamics. Palmitoylation of assembling α7 subunits in the endoplasmic reticulum has been shown to play a role in the formation of functional α-bungarotoxin sites [111, 112]. A linear relationship has been found between average nAChR half-life and the percentage of nAChRs with phosphorylated β subunit in cultured muscle cells. Phosphorylation occurs specifically at tyrosine residue 390 of the β subunit, and is induced by agrin. This unexpected role of agrin in downregulating nAChR turnover most likely stabilizes receptors at developing synapses and contributes to their extended half-life at adult NMJs [113]. Phosphorylation-induced global conformational changes have been recently proposed to be a universal phenomenon among

ligand-gated ion channels, and also to play a role in pathophysiological phenomena such as nicotine addiction in the specific case of the nAChR [114].

In addition to the above post-translational modifications, antibody crosslinking plays an important role in confining and immobilizing receptors under pathological conditions. Antibody-induced crosslinking results in a strong diminution of receptor mobility in developing rat myotubes in primary culture [115]. Neuromuscular dysfunction in the autoimmune disease myasthenia gravis is caused primarily by the crosslinking of autoantibodies to the muscle endplate nAChR, although other antigens such as muscle-specific tyrosine kinase and low-density lipoprotein receptor-related protein 4 are currently recognized as molecular targets in muscle [116]. Antibody binding results in impaired receptor function, diminished neuromuscular transmission and the characteristic weakness and rapid-onset fatigue clinical symptoms. The antibody binding also triggers the endocytic internalization of nAChRs in C2C12 muscle cells and in CHO-K1/A5 cells [69]. This is also observed using the SPT technique in adult-type nAChR expressed in CHO-K1/A5 cells. Instead of the long particle walks observed with the monovalent ligand α-BTX, the motion of antibody-crosslinked nAChR particles was restricted to much shorter trajectories confined within relatively small areas [80].

9.8 Residence Time, Mobility and Function of Neurotransmitter Receptors and Lipid Platforms in the Central Nervous System

In brain, neuronal excitability depends on the homeostatic equilibrium between inhibitory and excitatory neurotransmission, which is mainly mediated by GABA and glutamic acid, respectively, with additional contributions from other neurotransmitters. The principal excitatory neurotransmitter in brain is glutamic acid. There are various forms of glutamatergic ion channels. They include AMPA (α-amino-3-hydroxy-5-methyl-4-isoxazolepropionic acid), kainic acid and N-methyl-D-aspartic acid (NMDA) receptors. These macromolecules having both neurotransmitter receptor and ion channel properties fulfill quite different functions. AMPARs generate fast excitatory postsynaptic potentials by activating non-selective cationic channels permeable to Na^+ and K^+ with an equilibrium potential near 0 mV. AMPAR channels are responsible for most of the fast excitatory synaptic transmission in the central nervous system. They are heterotetramers composed of four subunits termed GluR1- GluR4 and contain PDZ-domains: GluR1 binds to SAP1 and GluR2 binds to PICK1 or GRIP/ABP. SAP97 has been postulated to intervene in the trafficking of AMPARs from peri-synaptic to the post-synaptic region and influence glutamatergic transmission. AMPARs do not bind to the ubiquitous PSD-95 scaffolding protein. Clathrin-dependent AMPAR endocytosis in the dendritic spines has been associated with the phenomenon of long-term depression [117].

NMDARs are also heterotetramers formed by two GluN1 and two GluN2 subunits surrounding a cation channel permeable to calcium [118–120]. NMDARs play a key role in synaptic plasticity and are associated with various forms of learning and memory. NMDARs have been reported to be associated with cholesterol-rich domains in the excitatory synapse [121], which might regulate NMDAR composition, trafficking and ion-channel permeability. Changes in cholesterol content were shown to inhibit NMDA-stimulated Ca^{2+} influx in hippocampal cells in culture [122]. Cholesterol diminution redistributed the NMDAR GluN2B subunit, from Lo to Ld membrane fractions [122].

The two most abundant forms of nAChR in brain are the heteropentameric oligomer formed by α4 and β2 subunits and the homopentameric receptor formed exclusively by α7 subunits [123]. The α7 nAChR is found in the neuronal soma and also in the pre-, post-and peri-synaptic regions. Presynaptic α7 nAChRs modulate the release of various neurotransmitters, and postsynaptic α7 nAChRs are involved in the generation of postsynaptic currents [124]. Postsynaptic α7 nAChRs can be associated with dendritic spines, in a peri-synaptic annulus [125]. Perisynaptic α7 nAChRs are found in the vicinity of GABAergic and glutamatergic synapses (see below and e.g. [126]). The α7 nAChR exhibits unique functional properties that distinguish it from other nicotinic receptors: (a) fast desensitizing kinetics, (b) unusually high Ca^{2+} permeability and (c) high affinity for binding α-bungarotoxin [127, 128]. The α7 nAChR is highly expressed in the hippocampus and in GABAergic interneurons in particular. The hippocampus is one of the brain regions mostly affected in Alzheimer's disease, where it regulates inhibition of hippocampal networks: activation of α7 nAChR blocks the induction of short-term potentiation as well as LTP. It is involved in cognition and has been associated with pathological states other than Alzheimer's disease, such as some forms of schizophrenia and Parkinson's disease [129].

The residence lifetime of neurotransmitter receptors in the synapse plays an important role in maintaining the inhibitory-excitatory balance. Most neurotransmitter receptors are not permanently anchored to diffusional traps or scaffolding domains at the synapse but appear to freely diffuse in the plane of the membrane at rates between 0.1 and 0.5 $\mu m^2\ s^{-1}$ [55, 57, 106, 130–133]. Glycine receptors [134] and α7 nAChR [126] display similar motional behavior: both exhibit high mobility in extrasynaptic areas and confined, low motion in perisynaptic and synaptic domains. Confinement is inversely correlated to mobility [126, 132, 133].

In brain, glycine receptors are stabilized by microtubules in extrasynaptic regions, and by gephyrin and actin filaments in synaptic regions [130]; AMPA receptors become stable upon interaction with the protein GRIP1, which binds in turn to microfilaments [135]. In addition to these anchoring heterotropic interactions with non-receptor proteins, excitatory GluR1 AMPA receptors are also immobilized transiently at individual synapses by activity, which is input-specific [132]. This relative "trapping" results from the reduction of the diffusional exchange between synaptic and extrasynaptic domains. In other words, AMPA receptors transiently accumulate at distinct sub-regions of the postsynaptic membrane, probably contained within distinct lipid platforms in which receptors

experience restricted mobility (median D 0.023 $\mu m^2\ s^{-1}$). In contrast, AMPA receptors at neighboring inactive synapses are highly mobile (median D 0.138 $\mu m^2\ s^{-1}$). However, these differences in diffusion coefficients do not account for the net difference in the number of receptors between active and inactive ("silent") synapses: AMPA receptors often escape from silent synapses, whereas they remain trapped in active synapses, which actually capture receptors by diffusional exchange.

In a recent study of inhibitory glycinergic receptors and their scaffolding anchorage protein at the postsynaptic density, gephyrin, PALM time-resolved superresolution microscopy showed that gephyrin clusters are comprised of several sub-clusters, and that these undergo dynamic changes in the time-course of minutes [136]. According to these authors, the morphological changes may correspond to the splitting and merging of gephyrin clusters in the postsynaptic density, whose size determines the number of receptors it can accommodate. Furthermore, the number of the two key inhibitory neurotransmitters—glycine and $GABA_A$—increased with the number of gephyrin clusters at spinal cord synapses. This is another reflection of gephyrin's ubiquity in inhibitory synapses: gephyrin is involved in the clustering of both glycine receptors and a major subset of $GABA_A$ receptors; both compete for the same sites on the gephyrin molecule. Palmitoylation of Cys212 and Cys284 in gephyrin has recently been reported to be critical for the association of this protein with the postsynaptic membrane and also essential for its clustering (trimers, hexamers and nonamers) [137]. Lack of palmitoylation leads to mislocalization of gephyrin in non-synaptic regions. Conversely, increased palmitoylation is associated with gain-of-function, i.e. augmented inhibitory GABAergic transmission.

In a study of α7 nAChR mobility in cultured hippocampal neurons, SPT was carried out on a small fraction of receptors labeled with quantum dot-coupled α-BTX [126]. It should be mentioned that in hippocampal neuronal cultures the GABAergic interneurons are not expected to receive cholinergic innervation, since they are deprived of inputs from distal anatomical brain regions such as the septum. In spite of the absence of synaptic input, α7 nAChRs clusters are present on the neuronal surface. Less than 20% of the receptors were found in clusters, categorized as "synaptic", as opposed to those labeled with the presynaptic marker synapsin 1, which were assigned to dendritic, postsynaptic, nicotinic sites. The majority (78%) of the receptors were found in the form of aggregates in extrasynaptic areas and were either classified as "axonal" (20%, highly mobile, $D > 0.1\ \mu m^2\ s^{-1}$, Brownian motion with mostly linear trajectories) or perisynaptic, i.e. in the vicinity of, but not co-localized with, excitatory glutamatergic (identified by mCherry-Homer 1c staining) and inhibitory GABAergic (labeled with EGFP-gephyrin) postsynaptic densities. The α7 nAChRs in perisynaptic locations differed in their mobility, too, with lowest receptor mobility (>66% of the "peri-GABAergic" with $D \sim 0.018 \pm 0.03\ \mu m^2\ s^{-1}$ and >70% of the "peri-glutamatergic" with $D \sim 0.028 \pm 0.04\ \mu m^2\ s^{-1}$), reflecting local confinement domains, these differences suggesting in turn that the tethering mechanisms holding these nicotinic receptors in the vicinity of excitatory and inhibitory synapses differed as well [126]. What are

the possible physiological implications of these findings? Stimulation of α7 nAChRs in hippocampal interneurons modulates GABAergic inhibitory postsynaptic potentials, depressing them in some cases [138] or exciting them in other instances [139]. In the latter case, the ACh-induced excitation of the bicuculline-sensitive GABAergic interneurons could in turn excite or inhibit pyramidal neurons in the CA1 region. Methyllycaconitine-sensitive α7 nAChRs also appear to affect glutamatergic synapses, modulating back-propagating dendritic action potentials and, hence, LTP [140]. Activation of α7 nAChRs influences postsynaptic NMDA receptors, relieving the Mg^{2+} block and thus enhancing the probability of LTP induction [141]. From this type of evidence, the conclusion was reached that their perisynaptic localization and their high Ca^{2+} permeability endows α7 nAChRs with the ability to regulate both excitatory and inhibitory CNS synapses independently of their endogenous transmitter [126].

In the synapses between pre- and post-ganglionic neurons in the mouse submandibular ganglion [142], the density of synaptic receptors is normally maintained by the combination of exchange of receptors with non-synaptic regions, a diffusional phenomenon occurring in the time course of minutes, and the turnover of cell surface receptors, taking place in the course of hours. To measure the kinetics of α7 nAChR, McCann et al. [142] resorted to various techniques. First, using fluorescent α-BTX they identified postsynaptic and non-synaptic populations of nAChRs. Postsynaptic nAChRs remained stable for days; non-synaptic nAChRs were more dynamic, being replaced in the course of days. Secondly, using the FRAP technique the authors studied nAChR lateral diffusion in the ganglionic neurons, measuring a $t_{1/2}$ of recovery of 47 ± 7 min and 11 ± 4 min for synaptic and non-synaptic α7 nAChR clusters, respectively. Thirdly, to measure the turnover rate of nAChRs *in vivo*, McCann et al. [142] resorted to a fluorescence and pulse-chase technique [143] which enabled them to follow the fate of the nAChRs in the living animal for several days. The rate of loss of cell-surface neuronal α7 nAChRs (350 ± 47 min) was found to be 60-fold faster than that of muscle-type nAChRs at the neuromuscular junction [143, 144]. If living ganglion cell axons were severed, synaptic receptors showed enhanced lateral mobility and insertion of new receptors dramatically decreased, leading to near-complete loss of synaptic receptors and to acute synaptic depression. Disappearance of postsynaptic spines and presynaptic terminals ensued [142]. The authors concluded that rapid changes in synaptic efficacy precede long-lasting structural changes in synaptic connectivity. FRAP continues to be applied to the study of neuronal nAChRs. In a recent study, FRAP revealed that the agonist nicotine, acting on α7 nAChRs in hippocampal postsynaptic neurons, induces the stabilization and accumulation of GluA1-type AMPA receptors [145].

Chick ciliary ganglion neurons in culture express homomeric α7 and heteromeric α3 nAChR at their surface. nAChR lateral mobility was measured using biotinylated α-BTX and biotinylated monoclonal antibody against α3 nAChRs, respectively, followed by streptavidin-coated quantum dots with an emission wavelength of 605 nm [146]. In the case of α3 nAChRs, only 34% were mobile. The resulting diffusion coefficient, D, was reported to be 0.070 $\mu m^2\ s^{-1}$ and

0.188 $\mu m^2 s^{-1}$ in synaptic (roughly 50%) and extrasynaptic regions, respectively. In the case of α7 nAChRs the mobile fraction was much higher (61%) and the measured D was 0.067 and 0.188 $\mu m^2 s^{-1}$ for synaptic and extrasynaptic locations, respectively [146]. The dwell time at the synaptic region was about 0.5 ms for the two types of neuronal nAChRs. Analysis of the MSD indicated that synaptic receptors exhibited constrained motion, and extrasynaptic receptors displayed Brownian motion. That is, when either type of receptors is able to diffuse freely, they do so at similar rates, but when their motion is restricted, their constraints differ. In adult ciliary ganglia in vivo α7 nAChRs are localized in the peri-synaptic region; in cultured neurons, wide-field microscopy immunocytochemistry showed puncta in close proximity to synaptophysin labeling [146].

9.9 Biomedical Implications

Keeping synaptic strength at an adequate level is a functional requisite of both peripheral and central nervous system synapses, and it is the combination and homeostasis of the +/− mechanisms outlined above that concertedly operate to maintain the functionally adequate density of neurotransmitter receptors. The mechanisms utilized by cells to achieve this equilibrium are complex, and vary between peripheral and CNS. A common feature is the transient immobilization of receptors in nanoscale compartments of the synapse as opposed to extrasynaptic regions, commonly achieved by clustering or by interaction with scaffolding non-receptor proteins and lipid platforms. Our ability to interrogate the dynamics of receptors is currently limited to brief glimpses of the molecules' entire lifetime, from synthesis to degradation, but nonetheless these snapshots provide useful hints about the organization and the functionally relevant spatiotemporal behavior of these important molecules in the synapse.

Several neurological and neuropsychiatric disorders have been associated with dysfunction of receptors and ion channels at the synapse, whose alterations can be encompassed under the term "synaptopathies". Diseases like depression, anxiety disorders, various forms of dementia, epilepsy, Parkinson's disease, autism spectrum disorder, migraine, fragile X syndrome, and schizophrenia are among these disorders, which cover a wide spectrum of pathological synaptic phenotypes, ranging from alterations in the number, size or morphology of dendritic spines, disposition of spines along the dendritic arborizations, etc. The related physiological alterations in these synaptopathies (either hypo- or hyper-function of the synapse) are assumed to depend in turn on the underlying dysfunction of the receptors and channels, the so-called channelopathies [147], which should now be extended to encompass scaffolding and other non-receptor proteins e.g. those misfolded and aggregated at the synapse, like in Alzheimer's, Huntington's or Parkinson's diseases (for recent reviews see e.g. [148, 149]).

Acknowledgements Experimental work quoted in this article was supported by grants PICT 2011-0604 from FONCYT, Ministry of Science and Technology and PIP No. N° 112-201101-01023 from the National Scientific and Technical Research Council of Argentina (CONICET).

References

1. Chen Y, Lagerholm BC, Yang B, Jacobson K. Methods to measure the lateral diffusion of membrane lipids and proteins. Methods. 2006;39(2):147–53.
2. Jacobson K, Mouritsen OG, Anderson RG. Lipid rafts: at a crossroad between cell biology and physics. Nat Cell Biol. 2007;9(1):7–14.
3. Kusumi A, Nakada C, Ritchie K, Murase K, Suzuki K, Murakoshi H, Kasai RS, Kondo J, Fujiwara T. Paradigm shift of the plasma membrane concept from the two-dimensional continuum fluid to the partitioned fluid: high-speed single-molecule tracking of membrane molecules. Annu Rev Biophys Biomol Struct. 2005;34:351–78.
4. Kusumi A, Sako Y, Yamamoto M. Confined lateral diffusion of membrane receptors as studied by single particle tracking (nanovid microscopy). Effects of calcium-induced differentiation in cultured epithelial cells. Biophys J. 1993;65(5):2021–40.
5. Suzuki K, Ritchie K, Kajikawa E, Fujiwara T, Kusumi A. Rapid hop diffusion of a G-protein-coupled receptor in the plasma membrane as revealed by single-molecule techniques. Biophys J. 2005;88(5):3659–80.
6. Rao M, Mayor S. Rafts: scale-dependent, active lipid organization at the cell surface. Traffic. 2004;5:231–40.
7. Rao M, Mayor S. Active organization of membrane constituents in living cells. Curr Opin Cell Biol. 2014;29:126–32.
8. Varma R, Mayor S. GPI-anchored proteins are organized in submicron domains at the cell surface. Nature. 1998;394:798–801.
9. Borroni MV, Vallés AS, Barrantes FJ. The lipid habitats of neurotransmitter receptors in brain. Biochim Biophys Acta Biomembr. 2016;1858(11):2662–70.
10. Barrantes FJ. Phylogenetic conservation of protein-lipid motifs in pentameric ligand-gated ion channels. Biochim Biophys Acta Biomembr. 2015;1848(9):1796–805.
11. Barrantes FJ, Fantini J. From hopanoids to cholesterol: molecular clocks of pentameric ligand-gated ion channels. Prog Lipid Res. 2016;63:1–13.
12. Kang M, Day CA, Drake K, Kenworthy AK, DiBenedetto E. A generalization of theory for two-dimensional fluorescence recovery after photobleaching applicable to confocal laser scanning microscopes. Biophys J. 2009;97(5):1501–11.
13. Petersen NO, Elson EL. Measurements of diffusion and chemical kinetics by fluorescence photobleaching recovery and fluorescence correlation spectroscopy. Methods Enzymol. 1986;130:454–84.
14. Andrade DM, Clausen MP, Keller J, Mueller V, Wu C, Bear JE, Hell SW, Lagerholm BC, Eggeling C. Cortical actin networks induce spatio-temporal confinement of phospholipids in the plasma membrane – a minimally invasive investigation by STED-FCS. Sci Rep. 2015;5. https://doi.org/10.1038/srep11454.
15. Eggeling C, Ringemann C, Medda R, Schwarzmann G, Sandhoff K, Polyakova S, Belov VN, Hein B, von Middendorff C, Schonle A, Hell SW. Direct observation of the nanoscale dynamics of membrane lipids in a living cell. Nature. 2009;457(7233):1159–62.
16. Elson EL. Quick tour of fluorescence correlation spectroscopy from its inception. J Biomed Opt. 2004;9(5):857–64.
17. Elson EL, Qian H. Interpretation of fluorescence correlation spectroscopy and photobleaching recovery in terms of molecular interactions. Methods Cell Biol. 1989;30:307–32.

18. Schwille P. Fluorescence correlation spectroscopy and its potential for intracellular applications. Cell Biochem Biophys. 2001;34(3):383–408.
19. Schwille P, Haupts U, Maiti S, Webb WW. Molecular dynamics in living cells observed by fluorescence correlation spectroscopy with one- and two-photon excitation. Biophys J. 1999;77 (4):2251–65.
20. Sengupta P, Balaji J, Maiti S. Measuring diffusion in cell membranes by fluorescence correlation spectroscopy. Methods. 2002;27(4):374–87.
21. Day CA, Kenworthy AK. Tracking microdomain dynamics in cell membranes. Biochim Biophys Acta. 2009;1788(1):245–53.
22. Qian H, Sheetz MP, Elson EL. Single particle tracking. Analysis of diffusion and flow in two-dimensional systems. Biophys J. 1991;60(4):910–21.
23. Saxton MJ. Single-particle tracking: effects of corrals. Biophys J. 1995;69(2):389–98.
24. Saxton MJ, Jacobson KA. Single-particle tracking: applications to membrane dynamics. Annu Rev Biophys Biomol Struct. 1997;26:373–99.
25. Simson R, Sheets ED, Jacobson K. Detection of temporary lateral confinement of membrane proteins using single-particle tracking analysis. Biophys J. 1995;69(3):989–93.
26. Simson R, Yang B, Moore SE, Doherty P, Wash FS, Jacobson KA. Structural mosaicism on the submicron sacale in the plasma membrane. Biophys J. 1998;74(1):297–308.
27. Wu H-M, Lin Y-H, Yen T-C, Hsieh C-L. Nanoscopic substructures of raft-mimetic liquid-ordered membrane domains revealed by high-speed single-particle tracking. Sci Rep. 2016;6:20542.
28. Kim SA, Schwille P. Intracellular applications of fluorescence correlation spectroscopy: prospects for neuroscience. Curr Opin Neurobiol. 2003;13:583–90.
29. Eggeling C, Willig KI, Barrantes FJ. STED microscopy of living cells—new frontiers in membrane and neurobiology. J Neurochem. 2013;126(2):203–12.
30. Digman M, Gratton E. Imaging barriers to diffusion by pair correlation functions. Biophys J. 2009;97:665–73.
31. Sahl S, Leutenegger M, Hell S, Eggeling C. High-resolution tracking of single-molecule diffusion in membranes by confocalized and spatially differentiated fluorescence photon stream recording. ChemPhysChem. 2014;15(4):771–83.
32. Dietrich C, Yang B, Fujiwara T, Kusumi A, Jacobson K. Relationship of lipid rafts to transient confinement zones detected by single particle tracking. Biophys J. 2002;82(1 Pt 1):274–84.
33. Kapitza HG, McGregor G, Jacobson KA. Direct measurement of lateral transport in membranes by using time-resolved spatial photometry. Proc Natl Acad Sci U S A. 1985;82 (12):4122–6.
34. Ladha S, Mackie AR, Clark DC. Cheek cell membrane fluidity measured by fluorescence recovery after photobleaching and steady-state fluorescence anisotropy. J Membr Biol. 1994;142(2):223–8.
35. Niv H, Gutman O, Kloog Y, Henis YI. Activated K-Ras and H-Ras display different interactions with saturable nonraft sites at the surface of live cells. J Cell Biol. 2002;157 (5):865–72.
36. Pucadyil TJ, Mukherjee S, Chattopadhyay A. Organization and dynamics of NBD-labeled lipids in membranes analyzed by fluorescence recovery after photobleaching. J Phys Chem B. 2007;111(8):1975–83.
37. Masson JB, Dionne P, Salvatico C, Renner M, Specht CG, Triller A, Dahan M. Mapping the energy and diffusion landscapes of membrane proteins at the cell surface using high-density single-molecule imaging and Bayesian inference: application to the multiscale dynapics of glycine receptors in the neuronal membrane. Biophys J. 2014;106:74–83.
38. Monnier N, Guo S-M, Mori M, He J, Lenart P, Bathe M. Bayesian approach to MSD-based analysis of particle motion in live cells. Biophys J. 2012;103:616–26.
39. Türkcan S, Alexandrou A, Masson JB. A Bayesian inference scheme to extract diffusivity and potential fields from confined single-molecule trajectories. Biophys J. 2012;102:2288–98.

40. Türkcan S, Masson JB. Bayesian decision free for the classification of the model of motion in single-molecule trajectories. PLoS One. 2013;8:e82799.
41. Manzo C, van Zanten TS, Saha S, Torreno-Pina JA, Mayor S, G.-P. M.F. PSF decomposition of nanoscopy images via Bayesian analysis unravels distinct molecular organization of the cell membrane. Sci Rep. 2014;4:4354.
42. Chenouard N, Smal I, de Chaumont F, Maška M, Sbalzarini IF, Gong Y, Cardinale J, Carthel C, Coraluppi S, Winter M, Cohen AR, Godinez WJ, Rohr K, Kalaidzidis Y, Liang L, Duncan J, Shen H, Xu Y, Magnusson KE, Jaldén J, Blau HM, Paul-Gilloteaux P, Roudot P, Kervrann C, Waharte F, Tinevez JY, Shorte SL, Willemse J, Celler K, van Wezel GP, Dan HW, Tsai YS, Ortiz de Solórzano C, Olivo-Marin JC, Meijering E. Objective comparison of particle tracking methods. Nat Methods. 2014;11:281–9.
43. Cecchini M, Changeux JP. The nicotinic acetylcholine receptor and its prokaryotic homologues: structure, conformational transitions & allosteric modulation. Neuropharmacology. 2015;96(Pt B):137–49.
44. Nys M, Kesters D, Ulens C. Structural insights into Cys-loop receptor function and ligand recognition. Biochem Pharmacol. 2013;86:1042–53.
45. Barrantes FJ. Modulation of nicotinic acetylcholine receptor function through the outer and middle rings of transmembrane domains. Curr Opin Drug Discov Devel. 2003;6(5):620–32.
46. Karlin A. Emerging structure of the nicotinic acetylcholine receptors. Nat Rev Neurosci. 2002;3:102–14.
47. Barrantes FJ. Endogenous chemical receptors: some physical aspects. Annu Rev Biophys Bioeng. 1979;8:287–321.
48. Sanes JR, Lichtman JW. Induction, assembly, maturation and maintenance of a postsynaptic apparatus. Nat Rev Neurosci. 2001;2(11):791–805.
49. Salpeter MM, Loring RH. Nicotinic acetylcholine receptors in vertebrate muscle: properties, distribution and neural control. Prog Neurobiol. 1985;25(4):297–325.
50. Pierron M, Pinan-Lucarre B, Bessereau JL. Preventing illegitimate extrasynaptic acetylcholine receptor clustering requires the RSU-1 protein. J Neurosci. 2016;36(24):6525–37.
51. Burden SJ, Yumoto N, Zhang W. The role of MuSK in synapse formation and neuromuscular disease. Cold Spring Harb Perspect Biol. 2013;5(5):a009167.
52. Picciotto MR, Higley MJ, Mineur YS. Acetylcholine as a neuromodulator: cholinergic signaling shapes nervous system function and behavior. Neuron. 2012;76(1):116–29.
53. Descarries L, Gisiger V, Steriade M. Diffuse transmission by acetylcholine in the CNS. Prog Neurobiol. 1997;53(5):603–25.
54. Descarries L, Parent M. Chapter 14 – Asynaptic and synaptic innervation by acetylcholine neurons of the central nervous system. In: Pickel V, Segal M, editors. The synapse. Boston: Academic Press; 2014. p. 447–66.
55. Choquet D, Triller A. The role of receptor diffusion in the organization of the postsynaptic membrane. Nat Rev Neurosci. 2003;4(4):251–65.
56. Choquet D, Triller A. The dynamic synapse. Neuron. 2013;80:691–703.
57. Holcman D, Triller A. Modeling synaptic dynamics driven by receptor lateral diffusion. Biophys J. 2006;91(7):2405–15.
58. Triller A, Choquet D. New concepts in synaptic biology derived from single-molecule imaging. Neuron. 2008;59(3):359–74.
59. Bear MF, Malenka RC. Synaptic plasticity: LTP and LTD. Curr Opin Neurobiol. 1994;4(3):389–99.
60. Kroker KS, Rast G, Rosenbrock H. Differential effects of subtype-specific nicotinic acetylcholine receptor agonists on early and late hippocampal LTP. Eur J Pharmacol. 2011;671(1–3):26–32.
61. Stevens C. A millon dollar question: does LTP = memory? Neuron. 1998;20:1–2.
62. Chen L, Yamada K, Nabeshima T, Sokabe M. α7 nicotinic acetylcholine receptor as a target to rescue deficit in hippocampal LTP induction in β-amyloid infused rats. Neuropharmacology. 2006;50(2):254–68.

63. Ma L, Turner D, Zhang J, Wang Q, Wang M, Shen J, Zhang S, Wu J. Deficits of synaptic functions in hippocampal slices prepared from aged mice null α7 nicotinic acetylcholine receptors. Neurosci Lett. 2014;570:97–101.
64. Ondrejcak T, Wang Q, Kew JNC, Virley DJ, Upton N, Anwyl R, Rowan MJ. Activation of α7 nicotinic acetylcholine receptors persistently enhances hippocampal synaptic transmission and prevents Aß-mediated inhibition of LTP in the rat hippocampus. Eur J Pharmacol. 2012;677(1–3):63–70.
65. Broide RS, Leslie FM. The alpha7 nicotinic acetylcholine receptor in neuronal plasticity. Mol Neurobiol. 1999;20(1):1–16.
66. Axelrod D, Koppel DE, Schlessinger J, Elson E, Webb WW. Mobility measurement by analysis of fluorescence photobleaching recovery kinetics. Biophys J. 1976;16(9):1055–69.
67. Heuser JE, Salpeter SR. Organization of acetylcholine receptors in quick-frozen, deep-etched, and rotary-replicated *Torpedo* postsynaptic membrane. J Cell Biol. 1979;82:150–73.
68. Roccamo AM, Pediconi MF, Aztiria E, Zanello L, Wolstenholme A, Barrantes FJ. Cells defective in sphingolipids biosynthesis express low amounts of muscle nicotinic acetylcholine receptor. Eur J Neurosci. 1999;11(5):1615–23.
69. Kumari S, Borroni V, Chaudhry A, Chanda B, Massol R, Mayor S, Barrantes FJ. Nicotinic acetylcholine receptor is internalized via a Rac-dependent, dynamin-independent endocytic pathway. J Cell Biol. 2008;181(7):1179–93.
70. Nehls S, Snapp EL, Cole NB, Zaal KJ, Kenworthy AK, Roberts TH, Ellenberg J, Presley JF, Siggia E, Lippincott-Schwartz J. Dynamics and retention of misfolded proteins in native ER membranes. Nat Cell Biol. 2000;2(5):288–95.
71. Zaal KJ, Smith CL, Polishchuk RS, Altan N, Cole NB, Ellenberg J, Hirschberg K, Presley JF, Roberts TH, Siggia E, Phair RD, Lippincott-Schwartz J. Golgi membranes are absorbed into and reemerge from the ER during mitosis. Cell. 1999;99(6):589–601.
72. Edidin M. Fluorescence photobleaching and recovery, FPR, in the analysis of membrane structure and dynamics. In: Damjanocich S, Edidin M, Szollosi J, editors. Mobility and proximity in biological membranes. Boca Raton, FL: CRC Press; 1994. p. 109–35.
73. Guo L, Har JY, Sankaran J, Hong Y, Kannan B, Wohland T. Molecular diffusion measurement in lipid bilayers over wide concentration ranges: a comparative study. ChemPhysChem. 2008;9(5):721–8.
74. Kenworthy AK, Nichols BJ, Remmert CL, Hendrix GM, Kumar M, Zimmerberg J, Lippincott-Schwartz J. Dynamics of putative raft-associated proteins at the cell surface. J Cell Biol. 2004;165(5):735–46.
75. Baier CJ, Gallegos CE, Levi V, Barrantes FJ. Cholesterol modulation of nicotinic acetylcholine receptor surface mobility. Eur Biophys J. 2010;39(2):213–27.
76. Stya M, Axelrod D. Mobility and detergent extractability of acetylcholine receptors on cultured rat myotubes: a correlation. J Cell Biol. 1983;97:48–51.
77. Stya M, Axelrod D. Mobility of extrajunctional acetylcholine receptors on denervated adult muscle fibers. J Neurosci. 1984;4:70–4.
78. Borroni V, Baier CJ, Lang T, Bonini I, White MM, Garbus I, Barrantes FJ. Cholesterol depletion activates rapid internalization of submicron-sized acetylcholine receptor domains at the cell membrane. Mol Membr Biol. 2007;24(1):1–15.
79. Kellner RR, Baier CJ, Willig KI, Hell SW, Barrantes FJ. Nanoscale organization of nicotinic acetylcholine receptors revealed by stimulated emission depletion microscopy. Neuroscience. 2007;144(1):135–43.
80. Almarza G, Sanchez F, Barrantes FJ. Transient cholesterol effects on nicotinic acetylcholine receptor cell-surface mobility. PLoS One. 2014;9(6):e100346.
81. Simonson PD, DeBerg HA, Ge P, Alexander JK, Jeyifous O, Green WN, Selvin PR. Counting bungarotoxin binding sites of nicotinic acetylcholine receptors in mammalian cells with high signal/noise ratios. Biophys J. 2010;99(10):L81–3.

82. Barrantes FJ, Neugebauer DC, Zingsheim HP. Peptide extraction by alkaline treatment is accompanied by rearrangement of the membrane-bound acetylcholine receptor from Torpedo marmorata. FEBS Lett. 1980;112(1):73–8.
83. Burden SJ, Depalma RL, Gottesman GS. Crosslinking of proteins in acetylcholine receptor-rich membranes: association between the β-subunit and the 43 kd subsynaptic protein. Cell. 1983;35:687–92.
84. Ramarao MK, Cohen JB. Mechanism of nicotinic acetylcholine receptor cluster formation by rapsyn. Proc Natl Acad Sci U S A. 1998;95:4007–12.
85. Piguet J, Schreiter C, Segura J, Voguel H, Hovius R. Acetylcholine receptor organization in membrane domains in muscle cells: evidence for rapsyn-independent and rapsyn-dependent mechanisms. Int J Biol Chem. 2011:363–9.
86. O'Connell KM, Tamkun MM. Targeting of voltage-gated potassium channel isoforms to distinct cell surface microdomains. J Cell Sci. 2005;118(Pt 10):2155–66.
87. Nishimura SY, Vrljic M, Klein LO, McConnell HM, Moerner WE. Cholesterol depletion induces solid-like regions in the plasma membrane. Biophys J. 2006;90(3):927–38.
88. Vrljic M, Nishimura SY, Moerner WE, McConnell HM. Cholesterol depletion suppresses the translational diffusion of class II major histocompatibility complex proteins in the plasma membrane. Biophys J. 2005;88(1):334–47.
89. Sun M, Northup N, Marga F, Huber T, Byfield FJ, Levitan I, et al. The effect of cellular cholesterol on membrane-cytoskeleton adhesion. J. Cell Sci. 2007;120(Pt 13):2223–31. doi:10.1242/jcs.001370.
90. Orr G, Hu D, Ozcelik S, Opresko LK, Wiley HS, Colson SD. Cholesterol dictates the freedom of EGF receptors and HER2 in the plane of the membrane. Biophys J. 2005;89(2):1362–73.
91. Oliferenko S, Paiha K, Harder T, Gerke V, Schwarzler C, Schwarz H, Beug H, Gunthert U, Huber LA. Analysis of CD44-containing lipid rafts: recruitment of annexin II and stabilization by the actin cytoskeleton. J Cell Biol. 1999;146(4):843–54.
92. Shvartsman DE, Gutman O, Tietz A, Henis YI. Cyclodextrins but not compactin inhibit the lateral diffusion of membrane proteins independent of cholesterol. Traffic. 2006;7(7):917–26.
93. Bruses J, Chauvet N, Rutishauser U. Membrane lipid rafts are necessary for the maintenance of the (alpha)7 nicotinic acetylcholine receptor in somatic spines of ciliary neurons. J Neurosci. 2001;21(2):504–12.
94. Gomez-Varela D, Kohl T, Schmidt M, Rubio ME, Kawabe H, Nehring RB, Schafer S, Stuhmer W, Pardo LA. Characterization of Eag1 channel lateral mobility in rat hippocampal cultures by single-particle-tracking with quantum dots. PLoS One. 2010;5(1):e8858.
95. Hotulainen P, Hoogenraad CC. Actin in dendritic spines: connecting dynamics to function. J Cell Biol. 2010;189(4):619–29.
96. Feder TJ, Brust-Mascher I, Slattery JP, Baird B, Webb WW. Constrained diffusion or immobile fraction on cell surfaces: a new interpretation. Biophys J. 1996;70(6):2767–73.
97. Bloch RJ, Velez M, Krikorian JG, Axelrod D. Microfilaments and actin-associated proteins at sites of membrane-substrate attachment within acetylcholine receptor clusters. Exp Cell Res. 1989;182:583–96.
98. Dai Z, Luo X, Xie H, Peng HB. The actin-driven movement and formation of acetylcholine receptor clusters. J Cell Biol. 2000;150(6):1321–34.
99. Pumplin DW, Strong JC. Acetylcholine receptor clusters of rat myotubes have at least three domains with distinctive cytoskeletal and membranous components. J Cell Biol. 1989;109:739–53.
100. Honigmann A, Sadeghi S, Keller J, Hell SW, Eggeling C, Vink R. A lipid bound actin meshwork organizes liquid phase separation in model membranes. Elife. 2014;3:e01671.
101. Lenne P-F, Wawrezinieck L, Conchonaud F, Wurtz O, Boned A, Guo X-J, et al. Dynamic molecular confinement in the plasma membrane by microdomains and the cytoskeleton meshwork. EMBO J. 2006;25:3245–56. doi:10.1038/sj.emboj.7601214.
102. Maxfield FR. Plasma membrane microdomains. Curr. Opin. Cell Biol. 2002;14:483–7. doi:10.1016/S0955-0674(02)00351-4.

103. Kwik J, Boyle S, Fooksman D, Margolis L, Sheetz MP, Edidin M. Membrane cholesterol, lateral mobility, and the phosphatidylinositol 4,5-bisphosphate-dependent organization of cell actin. Proc. Natl. Acad. Sci. U.S.A. 2003;100:13964–9. doi:10.1073/pnas.2336102100.
104. Saka SK, Honigmann A, Eggeling C, Hell SW, Lang T, Rizzoli SO. Multi-protein assemblies underlie the mesoscale organization of the plasma membrane. Nat Commun. 2014;5:1–14.
105. Kusumi A, Ike H, Nakada C, Murase K, Fujiwara T. Single-molecule tracking of membrane molecules: plasma membrane compartmentalization and dynamic assembly of raft-philic signaling molecules. Semin Immunol. 2005;17(1):3–21.
106. Triller A, Choquet D. Synaptic structure and diffusion dynamics of synaptic receptors. Biol Cell. 2003;95(7):465–76.
107. Kusumi A, Suzuki K. Toward understanding the dynamics of membrane-raft-based molecular interactions. Biochim Biophys Acta. 2005;1746(3):234–51.
108. Ritchie K, Shan XY, Kondo J, Iwasawa K, Fujiwara T, Kusumi A. Detection of non-Brownian diffusion in the cell membrane in single molecule tracking. Biophys J. 2005;88(3):2266–77.
109. Hoch W. Formation of the neuromuscular junction. Agrin and its unusual receptors. Eur. J. Biochem. 1999;265:1–10. doi:10.1046/j.1432-1327.1999.00765.x.
110. Wenz JJ, Borroni V, Barrantes FJ. Statistical analysis of high-resolution light microscope images reveals effects of cytoskeleton-disrupting drugs on the membrane organization of the nicotinic acetylcholine receptor. J Membr Biol. 2010;235(3):163–75.
111. Alexander JK, Govind AP, Drisdel RC, Blanton MP, Vallejo Y, Lam TT, Green WN. Palmitoylation of nicotinic acetylcholine receptors. J Mol Neurosci. 2010;40:12–20.
112. Drisdel RC, Manzana E, Green WN. The role of palmitoylation in functional expression of nicotinic alpha7 receptors. J Neurosci. 2004;24:10502–10.
113. Rudell JB, Ferns MJ. Regulation of muscle acetylcholine receptor turnover by β subunit tyrosine phosphorylation. Dev Neurobiol. 2013;73:399–410.
114. Talwar S, Lynch JW. Phosphorylation mediated structural and functional changes in pentameric ligand-gated ion channels: implications for drug discovery. Int J Biochem Cell Biol. 2014;53:218–23.
115. Axelrod D. Crosslinkage and visualization of acetylcholine receptors on myotubes with biotinylated alpha-bungarotoxin and fluorescent avidin. Proc Natl Acad Sci U S A. 1980;77 (8):4823–7.
116. Sieb JP. Myasthenia gravis: an update for the clinician. Clin Exp Immunol. 2014;175 (3):408–18.
117. Huganir RL, Nicoll RA. AMPARs and synaptic plasticity: the last 25 years. Neuron. 2013;80 (3):704–17.
118. Bashir ZI, Alford S, Davies SN, Randall AD, Collingridge GL. Long-term potentiation of NMDA receptor-mediated synaptic transmission in the hippocampus. Nature. 1991;349 (6305):156–8.
119. Cui Z, Wang H, Tan Y, Zaia KA, Zhang S, Tsien JZ. Inducible and reversible NR1 knockout reveals crucial role of the NMDA receptor in preserving remote memories in the brain. Neuron. 2004;41(5):781–93.
120. Li F, Tsien JZ. Memory and the NMDA receptors. N Engl J Med. 2009;361(3):302–3.
121. Besshoh S, Bawa D, Teves L, Wallace MC, Gurd JW. Increased phosphorylation and redistribution of NMDA receptors between synaptic lipid rafts and post-synaptic densities following transient global ischemia in the rat brain. J Neurochem. 2005;93(1):186–94.
122. Frank C, Giammarioli AM, Pepponi R, Fiorentini C, Rufini S. Cholesterol perturbing agents inhibit NMDA-dependent calcium influx in rat hippocampal primary culture. FEBS Lett. 2004;566(1–3):25–9.
123. Gotti C, Clementi F, Fornari A, Gaimarri A, Guiducci S, Manfredi I, Moretti M, Pedrazzi P, Pucci L, Zoli M. Structural and functional diversity of native brain neuronal nicotinic receptors. Biochem Pharmacol. 2009;78:703–11.

124. Cuevas J, Berg DK. Mammalian nicotinic receptors with alpha7 subunits that slowly desensitize and rapidly recover from alpha-bungarotoxin blockade. J Neurosci. 1998;18:10335–44.
125. Fabian-Fine R, Skehel P, Errington ML, Davies HA, Sher E, Stewart MG, Fine A. Ultrastructural distribution of the 7 nicotinic acetylcholine receptor subunit in rat hippocampus. J Neurosci. 2001;21:7993–8003.
126. Buerli T, Baer K, Ewers H, Sidler C, Fuhrer C, Fritschy JM. Single particle tracking of alpha7 nicotinic AChR in hippocampal neurons reveals regulated confinement at glutamatergic and GABAergic perisynaptic sites. PLoS One. 2010;5(7):e11507.
127. Alkondon M, Pereira EF, Barbosa CT, Albuquerque EX. Neuronal nicotinic acetylcholine receptor activation modulates gamma-aminobutyric acid release from CA1 neurons of rat hippocampal slices. Pharmacol Exp Ther. 1997;283:1396–411.
128. Alkondon MA, E.X. The nicotinic acetylcholine receptor subtypes and their function in the hippocampus and cerebral cortex. Prog Brain Res. 2004;145:109–20.
129. Banerjee C, Nyengaard JR, Wevers A, de Vos RA, Jansen Steur EN, Lindstrom J, Pilz K, Nowacki S, Bloch W, Schroder H. Cellular expression of alpha7 nicotinic acetylcholine receptor protein in the temporal cortex in Alzheimer's and Parkinson's disease—a stereological approach. Neurobiol Dis. 2000;7:666–72.
130. Charrier C, Ehrensperger MV, Dahan M, Levy S, Triller A. Cytoskeleton regulation of glycine receptor number at synapses and diffusion in the plasma membrane. J Neurosci. 2006;26:8502–11.
131. Dahan M, Levi S, Luccardini C, Rostaing P, Riveau B, Triller A. Diffusion dynamics of glycine receptors revealed by single-quantum dot tracking. Science. 2003;302(5644):442–5.
132. Ehlers MD, Heine M, Groc L, Lee MC, Choquet D. Diffusional trapping of GluR1 AMPA receptors by input-specific synaptic activity. Neuron. 2007;54(3):447–60.
133. Meier J, Vannier C, Serge A, Triller A, Choquet D. Fast and reversible trapping of surface glycine receptors by gephyrin. Nat Neurosci. 2001;4(3):253–60.
134. Ehrensperger MV, Hanus C, Vannier C, Triller A, Dahan M. Multiple associations states between glycine receptors and gephyrin identified by SPT analysis. Biophys J. 2007;92:442–5.
135. Allison DW, Gelfand VI, Spector I, Craig AM. Role of actin in anchoring postsynaptic receptors in cultured hippocampal neurons: differential attachment of NMDA versus AMPA receptors. J Neurosci. 1998;18:2423–36.
136. Specht C, Izeddin I, Rodriguez PC, El Beheiry M, Rostaing P, Darzacq X, Dahan M, Triller A. Quantitative nanoscopy of inhibitory synapses: counting gephyrin molecules and receptor binding sites. Neuron. 2013;79:308–21.
137. Dejanovic B, Semtner M, Ebert S, Lamkemeyer T, Neuser F, Lüscher B, Meier JC, Schwarz G. Palmitoylation of gephyrin controls receptor clustering and plasticity of GABAergic synapses. PLoS Biol. 2014;12:e1001908.
138. Wanaverbecq N, Semyanov A, Pavlov I, Walker MC, Kullmann DM. Cholinergic axons modulate GABAergic signaling among hippocampal interneurons via postsynaptic alpha 7 nicotinic receptors. J Neurosci. 2007;27:5683–93.
139. Ji D, Dani JA. Inhibition and disinhibition of pyramidal neurons by activation of nicotinic receptors on hippocampal interneurons. J Neurophysiol. 2000;83:2682–90.
140. Rosza B, Katona G, Kaszas A, Szipocs R, Vizi ES. Dendritic nicotinic receptors modulated backpropagating action potentials and long-term plasticity of interneurons. Eur J Neurosci. 2008;27:364–77.
141. Dani JA, Bertrand D. Nicotinic acetylcholine receptors and nicotinic cholinergic mechanisms of the central nervous system. Annu Rev Pharmacol Toxicol. 2007;47:699–729.
142. McCann CM, Tapia JC, Kim H, Coggan JS, Lichtman JW. Rapid and modifiable neurotransmitter receptor dynamics at a neuronal synapse in vivo. Nat Neurosci. 2008;11(7):807–15.
143. Akaaboune M, Cullican SM, Turney SG, Lichtman JW. Rapid and reversible effect of activity on acetylcholine receptor density at the neuromuscular junction in vivo. Science. 1999;286:503–7.

144. Bruneau EG, Akaaboune M. The dynamics of recycled acetylcholine receptors at the neuromuscular junction in vivo. Development. 2006;133(22):4485–93.
145. Halff AW, Gómez-Varela D, John D, Berg DK. A novel mechanism for nicotinic potentiation of glutamatergic synapses. J Neurosci. 2014;34(6):2051–64.
146. Fernandes CC, Berg DK, Gomez-Varela D. Lateral mobility of nicotinic acetylcholine receptors on neurons is determined by receptor composition, local domain, and cell type. J Neurosci. 2010;30(26):8841–51.
147. Kass RS. The channelopathies: novel insights into molecular and genetic mechanisms of human disease. J Clin Invest. 2005;115:1986–9.
148. Perez-Lloret S, Barrantes FJ. Deficits in cholinergic neurotransmission and their clinical correlates in Parkinson's disease. NPJ Parkinsons Dis. 2016;2:16001.
149. Remmers C, Sweet RA, Penzes P. Abnormal kalirin signaling in neuropsychiatric disorders. Brain Res Bull. 2014;103:29–38.

Chapter 10
Dynamics of Membrane Proteins

Sahil Lall and M.K. Mathew

Abstract Transmembrane proteins inhabit a highly asymmetric environment that is, to a first approximation, two-dimensional. Many of them serve to transmit information between aqueous compartments, while others serve as conduits for the transport of material between compartments. In serving these functions they have to adopt at least two stable structures and rapidly interconvert between them. The paucity of atomic resolution structures has been limiting in elucidating the mechanisms by which these proteins carry out their functions. However, this century has seen the determination of the three-dimensional structures of a number of membrane proteins, leading to the start of an understanding of the dynamics displayed by them within the bilayer. Without attempting to be exhaustive, we provide illustrative examples of dynamics in membrane proteins and review their underlying mechanisms as they insert, fold and function in biological membranes.

10.1 Introduction

Proteins can be broadly classified by the milieu they reside in. Those embedded in the non-polar environment of membranes and which have portions that traverse the membrane, are called integral membrane proteins. These proteins carry out a variety of functions ranging from providing a local structural framework at the membrane to the transmission of physiologically critical material and information across membranes. Inasmuch as they form the interface between the cell and its environment, plasma membrane resident proteins have been the subject of intense study. However, the detailed characterisation of these proteins and their mechanistic understanding has been impeded because of the challenge of obtaining purified protein in sufficient quantities. Nevertheless, there has been progress made into structure determination of membrane proteins over the past two decades. While only 1% or so of protein structures deposited in the Protein Data Bank (PDB) over this period are of membrane proteins, the number of membrane protein structures determined in the twenty-first century greatly exceed the total number determined

S. Lall • M.K. Mathew (✉)
National Centre for Biological Sciences, TIFR, Bangalore 560065, Karnataka, India
e-mail: mathew@ncbs.res.in

A. Chattopadhyay (ed.), *Membrane Organization and Dynamics*, Springer Series in Biophysics 20, DOI 10.1007/978-3-319-66601-3_10

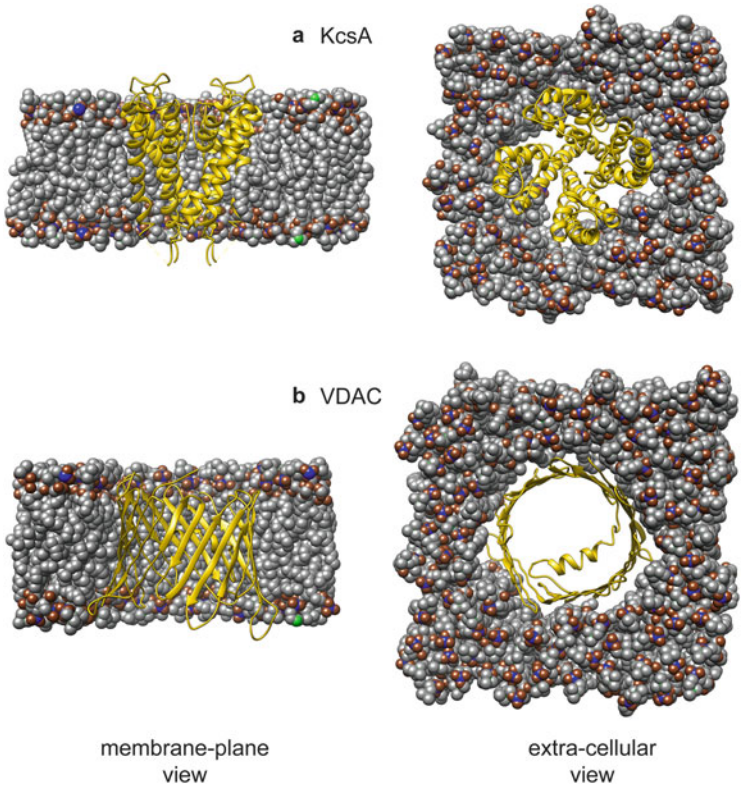

Fig. 10.1 Two major categories of membrane proteins. Integral Membrane Proteins are either all-helical as in **(a)** or β-barrel as in **(b)**. (**a**) KcsA—the first ion channel to be crystallised is an all helix protein; shown here embedded in the lipid bilayer. It is representative of the closed state of almost all potassium channels. The pore has a selectivity filter at the level of lipid head-groups in the upper leaflet visible in the cut-away model in the *left panel*. The C-terminus of the helices obstruct the channel. The *right panel* highlights the constricted channel aperture. On the other hand, there is Voltage Dependent Anion Channel (VDAC) (**b**). It is an interesting β-barrel protein found on the outer membrane of mitochondria. It posesses an atypical odd number of β-strands unlike other β-barrels which have an even number. The *right panel* shows the barrel from the top highlighting the lone helix that is hypothesised to alter the conductivity of the protein. Both (**a**) and (**b**) are drawn surrounded by a homogenous dipalmitoylphosphatidylcholine (DPPC) lipid bilayer modelled around the crystal structures available in PDB; [PDB id: 1BL8, 2JK4]

prior to this period. Armed with these static pictures, it is now becoming possible to understand the functional dynamics of membrane proteins.

The α-helix, first recognized by Linus Pauling 65 years ago [1] and the β-sheet, Pauling's "other" secondary structure [2], provided the only solutions to the problem of satisfying the hydrogen bonding requirements of the peptide bond within the bilayer (Fig. 10.1). The edges of a β-sheet would be unstable in a bilayer, hence it folds on itself to close and form a barrel in the membrane. β-barrels are seen primarily in proteins of the outer membranes of bacteria, mitochondria and plastids. While structures are available for a few β-barrel proteins (such as in Fig. 10.1),

considerably more structural and biochemical literature is available for proteins composed of transmembrane helices (TMHs). There is also a substantial bias towards information about plasma membrane proteins compared to those residing on endomembranes.

Proteins that mediate transduction of information and exchange matter across the membrane have to adopt at least two forms: one that facilitates transmission and another that does not. The interconversion between these forms is controlled by an external signal such as a ligand, voltage, pressure, temperature, etc. However, the proteins first have to be made on ribosomes as linear polypeptides, folded into their final three-dimensional (3D) structure and then be transported to their location of action where they function. Hence, the dynamics of such membrane proteins can be studied broadly at three stages: (i) insertion into the membrane and folding therein, (ii) transport to the appropriate organelle and (iii) interconversion between a transmission competent state and the ground state.

10.2 Membrane Protein Translocation/Insertional Dynamics

Protein dynamics initiate right when a polypeptide starts emerging from the ribosomal exit tunnel. The highly hydrophobic nascent polypeptides have to be folded and transported to their site of function. While there has been considerable progress studying the folding of soluble proteins, membrane proteins pose major difficulties. Unfolding membrane proteins to structure-less entities generally results in irreversible denaturation, while refolding from partially folded states fails to capture the entire process (reviewed by Stanley and Fleming [3]). A further complication occurs due to the fact that the membrane ambient into which the protein has to fold is not homogenous, being polar at the head-groups and very non-polar at the mid-plane [4].

Khorana's group showed that individual helices of bacteriorhodopsin (bR) can insert and fold independently, then assemble into a functional entity capable of binding retinal and pumping protons on absorbing light [5]. This led to the postulation of a two-stage folding process with independent insertion of individual helices, followed by their assembly into a higher order structure within the membrane [6]. Kaback's group expressed lactose permease as contiguous polypeptides and if the breaks between fragments are introduced in loop regions, the peptides could associate to mediate active lactose transport [7]. Thus, the case for two-stage folding is strong, but the data is limited to very few membrane proteins.

Recent experiments have used cell free translation systems to extend this knowledge to insertion of freshly synthesised bacteriorhodopsin into nanodiscs. These data indicate that, in this system, retinal is required for formation of the fully folded and functional form of the protein [8]. However, for most membrane proteins, we are limited to the knowledge of the machinery that promotes insertion into the membrane.

10.2.1 Prokaryotic Translocation Machinery

10.2.1.1 α-Helical Proteins

SecYEG Translocase

α-helical proteins are predominantly found in the inner membrane of Gram negative bacteria. The growing hydrophobic chain emerging from the ribosome exit tunnel is identified by a Signal Recognition Particle (SRP) [9]. A groove within the SRP recognises the non-polar signal peptide that might be the first TM segment or a region distal to it [10, 11]. The signal peptide loaded SRP is then transferred to the SecYEG translocon by the SRP-FtsY composite. FtsY is a receptor for SRP and utilises energy from GTP hydrolysis to load the nascent polypeptide on the SecYEG complex. SecY is a 10 transmembrane helix protein that appears to have two exit points [12]. One is a channel with a 3–5 Å hydrophobic constriction and the other permits lateral entry to the membrane [13, 14].

An α-helix blocks the channel in SecY and the lateral entry port between TM2-TM7 is also gated. The former is opened by signal peptide binding and the latter by protein translocation through the channel [14]. This process is initiated when the nascent polypeptide inserts into the channel as a loop. Signal peptide gets intercalated into the walls of SecY while the distal region gets close to the pore [15]. This binding moves the pore blocking helix by about 20 Å [16]. Subsequently, the lateral entry gate opens into the membrane on protein translocation into the channel, enabling insertion into the membrane. The signal sequence remains bound till the entire protein has passed through [17].

Peptide propulsion through SecY requires the force generated either by the ribosome itself [18] or by an ATPase-SecA [19] and a proton motif force [20]. SecA has a two helix finger domain which is found near the entrance of the SecYEG channel [21]. It is believed that this two helix finger pushes substrates in to the channel [22]. Moreover, binding of SecA to SecY creates a 5 Å gap in the lateral gate manned by TM2 and TM7 [21]. Hence, SecY in conjunction with SecA or the ribosome can mediate co- or post-translational insertion, respectively, in the inner membrane of Gram negative bacteria.

YidC Insertase

The YidC Insertase enables integration of membrane proteins in a SecYEG-independent manner [23]. In contrast to SecYEG translocon that can mediate both co- and post-translational translocation, YidC facilitates only post-translational translocation [24]. How a substrate protein chooses between alternate pathways to integrate into the membrane is not currently known. But, it is worth noting that YidC can associate with SecYEG to form a supercomplex [25].

The YidC structure reveals a novel fold. It has a cytoplasmic helical hairpin and a central membrane embedded groove that opens towards the cytoplasm and the

membrane. It is proposed that the cytoplasmic hairpin facilitates the entry of the substrate protein into the groove. The groove being blocked on the extracellular side, guides the processing TMH to slide into the bilayer core [26].

10.2.1.2 β-Barrel Proteins

β-barrel proteins are found in the outer membrane of Gram negative bacteria. The insertion of these outer-membrane proteins (OMPs) is mediated by a complex machinery composed of a Bam supercomplex and a few chaperones [27]. Upon synthesis in the cytoplasm, the polypeptide is carried across the inner membrane by the Sec translocon (Sect. 10.2.1.1). Once in the periplasmic space, it is bound by chaperones SurA and Skp which protect and escort the nascent OMP to the outer membrane [27]. A number of weak contacts mediate the transfer of the protein to the Bam complex where it is folded and passed into the membrane.

Multiple crystal structures are available for the 5 Bam(A–E) individual proteins that make up the supercomplex (reviewed by O'Neil et al. [28]). Moreover earlier this year, multiple groups solved the structure of the complete complex [29–31]. This has brought substantial advance into understanding the molecular architecture that inserts and aids the formation of tertiary structure of an OMP.

10.2.2 Eukaryotic Translocation Machinery

10.2.2.1 α-Helical Proteins

Despite the large number of membrane bound organelles, eukaryotes have only three sites of TMH insertion. Co-translational insertion occurs at the endoplasmic reticulum (ER), inner mitochondrial and the thylakoid membrane. Sec61 which is present on the ER membrane is a homologue of SecY [32]. Though absent in the ER, Oxa1 in the inner mitochondrial membrane and Alb3/Alb4 in chloroplasts appear to be YidC homologues in eukaryotes [24]. Post-translational translocation has also been observed at the ER mediated by Sec62 and Sec63. There are other proteins in the ER that aid the translocation in specific ways (reviewed in Denks et al. [33]) and include TRAM, TRAP, oligosaccharyl transferase, BiP, etc. The process of targeting proteins to different membranes is beyond the scope of this article but the reader is referred to an excellent review [34].

10.2.2.2 β-Barrel Proteins

In Eukaryotes, β-barrel proteins are found predominantly on the outer membrane of mitochondria and plastids. Homologues of the Prokaryotic OMP insertion and translocation machinery are found in the Eukaryotic organelles [35]. In the mitochondrion, polypeptides are imported from the cytoplasm through the TOM

(Translocase of Outer Membrane) complex where TOM40, itself a β-barrel, forms the protein conduction channel. The imported protein is stabilised by small TIM (Translocase of Inner Membrane) chaperones—Tim9 & Tim10 and MIA (Mitochondrial Inner membrane Assembly) chaperones. The SAM (Sorting and Assembly Machinery) complex finishes the insertion of β-barrel precursors into the outer membrane. In the SAM complex, SAM50 is thought to perform the same role as the Prokaryotic protein—BamA [36]. The chloroplast membrane protein insertion pathway remains relatively obscure with only a few implicated proteins (Tic-Toc complex) that have been characterised [37].

10.3 Energetics Underlying Protein Dynamics in Lipid Bilayers

Integral membrane proteins, especially TM helices, upon reaching their destination are met with similar and dissimilar hydrophobic molecules. In other words, they reside in a complex milieu where lateral interactions between adjacent helices occur in competition with interactions with surrounding lipids and also with the encapsulating water. Furthermore, there are global bilayer effects which arise due to the electric field across the membrane and phase separation amongst lipids. Several studies have been undertaken to elucidate the forces stabilising the final 3D structures adopted by TMHs. Some understanding of the energetics of transitions between stable states has also been obtained in a few cases.

10.3.1 Van der Waal's Interactions

Van der Waals (VdW) packing interactions contribute significantly to the integrity of the core of membrane proteins. This is in contrast to soluble proteins where the core is stabilised by hydrophobic interactions [38]. However, membrane proteins cannot utilise the entropic gain of partitioning away from water if their interactions occur in the interior of the bilayer. The first example that emphasized the importance of VdW interactions in membrane protein dynamics came from studying the transmembrane helix (TMH) of Glycophorin A (GpA) [39]. Interhelical packing in GpATM was more stabilising compared to helix-lipid interactions, thereby promoting its homo-dimerization. The dimer interface in GpA is formed by a GxxxG motif where the Glycines occur on the same side of the lone TMH of GpA [40]. GxxxG has become probably the most studied dimerization motif in membranes and we take it up in more detail in Sect. 10.4.1. In addition, the VdW packing in membrane proteins is optimized for function. For instance, bR has only a fourth of void space in the interior of the protein when compared to mechanosensitive channels like MscL (Mechanosensitive Channel of Large conductance) which are

loosely packed [41]. The empty pockets in receptors and channels allows for conformational flexibility required to undergo gating transitions [41].

10.3.2 Hydrogen Bonding

Hydrogen bonding is widespread in membrane proteins. Apart from participating in secondary structure formation, hydrogen bonding is also critical for tertiary structure formation. However, experimental determinations of the contribution of hydrogen bonds to stability fall short by 3.5–4.5 kcal mol^{-1} of the expected value in several cases [42]. Nevertheless, a single polar residue has been shown sufficient to drive homo-dimerization of an otherwise hydrophobic model TMH [43, 44]. The contribution of Glycines is also particularly well studied in the context of hydrogen bonding in membranes. Especially, the GAS_{Right}/GxxxG/GG4 motif has been shown to be partly stabilised by hydrogen-bonding [45].

10.3.3 Salt Bridges

Salt bridge interactions are thought to contribute over long range [46]. Debye lengths in the interior of membranes can be very long compared to those in the aqueous phase. Further, the energy of all electrostatic interactions is enhanced in the low dielectric of the bilayer. Making a salt-bridge in a hydrophobic membrane is also energetically favoured when the contributing charged residues are in close proximity as seen in bacteriorhodopsin [47, 48]. Since burying a charged residue in the bilayer core is energetically costly, salt-bridges often contribute to function. There is experimental evidence supporting the role of specific salt bridges in altering the functional state of α-helical membrane proteins such as CFTR (Cystic Fibrosis Transmembrane conductance Regulator), Kcv (Potassium channel chlorella virus) [49], rhodopsin and TCR (T-cell receptor). In CFTR, a change from such coulombic interactions between R347-D924-D993 to R352-D993 can change its conductance [50]. Notably, rhodopsin becomes constitutively active upon removal of one salt-bridge [51] and salt bridge formation can promote homo/hetero-dimerization of TMH in TCR α, β and ζζ [52]. Interestingly, the dimerization in TCR occur through Aspartate and Threonine residues in preference to Glycines of GxxxG which are also present in the latter protein.

10.3.4 Aromatic–Aromatic Interactions

The WxxW, WxxY, YxxY motifs have also been shown to drive dimerization of TMHs through aromatic-aromatic interactions between Tryptophan and Tyrosine

residues [53]. These are long range (approx. 7 Å) interactions, usually considered in the context of strengthening the tertiary folded structure of integral membrane proteins [54], e.g. there are seven aromatic pairs that form in KcsA. Also, a ZAX motif, where Z = Alanine, Tryptophan, Phenylalanine, or Tyrosine and X = Alanine, Histidine, Lysine, Arginine show very high dimerization affinity in TMHs. This motif is stabilised by cation-π interactions [55]. It is the same cation-π interactions between protein and lipids that preferentially stabilise Tryptophan and Tyrosine residues at the membrane-water interface [56] and sometimes promote tilts in TM helices [57].

It should be noted that lipids in the bilayer have also been implicated in enabling interaction of TMHs and affecting function (reviewed in [58]). These interactions may be specific or non-specific and manifest themselves as change in helical tilts, perpendicular shifts of helices with respect to the membrane normal (reviewed by Lee [59]) or even inversion of helical topology post-insertion [60]. Lipids can also modulate the strength of existing dimers, shifting their dynamic equilibrium, like it is shown for the Glycophorin A TM dimer [61].

10.4 Dynamics of Helix Dimerization

The binding of ligands to signal transducing receptors on one side of the membrane, results in conformational rearrangements leading to changes in accessibility of critical residues on the other side. This alters protein-protein interactions with downstream binding partners that translates to a signal being transduced in the far compartment. Transmission of binding information across the membrane may be expected to implicate conformational rearrangements of transmembrane helices. The simplest case would involve proteins with a single transmembrane helix. We review instances of protein-protein interactions mediated by a single transmembrane helix (TMH) in different contexts focussing on well-characterised instances of bitopic proteins.

10.4.1 GxxxG Motif

The GxxxG/GG4 or the GAS_{Right} motif is a *bona-fide* motif that induces dimerization of α-helices both in bilayers and micelles. This motif was first observed in Glycophorin A (GpA) [39, 62] which itself was one of the first membrane proteins to be sequenced [63]. Shortly after the protein was sequenced, it was observed that the TM region of GpA (GpATM) is responsible for dimerization of the protein [64]. This was inferred from Dodecyl Polyacrylamide gels (SDS-PAGE) of erythrocyte ghosts and it wasn't until a decade after, that dimerization in gels could be reproduced synthetically in liposomes [65]. On mapping the dimerization interface of GpATM, it was found that a minimal sequence of GxxxG, where the 'x'

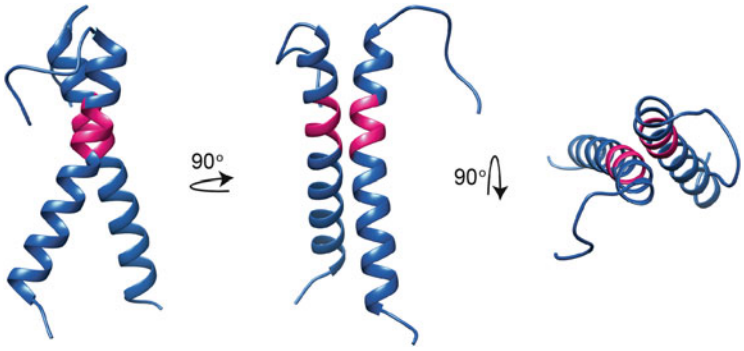

Fig. 10.2 Dimerization of Glycophorin A TM (GpATM) helix. GpATM is one of the most studied examples in the context of helical dimerization in membranes (see Sect. 10.4.1 in the main text for more details). The GxxxG motif (shown in *pink*) utilises hydrogen bonding and Van der Waals interactions to stabilise an SDS resistant helical dimer

represent dimerization insensitive amino-acids, could cause dimerization of unrelated transmembrane helices [66]. This discovery marked GxxxG as a common dimerization motif. Subsequent work which produced a NMR (Nuclear Magnetic Resonance) structure of the GpATM validated the biochemically identified interface (Fig. 10.2) [40]. Also, a search through the sequences of transmembrane helices available at the time revealed an enrichment of the said motif pointing to its physiological importance [67].

Proteins apart from GpA, like EGFR [68], ErbB4 [69], BNIP3 [70], etc. carrying a GxxxG motif form similar right handed helical TM dimers with a crossing angle of –40°. Of all the 3D structures of TM helices—bitopic and polytopic—in membrane proteins, when clustered pairwise, 12.8% had similar parallel, right-handed geometry as dimeric GpATM [71]. Proteins like RTKs (Receptor Tyrosine Kinases—ErbBs), neuropilins [72], immunologically important receptors like TLRs (Toll-like Receptors) [73], MHC (Major Histocompatibility Complex) [74] and Integrins [75, 76] have all been shown to use the GxxxG motif to dimerise. This geometry is stabilised by Van der Waals packing and hydrogen bonding (Sect. 10.3) [45].

10.4.1.1 GxxxG Is Not Sufficient for Dimerization

The experimental tools developed during discovery of GxxxG as a dimerization motif spawned a great deal of research on finding other such motifs. These validation tools utilise a similar concept of expressing TMH of interest fused with a protein that is active only as a dimer. First of these was ToxR, where the TMH dimerization induces ToxR dimerization leading to controlled expression of β-galactosidase enzyme which can be monitored [77]. Variations of this method include TOXCAT [78], POSSYCCAT [79], GALLEX [80], BACTH [81], AraTM [82] and MaMTH [83]. As a result, polar motifs (SxxxSSxxT and SxxxSSxxT) [84],

glycine zipper (GxxxGxxxG) and its variants with SAT substitutions [85], WxxW, WxxY and YxxY [53] have been shown to cause association of monomeric TMHs. Still, these dimer interfaces have limited associated literature which has been mentioned at the appropriate places.

These observations lead to the idea that any small-xxx-small motif could cause dimerization. However, this assumption was proved incorrect and believably so, as more than 55% of all predicted TM helices have a small-xxx-small motif [86]. On similar lines, it was also found that GxxxG in GpATM is also sensitive to the sequence context in which it occurs [87, 88]. Neither artificially enriching transmembrane sequences from a randomised pool nor searching the entire sequence space of naturally occurring sequences carrying the dimerization motif, reveals any common contextual scaffolding pattern for GxxxG [86].

Studying GxxxG on more proteins revealed that the presence of GxxxG by itself does not cause dimerization. When recording dimerization status of peptides in denaturing polyacrylamide gels, unlike GpATM, a vast majority do not show association [89]. Even a high sequence conservation does not ensure that the GAS_{Right} motif will convey association of the TMHs [90, 91]. In the same vein, its corollary is also true; not every TM helical interaction relies on GxxxG or small-xxx-small motif. For instance, Dap12 which is an immunologically important, signalling competent receptor that associates with other proteins such as the T-cell receptor was shown to use a polar residue to dimerise in spite of the presence of a GxxxG motif [92] (See also Sect. 10.3.3). Another example illustrating the same is discussed in Sect. 10.4.2.1.

10.4.1.2 Ab Initio Prediction of Dimerization

Despite the advancement of technology, most simulations of transbilayer segments are computationally limiting. The application of force-field based modelling has remained the only option for membrane biologists trying to study helical interactions until recently. Nevertheless, simplified approaches are being developed to circumvent the issue. PREDDIMER is one such algorithm that is available through a web server [93]. Another method—CATM, is available as an open-source compilable C++ library on the internet [45]. CATM screens the helical interface with respective to a set of 463 geometries that any GxxxG motif can afford and then optimises the resulting structure using Monte Carlo simulations. While CATM presently only computes homo-dimeric interactions, PREDDIMER can be used for both homo- and hetero-dimeric structures. Both these solutions have stood validation against the experimentally solved available 3D structures for interacting TM helices.

In summary, we can explain some of the available structures containing the GAS_{Right} motif invoking hydrogen bonding and Van der Waals forces which has enabled respectable prediction of helical dimerization in membranes. However, more work is needed to have a unifying model to understand and predict the mechanism of GxxxG driven dynamics in natural membranes.

10.4.2 Beyond a Passive GxxxG Motif

A high resolution 3D structure alone isn't enough to furnish mechanistic information about a protein. Nevertheless, it allows for more guided experiments to be performed. More importantly, it provides researchers with a starting point for simulating the molecules. Once, arguably the largest barrier for computational biologists—*de novo* tertiary structure prediction is surpassed, molecular dynamics (MD) simulations can help in understanding their dynamics in nature [94]. This approach has helped gain deeper insights into GxxxG driven dimerization and glean more general principles which can be applied to complex polytopic transmembrane proteins such as ion channels (KcsA, MscL; Sect. 10.6.1) that have a glycine zipper motif.

10.4.2.1 GxxxG Motif as a TM Switch

The signalling proteins mentioned in Sect. 10.4.1 use as diverse a range of domains on extracellular and intracellular side of the plasma membrane as the number of signals themselves. Despite the multitude of folds and structures on either side of the membrane, all these proteins traverse the plasma membrane using a single TM helix. The GxxxG motif has been implicated in stabilising the dimerization of such TMHs. But there are instances, where using two GxxxG motifs, a TMH could go from one dimeric conformation to another. If two GxxxG motifs occur at the N- and C-termini of the same helix, then it becomes straightforward to imagine how two motifs can enable two structurally distinct forms to exist (Fig. 10.3). Also, one could hypothesize the introduction of an energy barrier between the two, such that interconversion between these two forms can be coupled to another process. Thus, hinting at the potential of GxxxG as a naturally occurring intramembranous molecular switch.

It was in 2002 that the role of GxxxG as a switch was first formally hypothesised [95]. However, it was not until 11 years later that experimental evidence supporting the hypothesis was obtained in a plasma membrane bitopic receptor protein—EGFR (Epidermal Growth Factor Receptor) [68, 94]. EGFR or ErbB1 is one of the four Erb receptors of the Receptor Tyrosine Kinase family and being the cell surface receptor of the EGF peptide ligand, it has a crucial signalling role in cellular proliferation, migration and differentiation. But, its ligand-mediated activation was not clear until the TMH was studied. EGFR/ErbB1 was found to go from an active to inactive state utilising the two small-xxx-small motifs in its TMH (Fig. 10.3). Performing MD simulations on the structures of transmembrane and juxtamembrane segment obtained by NMR spectroscopy, it was demonstrated that the TMH of ErbB1/EGFR can indeed stabilise in either of the N- or C-terminal dimers. This change in the mode of dimerization controlled by EGF binding/unbinding modulates the activity of cytosolic kinase domains of EGFR [68] that has been implicated in certain cancers for over 30 years.

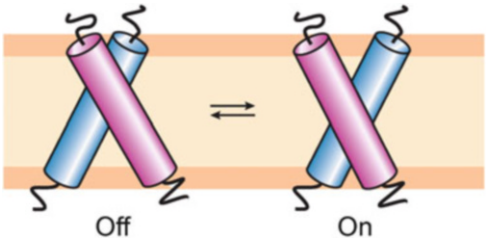

Fig. 10.3 Small-xxx-small motif in intra-membrane dynamics. A cartoon depiction of EGFR TM helices. The *helices* are proposed to switch from one conformation to another to shuttle between a signalling "On" state and an "Off" state. With both these interfaces stabilised by the small-xxx-small motif, the helices can lock-in either of them, affecting the interaction of the juxtamembrane region. This transduces the activation caused by extracellular ligand binding to kinase activity in the cytoplasm

Another notable example that demands a mention here is that of ErbB2 or HER2 (Human EGF Receptor 2). ErbB2, like EGFR, has two small-xxx-small motifs in its TMH [96]. It was shown that mutating the C-terminal GxxxG motif did not affect the dimerization potential to any significant degree [96]. Moreover, from the NMR structure it was found that ErbB2 used the N-terminal motif for homo-dimerization [97] This observation would appear confounding to the argument to have two dimerization motifs on a transmembrane helix for switching between active and inactive states. However, earlier this year another NMR structure of ErbB2 was solved [98]. Surprisingly, it was found that the TM helix of ErbB2 can indeed form a C-terminal right-handed dimer but without using the GxxxG motif. Instead, it uses an unusual (Sect. 10.4.1.1), highly hydrophobic stretch of residues IxxxVxxLLxxVLxxVFxxL. Thus, even ErbB2 can form both N- and C-terminal dimers with their potential use as a switch. Also, the C-terminal GxxxG motif of ErbB2 is suggested to be involved in hetero-dimerization [99].

10.5 TM Helices in Endomembranes

There is some evidence that STIM1 (Stromal Interaction Molecule 1) on the metazoan endoplasmic reticulum (ER) membranes can also form dimers with the small-xxx-small motif in its single transmembrane helix [100]. This dimerization has implications for the conversion of STIM1 from inactive to active state. The inactive to active state conversion is initiated by depletion of Ca^{2+} in the lumen of the ER. This signal is translocated across the ER membrane to activate Orai1, a highly selective, STIM1 gated Ca^{2+} channel. STIM together with Orai orchestrates the process of Store Operated Calcium Entry (SOCE) which is crucial for immunological signalling and cellular Ca^{2+} homeostasis; reviewed by Prakriya and Lewis [101].

ADCK3 (AarF Domain Containing Kinase 3) is a mitochondrial inner membrane protein which has been categorically studied in the context of helical dimerization. It also utilises a Glycine zipper motif (Sect. 10.4.1.1) to form homodimers [102]. ADCK3 protein has a role in Coenzyme Q (Ubiquinone) biosynthesis and a naturally occurring mutation in ADCK3 has been correlated to respiratory phenotypes and cerebellar ataxia [103]. However, the physiological relevance of homodimerization of ADCK3 TMH remains a speculation. Thus, despite the unarguable biological importance of integral proteins on endomembrane organelles, the transmembrane region of these protein remain understudied. This is exemplified by almost no literature highlighting more than a passive role for the TM region of such proteins.

10.6 Dynamics of Ion Channels

The extension of dimerization studies to multi-pass membrane proteins has been limited, due in part to the relatively small number of well characterized instances where a reversible equilibrium association can be observed and manipulated in native membranes. One system that has been studied, is the homo-dimeric ClC-ec1 Cl^-/H^+ antiporter of *Escherichia coli*. This 50-kDa membrane protein dimerizes via a membrane embedded, non-polar interface lined mainly by Isoleucines and Leucines. Chadda et al. [104] have diluted this protein into liposomes to the point where monomers and dimers can both be observed by single molecule fluorescence. Such an approach has allowed the extraction of thermodynamic parameters, including the free energy of dimerization, but fails to provide atomic level information of the dimerization process [104].

There are relatively few multi-pass membrane proteins for which a mechanism of transition between stable states has been worked out at atomic resolution. Of these, ion transporters are probably the best understood and have been extensively studied for four decades. The first structure of a membrane protein [105] was of bacteriorhodopsin (bR)—a light-driven H^+ pump—which is also the first membrane protein to have essentially all its characterised intermediates crystallised. These structures and a vast body of biophysical and mutagenesis studies have revealed individual steps of proton translocation through the protein coupled to movements of transmembrane helices. These include long range proton migration using a hydrogen-bonded chain, proton transfer between protonable groups within the membrane and also proton transfer utilising water molecules present between protein residues [106]. Consequently, it is the best understood membrane protein today. After bR, the protein that attracted concerted attention was the voltage gated potassium channel that is involved in the generation of action potentials in excitable tissues. Ion channels constitute a class of transporters that stabilize an aqueous pore across the membrane through which ions can diffuse down their electro-chemical gradient. These pores are responsible for electrical signalling in the nervous system, volume regulation and other critical physiological processes. The appearance of a

series of high resolution structures of ion channels makes it possible to infer the stimulus-driven conformational changes underlying the transition from conducting to non-conducting states and *vice-versa*.

Ion channels stabilise columns of water that traverse the membrane and hence the functional channel has multiple pore-lining helices. For a given stoichiometry of ideal helices lining the conducting pore, the enclosed pore radius depends on the tilt of the helices with respect to the membrane normal. Conversely, for a given helical tilt, the pore radius increases with the number of constituent helices. Thus, gating transitions from conducting to non-conducting states can be achieved by altering helical tilt or by changing the number of constituent helices. The disposition of side chains that project into the pore lumen is another critical feature determining effective pore radius.

10.6.1 Voltage Gated K^+ Channels

Voltage gated ion channels are tetrameric proteins contributing one helix per subunit to the aqueous pore. These channels are strongly ion-selective. Selectivity is conferred by a selectivity filter which is non-helical and tightly packed against the pore helix. This ensures that interatomic distances within the filter remain constant so as to achieve selectivity between ions as similar as Na^+ and K^+ (Fig. 10.4). Much of our knowledge of ion channel structure starts with a series of crystal structures of prokaryotic channels solved by Rod MacKinnon. The first such structure was that of the KcsA, a homo-tetrameric K^+ channel that crystallised in the Closed State [107] (Figs. 10.1 and 10.4). The protein has two transmembrane helices, one of which contributes to the lining of the aqueous pore. The re-entrant loop connecting these helices contains the selectivity filter. The pore-lining helices are at an angle to the membrane normal, and the point of closest approach or the "bundle crossing" point between them leaves insufficient room for a hydrated K^+ ion to pass. The MacKinnon group subsequently solved the structure of the MthK channel, which is also K^+ conducting, but crystallised in the Open State [108]. A comparison of these structures revealed that channel opening and closing probably proceeds through an iris-type opening, involving bending of the four pore-lining helices so that the diameter at the narrowest point is about 12 Å (Fig. 10.4).

Voltage gated ion channels undergo a transition between the Open (or conducting) and Closed (or non-conducting) States in response to changes in transmembrane electric field. These two stable states differ by about 10 Kcal mol^{-1} in energy at resting membrane potentials. For simplicity, we will not consider other states such as an activated state or any of the inactivated states, all of which are non-conducting. Each subunit of voltage gated K^+ channels (K_v channels) has six transmembrane helices with a re-entrant loop, containing the selectivity filter, connecting the last two helices. These last two helices and included loop are analogous to the KcsA and MthK channels. The last helix, S6, lines the pore while the positively charged fourth helix, S4, constitutes the voltage sensor. This

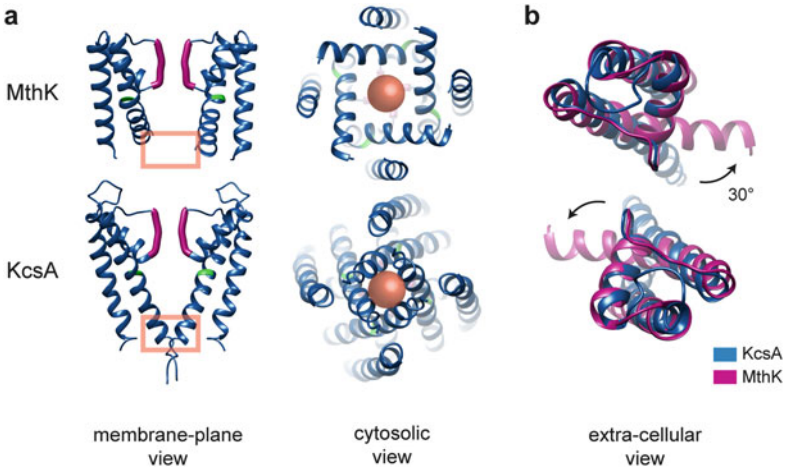

Fig. 10.4 The Open ↔ Closed transition in ion channels. The bacterial potassium channels KcsA and MthK crystallised in the Closed and Open States respectively. (**a**) Views of the two tetrameric structures without lipid and with two chains omitted for clarity. *Top*: MthK which crystallised in the Open State. Highlighted in *green* is the conserved Glycine residue that allows a kink in the pore lining helix. *Bottom*: KcsA which crystallised in the Closed State. Note the bundle crossing of the helices highlighted by a rectangle in the view at *left*. The non-helical, tightly-packed selectivity filter is shown in *magenta*. The *orange spheres* represent the space between the helix backbones towards the cytosolic end of the pore as viewed from a cytosolic vantage point. The bend in the helix in MthK that occurs around the highlighted Glycine is responsible for opening of the pore by about 12 Å to allow for a hydrated K^+ to pass. The pore lining helices splay about 30° to open the channel as represented in (**b**); [PDB id: 1BL8, 3LDC]

basic architecture of the channel is shared by all voltage gated channels whose structure has been solved to date.

The determination of crystal structures of rat $K_v1.2$ in the Open State [109] provided a starting point to understand the dynamics of the voltage driven Open to Closed transition of the channel. Deducing a model for the Closed State starting from an open structure requires integrating the vast body of biochemical and electrophysiological work, coupled with data on the mutagenesis of a significant fraction of the residues to elucidate conformational switching in these proteins. This challenge has been approached by several groups [110–112]. Unfortunately, in the absence of an experimentally determined structure for the Closed State, there is no final answer at this time. Upadhyay et al. [111] started with the crystal structure of $K_v1.2$, which has a bent S6 as in MthK (Fig. 10.4) and modelled the Closed State of the pore based on the structure of KcsA [107]. The pore lining S6 helix had to be remodelled by the action of the electric field so as to achieve the narrow "bundle crossing" seen in the KcsA structure. This involves straightening of the S6 helix, resulting in closure of the channel inasmuch as the C-γ of V408 in diagonally opposite subunits are positioned around 5.3 Å apart. This spacing generates a constriction too small to be negotiated by a hydrated K^+ ion (which is over 8 Å in diameter).

Like the potassium channels (K_v), voltage gated Na^+ channel and Ca^{2+} channels, are Closed at the resting potentials of neuronal cells, around −60 mV. They open on depolarising the cells—i.e. going to less negative potentials. The early view of channel gating was that electric field actively forced the channels into opening from a "ground" Closed State. On the other hand, Upadhyay et al argued that since the crystals were formed in the absence of a bilayer, they are perforce zero-field structures. Which is to say that the Open State of the channel is the "ground state" of the channel. This is supported by the observation that all available structures of voltage gated channels are of the Open State. The application of an inside-negative electric field applies force on the voltage sensing helix, S4, moving it towards the cytoplasmic side of the plasma membrane. S4, in turn, tugs on the S4–S5 linker so that S5 prods S6, resulting in its "unkinking" and straightening, which constricts the spacing at the bundle crossing point. The Closed State is thus a "cocked gun" kept closed by action of the electric field. Once this is relieved by depolarising the membrane, S5 (by the action of S4) moves away from S6 allowing it to swing open rapidly resulting in channel opening. Since the electric field is used to constrain S6 into the Closed State, an S4 with significantly lower charge would require a greater electric field to apply the same pressure on S6 to keep it closed. The most dramatic instance of such a shift in the voltage of channel opening is probably that reported by Miller and Aldrich [113] for the double mutant R365N: R371I of the Shaker channel which has a mid-point of activation at −180 mV as compared to the wild type channel which opens at −20 mV.

10.6.2 Ligand Gated Ion Channels

Ligand gated channels can be broadly classified, for the purposes of this review, into two classes—those with four subunits and those with five. Glutamate receptor channels are the prototypic tetrameric neurotransmitter receptors while serotonin, GABA, glycine, and acetylcholine gate pentameric receptors. Though structures of ligand binding domains have been available for some time in both liganded and free states, an understanding of how ligand binding leads to channel opening requires the structure of the full length channel. These have been elucidated over the past few years allowing the examination of plausible pathways to ligand driven transitions in these proteins.

Glutamate receptors come in several flavours, named after ligands that can activate the channel (apart from glutamate, which opens all GluRs). Structures of full length AMPA channels have been solved with either an antagonist bound [114] or with an auxiliary subunit called TARP bound to it [115]. In both cases, the channel is in a closed state. Here the narrowest point of the channel is the bundle crossing point of the M2 helices from each of the subunits, which is structurally similar to the bundle crossing seen in the S6 helices of voltage gated K^+ channels. Thus, channel opening is presumed to follow an iris opening transition as inferred for the K^+ channels. The conformational changes in the ligand binding domain effected by binding of ligand

have been observed in crystal structures of the isolated domain and the manner in which this is likely to affect the transmembrane helices is apparent [116].

The pentameric ligand gated receptor family includes receptors for nicotinic acetylcholine (nAChRs), serotonin (5-HT3Rs), glycine (GlyRs) and GABA (GABAARs). X-ray structures of the ancestral prokaryotic receptor channels were solved almost a decade ago [117–119]. These channels are symmetric homo-pentamers, whereas eukaryotic channels are often hetero-multimeric. Nonetheless, the prokaryotic channels probably represent a common minimal core. Indeed, more recent structures of a mouse serotonin receptor [120], a human GABA receptor [121] and glycine receptors from humans [122] and zebrafish [123] confirm this conservation.

The transition between Open and Closed States can be clearly seen in comparing crystal structures of the channels in the respective states. Fortunately, there are structures of the Closed State of unliganded channels (GLIC at pH 7 and the Glutamate gated Chloride channel [117, 119, 124]) as well as the strychnine-bound state of the Gly receptors [123]. In all of these structures, side chains of long, hydrophobic amino acid residues point into the lumen of the pore restricting it to under 2 Å radius precluding the transport of hydrated ions like Na^+. The presence of the hydrophobic side chains prevents passage of desolvated ions, which would need compensatory ligands from the channel lining residues. Open State structures of GLIC at pH 4 [117, 119, 124], glutamate activated chloride channel in the presence of agonists [125, 126] and the glycine receptor bound to glycine [122] are also available. The pore-lining M2 helices move outwards towards the M3 helices of the same subunit and also undergo an anticlockwise rotation which move the constricting Isoleucine side chains away from the pore and towards the helical interface. This results in an opening of the pore to allow the passage of hydrated ions. Such a model of channel opening is consistent with a variety of mutagenesis studies which implicate an activation-gate hydrophobic block in the nAChR [127], as well as the finding that mutation of the critical hydrophobic resides to polar residues results in stabilisation of the Open State.

10.7 Concluding Remarks

There are several stages in the life of a membrane protein where dynamics play a critical role. We have very little information on the folding of membrane proteins, although the machinery involved has been identified. It may be, that the process will have to be studied with the full panoply of the cellular machinery intact. Trafficking of the membrane integrated protein to its target location is well studied. Operation of the protein in its native location requires the elucidation of structures of the protein in the various stable states that it adopts. The gradually increasing repository of atomic resolution structures provide a starting point for understanding how these remarkable proteins do what they do.

References

1. Pauling L, Corey RB, Branson HR. The structure of proteins; two hydrogen-bonded helical configurations of the polypeptide chain. Proc Natl Acad Sci U S A. 1951;37:205–11.
2. Pauling L, Corey RB. The pleated sheet, a new layer configuration of polypeptide chains. Proc Natl Acad Sci U S A. 1951;37:251–6.
3. Stanley AM, Fleming KG. The process of folding proteins into membranes: challenges and progress. Arch Biochem Biophys. 2008;469:46–66.
4. White SH, Wimley WC. Hydrophobic interactions of peptides with membrane interfaces. Biochim Biophys Acta. 1998;1376:339–52.
5. Liao MJ, Huang KS, Khorana HG. Regeneration of native bacteriorhodopsin structure from fragments. J Biol Chem. 1984;259:4200–4.
6. Popot JL, Engelman DM. Membrane-protein folding and oligomerization—the 2-stage model. Biochemistry. 1990;29:4031–7.
7. Zen KH, Mckenna E, Bibi E, Hardy D, Kaback HR. Expression of lactose permease in contiguous fragments as a probe for membrane-spanning domains. Biochemistry. 1994;33:8198–206.
8. Baumann A, Kerruth S, Fitter J, Buldt G, Heberle J, Schlesinger R, Ataka K. In-situ observation of membrane protein folding during cell-free expression. PLoS One. 2016;11: e0151051.
9. Berndt U, Oellerer S, Zhang Y, Johnson AE, Rospert S. A signal-anchor sequence stimulates signal recognition particle binding to ribosomes from inside the exit tunnel. Proc Natl Acad Sci U S A. 2009;106:1398–403.
10. Batey RT, Rambo RP, Lucast L, Rha B, Doudna JA. Crystal structure of the ribonucleoprotein core of the signal recognition particle. Science. 2000;287:1232–9.
11. Janda CY, Li J, Oubridge C, Hernandez H, Robinson CV, Nagai K. Recognition of a signal peptide by the signal recognition particle. Nature. 2010;465:507–10.
12. Van den Berg B, Clemons WM Jr, Collinson I, Modis Y, Hartmann E, Harrison SC, Rapoport TA. X-ray structure of a protein-conducting channel. Nature. 2004;427:36–44.
13. Cannon KS, Or E, Clemons WM Jr, Shibata Y, Rapoport TA. Disulfide bridge formation between SecY and a translocating polypeptide localizes the translocation pore to the center of SecY. J Cell Biol. 2005;169:219–25.
14. du Plessis DJ, Berrelkamp G, Nouwen N, Driessen AJ. The lateral gate of SecYEG opens during protein translocation. J Biol Chem. 2009;284:15805–14.
15. Shaw AS, Rottier PJM, Rose JK. Evidence for the loop model of signal-sequence insertion into the endoplasmic-reticulum. Proc Nat Acad Sci U S A. 1988;85:7592–6.
16. Harris CR, Silhavy TJ. Mapping an interface of SecY (PrlA) and SecE (PrlG) by using synthetic phenotypes and in vivo cross-linking. J Bacteriol. 1999;181:3438–44.
17. Plath K, Mothes W, Wilkinson BM, Stirling CJ, Rapoport TA. Signal sequence recognition in posttranslational protein transport across the yeast ER membrane. Cell. 1998;94:795–807.
18. Connolly T, Gilmore R. Formation of a functional ribosome-membrane junction during translocation requires the participation of a GTP-binding protein. J Cell Biol. 1986;103:2253–61.
19. Osborne AR, Clemons WM Jr, Rapoport TA. A large conformational change of the translocation ATPase SecA. Proc Natl Acad Sci U S A. 2004;101:10937–42.
20. Schiebel E, Driessen AJM, Hartl F-U, Wickner W. ΔμH+ and ATP function at different steps of the catalytic cycle of preprotein translocase. Cell. 1991;64:927–39.
21. Zimmer J, Nam Y, Rapoport TA. Structure of a complex of the ATPase SecA and the protein-translocation channel. Nature. 2008;455:936–43.
22. Erlandson KJ, Miller SB, Nam Y, Osborne AR, Zimmer J, Rapoport TA. A role for the two-helix finger of the SecA ATPase in protein translocation. Nature. 2008;455:984–7.
23. Samuelson JC, Chen M, Jiang F, Moller I, Wiedmann M, Kuhn A, Phillips GJ, Dalbey RE. YidC mediates membrane protein insertion in bacteria. Nature. 2000;406:637–41.

24. Dalbey RE, Kuhn A, Zhu L, Kiefer D. The membrane insertase YidC. Biochim Biophys Acta. 2014;1843:1489–96.
25. Houben EN, Ten Hagen-Jongman CM, Brunner J, Oudega B, Luirink J. The two membrane segments of leader peptidase partition one by one into the lipid bilayer via a Sec/YidC interface. EMBO Rep. 2004;5:970–5.
26. Kumazaki K, Chiba S, Takemoto M, Furukawa A, Nishiyama K, Sugano Y, Mori T, Dohmae N, Hirata K, Nakada-Nakura Y, Maturana AD, Tanaka Y, Mori H, Sugita Y, Arisaka F, Ito K, Ishitani R, Tsukazaki T, Nureki O. Structural basis of Sec-independent membrane protein insertion by YidC. Nature. 2014;509:516–20.
27. Hagan CL, Silhavy TJ, Kahne D. beta-Barrel membrane protein assembly by the Bam complex. Annu Rev Biochem. 2011;80:189–210.
28. O'neil PK, Rollaer SE, Noinaj N, Buchanan SK. Fitting the pieces of the beta-barrel assembly machinery complex. Biochemistry. 2015;54:6303–11.
29. Bakelar J, Buchanan SK, Noinaj N. The structure of the beta-barrel assembly machinery complex. Science. 2016;351:180–6.
30. Gu Y, Li H, Dong H, Zeng Y, Zhang Z, Paterson NG, Stansfeld PJ, Wang Z, Zhang Y, Wang W, Dong C. Structural basis of outer membrane protein insertion by the BAM complex. Nature. 2016;531:64–9.
31. Han L, Zheng J, Wang Y, Yang X, Liu Y, Sun C, Cao B, Zhou H, Ni D, Lou J, Zhao Y, Huang Y. Structure of the BAM complex and its implications for biogenesis of outer-membrane proteins. Nat Struct Mol Biol. 2016;23:192–6.
32. Voorhees RM, Fernandez IS, Scheres SH, Hegde RS. Structure of the mammalian ribosome-Sec61 complex to 3.4 A resolution. Cell. 2014;157:1632–43.
33. Denks K, Vogt A, Sachelaru I, Petriman NA, Kudva R, Koch HG. The Sec translocon mediated protein transport in prokaryotes and eukaryotes. Mol Membr Biol. 2014;31:58–84.
34. Mellman I, Nelson WJ. Coordinated protein sorting, targeting and distribution in polarized cells. Nat Rev Mol Cell Biol. 2008;9:833–45.
35. Dolezal P, Likic V, Tachezy J, Lithgow T. Evolution of the molecular machines for protein import into mitochondria. Science. 2006;313:314–8.
36. Dukanovic J, Rapaport D. Multiple pathways in the integration of proteins into the mitochondrial outer membrane. Biochim Biophys Acta. 2011;1808:971–80.
37. Soll J, Schleiff E. Protein import into chloroplasts. Nat Rev Mol Cell Biol. 2004;5:198–208.
38. Harpaz Y, Gerstein M, Chothia C. Volume changes on protein folding. Structure. 1994;2:641–9.
39. Lemmon MA, Flanagan JM, Treutlein HR, Zhang J, Engelman DM. Sequence specificity in the dimerization of transmembrane alpha-helices. Biochemistry. 1992;31:12719–25.
40. Mackenzie KR, Prestegard JH, Engelman DM. A transmembrane helix dimer: structure and implications. Science. 1997;276:131–3.
41. Adamian L, Liang J. Helix-helix packing and interfacial pairwise interactions of residues in membrane proteins. J Mol Biol. 2001;311:891–907.
42. Bowie JU. Membrane protein folding: how important are hydrogen bonds? Curr Opin Struct Biol. 2011;21:42–9.
43. Choma C, Gratkowski H, Lear JD, Degrado WF. Asparagine-mediated self-association of a model transmembrane helix. Nat Struct Biol. 2000;7:161–6.
44. Gratkowski H, Lear JD, Degrado WF. Polar side chains drive the association of model transmembrane peptides. Proc Natl Acad Sci U S A. 2001;98:880–5.
45. Mueller BK, Subramaniam S, Senes A. A frequent, GxxxG-mediated, transmembrane association motif is optimized for the formation of interhelical C alpha-H hydrogen bonds. Proc Nat Acad Sci U S A. 2014;111:E888–95.
46. Kumar S, Nussinov R. Salt bridge stability in monomeric proteins. J Mol Biol. 1999;293:1241–55.
47. Balashov SP, Imasheva ES, Govindjee R, Sheves M, Ebrey TG. Evidence that aspartate-85 has a higher pK(a) in all-trans than in 13-cis Bacteriorhodopsin. Biophys J. 1996;71:1973–84.

48. Eisenstein L, Lin SL, Dollinger G, Odashima K, Termini J, Konno K, Ding WD, Nakanishi K. Ftir difference studies on apoproteins - Protonation states of aspartic and glutamic-acid residues during the photocycle of bacteriorhodopsin. J Am Chem Soc. 1987;109:6860–2.
49. Hertel B, Tayefeh S, Kloss T, Hewing J, Gebhardt M, Baumeister D, Moroni A, Thiel G, Kast SM. Salt bridges in the miniature viral channel Kcv are important for function. Eur Biophys J. 2010;39:1057–68.
50. Cui G, Freeman CS, Knotts T, Prince CZ, Kuang C, Mccarty NA. Two salt bridges differentially contribute to the maintenance of cystic fibrosis transmembrane conductance regulator (CFTR) channel function. J Biol Chem. 2013;288:20758–67.
51. Kim JM, Altenbach C, Kono M, Oprian DD, Hubbell WL, Khorana HG. Structural origins of constitutive activation in rhodopsin: role of the K296/E113 salt bridge. Proc Natl Acad Sci U S A. 2004;101:12508–13.
52. Call ME, Pyrdol J, Wiedmann M, Wucherpfennig KW. The organizing principle in the formation of the T cell receptor-CD3 complex. Cell. 2002;111:967–79.
53. Sal-Man N, Gerber D, Bloch I, Shai Y. Specificity in transmembrane helix-helix interactions mediated by aromatic residues. J Biol Chem. 2007;282:19753–61.
54. Hong H, Park S, Jimenez RH, Rinehart D, Tamm LK. Role of aromatic side chains in the folding and thermodynamic stability of integral membrane proteins. J Am Chem Soc. 2007;129:8320–7.
55. Johnson RM, Hecht K, Deber CM. Aromatic and cation-pi interactions enhance helix-helix association in a membrane environment. Biochemistry. 2007;46:9208–14.
56. Yau WM, Wimley WC, Gawrisch K, White SH. The preference of tryptophan for membrane interfaces. Biochemistry. 1998;37:14713–8.
57. Van der Wel PCA, Strandberg E, Killian JA, Koeppe RE. Geometry and intrinsic tilt of a tryptophan-anchored transmembrane α-helix determined by 2H NMR. Biophys J. 2002;83:1479–88.
58. Mcintosh TJ, Simon SA. Roles of bilayer material properties in function and distribution of membrane proteins. Annu Rev Biophys Biomol Struct. 2006;35:177–98.
59. Lee AG. How lipids affect the activities of integral membrane proteins. Biochim Biophys Acta. 2004;1666:62–87.
60. Bogdanov M, Heacock PN, Dowhan W. A polytopic membrane protein displays a reversible topology dependent on membrane lipid composition. EMBO J. 2002;21:2107–16.
61. Anbazhagan V, Schneider D. The membrane environment modulates self-association of the human GpA TM domain—implications for membrane protein folding and transmembrane signaling. Biochim Biophys Acta. 2010;1798:1899–907.
62. Lemmon MA, Flanagan JM, Hunt JF, Adair BD, Bormann BJ, Dempsey CE, Engelman DM. Glycophorin-a dimerization is driven by specific interactions between transmembrane alpha-helices. J Biol Chem. 1992;267:7683–9.
63. Segrest JP, Jackson RL, Marchesi VT, Guyer RB, Terry W. Red cell membrane glycoprotein: amino acid sequence of an intramembranous region. Biochem Biophys Res Commun. 1972;49:964–9.
64. Furthmayr H, Marchesi VT. Subunit structure of human erythrocyte glycophorin A. Biochemistry. 1976;15:1137–44.
65. Bormann BJ, Knowles WJ, Marchesi VT. Synthetic peptides mimic the assembly of transmembrane glycoproteins. J Biol Chem. 1989;264:4033–7.
66. Lemmon MA, Treutlein HR, Adams PD, Brunger AT, Engelman DM. A dimerization motif for transmembrane alpha-helices. Nat Struct Biol. 1994;1:157–63.
67. Senes A, Gerstein M, Engelman DM. Statistical analysis of amino acid patterns in transmembrane helices: the GxxxG motif occurs frequently and in association with beta-branched residues at neighboring positions. J Mol Biol. 2000;296:921–36.
68. Endres NF, Das R, Smith AW, Arkhipov A, Kovacs E, Huang Y, Pelton JG, Shan Y, Shaw DE, Wemmer DE, Groves JT, Kuriyan J. Conformational coupling across the plasma membrane in activation of the EGF receptor. Cell. 2013;152:543–56.

69. Bocharov EV, Mineev KS, Goncharuk MV, Arseniev AS. Structural and thermodynamic insight into the process of "weak" dimerization of the ErbB4 transmembrane domain by solution NMR. Biochim Biophys Acta. 2012;1818:2158–70.
70. Sulistijo ES, Mackenzie KR. Structural basis for dimerization of the BNIP3 transmembrane domain. Biochemistry. 2009;48:5106–20.
71. Walters RF, Degrado WF. Helix-packing motifs in membrane proteins. Proc Natl Acad Sci U S A. 2006;103:13658–63.
72. Sawma P, Roth L, Blanchard C, Bagnard D, Cremel G, Bouveret E, Duneau JP, Sturgis JN, Hubert P. Evidence for new homotypic and heterotypic interactions between transmembrane helices of proteins involved in receptor tyrosine kinase and neuropilin signaling. J Mol Biol. 2014;426:4099–111.
73. Godfroy JI 3rd, Roostan M, Moroz YS, Korendovych IV, Yin H. Isolated Toll-like receptor transmembrane domains are capable of oligomerization. PLoS One. 2012;7:e48875.
74. Dixon AM, Drake L, Hughes KT, Sargent E, Hunt D, Harton JA, Drake JR. Differential transmembrane domain GXXXG motif pairing impacts major histocompatibility complex (MHC) class II structure. J Biol Chem. 2014;289:11695–703.
75. Li R, Gorelik R, Nanda V, Law PB, Lear JD, Degrado WF, Bennett JS. Dimerization of the transmembrane domain of Integrin alphaIIb subunit in cell membranes. J Biol Chem. 2004;279:26666–73.
76. Schneider D, Engelman DM. Involvement of transmembrane domain interactions in signal transduction by alpha/beta integrins. J Biol Chem. 2004;279:9840–6.
77. Langosch D, Brosig B, Kolmar H, Fritz HJ. Dimerisation of the glycophorin A transmembrane segment in membranes probed with the ToxR transcription activator. J Mol Biol. 1996;263:525–30.
78. Russ WP, Engelman DM. The GxxxG motif: a framework for transmembrane helix-helix association. J Mol Biol. 2000;296:911–9.
79. Gurezka R, Langosch D. In vitro selection of membrane-spanning leucine zipper protein-protein interaction motifs using POSSYCCAT. J Biol Chem. 2001;276:45580–7.
80. Schneider D, Engelman DM. GALLEX, a measurement of heterologous association of transmembrane helices in a biological membrane. J Biol Chem. 2003;278:3105–11.
81. Karimova G, Pidoux J, Ullmann A, Ladant D. A bacterial two-hybrid system based on a reconstituted signal transduction pathway. Proc Natl Acad Sci U S A. 1998;95:5752–6.
82. Su PC, Berger BW. Identifying key juxtamembrane interactions in cell membranes using AraC-based transcriptional reporter assay (AraTM). J Biol Chem. 2012;287:31515–26.
83. Petschnigg J, Groisman B, Kotlyar M, Taipale M, Zheng Y, Kurat CF, Sayad A, Sierra JR, Mattiazzi Usaj M, Snider J, Nachman A, Krykbaeva I, Tsao MS, Moffat J, Pawson T, Lindquist S, Jurisica I, Stagljar I. The mammalian-membrane two-hybrid assay (MaMTH) for probing membrane-protein interactions in human cells. Nat Methods. 2014;11:585–92.
84. Dawson JP, Weinger JS, Engelman DM. Motifs of serine and threonine can drive association of transmembrane helices. J Mol Biol. 2002;316:799–805.
85. Kim S, Jeon TJ, Oberai A, Yang D, Schmidt JJ, Bowie JU. Transmembrane glycine zippers: physiological and pathological roles in membrane proteins. Proc Natl Acad Sci U S A. 2005;102:14278–83.
86. Teese MG, Langosch D. Role of GxxxG motifs in transmembrane domain interactions. Biochemistry. 2015;54:5125–35.
87. Doura AK, Fleming KG. Complex interactions at the helix-helix interface stabilize the glycophorin A transmembrane dimer. J Mol Biol. 2004;343:1487–97.
88. Doura AK, Kobus FJ, Dubrovsky L, Hibbard E, Fleming KG. Sequence context modulates the stability of a GxxxG-mediated transmembrane helix-helix dimer. J Mol Biol. 2004;341:991–8.
89. He L, Hoffmann AR, Serrano C, Hristova K, Wimley WC. High-throughput selection of transmembrane sequences that enhance receptor tyrosine kinase activation. J Mol Biol. 2011;412:43–54.

90. Domanska G, Motz C, Meinecke M, Harsman A, Papatheodorou P, Reljic B, Dian-Lothrop EA, Galmiche A, Kepp O, Becker L, Gunnewig K, Wagner R, Rassow J. Helicobacter pylori VacA toxin/subunit p34: targeting of an anion channel to the inner mitochondrial membrane. PLoS Pathog. 2010;6:e1000878.
91. Toutain CM, Clarke DJ, Leeds JA, Kuhn J, Beckwith J, Holland IB, JACQ A. The transmembrane domain of the DnaJ-like protein DjlA is a dimerisation domain. Mol Genet Genomics. 2003;268:761–70.
92. Call ME, Wucherpfennig KW, Chou JJ. The structural basis for intramembrane assembly of an activating immunoreceptor complex. Nat Immunol. 2010;11:1023–9.
93. Polyansky AA, Chugunov AO, Volynsky PE, Krylov NA, Nolde DE, Efremov RG. PREDDIMER: a web server for prediction of transmembrane helical dimers. Bioinformatics. 2014;30:889–90.
94. Arkhipov A, Shan Y, Das R, Endres NF, Eastwood MP, Wemmer DE, Kuriyan J, Shaw DE. Architecture and membrane interactions of the EGF receptor. Cell. 2013;152:557–69.
95. Fleishman SJ, Schlessinger J, Ben-Tal N. A putative molecular-activation switch in the transmembrane domain of erbB2. Proc Natl Acad Sci U S A. 2002;99:15937–40.
96. Mendrola JM, Berger MB, King MC, Lemmon MA. The single transmembrane domains of ErbB receptors self-associate in cell membranes. J Biol Chem. 2002;277:4704–12.
97. Bocharov EV, Mineev KS, Volynsky PE, Ermolyuk YS, Tkach EN, Sobol AG, Chupin VV, Kirpichnikov MP, Efremov RG, Arseniev AS. Spatial structure of the dimeric transmembrane domain of the growth factor receptor ErbB2 presumably corresponding to the receptor active state. J Biol Chem. 2008;283:6950–6.
98. Bragin PE, Mineev KS, Bocharova OV, Volynsky PE, Bocharov EV, Arseniev AS. HER2 transmembrane domain dimerization coupled with self-association of membrane-embedded cytoplasmic juxtamembrane regions. J Mol Biol. 2016;428:52–61.
99. Gerber D, Sal-Man N, Shai Y. Two motifs within a transmembrane domain, one for homodimerization and the other for heterodimerization. J Biol Chem. 2004;279:21177–82.
100. Ma G, Wei M, He L, Liu C, Wu B, Zhang SL, Jing J, Liang X, Senes A, Tan P, Li S, Sun A, Bi Y, Zhong L, Si H, Shen Y, Li M, Lee MS, Zhou W, Wang J, Wang Y, Zhou Y. Inside-out Ca(2+) signalling prompted by STIM1 conformational switch. Nat Commun. 2015;6:7826.
101. Prakriya M, Lewis RS. Store-operated calcium channels. Physiol Rev. 2015;95:1383–436.
102. Khadria AS, Mueller BK, Stefely JA, Tan CH, Pagliarini DJ, Senes A. A Gly-zipper motif mediates homodimerization of the transmembrane domain of the mitochondrial kinase ADCK3. J Am Chem Soc. 2014;136:14068–77.
103. Liu YT, Hersheson J, Plagnol V, Fawcett K, Duberley KE, Preza E, Hargreaves IP, Chalasani A, Laura M, Wood NW, Reilly MM, Houlden H. Autosomal-recessive cerebellar ataxia caused by a novel ADCK3 mutation that elongates the protein: clinical, genetic and biochemical characterisation. J Neurol Neurosurg Psychiatry. 2014;85:493–8.
104. Chadda R, Krishnamani V, Mersch K, Wong J, Brimberry M, Chadda A, Kolmakova-Partensky L, Friedman LJ, Gelles J, Robertson JL. The dimerization equilibrium of a ClC Cl(-)/H(+) antiporter in lipid bilayers. Elife. 2016;5:e17438.
105. Henderson R, Unwin PNT. Three-dimensional model of purple membrane obtained by electron microscopy. Nature. 1975;257:28–32.
106. Lanyi JK. Proton transfers in the bacteriorhodopsin photocycle. Biochim Biophys Acta Bioenergetics. 2006;1757:1012–8.
107. Doyle DA, Morais Cabral J, Pfuetzner RA, Kuo A, Gulbis JM, Cohen SL, Chait BT, Mackinnon R. The structure of the potassium channel: molecular basis of K+ conduction and selectivity. Science. 1998;280:69–77.
108. Jiang Y, Lee A, Chen J, Cadene M, Chait BT, Mackinnon R. The open pore conformation of potassium channels. Nature. 2002;417:523–6.
109. Long SB, Campbell EB, Mackinnon R. Crystal structure of a mammalian voltage-dependent Shaker family K+ channel. Science. 2005;309:897–903.

110. Grabe M, Lai HC, Jain M, Jan YN, Jan LY. Structure prediction for the down state of a potassium channel voltage sensor. Nature. 2007;445:550–3.
111. Upadhyay SK, Nagarajan P, Mathew MK. Potassium channel opening: a subtle two-step. J Physiol. 2009;587:3851–68.
112. Yarov-Yarovoy V, Baker D, Catterall WA. Voltage sensor conformations in the open and closed states in ROSETTA structural models of K(+) channels. Proc Natl Acad Sci U S A. 2006;103:7292–7.
113. Miller AG, Aldrich RW. Conversion of a delayed rectifier K+ channel to a voltage-gated inward rectifier K+ channel by three amino acid substitutions. Neuron. 1996;16:853–8.
114. Sobolevsky AI, Rosconi MP, Gouaux E. X-ray structure, symmetry and mechanism of an AMPA-subtype glutamate receptor. Nature. 2009;462:745–56.
115. Zhao Y, Chen S, Yoshioka C, Baconguis I, Gouaux E. Architecture of fully occupied GluA2 AMPA receptor-TARP complex elucidated by cryo-EM. Nature. 2016;536:108–11.
116. Sobolevsky AI. Structure and gating of tetrameric glutamate receptors. J Physiol. 2015;593:29–38.
117. Bocquet N, Nury H, Baaden M, Le Poupon C, Changeux JP, Delarue M, Corringer PJ. X-ray structure of a pentameric ligand-gated ion channel in an apparently open conformation. Nature. 2009;457:111–4.
118. Hilf RJ, Dutzler R. X-ray structure of a prokaryotic pentameric ligand-gated ion channel. Nature. 2008;452:375–9.
119. Hilf RJ, Dutzler R. Structure of a potentially open state of a proton-activated pentameric ligand-gated ion channel. Nature. 2009;457:115–8.
120. Hassaine G, Deluz C, Grasso L, Wyss R, Tol MB, Hovius R, Graff A, Stahlberg H, Tomizaki T, Desmyter A, Moreau C, Li XD, Poitevin F, Vogel H, Nury H. X-ray structure of the mouse serotonin 5-HT3 receptor. Nature. 2014;512:276–81.
121. Miller PS, Aricescu AR. Crystal structure of a human GABAA receptor. Nature. 2014;512:270–5.
122. Huang X, Chen H, Michelsen K, Schneider S, Shaffer PL. Crystal structure of human glycine receptor-alpha3 bound to antagonist strychnine. Nature. 2015;526:277–80.
123. Du J, Lu W, Wu S, Cheng Y, Gouaux E. Glycine receptor mechanism elucidated by electron cryo-microscopy. Nature. 2015;526:224–9.
124. Sauguet L, Shahsavar A, Poitevin F, Huon C, Menny A, Nemecz A, Haouz A, Changeux JP, Corringer PJ, Delarue M. Crystal structures of a pentameric ligand-gated ion channel provide a mechanism for activation. Proc Natl Acad Sci U S A. 2014;111:966–71.
125. Althoff T, Hibbs RE, Banerjee S, Gouaux E. X-ray structures of GluCl in apo states reveal a gating mechanism of Cys-loop receptors. Nature. 2014;512:333–7.
126. Hibbs RE, Gouaux E. Principles of activation and permeation in an anion-selective Cys-loop receptor. Nature. 2011;474:54–60.
127. Purohit P, Gupta S, Jadey S, Auerbach A. Functional anatomy of an allosteric protein. Nat Commun. 2013;4:2984.

Chapter 11
G-Protein-Coupled Receptors: Membrane Diffusion and Organization Matter

Evert Haanappel and Laurence Salomé

Abstract G-protein coupled receptors constitute an important family of membrane proteins. They are involved in numerous signaling pathways. The efficiency and regulation of these signaling events depend on the organization of the receptors with their different partners in the plasma membrane, and the way this organization influences the encounters between them. By studying the dynamics of the receptors and their partners in the plasma membrane, important information can be obtained on this membrane organization. In this chapter, we will first review experimental techniques used to study receptor dynamics. Then we discuss how the membrane environment influences receptor dynamics, and how measurements of this dynamics can inform us on interactions of the receptors with their signaling partners and on the effect of ligands. We finish by discussing recent theoretical advances on models of receptor organization, in particular the cluster phases, which provide a coherent framework for the understanding of this organization.

11.1 Introduction

As soon as it had been established that plasma membranes were highly heterogeneous yet dynamically organized, a relationship was postulated between the lateral distribution and mobility of membrane proteins and the cellular functions in which they are involved [1]. In a similar vein, and on the basis of mainly biochemical data, Neubig [2] had suggested earlier that G-protein-coupled receptors (GPCRs) form supramolecular complexes with their signaling partners, hence accounting for the specificity of their interactions. Addressing this question represents a major challenge in membrane biology. GPCRs constitute the largest family of membrane proteins with more than 800 members in humans. GPCRs mediate intracellular responses upon activation by a wide variety of extracellular stimuli, including photons, ions, diverse molecules and proteins. GPCRs are involved in almost all known physiological processes and are the target of about 50% of current drugs.

E. Haanappel • L. Salomé (✉)
Institut de Pharmacologie et de Biologie Structurale, Université de Toulouse, CNRS, UPS, Toulouse, France
e-mail: laurence.salome@ipbs.fr

A. Chattopadhyay (ed.), *Membrane Organization and Dynamics*, Springer Series in Biophysics 20, DOI 10.1007/978-3-319-66601-3_11

This superfamily of membrane receptors, also called seven transmembrane (7TM) receptors, is divided into several classes based on sequence homology (according to the International Union of Basic and Clinical Pharmacology). The class A or rhodopsin-like receptors represent the vast majority of the GPCRs and will be the main focus of this chapter. While tremendous progress has been made in obtaining crystallographic structures of these receptors, following the breakthrough by Kobilka and coworkers [3], a lot remains to be done to unveil the signaling processes of GPCRs in their biological context [4]. Their interaction with one or more members of the G-protein family upon stimulation was long thought to be the only signaling pathway enabling GPCRs to regulate the activity of various ion channels and enzymes. However, alternative non-G-protein dependent pathways have been discovered, among which the one mediated by β-arrestin is the most important. The emerging view of the successive membrane steps involved in signaling is that the binding of an agonist ligand to the receptor induces its coupling with a heterotrimeric G protein which, after exchanging GDP for GTP, can in turn activate an effector. This is followed by the phosphorylation of the receptor by GPCR kinases (GRKs). The subsequent binding of β-arrestin to the phosphorylated intracellular domain promotes the internalization of the receptor mediated by clathrin-coated pits and also triggers G-protein-independent downstream signals (Fig. 11.1) [5]. In this context, the concept of biased agonism has emerged, which states that ligands can selectively stabilize distinct subsets of receptor conformations promoting different cellular responses [6]. Together with the observation that a receptor's function is modulated by its membrane environment, this revives the need to fully understand the coupling of the receptor's signaling with its dynamics and organization in the membrane. This question is relevant both at the molecular and supramolecular level. At the molecular level, progress made through a

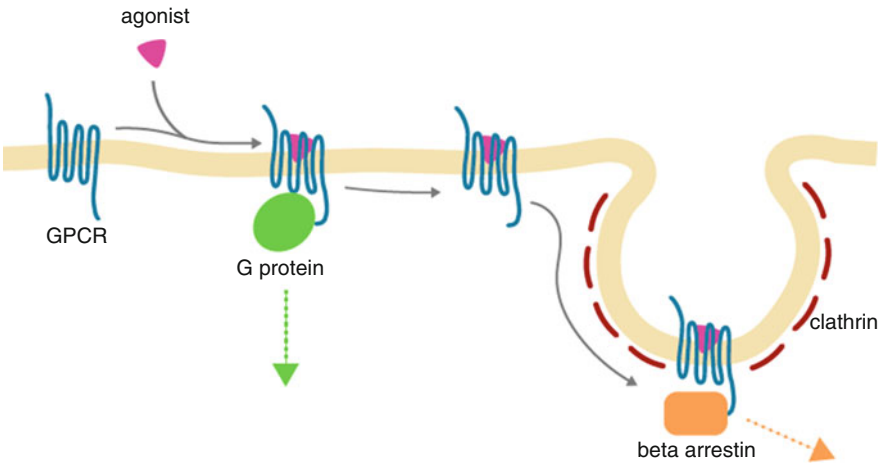

Fig. 11.1 Schematic view of the cascade of events occurring at the plasma membrane after an agonist binding to a GPCR, leading to G-protein and beta-arrestin dependent signaling

combination of crystallographic and computational methods gives insight into the influence of the membrane environment on the structural features of the receptors [7]. At the supramolecular level, fluorescence-based microscopy techniques, in particular those probing lateral diffusion, have yielded precious information on the dynamic organization of the receptors at the nm to μm scale [8, 9].

The hypothesis of a subtle arrangement of the receptors with their signaling partners makes sense in the context of the plasma membrane which is highly compartmentalized at various spatiotemporal scales [10]. As foreseen by Neubig, the confinement of the receptors with their partners in the same compartment could promote rapid and selective signaling. It could also modulate or impede interferences between distinct signaling pathways. The main sources identified so far for the existence of more or less specialized membrane domains are the obstruction to diffusion via the underlying cytoskeleton and the membrane proteins anchored to it [11], specific lipid-lipid interactions leading to the formation of nanodomains enriched in cholesterol and sphingolipids [12] and protein-protein interactions [13, 14]. In this chapter, we will first review the main experimental techniques and labeling methods available for the study of receptor lateral diffusion. Then through a selection of studies performed on distinct GPCRs we will examine the emerging features of the behavior of GPCRs. We will first consider GPCRs in their basal state and discuss the type of behavior GPCRs exhibit in this state and how it is influenced by various factors from the membrane environment. Second, we will attempt to identify the dynamic signatures of the various functional states at the different steps of the signaling process.

11.2 Experimental Techniques to Analyze Lateral Diffusion in Membranes

To characterize the lateral diffusion properties of membrane constituents, three methods are commonly used which are schematized in Fig. 11.2.

Fluorescence Recovery After Photobleaching (FRAP) analyzes the diffusional behavior of a population of fluorescently labeled receptors (Fig. 11.2a). A short intense pulse of laser light photobleaches the fluorescent markers in a small region of the membrane. Due to receptor diffusion, the fluorescence returns in the bleached region. The recovery curve contains information on the dynamic parameters of the receptors [15], in particular their diffusion coefficient D and their mobile fraction M. By changing the size of the bleached region, additional information can be obtained on compartmentalization of the receptors [16] down to domain sizes of 150–200 nm.

In Fluorescence Correlation Spectroscopy (FCS) [17, 18], a low-intensity laser beam is focused on a membrane region containing a low density of fluorescently labeled receptors (Fig. 11.2b). As a result of molecules diffusing into and out of the observation area, the fluorescence intensity fluctuates on a time scale characteristic of the residence time (typically microseconds to milliseconds) of a molecule in this

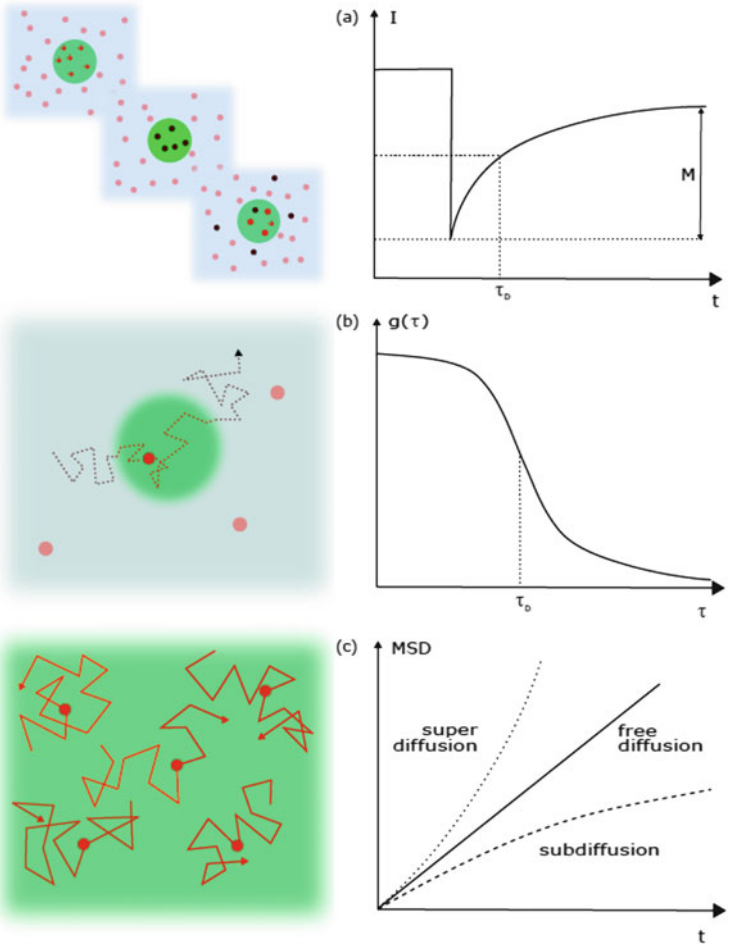

Fig. 11.2 Outline of the experimental techniques discussed in this chapter. (**a**) Fluorescence recovery after photobleaching (FRAP). An intense laser pulse photobleaches the fluorescence of labeled receptors in a small region. The fluorescence intensity I recovers due to receptor mobility with a characteristic time scale τ_d up to a level dependent on the mobile fraction M. (**b**) Fluorescence Correlation Spectroscopy (FCS). Fluorescently labeled receptors diffusing through the detection region generate a fluctuating fluorescence signal, whose autocorrelation function $g(\tau)$ contains information on the dynamics of the receptor. (**c**) Single Particle Tracking (SPT) Individual labeled receptors are tracked and their trajectories reconstructed. The Mean Square Displacement (MSD) is sketched for three different diffusion modes: directed (super-), Brownian (free) and confined (sub-) diffusion

area. The fluorescence autocorrelation function contains information on the diffusion constant, the average number of molecules in the observation region and on receptor interactions and binding. By varying the diameter of the waist of the laser beam, receptor compartmentalization can be studied [19, 20].

Single Particle/Molecule Tracking (SPT/SMT) allows the study of the dynamics of individual membrane receptors with nanometer-scale spatial and millisecond-scale temporal resolution [21–24] (Fig. 11.2c). Here the receptors are labeled with a nanoparticle (SPT) or a fluorescent molecule (SMT) and the receptor movements are tracked using videomicroscopy. Individual particles are localized with high precision [25, 26] in each image and the positions are connected using advanced algorithms [27–29] to reconstruct the trajectory of the receptor. Trajectory analysis allows the correct identification of the diffusion mode of the receptors [30–32], as well as the numerical estimation of the associated dynamic parameters from a fit of the Mean Square Displacement (MSD) [21, 33]. Recently, Bayesian inference techniques have been developed enabling to map the force and diffusion constants over the cell surface [34, 35].

All techniques have in common that the analysis of receptor diffusion generally assumes a flat membrane perpendicular to the direction of observation. In reality, cells and other biological structures are 3D, highly corrugated entities showing membrane ruffling, invaginations or spines. The complex membrane geometry has a significant influence on the measured dynamics properties of receptors [36] and ideally should be taken into account, e.g. by doing full 3D particle localization and tracking [37, 38].

Receptors must be labeled with an appropriate probe: either a fluorescent molecule (for FRAP, FCS and SMT) or a nanoparticle (for SPT). A large variety of probes with different properties exist [39]. The best choice of probe depends on the experimental design and involves considerations of probe size, wavelength range, brightness, photobleaching and blinking, ease of labeling, influence of the probe on the properties of the receptor of interest.

Several types of probes are commonly used. *Organic dyes* are small (less than 1 kDa) molecules that combine a fluorescent moiety with a chemically reactive group to allow covalent attachment to a molecule of interest. Their small size represents only a small perturbation to the labeled molecule, but they are prone to photobleaching, intensity fluctuations and blinking. A large family of *fluorescent proteins* (FPs) exist with different properties [40, 41], including versions that can be photoconverted or photoactivated. Their main advantage is that they can be expressed by the cell, as fusion proteins by conjugating the sequence of the FP to that of the protein of interest. FPs also suffer from fluorescence blinking and photobleaching, although genetic engineering has resulted in improved stabler and brighter versions. *Nanoparticles* are used for particle tracking applications. Quantum Dots (QDs) are very common [42] but they suffer from an intermittent fluorescence emission (“blinking”). Small fluorescent polystyrene (“latex”) particles are a non-blinking alternative to QDs [43]. Colloidal Au particles were used in the original SPT experiments [44] and recently in high-speed SPT [11, 45, 46].

A recurring and legitimate question is whether the nanoparticle modifies the dynamic properties of the receptor. The influence of the probe has been studied experimentally [43, 47]. Tracking studies on lipids in supported bilayers labeled with different types and sizes of nanoparticles showed that QDs and ϕ40 nm latex

particles had negligible influence on lipid diffusion, whereas larger latex particles and ϕ40 nm Au colloidal particles significantly did reduce the measured diffusion coefficient [43].

Conjugation Techniques To label a receptor with a fluorescent protein (FP), a fusion protein must be created where the FP is conjugated directly to the receptor of interest. The FP can be intracellular or extracellular. It must be verified that the fusion protein still is a functional receptor. In addition, the expression rate of the fusion protein is usually different from that of the native protein, which can lead to non-physiological results. Alternatively, a short tag (ACP tag, SNAP/CLIP tag, T7 tag) can be fused to the extracellular terminus of the receptor, that can be labeled chemically or via an antibody.

Native endogenous membrane receptors can be labeled with high specificity using an antibody directed against the receptor. This antibody can either be fluorescent or labeled with a reactive group, *e.g.* biotin. In the latter case, streptavidin or neutravidin-coated nanoparticles can attach to a biotin group on the antibody, leading to receptor labeling. Antibodies are large (~150 kDa) proteins potentially leading to modified receptor behavior. Single-domain antibodies from camelids (nanobodies) are much smaller (12–15 kDa) and have recently been applied for dual-color receptor labeling [48].

An alternative labeling strategy for GPCRs uses fluorescent ligands, consisting of an agonist or antagonist conjugated to a fluorophore, that bind to the receptor of interest with high specificity [49, 50]. Binding of the ligand leads to a specific functional state of the receptor, and may induce internalization. The ideal method for receptor labeling would be to covalently attach a fluorescent label to an endogenous receptor of interest, while maintaining full receptor functionality and dynamical properties. A promising way to reach this goal is provided by the traceless affinity-based labeling technique [51]. Here a ligand of the receptor, covalently coupled to a fluorescent probe via a chemically reactive linker, binds to the receptor's binding site. The reactive linker subsequently reacts with a residue on the receptor, binding the fluorescent moiety to the receptor while the ligand is released after a washing step. The feasibility of this method has been demonstrated for the bradykinin B_2 receptor [51].

11.3 Receptor Diffusion Is Under the Influence of the Membrane Environment

The influence of cholesterol on the function and signaling of GPCRs has been well documented [52], but its influence on the dynamic properties of GPCRs has rarely been studied. This is surprising because cholesterol profoundly modulates the membrane's properties. It induces the emergence of the liquid-ordered membrane phase with reduced lipid lateral diffusion. Membrane nanodomains enriched in cholesterol and sphingolipids ("*rafts*") may provide a favorable environment for

certain GPCRs and may constitute platforms for receptor signaling [53]. In addition, specific cholesterol-GPCR interactions might induce conformational changes in GPCRs, modulating their diffusional properties or interactions with other receptors. This could influence the formation of receptor oligomers with different diffusion properties than the monomer. Indeed, specific cholesterol binding sites exist in the structures of a number of GPCRs [54].

The influence of the membrane environment on the properties of the serotonin$_{1A}$ receptor has been extensively studied in the group of Chattopadhyay by a combination of techniques. Using variable-radius FRAP, Pucadyil and Chattopadhyay [55] found that, in normal CHO cells, the diffusion coefficient and mobile fraction of serotonin$_{1A}$ receptor-EYFP were independent of the radius of the bleached area, indicating that the receptor diffuses in a homogeneous membrane environment. Upon cholesterol depletion by methyl-β-cyclodextrin treatment, both the diffusion coefficient and mobile fraction of the serotonin$_{1A}$ receptor showed a marked dependence on the bleach radius, suggesting that cholesterol depletion leads to a dynamic confinement of the receptor attributed to a membrane organization in domains. Using z-scan FCS, they found that the same receptor was confined at a length scale of ~210 nm in normal cells [56] and that cholesterol depletion reduced receptor confinement. The discrepancy between results obtained by FRAP and by zFCS was attributed to the fact that these techniques probe different spatial and temporal regimes.

Not only cholesterol, but also sphingomyelin had an influence on the dynamics of the serotonin$_{1A}$ receptor. Metabolic depletion of sphingomyelin induced an increase of the mobile fraction of the receptor, but had no influence on its diffusion coefficient [57]. Other substances affecting membrane fluidity have also been found to influence the dynamics of GPCRs. As an example, Vukojevic et al. [58] found by FCS that ethanol at concentrations relevant in alcohol consumption increases the lateral mobility and surface density of the μ-opioid receptor in PC12 cells, while the antagonist naltrexone, used to prevent relapse in alcoholism, reverses this effect.

Cholesterol removal from the plasma membrane is expected to increase its fluidity leading to an increase of the mobility of a GPCR. The actual observation that cholesterol depletion induced a confinement of the serotonin$_{1A}$ receptor is therefore paradoxical [59] and suggests that other factors are influenced by cholesterol depletion. Studying the influence of cholesterol depletion on the diffusion of HLA, a non-GPCR, Kwik et al. [60] observed a reduction of the lateral mobility of this protein after cholesterol depletion. This reduction was demonstrated to be a consequence of the reorganization of the actin cytoskeleton, related to a redistribution of phosphatidylinositol 4,5-bisphosphate [PI(4,5)P2]. Cholesterol depletion interfered with the interactions of PI(4,5)P2 with other partners controlling the organization of the actin cytoskeleton. Earlier observations had already shown that the actin cytoskeleton is involved in receptor dynamics. Jans et al. [61] observed a decrease in the diffusion coefficient and the mobile fraction of the vasopressin receptor after treatment with cytochalasin B, a drug that interferes with actin polymerization. On the other hand, Roess et al. [62] observed an increase of the rotational diffusion of the LH receptor after treatment with cytochalasin D. In

studies of the interaction of different GPCRs with the actin cytoskeleton, Wheeler et al. [63] showed that this interaction may be different for different receptors. The β2-adrenergic receptor and the parathyroid hormone receptor (PTH1R) were shown to interact with the cytoskeleton via one or several partners, in particular NHERF-1, but the calcium-sensing receptor (CaSR) was not influenced by the cytoskeleton. Even structurally related receptors may show different interactions with the actin cytoskeleton. Valentine and Haggie [64] studied the diffusional behavior of the β_1- and β_2-adrenergic receptors (AR). They found that the unstimulated β_1-AR and β_2-AR are highly confined in the cell membrane, and that the interaction of these GPCRs is due to interaction of their C-terminus with different scaffold proteins.

Taken together, these results imply that GPCR diffusion in the plasma membrane may be regulated by multiple factors: cholesterol, the actin cytoskeleton and a number of partner proteins interacting with actin.

As an aside, the other main component of the cytoskeleton, the microtubules which also extend out close to the plasma membrane [65], also play a role in receptor diffusion, as illustrated *e.g.* by the observation by de Keijzer et al. [66] that the mobility of the cAMP receptor cAR1 was abolished upon microtubule disruption. We will not discuss this further.

Apart from being the support of scaffold proteins responsible for the tethering of receptors, actin is also thought to operate as a physical barrier to the diffusion of proteins and lipids. Indeed, according to the "fence and picket" model, the actin-based membrane skeleton itself and the transmembrane proteins anchored to it act in concert to confine the movement of membrane constituents within compartments over short timescales [11]. Supporting this model is the interpretation of single-molecule trajectories of proteins, and also lipids, as due to hop-diffusion: a short-term confined diffusion with jumps between adjacent domains on a longer time scale. Such a diffusive behavior, with nested double compartments and consistent with an actin-based compartmentalization, was inferred from single-molecule tracking experiments of the human μ-opioid receptor (hMOR) [67]. However, due to the statistical fluctuations inherent to diffusion of the membrane constituents, detecting jumps within a trajectory is extremely delicate and requires sophisticated mathematical tools. After the development of a rigorous algorithm for the detection of confinement and jumps [68], we revisited the analysis of trajectories acquired previously for the same hMOR receptor [69]. These trajectories have roughly the same features as those obtained by Suzuki et al., namely a long-term slow diffusion superimposed on a short-term confined diffusion. The analysis revealed that the frequency of jumps was low, too low in fact to account for the long-term diffusion. It rather suggested a predominant involvement of interprotein interactions that would lead to dynamic protein assemblies [69]. These protein domains are not static and should be seen as dynamic protein clusters, stabilized by short-range attractive and long-range repulsive forces, diffusing themselves and exchanging components over large distances [70]. Interestingly, some theoretical developments predict that such clusters can selectively segregate distinct proteins [14, 71]. Along these lines, an attractive recent model proposes that the clusters are grouped into mesoscale assemblies of several hundred nanometers [13]. Such a double scale

self-organization of the membrane proteins combined with a potential role of the cytoskeleton via anchoring proteins offers a coherent view of receptor diffusion able to account for all aspects of the observed single-molecule trajectories.

11.4 The Choreography of Signaling Receptors

The model of dynamic nanodomains or cluster phases presented in the last section constitutes a conceptual framework for explaining the spatiotemporal features of receptor signaling and reconciling their different aspects.

First of all, the possible existence of nanoclusters of proteins is consistent with the observed multimerization of receptors. The question of the exact structure of receptor multimers, whether they are dimers or higher order oligomers, and their physiological relevance is still under debate but a significant body of evidence of their existence has now been accumulated [72–75]. Initially deduced from biochemical experiments, the aggregation of receptors was further characterized by *in vitro* and *in vivo* biophysical approaches. The dimerization or oligomerization below a very high order cannot be identified from a simple measurement of the diffusion coefficient of receptors as the Saffman-Delbrück theory predicts that the diffusion coefficient of a protein depends weakly on its radius [76]. However, a cunning approach using dual-color FRAP with antibodies to immobilize a fraction of the receptor population made it possible to distinguish transient and stable interactions between receptors for the β_1-AR and β_2-AR, respectively [77]. Using the same approach, the D2 dopamine receptors were shown to interact only transiently to form oligomers [78]. In a more resolutive manner, the direct visualization of individual muscarinic, β_1- and β_2-adrenergic receptors and N-formyl peptide receptors by Single Molecule Tracking revealed the transient formation of dimers, with about 30–50% of receptors involved in dimers at any moment [79–83], in agreement with the popular resonance energy transfer approaches such as FRET or BRET [84]. The analysis of the oligomerization state of receptors previously studied by FRET or related techniques should be revisited by these powerful super-resolutive methods in order to update the data and obtain a dynamic view of these assemblies. To make the findings fully relevant, studies should preferably be performed on endogenous receptors expressed in their native environment [85]. Considering the evidence of multimerization of GPCRs, its role in the receptor signaling function will need to be understood.

The cluster phase model predicting the formation of dynamic assemblies maintaining several distinct proteins in close proximity, provides a theoretical basis for the hypothesized signalosomes or signal transduction platforms that are thought to assemble receptors and G proteins and presumably effectors and other signaling partners. Let us consider the question of the mechanism of coupling between the receptors and their G proteins. Two conflicting models have been examined by biophysical approaches: the classical “collision coupling” model supposing a free diffusion of both molecules that accounts for the diffusion

facilitated encounter between the signaling partners, and the "physical scaffold" supposing the existence of pre-coupled GPCR—G protein complexes. Overall, experimental results are compatible with an assembly of the receptors and associated G proteins in dynamic [86–89].

The observed changes in the membrane dynamics of the receptor after activation by an agonist ligand is probably the most convincing demonstration of the interplay between signaling and membrane organization of GPCRs. In contrast to the binding of antagonists, which generally does not induce modifications of the diffusion parameters of the receptors, the activation of receptors by agonists is generally accompanied by a decrease of receptor mobility [8] with a few exceptions, *e.g.* for the serotonin$_{1A}$ receptor [88], and some contradictory results, *e.g.* for the β_2-adrenergic receptors [79, 90]. Studies covering a large variety of receptors coupled to various G proteins used tools that allowed to deepen the analysis of the diffusion of the agonist bound receptors. All studies converge and show an increase of the population of confined receptors together with a decrease of the domain size and of the diffusion coefficient of the receptors inside the domains [90–98]. Of particular physiological relevance are the differences observed for distinct agonists. We focus in the following on the μ-opioid receptor (MOR), the main target of morphine, an opioid analgesic predominantly used in severe pain treatment despite its important side effects [99]. Our own work on MOR using extensive variable-radius FRAP (vrFRAP) experiments showed that morphine and DAMGO caused markedly different modifications of MOR diffusion [94]. Morphine maintained the confinement in permeable domains that was observed for receptors in their basal state but with smaller domain size. This effect was abolished by the inhibition of G-protein activation but persisted upon inhibition of internalization. DAMGO induced a redistribution of the receptors between a freely diffusing population and a population with slow diffusion in small closed domains, this latter being attributed to receptors entering the internalization pathway via clathrin-coated pits. Considering the agonist-selective phosphorylation of MOR [100], we argued that the slow phosphorylation of the receptors following morphine binding allows to observe the dynamic changes related to G-protein activation, while these changes could not be detected due to the rapid receptor phosphorylation induced by DAMGO binding. It should be noted that the results of a recent independent study of MOR signaling in response to the same ligands quite consistently point to a relationship between the dynamic organization of MOR and its spatiotemporal signaling [101]. Different agonists are likely to stabilize or induce distinct conformational states of the receptors that in turn trigger the cascade of interactions favoring particular partners among the different ones available and involving distinct patterns of the membrane organization.

A similar mechanism seems to be involved in formation of heteromers which are accompanied by a modulation of their signaling properties [102, 103]. Again taking MOR as an example, our vrFRAP analysis showed a modification of MOR dynamics after the activation of α_2-adrenergic and $NPFF_2$ receptors known to functionally interact with MOR [104]. The activation of the Neuropeptide Y receptor, that is not described to interact with MOR, did not affect MOR diffusion. FRET experiments

could demonstrate that the crosstalk between MOR and α_2-AR is mediated by conformational changes propagating from one receptor to the other [105]. Here again, conformational changes could impact the interactions of the receptors with their partners and be responsible for the changes in diffusional behavior. However, as demonstrated by vrFRAP combined with bimolecular fluorescence complementation, the MOR/NPFF2 heterodimer adopts a specific dynamical behavior corresponding to a mix of the properties of both monomers [104]. A similar earlier FCS study of the A1/A2 adenosin receptor heteromer led to similar observations [106].

11.5 Concluding Remarks

We believe that a coherent explanatory model is emerging from the experimental and theoretical developments presented here. This model will go beyond an oversimplified representation and propose a robust framework to interpret the cell surface choreography of G-protein coupled receptors with their partners during the signaling events. Ultimately, and integrating the impressive biochemical and structural knowledge accumulated, it should also substitute physical interactions for the arrows habitually used in schematic representations of signaling pathways.

Further research using advanced methods is still needed to refine our description of the mechanisms at play. Efforts should be put into monitoring individual receptors at normal and high temporal resolution during a binding event to obtain the full spatiotemporal information on the processes [93]. In addition, model experiments on receptors reconstituted in biomimetic membranes [107] or on isolated cell plasma membranes [108], combined with micropatterning [109], will allow to test the validity of the theory and establish which are the dominating interactions and their regulation mode. In this respect, recent progress on the purification of GPCRs in lipid nanodiscs offer promising perspectives [110].

References

1. Jacobson K, Sheets ED, Simson R. Revisiting the fluid mosaic model of membranes. Science. 1995;268:1441–2.
2. Neubig RR. Membrane organization in G-protein mechanisms. FASEB J. 1994;8:939–46.
3. Kobilka B. The structural basis of G-protein-coupled receptor signaling (Nobel lecture). Angew Chem Int Ed. 2013;52:6380–8.
4. Venkatakrishnan AJ, Deupi X, Lebon G, Tate CG, Schertler GF, Babu MM. Molecular signatures of G-protein-coupled receptors. Nature. 2013;494:185–94.
5. Jacobson KA. New paradigms in GPCR drug discovery. Biochem Pharmacol. 2015;98:541–55.
6. Violin JD, Crombie AL, Soergel DG, Lark MW. Biased ligands at G-protein-coupled receptors: promise and progress. Trends Pharmacol Sci. 2014;35:308–16.

7. Mondal S, Khelashvili G, Johner N, Weinstein H. How the dynamic properties and functional mechanisms of GPCRs are modulated by their coupling to the membrane environment. Adv Exp Med Biol. 2014;796:55–74.
8. Baker A, Sauliere A, Dumas F, Millot C, Mazeres S, Lopez A, Salome L. Functional membrane diffusion of G-protein coupled receptors. Eur Biophys J. 2007;36:849–60.
9. Barden AO, Goler AS, Humphreys SC, Tabatabaei S, Lochner M, Ruepp M-D, Jack T, Simonin J, Thompson AJ, Jones JP, Brozik JA. Tracking individual membrane proteins and their biochemistry: the power of direct observation. Neuropharmacology. 2015;98:22–30.
10. Truong Quang B-A, Lenne P-F. Membrane microdomains: from seeing to understanding. Front Plant Sci. 2014;5:18.
11. Fujiwara T, Ritchie K, Murakoshi H, Jacobson K, Kusumi A. Phospholipids undergo hop diffusion in compartmentalized cell membrane. J Cell Biol. 2002;157:1071–81.
12. Sevcsik E, Schutz GJ. With or without rafts? Alternative views on cell membranes. Bioessays. 2016;38(2):129–39.
13. Destainville N, Schmidt TH, Lang T. Where biology meets physics-a converging view on membrane microdomain dynamics. Curr Top Membr. 2016;77:27–65.
14. Meilhac N, Destainville N. Clusters of proteins in biomembranes: insights into the roles of interaction potential shapes and of protein diversity. J Phys Chem B. 2011;115:7190–9.
15. Sprague BL, Mcnally JG. FRAP analysis of binding: proper and fitting. Trends Cell Biol. 2005;15:84–91.
16. Salome L, Cazeils JL, Lopez A, Tocanne JF. Characterization of membrane domains by FRAP experiments at variable observation areas. Eur Biophys J. 1998;27:391–402.
17. Haustein E, Schwille P. Fluorescence correlation spectroscopy: novel variations of an established technique. Annu Rev Biophys Biomol Struct. 2007;36:151–69.
18. Ries J, Schwille P. Fluorescence correlation spectroscopy. Bioessays. 2012;34(5):361–8.
19. Wawrezinieck L, Rigneault H, Marguet D, Lenne PF. Fluorescence correlation spectroscopy diffusion laws to probe the submicron cell membrane organization. Biophys J. 2005;89 (6):4029–42.
20. Wenger J, Conchonaud F, Dintinger J, Wawrezinieck L, Ebbesen TW, Rigneault H, Marguet D, Lenne PF. Diffusion analysis within single nanometric apertures reveals the ultrafine cell membrane organization. Biophys J. 2007;92(3):913–9.
21. Saxton MJ, Jacobson K. Single-particle tracking: applications to membrane dynamics. Annu Rev Biophys Biomol Struct. 1997;26:373–99.
22. Wieser S, Schutz GJ. Tracking single molecules in the live cell plasma membrane-do's and don't's. Methods. 2008;46(2):131–40.
23. Kusumi A, Tsunoyama TA, Hirosawa KM, Kasai RS, Fujiwara TK. Tracking single molecules at work in living cells. Nat Chem Biol. 2014;10(7):524–32.
24. Manzo C, Garcia-Parajo MF. A review of progress in single particle tracking: from methods to biophysical insights. Rep Prog Phys. 2015;78(12):124601.
25. Small A, Stahlheber S. Fluorophore localization algorithms for super-resolution microscopy. Nat Methods. 2014;11(3):267–79.
26. Deschout H, Cella Zanacchi F, Mlodzianoski M, Diaspro A, Bewersdorf J, Hess ST, Braeckmans K. Precisely and accurately localizing single emitters in fluorescence microscopy. Nat Methods. 2014;11(3):253–66.
27. Serge A, Bertaux N, Rigneault H, Marguet D. Dynamic multiple-target tracing to probe spatiotemporal cartography of cell membranes. Nat Methods. 2008;5(8):687–94.
28. Jaqaman K, Loerke D, Mettlen M, Kuwata H, Grinstein S, Schmid SL, Danuser G. Robust single-particle tracking in live-cell time-lapse sequences. Nat Methods. 2008;5(8):695–702.
29. Chenouard N, Smal I, de Chaumont F, Maska M, Sbalzarini IF, Gong Y, Cardinale J, Carthel C, Coraluppi S, Winter M, Cohen AR, Godinez WJ, Rohr K, Kalaidzidis Y, Liang L, Duncan J, Shen H, Xu Y, Magnusson KE, Jalden J, Blau HM, Paul-Gilloteaux P, Roudot P, Kervrann C, Waharte F, Tinevez JY, Shorte SL, Willemse J, Celler K, van Wezel GP, Dan HW, Tsai YS, Ortiz de Solorzano C, Olivo-Marin JC, Meijering E. Objective comparison of particle tracking methods. Nat Methods. 2014;11(3):281–9.

30. Meilhac N, Le Guyader L, Salome L, Destainville N. Detection of confinement and jumps in single-molecule membrane trajectories. Phys Rev E Stat Nonlin Soft Matter Phys. 2006;73 (1 Pt 1):011915.
31. Huet S, Karatekin E, Tran VS, Fanget I, Cribier S, Henry JP. Analysis of transient behavior in complex trajectories: application to secretory vesicle dynamics. Biophys J. 2006;91 (9):3542–59.
32. Bouzigues C, Dahan M. Transient directed motions of GABA(A) receptors in growth cones detected by a speed correlation index. Biophys J. 2007;92(2):654–60.
33. Michalet X. Mean square displacement analysis of single-particle trajectories with localization error: Brownian motion in an isotropic medium. Phys Rev E Stat Nonlin Soft Matter Phys. 2010;82(4 Pt 1):041914.
34. El Beheiry M, Dahan M, MASSON JB. Inference MAP: mapping of single-molecule dynamics with Bayesian inference. Nat Methods. 2015;12:594–5.
35. Masson JB, CASANOVA D, Turkcan S, Voisinne G, Popoff MR, Vergassola M, Alexandrou A. Inferring maps of forces inside cell membrane microdomains. Phys Rev Lett. 2009;102:048103.
36. Adler J, Shevchuk AI, Novak P, Korchev YE, Parmryd I. Plasma membrane topography and interpretation of single-particle tracks. Nat Methods. 2010;7:170–1.
37. Dupont A, Lamb DC. Nanoscale three-dimensional single particle tracking. Nanoscale. 2011;3:4532–41.
38. Wells NP, Lessard GA, Goodwin PM, Phipps ME, Cutler PJ, Lidke DS, Wilson BS, Werner JH. Time-resolved three-dimensional molecular tracking in live cells. Nano Lett. 2010;10:4732–7.
39. Giepmans BN, Adams SR, Ellisman MH, Tsien RY. The fluorescent toolbox for assessing protein location and function. Science. 2006;312:217–24.
40. Chudakov DM, Matz MV, Lukyanov S, Lukyanov KA. Fluorescent proteins and their applications in imaging living cells and tissues. Physiol Rev. 2010;90:1103–63.
41. Shaner NC, Patterson GH, Davidson MW. Advances in fluorescent protein technology. J Cell Sci. 2007;120:4247–60.
42. Pinaud F, Clarke S, Sittner A, Dahan M. Probing cellular events, one quantum dot at a time. Nat Methods. 2010;7:275–85.
43. Haanappel E, Mascalchi P, Carayon K, Mazères S, Salomé L. Probing the influence of the particle in Single Particle Tracking measurements of lipid diffusion. Soft Matter. 2012;8:4462–70.
44. Geerts H, De Brabander M, Nuydens R, Geuens S, Moeremans M, De Mey J, Hollenbeck P. Nanovid tracking: a new automatic method for the study of mobility in living cells based on colloidal gold and video microscopy. Biophys J. 1987;52:775–82.
45. Spillane KM, Ortega-Arroyo J, De Wit G, Eggeling C, Ewers H, Wallace MI, Kukura P. High-speed single-particle tracking of GM1 in model membranes reveals anomalous diffusion due to interleaflet coupling and molecular pinning. Nano Lett. 2014;14:5390–7.
46. Wu HM, Lin YH, Yen TC, Hsieh CL. Nanoscopic substructures of raft-mimetic liquid-ordered membrane domains revealed by high-speed single-particle tracking. Sci Rep. 2016;6:20542.
47. Clausen MP, Lagerholm BC. Visualization of plasma membrane compartmentalization by high-speed quantum dot tracking. Nano Lett. 2013;13:2332–7.
48. Albrecht D, Winterflood CM, Ewers H. Dual color single particle tracking via nanobodies. Methods Appl Fluoresc. 2015;3(2):024001.
49. Sridharan R, Zuber J, Connelly SM, Mathew E, Dumont ME. Fluorescent approaches for understanding interactions of ligands with G protein coupled receptors. Biochim Biophys Acta. 2014;1838:15–33.
50. Stoddart LA, Kilpatrick LE, Briddon SJ, Hill SJ. Probing the pharmacology of G protein-coupled receptors with fluorescent ligands. Neuropharmacology. 2015;98:48–57.
51. Hayashi T, Hamachi I. Traceless affinity labeling of endogenous proteins for functional analysis in living cells. Acc Chem Res. 2012;45:1460–9.

52. Burger K, Gimpl G, Fahrenholz F. Regulation of receptor function by cholesterol. Cell Mol Life Sci. 2000;57:1577–92.
53. Lingwood D, Simons K. Lipid rafts as a membrane-organizing principle. Science. 2010;327:46–50.
54. Gater DL, Saurel O, Iordanov I, Liu W, Cherezov V, Milon A. Two classes of cholesterol binding sites for the beta2AR revealed by thermostability and NMR. Biophys J. 2014;107:2305–12.
55. Pucadyil TJ, Chattopadhyay A. Cholesterol depletion induces dynamic confinement of the G-protein coupled serotonin(1A) receptor in the plasma membrane of living cells. Biochim Biophys Acta. 2007;1768:655–68.
56. Ganguly S, Chattopadhyay A. Cholesterol depletion mimics the effect of cytoskeletal destabilization on membrane dynamics of the serotonin1A receptor: a zFCS study. Biophys J. 2010;99:1397–407.
57. Ganguly S, Paila YD, Chattopadhyay A. Metabolic depletion of sphingolipids enhances the mobility of the human serotonin1A receptor. Biochem Biophys Res Commun. 2011;411:180–4.
58. Vukojevic V, Ming Y, D'addario C, Rigler R, Johansson B, Terenius L. Ethanol/naltrexone interactions at the mu-opioid receptor CLSM/FCS study in live cells. PLoS One. 2008;3:e4008.
59. Ayee MA, Levitan I. Paradoxical impact of cholesterol on lipid packing and cell stiffness. Front Biosci. 2016;21:1245–59.
60. Kwik J, Boyle S, Fooksman D, Margolis L, Sheetz MP, Edidin M. Membrane cholesterol, lateral mobility, and the phosphatidylinositol 4,5-bisphosphate-dependent organization of cell actin. Proc Natl Acad Sci USA. 2003;100:13964–9.
61. Jans DA, Peters R, Jans P, Fahrenholz F. Ammonium chloride affects receptor number and lateral mobility of the vasopressin V2-type receptor in the plasma membrane of LLC-PK1 renal epithelial cells: role of the cytoskeleton. Exp Cell Res. 1990;191:121–8.
62. Roess DA, Jewell MA, Philpott CJ, Barisas BG. The rotational diffusion of LH receptors differs when receptors are occupied by hCG versus LH and is increased by cytochalasin D. Biochim Biophys Acta. 1997;1357:98–106.
63. Wheeler D, Sneddon WB, Wang B, Friedman PA, Romero G. NHERF-1 and the cytoskeleton regulate the traffic and membrane dynamics of G protein-coupled receptors. J Biol Chem. 2007;282:25076–87.
64. Valentine CD, Haggie PM. Confinement of beta(1)- and beta(2)-adrenergic receptors in the plasma membrane of cardiomyocyte-like H9c2 cells is mediated by selective interactions with PDZ domain and A-kinase anchoring proteins but not caveolae. Mol Biol Cell. 2011;22:2970–82.
65. Huet S, Karatekin E, Tran VS, Fanget I, Cribier S, Henry JP. Analysis of transient behavior in complex trajectories: application to secretory vesicle dynamics. Biophys J. 2006;91:3542–59.
66. De Keijzer S, Galloway J, Harms GS, Devreotes PN, Iglesias PA. Disrupting microtubule network immobilizes amoeboid chemotactic receptor in the plasma membrane. Biochim Biophys Acta Biomembr. 2011;1808:1701–8.
67. Suzuki K, Ritchie K, Kajikawa E, Fujiwara T, Kusumi A. Rapid hop diffusion of a G-protein-coupled receptor in the plasma membrane as revealed by single-molecule techniques. Biophys J. 2005;88:3659–80.
68. Meilhac N, Le Guyader L, Salome L, Destainville N. Detection of confinement and jumps in single-molecule membrane trajectories. Phys Rev E: Stat Nonlinear Soft Matter Phys. 2006;73:011915.
69. Daumas F, Destainville N, Millot C, Lopez A, Dean D, Salome L. Confined diffusion without fences of a g-protein-coupled receptor as revealed by single particle tracking. Biophys J. 2003;84:356–66.
70. Destainville N. Cluster phases of membrane proteins. Phys Rev E: Stat Nonlinear Soft Matter Phys. 2008;77:011905.
71. Destainville N. An alternative scenario for the formation of specialized protein nano-domains (cluster phases) in biomembranes. EPL. 2010;91:58001.

72. Bouvier M, Hebert TE. CrossTalk proposal: weighing the evidence for Class A GPCR dimers, the evidence favours dimers. J Physiol Lond. 2014;592:2439–41.
73. Bouvier M, Hebert TE. Rebuttal from Michel Bouvier and Terence E Hebert. J Physiol Lond. 2014;592:2447.
74. Lambert NA, Javitch JA. CrossTalk opposing view: weighing the evidence for classA GPCR dimers, the jury is still out. J Physiol Lond. 2014;592:2443–5.
75. Lambert NA, Javitch JA. Rebuttal from Nevin A. Lambert and Jonathan A Javitch. J Physiol Lond. 2014;592:2449.
76. Saffman PG, Delbrück M. Brownian motion in biological membranes. Proc Natl Acad Sci USA. 1975;72(8):3111–3.
77. Dorsch S, Klotz KN, Engelhardt S, Lohse MJ, Bunemann M. Analysis of receptor oligomerization by FRAP microscopy. Nat Methods. 2009;6:225–30.
78. Fonseca JM, Lambert NA. Instability of a class A G protein-coupled receptor oligomer interface. Mol Pharmacol. 2009;75:1296–9.
79. Calebiro D, Rieken F, Wagner J, Sungkaworn T, Zabel U, Borzi A, Cocucci E, Zurn A, Lohse MJ. Single-molecule analysis of fluorescently labeled G-protein-coupled receptors reveals complexes with distinct dynamics and organization. Proc Natl Acad Sci USA. 2013;110:743–8.
80. Hern JA, Baig AH, Mashanov GI, Birdsall B, Corrie JE, Lazareno S, Molloy JE, Birdsall NJ. Formation and dissociation of M1 muscarinic receptor dimers seen by total internal reflection fluorescence imaging of single molecules. Proc Natl Acad Sci USA. 2010;107:2693–8.
81. Kasai RS, Suzuki KGN, Prossnitz ER, Koyama-Honda I, Nakada C, Fujiwara TK, Kusumi A. Full characterization of GPCR monomer–dimer dynamic equilibrium by single molecule imaging. J Cell Biol. 2011;192:463–80.
82. Kusumi A, Suzuki KG, Kasai RS, Ritchie K, Fujiwara TK. Hierarchical mesoscale domain organization of the plasma membrane. Trends Biochem Sci. 2011;36:604–15.
83. Scarselli M, Annibale P, Mccormick PJ, Kolachalam S, Aringhieri S, Radenovic A, Corsini GU, Maggio R. Revealing G-protein-coupled receptor oligomerization at the single-molecule level through a nanoscopic lens: methods, dynamics and biological function. FEBS J. 2016;283:1197–217.
84. Kaczor AA, Makarska-Bialokoz M, Selent J, De La Fuente RA, Marti-Solano M, Castro M. Application of BRET for studying G protein-coupled receptors. Mini Rev Med Chem. 2014;14:411–25.
85. Herrick-Davis K, Grinde E, Lindsley T, Teitler M, Mancia F, Cowan A, Mazurkiewicz JE. Native serotonin 5-HT2C receptors are expressed as homodimers on the apical surface of choroid plexus epithelial cells. Mol Pharmacol. 2015;87:660–73.
86. Mystek P, Tworzydlo M, Dziedzicka-Wasylewska M, Polit A. New insights into the model of dopamine D1 receptor and G-proteins interactions. Biochim Biophys Acta. 2015;1853:594–603.
87. Perez JB, Segura JM, Abankwa D, Piguet J, Martinez KL, Vogel H. Monitoring the diffusion of single heterotrimeric G proteins in supported cell-membrane sheets reveals their partitioning into microdomains. J Mol Biol. 2006;363:918–30.
88. Pucadyil TJ, Kalipatnapu S, Harikumar KG, Rangaraj N, Karnik SS, Chattopadhyay A. G-protein-dependent cell surface dynamics of the human serotonin1A receptor tagged to yellow fluorescent protein. Biochemistry. 2004;43:15852–62.
89. Qin K, Sethi PR, Lambert NA. Abundance and stability of complexes containing inactive G protein-coupled receptors and G proteins. FASEB J. 2008;22:2920–7.
90. Hegener O, Prenner L, Runkel F, Baader SL, Kappler J, Haberlein H. Dynamics of beta2-adrenergic receptor-ligand complexes on living cells. Biochemistry. 2004;43:6190–9.
91. Cezanne L, Lecat S, Lagane B, Millot C, Vollmer JY, Matthes H, Galzi JL, Lopez A. Dynamic confinement of NK2 receptors in the plasma membrane. Improved FRAP analysis and biological relevance. J Biol Chem. 2004;279:45057–67.

92. Jacquier V, Prummer M, Segura JM, Pick H, Vogel H. Visualizing odorant receptor trafficking in living cells down to the single-molecule level. Proc Natl Acad Sci USA. 2006;103:14325–30.
93. Lill Y, Martinez KL, Lill MA, Meyer BH, Vogel H, Hecht B. Kinetics of the initial steps of G protein-coupled receptor-mediated cellular signaling revealed by single-molecule imaging. Chemphyschem. 2005;6:1633–40.
94. Sauliere-Nzeh Ndong A, Millot C, Corbani M, Mazeres S, Lopez A, Salome L. Agonist-selective dynamic compartmentalization of human Mu opioid receptor as revealed by resolutive FRAP analysis. J Biol Chem. 2010;285:14514–20.
95. Smith SM, Lei Y, Liu J, Cahill ME, Hagen GM, Barisas BG, Roess DA. Luteinizing hormone receptors translocate to plasma membrane microdomains after binding of human chorionic gonadotropin. Endocrinology. 2006;147:1789–95.
96. Thurner P, Gsandtner I, Kudlacek O, Choquet D, Nanoff C, Freissmuth M, Zezula J. A two-state model for the diffusion of the A2A adenosine receptor in hippocampal neurons: agonist-induced switch to slow mobility is modified by synapse-associated protein 102 (SAP102). J Biol Chem. 2014;289:9263–74.
97. Veya L, Piguet J, Vogel H. Single molecule imaging deciphers the relation between mobility and signaling of a prototypical G protein-coupled receptor in living cells. J Biol Chem. 2015;290:27723–35.
98. Wolf-Ringwall AL, Winter PW, Liu J, Van Orden AK, Roess DA, Barisas BG. Restricted lateral diffusion of luteinizing hormone receptors in membrane microdomains. J Biol Chem. 2011;286:29818–27.
99. Ahlbeck K. Opioids: a two-faced Janus. Curr Med Res Opin. 2011;27:439–48.
100. Kelly E, Bailey CP, Henderson G. Agonist-selective mechanisms of GPCR desensitization. Br J Pharmacol. 2008;153(Suppl 1):S379–88.
101. Hall D. Analysis and interpretation of two-dimensional single-particle tracking microscopy measurements: effect of local surface roughness. Anal Biochem. 2008;377:24–32.
102. Bellot M, Galandrin S, Boularan C, Matthies HJ, Despas F, Denis C, Javitch J, Mazeres S, Sanni SJ, Pons V, Seguelas MH, Hansen JL, Pathak A, Galli A, Senard JM, Gales C. Dual agonist occupancy of AT1-R-alpha2C-AR heterodimers results in atypical Gs-PKA signaling. Nat Chem Biol. 2015;11:271–9.
103. Parmentier M. GPCRs: heterodimer-specific signaling. Nat Chem Biol. 2015;11:244–5.
104. Carayon K, Mouledous L, Combedazou A, Mazeres S, Haanappel E, Salome L, Mollereau C. Heterologous regulation of Mu-opioid (MOP) receptor mobility in the membrane of SH-SY5Y cells. J Biol Chem. 2014;289:28697–706.
105. Vilardaga J-P, Nikolaev VO, Lorenz K, Ferrandon S, Zhuang Z, Lohse MJ. Conformational cross-talk between [alpha]2A-adrenergic and [mu]-opioid receptors controls cell signaling. Nat Chem Biol. 2008;4:126–31.
106. Briddon SJ, Gandia J, Amaral OB, Ferre S, Lluis C, Franco R, Hill SJ, Ciruela F. Plasma membrane diffusion of G protein-coupled receptor oligomers. Biochim Biophys Acta. 2008;1783:2262–8.
107. Alves ID, Salamon Z, Hruby VJ, Tollin G. Ligand modulation of lateral segregation of a G-protein-coupled receptor into lipid microdomains in sphingomyelin/phosphatidylcholine solid-supported bilayers. Biochemistry. 2005;44:9168–78.
108. Danelon C, Terrettaz S, Guenat O, Koudelka M, Vogel H. Probing the function of ionotropic and G protein-coupled receptors in surface-confined membranes. Methods. 2008;46:104–15.
109. Wedeking T, Löchte S, Birkholz O, Wallenstein A, Trahe J, Klingauf J, Piehler J, You C. Spatiotemporally controlled reorganization of signaling complexes in the plasma membrane of living cells. Small. 2015;11:5912–8.
110. Rues R-B, Dötsch V, Bernhard F. Co-translational formation and pharmacological characterization of beta1-adrenergic receptor/nanodisc complexes with different lipid environments. Biochim Biophys Acta Biomembr. 2016;1858:1306–16.

Chapter 12
Role of Membrane Microdomains in Serotonin Receptor Functions

Josephine Labus, Alexander Wirth, Andre Zeug, and Evgeni Ponimaskin

Abstract The plasma membrane is a highly compartmentalised organelle containing specialised lipid microdomains or lipid rafts that enable the spatial regulation of signal transduction. Lipid microdomains are enriched in sphingolipids and cholesterol that are arranged in a highly ordered state. Functionally, they contribute to a lesser fluidity compared to the surrounding membrane. Besides their unique lipid composition, these domains are characterised by the accumulation of various signalling molecules, including G protein-coupled receptors (GPCRs) and its downstream effectors. In this way lipid microdomains can integrate a plethora of signalling cascades and thereby modulate the functions of e.g. GPCRs. Here, we provide a short overview about the role of lipid microdomains in the distribution and signalling of GPCRs with particular focus on serotonin receptors. Since recent investigations dealing with lipid microdomain functions revealed the participation of these membrane domains in various pathophysiological processes, we also discuss a possible link between lipid microdomains and serotonin receptor functions in the pathogenesis of depression.

List of Abbreviations

HMG-CoA	3-Hydroxy-3-Methylglutaryl-Coenzyme-A
5-HTRs	5-HT receptors
5-HT	5-Hydroxytrympamine
a-SMase	Acid sphingomyelinase
AC	Adenylyl cyclase
DHHC	Aspartate-histidine-histidine-cysteine
AFM	Atomic force microscopy
CREB	cAMP response element-binding protein
CNS	Central nervous system
cAMP	Cyclic adenosine monophosphate

J. Labus • A. Wirth • A. Zeug • E. Ponimaskin (✉)
Department of Cellular Neurophysiology, Hannover Medical School, Carl-Neuberg-Strasse 1, Hannover 30625, Germany
e-mail: Ponimaskin.Evgeni@mh-hannover.de

A. Chattopadhyay (ed.), *Membrane Organization and Dynamics*, Springer Series in Biophysics 20, DOI 10.1007/978-3-319-66601-3_12

DRMs	Detergent-resistant membranes
PDMP	D-threo-1-phenyl-2-decanoylamino-3-morpholino-1-propanol
ER	Endoplasmic reticulum
ERK	Extracellular-activated kinase
FCS	Fluorescence correlation spectroscopy
FLIM	Fluorescence lifetime imaging
FRAP	Fluorescence recovery after photobleaching
FRET	Förster resonance energy transfer
GRKs	G protein-coupled receptor kinases
GPCRs	G protein-coupled receptors
GPI	Glycosylphosphatidylinositol
G proteins	Guanine nucleotide-binding proteins
IP_3	Inositol-1,4,5-triphosphate
β-MCD	Methyl-β-cyclodextrin
MAPK	Mitogen-activated protein kinases
PATs	Palmitoyl-acyl transferases
PLCβ	Phospholipase Cβ
PALM	Photoactivated localisation microscopy
PET	Positron emission tomography
SNOM	Scanning optical microscopy
STED	Stimulated emission depletion
STORM	Stochastic optical reconstruction microscopy
SIM	Structured illumination microscopy

12.1 The Concept of Lipid Microdomains

12.1.1 Structure and Function of Lipid Microdomains

Unlike postulated by Singer and Nicolson in the early 1970s, lipids and proteins are not randomly distributed in the phospholipid bilayer [1]. According to the current understanding, the plasma membrane is compartmentalised into various domains that differ in their structure and composition, and thus enable spatially restricted signal transduction. Depending on the protein and lipid content, protein-based and lipid-based membrane domains can be distinguished [2].

Lipid rafts are planar lipid microdomains of about 10–200 nm diameter which are enriched in sphingolipids and cholesterol [3]. In these structures, the sphingolipid head groups associate laterally with one another in the outer leaflet of the membrane and their long, largely saturated acyl chains are densely packed inside the membrane. In addition, rigid cholesterol molecules intercalate into hydrophobic gaps of the acyl chains [4]. This special lipid organisation causes the characteristic, highly ordered and less fluid state of lipid rafts (also referred to as liquid-ordered

phase) separating them from the surrounding membrane, which is characterised by a greater fluidity resulting from the presence of phospholipids with kinked unsaturated acyl groups (also referred to as liquid-disordered phase) [5, 6].

Another type of lipid-based microdomains are caveolae, which are small (50–100 nm diameter) flask-shaped invaginations of the plasma membrane [7, 8]. Although the lipid composition is similar to lipid rafts and caveolae are often regarded as non-planar subtype of lipid rafts, they rather seem to be biochemically different [6]. In contrast to planar rafts, caveolae express the transmembrane protein caveolin, which exists in three different isoforms (Caveolin-1, -2 and -3). Since caveolin molecules can oligomerise in large clusters, this protein was thought to be the structural protein coating membrane invaginations [9, 10]. However, more recently, an additional protein named cavin was identified as novel integral component for the caveolae formation [11, 12]. Lipid rafts are found in nearly all cell types, whereas caveolae are not formed in neurons, erythrocytes and lymphocytes [5], although these cells have been shown to express caveolin and form planar rafts [13].

Besides their unique lipid composition, lipid microdomains are characterised by the accumulation of signalling molecules including glycosylphosphatidylinositol (GPI)-anchored proteins, G protein-coupled receptors (GPCRs), heterotrimeric G proteins, membrane-associated kinases, and various cytoplasmic effector proteins [4, 6]. Furthermore, also cytoskeletal proteins such as actin, tubulin, vinculin, filamin, actinin and tau are enriched in lipid rafts [14, 15]. It has been suggested that these proteins are important for forming and maintaining the structure of lipid rafts by tethering the plasma membrane to the underlying cytoskeleton [14]. In addition, the actin cytoskeleton, which is organised in a lattice network, might have an ordering effect on lipid domains [16].

Lipid rafts and caveolae function as specific compartments within the plasma membrane that spatially regulate the interaction of signalling molecules [17]. By facilitating the formation of large protein clusters, these lipid domains enable a rapid and site-specific activation of signalling cascades. However, complexes of lipids and/or proteins within these structures can also inhibit activity of signalling molecules leading to attenuated signal transduction. Consequently, lipid microdomains have been found to be involved in the regulation of the numerous cellular functions, including protein sorting, endocytosis, exocytosis and transcytosis, cell polarity, homeostasis of cholesterol, nutrient transport, signalling cascades of receptors and ion channels as well as entry of viruses, bacteria, toxins and nanoparticles [3, 5, 9, 15].

Lipid rafts and caveolae are dynamic structures underlying continuous changes in size, individual composition of lipids and proteins as well as stability. Generally, two raft states can be defined: small, metastable assemblies referred to as “reserve rafts” and larger, stabilised “receptor-cluster rafts” [18]. Stabilisation of reserve rafts, which are mainly found in resting cells, is induced by specific interaction between rafts components, which get recruited into lipid rafts upon stimulation [18, 19]. The lateral diffusion of proteins and lipids inside and outside of rafts is partly mediated by the actin cytoskeleton [15]. Raft size can be further increased by

ligand-induced oligomerisation of proteins as well as by protein modifications like phosphorylation, leading to the generation of more potent signalling platforms [19].

12.1.2 Methods to Investigate Lipid Microdomains

Various biochemical, spectroscopic and microscopic approaches have been developed to study the structure of lipid rafts and their possible role in signalling events. One of the commonly used method to isolate lipid rafts from cell membranes is based on its insolubility in detergents [20]. Due to the accumulation of lipids in the highly ordered state, rafts are resistant to treatment with non-ionic detergents, such as Triton X-100, Brji 96 or CHAPS, and float into fractions of low density within a sucrose gradient upon ultracentrifugation [20–22]. These so-called detergent-resistant membranes (DRMs) contain a couple of specific protein markers including caveolin [5], which is specific for caveolae, CD55 and alkaline phosphatase. In addition, pore-forming toxins like cholera toxin B, which binds ganglioside GM1, are also enriched in rafts [23]. Another raft marker for cells which do not form caveolae, such as blood [24] and neural cells [25] is flotilin. Non-raft fractions can be verified by the presence of transferrin receptor, CD71 and geranylated proteins [26, 27]. Depending on the choice of the used detergent, DRMs can differ in their composition of the lipid raft components as well as in their distribution within the low density fraction [5, 28]. For that reason, the detergent-extraction of lipid rafts was controversially discussed [29, 30], leading to the development of detergent-free isolation methods [31, 32]. These techniques allow the fine disruption of the membrane and the extraction of a larger portion of the inner leaflet by sonication, which results in more reproducible outcomes [33].

The most direct method to study lipid rafts is based on monitoring chemical (lipid) composition of the cell membranes with mass spectrometry [34–36]. Although nuclear magnetic resonance spectroscopy provides direct information about the order of lipid head groups and fatty acid chains, it is limited to model membranes with simple lipid compositions [37–39]. A chemical cross-linking method was also proposed, which provides evidence for the proximity between sphingomyelin and cholesterol species [40]. Though this method could be extended to a variety of lipid species and even to proteins, it is invasive and requires destruction of the cell membranes.

Direct visualisation of lipid rafts is rather challenging due to their typical size below diffraction limit and their high dynamics. Thus, postulating the concept of membrane compartmentalisation let to a controversial discussion and low acceptance of the raft concept over the years [41]. Nowadays, Atomic Force Microscopy (AFM) provide the necessary resolution [42] and can clearly distinguish between raft and non-raft segments of the membrane [43]. However, AFM usually requires modelled or isolated native membranes immobilised on surfaces. The AFM related near-field scanning optical microscopy (NSOM or SNOM) uses a fibre probe with an aperture below wavelength to scan the sample and is able to provide structural information below the far field resolution limit [44]. Thus, SNOM was successfully

applied to study the nanoscale organisation of membrane surfaces and enables the investigation of lipid rafts in both model-supported and cellular membranes [45, 46].

In addition, recent improvements in light microscopy allow to apply single molecule spectroscopy and microscopy techniques to study the biophysical properties of lipid rafts as well as the localisation and distribution of receptors at nanometre resolution. The spectroscopic and microscopic methods, however, intrinsically require the implementation of fluorescent probes or contrast agents to the lipid raft structure since such biological systems are poor in autofluorescence. Meanwhile, lipid rafts have been visualised in numerous studies using fluorescent probes that partition specifically into liquid-ordered or liquid-disordered phases [47]. For example, Schütz et al. [48] imaged the distribution of fluorescein–polyethylene glycol–cholesterol in comparison to Cy5-dimyristoyl-sn-glycero-phosphatidylethanolamine in native cell membranes on a millisecond time scale and with positional accuracy of approximately 50 nm using single molecule tracking. They characterised small areas in a liquid-ordered phase and identified those as lipid rafts. Sato et al. [49] extended such investigations to membrane fragment clustering of the Golgi apparatus. In addition, Sharma et al. [50] used green fluorescent protein coupled GPI-anchored proteins to visualise microdomains. They used Förster resonance energy transfer (FRET)-microscopy to determine the size and structure of GPI-anchored protein organisation. In other studies, non-toxic recombinant derivatives of pore-forming toxins, such as lysenin, cholera toxin subunit B, and aerolysin, have been used as lipid raft markers since they specifically bind to sphingomyelin, glycosphingolipid GM1, and GPI-associated proteins, respectively [23, 51–53]. Alternatively, environment-sensitive membrane dyes have been developed, which show different fluorescence properties depending on the membrane phases. The classical example for these probes is laurdan, which is among the first probes introduced for imaging liquid-ordered or liquid-disordered phases in model membranes [54]. Such probes can directly address the properties of each separate phase, but their cellular applications are still limited. An ample collection was recently provided by Klymchenko and Kreder [55]. These fluorescent analogues and probes are useful tools to visualise lipid microdomains, although the size of the individual raft seems to be beyond the resolution of the current conventional microscopy. A comprehensive collection of specific optical methods visualising membrane rafts was reviewed by Lagerholm et al. [56].

The development of super-resolution imaging techniques surpassed the diffraction-limited resolution of optical systems and enables the direct observation of small membrane clusters with the size of lipid rafts. Stimulated emission depletion (STED) in combination with fluorescence recovery after photobleaching (FRAP) analysis was applied for the first time by Siebert and colleagues to investigate lipid microdomains [57]. Later STED was combined with fluorescence

correlation spectroscopy (STED-FCS) to overcome the poor spatial resolution of standard FCS and to diminish the statistical extrapolations [58, 59]. Fluorescence fluctuation methods including photoactivated localisation microscopy (PALM) and stochastic optical reconstruction microscopy (STORM) were also exploited to directly prove existence of the nano-scaled lipid complexes and meso-scaled lipid domains in cell membranes [60–62]. In line with the mentioned super-resolution techniques, structured illumination microscopy (SIM) was recently applied to analyse biopsies of patients suffering from pemphigus vulgaris, an autoimmune epidermal blistering disease, to better understand how autoantibodies alter desmosome morphology and function in vivo [63].

Various additional cutting-edge optical methods have also been applied to investigate the functional properties of lipid rafts, such as FRET, fluorescence lifetime imaging (FLIM), FRAP, and FCS [56, 64, 65]. These optical techniques in combination with super-resolution approaches are expected to provide more accurate information about lipid raft dynamics and the spatiotemporal signalling events at these microdomains.

One common approach to evaluate the functional role of lipid rafts in cell signalling is their targeted disruption. This can be achieved by modifying the content of its lipid components, especially cholesterol, and is confirmed by the redistribution of raft markers from low density to high density fractions upon density gradient centrifugation. Several antimycotics, such as filipin, nystatin and amphotericin, destabilise lipid raft integrity by binding and sequestering membrane cholesterol [66–69]. Depletion of plasma membrane cholesterol using methyl-β-cyclodextrin (β-MCD) is another often applied method [70]. However, it has been shown that β-MCD only partially removes membrane cholesterol at concentrations that retain cell viability leading rather to the impairment than to a complete disruption of lipid microdomains [71–73]. Besides directly altering the cholesterol content in the plasma membrane, lipid raft's integrity can be influenced indirectly by interfering with the lipid biosynthesis. Statins, such as simvastatin, lovastatin and mevastatin [67, 74, 75], as well as mevalonate are used to inhibit 3-Hydroxy-3-Methylglutaryl-Coenzyme-A (HMG-CoA) reductase, the rate-limiting enzyme of cholesterol synthesis. Moreover, blocking sphingolipid and ganglioside biosynthesis by fumusonisin [76] or D-threo-1-phenyl-2-decanoylamino-3-morpholino-1-propanol (PDMP) [77] can be used to induce lipid raft disruption. In addition to these biochemical methods, genetic approaches to disrupt caveolae have been developed including caveolin-1 knockout mice [78] or silencing caveolin-1 in cell lines by RNA interference [79]. Since all techniques mentioned above bear the inherent disadvantage to interfere with the lipid raft structure, an alternative conceptual approach focusses on the specificity of the lipid raft downstream signalling in comparison to non-raft region signalling. For example, Agarwal and colleagues employed different genetically encoded FRET-based biosensors Epac2, which are specifically targeted to lipid rafts (Epac2-MyrPalm) and non-raft domains (Epac2-CAAX) [80]. These sensors were used to monitor local cyclic adenosine monophosphate (cAMP) synthesis near the plasma membrane in comparison to the freely diffusible Epac2-camps, which monitors the global [cAMP] [80].

12.1.3 Targeting Proteins into Lipid Microdomains

Since lipid microdomains represent signalling hot spots, the association and dissociation of defined signalling proteins with lipid rafts have to be highly regulated. Central mechanisms responsible for the targeting of proteins into lipid rafts include different co- and post-translational modifications.

One of the prominent lipid raft targeting signals is the GPI anchor. This protein modification occurs in the endoplasmic reticulum (ER) by covalent attachment of the protein-bound core oligosaccharide to a phosphoinositide residue to the outer leaflet of the subsequent plasma membrane. GPI-anchored proteins include enzymes such as placental alkaline phosphatase, cell adhesion molecules like NCAM as well as several receptors (e.g. growth hormone receptors and glial-cell derived neurotrophic factor receptor) [81].

Another common signal to guide proteins into the lipid rafts is S-palmitoylation (in the following designated as palmitoylation), a widespread post-translational lipid modification [82, 83]. Palmitoylation is the covalent attachment of the saturated (C16:0) fatty acid palmitate to free thiol groups of cysteine side chain(s) via a labile thioester bond. Palmitoylation is an enzymatic process mediated by at least 23 palmitoyl-acyl transferases (PATs) in mammals [82]. The catalytic centre of these proteins contains an aspartate-histidine-histidine-cysteine (DHHC)-motif, which mediates the palmitoyl transfer to the target protein [84]. Generally, palmitoylation takes place at the ER and the Golgi apparatus, but can also be carried out at the plasma membrane [85, 86]. Three depalmitoylation enzymes have been characterised: Acyl protein thioesterases 1 and 2 (APT1 and APT2) and palmitoyl protein thioesterase 1 (PPT1). APT1 and APT2 mediate depalmitoylation of many proteins in the cytosol, whereas PPT1 resides in lysosomes and participates in depalmitoylation during protein degradation [87]. Quite recently, Lin et al. found that proteins of the ABHD17 protein family also possess functions of the depalmitoylation enzymes. Using a dual pulse-chase approach, they demonstrated that ABHD17 proteins can remove palmitate from PSD-95 and N-Ras [88]. These results point to more complex depalmitoylation mechanisms than thought.

Palmitoylation *per se* increases hydrophobicity and thus affinity of proteins towards membranes. Thereby, it can influence subcellular localisation, conformation and stability, but also protein-protein interactions as well as protein degradation [89]. In case of soluble proteins like Src family kinases, heterotrimeric G proteins and small GTPases such as Ras and Rho GTPases, palmitoylation facilitates the access to the plasma membrane [90–92]. Palmitoylation often assists other protein modifications such as N-myristoylation in guiding peripheral proteins to liquid-ordered membrane domains [93]. Transmembrane proteins, such as GPCRs, are often palmitoylated on cysteine residues in close proximity to their transmem-

brane segment, and GPCR palmitoylation might act as guidance cue to lipid rafts [94]. The palmitoylation of juxtamembrane cysteines can tilt transmembrane domains [95] and can also be responsible for the formation of a fourth C-terminal intracellular loop, which might be of importance for proper signalling [96].

However, palmitoylated transmembrane proteins reside not exclusively in lipid rafts. The best example is the transferrin-receptor, a palmitoylated non-raft marker [97]. This highlights the need to further study molecular processes induced by palmitoylation of membrane-spanning proteins.

Interestingly, other co- or post-translational modifications of soluble proteins with unsaturated fatty acids, like prenylation, prevent proteins from inserting into lipid microdomains. It can be explained by the appearance of lipid rafts as liquid-ordered membranes, in which branched fatty acids and isoprenyl or geranyl-geranyl moieties do not fit as good as unbranched fatty acids [98].

Although GPI-anchoring and acylation are the most common signals to target proteins into lipid rafts, there might be other mechanisms. A recent study demonstrated that upon depalmitoylation and removal of GPI-anchors a small percentage of proteins still reside in lipid rafts [99]. This group of proteins might interact directly with raft lipids, such as cholesterol and sphingolipids [9, 19]. Furthermore, the direct interaction of the cytoplasmic N-terminus of caveolin-1 with numerous raft proteins was shown, including G proteins, growth hormone receptors and various kinases [100–102]. In addition, it has been suggested that transmembrane proteins can be targeted into lipid microdomains by their C-terminal amino acid sequence [103, 104].

12.2 GPCR Signalling Complexes and Lipid Microdomains

12.2.1 G Protein-Coupled Receptors

Lipid rafts form an important platform for GPCR-mediated signalling, since GPCRs as well as multiple downstream effectors are often targeted to lipid rafts. GPCRs represent the largest and most diverse superfamily of transmembrane receptors. They can be divided into five families: rhodopsin, secretin, glutamate, adhesion and frizzled receptors [105]. All GPCRs belong to the family of seven transmembrane receptors, which feature seven membrane spanning helices with an extracellular amino-terminus and an intracellular carboxy-terminus. Ligand binding to different domains within the receptor's outer surface leads to conformational changes within the transmembrane segments which in turn results in activation of multiple downstream effectors [106]. In this way, GPCRs translate extracellular cues into intracellular, which influence a plethora of signalling cascades [107].

The best characterised downstream effectors of GPCRs are heterotrimeric G proteins. They are comprised of three subunits: α, β, γ and act as molecular

switches, cycling between inactive GDP-state and active GTP-state [108]. Heterotrimeric G proteins can be divided into several subgroups according to their Gα-subunits: $G\alpha_S$ proteins activate adenylyl cyclases (AC) and are referred to as stimulatory G proteins. In contrast, inhibitory G proteins, $G\alpha_{i/o}$, inhibit ACs. Another class of heterotrimeric G proteins, $G\alpha_{q/11}$, couples to phospholipase Cβ (PLCβ), resulting in the production of inositol-1,4,5-triphosphate (IP_3) and leading to calcium mobilisation. The last subgroup of heterotrimeric G proteins is termed G_{12} and consists of $G\alpha_{12}$ and $G\alpha_{13}$, both activating different RhoGEFs, linking GPCR signalling to Rho GTPases [109, 110]. Even though heterotrimeric G proteins are clustered according to their α-subunits, βγ dimers have also been shown to act as effectors of GPCRs signalling [111, 112].

GPCRs transduce extracellular stimuli not exclusively via trimeric G proteins. Well-studied heterotrimeric G protein-independent signalling is mediated by arrestins [113, 114]. Canonically, the C-termini of GPCRs get phosphorylated by G protein-coupled receptor kinases (GRKs), followed by binding of β-arrestin 1 and 2 [115]. In turn, arrestins can switch off G protein-dependent signalling [116]. Further evidence points towards the participation of arrestins in receptor trafficking, internalisation, non-receptor tyrosine kinase signalling (e.g. c-Src) and mitogen-activated protein kinases (MAPK) [117].

In the following section, we will provide a short overview of the role of lipid microdomains in the distribution and signalling functions of the defined serotonin GPCRs.

12.2.2 Influence of Lipid Microdomains on Serotonin Receptor Functions

Serotonin (5-hydroxytrympamine or 5-HT) is an important neurotransmitters within the central nervous system (CNS) as well as in the periphery. It is critically involved in regulation of multiple physiological and pathological processes, including body temperature, appetite, breathing, sleep and mood [118, 119]. Serotonin can activate a large family of 5-HT receptors (5-HTRs) belonging to the seven distinct classes. The majority of the 5-HTRs belongs to the family of the G-protein coupled receptors (GPCRs), with only the 5-HT3R being a ligand-gated ion channel.

Several 5-HTRs, including 5-HT_{1A}R, 5-HT_2R and 5-HT_7R, have been shown to be localised in caveolae and/or planar lipid rafts. Furthermore, several studies provide evidence for the importance of raft localisation in terms of the regulation of 5-HTR functions, including ligand binding properties, trafficking, internalisation and/or signalling.

12.2.2.1 5-HT$_{1A}$R

The 5-HT$_{1A}$R is the most extensively studied member of the serotonin receptor family. This receptor is highly expressed in the cerebral cortex, hippocampus and raphe nuclei, but it is also present in the gastrointestinal tract and platelets [96]. Functionally, 5-HT$_{1A}$Rs are involved in a wide range of physiological processes including the regulation of mood, sleep, appetite, body temperature, sexual behaviour, learning and memory as well as the control of respiration, blood pressure and heart rate [96, 120, 121]. Considerable interest in this receptor has been raised due to its involvement in the pathogenesis of neurological disorders such as depression and anxiety [122].

On the molecular level, 5-HT$_{1A}$Rs can couple to heterotrimeric G proteins of the $G_{i/o}$ family leading to AC inhibition and a subsequent decrease in cAMP levels. In addition, 5-HT$_{1A}$Rs are involved in opening of K^+ channels, closing of Ca^{2+} channels as well as activation of the extracellular-activated kinase (ERK) and PLCβ by signalling via $G_{\beta\gamma}$ subunits [123].

The localisation of the 5-HT$_{1A}$R in lipid rafts was firstly demonstrated in CHO cells stably transfected with a YFP-tagged recombinant 5-HT$_{1A}$R using an microscopic approach [124]. In these experiments, a small yet significant percentage of 5-HT$_{1A}$R-eYFP retained in the plasma membrane after treatment with the non-ionic detergent Triton X-100, indicating the association with lipid rafts. However, since the fluorescence intensity was significantly decreased upon Triton X-100 treatment, the authors concluded that only a small fraction of 5-HT$_{1A}$R is associated with lipid rafts [124]. Furthermore, agonist stimulation of 5-HT$_{1A}$R did not increase the amount of 5-HT$_{1A}$R in detergent-insoluble membrane domains suggesting that receptor activation is not involved in translocation into rafts [125]. The raft localisation of a small portion of 5-HT$_{1A}$R in CHO cells as well as in bovine hippocampal neurons was further confirmed using a detergent-free approach [126]. In the follow-up study, by applying z-scan FCS (zFCS), Ganguly and Chattopadhyay have shown that 5-HT$_{1A}$R exhibits confinement in cell membranes, which was altered by the depletion of membrane cholesterol [127]. It appears to reduce receptor confinement in a manner similar to that observed in the case of cytoskeletal destabilisation, implying possible changes in the actin cytoskeleton induced upon cholesterol depletion. In addition, raft association of 5-HT$_{1A}$R was studied after its incorporation into the artificial system of giant unilamellar vesicles using an agarose rehydration method [128]. In this study, the preferential segregation of 5-HT$_{1A}$R into the cholesterol-poor liquid-disordered phase of the membrane was observed with fluorescence techniques. Noteworthy, modifying the concentration of cholesterol and sphingomyelin does not alter 5-HT$_{1A}$R segregation into the liquid disordered phase.

In our own studies we have demonstrated that the murine 5-HT$_{1A}$R undergoes palmitoylation at its cysteine residues 417 and 420 within the proximal C-terminal domain [129]. Using gradient centrifugation and copatching assays, we have demonstrated that a significant fraction of 5-HT$_{1A}$R (app. 30%) resides in lipid rafts in a

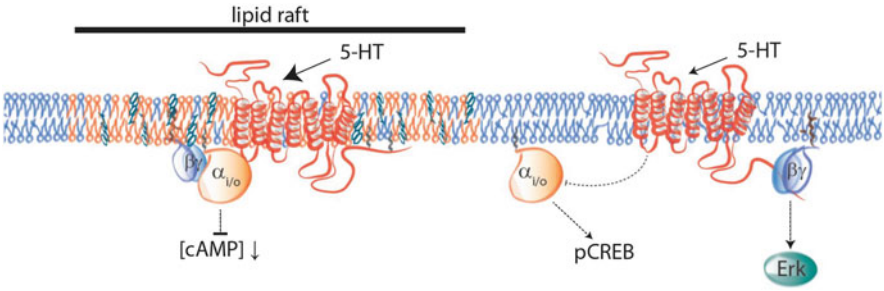

Fig. 12.1 5-HT_{1A}R signalling in lipid microdomains. Palmitoylated 5-HT_{1A}Rs are recruited into lipid microdomains, where they couple to $G\alpha_{i/o}$ subunit leading to agonist-induced inhibition of AC and decreased cAMP levels. Non-palmitoylated 5-HT_{1A}Rs are excluded from the lipid raft domains, which results in impaired signalling towards $G\alpha_i$-mediated AC inhibition and increased phosphorylation of ERK via $G\beta\gamma$ subunits

palmitoylation-dependent manner, suggesting that palmitoylation functions as a targeting signal for lipid rafts [52]. The importance of 5-HT_{1A}R palmitoylation for receptor localisation in lipid rafts was further confirmed in two follow-up studies using a FRET-based approach [130, 131]. Investigations in our lab also suggest that the palmitoylation-dependent raft localisation of the receptor is critically involved in the regulation of signalling processes. Characterisation of non-palmitoylated 5-HT_{1A}R mutants revealed the importance of receptor palmitoylation for signalling. In particular, non-palmitoylated mutants of 5-HT_{1A}R showed reduced coupling to the $G\alpha_{i/o}$ protein and impairment in the inhibition of AC leading to high forskolin-induced cAMP levels [129]. Furthermore, the phosphorylation of ERK was increased, indicating a preference for the coupling of non-palmitoylated 5-HT_{1A}R to $G\beta\gamma$ over $G\alpha_{i/o}$ outside of lipid rafts. Similar effects have been observed in human primary neuronal cultures [132].

These findings clearly demonstrate the importance of raft localisation of 5-HT_{1A}R for the regulation of the receptor-mediated signalling (Fig. 12.1).

12.2.2.2 5-HT_2R

The 5-HT_2Rs comprise three subtypes—5-HT_{2A}R, 5-HT_{2B}R and 5-HT_{2C}R—and are involved in the regulation of learning, memory, sleep, mood and appetite [121]. The 5-HT_2Rs have also been implicated in pathological conditions such as migraine, depression, anxiety and sleep disorders [133]. 5-HT_2Rs couple to heterotrimeric G_q/G_{11} proteins, which in turn activate PLCβ, leading to increased accumulation of IP_3 and the stimulation of Ca^{2+} release from the ER.

The localisation of 5-HT_2Rs in caveolae has been reported in smooth muscle cell of the murine intestine [134] and the bovine trachea [135] as well as in rat endothelial cells [135–137]. Furthermore, Bhatnagar et al. demonstrated that 5-HT_2Rs can be co-immunoprecipitated with the caveoale marker caveolin-1 in C6 glioma

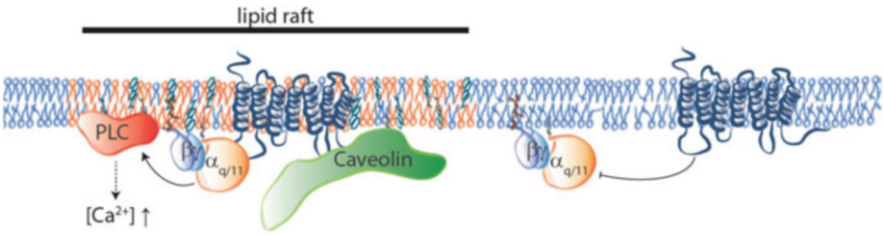

Fig. 12.2 5-HT_2R signalling in lipid microdomains. Direct interaction of 5-HT_2Rs with caveolin facilitates receptor coupling to $G\alpha_{q/11}$ and induces PLCβ-mediated Ca^{2+} signalling. Decreased concentrations of caveolin and/or cholesterol in non-raft membranes reduce 5-HT_2R binding to $G\alpha_{q/11}$ leading to impaired downstream signalling

cells and in rat synaptic membrane preparations, indicating the interaction of both proteins in caveolin-enriched lipid microdomains [79]. However, in smooth muscle cells this interaction seems to be also existent in non-caveolar fractions [135]. Nonetheless, siRNA induced knockdown of caveolin significantly reduced coupling of 5-HT_2Rs to $G\alpha_{q/11}$ proteins in the absence of agonist, pointing to a functional significance of the 5-HT_2R/caveolin interaction for 5-HT_2R-mediated signalling [79]. Potential interaction of the receptor with cholesterol might also be relevant for 5-HT_2R functions, since cholesterol depletion by β-MCD impaired the agonist-induced Ca^{2+} signalling in myocytes and endothelial cells [135, 136]. These studies indicate that the proper function of the 5-HT_2R is dependent on a unique membrane organisation mediated by its interaction with cholesterol and rafts associated proteins, such as caveolin-1 (Fig. 12.2).

12.2.2.3 5-HT_7R

The 5-HT_7R is abundantly expressed in smooth muscle cells of vessels and in the gastrointestinal tract [121]. In the CNS, 5-HT_7Rs are located in the spinal cord, thalamus, hypothalamus, hippocampus, prefrontal cortex, amygdala, raphe nuclei and suprachiasmatic nucleus [138]. With regard to its function, 5-HT_7Rs have been implicated in the regulation of circadian rhythm, sleep-wake cycle, body core temperature, locomotion as well as learning and memory processes [139, 140]. A large body of evidence indicates the involvement of the 5-HT_7Rs in anxiety and depression, and recent studies suggest that 5-HT_7Rs can be highly relevant for the treatment of major depressive disorders [141]. At the cellular level, 5-HT_7Rs couple to the stimulatory G_s proteins which results in the activation of AC leading to a rise in cAMP concentration. Receptor stimulation can also activate small GTPases of the Rho family by signalling via G_{12} proteins.

5-HT_7Rs have been shown to co-localise with the caveolae marker caveolin in Triton X-100-resistant fractions. However, this receptor was also detected in non-raft fractions after sucrose gradient centrifugation [142]. This indicates that the 5-HT_7R can be localised both inside as well as outside of lipid rafts. In contrast

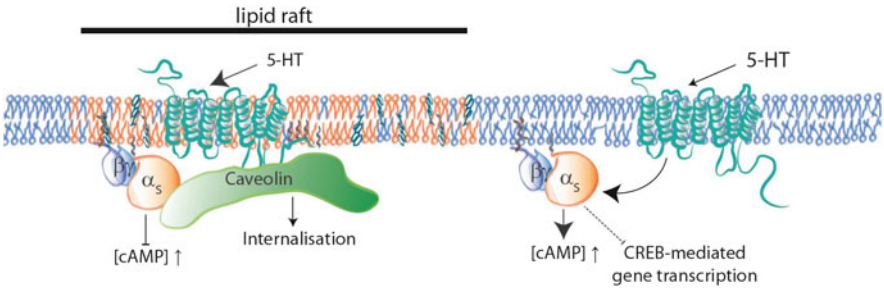

Fig. 12.3 5-HT$_7$R signalling in lipid microdomains. 5-HT$_7$Rs can be recruited into lipid microdomains either by direct interaction with caveolin or via palmitoylation. Agonist-dependent internalisation of the 5-HT$_7$R-caveolin-Gα_s-complex from lipid microdomains can result in the impairment of the 5-HT$_7$R-mediated signalling. 5-HT$_7$R residing outside of lipid raft possesses a high constitutive activity towards Gα_s-mediated activation of AC

to the 5-HT$_{1A}$R, signal(s) responsible for targeting the 5-HT$_7$R into lipid microdomains have not been investigated yet. Since palmitoylation is a known regulator for raft localisation of the 5-HT$_{1A}$R, this post-translational modification might also be responsible for raft targeting of the 5-HT$_7$R. Indeed, 5-HT$_{7(a)}$R has been shown to undergo palmitoylation at its C-terminal cysteine residues 404, 438 and 441 in an agonist-dependent manner [143]. Functionally, 5-HT$_7$R palmitoylation negatively regulates the constitutive, Gα_s-mediated activity of the receptor, while agonist-induced activation of Gα_s and Gα_{12} were not altered in palmitoylation-deficient mutants [140, 143]. In addition, it has been demonstrated that the specific composition of lipids in the plasma membrane can regulate 5-HT$_7$R-mediated signalling. Depletion of membrane cholesterol either by β-MCD treatment or inhibition of cholesterol biosynthesis results in reduced agonist and antagonist binding to 5-HT$_7$R as well as in decreased agonist-induced phosphorylation of the cAMP response element-binding protein (CREB) and of the activating transcription factor 1 [144]. Reduction in agonist and antagonist binding was also reported after inhibition of sphingolipid and ganglioside biosynthesis and caveolin-1 knockdown [142, 145]. Furthermore, proper caveolin-1 expression is necessary for the recruitment of 5-HT$_7$Rs to the cell surface as well as for its agonist-induced internalisation [142]. These results suggest that 5-HT$_7$R signalling and internalisation might be influenced by its localisation in lipid microdomains (Fig. 12.3).

12.2.3 Role of Lipid Microdomains in Functional Regulation of G Proteins and Their Effectors

Lipid rafts act as potent signalling platforms, and nearly each type of Gα subunit has been shown to be localised in lipid rafts [17]. For example, raft association of

the $G\alpha_{i/o}$ subunits coupled to the 5-HT_1R and 5-HT_2R has been reported in cardiac myocytes [146], fibroblasts [147], smooth muscle cells [21], epithelial cells [22, 32, 147–149] and endothelial cells [149]. The $G\alpha_{q/11}$subunit, which can be activated via 5-HT_2R, resides in caveolae of endothelial and epithelial cells [22, 149, 150]. The $G\alpha_s$ protein is also localised in lipid rafts in different cell types, including glioma cells [151, 152], breast cancer cells [152], cardiac myocytes [146], smooth muscle cells [21], epithelial cells [149, 153, 154] and endothelial cells [149]. Also the $G\alpha_{12}$ protein is localised within lipid rafts in fibroblasts [155] and epithelial cells [153, 155]. In addition, Gβ-subunits reside in plasma membrane microdomains in fibroblasts [31], epithelial cells [32] and endothelial cells [149]. However, the individual Gα protein subtype seems to differ in the distribution between raft and non-raft domains as well as in their preference for association with planar lipid rafts or caveolae. For example, in endothelial cells $G\alpha_{q/11}$ preferentially localises into caveolin-rich caveolae, while $G\alpha_{i/o}$, $G\alpha_s$ and Gβ concentrates in lipid rafts enriched in GPI-anchored proteins [149].

The recruitment of G proteins to lipid rafts can be mediated by different mechanisms. One important raft targeting signal is palmitoylation of G protein subunits. It has been shown that palmitoylation-deficient mutants of $G\alpha_s$ [151] as well as $G\alpha_{12}$ are not associated with lipid rafts, while myristoylation of the $G\alpha_{12}$ subunit can partially restore its raft localisation [155]. In addition, dual acylation by myristoylation and palmitoylation was found to be sufficient to recruit $G\alpha_{i/o}$ into lipid microdomains [147, 148, 156]. Interestingly, not all acylated G proteins are necessarily targeted to lipid rafts. Although $G\alpha_{13}$ is palmitoylated at three different cysteine residues [157], it can only be detected within non-raft domains in fibroblasts and endothelial cells [155]. Furthermore, the prenylated Gβγ subunit is also excluded from lipid raft domains within reconstituted membranes or liposomes [156]. Another possible mechanism to recruit G proteins to lipid microdomains is their interaction with scaffolding proteins. Several Gα subunits including $G\alpha_{i/0}$, $G\alpha_{q/11}$, $G\alpha_s$ and $G\alpha_{12}$ have been demonstrated to directly interact with the N-terminus of caveolin [147, 149, 153], and palmitoylation of caveolin seems to be important for the proper interaction [147]. In addition, the activation state of G proteins can influence its binding affinity for caveolin. It has been shown that the constitutive active mutant of the $G\alpha_s$ subunit is not able to interact with caveolin and thus fails to translocate into lipid rafts [153]. Furthermore, caveolin-1 knockdown decreases $G\alpha_s$ association with lipid rafts supporting the fact that binding to caveolin is an important signal for raft targeting [151]. It has been suggested that caveolin can negatively regulate GTPase activity and GTP binding of G proteins, which in turn stabilises the inactive conformation of G proteins during their localisation in caveolae [153]. Besides caveolin, another component of lipid rafts tubulin can interact with various G protein subunits, including $G\alpha_i$, $G\alpha_q$ and $G\alpha_s$, thus facilitating their localisation into lipid microdomains [158, 159].

As mentioned above, lipid rafts can be involved in activity-dependent G protein trafficking, internalisation and signalling. For example, thyrotropin-releasing hormone receptor-mediated $G\alpha_{q/11}$ activation results in decreased raft association [150]. In contrast, $G\alpha_s$ gets enriched in caveolae and subsequently internalised

upon GPCR-mediated activation [152]. In addition, it has been shown that endocytosis of $G\alpha_s$ is dependent on the integrity of caveolae since their its disruption by β-MCD or caveolin-1 knockdown prevents proper $G\alpha_s$ internalisation [151, 152]. Furthermore, depletion of cholesterol, sphingolipids or caveolin from the plasma membrane prevents $G\alpha_s$ localisation in lipid rafts, which in turn modifies $G\alpha_s$/AC downstream signalling leading to increased receptor-mediated cAMP production [146, 151, 154].

In addition to the heterotrimeric G proteins, also their downstream effectors are often localised in lipid microdomains. For example, Ca^{2+}-sensitive isoforms of AC are localised in lipid rafts [146, 160–162], where they interact with caveolin-3 and other membrane components via their cytoplasmic C1 and C2 loops [103, 146, 163]. Cholesterol depletion by treatment with β-MCD as well as caveolin-1 knockdown results in relocation of AC to non-raft membranes and in the enhancement of AC-mediated cAMP signalling [146, 151]. Similar effects have been observed after disruption of the actin and microtuble cytoskeleton [15], suggesting that raft association can lead to inhibition of AC activity followed by lowering the cAMP levels. This is in line with a recently published study demonstrating a higher basal AC activity in non-raft domains by applying different spatially restricted FRET-based cAMP biosensors [80]. In addition, lipid raft disruption by cholesterol depletion has been shown to selectively alter cAMP responses of receptors found in those membrane domains [80].

Besides AC, the $G\alpha_{q/11}$ effector PLCβ has recently been shown to translocate into lipid rafts of astrocytes upon agonist stimulation [164]. Furthermore, the PLCγ resides in lipid rafts and PLCγ palmitoylation seems to be necessary for raft recruitment. From the functional point of view, PLCγ association with lipid rafts is sufficient to promote its phosphorylation-induced activation [165]. Furthermore, lipid raft disruption delayed agonist-evoked calcium waves propagation, indicating that intact lipid rafts are important for GPCR-induced Ca^{2+} signalling [164].

12.3 Role of Lipid Microdomains and Serotonin Receptors in Depression

Lipid microdomains are important for many physiological processes and their integrity is essential for 5-HTR functions under physiological conditions. Accordingly, changes in the composition of lipid domains have been implicated in the development and progression of brain pathologies such as Alzheimer's Disease, Parkinson's Disease, schizophrenia and depression [166, 167]. In the following section, we will focus on the possible role of membrane lipid rafts and 5-HTR signalling in depression.

12.3.1 The Possible Role of Lipid Composition in Depression

Depression is a major neurological disorder characterised by altered mood, impaired concentration and a couple of neuro-vegetative symptoms. One key factor for the pathogenesis of depression is chronic stress, which is used in animal models to induce depression and anxiety-like behaviours. Several recent studies suggested a correlation between depression-like behaviours and modified membrane lipid composition. For example, chronic stress has been reported to induce a general dysregulation in lipid metabolism by increasing the transcriptional activity of genes involved in lipid synthesis [168]. Furthermore, Faria et al. investigated the brain's phospholipid content in a mouse model of depression [169]. They observed significantly reduced levels of phosphatidylinositol and increased levels of phosphatidylcholine as well as phosphatidylethanolamine in the whole brain. A recently published study suggests a brain area-specific regulation of phospholipid levels during depression [170]. In this study authors demonstrated that chronic unpredictable stress induces an increase in the amount of phosphatidylinositol in rat hippocampus, while phosphatidylethanolamine levels decreases in rat prefrontal cortex. In addition, the lack of n-3 polyunsaturated fatty acids in the brain might be involved in the development of depression/anxiety [167].

Besides general alteration in lipid synthesis, the metabolism of sphingomyelin is particularly influenced by depressive conditions. Lipid rafts have been suggested to be specific sites for the activation of acid sphingomyelinase (a-SMase), which hydrolyses sphingomyelin to ceramide in response to various stimuli, e.g. stress as well as bacterial and viral infection [167, 171]. In patients with severe depression, the activity of a-SMase is dramatically enhanced and a-SMase activity has been shown to correlate with the severity of depression [172]. In line with these observations, reduced levels of sphingomyelin and increased levels of ceramide have been detected in the prefrontal cortex and hippocampus of rats exposed to chronic unpredictable stress over a period of four weeks [170]. Furthermore, direct injection of C16 ceramide into the hippocampus of wild-type C57BL/6 mice induces depression-like symptoms even in the absence of stress [173]. Altogether, these findings indicate that enhanced a-SMase activity and subsequent ceramide release might contribute to the pathogenesis of depression. However, the mechanisms involved in ceramide-related control of depressive behaviours need to be elucidated.

One possible scenario implicates spatial regulation and signalling of monoaminergic receptors by modifying their lipid environment. Indeed, released ceramide can associate with each other to form small ceramide-rich domains, which can further fuse to larger platforms serving as signalling hot spots. Consequently, the tight packing and the high hydrophobicity of ceramide molecules can cause the removal of cholesterol from the membrane. Changes in the biophysical properties of membrane domains in turn might contribute to reorganisation of signalling receptors, e.g. 5-HTRs, or modification of its activation states [171]. Furthermore, a high concentration of ceramide molecules can result in the formation of ceramide channels which have been implicated in apoptosis [174].

Since enhanced a-SMase activity can directly influence depression-like behaviours, this enzyme has emerged as possible target for the treatment of depression. Different tricyclic and tetracyclic anti-depressant drugs (e.g. desipramine, imipramine and amitriptyline) functionally inhibit the activity of a-SMase by induction of the proteolytic degradation of the enzyme inhibiting activity of a-SMase [175–177]. In addition, the anti-depressants amitriptyline and fluoxetine were shown to reduce acid sphingomyelinase activity and ceramide concentrations in the hippocampus [173]. Furthermore, treatment with these drugs increased neuronal proliferation, maturation and survival, and improve depression-like behaviour in a rodent model of depression, while anti-depressive effects were not observed in a-SMase deficient mice [173], indicating an important role of a-SMase as therapeutic target in the treatment of depression.

12.3.2 The Role of Serotonin Receptors in Depression

An imbalance in monoaminergic neurotransmission and in particular alteration in the serotonergic system are tightly associated with the pathogenesis of depression [178]. In addition, abnormalities in the expression or signalling of different 5-HTRs have been implicated in the pathophysiology of this disease. Analysis of post-mortem brains of subjects suffering from depression revealed reduced postsynaptic 5-HT_{1A}R mRNA levels in the hippocampus and prefrontal cortex [179]. Several Positron emission tomography (PET) studies confirmed a decreased 5-HT_{1A}R density in the prefrontal cortex of patients with major depression [180–182]. Consistent with a lowered expression of 5-HT_{1A}R in depression, attenuated 5-HT_{1A}R-mediated signalling was also observed in tissue depressed suicide victims [183]. In addition, it has been shown that transgenic mice with low expression of 5-HT_{1A} autoreceptors exhibit increased resistance to chronic stress as compared to mice with high expression of presynaptic 5-HT_{1A}R [184]. Besides 5-HT_{1A}R, also 5-HT_7R has been implicated in the pathogenesis of depression, since pharmacological blockage of 5-HT_7R or genetic knockout of this receptor result in anti-depressive effects [185–189].

Numerous drugs used to treat depressive disorders affect the serotonin levels in the brain. They mainly increase extracellular serotonin concentrations by blocking the presynaptic reuptake [178]. Furthermore, some anti-depressants directly influence serotonergic signalling by acting as agonist for 5-HT_{1A}R (e.g. buspirone and vilazodone) or antagonist for 5-HT_7R (e.g. imipramine, desipramine, fluoxetine and vortioxtine). In addition, various pharmaceuticals applied in the treatment of depression have been shown to modify 5-HTR signalling indirectly by affecting the rafts translocation of the corresponding G proteins and its effectors. Some anti-depressants such as desipramine, fluoxetine, and reboxetine have been found to accumulate in lipid rafts without influencing the cholesterol content [190]. Furthermore, several studies demonstrated that chronic treatment with anti-depressants results in the translocation of $G\alpha_s$ out of lipid rafts [191–195]. The analysis of post-

mortem brains from suicide victims with a confirmed unipolar depression revealed an increased localisation of $G\alpha_s$ in DRM of cerebellum indicating altered raft association of $G\alpha_s$ in depression [196]. Anti-depressants seem to affect not only the localisation of G proteins, but also its downstream signalling. For example, coupling of $G\alpha_s$ to AC is enhanced upon anti-depressant treatment [197], which correlates with an increase in cAMP levels [198]. These data suggest that altering the lipid raft environment by anti-depressants can promote trafficking of $G\alpha_s$ into non-raft domains, which facilitates interaction and activation of AC leading to increased cAMP production.

Acknowledgement The work was supported by DFG grant PO732 to EP, by the DFG excellence cluster REBIRTH as well as by the EU funding of the European collaborative project Target ECM.

References

1. Singer SJ, Nicolson GL. The fluid mosaic model of the structure of cell membranes. Science. 1972;175:720–31. https://doi.org/10.1126/science.175.4023.720.
2. Lindner R, Naim HY. Domains in biological membranes. Exp Cell Res. 2009;315:2871–8. https://doi.org/10.1016/j.yexcr.2009.07.020.
3. Patel HH, Murray F, Insel PA. G-protein-coupled receptor-signaling components in membrane raft and caveolae microdomains. In: Klussmann DE, Scott J, editors. Protein-protein interactions as new drug targets. Berlin: Springer; 2008. p. 167–84.
4. Simons K, Ikonen E. Functional rafts in cell membranes. Nature. 1997;387:569–72. https://doi.org/10.1038/42408.
5. Insel PA, Head BP, Patel HH, et al. Compartmentation of G-protein-coupled receptors and their signalling components in lipid rafts and caveolae. Biochem Soc Trans. 2005;33:1131–4. https://doi.org/10.1042/BST0331131.
6. Tsui-Pierchala BA, Encinas M, Milbrandt J, Johnson EM Jr. Lipid rafts in neuronal signaling and function. Trends Neurosci. 2002;25:412–7. https://doi.org/10.1016/S0166-2236(02)02215-4.
7. Palade GE. Fine structure of blood capillaries. J Appl Phys. 1953;24:1424–36. https://doi.org/10.1161/01.RES.27.3.482.
8. Yamada E. The fine structure of the gall bladder epithelium of the mouse. J Biophys Biochem Cytol. 1955;1:445–58. https://doi.org/10.1083/jcb.1.5.445.
9. Chini B, Parenti M. G-protein coupled receptors in lipid rafts and caveolae: how, when and why do they go there? J Mol Endocrinol. 2004;32:325–38. https://doi.org/10.1677/jme.0.0320325.
10. Rothberg KG, Heuser JE, Donzell WC, et al. Caveolin, a protein component of caveolae membrane coats. Cell. 1992;68:673–82. https://doi.org/10.1016/0092-8674(92)90143-Z.
11. Hill MM, Bastiani M, Luetterforst R, et al. PTRF-Cavin, a conserved cytoplasmic protein required for caveola formation and function. Cell. 2008;132:113–24. https://doi.org/10.1016/j.cell.2007.11.042.
12. Liu L, Pilch PF. A critical role of cavin (polymerase I and transcript release factor) in caveolae formation and organization. J Biol Chem. 2008;283:4314–22. https://doi.org/10.1074/jbc.M707890200.

13. Head BP, Insel PA. Do caveolins regulate cells by actions outside of caveolae? Trends Cell Biol. 2007;17:51–7. https://doi.org/10.1016/j.tcb.2006.11.008.
14. Chichili GR, Rodgers W. Cytoskeleton–membrane interactions in membrane raft structure. Cell Mol Life Sci. 2009;66:2319–28. https://doi.org/10.1007/s00018-009-0022-6.
15. Head BP, Patel HH, Insel PA. Interaction of membrane/lipid rafts with the cytoskeleton: impact on signaling and function: membrane/lipid rafts, mediators of cytoskeletal arrangement and cell signaling. Biochim Biophys Acta BBA Biomembr. 2014;1838:532–45. https://doi.org/10.1016/j.bbamem.2013.07.018.
16. Liu AP, Fletcher DA. Actin Polymerization serves as a membrane domain switch in model lipid bilayers. Biophys J. 2006;91:4064–70. https://doi.org/10.1529/biophysj.106.090852.
17. Allen JA, Halverson-Tamboli RA, Rasenick MM. Lipid raft microdomains and neurotransmitter signalling. Nat Rev Neurosci. 2007;8:128–40. https://doi.org/10.1038/nrn2059.
18. Kusumi A, Koyama-Honda I, Suzuki K. Molecular dynamics and interactions for creation of stimulation-induced stabilized rafts from small unstable steady-state rafts. Traffic. 2004;5:213–30. https://doi.org/10.1111/j.1600-0854.2004.0178.x.
19. Simons K, Sampaio JL. Membrane organization and lipid rafts. Cold Spring Harb Perspect Biol. 2011;3:a004697. https://doi.org/10.1101/cshperspect.a004697.
20. Brown DA, Rose JK. Sorting of GPI-anchored proteins to glycolipid-enriched membrane subdomains during transport to the apical cell surface. Cell. 1992;68:533–44. https://doi.org/10.1016/0092-8674(92)90189-J.
21. Chang WJ, Ying YS, Rothberg KG, et al. Purification and characterization of smooth muscle cell caveolae. J Cell Biol. 1994;126:127–38. https://doi.org/10.1083/jcb.126.1.127.
22. Sargiacomo M, Sudol M, Tang Z, Lisanti MP. Signal transducing molecules and glycosyl-phosphatidylinositol-linked proteins form a caveolin-rich insoluble complex in MDCK cells. J Cell Biol. 1993;122:789–807. https://doi.org/10.1083/jcb.122.4.789.
23. Skocaj M, Bakrac B, Krizaj I, et al. The sensing of membrane microdomains based on pore-forming toxins. Curr Med Chem. 2013;20:491–501. https://doi.org/10.2174/0929867311320040002.
24. Salzer U, Prohaska R. Stomatin, flotillin-1, and flotillin-2 are major integral proteins of erythrocyte lipid rafts. Blood. 2001;97:1141–3. https://doi.org/10.1182/blood.V97.4.1141.
25. Huang P, Xu W, Yoon S-I, et al. Cholesterol reduction by methyl-beta-cyclodextrin attenuates the delta opioid receptor-mediated signaling in neuronal cells but enhances it in non-neuronal cells. Biochem Pharmacol. 2007;73:534–49. https://doi.org/10.1016/j.bcp.2006.10.032.
26. Boesze-Battaglia K. Isolation of membrane rafts and signaling complexes. In: Ali H, Haribabu B, editors. Transmembrane signaling protocols. Humana Press; 2006. p. 169–79.
27. Magee AI, Adler J, Parmryd I. Cold-induced coalescence of T-cell plasma membrane microdomains activates signalling pathways. J Cell Sci. 2005;118:3141–51. https://doi.org/10.1242/jcs.02442.
28. Foster LJ, De Hoog CL, Mann M. Unbiased quantitative proteomics of lipid rafts reveals high specificity for signaling factors. Proc Natl Acad Sci. 2003;100:5813–8. https://doi.org/10.1073/pnas.0631608100.
29. Babiychuk EB, Draeger A. Biochemical characterization of detergent-resistant membranes: a systematic approach. Biochem J. 2006;397:407–16. https://doi.org/10.1042/BJ20060056.
30. Lichtenberg D, Goñi FM, Heerklotz H. Detergent-resistant membranes should not be identified with membrane rafts. Trends Biochem Sci. 2005;30:430–6. https://doi.org/10.1016/j.tibs.2005.06.004.
31. Smart EJ, Ying Y-S, Mineo C, Anderson RG. A detergent-free method for purifying caveolae membrane from tissue culture cells. Proc Natl Acad Sci. 1995;92:10104–8.

32. Song KS, Li S, Okamoto T, et al. Co-purification and direct interaction of Ras with caveolin, an integral membrane protein of caveolae microdomains detergent-free purification of caveolae membranes. J Biol Chem. 1996;271:9690–7. https://doi.org/10.1074/jbc.271.16.9690.
33. Villar VAM, Cuevas S, Zheng X, Jose PA. Chapter 1—Localization and signaling of GPCRs in lipid rafts. In: Shukla AK, editor. Methods in cell biology. Academic; 2016. p. 3–23.
34. Boxer SG, Kraft ML, Weber PK. Advances in imaging secondary ion mass spectrometry for biological samples. Annu Rev Biophys. 2009;38:53–74. https://doi.org/10.1146/annurev.biophys.050708.133634.
35. Kraft ML, Weber PK, Longo ML, et al. Phase separation of lipid membranes analyzed with high-resolution secondary ion mass spectrometry. Science. 2006;313:1948–51. https://doi.org/10.1126/science.1130279.
36. Lozano MM, Liu Z, Sunnick E, et al. Colocalization of the ganglioside GM1 and cholesterol detected by secondary ion mass spectrometry. J Am Chem Soc. 2013;135:5620–30. https://doi.org/10.1021/ja310831m.
37. Filippov A, Orädd G, Lindblom G. The effect of cholesterol on the lateral diffusion of phospholipids in oriented bilayers. Biophys J. 2003;84:3079–86. https://doi.org/10.1016/S0006-3495(03)70033-2.
38. Guo W, Kurze V, Huber T, et al. A solid-state NMR study of phospholipid-cholesterol interactions: sphingomyelin-cholesterol binary systems. Biophys J. 2002;83:1465–78. https://doi.org/10.1016/S0006-3495(02)73917-9.
39. Soni SP, LoCascio DS, Liu Y, et al. Docosahexaenoic acid enhances segregation of lipids between raft and nonraft domains: 2H-NMR study. Biophys J. 2008;95:203–14. https://doi.org/10.1529/biophysj.107.123612.
40. Sugahara M, Uragami M, Regen SL. Selective association of cholesterol with long-chain phospholipids in liquid-ordered bilayers: support for the existence of lipid rafts. J Am Chem Soc. 2003;125:13040–1. https://doi.org/10.1021/ja038102n.
41. Simons K, Toomre D. Lipid rafts and signal transduction. Nat Rev Mol Cell Biol. 2000;1:31–9. https://doi.org/10.1038/35036052.
42. Binnig G, Quate CF, Gerber C. Atomic force microscope. Phys Rev Lett. 1986;56:930–3. https://doi.org/10.1103/PhysRevLett.56.930.
43. Henderson RM, Edwardson JM, Geisse NA, Saslowsky DE. Lipid rafts: feeling is believing. Physiology. 2004;19:39–43. https://doi.org/10.1152/nips.01505.2003.
44. Dürig U, Pohl DW, Rohner F. Near-field optical-scanning microscopy. J Appl Phys. 1986;59:3318–27. https://doi.org/10.1063/1.336848.
45. Ianoul A, Johnston L. Near-field scanning optical microscopy to identify membrane microdomains. In: Dopico A, editor. Methods in membrane lipids. Totowa, NJ: Humana Press; 2007. p. 469–80.
46. Ianoul A, Street M, Grant D, et al. Near-field scanning fluorescence microscopy study of ion channel clusters in cardiac myocyte membranes. Biophys J. 2004;87:3525–35. https://doi.org/10.1529/biophysj.104.046383.
47. Ishitsuka R, Sato SB, Kobayashi T. Imaging lipid rafts. J Biochem (Tokyo). 2005;137:249–54. https://doi.org/10.1093/jb/mvi041.
48. Schütz GJ, Kada G, Pastushenko VP, Schindler H. Properties of lipid microdomains in a muscle cell membrane visualized by single molecule microscopy. EMBO J. 2000;19:892–901. https://doi.org/10.1093/emboj/19.5.892.
49. Sato SB, Ishii K, Makino A, et al. Distribution and transport of cholesterol-rich membrane domains monitored by a membrane-impermeant fluorescent polyethylene glycol-derivatized cholesterol. J Biol Chem. 2004;279:23790–6. https://doi.org/10.1074/jbc.M313568200.
50. Gousset K, Krishnamoorthy G, Rao M, Mayor S with Sharma P, Varma R, Sarasij RC, Ira. Nanoscale organization of multiple GPI-anchored proteins in living cell membranes. Cell. 2004;116:577–89. doi: https://doi.org/10.1016/S0092-8674(04)00167-9.

51. Kenworthy AK, Petranova N, Edidin M. High-resolution FRET microscopy of cholera toxin B-subunit and GPI-anchored proteins in cell plasma membranes. Mol Biol Cell. 2000;11:1645–55. https://doi.org/10.1091/mbc.11.5.1645.
52. Renner U, Glebov K, Lang T, et al. Localization of the mouse 5-hydroxytryptamine1A receptor in lipid microdomains depends on its palmitoylation and is involved in receptor-mediated signaling. Mol Pharmacol. 2007;72:502–13. https://doi.org/10.1124/mol.107.037085.
53. Shakor A-BA, Czuryło EA, Sobota A. Lysenin, a unique sphingomyelin-binding protein. FEBS Lett. 2003;542:1–6. https://doi.org/10.1016/S0014-5793(03)00330-2.
54. Parasassi T, Gratton E, Yu WM, et al. Two-photon fluorescence microscopy of laurdan generalized polarization domains in model and natural membranes. Biophys J. 1997;72:2413–29. https://doi.org/10.1016/S0006-3495(97)78887-8.
55. Klymchenko AS, Kreder R. Fluorescent probes for lipid rafts: from model membranes to living cells. Chem Biol. 2014;21:97–113. https://doi.org/10.1016/j.chembiol.2013.11.009.
56. Lagerholm BC, Weinreb GE, Jacobson K, Thompson NL. Detecting microdomains in intact cell membranes. Annu Rev Phys Chem. 2005;56:309–36. https://doi.org/10.1146/annurev.physchem.56.092503.141211.
57. Sieber JJ, Willig KI, Kutzner C, et al. Anatomy and dynamics of a supramolecular membrane protein cluster. Science. 2007;317:1072–6. https://doi.org/10.1126/science.1141727.
58. Eggeling C, Ringemann C, Medda R, et al. Direct observation of the nanoscale dynamics of membrane lipids in a living cell. Nature. 2009;457:1159–62. https://doi.org/10.1038/nature07596.
59. Sezgin E, Levental I, Grzybek M, et al. Partitioning, diffusion, and ligand binding of raft lipid analogs in model and cellular plasma membranes. Biochim Biophys Acta BBA Biomembr. 2012;1818:1777–84. https://doi.org/10.1016/j.bbamem.2012.03.007.
60. Owen DM, Gaus K. Imaging lipid domains in cell membranes: the advent of super-resolution fluorescence microscopy. Plant Cell Biol. 2013;4:503. https://doi.org/10.3389/fpls.2013.00503.
61. Owen DM, Williamson D, Magenau A, et al. Optical techniques for imaging membrane domains in live cells (live-cell palm of protein clustering). Methods Enzymol. 2012;504:221–35.
62. Simons K, Gerl MJ. Revitalizing membrane rafts: new tools and insights. Nat Rev Mol Cell Biol. 2010;11:688–99. https://doi.org/10.1038/nrm2977.
63. Stahley SN, Warren MF, Feldman RJ, et al. Super-resolution microscopy reveals altered desmosomal protein organization in tissue from patients with Pemphigus vulgaris. J Invest Dermatol. 2016;136:59–66. https://doi.org/10.1038/JID.2015.353.
64. De Almeida RFM, Loura LMS, Prieto M. Membrane lipid domains and rafts: current applications of fluorescence lifetime spectroscopy and imaging. Chem Phys Lipids. 2009;157:61–77. https://doi.org/10.1016/j.chemphyslip.2008.07.011.
65. Rao M, Mayor S. Use of Forster's resonance energy transfer microscopy to study lipid rafts. Biochim Biophys Acta BBA Mol Cell Res. 2005;1746:221–33. https://doi.org/10.1016/j.bbamcr.2005.08.002.
66. Brown DA, London E. Structure and function of sphingolipid- and cholesterol-rich membrane rafts. J Biol Chem. 2000;275:17221–4. https://doi.org/10.1074/jbc.R000005200.
67. Drake DR, Braciale TJ. Cutting edge: lipid raft integrity affects the efficiency of MHC class I tetramer binding and cell surface TCR arrangement on CD8+ T cells. J Immunol. 2001;166:7009–13.
68. Oakley FD, Smith RL, Engelhardt JF. Lipid rafts and caveolin-1 coordinate interleukin-1beta (IL-1beta)-dependent activation of NFkappaB by controlling endocytosis of Nox2 and IL-1beta receptor 1 from the plasma membrane. J Biol Chem. 2009;284:33255–64. https://doi.org/10.1074/jbc.M109.042127.
69. Wysoczynski M, Reca R, Ratajczak J, et al. Incorporation of CXCR4 into membrane lipid rafts primes homing-related responses of hematopoietic stem/progenitor cells to an SDF-1 gradient. Blood. 2005;105:40–8. https://doi.org/10.1182/blood-2004-04-1430.

70. Ohtani Y, Irie T, Uekama K, et al. Differential effects of alpha-, beta- and gamma-cyclodextrins on human erythrocytes. Eur J Biochem FEBS. 1989;186:17–22.
71. Christian AE, Haynes MP, Phillips MC, Rothblat GH. Use of cyclodextrins for manipulating cellular cholesterol content. J Lipid Res. 1997;38:2264–72.
72. Kilsdonk EPC, Yancey PG, Stoudt GW, et al. Cellular cholesterol efflux mediated by cyclodextrins. J Biol Chem. 1995;270:17250–6. https://doi.org/10.1074/jbc.270.29.17250.
73. Yancey PG, Rodrigueza WV, Kilsdonk EPC, et al. Cellular cholesterol efflux mediated by cyclodextrins demonstration of kinetic pools and mechanism of efflux. J Biol Chem. 1996; 271:16026–34. https://doi.org/10.1074/jbc.271.27.16026.
74. Hering H, Lin C-C, Sheng M. Lipid rafts in the maintenance of synapses, dendritic spines, and surface AMPA receptor stability. J Neurosci. 2003;23:3262–71.
75. Meszaros P, Klappe K, Hummel I, et al. Function of MRP1/ABCC1 is not dependent on cholesterol or cholesterol-stabilized lipid rafts. Biochem J. 2011;437:483–91. https://doi.org/10.1042/BJ20110427.
76. Naslavsky N, Shmeeda H, Friedlander G, et al. Sphingolipid depletion increases formation of the scrapie prion protein in neuroblastoma cells infected with prions. J Biol Chem. 1999;274: 20763–71. https://doi.org/10.1074/jbc.274.30.20763.
77. Nagafuku M, Kabayama K, Oka D, et al. Reduction of glycosphingolipid levels in lipid rafts affects the expression state and function of glycosylphosphatidylinositol-anchored proteins but does not impair signal transduction via the T cell receptor. J Biol Chem. 2003;278: 51920–7. https://doi.org/10.1074/jbc.M307674200.
78. Trushina E, Du Charme J, Parisi J, McMurray CT. Neurological abnormalities in caveolin-1 knock out mice. Behav Brain Res. 2006;172:24–32. https://doi.org/10.1016/j.bbr.2006.04.024.
79. Bhatnagar A, Sheffler DJ, Kroeze WK, et al. Caveolin-1 interacts with 5-HT2A serotonin receptors and profoundly modulates the signaling of selected Gαq-coupled protein receptors. J Biol Chem. 2004;279:34614–23. https://doi.org/10.1074/jbc.M404673200.
80. Agarwal SR, Yang P-C, Rice M, et al. Role of membrane microdomains in compartmentation of cAMP signaling. PLoS One. 2014;9:e95835. https://doi.org/10.1371/journal.pone.0095835.
81. Levental I, Grzybek M, Simons K. Greasing their way: lipid modifications determine protein association with membrane rafts. Biochemistry (Mosc). 2010;49:6305–16. https://doi.org/10.1021/bi100882y.
82. Fukata Y, Fukata M. Protein palmitoylation in neuronal development and synaptic plasticity. Nat Rev Neurosci. 2010;11:161–75. https://doi.org/10.1038/nrn2788.
83. Lucero HA, Robbins PW. Lipid rafts–protein association and the regulation of protein activity. Arch Biochem Biophys. 2004;426:208–24. https://doi.org/10.1016/j.abb.2004.03.020.
84. Roth AF, Feng Y, Chen L, Davis NG. The yeast DHHC cysteine-rich domain protein Akr1p is a palmitoyl transferase. J Cell Biol. 2002;159:23–8. https://doi.org/10.1083/jcb.200206120.
85. Greaves J, Chamberlain LH. DHHC palmitoyl transferases: substrate interactions and (patho) physiology. Trends Biochem Sci. 2011;36:245–53. https://doi.org/10.1016/j.tibs.2011.01.003.
86. Ohno Y, Kashio A, Ogata R, et al. Analysis of substrate specificity of human DHHC protein acyltransferases using a yeast expression system. Mol Biol Cell. 2012;23:4543–51.
87. Zeidman R, Jackson CS, Magee AI. Protein acyl thioesterases (Review). Mol Membr Biol. 2009;26:32–41. https://doi.org/10.1080/09687680802629329.
88. Lin DTS, Conibear E. ABHD17 proteins are novel protein depalmitoylases that regulate N-Ras palmitate turnover and subcellular localization. elife. 2015;4:e11306. https://doi.org/10.7554/eLife.11306.
89. Conibear E, Davis NG. Palmitoylation and depalmitoylation dynamics at a glance. J Cell Sci. 2010;123:4007–10. https://doi.org/10.1242/jcs.059287.
90. Aicart-Ramos C, Valero RA, Rodriguez-Crespo I. Protein palmitoylation and subcellular trafficking. Biochim Biophys Acta. 2011;1808:2981–94. https://doi.org/10.1016/j.bbamem.2011.07.009.

91. Chamberlain LH, Lemonidis K, Sanchez-Perez M, et al. Palmitoylation and the trafficking of peripheral membrane proteins. Biochem Soc Trans. 2013;41:62–6. https://doi.org/10.1042/BST20120243.
92. Rocks O, Gerauer M, Vartak N, et al. The palmitoylation machinery is a spatially organizing system for peripheral membrane proteins. Cell. 2010;141:458–71. https://doi.org/10.1016/j.cell.2010.04.007.
93. Wang T-Y, Leventis R, Silvius JR. Partitioning of lipidated peptide sequences into liquid-ordered lipid domains in model and biological membranes. Biochemistry (Mosc). 2001;40:13031–40. https://doi.org/10.1021/bi0112311.
94. Brown DA. Lipid rafts, detergent-resistant membranes, and raft targeting signals. Physiology. 2006;21:430–9. https://doi.org/10.1152/physiol.00032.2006.
95. Blaskovic S, Blanc M, van der Goot FG. What does S-palmitoylation do to membrane proteins? FEBS J. 2013;280:2766–74. https://doi.org/10.1111/febs.12263.
96. Gorinski N, Ponimaskin E. Palmitoylation of serotonin receptors. Biochem Soc Trans. 2013;41:89–94. https://doi.org/10.1042/BST20120235.
97. Macdonald JL. A simplified method for the preparation of detergent-free lipid rafts. J Lipid Res. 2005;46:1061–7. https://doi.org/10.1194/jlr.D400041-JLR200.
98. Melkonian KA, Ostermeyer AG, Chen JZ, et al. Role of lipid modifications in targeting proteins to detergent-resistant membrane rafts. Many raft proteins are acylated, while few are prenylated. J Biol Chem. 1999;274:3910–7.
99. Levental I, Lingwood D, Grzybek M, et al. Palmitoylation regulates raft affinity for the majority of integral raft proteins. Proc Natl Acad Sci. 2010;107:22050–4. https://doi.org/10.1073/pnas.1016184107.
100. Liu P, Rudick M, Anderson RGW. Multiple functions of caveolin-1. J Biol Chem. 2002;277:41295–8. https://doi.org/10.1074/jbc.R200020200.
101. Okamoto T, Schlegel A, Scherer PE, Lisanti MP. Caveolins, a family of scaffolding proteins for organizing "preassembled signaling complexes" at the plasma membrane. J Biol Chem. 1998;273:5419–22. https://doi.org/10.1074/jbc.273.10.5419.
102. Razani B, Rubin CS, Lisanti MP. Regulation of cAMP-mediated signal transduction via interaction of caveolins with the catalytic subunit of protein kinase A. J Biol Chem. 1999;274:26353–60. https://doi.org/10.1074/jbc.274.37.26353.
103. Crossthwaite AJ, Seebacher T, Masada N, et al. The cytosolic domains of Ca2+−sensitive adenylyl cyclases dictate their targeting to plasma membrane lipid rafts. J Biol Chem. 2005;280:6380–91. https://doi.org/10.1074/jbc.M411987200.
104. Yamabhai M, Anderson RGW. Second cysteine-rich region of epidermal growth factor receptor contains targeting information for caveolae/rafts. J Biol Chem. 2002;277:24843–6. https://doi.org/10.1074/jbc.C200277200.
105. Bjarnadottir TK, Gloriam DE, Hellstrand SH, et al. Comprehensive repertoire and phylogenetic analysis of the G protein-coupled receptors in human and mouse. Genomics. 2006;88:263–73. https://doi.org/10.1016/j.ygeno.2006.04.001.
106. Kobilka BK. G protein coupled receptor structure and activation. Biochim Biophys Acta. 2007;1768:794–807. https://doi.org/10.1016/j.bbamem.2006.10.021.
107. Thompson MD, Cole DE, Jose PA. Pharmacogenomics of G protein-coupled receptor signaling: insights from health and disease. Methods Mol Biol. 2008;448:77–107. https://doi.org/10.1007/978-1-59745-205-2_6.
108. Cabrera-Vera TM, Vanhauwe J, Thomas TO, et al. Insights into G protein structure, function, and regulation. Endocr Rev. 2003;24:765–81. https://doi.org/10.1210/er.2000-0026.
109. Kristiansen K. Molecular mechanisms of ligand binding, signaling, and regulation within the superfamily of G-protein-coupled receptors: molecular modeling and mutagenesis approaches to receptor structure and function. Pharmacol Ther. 2004;103:21–80. https://doi.org/10.1016/j.pharmthera.2004.05.002.
110. Pierce KL, Premont RT, Lefkowitz RJ. Seven-transmembrane receptors. Nat Rev Mol Cell Biol. 2002;3:639–50. https://doi.org/10.1038/nrm908.

111. Logothetis DE, Kurachi Y, Galper J, et al. The beta gamma subunits of GTP-binding proteins activate the muscarinic K+ channel in heart. Nature. 1987;325:321–6. https://doi.org/10.1038/325321a0.
112. Woehler A, Ponimaskin EG. G protein-mediated signaling: same receptor, multiple effectors. Curr Mol Pharmacol. 2009;2:237–48.
113. Krupnick JG, Benovic JL. The role of receptor kinases and arrestins in G protein-coupled receptor regulation. Annu Rev Pharmacol Toxicol. 1998;38:289–319. https://doi.org/10.1146/annurev.pharmtox.38.1.289.
114. Lefkowitz RJ, Shenoy SK. Transduction of receptor signals by beta-arrestins. Science. 2005;308:512–7. https://doi.org/10.1126/science.1109237.
115. Gehret AU, Hinkle PM. Importance of regions outside the cytoplasmic tail of G-protein-coupled receptors for phosphorylation and dephosphorylation. Biochem J. 2010;428:235–45. https://doi.org/10.1042/BJ20100139.
116. Perry SJ, Baillie GS, Kohout TA, et al. Targeting of cyclic AMP degradation to beta 2-adrenergic receptors by beta-arrestins. Science. 2002;298:834–6. https://doi.org/10.1126/science.1074683.
117. Shenoy SK, Lefkowitz RJ. Multifaceted roles of beta-arrestins in the regulation of seven-membrane-spanning receptor trafficking and signalling. Biochem J. 2003;375:503–15. https://doi.org/10.1042/BJ20031076.
118. Arreola R, Becerril-Villanueva E, Cruz-Fuentes C, et al. Immunomodulatory effects mediated by serotonin, immunomodulatory effects mediated by serotonin. J Immunol Res. 2015;2015:e354957. https://doi.org/10.1155/2015/354957.
119. Mössner R, Lesch K-P. Role of serotonin in the immune system and in neuroimmune interactions. Brain Behav Immun. 1998;12:249–71. https://doi.org/10.1006/brbi.1998.0532.
120. Glikmann-Johnston Y, Saling MM, Reutens DC, Stout JC. Hippocampal 5-HT1A receptor and spatial learning and memory. Neuropharmacology. 2015;289. https://doi.org/10.3389/fphar.2015.00289.
121. Pytliak M, Vargová V, Mechírová V, Felšöci M. Serotonin receptors—from molecular biology to clinical applications. Physiol Res Acad Sci Bohemoslov. 2011;60:15–25.
122. Kaufman J, DeLorenzo C, Choudhury S, Parsey RV. The 5-HT1A receptor in major depressive disorder. Eur Neuropsychopharmacol. 2016;26:397–410. https://doi.org/10.1016/j.euroneuro.2015.12.039.
123. Albert PR, Tiberi M. Receptor signaling and structure: insights from serotonin-1 receptors. Trends Endocrinol Metab. 2001;12:453–60. https://doi.org/10.1016/S1043-2760(01)00498-2.
124. Kalipatnapu S, Chattopadhyay A. A GFP fluorescence-based approach to determine detergent insolubility of the human serotonin1A receptor. FEBS Lett. 2004;576:455–60. https://doi.org/10.1016/j.febslet.2004.09.055.
125. Kalipatnapu S, Chattopadhyay A. Membrane organization of the human serotonin1A receptor monitored by detergent insolubility using GFP fluorescence. Mol Membr Biol. 2005;22:539–47. https://doi.org/10.1080/09687860500421738.
126. Kalipatnapu S, Chattopadhyay A. Membrane organization of the serotonin 1A receptor monitored by a detergent-free approach. Cell Mol Neurobiol. 2007;27:463–74. https://doi.org/10.1007/s10571-007-9138-0.
127. Ganguly S, Chattopadhyay A. Cholesterol depletion mimics the effect of cytoskeletal destabilization on membrane dynamics of the serotonin1A receptor: a zFCS study. Biophys J. 2010;99:1397–407. https://doi.org/10.1016/j.bpj.2010.06.031.
128. Gutierrez MG, Malmstadt N. Human serotonin receptor 5-HT1A preferentially segregates to the liquid disordered phase in synthetic lipid bilayers. J Am Chem Soc. 2014;136:13530–3. https://doi.org/10.1021/ja507221m.
129. Papoucheva E, Dumuis A, Sebben M, et al. The 5-hydroxytryptamine(1A) receptor is stably palmitoylated, and acylation is critical for communication of receptor with Gi protein. J Biol Chem. 2004;279:3280–91. https://doi.org/10.1074/jbc.M308177200.

130. Kobe F, Renner U, Woehler A, et al. Stimulation- and palmitoylation-dependent changes in oligomeric conformation of serotonin 5-HT1A receptors. Biochim Biophys Acta BBA Mol Cell Res. 2008;1783:1503–16. https://doi.org/10.1016/j.bbamcr.2008.02.021.
131. Woehler A, Wlodarczyk J, Ponimaskin EG. Specific oligomerization of the 5-HT1A receptor in the plasma membrane. Glycoconj J. 2008;26:749–56. https://doi.org/10.1007/s10719-008-9187-8.
132. Sjögren B, Csöregh L, Svenningsson P. Cholesterol reduction attenuates 5-HT1A receptor-mediated signaling in human primary neuronal cultures. Naunyn Schmiedeberg's Arch Pharmacol. 2008;378:441–6. https://doi.org/10.1007/s00210-008-0323-6.
133. Landolt H-P, Wehrle R. Antagonism of serotonergic 5-HT2A/2C receptors: mutual improvement of sleep, cognition and mood? Eur J Neurosci. 2009;29:1795–809. https://doi.org/10.1111/j.1460-9568.2009.06718.x.
134. Fiorica-Howells E, Hen R, Gingrich J, et al. 5-HT2A receptors: location and functional analysis in intestines of wild-type and 5-HT2A knockout mice. Am J Physiol Gastrointest Liver Physiol. 2002;282:G877–93. https://doi.org/10.1152/ajpgi.00435.2001.
135. Sommer B, Montaño LM, Carbajal V, et al. Extraction of membrane cholesterol disrupts caveolae and impairs serotonergic (5-HT2A) and histaminergic (H1) responses in bovine airway smooth muscle: role of Rho-kinase. Can J Physiol Pharmacol. 2009;87:180–95. https://doi.org/10.1139/Y08-114.
136. Dreja K, Voldstedlund M, Vinten J, et al. Cholesterol depletion disrupts caveolae and differentially impairs agonist-induced arterial contraction. Arterioscler Thromb Vasc Biol. 2002;22:1267–72. https://doi.org/10.1161/01.ATV.0000023438.32585.A1.
137. Fiorica-Howells E, Maroteaux L, Gershon MD. Serotonin and the 5-HT2B receptor in the development of enteric neurons. J Neurosci. 2000;20:294–305.
138. Wirth A, Holst K, Ponimaskin E. How serotonin receptors regulate morphogenic signalling in neurons. Prog Neurobiol. 2016. https://doi.org/10.1016/j.pneurobio.2016.03.007.
139. Gellynck E, Heyninck K, Andressen KW, et al. The serotonin 5-HT7 receptors: two decades of research. Exp Brain Res. 2013;230:555–68. https://doi.org/10.1007/s00221-013-3694-y.
140. Guseva D, Wirth A, Ponimaskin E. Cellular mechanisms of the 5-HT $_7$ receptor-mediated signaling. Front Behav Neurosci. 2014;8:306. https://doi.org/10.3389/fnbeh.2014.00306.
141. Naumenko VS, Popova NK, Lacivita E, et al. Interplay between serotonin 5-HT1A and 5-HT7 receptors in depressive disorders. CNS Neurosci Ther. 2014;20:582–90. https://doi.org/10.1111/cns.12247.
142. Sjögren B, Svenningsson P. Caveolin-1 affects serotonin binding and cell surface levels of human 5-HT7(a) receptors. FEBS Lett. 2007;581:5115–21. https://doi.org/10.1016/j.febslet.2007.09.059.
143. Kvachnina E. 5-HT7 receptor is coupled to G subunits of heterotrimeric G12-protein to regulate gene transcription and neuronal morphology. J Neurosci. 2005;25:7821–30. https://doi.org/10.1523/JNEUROSCI.1790-05.2005.
144. Sjögren B, Hamblin MW, Svenningsson P. Cholesterol depletion reduces serotonin binding and signaling via human 5-HT7(a) receptors. Eur J Pharmacol. 2006;552:1–10. https://doi.org/10.1016/j.ejphar.2006.08.069.
145. Sjögren B, Svenningsson P. Depletion of the lipid raft constituents, sphingomyelin and ganglioside, decreases serotonin binding at human 5-HT7(a) receptors in HeLa cells. Acta Physiol. 2007;190:47–53. https://doi.org/10.1111/j.1365-201X.2007.01687.x.
146. Rybin VO, Xu X, Lisanti MP, Steinberg SF. Differential targeting of β-adrenergic receptor subtypes and adenylyl cyclase to cardiomyocyte caveolae a mechanism to functionally regulate the cAMP signaling pathway. J Biol Chem. 2000;275:41447–57. https://doi.org/10.1074/jbc.M006951200.

147. Galbiati F, Volonté D, Meani D, et al. The dually acylated NH2-terminal domain of Gi1α Is sufficient to target a green fluorescent protein reporter to caveolin-enriched plasma membrane domains palmitoylation of caveoLIN-1 is required for the recognition of dually acylated G-protein α subunits in vivo. J Biol Chem. 1999;274:5843–50. https://doi.org/10.1074/jbc.274.9.5843.
148. Dunphy JT, Greentree WK, Linder ME. Enrichment of G-protein palmitoyltransferase activity in low density membranes in vitro reconstitution of gαi to these domains requires palmitoyltransferase activity. J Biol Chem. 2001;276:43300–4. https://doi.org/10.1074/jbc.M104275200.
149. Oh P, Schnitzer JE. Segregation of heterotrimeric G proteins in cell surface microdomains Gq binds caveolin to concentrate in caveolae, whereas Gi and Gs target lipid rafts by default. Mol Biol Cell. 2001;12:685–98. https://doi.org/10.1091/mbc.12.3.685.
150. Pešanová Z, Novotný J, Černý J, et al. Thyrotropin-releasing hormone-induced depletion of Gqα/G11α proteins from detergent-insensitive membrane domains. FEBS Lett. 1999;464:35–40. https://doi.org/10.1016/S0014-5793(99)01666-X.
151. Allen JA, Yu JZ, Dave RH, et al. Caveolin-1 and lipid microdomains regulate Gs trafficking and attenuate Gs/adenylyl cyclase signaling. Mol Pharmacol. 2009;76:1082–93. https://doi.org/10.1124/mol.109.060160.
152. Allen JA, Yu JZ, Donati RJ, Rasenick MM. β-adrenergic receptor stimulation promotes Gαs internalization through lipid rafts: a study in living cells. Mol Pharmacol. 2005;67:1493–504. https://doi.org/10.1124/mol.104.008342.
153. Li S, Okamoto T, Chun M, et al. Evidence for a regulated interaction between heterotrimeric G proteins and caveolin. J Biol Chem. 1995;270:15693–701.
154. Miura Y, Hanada K, Jones TLZ. Gs signaling is intact after disruption of lipid rafts. Biochemistry (Mosc). 2001;40:15418–23. https://doi.org/10.1021/bi015574a.
155. Waheed AA, Jones TLZ. Hsp90 interactions and acylation target the G protein Gα12 but not Gα13 to lipid rafts. J Biol Chem. 2002;277:32409–12. https://doi.org/10.1074/jbc.C200383200.
156. Moffett S, Brown DA, Linder ME. Lipid-dependent targeting of G proteins into rafts. J Biol Chem. 2000;275:2191–8. https://doi.org/10.1074/jbc.275.3.2191.
157. Ponimaskin E, Behn H, Adarichev V, et al. Acylation of Gα13 is important for its interaction with thrombin receptor, transforming activity and actin stress fiber formation. FEBS Lett. 2000;478:173–7. https://doi.org/10.1016/S0014-5793(00)01845-7.
158. Popova JS, Garrison JC, Rhee SG, Rasenick MM. Tubulin, Gq, and phosphatidylinositol 4,5-bisphosphate interact to regulate phospholipase Cβ1 signaling. J Biol Chem. 1997;272:6760–5. https://doi.org/10.1074/jbc.272.10.6760.
159. Wang N, Yan K, Rasenick MM. Tubulin binds specifically to the signal-transducing proteins, Gs alpha and Gi alpha 1. J Biol Chem. 1990;265:1239–42.
160. Cooper DMF, Crossthwaite AJ. Higher-order organization and regulation of adenylyl cyclases. Trends Pharmacol Sci. 2006;27:426–31. https://doi.org/10.1016/j.tips.2006.06.002.
161. Fagan KA, Smith KE, Cooper DMF. Regulation of the Ca2+-inhibitable adenylyl cyclase type VI by capacitative Ca2+ entry requires localization in cholesterol-rich domains. J Biol Chem. 2000;275:26530–7. https://doi.org/10.1074/jbc.M001369200.
162. Smith KE, Gu C, Fagan KA, et al. Residence of adenylyl cyclase type 8 in caveolae is necessary but not sufficient for regulation by capacitative Ca2+ entry. J Biol Chem. 2002;277:6025–31. https://doi.org/10.1074/jbc.M109615200.
163. Toya Y, Schwencke C, Couet J, et al. Inhibition of adenylyl cyclase by caveolin peptides. Endocrinology. 1998;139:2025–31. https://doi.org/10.1210/endo.139.4.5957.
164. Weerth SH, Holtzclaw LA, Russell JT. Signaling proteins in raft-like microdomains are essential for Ca2+ wave propagation in glial cells. Cell Calcium. 2007;41:155–67. https://doi.org/10.1016/j.ceca.2006.06.006.
165. Verí M-C, KE DB, Seminario M-C, et al. Membrane raft-dependent regulation of phospholipase Cγ-1 activation in T lymphocytes. Mol Cell Biol. 2001;21:6939–50. https://doi.org/10.1128/MCB.21.20.6939-6950.2001.

166. Bienias K, Fiedorowicz A, Sadowska A, et al. Regulation of sphingomyelin metabolism. Pharmacol Rep. 2016;68:570–81. https://doi.org/10.1016/j.pharep.2015.12.008.
167. Müller CP, Reichel M, Mühle C, et al. Brain membrane lipids in major depression and anxiety disorders. Biochim Biophys Acta BBA Mol Cell Biol Lipids. 2015;1851:1052–65. https://doi.org/10.1016/j.bbalip.2014.12.014.
168. Chuang J-C, Cui H, Mason BL, et al. Chronic social defeat stress disrupts regulation of lipid synthesis. J Lipid Res. 2010;51:1344–53. https://doi.org/10.1194/jlr.M002196.
169. Faria R, Santana MM, Aveleira CA, et al. Alterations in phospholipidomic profile in the brain of mouse model of depression induced by chronic unpredictable stress. Neuroscience. 2014; 273:1–11. https://doi.org/10.1016/j.neuroscience.2014.04.042.
170. Oliveira TG, Chan RB, Bravo FV, et al. The impact of chronic stress on the rat brain lipidome. Mol Psychiatry. 2016;21:80–8. https://doi.org/10.1038/mp.2015.14.
171. Gulbins E, Walter S, Becker KA, et al. A central role for the acid sphingomyelinase/ceramide system in neurogenesis and major depression. J Neurochem. 2015;134:183–92. https://doi.org/10.1111/jnc.13145.
172. Kornhuber J, Medlin A, Bleich S, et al. High activity of acid sphingomyelinase in major depression. J Neural Transm. 2005;112:1583–90. https://doi.org/10.1007/s00702-005-0374-5.
173. Gulbins E, Palmada M, Reichel M, et al. Acid sphingomyelinase-ceramide system mediates effects of antidepressant drugs. Nat Med. 2013;19:934–8. https://doi.org/10.1038/nm.3214.
174. Siskind LJ, Colombini M. The lipids C2- and C16-ceramide form large stable channels. Implications for apoptosis. J Biol Chem. 2000;275:38640–4. https://doi.org/10.1074/jbc.C000587200.
175. Hurwitz R, Ferlinz K, Sandhoff K. The tricyclic antidepressant desipramine causes proteolytic degradation of lysosomal sphingomyelinase in human fibroblasts. Biol Chem Hoppe Seyler. 1994;375:447–50.
176. Kölzer M, Werth N, Sandhoff K. Interactions of acid sphingomyelinase and lipid bilayers in the presence of the tricyclic antidepressant desipramine. FEBS Lett. 2004;559:96–8. https://doi.org/10.1016/S0014-5793(04)00033-X.
177. Kornhuber J, Tripal P, Reichel M, et al. Identification of new functional inhibitors of acid sphingomyelinase using a structure-property-activity relation model. J Med Chem. 2008;51:219–37. https://doi.org/10.1021/jm070524a.
178. Köhler S, Cierpinsky K, Kronenberg G, Adli M. The serotonergic system in the neurobiology of depression: relevance for novel antidepressants. J Psychopharmacol (Oxf). 2016;30:13–22. https://doi.org/10.1177/0269881115609072.
179. López-Figueroa AL, Norton CS, López-Figueroa MO, et al. Serotonin 5-HT1A, 5-HT1B, and 5-HT2A receptor mRNA expression in subjects with major depression, bipolar disorder, and schizophrenia. Biol Psychiatry. 2004;55:225–33. https://doi.org/10.1016/j.biopsych.2003.09.017.
180. Drevets WC, Frank E, Price JC, et al. Serotonin type-1A receptor imaging in depression. Nucl Med Biol. 2000;27:499–507.
181. Neumeister A, Young T, Stastny J. Implications of genetic research on the role of the serotonin in depression: emphasis on the serotonin type 1A receptor and the serotonin transporter. Psychopharmacology. 2004;174:512–24. https://doi.org/10.1007/s00213-004-1950-3.
182. Sargent PA, Rabiner EA, Bhagwagar Z, et al. 5-HT(1A) receptor binding in euthymic bipolar patients using positron emission tomography with [carbonyl-(11)C]WAY-100635. J Affect Disord. 2010;123:77–80. https://doi.org/10.1016/j.jad.2009.07.015.
183. Hsiung S, Adlersberg M, Arango V, et al. Attenuated 5-HT1A receptor signaling in brains of suicide victims: involvement of adenylyl cyclase, phosphatidylinositol 3-kinase, Akt and mitogen-activated protein kinase. J Neurochem. 2003;87:182–94. https://doi.org/10.1046/j.1471-4159.2003.01987.x.
184. Richardson-Jones JW, Craige CP, Guiard BP, et al. 5-HT1A autoreceptor levels determine vulnerability to stress and response to antidepressants. Neuron. 2010;65:40–52. https://doi.org/10.1016/j.neuron.2009.12.003.

185. Guscott M, Bristow LJ, Hadingham K, et al. Genetic knockout and pharmacological blockade studies of the 5-HT7 receptor suggest therapeutic potential in depression. Neuropharmacology. 2005;48:492–502. https://doi.org/10.1016/j.neuropharm.2004.11.015.
186. Hedlund PB, Huitron-Resendiz S, Henriksen SJ, Sutcliffe JG. 5-HT7 receptor inhibition and inactivation induce antidepressant like behavior and sleep pattern. Biol Psychiatry. 2005;58:831–7. https://doi.org/10.1016/j.biopsych.2005.05.012.
187. Wesołowska A, Nikiforuk A, Stachowicz K. Potential anxiolytic and antidepressant effects of the selective 5-HT7 receptor antagonist SB 269970 after intrahippocampal administration to rats. Eur J Pharmacol. 2006;553:185–90. https://doi.org/10.1016/j.ejphar.2006.09.064.
188. Wesołowska A, Nikiforuk A, Stachowicz K, Tatarczyńska E. Effect of the selective 5-HT7 receptor antagonist SB 269970 in animal models of anxiety and depression. Neuropharmacology. 2006;51:578–86. https://doi.org/10.1016/j.neuropharm.2006.04.017.
189. Wesołowska A, Tatarczyńska E, Nikiforuk A, Chojnacka-Wójcik E. Enhancement of the anti-immobility action of antidepressants by a selective 5-HT7 receptor antagonist in the forced swimming test in mice. Eur J Pharmacol. 2007;555:43–7. https://doi.org/10.1016/j.ejphar.2006.10.001.
190. Eisensamer B, Uhr M, Meyr S, et al. Antidepressants and antipsychotic drugs colocalize with 5-HT3 receptors in raft-like domains. J Neurosci. 2005;25:10198–206. https://doi.org/10.1523/JNEUROSCI.2460-05.2005.
191. Donati RJ, Rasenick MM. Chronic antidepressant treatment prevents accumulation of gsalpha in cholesterol-rich, cytoskeletal-associated, plasma membrane domains (lipid rafts). Neuropsychopharmacology. 2005;30:1238–45. https://doi.org/10.1038/sj.npp.1300697.
192. Donati RJ, Schappi J, Czysz AH, et al. Differential effects of antidepressants escitalopram versus lithium on Gs alpha membrane relocalization. BMC Neurosci. 2015;16:40. https://doi.org/10.1186/s12868-015-0178-y.
193. Donati RJ, Thukral C, Rasenick MM. Chronic treatment of C6 glioma cells with antidepressant drugs results in a redistribution of Gsα. Mol Pharmacol. 2001;59:1426–32. https://doi.org/10.1124/mol.59.6.1426.
194. Toki S, Donati RJ, Rasenick MM. Treatment of C6 glioma cells and rats with antidepressant drugs increases the detergent extraction of Gsα from plasma membrane. J Neurochem. 1999;73:1114–20. https://doi.org/10.1046/j.1471-4159.1999.0731114.x.
195. Zhang L, Rasenick MM. Chronic treatment with escitalopram but not R-citalopram translocates gαs from lipid raft domains and potentiates adenylyl cyclase: a 5-hydroxytryptamine transporter-independent action of this antidepressant compound. J Pharmacol Exp Ther. 2010;332:977–84. https://doi.org/10.1124/jpet.109.162644.
196. Donati RJ, Dwivedi Y, Roberts RC, et al. Postmortem brain tissue of depressed suicides reveals increased Gsα localization in lipid raft domains where it is less likely to activate adenylyl cyclase. J Neurosci. 2008;28:3042–50. https://doi.org/10.1523/JNEUROSCI.5713-07.2008.
197. Chen J, Rasenick MM. Chronic Treatment of C6 glioma cells with antidepressant drugs increases functional coupling between a G protein (GS) and adenylyl cyclase. J Neurochem. 1995;64:724–32. https://doi.org/10.1046/j.1471-4159.1995.64020724.x.
198. Gur TL, Conti AC, Holden J, et al. cAMP response element-binding protein deficiency allows for increased neurogenesis and a rapid onset of antidepressant response. J Neurosci. 2007;27:7860–8. https://doi.org/10.1523/JNEUROSCI.2051-07.2007.

Chapter 13
Rotation of Single Cell Surface Receptors Examined by Quantum Dot Probes

Dongmei Zhang, Peter W. Winter, Deborah A. Roess, and B. George Barisas

Abstract Rotational diffusion, which depends linearly on the in-membrane volume of the rotating molecule, is, relative to lateral diffusion, a more sensitive probe of an individual molecule's size and local environment. Single-particle tracking has provided new perspectives on lateral compartmentalization of membrane proteins. However, little is known at present about rotational motions of single membrane protein molecules. We discuss correlation analysis of fluctuations in fluorescence polarization from proteins labeled by asymmetric quantum dots. Such analysis provides rotational information on single membrane molecules which can be directly related to that from ensemble measurements of cell surface protein rotation. We have used asymmetric quantum dots to examine individual Type I Fcε receptors on 2H3-RBL cells and to conduct imaging measurements of receptor rotational diffusion on timescales down to 10 ms per frame. To achieve removal of blinking-based contributions to rotation measurements, we discuss an approach based on the necessary statistical independence of polarization and intensity fluctuations. Imaging results demonstrate rotational correlation times broadly ranging from 50 to 500 ms among individual molecules of the same type. The magnitude of these orientational fluctuations is comparable to the fraction of molecules which appear rotationally immobile when examined on the microsecond timescale by time-

D. Zhang • B. George Barisas (✉)
Department of Chemistry, Colorado State University, 1301 Center Ave, Fort Collins CO 80523, USA
e-mail: dongmei.zhang@colostate.edu; george.barisas@colostate.edu

P.W. Winter
Department of Chemistry, Colorado State University, 1301 Center Ave, Fort Collins CO 80523, USA

U.S. Department of Energy, 1000 Independence Ave SW, Washington, DC 20560, USA
e-mail: peter.w.winter@gmail.com

D.A. Roess
Department of Biomedical Sciences, Colorado State University, Fort Collins CO 80523, USA
e-mail: deborah.roess@colostate.edu

A. Chattopadhyay (ed.), *Membrane Organization and Dynamics*, Springer Series in Biophysics 20, DOI 10.1007/978-3-319-66601-3_13

resolved phosphorescence anisotropy. These slow motions, not observable previously, appear to be a property of the membrane rather than the receptor state. Our results suggest that individual mesoscale membrane regions may rotate or liberate with respect to the overall cell surface.

Abbreviations

FcεRI	Type I Fcε receptor
FRET	Fluorescence resonant energy transfer
MSD	Mean square displacement
NP	Nanoparticle
PBS	Phosphate-buffered saline
QD	Quantum dot
ROI	Region of interest
TACF	Time autocorrelation function
TPA	Time-resolved phosphorescence anisotropy

13.1 Optical Methods Permit Examination of Rotational Motions of Cell Surface Receptors

Protein function and interactions between proteins in local cell environments are central areas of interest in contemporary cell biology. Techniques for observing proteins within specialized environments and interactions within those compartments on viable cells are limited by the small numbers of a particular molecule. When both partners in an intermolecular interaction are known, fluorescence resonant energy transfer (FRET) measurements permit the changes in the intermolecular distance to be evaluated. However, to evaluate intermolecular interactions of a single known molecule with *unknown* species or structures or the effects of conformation change or local environment on protein molecular motions, kinetic approaches based on rotational or lateral diffusion provide the most practical tools.

Protein lateral and rotational diffusion reflect the size, interactions, environment and temperature of the molecule examined. If a molecule self-associates or interacts with other molecules or structures, whether in solution, in the cytoplasm or in membranes, other factors being held constant, slower rotational and lateral diffusion necessarily result. For example, for two-dimensional diffusion in membranes, the Saffman-Delbrück treatment shows the translational diffusion coefficient to vary inversely with the logarithm of the particle radius. This represents a very weak dependence on particle size [1]. By contrast, the rotational correlation time varies according to the in-membrane volume of the rotating protein [1, 2]. In particular, for a spherical particle of hydrated volume V_{hyd} in a medium of viscosity η, this correlation time is $1/6D_{rot}$ or $\eta V_{hyd}/kT$. Thus measurements of rotational motions are highly sensitive to the size and shape of the protein and as well as to the viscosity of the surrounding environment. Rotational diffusion measurements

provide a rather sensitive method to investigate the structure of large macromolecular complexes and are sensitive enough to reveal receptor oligomerization and aggregation events [3–5].

Further, cell membranes are dynamic structures with complex, non-homogeneous organization [6] including membrane microdomains within the plasma membrane and protein organizational effects created by the membrane cytoskeleton. Due to compartmentalization of the plasma membrane and the formation of membrane microdomains, receptors are distributed in a variety of environments in the cell surface. Particular receptors function only in specific lateral environments, such as lipid rafts, and depend on co-localization there of other proteins [7]. In particular, rotational parameters of individual copies of a particular receptor should indicate differences in receptor aggregation state and local environment. However, only by studies of single molecules can such heterogeneity in behavior among different copies of the same molecule be examined.

To measure rotation of a particular receptor type on a selected cell, only optical methods have adequate sensitivity. All such optical approaches are based on measuring polarization of light emitted, absorbed or scattered from molecules, since only polarization phenomena reflect molecular orientation. Before discussing specific techniques applicable to examination of *single protein molecules* on cell surfaces, we should note some of the various techniques that have been applied in earlier cellular studies of rotational motions within *ensembles* of molecules, either on individual cells or in cell suspensions. Rotation of fluorescent lipid probes in membranes occurs on the few-nanosecond timescale and so time-resolved fluorescence anisotropy is an effective technique for measuring such rotation. However, unhindered rotational diffusion of cell surface proteins occurs on the 10–100 μs timescale, so that fluorescence anisotropy is not applicable. Rotation of proteins on or in cells has been studied using various methods based on generation of anisotropic distributions of long-lived, typically triplet, species and subsequent examination of the decay of the distribution's asymmetry. Such techniques have included linear dichroism [8], delayed or E-type fluorescence [9], time-resolved phosphorescence anisotropy (TPA; [10]) and fluorescence depletion anisotropy [11, 12]. Cellular studies demand robust, broadly-applicable methods and measurements of phosphorescence and E-type fluorescence anisotropy decay, being the most straightforward to conduct, have been most widely used.

These techniques use luminescent dye molecules as probes. Rotational motion of membrane proteins can only be measured within a critical time window that is determined by the limited lifetime of probe luminescence. For example, time-resolved phosphorescence anisotropy can measure rotational diffusion times up to a few times the phosphorescence lifetime of the probe, typically <500 μs for phosphors like erythrosin, and so provides little information on motions slower than about 5 ms. Polarized photobleaching [2] is applicable to very slow motions but requires at least 100 ms to bleach fluorophores and cannot be used to examine faster rotational motions. Thus there is a time window, extending from perhaps 5 to 500 ms, within which little is known about rotation motions of membrane receptors, whether in ensembles or as single molecules.

The development of asymmetric, typically rod-shaped, nanoparticles capable of attachment to specific cell surface proteins has made possible measurement of rotational dynamics of individual molecules in vivo within the aforementioned time frame. The most commonly used rod-shaped nanoparticles are gold nanorods and asymmetric fluorescent nanocrystals [13] including commercial quantum dots [14]. Quantum dots emit high brightness polarized fluorescence [15]. Nanorods scatter light preferentially along their long axis [16]. Both types of nanoparticles are stable under normal levels of illumination and so permit extended examination of samples labeled with these materials.

A key issue involving nanoparticle probes is whether quantum dots or nanorods might significantly inhibit rotation of membrane proteins which they label. In fact, physical considerations indicate that nanoparticle probes should not significantly restrict the rotation of membrane proteins. The rotational correlation time τ of a randomly-oriented molecular complex depends on the rotational correlation times τ_A, τ_B of its parts as $\tau = \tau_A \tau_B/(\tau_A + \tau_B)$ since the friction coefficients of its parts in their respective environments must be additive. The quantum dots we have studied most extensively, Invitrogen's Qdot655, measure ~5.8 × 12.8 nm and, even if labeling a membrane protein, the particle itself must nonetheless exist primarily in the aqueous extracellular fluid. The slower rotational correlation time of such a particle, reflecting rotation about one of the degenerate short axes, is calculated to be approximately 0.27 μs [17]. By contrast, relatively small proteins such as major histocompatibility complex (MHC) class I and class II antigens [18–20] exhibit rotational correlation times of 25–30 μs. Thus the perturbation of the rotation rate of a membrane protein by conjugation of an extra-cellular quantum dot should be negligible. Because gold nanorods are larger than quantum dots, their possible effects on membrane proteins can be more problematic.

A quantum dot property of concern in measurements of protein rotational diffusion is their "blinking" noted, for example, by Nirmal et al. in 1996 [21]. Individual QDs display intermittent blinking with continuous excitation, alternating between an emitting state (on) and a non-emitting state (off) with blinking timescales ranging from nanoseconds to hundreds of seconds [22, 23]. The presence of a single QD can in fact be confirmed from this blinking. The probabilities $P(\tau)$ of observing a given "on" time or "off" time τ both follow power law distributions $P(\tau) \propto \tau^{-\mu}$ where the exponents μ~1.1–2.2 are largely independent of sample temperature and nanoparticle shape and size. Blinking "off" times are largely independent of temperature and excitation intensity, but "on" times vary with these factors [24]. Compensating for QD blinking is a challenge in lateral diffusion measurements such as single particle tracking where an "off" state leads to uncertainty in the identification of a particular particle once it again becomes "on". For rotational motion measurements, polarization or anisotropy of quantum dot fluorescence, being ratios of measured fluorescence intensities, would seem to be immune to blinking effects. However, in practical terms, blinking is a key problem in calculating rotation rates of quantum dot-labeled proteins, as will be discussed subsequently.

Most previous work using nanoparticle probes of single molecule rotation has involved gold nanorods. Although our own work utilizes asymmetric quantum dots, some important nanorod studies should be mentioned as they inform certain aspects

of our own work. Rotational motion measurement of gold nanorods was first performed using dark field microscopy by Sönnichsen and Alivisatos [16]. Polarization fluctuations in light scattered by gold nanorods, loosely attached to a glass surface in a solution at pH 8.0, exhibited two-dimensional rotation with a rapid rotational correlation time of about 60 ms. Pierrat and his coworker, monitoring rotational diffusion of polymer-coated gold nanorods attached to artificial biomembranes on solid supports using polarization contrast microscopy [25], demonstrated that rotational diffusion times of about 100 ms could obtained. Spetzler and coworkers observed the rotation of ATPase molecular motors using dark-field microscopy. A single gold nanorod, attached to the rotating γ-subunit of an immobilized F1-ATPase molecule on a glass slide, exhibited rotation rates of 7.62 rad/ms with a time resolution of 2.5 μs [26]. Chang and coworkers determined the rotational motion of gold nanorods using a polarization-sensitive instrument to measure the orientation of a 25 × 73 nm nanorod from either the longitudinal or the transverse surface plasmon resonance [27]. Wang and coworkers were the first investigators to successfully use gold nanorod probes to track the rotational motions of proteins on a live cell. Derivatized gold nanorods were internalized by A549 human lung cancer cells and transported by the cytoskeleton. Orientational information on moving nanoparticles was extracted from asymmetries in nanorod DIC images [28]. Xiao and coworkers directly tracked the rotational diffusion of individual nanorods being transported by kinesin motor protein along microtubule networks inside live cells. They illuminated gold nanorods with two orthogonal sheets of light instead of using dark-field illumination. This method allowed determination of three-dimensional orientation of single gold nanorods [29].

13.2 Evaluating Orientational Changes of Nanoparticles

Both physical considerations and existing literature suggest that measurement of single nanoparticle rotation is necessarily based on examination of the spontaneous orientational fluctuations of an individual nanoparticle-protein complex. The obvious analogy is with determination of molecular lateral diffusion by single particle tracking [30]. In such studies, the position of a particle is determined over time and used to determine the mean square displacement (MSD) occurring within a given time interval. Such a calculation is effectively a determination of the time autocorrelation function for fluctuations in particle *position*. For rotational studies, an analogous approach would be to evaluate fluctuations in some function of particle *orientation* related to particle rotational motion. Correlation analysis of single molecule orientational fluctuations yields the same rotational information as would be available in ensemble methods like time-resolved fluorescence or phosphorescence anisotropy.

Consider a quantum dot emitting polarized fluorescence resulting from polarized illumination, whether an excitation pulse or continuous light. This description also applies to a nanorod exhibiting polarized light scattering. Emission intensities

polarized parallel and perpendicular with respect to the x-polarized exciting light can be recorded using polarizer-equipped detectors to select x- and y-polarized emission. Each signal is corrected for any background signal and for unequal response by the two detectors [31]. This latter correction is achieved by multiplying raw y-channel data by the so-called "g-factor", namely the ratio of a nonpolarized signal detected in the x-signal to that detected in the y-channel. We denote the corrected intensities as $I_{\parallel}(t)$ and $I_{\perp}(t)$ to indicate their relation to the excitation polarization. Various functions using such measurements reflect orientation of the fluorescent particle(s). One such function is emission anisotropy r

$$r(t) = \left[I_{||}(t) - I_{\perp}(t)\right] / \left[I_{||}(t) + 2I_{\perp}(t)\right] \tag{13.1}$$

while the other, the polarization p, is

$$p(t) = \left[I_{||}(t) - I_{\perp}(t)\right] / \left[I_{||}(t) + I_{\perp}(t)\right]. \tag{13.2}$$

It is important to note that polarization and anisotropy are defined empirically here as functions of signals measured in two orthogonally-polarized detectors, whatever the light signal and independent of the nature of illumination. In particular, it is not necessary that the exciting light be polarized. Consider a single molecule illuminated with non-polarized light. When the molecule points in the x-direction, signal will appear in the $\parallel$-channel but if it diffuses orientationally its signal may appear mainly in the $\perp$-channel. Thus a time-dependent polarization or anisotropy can be calculated. The two functions contain essentially the same information and, for an ensemble of randomly oriented molecules, can be interconverted as $p = 3r/(2 + r)$ and $r = 2p/(3 - p)$.

In the majority of our experiments, we have measured the fluctuations in apparent fluorescence polarization from single quantum dots illuminated by constant, non-polarized light. We first showed that such experiments provide information on the rotational correlation time of the quantum dot probe. Then we compared these results with those obtainable from hypothetical time-resolved fluorescence anisotropy measurements on an ensemble of such systems if the quantum dot fluorescence lifetime were sufficiently long. This comparison shows that both approaches yield qualitatively comparable information.

The Qdot655 asymmetric quantum dots we used experimentally have been shown to exhibit a "two-dimensional" absorption dipole [32]. Such a molecule or particle possesses a degenerate transition dipole uniformly distributed around a molecular "bright plane" and a "dark axis", light polarized along which cannot excite the molecule [33]. Such a situation obtains for CdSe nanoparticles with a wurtzite crystal structure and an aspect ratio less than about 2. For these structures, the dark axis is the long (C3) axis of the crystal and the bright plane, the equatorial plane, here is symmetrical [34]. Such a system exhibits substantially different fluorescence polarization behavior than that arising from one-dimensional absorbers. Rotational fluctuation correlation calculations for 1D transitions have been described elsewhere [35]. We consider the simplified case of such a rapidly-fluorescing 2D fluorophore observed along the optical (z-) axis of a microscope,

along which either x-polarized or non-polarized excitation is applied. The molecule's long or "dark" axis has an orientation (θ, φ) in the corresponding spherical coordinates. Because of the both physical and optical symmetry of the nanoparticle about the dark axis, we need not consider rotation about this axis and so need only consider diffusion of the dark axis in θ and φ. The applicable rotational diffusion equation is then

$$\frac{\partial c}{\partial t} = D_r \nabla^2 c = D_r \left[\frac{1}{\sin\theta} \frac{\partial}{\partial \theta} \left(\sin\theta \frac{\partial c}{\partial \theta} \right) + \frac{1}{\sin^2\theta} \frac{\partial^2 c}{\partial \varphi^2} \right] \tag{13.3}$$

where D_r is the mean rotational diffusion constant. If the molecule is oriented at (θ_1, φ_1) at $t = t_1$ then Eq. (13.3) can be solved to yield the probability $c(t_2, t_1, \theta_2, \phi_2, \theta_1, \phi_1, D_r)$ of finding the molecule at a new orientation (θ_2, φ_2) at a subsequent time t_2 in terms of a series of spherical harmonics Y_n^m of even order [36]:

$$c(t_2,t_1,\theta_2,\varphi_2,\theta_1,\varphi_1,D_r) = \sum_{n=0}^{\infty} \sum_{m=-n}^{n} e^{-n(n+1)D_r(t_2-t_1)} Y_n^m(\theta_1,\varphi_1)^* Y_n^m(\theta_2,\varphi_2) \tag{13.4}$$

If the integral of c over θ_1 and φ_1 is unity at a time t_1, then the integral is also unity at any subsequent time any time t_2, as physical reality requires. For a molecular orientation (θ, φ), the fluorescences recorded in the ∥-and ⊥-channel detectors and, if present, in a z-polarized detector at 90° to the optical axis, i.e. x-, y- and z-respectively, for x-polarized excitation are then (Barisas, unpublished)

$$\begin{aligned} F_{xx}(t,\theta,\varphi) &= F_0(t)\ (\cos^2\theta \sin^2\phi + \cos^2\phi)^2 \\ F_{xy}(t,\theta,\varphi) &= F_0(t)\ (\cos^2\theta \sin^2\phi + \cos^2\phi)(\cos^2\theta \cos^2\phi + \sin^2\phi) \\ F_{xz}(t,\theta,\varphi) &= F_0(t)\ (\cos^2\theta \sin^2\phi + \cos^2\phi)\sin^2\theta \end{aligned} \tag{13.5}$$

and, for non-polarized excitation of equal intensity,

$$\begin{aligned} F_{nx}(t,\theta,\varphi) &= \frac{1}{2} F_0(t)\ \left(1+\cos^2\theta\right)\left(\cos^2\theta \sin^2\phi + \cos^2\phi\right) \\ F_{ny}(t,\theta,\varphi) &= \frac{1}{2} F_0(t)\ \left(1+\cos^2\theta\right)\left(\cos^2\theta \cos^2\phi + \sin^2\phi\right) \\ F_{nz}(t,\theta,\varphi) &= \frac{1}{2} F_0(t)\ \left(1+\cos^2\theta\right)\sin^2\theta \end{aligned} \tag{13.6}$$

where $F_0(t)$ is a time-dependent quantity reflecting exciting light intensity, fluorophore absorption cross-section, fluorescence lifetime and quantum yield, detection efficiency and, most importantly, any blinking of the QD. For this particle oriented at (θ, φ), the apparent polarization p and anisotropy r, being ratios of fluorescences, are independent of $F_0(t)$. For both x-polarized and non-polarized excitation, the *single-molecule* polarization and anisotropy signals are defined as

$$p = \frac{\cos 2\varphi \sin^2\theta}{1+\cos^2\theta};$$
$$r = \frac{1}{2}\cos 2\varphi \sin^2\theta \tag{13.7}$$

However, to simplify calculations, we approximate p with 3r/2 with the result

$$p \approx \frac{3f}{4}\cos 2\varphi \sin^2\theta \tag{13.8}$$

The factor f in Eq. (13.8) reflects the fact that molecules typically exhibit a polarization less than that expected theoretically. This can arise, for example, from chromophore motion too rapid to be observed directly.

We require the time-autocorrelation function G(τ) of p, assuming unrestricted rotation over θ and φ for a given correlation time τ. It is given by the average

$$\begin{aligned} G(\tau) = &< (\text{polarization of molecule at time } t_2 = t_1 + \tau) \\ &\times (\text{probability of finding molecule at } (\theta_2, \varphi_2) \\ &\quad \text{at time } t_2 \text{ if it was at } (\theta_1, \varphi_1) \text{ at time } t_1) \\ &\times (\text{polarization of molecule at time } t_1) \\ &\times (\text{probability of finding molecule at } (\theta_1, \varphi_1) \text{ at time } t_1) > \end{aligned} \tag{13.9}$$

One assumes that, over a sufficiently long measurement times T, the molecule explores all initial orientations φ_1 equally so that $c_1(t_1, \theta_1, \varphi_1, D_r) = 1/4\pi$. This also implies that final orientations θ_2, φ_2 are also explored without bias. Averages over θ_1, φ_1 and θ_2, φ_2 effectively imply an arbitrarily long experiment time. Given a long experiment and unrestricted rotation, the average polarization must be zero so G(τ) is also the time-autocorrelation function for *fluctuations* in p. Expanding Eq. (13.9) using the notation

$$\int_S F(\theta,\varphi) = \int_{\varphi=0}^{2\pi}\int_{\theta=0}^{\pi} F(\theta,\varphi)\,\sin\theta\, d\theta\, d\varphi \tag{13.10}$$

for integration of an arbitrary function F(θ, ϕ) over the surface of a sphere, we obtain

$$\begin{aligned} G(\tau) = &\lim_{T\to\infty}\frac{1}{T}\int_{t_1=0}^{T-\tau}\int_{S_2}\left(\frac{3f}{4}\cos 2\varphi_2 \sin^2\theta_2\right)\int_{S_1} c(t_1+\tau, t_1, \theta_2, \varphi_2, \theta_1, \varphi_1, D_r) \\ &\times\left(\frac{3f}{4}\cos 2\varphi_1 \sin^2\theta_1\right)\left(\frac{1}{4\pi}\right) dS_1 dS_2 dt_1 \\ = &\frac{3f^2}{20}e^{-6D_r\tau} \end{aligned} \tag{13.11}$$

The constant f where $0 \le f \le 1$ reflects either photophysical aspects of the chromophore or depolarization too rapid to be observed. The expected initial

amplitude G(0) of the polarization fluctuation TACF can be predicted from measurements of time-resolved fluorescence anisotropy (see below). These provide an estimate of the constant f in terms of the measured initial anisotropy r_0 as 5 r_0. The apparent rotational correlation time τ_c is $1/(6D_r)$.

It is important to note that rotational motion measurements on a single molecule will yield useful information *only* if the individual molecule's measured rate of fluorescence emission is sufficiently rapid. At least one photon must be detected per rotational correlation time of the molecule, otherwise data acquired over time contain essentially no rotational information.

The mean rotational correlation time exhibited by molecules in an *ensemble* is typically measured by time-resolved fluorescence or phosphorescence anisotropy. An anisotropic distribution of excited states is produced by a rapid pulse of light and the decay of luminescence polarization or anisotropy reflects orientational randomization. We can consider a situation where the luminescence lifetime of the molecule is much longer than its expected rotational correlation time so that excited state decay need not be considered. At a time t after excitation by polarized light, the excited state distribution function c_e for the ensemble is

$$c_e(t,\theta,\varphi) = \frac{1}{\sqrt{4\pi}}\left\{ Y_0^0(\theta,\varphi) + \left[\frac{1}{2\sqrt{5}}Y_2^0(\theta,\varphi) + \frac{1}{2}\sqrt{\frac{3}{10}}Y_2^2(\theta,\varphi) + \frac{1}{2}\sqrt{\frac{3}{10}}Y_2^{-2}(\theta,\varphi)\right] e^{-6D_r t}\right\} \tag{13.12}$$

The signals $I_{\parallel}(t)$ and $I_{\perp}(t)$ detected in the x- and y-channels, respectively, and in the 90° z-channel if available, are then

$$\begin{aligned} I_x(t) &= A\, n_e \int_S c_e(t,\theta,\varphi)\cos^2\varphi\, \sin^2\theta dS = \frac{1}{3}\left(1 + \frac{1}{5}e^{-6\,D_r t}\right); \\ I_y(t) &= A\, n_e \int_S c_e(t,\theta,\varphi)\sin^2\varphi\, \sin^2\theta dS = \frac{1}{3}\left(1 - \frac{2}{5}e^{-6\,D_r t}\right); \\ I_z(t) &= A\, n_e \int_S c_e(t,\theta,\varphi)\cos^2\theta dS = \frac{1}{3}\left(1 + \frac{1}{5}e^{-6\,D_r t}\right); \end{aligned} \tag{13.13}$$

where n_e is the total number of excited state molecules produced and A is the detected photon count rate per molecule. The anisotropy and polarization are then

$$\begin{aligned} r(t) &= \frac{f}{5}e^{-6D_r t} = r_0 e^{-6D_r t}; \\ p(t) &= \frac{3f}{10}\,\frac{e^{-6D_r t}}{1 - {}^{1}\!/_{10}e^{-6D_r t}} \approx \frac{3f}{10}\,e^{-6D_r t} = p_0 e^{-6D_r t} \end{aligned} \tag{13.14}$$

Thus the initial anisotropy r_0 expected theoretically is 1/5 but lower values will be observed in practice. Similarly the theoretical initial polarization, if measured,

would be 3/10 or lower. These equations allow estimation of f as 5 r_0 and thus prediction of what value of G(0) would be consistent with the direct measurements.

Comparison of G(τ) in Eq. (13.11) with p(t) in Eq. (13.14) shows that single-molecule correlation experiments and pulsed-excitation ensemble measurements provide the same kinetic information on rates of orientational relaxation and that the amplitudes of relaxations curves yielded by the two methods are related in a simple, known way.

13.3 Evaluating Quantum Dot Probes for Measuring Receptor Rotational Diffusion

Experimentally, we evaluated the use of QD probes for measurements of single receptor rotational diffusion on cell surfaces. QD polarization was examined on RBL-2H3 cells expressing the Type I Fcε Receptor (FcεRI), a useful cell system for studying protein rotational diffusion. This receptor has been extensively studied by both TPA and fluorescence depletion anisotropy [37, 38]. FcεRI bind IgE with a stoichiometry of 1:1 and crosslinking of receptor-bound IgE by polyvalent allergen initiates a signaling cascade leading to mast cell degranulation, i.e. the release of vesicle contents from the cell. Receptor crosslinking is accompanied by formation of large receptor-containing complexes and virtual immobilizes the protein on the microsecond-timescale where its hydrodynamic rotation is otherwise observed [39].

Streptavidin-conjugated quantum dots Qdot655 and Qdot605 (Invitrogen) were selected on account of their asymmetry, commercial availability as streptavidin conjugates and wide use by other investigators. QD size was estimated from TEM images (Fig. 13.1) and yielded average sizes of 5.1 nm × 10.9 nm for Qdot 605 and 5.8 nm × 12.8 nm for Qdot 655. Dimensions of approximately 5 nm × 12 nm and 8 nm × 15 nm, respectively, are listed by the Manufacturer [40]. Fluorescence lifetimes and anisotropies (Fig. 13.2) were estimated using an IBH 5000U lifetime fluorometer with 456 nm NanoLED excitation and 605 or 655 nm emission

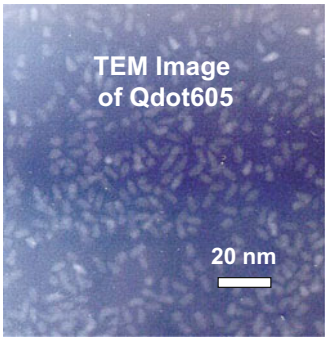

Fig. 13.1 TEM image of Qdot605 showing an average size of 10.9 × 5.1 nm

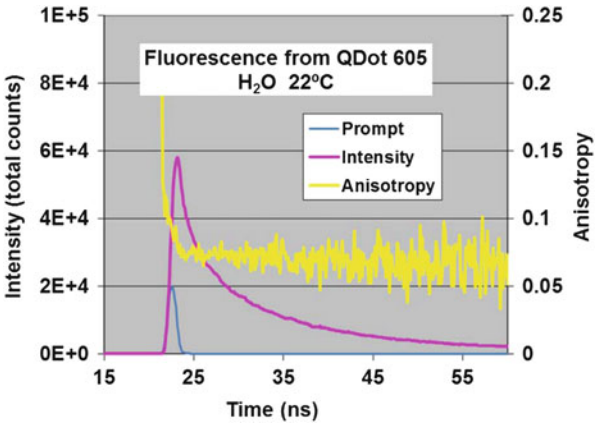

Fig. 13.2 Time-resolved fluorescence anisotropy of Qdot 605 in water at room temperature. The apparent fluorescence lifetime is ~5.5 ns and the initial anisotropy is 0.079

monochromator settings at 32 nm bandpass. Qdot 605 exhibit an initial anisotropy in solution of approximately 0.079 while a value of 0.085 is cited by Grecco et al. [15]. We estimate a rotational correlation time in solution of about 0.2 μs, through this is very approximate given the short fluorescence lifetime of the material. For Qdot 655, initial anisotropy was measured at 0.042 and the rotational correlation time estimated at about 0.3 μs. Biotinylated DNP-specific A2 IgE antibody, a kind gift from Dr. Israel Pecht of the Weizmann Institute of Science, Rehovoth, Israel, has very high affinity for FcεRI and provided the link between the receptor and streptavidin quantum dots. A published protocol from the Invitrogen company [41] was used to conjugate one QD or less per protein molecule.

Untreated and treated cells were maintained in pH 7.4 PBS solution. Images from cells were collected by fluorescence microscopy using a Zeiss Axiovert 200M microscope with a Zeiss αPlan-Fluar 100x NA 1.45 oil objective and custom Chroma filter sets including excitation filter (460/50 nm), dichroic beam splitter (475 nm) and emission filter (655/40 nm). At 600 nm the Airy radius on the sample was 252 nm [42]. Fluorescence from cell-bound quantum dots was excited by illumination from a 100 W arc lamp. In most experiments, non-polarized exciting light was used but some measurements involved exciting light vertically polarized at the sample, i.e. x-polarized. A Princeton Instruments Dual View image splitter equipped with a polarizing beamsplitter allowed recording of image sequences containing simultaneous x- and y-polarized sub-images in each frame. Orthogonally polarized images were collected every 10 ms for a typical duration of 1000 frames at a final magnification of 100x after 5x binning to enhance acquisition rates. An Andor Ixon Andor DU897E EMCCD camera having 512 × 512 16 μm × 16 μm pixels was used. Figure 13.3 provides a diagram of image data acquisition including a low resolution image of Qdot655 on a 2H3 cell surface. Dry QD on glass were

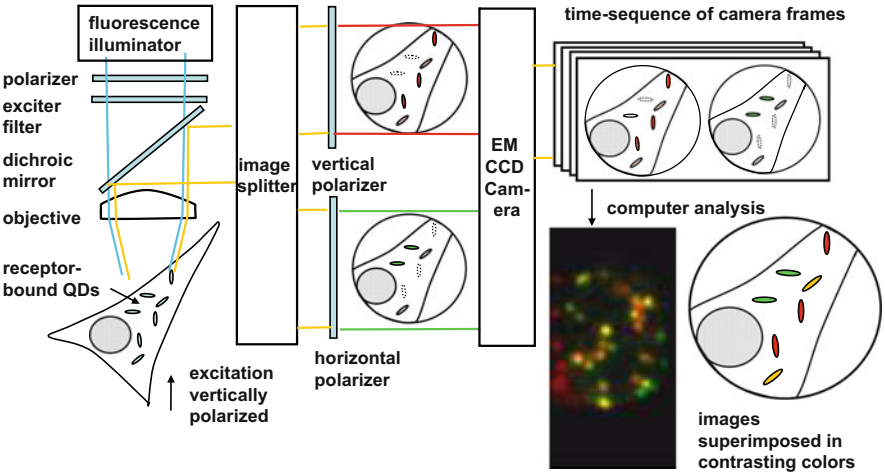

Fig. 13.3 Equipment for imaging measurement of slow QD rotation on cell surfaces. The *inset* image shows vertically- and horizontally-polarized fluorescence from Qdot655 on 2H3 cell FcεRI overlaid in *green* and *red*, respectively, to indicate different orientations of individual QD. Color differences among various QD are enhanced for clarity

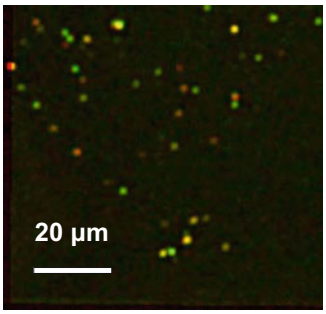

Fig. 13.4 Vertically- and horizontally-polarized fluorescence images of dry Qdot605 superimposed in *green* and *red*, respectively, to indicate different orientations of individual QD. Color differences among various QD are enhanced for clarity

imaged in the same way as cell-bound QD. An image of dry Qdot605 on glass is shown in Fig. 13.4. In both figures, to indicate varying orientations among dots, vertically and horizontally polarized images are presented superimposed in contrasting green and red colors, respectively, after alignment and correction by an appropriate g-factor.

13.4 Initial Processing of Image Sequences

Image stacks collected were analyzed using NIH Image J and expanded five-fold in each dimension to 510 × 510 pixels, each corresponding to 32 nm × 32 nm on the sample. For convenience in notation, we considered the x-axis to be the vertical direction as observed in the microscope and that polarization, if any, of exciting light is also in this direction. Thus $I_v(t) \equiv I_{\parallel}(t)$ and $I_h(t) \equiv I_{\perp}(t)$. Moreover we typically omitted "(t)" so that $v = I_v(t)$ and $h = I_h(t)$. Sub-pixel alignment of the vertically- and horizontally-polarized sub-images was necessary for rotational correlation calculations but could not be achieved mechanically, even with careful alignment of the Dual-View before the start of every experiment. Therefore, image stacks of QD on a cell or surface were segmented into substacks containing vertically and horizontally-polarized images. Each stack was flattened, i.e. averaged, and the horizontally-polarized average image adjusted with respect to the vertically-polarized one to correct for displacement, rotation and dilation of one image relative to the other. The parameters of this adjustment were then used to correct the entire horizontally-polarized stack to achieve sub-pixel alignment with the vertically-polarized one. Given the image expansion, the alignment parameters were accurate to ±1/5 of a pixel with respect to the original image. 25- and 50-pixel diameter regions of interest (ROI; 0.8 and 1.6 μm diameter, respectively) were centered around individual QD at the same locations in the aligned vertically- and horizontally-polarized images. The diameters of the Airy disc calculated previously for the microscope showed that these regions contain 0.90 and 0.95 of each dot's total image intensity. Figure 13.5 shows 800 nm ROI around several QD on a 2H3 cell surface while Fig. 13.6 shows the blinking of an individual quantum dot in such a region. Typically ten or more QD were examined per cell. ROIs in background areas, well away from any QD, were also selected for each cell. For each image sequence, and the average v- and h-polarized intensities in the ROI surrounding each dot plus the averaged v- and h-polarized intensities in each background ROI region were measured in Image J and exported as a CSV file.

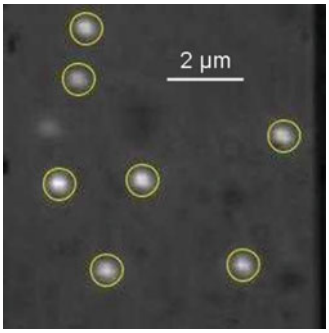

Fig. 13.5 Section of fluorescence image showing Qdot655 bound to 2H3 cell FcεRI. Indicated *circular* regions are 25 pixels or 800 nm in diameter and contain ~91% of the intensity in the QD Airy disc

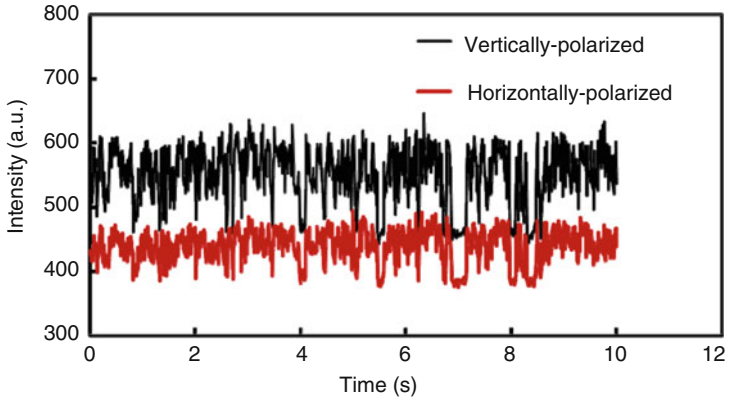

Fig. 13.6 Raw fluorescence data from an 800 nm ROI surrounding an individual Qdot655 bound to a 2H3 cell FcεRI. Signals from the vertically- and horizontally-polarized images are shown in *black* and *red*, respectively. Both traces show the QD's random blinking on various timescales

13.5 Removal of Blinking Effects and Correlation Calculations

Complete removal of quantum dot blinking effects is the critical step in data analysis. Polarization is defined as $(v - h)/(v + h)$ where v and h are true intensities of the two fluorescence signals. However, correction of observed fluorescences v_{obs} and h_{obs} to obtain true values involves experimental parameters such as the "g-factor", camera background and local cell background which can change between QDs, even in the same image. For computational reasons, we replace g with $(1 + g')$ and correspondingly multiplied v_{obs} by $(1 - g')$. We then have

$$\begin{aligned} v_{obs} &= \frac{1}{1-g'}(v + b_v) + c; \\ h_{obs} &= \frac{1}{1+g'}(h + b_h) + c \end{aligned} \tag{13.15}$$

where g' is the new g-correction as described, c is a camera background signal constant across the image and containing both CCD dark counts and offset intentionally added by the camera driver. b_v and b_h represent actual background fluorescences present in the image. We have measured background signals averaged over QD-free regions but might expect the backgrounds applicable to a particular dot to differ from the all-cell average by constants b_{dv} and b_{dh}. This gave the following equations

$$\begin{aligned} v &= (1-g')(v_{obs}-b_{vobs})-(1-g')b_{dv};\\ h &= (1+g')(h_{obs}-b_{hobs})-(1+g')b_{dh}. \end{aligned} \tag{13.16}$$

Three constants g', b_{dv} and b_{dh} are therefore needed to correct raw intensities and these constants vary slightly from cell to cell and from dot to dot. Hence calibration in independent experiments is not possible. Corrected intensities were used to calculate the intensity function s = v + h and the polarization p = (v − h)/s, the true values of which are necessarily statistically independent. However, if the three constants are not properly chosen, calculated polarization values p can contain a contribution from the intensity function s which varies with QD blinking. When, in turn, polarization fluctuations are correlated to obtain the polarization time autocorrelation function (TACF) to quantitate molecular rotation, errors in these parameters can introduce into the polarization TACF a contribution from the intensity fluctuation TACF arising from QD blinking.

A non-linear procedure in Mathematica was applied to each QD to select values for the adjustable constants yielding maximum statistical independence of p and s as assessed by the weighted correlation coefficient. Other factors, such as non-negativity of corrected intensities provided additional necessary constraints. For some QD, typically less than 20% of the total, optimizations of instrumental parameters failed, typically by failure to converge or by converging to physically impossible values such as negative g-factors. Such QD were not examined further.

Once corrected intensities were obtained for a given QD, polarization p was calculated for each frame. The time-autocorrelation functions $g_p(\tau)$ and $g_s(\tau)$ for polarization and intensity fluctuations, respectively, about the appropriate long-time means are given by

$$G_p(\tau)=\frac{1}{T}\sum_{t=0}^{T-\tau-1}\left[p(t)-\overline{p_t}\right]\left[p(t+\tau)-\overline{p_{t+\tau}}\right]w(t)w(t+\tau)\Big/\sum_{t=0}^{T-\tau-1}w(t)w(t+\tau) \tag{13.17}$$

$$G_s(\tau)=\frac{1}{T}\sum_{t=0}^{T-\tau-1}\left[s(t)-\overline{s_t}\right]\left[s(t+\tau)-\overline{s_{t+\tau}}\right] \tag{13.18}$$

where τ is correlation time in frames and T is the total number of frames recorded. Because integrated QD and background intensities in each ROI were substantial (Fig. 13.6), the uncertainty in corrected intensity was assumed to be constant for each QD. Thus, in the calculation of the polarization fluctuation TACF, the weight factors w(t) for each point were set to the intensity function s_t for that point. For each dot analyzed, the various numeric parameters and graphs obtained were saved automatically in a CSV file and PDF files, respectively. Subsequently, a model consisting of a single exponential decaying to zero at long times was least-squares fitted to the TACF decay for each dot. The resulting fitted parameters, RCT and G (0), were recorded for each QD and statistics of data from similarly treated cells computed.

13.6 Perspectives and Conclusions

Our measurements indicate initial anisotropies of 0.079 and 0.042 for Qdot605 and Qdot655, respectively. Considered as 2D fluorophores emitting and absorbing in an equatorial "bright plane", Eq. (13.14) suggests these materials should exhibit initial solution anisotropies of 1/5. Both QD have aspect ratios of about 2. At aspect ratios only slightly higher, CdSe nanocrystals apparently transition to 1D emitters, absorbing and emitting along the crystal long axis [43]. Thus one explanation for the observed anisotropies would be participation of this 1D transition, increasing the effective optical symmetry of the molecule and reducing measured fluorescence anisotropy.

Fluctuations of QD fluorescence polarization of ~300 Qdot655 bound to 2H3 cell FcεRI were examined and the TACF for each QD's fluctuations plotted vs. apparent rotational correlation time. Figure 13.7 shows a composite of 85 such traces. It is apparent that, among individual QD, substantial variation exists in both RCT and TACF initial amplitude. The average features of such decay are presented in Fig. 13.8 for subsets of the Qdot655 bound to 2H3 cell FcεRI and dry Qdot655 examined. Inspection suggests, for cell bound QD, an initial amplitude of about 0.0014 and multi-exponential decay with a mean RCT of perhaps 200 ms. By contrast, the dry dots exhibit essentially flat decay curves with an average G(0) of about 0.0002. Moreover, the intensity fluctuation TACF for cell-bound dots has substantially different kinetics from the polarization fluctuation TACF (results not shown). This, to our thinking, largely eliminates the possibility that the exponential decay of polarization fluctuation TACF decay is a artifact of feed-through of quantum dot blinking into the TACF. This is because the dry dots blink much like cell bound ones, yet their decay curves differ as shown.

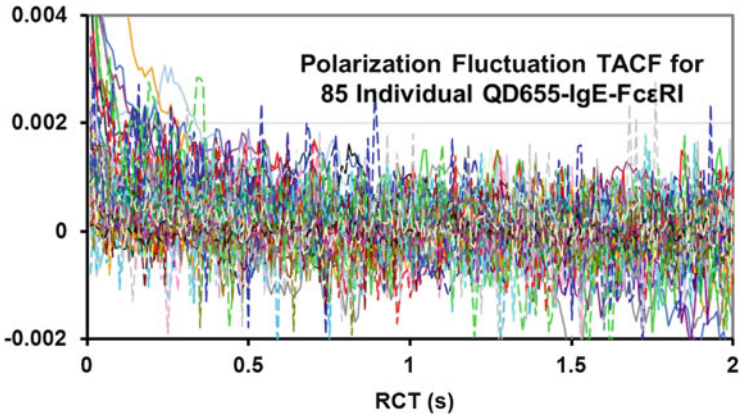

Fig. 13.7 Composite plot of polarization fluctuation TACF vs. time for 85 individual Qdot655 bound to 2H3 cell FcεRI

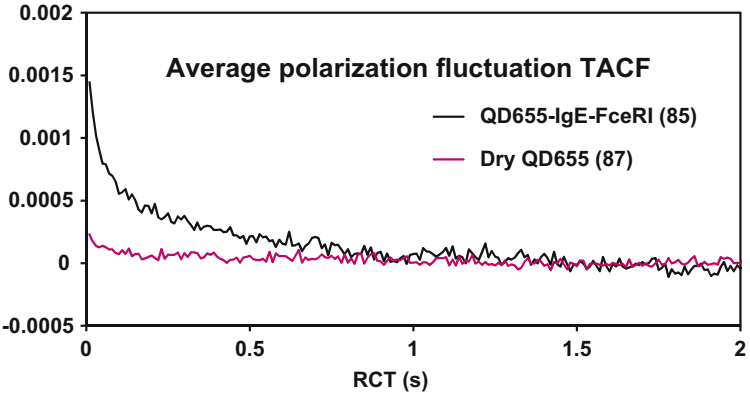

Fig. 13.8 Average polarization fluctuation TACF decay for 87 Qdot655 bound to 2H3 cell FcεRI (*black trace*) compared to decay for 85 dry Qdot655 on glass (*red trace*)

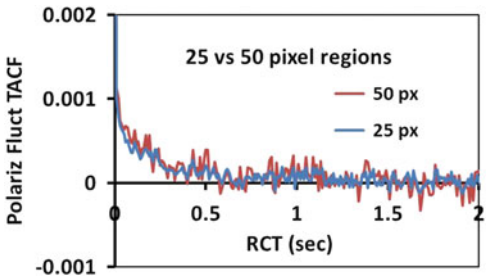

Fig. 13.9 Average polarization fluctuation TACF decay for 35 Qdot655 bound to 2H3 cell FcεRI as determined from fluorescence in 25- and 50-pixel ROIs surrounding the same QD. The traces for the 25- and 50-pixel ROIs are shown in *blue* and *red*, respectively. The absence of significant difference in the traces demonstrates that receptor lateral diffusion does not combine with ROI misalignment between vertically- and horizontally polarized images to produce apparent QD rotation as an artifact

Cell surface features which might cause apparent polarization fluctuations need to be considered. The most important of these is lateral diffusion of cell surface receptors. If the ROI surrounding the QD in the v- and h-images were displaced somewhat one to another, then receptor lateral diffusion into the v-channel ROI and out of the h-channel would increase the v-signal relative to the h-signal giving rise to time-dependent fluctuation in the apparent polarization. Two experimental facts argue against the presence of such an artifact. Figure 13.9 shows averaged TACF decay traces for 35 Qdot655 on 2H3 cell FceRI examined using both 800 nm and 1600 nm ROI for each QD. The traces are essentially indistinguishable, the increased noise in the 1600 nm trace being due to increased background signal in the larger ROI. Additionally, paraformaldehyde fixation, presumably reducing receptor lateral diffusion substantially [20], caused no significant changes in

TACF decay, as is described subsequently. Moreover, physical considerations make lateral diffusion effects unlikely. Assuming the QD are well-centered in the ROI as shown in Fig. 13.9, the amplitudes of such fluctuations would be negligible. The timescale of such fluctuations can also be estimated from the possible misalignment Δx of the ROI and the lateral microscopic diffusion constant D_{micro} of a typical receptor as $\Delta x^2/2D_{micro}$. Assuming worst-case values of 10 nm for Δx and a very slow D_{micro} of 5×10^{-11} cm^2 s^{-2} [44], such fluctuations would be 10 ms or faster, much faster than the receptor motions implied by our rotational correlation results.

Various treatments cause changes in cell membranes and/or membrane receptors that affect molecular motions of these receptors. Samples were treated at room temperature with either 0.01% DNP-BSA in PBS for 1 h, 4% paraformaldehyde in PBS for 45 min, 0.01% methyl-β-cyclodextrin (MBCD) in PBS for 1 h or 40 μM cytochalasin D in PBS for 1 h. Cells were washed and then incubated with 100 pM streptavidin-QD for 10 min and washed before imaging. Labeling was adjusted to give approximately ten suitably located QD per cell. In some experiments, the order of FcεRI loading with IgE and treatments were reversed. We examined the rotational fluctuation TACF of Qdot655 bound to 2H3 cell FcεRI on cells subjected to these four such treatments and on control cells pre-loaded with IgE alone. Figure 13.10 shows histograms of RCT distributions on the variously-treated cells while Tables 13.1 and 13.2 provide statistics on the geometric mean RCT and fitted initial TACF, respectively.

If 2H3 cell FcεRI are pre-loaded with DNP-specific A2 IgE, subsequent treatment with DNP-BSA substantially increases the receptor limiting anisotropy observed in TPA experiments, implying rotational immobilization of the 100 μs timescale [37]. Similarly, paraformaldehyde fixation effectively eliminates membrane protein rotation [20]. Methyl-β-cyclodextrin extracts membrane cholesterol and so a variety of effects resulting from such treatment can be rationalized. For example, Shvartsman et al. report that methyl-β-cyclodextrin inhibits membrane protein lateral diffusion although other cholesterol-depleting treatments accelerate such motions [45]. Finally, cytochalasin D disrupts actin filaments and so, for example, reduces the lateral mobility of the luteinizing hormone receptor, a G protein-coupled receptor [46]. For both these latter treatments, effects on membrane protein *rotation* remain to be determined.

Results shown in Fig. 13.10 demonstrate that FcεRI, both on untreated cells and on cells treated with DNP-BSA, paraformaldehyde, methyl-β-cyclodextrin or cytochalasin D, all exhibit broad ranges of rotational correlation times. This is also independent of the order in which IgE and treatment reagents are applied. Figure 13.10 shows that each of the treatment groups exhibits rotational kinetics covering a greater than ten-fold range of RCT. Because of the wide range of RCT, we present geometric averages of RCT in Table 13.1. Among the various treatment groups, no substantial differences in histograms or statistics are apparent; the histograms are very similar regardless of treatment with geometric averages of 150–250 ms. The standard deviation of $\log_{10}$RCT is quite constant at about 0.5, indicating that about the RCT of about 70% of QD fall within a tenfold range.

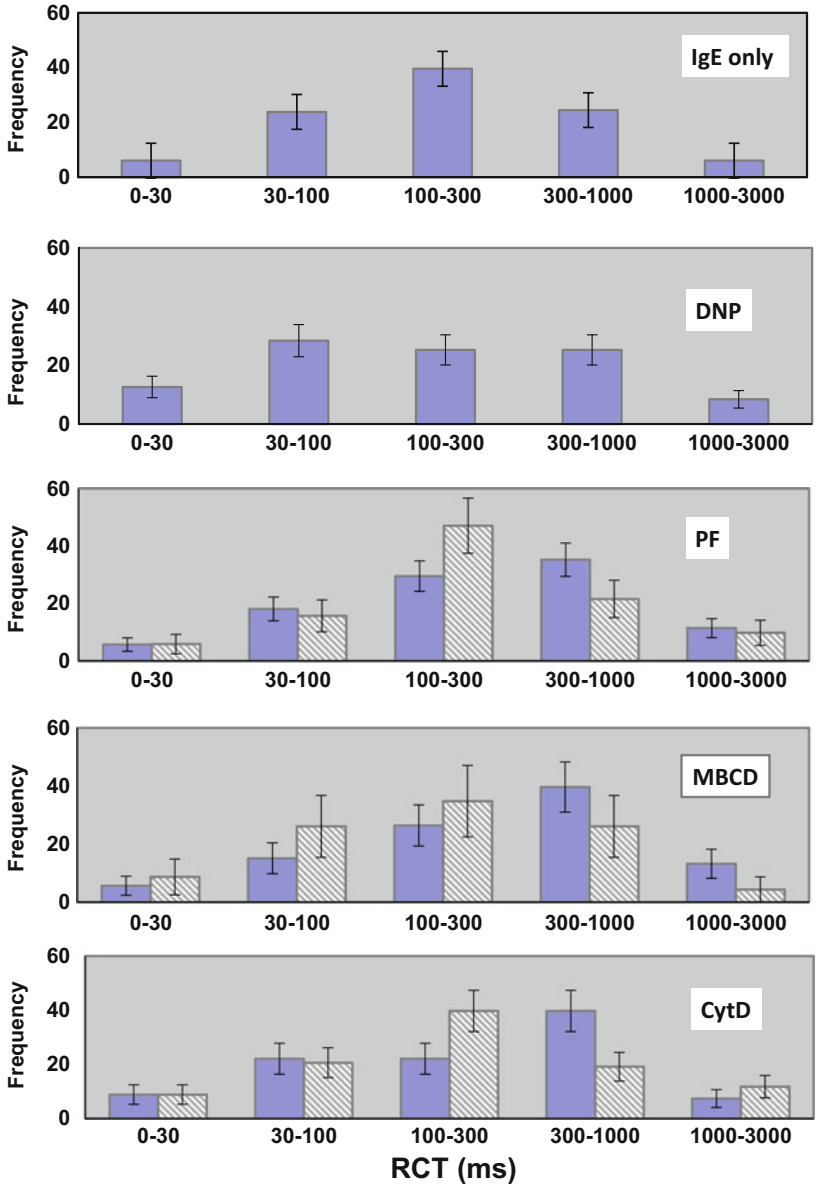

Fig. 13.10 Histograms of rotational correlation times for Qdot655 bound to FcεRI on variously-treated cells. Abbreviations indicating treatment groups are: IgE, IgE only; DNP, DNP-BSA; PF, paraformaldehyde; MBCD, methyl-β-cyclodextrin; cytD, cytpochalasin D. Frequencies are given as percents of the numbers of QD indicated in Table 13.1. The left-hand bar (*solid fill*) of each pair represents cells loaded with IgE before the indicated treatment while the right-hand bar if any (*hatched fill*) denotes cells treated before IgE loading

Table 13.1 Statistics of RCTs exhibited by Qdot655 bound to FcεRI on variously-treated cells

1st reagent	2nd reagent	Geometric Avg RCT	SD of $\log_{10}$ (RCT)	Total QD
IgE	–	175.1	0.475	298
IgE	DNP	150.1	0.481	95
IgE	PF	238.1	0.488	105
PF	IgE	208.2	0.491	51
IgE	MBCD	259.3	0.435	53
MBCD	IgE	148.9	0.482	23
IgE	CytD	203.5	0.564	68
CytD	IgE	164.3	0.522	68

Abbreviations indicating various treatment groups are the same as those used in Fig. 13.10. The geometric mean of the RCT in each treatment group is provided, together with the standard deviation of $\log_{10}$ (RCT) and the number of QD examined in each group

Table 13.2 Statistics of initial amplitudes of the polarization fluctuation TACF exhibited by Qdot655 bound to FcεRI on variously-treated cells

1st reagent	2nd reagent	Avg fitted Gr(0)	SD	Total QD
IgE	–	0.001243	0.001206	298
IgE	DNP	0.000978	0.000877	95
IgE	PF	0.000971	0.000797	105
PF	IgE	0.001311	0.001299	51
IgE	Mbcd	0.000905	0.000900	53
Mbcd	IgE	0.001595	0.001814	23
IgE	CytD	0.000895	0.000667	68
CytD	IgE	0.001774	0.001759	68

Abbreviations indicating various treatment groups are the same as those used in Fig. 13.10. The mean initial amplitude for each treatment group is provided, as is the standard deviation of these amplitudes and the number of QD examined in each group

The initial fitted values G(0) of the TACF (Table 13.2) are also grossly similar for all treatment groups. Nonetheless, *if applied after IgE loading,* DNP-BSA, methyl-β-cyclodextrin, paraformaldehyde and cytochalasin D seem to reduce the TACF amplitude significantly relative to IgE control cells, suggesting these treatments have affected more or less complete immobilization of a fraction of receptors, thus removing their contribution to the TACF which considers only receptors with RCT below about 2 s. Treated cells also exhibit slightly reduced standard deviation. This might be rationalized by suggesting that these treatments essentially immobilize an otherwise highly mobile fraction of receptors thus reducing both the average G(0) and the heterogenity of the receptor population. By contrast, if cells are first exposed to treatment reagents, not including DNP-BSA, and then loaded with IgE, both the average G(0) and the standard deviation are slightly increased, precisely the opposite of that observed when cell are treated immediately before QD binding. It is difficult to rationalize this difference.

A major question is what broader relevance the observed polarization fluctuation TACFs of initial amplitude ~0.0012 and RCTs of about 200 ms might have to membrane protein dynamics. TPA measurements on cell suspensions are limited by

the lifetime of organic phosphorescent probes and hence molecules rotating more slowly than about 1 ms appear rotationally immobile in such experiments. Data on all cell types typically show a "limiting anisotropy" which does not decay on microsecond timescale. For example, we have examined the rotation of erythrosin-labeled IgE-FcεRI complex on suspended 2H3 cells [37]. The ~80 μs anisotropy decays of both the receptor and the MAFA regulatory protein are understandable as hydrodynamic rotation of the proteins' transmembrane domains. However, residual anisotropies of 0.039 and 0.047, respectively, remain at 350 μs after excitation. We have noted [47] that, for FcεRI, the limiting anisotropies observed in fluorescence depletion anisotropy experiments represent about 1/6 of the photophysical maximum. If Qdot655 behaves as an ideal symmetric 2D chromophore and if its initial anisotropy of 0.042, as determined by time-resolved nanosecond fluorescence anisotropy measurements, represents the actual limiting photophysical anisotropy, then we would predict that G(0) should be about 0.0066. Our correlation experiments yield a G(0) of about 0.0012 for motion between about 10 ms and 2 s. The ratio of the measured G(0) to that predicted from time-resolved fluorescence anisotropy experiments is also about 1/6. This suggests that these orientational fluctuations of quantum dots on the 20–2000 ms timescale might account for a substantial fraction of the apparent rotational immobility exhibited by membrane receptors examined with faster techniques.

The other key question is why the various treatments such as receptor crosslinking by polyvalent DNP-antigens have such limited effects on receptor rotational dynamics. One explanation could be that the slow QD motions shown in TACF decay reflect properties of the membrane itself, rather than properties of the embedded receptors. Lateral motions of "lipid rafts" within the cell surface are well-known. Likewise, a rigid cylindrical membrane region would be expected to rotate as well. The relation between region size and RCT is easily calculated [1]. To exhibit *unhindered* rotation with an RCT of 200 ms, a structure in a 5 nm-thick membrane of viscosity 3 Poise would need a radius of 400 nm. However, such times could arise from *much smaller* domains whose motion was hindered by cytoplasmic species attached to embedded proteins. Thus, our results may indicate that individual mesoscale membrane regions rotate or librate somewhat with respect to the overall cell surface and that receptor-bound quantum dots share this overall motion.

References

1. Saffman PG, Delbrück M. Brownian motion in biological membranes. Proc Natl Acad Sci U S A. 1975;72(8):3111–3.
2. Fooksman DR, Edidin M, Barisas BG. Measuring rotational diffusion of MHC class I on live cells by polarized FPR. Biophys Chem. 2007;130(1–2):10–16.
3. Rahman NA, Philpott CJ, Barisas BG, Roess DA. Gonadotropin effects on luteinizing hormone receptor structure examined by time-resolved phosphorescence anisotropy and photoproximity labeling. FASEB J. 1992;6:A018.

4. Damjanovich S, Tron L, Szollosi J, Zidovetzki R, Vaz WLC, Regateiro F, Arndt-Jovin DJ, Jovin TM. Distribution and mobility of murine histocompatibility H-2K^k antigen in the cytoplasmic membrane. Proc Natl Acad Sci U S A. 1983;80:5985–9.
5. Zidovetzki R, Yarden Y, Schlessinger JD, Jovin TM. Rotational diffusion of epidermal growth factor complexes to cell surface receptors reflect rapid microaggregation and endocytosis of occupied receptors. Proc Natl Acad Sci U S A. 1985;8:1337–41.
6. van Meer G. Cellular lipidomics. EMBO J. 2005;24(18):3159–65.
7. Field KA, Apgar JR, Hong-Geller E, Siraganian RP, Baird B, Holowka D. Mutant RBL mast cells defective in Fc epsilon RI signaling and lipid raft biosynthesis are reconstituted by activated Rho-family GTPases. Mol Biol Cell. 2000;11(10):3661–73.
8. Cone RA. Rotational diffusion of rhodopsin in the visual receptor membrane. Nat New Biol. 1972;236:39–43.
9. Greinert R, Staerk H, Stier A, Weller A. E-type delayed fluorescence depolarization, technique to probe rotational motion in the microsecond range. J Biochem Biophys Methods. 1979;1(2): 77–83.
10. Austin RH, Chan SS, Jovin TM. Rotational diffusion of cell surface components by time-resolved phosphorescence anisotropy. Proc Natl Acad Sci U S A. 1979;76(11):5650–4.
11. Johnson P, Garland P. Fluorescent triplet probes for measuring the rotational diffusion of membrane proteins. Biochem J. 1982;203:313–21.
12. Johnson P, Garland PB. Depolarization of fluorescence depletion. A microscopic method for measuring rotational diffusion of membrane proteins on the surface of a single cell. FEBS Lett. 1981;132(2):252–6.
13. Pinaud F, King D, Moore HP, Weiss S. Bioactivation and cell targeting of semiconductor CdSe/ZnS nanocrystals with phytochelatin-related peptides. J Am Chem Soc. 2004;126(19): 6115–23.
14. Corporation I. Qdot® biotin conjugates user manual. Carlsbad, CA: Invitrogen Corp; 2006.
15. Grecco HE, Lidke KA, Heintzmann R, Lidke DS, Spagnuolo C, Martinez OE, Jares-Erijman EA, Jovin TM. Ensemble and single particle photophysical properties (two-photon excitation, anisotropy, FRET, lifetime, spectral conversion) of commercial quantum dots in solution and in live cells. Microsc Res Tech. 2004;65(4-5):169–79.
16. Sönnichsen C, Alivisatos A. Gold Nanorods as novel nonbleaching plasmon-based orinetation sensors for polarized single-particle microscopy. Nano Lett. 2005;5(2):301–4.
17. Cantor CR, Schimmel PR. Techniques for the study of biological structure and function. In: Freeman WH, editor. Biophysical chemistry II. San Francisco: W. H. Freeman; 1980. p. 441.
18. Philpott CJ, Rahman NA, Kenny N, Londo TR, Young RM, Barisas BG, Roess DA. Rotational dynamics of luteinizing hormone receptors and MHC class I antigens on murine Leydig cells. Biochim Biophys Acta. 1995;1235(1):62–8.
19. Munnelly HM, Brady CJ, Wade WF, Roess DA, Barisas BG. Lateral and rotational dynamics of I-A^k molecules expressing cytoplasmic truncations. Int Immunol. 2000;12(9):1319–28.
20. Barisas BG, Wade WF, Jovin TM, Arndt-Jovin D, Roess DA. Dynamics of molecules involved in antigen presentation: effects of fixation. Mol Immunol. 1999;36(11-12):701–8.
21. Nirmal M, Dabbousi BO, Bawendi MG, Macklin JJ, Trautman JK, Harris TD, Brus LE. Fluorescence intermittency in single cadmium selenide nanocrystals. Nature. 1996; 383(6603):802–4.
22. Rosenthal SJ, Chang JC, Kovtun O, McBride JR, Tomlinson ID. Biocompatible quantum dots for biological applications. Chem Biol. 2011;18(1):10–24.
23. Fu Y, Zhang J, Lakowicz JR. Suppressed blinking in single quantum dots (QDs) immobilized near silver island films (SIFs). Chem Phys Lett. 2007;447(1–3):96–100.
24. Shimizu KT, Neuhauser RG, Leatherdale CA, Empedocles SA, Woo WK, Bawendi MG. Blinking statistics in single semiconductor nanocrystal quantum dots. Phys Rev B. 2001; 63(20):205316.
25. Pierrat S, Zins I, Breivogel A, Sonnichsen C. Self-assembly of small gold colloids with functionalized gold nanorods. Nano Lett. 2007;7(2):259–63.

26. Spetzler D, York J, Daniel D, Fromme R, Lowry D, Frasch W. Microsecond time scale rotation measurements of single F1-ATPase molecules. Biochemistry. 2006;45(10):3117–24.
27. Chang W-S, Ha JW, Slaughter LS, Link S. Plasmonic nanorod absorbers as orientation sensors. Proc Natl Acad Sci U S A. 2010;107(7):2781–6.
28. Wang G, Sun W, Luo Y, Fang N. Resolving rotational motions of nano-objects in engineered environments and live cells with gold nanorods and differential interference contrast microscopy. J Am Chem Soc. 2010;132(46):16417–22.
29. Xiao L, Qiao Y, He Y, Yeung ES. imaging translational and rotational diffusion of single anisotropic nanoparticles with planar illumination microscopy. J Am Chem Soc. 2011;133:10638–45.
30. Barisas BG, Smith SM, Liu J, Song J, Hagen GM, Pecht I, Roess DA. Compartmentalization of the Type I Fc epsilon receptor and MAFA on mast cell membranes. Biophys Chem. 2007; 126(1–3):209–17.
31. Lakowicz JR. Principles of fluorescence spectroscopy. 3rd ed. New York: Springer; 2006.
32. Li J, Kwok K-C, Cheung N-H. Determination of the dipole geometry of fluorescent nanoparticles by polarized excitation and emission analysis. Appl Spectrosc. 2016;70(2):302–11.
33. Empedocles SA, Neuhauser R, Bawendi MG. Three-dimensional orientation measurements of symmetric single chromophores using polarization microscopy. Nature. 1999;399(6732): 126–30.
34. Shapiro IRM. Observation of single-molecule rotational diffusion at microsecond timescales by polarized fluorescence correlation spectroscopy. Ph.D.dissertation, California Institute of Technology; 2009
35. Aragón SR, Pecora R. Fluorescence correlation spectroscopy and Brownian rotational diffusion. Biopolymers. 1975;14(1):119–37.
36. Jackson JD. Mathematics for quantum mechanics: an introductory survey of operators, eigenvalues, and linear vector spaces. 1st ed. New York: W.A. Benjamin Inc.; 1962.
37. Song J, Hagen G, Roess DA, Pecht I, Barisas BG. Time-resolved phorescence anisotropy studies of the mast cell function-associated antigen and its interactions with the Type I Fce receptor. Biochemistry. 2002;41:880–9.
38. Rahman NA, Pecht I, Roess DA, Barisas BG. Rotational dynamics of Fc receptors on individually-selected rat mast cells studied by polarized fluorescence depletion. Biophys J. 1992;161:334–61.
39. Roess DA, Brady CJ, Barisas BG. Biological function of the LH receptor is associated with slow receptor rotational diffusion. Biochim Biophys Acta. 2000;1464(2):242–50.
40. Whaley P. Qdot conjugates: sensitive, multicolor, stable fluorescence. Carlsbad California: Invitrogen Corporation; 2006.
41. Corporation I. Qdot biotin conjugates user manual. Carlsbad California: Invitrogen Corporation; 2006.
42. Born M, Wolf E. Principles of optics: electromagnetic theory of propagation, interference and diffraction of light. Pergamon: Elsevier; 1980.
43. Efros AL, Rodina AV. Band-edge absorption and luminescence of nonspherical nanometer-size crystals. Phys Rev B. 1993;47(15):10005–7.
44. Barisas BG, Smith S, Liu J, Song J, Hagen G, Pecht I, Roess D. Compartmentalization of the Type I Fc epsilon receptor and MAFA on 2H3 cell membranes. Biophys Chem. 2006;126: 209–17.
45. Shvartsman DE, Gutman O, Tietz A, Henis YI. Cyclodextrins but not compactin inhibit the lateral diffusion of membrane proteins independent of cholesterol. Traffic. 2006;7(7):917–26.
46. Roess DA, Niswender GD, Barisas BG. Cytochalasins and colchicine increase the lateral mobility of human chorionic gonadotropin-occupied luteinizing hormone receptors on ovine luteal cells. Endocrinology. 1988;122(1):261–9.
47. Rahman NA, Pecht I, Roess DA, Barisas BG. Rotational dynamics of type I Fce receptors on individually-selected rat mast cells studied by polarized fluorescence depletion. Biophys J. 1992;61(2):334–46.

Chapter 14
Combining NMR Spectroscopy and Molecular Dynamics Simulation to Investigate the Structure and Dynamics of Membrane-Associated Proteins

Alexander Vogel and Daniel Huster

Abstract Nuclear magnetic resonance (NMR) spectroscopy and molecular dynamics (MD) simulations are both powerful methods for the investigation of the structure and dynamics of biological membranes and membrane proteins but like every scientific method they both have their inherent advantages and disadvantages. Fortunately, these strengths and weaknesses are rather complementary to each other. Typically, MD simulations perform best on model systems with a limited number of molecules, while NMR methods can be applied to much larger and more complex systems. Furthermore, MD simulations are very limited in the size of the systems and the timescales which can be simulated, while NMR is an ensemble technique that is sensitive to a very broad window of timescales. However, interactions of the like molecules of the ensemble are difficult to study which does not pose a problem in MD simulations. In complex systems that do not provide atomistic resolution, tracing an NMR result to its molecular origin can be very difficult while MD simulations offer a complete atomistic representation of the system. This all argues that a combination of the two methods can produce synergies that lead to a much deeper understanding of a specific research question. In this chapter, we address how experimental results can be used to guide MD simulation setup and validate its results and how these results can be used to obtain a much more detailed picture of the processes that occur in the investigated system. The combined use of both methods is illustrated on several examples of investigations on the human N-Ras protein, which represents a membrane-associated small GTPase.

A. Vogel • D. Huster (✉)
Institute for Medical Physics and Biophysics, Leipzig University, Härtelstr. 16-18, 04107 Leipzig, Germany
e-mail: daniel.huster@medizin.uni-leipzig.de

A. Chattopadhyay (ed.), *Membrane Organization and Dynamics*, Springer Series in Biophysics 20, DOI 10.1007/978-3-319-66601-3_14

14.1 Introduction

Biological membranes are highly important interfaces and represent a mediator of many crucial functions of life. They consist of a double layer of lipids composed of a multitude of chemical structures, in which a huge variety of proteins and also other molecules is embedded. While the lipid moiety of the membrane itself was viewed only as a passive matrix that represents the solvent for proteins for a long time, a picture has emerged now, in which the membrane actively participates in many biological functions in various ways. For instance, lipid molecules have been identified as second messengers that are involved in signaling [1–3] or as cofactors for membrane proteins [4, 5]. Furthermore, in contrast to the Singer Nicolson model [6], the lipid phase of the membrane is not homogeneous but represents a dynamic assembly of inhomogeneously mixed lipids that organize in small domains, which are often referred to as rafts [7, 8]. Both membrane-embedded and membrane-associated proteins have a certain propensity to partition into specific domains most likely driven by preferential interactions with particular lipids that enables specific functions. Furthermore, increased protein concentration at the domain boundaries may indicate storage of inactive proteins that can be activated by partitioning into the respective domain [9, 10].

Lipid membranes are highly dynamic. Lipid molecules undergo a multitude of structural transitions on several time scales that have been revealed by diffraction methods [11–13], NMR spectroscopy [14–16], and molecular dynamics (MD) simulations [17, 18]. A cartoon representation of the lipid dynamics in membranes is given in Fig. 14.1. Amplitudes of motion are large such that contacts between lipid headgroups and the hydrocarbon tail ends are possible and frequently observed [13, 14, 16]. Furthermore, both membrane-embedded and membrane-associated proteins have been reported to be highly mobile as also indicated in Fig. 14.1 [19, 20].

In this chapter, we shall address the combined use of nuclear magnetic resonance (NMR) spectroscopy and molecular dynamics (MD) simulations for the investigation of membrane structure and dynamics with particular emphasis on membrane-associated proteins. Both represent powerful methods by themselves to obtain detailed information about membrane constituents and in particular membrane proteins. However, the combination of both produces synergies with the benefit to lead to a much deeper understanding of the molecular details of the underlying mechanisms of a respective research question. Obviously, both methods have strengths and weaknesses that in the best case perfectly complement each other. This is expressed by the fact that MD simulations perform best on model systems with a limited number of molecules, while NMR methods can be applied to much more complex systems and even live cells [22–24]. MD simulations are very limited in the size of the systems that can be simulated, while NMR methods are able to study long range interactions. The same applies for the timescales, which again are very limited in MD simulations, rarely reaching the microsecond regime for all-atom simulations, while NMR methods can cover many different timescales

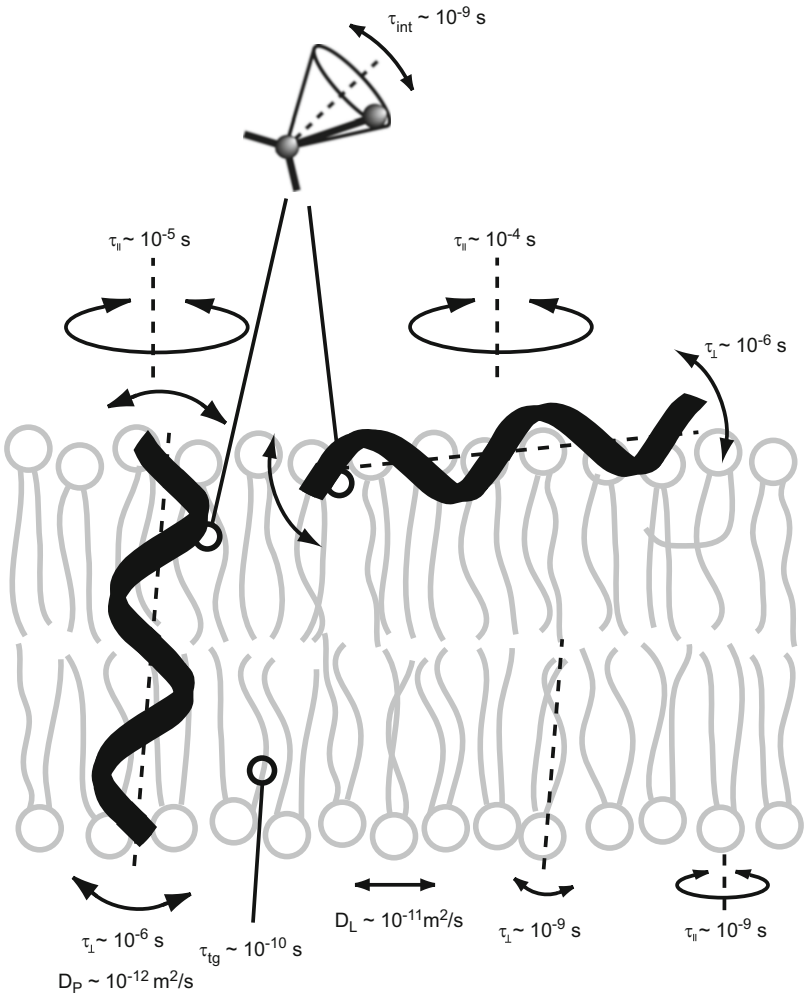

Fig. 14.1 Cartoon representation of the typical motions in biological membranes and the time scales on which they typically occur. Reprinted from [21], Copyright (2005), with permission from Elsevier

depending on the experimental setup. This also means that MD simulations are very dependent on their starting conformation since equilibration in many cases is performed for a fraction of the actual simulation time. If the system is far from equilibrium, the short available equilibration time will not be sufficient to actually reach equilibrium. NMR is an ensemble technique and specific interactions for instance between lipids and proteins can only be studied with great effort, while MD simulations can easily highlight the role of specific lipids in a simulation.

To mitigate some of the disadvantages of MD simulations, their setup should be guided by experimental data as much as possible, such that the simulated system is

a good representation of the experimental one. In addition, the results of the simulation should be carefully checked against experimental data for validity to ensure that the simulated system evolves as in the experiments. However, if both these criteria are met, the main strength of MD simulations can be exploited, which is the amount of detail (atomistic) simulations provide. Particularly in membrane biophysics, NMR parameters are often difficult to interpret with respect to molecular specificity. Isotope labeling helps, but molecules with specific isotopic labels are sometimes difficult to prepare and often not commercially available with respect to specific lipids. Due to the low intrinsic sensitivity of NMR, the influence of very low abundant membrane constituents is also difficult to track. The application of sometimes very complex models can help in such cases but even then the results tend to be model dependent. Furthermore, the interpretation of the results in terms of the underlying mechanisms often remains in the realm of speculation. In such cases, MD simulations can greatly support the interpretation of experimental results as basically all information is contained in the simulation trajectory. The difficult part is to extract this information since it is often not immediately obvious why for instance an order parameter is low or a correlation time long by looking at snapshots or movies of the trajectory. Hence, the most time consuming and difficult part, when conducting a MD simulation actually is data analysis after the simulation run is completed.

Since both NMR spectroscopy and MD simulations are complex matters by themselves, in the following both will be briefly introduced individually. Next, the benefits of combining both approaches will be detailed followed by an example, in which the combination of both methods has been applied successfully multiple times and led to very detailed understanding of the structure and dynamics of the membrane-associated human N-Ras protein.

14.2 NMR Spectroscopy

14.2.1 ^{2}H NMR Spectroscopy

One of the most powerful tools for the investigation of the structure and dynamics of biological membranes is ^{2}H NMR spectroscopy [25, 26]. Various lipids with different deuteration schemes are commercially available and can be used to elucidate their structure and dynamics and the influences that e.g. membrane peptides/proteins or small molecules have on membrane structure and dynamics. Deuterated fatty acids are also available and can be used to synthesize ^{2}H labeled lipid-modified proteins allowing their direct investigation [27]. From these molecules, samples can be prepared and NMR spectra recorded. One advantage of this approach is that the natural abundance of deuterium is very low and even in dilute samples only the labeled molecules are detected in the ^{2}H NMR spectra. Only when the molecule of interest is extremely diluted, a peak from natural abundance

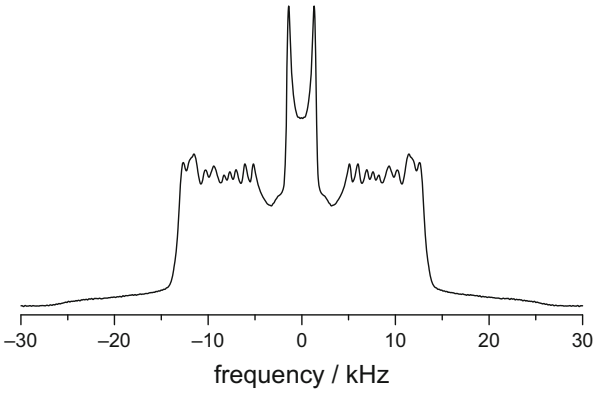

Fig. 14.2 ^{2}H NMR spectrum of dimyristoylphosphatidylcholine (DMPC-d_{54}) membranes at 30 °C

deuterium in water may show up, which can largely be suppressed by using deuterium-depleted water. The position of this peak is always in the center of the spectrum due to the large mobility of water and, therefore, often does not interfere with data analysis of the quadrupolar splittings that represent the dominating interaction in ^{2}H NMR. Another advantage of selective labeling is that in samples with a mix of different lipids or lipid modified proteins, different samples can be prepared, in which each molecular species is labeled at the time, allowing the selective investigation of each species.

A typical ^{2}H NMR spectrum of DMPC-d_{54}, where both acyl chains are fully deuterated is shown in Fig. 14.2. It consists of a superposition of several Pake doublets that originate from the individual deuterated carbon positions in the acyl chains [28]. The intense Pake doublet in the center of the spectrum represents the terminal methyl groups of both chains.

From the ^{2}H NMR spectra, a wealth of information can be obtained. Most easily, order parameters can be extracted that are indicative of the amplitude of motion of the C-D bond vector in the labeled position [25]. The order parameter is defined as

$$S_{\mathrm{CD}}^{(i)} = 1/2\left\langle 3\cos^2\beta_i - 1\right\rangle, \tag{14.1}$$

where β is the angle between the C-D bond orientation and membrane normal and the angular brackets indicate the ensemble average. Since experimentally only the absolute value is accessible, the order parameter ranges from 0 to 1, where a value of zero indicates that the C-D bond vector undergoes isotropic motion while a value of 1 indicates a totally rigid C-D bond. However, in reality, the problem is more complex since the average orientation of the C-D bond with respect to the external magnetic field also influences the magnitude of the order parameter and information of this average orientation is required for interpretation. For lipids or lipid modifications of proteins, it is usually assumed that the C-D bonds are on average perpendicular on the membrane normal, which is true for most cases and most

positions in the acyl chain. Since lipids in the liquid crystalline phase state undergo rapid rotation around an axis parallel to the membrane normal, the angle of 90° leads to a reduction of the order parameter by 50% such that it only ranges from 0 to 0.5. Experiments with selectively labeled lipids have shown that the uppermost segments of lipid acyl chains that are directly connected to the carboxyl group deviate from this orientation, which leads to an additional apparent reduction in their order parameter. Experimentally, the absolute values of the order parameters are easily determined from the quadrupolar splitting ($\Delta\nu_Q$) that can be measured directly in the ^{2}H NMR spectrum as the distance between the two maxima in the Pake doublet

$$\left|\Delta\nu_Q^{(i)}\right| = \frac{3}{4}\chi_Q\left|S_{CD}^{(i)}\right|, \tag{14.2}$$

where $\chi_Q = e^2qQ/\hbar$ represents the quadrupolar coupling constant (167 kHz for ^{2}H in an aliphatic C-^{2}H bond) [29]. Since experimentally mostly lipids with acyl chains are used, in which all positions are deuterated simultaneously, the ^{2}H NMR spectra of such lipids consist of a superposition of numerous Pake doublets as in Fig. 14.2 and it is almost impossible to assign the individual segments to the individual doublets. Therefore, commonly the order parameters are assigned consecutively with the largest values at the top of the chain and the smallest for the terminal methyl group resulting in an order profile of the entire lipid chain. The order profile that was obtained from the ^{2}H NMR spectrum shown in Fig. 14.2 is shown in Fig. 14.3A.

These order parameters provide valuable information on the dynamics of the membrane as they are directly related to the amplitude of motion. In addition, using advanced methods, much more information about the structure of the membrane is accessible, since in the highly dynamic membrane environment structure and dynamics are closely related. Accessible values include but are not limited to the length of the acyl chain, area per acyl chain, and hydrocarbon thickness of the membrane. One of the most successful models for obtaining these values is the mean torque model that has been developed with the help of MD simulations [30]. It allows the prediction of the aforementioned values based upon a potential of mean torque that governs the distribution of angles between C-D bond and membrane normal. The most important value for calculating the structural parameters is the average travel $\langle D_i\rangle$ of each carbon segment i along the bilayer normal, which can have a maximum value of $D_M = 2.54$ Å. For each carbon segment $\langle D_i\rangle$ can be calculated from

$$\langle D_i\rangle = D_M\langle\cos\beta_i\rangle = \langle z_{i-1}\rangle - \langle z_{i+1}\rangle, \tag{14.3}$$

where z_{i-1} and z_{i+1} denote the positions of carbon segments $i-1$ and $i+1$ along the membrane normal. The calculation of $\langle\cos\beta_i\rangle$ will be detailed later. Therefore, knowing the travel for all carbon segments, chain extension plots can be calculated. For this first $\langle D_{\omega-1}\rangle$ has to be calculated, where ω represents the terminal methyl

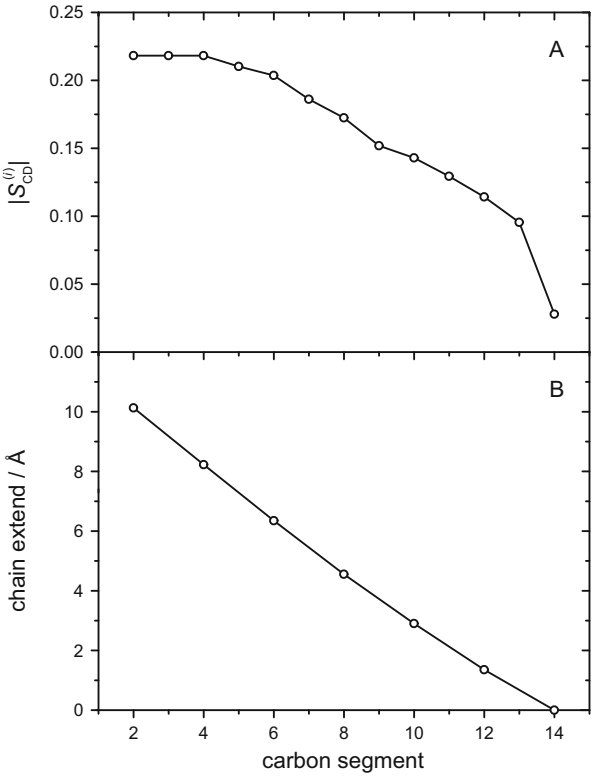

Fig. 14.3 Order parameter profile (**a**) and chain extension plot (**b**) of DMPC-d_{54} membranes at 30 °C obtained from the ^{2}H NMR spectrum shown in Fig. 14.2 using the mean torque model

position of the acyl chain. Therefore, this is the average travel for the methylene segment directly preceding the terminal methyl group and gives the distance between the terminal methyl ω and the next but one methylene group ω−2. Next, the value for $\langle D_{\omega-3} \rangle$ has to be calculated, which is the distance between ω−2 and ω−4. Continuing this procedure until the top of the chain is reached, a chain extension profile can be created, in which usually the position of the terminal methyl is fixed at 0 along the membrane normal and the position of every other carbon position before that is plotted as shown in Fig. 14.3B. From this, the distance L_C* between position 2 and the terminal methyl ω projected onto the membrane normal can be extracted via [31]

$$L_C^* = \langle z_2 \rangle - \langle z_\omega \rangle = \sum_{i=3,5\ldots}^{\omega-1} \langle D_i \rangle. \tag{14.4}$$

Taking the size of the terminal methyl and the first position of the chain into account the more realistic chain length L_C can be calculated using [31]

$$L_C = \frac{1}{2}\sum_{i=2}^{\omega-1}\langle D_i\rangle + \langle D_{\omega-1}\rangle. \tag{14.5}$$

Besides this chain length, further structural parameters such as the area per lipid chain $\langle A\rangle$ and the hydrocarbon thickness of the membrane D_C can be calculated. For this, however, not the complete order profile is used but just the so called plateau peak. This peak typically has the highest order and is very intense because it corresponds to carbon segments in the upper part of the chain that all have very similar order and, therefore, overlap in one single peak. Assuming that the acyl chain has the shape of a cylinder or cuboid, its average cross-sectional area can be expressed by

$$\langle A\rangle = \frac{2V_{CH_2}}{D_M}\left\langle\frac{1}{\cos\beta}\right\rangle, \tag{14.6}$$

where V_{CH2} is the volume of a single methylene group. For disaturated phospholipids, the volume of a single methylene group V_{CH2}, which is a function of absolute temperature T, can be approximated by

$$V_{CH_2}(T) \approx V^0_{CH_2} + \alpha_{CH_2}(T - 273.15\text{K}) \tag{14.7}$$

with the empirical parameters $V^0_{CH_2} = 26.5\ \text{Å}^3$ and $\alpha_{CH_2} = 0.0325\ \text{Å}^3/\text{K}$. The hydrocarbon thickness can be expressed by

$$D_C = \frac{1}{2}n_C D_M\left\langle\frac{1}{\cos\beta}\right\rangle^{-1} \tag{14.8}$$

using the same assumption of a cylindrical or cuboidal chain. For the calculation of both $\langle A\rangle$ and D_C the value of $\langle 1/\cos\beta\rangle$ is needed, which can be approximated by

$$\left\langle\frac{1}{\cos\beta}\right\rangle \approx 3 - 3\langle\cos\beta\rangle + \langle\cos^2\beta\rangle. \tag{14.9}$$

Therefore, the moments $\langle\cos\beta\rangle$ and $\langle\cos^2\beta\rangle$ are needed and can be obtained from the measured order parameters. The calculation of $\langle\cos^2\beta\rangle$ is straightforward and is given by

$$\langle\cos^2\beta\rangle = \frac{1 - 4S_{CD}}{3} \tag{14.10}$$

where S_{CD} is the order parameter of the plateau peak. The calculation of $\langle\cos\beta\rangle$, which also is required to calculate the average travel $\langle D_i\rangle$ of each carbon segment i along the bilayer normal is more difficult and the following approximate result has been obtained [31]

$$\langle \cos\beta \rangle = \frac{1}{2}\left(1 + \sqrt{\frac{-8S_{CD} - 1}{3}}\right), \tag{14.11}$$

where S_{CD} either is the order parameter of the plateau peak or the order parameter of the carbon position, for which the average travel $\langle D_i \rangle$ will be calculated. This approximation works well for order parameters larger than 0.2 but for smaller order parameters, it is preferable to numerically solve the following system of coupled equations for a more accurate result [31]

$$\langle \cos\beta_i \rangle = \frac{1}{Z}\int_{-1}^{1} \cos\beta_i \exp\left(\frac{-U_i \cos\beta_i}{k_B T}\right) \mathrm{d}\cos\beta_i = \coth\left(-\frac{U_i}{k_B T}\right) + \frac{k_B T}{U_i} \tag{14.12}$$

$$\begin{aligned} \langle \cos^2\beta_i \rangle &= \frac{1}{Z}\int_{-1}^{1} \cos^2\beta_i \exp\left(\frac{-U_i \cos\beta_i}{k_B T}\right) \mathrm{d}\cos\beta_i \\ &= 1 + 2\left(\frac{-k_B T}{U_i}\right)^2 + \frac{2k_B T}{U_i}\coth\left(-\frac{U_i}{k_B T}\right). \end{aligned} \tag{14.13}$$

While the order parameter is indicative of the amplitude of the motions of the C-^{2}H bond, the corresponding correlation times can be investigated by means of NMR relaxation experiments. For this, the spin system is prepared in a non-equilibrium state and the return to equilibrium is observed. This relaxation process is facilitated by molecular motions that result in randomly fluctuating electromagnetic fields at the location of the nucleus and, thereby, the relaxation time or the inverse relaxation rate contains information about these motions. While measurement of the relaxation rates is fairly straightforward, the interpretation of these rates is not. There are some simple ways of model-free interpretation but for an in-depth analysis, models of the molecular motions are needed. In the case of ^{2}H NMR spectroscopy, a simple empirical representation of the data is the so-called square-law plot and an example is shown in Fig. 14.4 [32]. In this plot, the R_1 relaxation rate is plotted against the square of the order parameter S_{CD} for all positions in the acyl chain. For disaturated phospholipids, straight lines are observed and their slope provides qualitative information on the elasticity and flexibility of the membrane [33]. In Fig. 14.4, data is shown for DMPC membranes alone as well as in the presence of either cholesterol or the detergent $C_{12}E_8$. It is immediately obvious that the plot is much shallower in the presence of cholesterol, which significantly stiffens the membrane und much steeper in the presence of $C_{12}E_8$ that renders the membrane softer. In addition, the plot in the presence of $C_{12}E_8$ deviates from a purely linear dependence and instead acquires a curved shape. Therefore, such plots can be used to judge the flexibility of the membrane lipids over relatively short distances approaching the molecular dimensions.

For a deeper understanding of the motions, a number of different models exists that can be fitted to the obtained relaxation rates [34, 35]. To this end, it is advisable

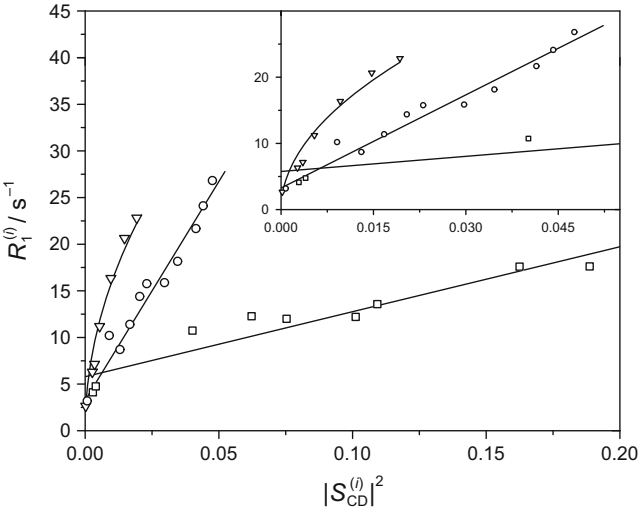

Fig. 14.4 Square-law plot of DMPC-d_{54} membranes (*circles*) and DMPC-d_{54}/cholesterol (1:1 mol/mol) membranes (*squares*) at 30 °C, and DMPC-d_{54}/$C_{12}E_8$ (2:1 mol/mol) membranes (*triangles*) at 40 °C. All data was obtained at a ^{2}H Larmor frequency of 115.1 MHz. The inset shows an expansion of the data for DMPC-d_{54} and DMPC-d_{54}/$C_{12}E_8$. Lines are drawn to guide the eye. Reprinted from [33], Copyright (2005), with permission from the American Chemical Society

to record the relaxation rates in dependence on various physical quantities such as temperature, magnetic field strength, or orientation of an oriented sample in the magnetic field. Then, the models can be fitted to the data obtaining a number of fitting parameters such as order parameters, correlation times, parameters describing the membrane flexibility, and so forth. However, the sheer number of models and their complexity is beyond the scope of this chapter and the interested reader is referred to the literature and the example at the end of this chapter (*vide infra*).

14.2.2 ^{13}C/^{15}N NMR Spectroscopy

Since biological molecules and in particular membrane proteins contain many carbons and nitrogens, these nuclei can also be used to investigate the structure and dynamics of the proteins as well as their interaction with lipids. For NMR spectroscopy, the isotopes ^{13}C and ^{15}N have to be used and amino acids with various labeling patterns are commercially available for the synthesis of labeled peptides/proteins as well as a host of other labeled molecules. Again, this selective labeling of certain positions does allow site specific resolution in the molecule under investigation. If the concentration of the molecule is high, the natural abundance of these nuclei (^{13}C: ~1.1% or ^{15}N: ~0.4%) can also be exploited to

investigate unlabeled samples. Typically, uniform labeling of the protein is used in biosynthesis, but techniques to achieve selective labeling are also available.

As membrane proteins move only slowly with respect to the NMR timescale, NMR spectra of these molecules are broadened by the orientation dependence of the NMR frequencies [36]. This can be overcome by application of magic angle spinning (MAS) in combination with ^{1}H decoupling, which results in narrow lines and in some cases allows detection of individual sites on the single amino acid basis [37, 38]. For MAS, the sample is located in a small rotor, oriented at 54.74° with respect to the external magnetic field (the magic angle) and spun at frequencies between 5 and 35 kHz. More recently, the technology to carry out fast and ultrafast MAS up to about 100 kHz has been developed such that ^{1}H detection becomes an attractive alternative to heteronucleus detection due to the much higher intrinsic sensitivity [38, 39].

A huge number of ^{13}C/^{15}N NMR experiments exists that can be used to obtain information about the labeled molecule [40]. In this chapter, we will focus on some selected examples that are used rather commonly and are well-suited for combination with MD simulations. Particularly useful for the setup of MD simulations is information on the structure of the simulated molecules. A large number of sophisticated experiments exist that provide distance constraints, which are useful in structure determination [40]. However, there are also more simple methods, and one of the simplest is based on the chemical shift of the amino acid carbons, which is easy to obtain if the assignment of the signals in the NMR spectrum is known. The reason for this is that the chemical shift of C_α, C_β, and CO contains information on the torsion angles in the protein backbone that determine the backbone structure as shown in Fig. 14.5. As can be seen, relative to the chemical shift in a random coil structure the NMR signals of C_α and CO move downfield (i.e. to higher ppm values) and the C_β signals move upfield (i.e. to lower ppm values) in an α-helix and opposite in a β-sheet. Therefore, in such investigations the difference between the chemical shifts of C_α and C_β often is used, which is larger in an α-helix than in a β-sheet. Database approaches have been developed that exploit this empirical correlation. In these databases, proteins for which the structure as well as the chemical shifts are known are collected. Based on the amino acid sequence and the measured chemical shifts of the target protein predictions about its structure can be made. The most often used implementation of this approach is called torsion angle likelihood obtained from shift and sequence similarity (TALOS) and its successor TALOS+ [41, 42].

While this is useful to obtain information about the structure of molecules in membranes, ^{13}C/^{15}N NMR experiments can also be used to investigate the dynamics of the molecule. One of many examples is the dipolar chemical shift correlation (DIPSHIFT) experiment that can be used to determine the ^{1}H-X dipolar coupling strength and thus molecular order parameters under MAS conditions [43, 44]. In this experiment, the strength of the dipolar coupling between either ^{13}C or ^{15}N and a directly bound ^{1}H nucleus is measured. In the static case it has a strength of 22.7 kHz for a ^{13}C-^{1}H bond and 10.9 kHz for a ^{15}N-^{1}H bond. If the bond orientation fluctuates, this value is reduced due to partial averaging. Therefore, by measuring

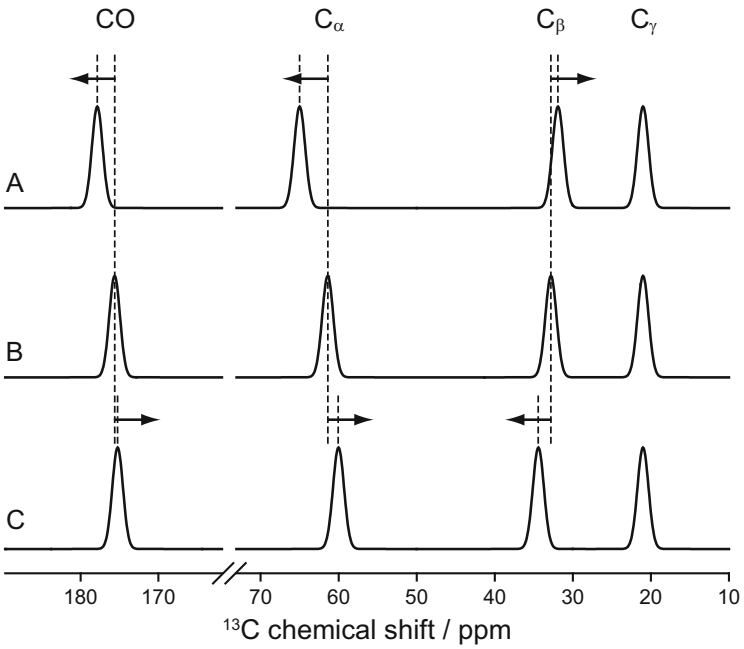

Fig. 14.5 Illustration how the ^{13}C chemical shift of C_α, C_β, C_γ, and CO carbons in a valine residue report the secondary structure of the peptide backbone. Typical random coil shifts for valine are shown in (**B**). If the same amino acid resides in an α-helix structure C_α and CO signal are shifted to higher ppm values and C_β to lower values (**A**) while shifts in the opposite directions are observed in a β-sheet (**C**). The values of C_γ and further side chain signals in other amino acids are typically uninfluenced by secondary structure. Reprinted from [21], Copyright (2005), with permission from Elsevier

the residual dipolar coupling the order parameter can be calculated as the ratio of the residual and static dipolar coupling constant. One difference to the order parameters measured by ^2H NMR spectroscopy is the timescale, on which they are defined. For ^2H NMR order parameters the timescale of the NMR experiment and therefore the time over which the quadrupolar coupling is averaged is <6 μs. In the DIPSHIFT experiment this timescale is <44 μs, which means that also slower motions contribute to the reduction of these order parameters. As before, the order parameter is indicative of the amplitude of motion. To also investigate the correlation time of the motion, again relaxation experiments are very useful. The collection of the data is relatively simple and should be conducted in dependence on as many experimental parameters as possible, such as temperature or magnetic field strength. This data can be interpreted by various complex motional models, but here also a relatively simple model-free approach exists. In the Lipari-Szabo model, it is assumed that the relaxation process is governed by a single internal motion in addition to overall isotropic reorientation of the molecule [45]. The correlation function $G(t)$ for this model is

$$G(t) = \frac{1}{5}\left(S^2 e^{\frac{-t}{\tau_M}} + \left[1 - S^2\right] e^{\frac{-t}{\tau}}\right) \tag{14.14}$$

with

$$\tau^{-1} = \tau_M^{-1} + \tau_e^{-1}, \tag{14.15}$$

where τ_M is the correlation time of the overall isotropic tumbling of the protein in solution and τ_e is the effective correlation time of the internal motion. The order parameter describes the amplitude of the internal motion. The nature of the internal motion is not relevant in this model (thereby this is a model-free approach) and is approximated by a single exponential decay as is the overall isotropic motion. The overall isotropic reorientation was included for soluble proteins that tumble freely in solution. Since this is not the case for membrane proteins, it is assumed that the overall isotropic tumbling correlation time τ_M is infinite, which simplifies the calculation. This model can then be fitted to relaxation rates by converting the correlation function into a spectra density. The spectral density $J(\omega)$ is a measure of how often certain frequencies occur in the randomly fluctuating electromagnetic fields that are caused by the dynamics of the molecules. It is defined as the Fourier transform of the correlation function:

$$J(\omega) = \mathrm{Re} \int_{-\infty}^{\infty} G(t) e^{-i\omega t} dt. \tag{14.16}$$

Solving the integral for the correlation function from Eq. (14.14) yields

$$J(\omega) = \frac{2}{5}\left(\frac{S^2 \tau_M}{1 + (\omega\tau_M)^2} + \frac{(1 - S^2)\tau}{1 + (\omega\tau)^2}\right). \tag{14.17}$$

This spectral density can then be used to calculate relaxation rates where the exact nature of the equation depends on the relaxation mechanism. In $^{13}C/^{15}N$ NMR often dipolar relaxation by directly bound ^1H atoms is predominant and the resulting relaxation rates R_1 and $R_{1\rho}$ (which are the inverse of the relaxation times T_1 and $T_{1\rho}$) can be calculated via

$$R_1 = \frac{1}{T_1} = n_H \pi^2 \chi_D^2 [J(\omega_H - \omega_C) + 3J(\omega_C) + 6J(\omega_H + \omega_C)] + \left(\frac{\omega_C \Delta\sigma}{\sqrt{3}}\right)^2 J(\omega_C) \tag{14.18}$$

and

$$R_{1\rho}=\frac{1}{T_{1\rho}}=\frac{1}{6}n_H\pi^2\chi_D^2\left[3J(\omega_H)+\frac{1}{3}J(\omega_e-2\omega_r)+\frac{2}{3}J(\omega_e-\omega_r)+\frac{2}{3}J(\omega_e+\omega_r)+\frac{1}{3}J(\omega_e+2\omega_r)\right]$$
$$+\frac{1}{6}(\omega_C\Delta\sigma)^2\left[\frac{1}{2}J(\omega_e-2\omega_r)+J(\omega_e-\omega_r)+J(\omega_e+\omega_r)+\frac{1}{2}J(\omega_e+2\omega_r)\right]+\frac{1}{2}R_1 \tag{14.19}$$

from the spectral densities.

In cases, where the molecule of interest is relatively mobile, also T_2 relaxation rates may be useful and can be calculated as

$$R_2=\frac{1}{T_2}=\frac{n_H\pi^2\chi_D^2}{2}[4J(0)+J(\omega_H-\omega_C)+3J(\omega_C)+6J(\omega_H)+6J(\omega_H+\omega_C)]$$
$$+\left(\frac{\omega_C\Delta\sigma}{\sqrt{18}}\right)^2[4J(0)+3J(\omega_C)]. \tag{14.20}$$

In these equations, n_H is the number of hydrogens bound to the $^{13}C/^{15}N$ nucleus, χ_D is the dipolar coupling constant, $\Delta\sigma$ is the span of the chemical shift anisotropy tensor and ω_X is the Lamor frequency of nucleus X. The frequencies ω_e and ω_r correspond to the spinlock field strength and the MAS frequency, respectively. Now using Eq. (14.17) and (14.18), (14.19) or (14.20) temperature and/or field strength dependent $^{13}C/^{15}N$ NMR relaxation data can be fitted obtaining the order parameter S and the correlation times τ_M and τ_e as fitting parameters. The temperature dependence of the correlation times often is modeled via an Arrhenius approach

$$\tau=\tau_0\cdot e^{\frac{E_A}{RT}}, \tag{14.21}$$

where E_A is the activation energy and R the gas constant. Numerous variants of the Lipari-Szabo model exist, e.g. considering anisotropic overall motion [45] or two separated internal motions with a fast and a slow motion [46]. Furthermore, a wealth of other models exists that make certain assumptions about the nature of the system and are therefore useful for certain systems. A particularly useful model for membrane constituents is modeling the overall motion of the molecule as restricted rotational diffusion with different correlation times parallel and perpendicular to the membrane normal [47].

Interpretation of such order parameters and correlation times however often proves to be difficult. First, various assumptions about the system have to be made that might impact the accuracy of the results. Examples from this section are:

- C-D bond vectors are perpendicular on the membrane normal.
- The order parameters drop monotonically from the top of the acyl chain towards the terminal methyl group.
- Overall isotropic protein tumbling can be neglected for membrane proteins in the Lipari-Szabo model.
- Chemical shift in a certain secondary structure motif is always similar.

Second, even if complex models are used for the interpretation and values such as order parameters, chain lengths, or correlation times are obtained the underlying mechanisms that lead to these values or changes in them often still are a matter of speculation. In such cases, MD simulations can provide valuable insights into the system that lead to much better understanding.

14.3 MD Simulations

Compared to NMR experiments; MD simulations represent a relatively new method. The first molecular simulations were conducted in the late 1950s and with the increasing success of modern computers the method became more popular [48]. Today, MD simulations are one of the most commonly used methods in biophysics despite the fact that until recently running all-atom MD simulations of reasonably sized systems (e.g. 100,000 atoms for a patch of membrane with an incorporated membrane protein) for the duration of a microsecond still required months of computing time on a small Linux cluster. The situation has considerably improved in the recent years with the rapid development of new graphics processing units (GPU) for gaming graphics cards. While the newest generations of GPUs are still far from being as flexible as classical CPUs, they are extremely efficient at calculating simple mathematical equations. Since MD simulations mostly consist of huge amounts of rather simple calculations, they are a perfect case for GPU acceleration and speedups of up to 20-fold have been reported for e.g. NAMD v2.11. This now even allows smaller workstations with GPUs to reach the performance levels that just a few years ago were only achievable by Linux clusters with many CPUs running in parallel. However, despite the many advances in the usability of the software and power of the hardware, which even allows beginners to conduct MD simulations rather easily [49], the methods that are employed in the background are a very complex matter. The reason for this is that the length and time scales available to current MD simulations are still very limited. The largest simulations published today contain millions of atoms (where one million atoms correspond to a total mass of about 10^{-17} g) but the timescale of such large simulations usually is on the order of 100 ns and huge computational effort is necessary to conduct these simulations often involving many thousands of CPUs and GPUs [50]. Since the computational demand of running MD simulations is so high, many different optimizations are used allowing the simulation to run faster without sacrificing too much accuracy. Therefore, it is important to understand how MD simulations and the various performance optimizations work, what their advantages/disadvantages are, and also what the general capabilities and limitations of MD simulations are.

An MD simulation is a computer simulation of the evolution of a fixed number of atoms under the laws of physics. To conduct a MD simulation, first a set of starting coordinates has to be generated and the exact details of how the simulation will be run have to be determined. These arguably are the most important steps of running a

MD simulation since any decision made at this stage is difficult or impossible to reverse later. First, it has to be decided what the system should contain and how big the simulation is going to be. There, a compromise has to be found such that the system is large enough to contain all molecules of interest without causing boundary effects while still being small enough to be computationally feasible. Then, a starting structure has to be built, which should be as close to reality as possible, because many equilibration processes (e.g. structural transitions) are much slower than the timescale that is accessible to MD simulations [51, 52]. For the starting structure of membrane simulations, usually pre-equilibrated lipid structures are taken from libraries and distributed in the membrane plane [49]. If other molecules such as proteins or peptides or are part of the simulation, for them also a starting structure has to be used. If a structure is available from crystallography or NMR, this is easy. However, since structures of membrane proteins are scarcely known, often a model has to be generated (e.g. via homology modeling or structure prediction) and the success of the simulation will strongly depend on the quality of the model [53, 54]. Subsequently, the simulation has to be hydrated and neutralized by the addition of ions. If the system is relatively uncomplicated, automated input generators such as the membrane builder on charmm-gui.org are available [49]. After the starting coordinates are created, first minimization of the system is performed to remove bad contacts before equilibration is started. The equilibration period often is a normal MD run, which is not used for data evaluation. Sometimes, the system is heated up to higher temperatures during equilibration to increase the probability of structural transitions. To keep certain molecules in their intended positions/structures, often constraints are used during equilibration which are subsequently weakened and finally switched off.

The actual procedure of calculating the trajectory is fairly straightforward. After the starting structure is defined forces between all atoms are calculated. For this, a force field such as CHARMM is used that contains parameters, which allow calculating the force between given atoms in the simulation [55]. In the case of two atoms that are directly bonded to each other, their interaction force is typically approximated by a spring and the stored values in the force field are the equilibrium bond length and the spring constant. Similar approaches are used for angles between three bonded atoms and dihedral angles as well as improper torsions of four connected atoms. The most demanding calculations, however, are the through space forces such as steric interactions as well as electrostatic forces due to the sheer number of atom pairs that need to be considered. Therefore, much optimization happens in this calculation step. First, these forces are only directly calculated for atoms that are within a certain distance from each other that is called cutoff and has a typical value of 12 Å. To avoid jumps in the force, when an atom enters the cutoff distance during the simulation, the forces are switched off gradually over a region of typically 10–12 Å. Longer range electrostatics are approximated by Fourier space based methods such as Particle Mesh Ewald, which are much faster but still highly accurate [56]. Such force fields now allow calculating the total force that is exerted on any atom in the system. Next, each atom is moved according to this force for the duration of one time step. Since the atoms have changed their

positions, the interaction forces have changed as well and need to be recalculated. This procedure is conducted in an iterative manner to create the trajectory of the simulation. The choice of the time step is crucial as it will determine the number of times all forces need to be calculated to reach a certain simulation length. In many all-atom MD simulations, a time step of 1 fs is used since the fastest bond length fluctuations in MD simulations that involve hydrogens are then still sampled reasonably well without introducing artifacts. A useful simplification to double the performance of the simulation is the use of an algorithm called SHAKE that fixes the length of all bonds involving hydrogens to their equilibrium length allowing to increase the time step to 2 fs. since all other fluctuations are accordingly slower [57]. A further optimization that is sometimes used is to calculate the long-range electrostatic interactions not for every time step but rather only every second or fourth step since changes in these forces are slow.

To avoid inconsistent forces at the boundaries of the simulation cell, periodic boundary conditions are used, which means that copies of the system are added to each of its sides. If a molecule moves in the main system, it also moves within all copies and if an atom leaves the main cell on one side it reenters the cell on the opposite side. Thereby, any atom on the boundary of the simulation cell still "feels" all relevant forces and is not exposed to vacuum or a hard wall. The size and shape of the periodic boundary cell can fluctuate in such a setup depending on the choice of the so-called ensemble. An ensemble is a choice of values that are kept constant during the simulation. Often used ensembles are NPT, NVT, or NVE. In the first ensemble the number of atoms (N), pressure (P), and temperature (T) are kept constant via various methods (e.g. barostat and thermostat) while energy (E) and volume (V) can fluctuate. The other ensembles apply constant number of atoms, volume, and temperature or energy, respectively. A particularly useful variation is the NPγT ensemble, which is identical to the NPT ensemble with the addition of forces that solely act within one plane of the simulation (described via the surface tension γ). This can be used to counter inaccuracies in the area per lipid that often occur due to force field inaccuracies, while retaining flexibility of the system size in this plane.

The methods described so far are the most commonly used approaches for MD simulations, where all atoms are represented and a single system is simulated for a certain number of time steps. However, many variations exist and some of them will be summarized briefly in the following. Taken together, a number of methods exists, which aim to improve the sampling of conformational states of the system, which is one of the most common problems. Some approaches modify the force field to lower energy barriers for the transition, but one particularly intriguing approach is called replica exchange. In this method, not just a single copy of the system is simulated, but rather a number of replicas at ever increasing temperatures [58]. Each replica of the system is simulated independently for a certain (short) amount of time before systems at neighboring temperatures can swap their coordinates based on their temperature and potential energy. This way during the simulation a certain copy of the system can start at the lowest temperature bath, which usually is the temperature of interest, and then subsequently travel to much higher

temperature baths, where structural transitions are much more likely to occur than at the lowest temperature. When the system returns, the new conformations also show up at the lowest temperature bath, where usually all data analysis is performed. Disadvantages of the replica exchange method are that the system can only be rather small and that the simulation time of each replica will be much shorter than a classical simulation due to the number of copies. However this shorter simulation time is more than compensated for by the much better sampling due to the use of higher temperatures.

Another often used approach to overcome limitations in system size and/or simulation length is called coarse grained MD simulations. In these simulations, several atoms are united into one particle to save computation time and specifically adjusted force fields such as MARTINI are used [59]. These simulations can run much faster, but lose some of the detail inherent in all-atom MD simulations. Furthermore, time progresses faster in these simulations due to the reduced number of atoms and thereby interactions between them, which further helps in extending the simulation timescale. Coarse grained MD simulations are particularly useful in cases, where principal physical effects such as hydrophobic mismatch are studied. However, it is difficult to extract NMR observables from these simulations due to the loss of bonds, whose orientation is crucial in NMR as well as the accelerated progression of time. Therefore, their potential for combination with NMR methods is limited.

In summary, MD simulations are a highly versatile method that can be used to investigate many different aspects of biological membranes. However a number of limitations exist that may compromise the validity of the results. Therefore, MD simulation can greatly benefit from the use of experimental data to improve the simulation setup as well as to validate the obtained results.

14.4 Combining NMR Spectroscopy and MD Simulations

14.4.1 Using NMR Data to Setup MD Simulations

As mentioned before, MD simulations offer many possibilities but also suffer from several weaknesses. Since they are computationally very demanding the main limiting factor is computational power. This results in the fact that MD simulations are very limited in size and timescale. Therefore, MD simulations are not well suited to equilibrate systems that are far from equilibrium and are very dependent on good starting coordinates and as much knowledge and effort as possible should be invested into the starting model of an MD simulation. One of the best ways to improve simulation quality is the constant use of experimental results to guide simulation setup and in particular NMR is able to contribute parameters that significantly improve simulation setup.

Membrane simulations often contain membrane bound or inserted peptides or proteins. However, structural information for membrane proteins is scarce and the RCSB protein data bank to date only contains 615 unique structures of membrane proteins. The reason is that membrane proteins are notoriously difficult to investigate and so far no standard method has been developed for their structure determination. It is unlikely that the huge effort required to determine the structure of a membrane protein will be undertaken just for the sake of running a MD simulation. In such cases, homology models are a good compromise. These models are generated by looking for template proteins of known structure that are as similar to the target protein as possible. Various methods exist to align the two sequences and predict a structure of the target protein based on the template protein.

Depending on the similarity of the two proteins the quality of the homology model can vary greatly. For two very similar proteins, the obtained homology structure might be of very high quality, while it will be much worse for proteins that show little similarity. But even in the case of very similar proteins, parts of the molecule might not agree or even be missing in the template protein. Again a number of methods exist to build loops or other protein segments de novo but in the end, the final model will have uncertainties and it has been shown that experimental data from many different sources can be used to significantly improve their quality. For such approaches, distance constraints and in particular long range constraints that help defining the global protein structure are useful and again NMR is a tool well suited to obtain such information. A host of experiments can provide quantities that are related to the structure of proteins and other molecules. Among them are distance restraints obtained via the nuclear Overhauser effect, torsion angle restraints, various NMR coupling strengths, or pseudo-contact shifts. From this information a structure obtained via homology modeling or database approaches such as TALOS can be refined via simulated annealing with the various experimental restraints. In addition, the structure can also be refined by methods that significantly speed up equilibration in MD simulations such as replica exchange.

Another important aspect is the topology of the membrane protein. Often, it is useful to have information about the amino acids that are located in the interface of the membrane to find the correct insertion depth for the start of the simulation. This is even more complicated for proteins or peptides that are membrane associated but do not span the membrane. In such cases, it often is not clear which parts of the protein exactly are in contact with the membrane surface and which parts embed into the hydrophobic region. Experimental methods can provide crucial data and again NMR spectroscopy offers various ways to obtain this information. E.g., the effect of spin diffusion can be used in which the magnetization is transferred between nuclei that are close in space [60]. If such a magnetization transfer is observed between certain amino acids of the protein and other membrane constituents such as lipids they must be in close proximity. However, depending on the experimental setup this method might not work very well in biological membranes as their high mobility impairs spin diffusion [14]. Also, paramagnetic probes either in the solution or attached to the molecules can be used. They cause paramagnetic relaxation of the spins in close vicinity that results in a broadening of the

corresponding signals in the spectrum [61–63]. This again can be used to identify positions that are in close proximity.

Another problematic topic concerns the area per phospholipid in the membrane. When setting up a membrane simulation, it is crucial to match it as closely as possible, because otherwise membrane structure and dynamics will be significantly impaired. For simple bilayers consisting of just a single lipid species values can be found in the literature, but for more complex systems, in particular mixtures of lipids or in presence of cholesterol, this is more complicated. For such cases experimental areas per lipid can be obtained in various ways such as X-ray diffraction or ^{2}H NMR spectroscopy. As an alternative, the area per lipid can be tuned during equilibration of the MD simulation until other values that are sensitive to it (e.g. order parameters or membrane thickness) are matched to experimental values.

14.4.2 Extracting NMR Observables from MD Simulations

While experimental data is extremely valuable for setting up MD simulations, they have further use in the validation of simulation results. The need for this again lies in the computational demands of MD simulations. This not only limits size and timescale of the simulations, but also the force field, which can be used. Ideally, one would like to use pure quantum mechanical (QM) force fields, but this is not feasible with the current computing power available. Hybrid QM/MM variants have been developed as a compromise that simulate only a small fraction of the molecules (most often just a single small molecule) with QM accuracy but also these force fields are very slow. Therefore, the force fields will remain classical in the foreseeable future and even simple QM calculations will remain limited to either small molecules and/or very short simulation times. The fastest all-atom force fields in terms of computing time such as CHARMM, AMBER, GROMOS, or OPLS are much faster than any QM variant but are very simple with purely classical terms and it actually is surprising that they reproduce experimental values as good as they do. Nevertheless, the classical force field values used today are still far from perfect. Despite constant tuning guided by experimental results, which tremendously improved simulation accuracy in last decades a lot of work remains in this field. For instance, the problem of matching area per lipid has been considerably improved in the CHARMM force field recently but still deviations remain in particular when different lipid types are mixed or non lipid molecules are added to the membrane [55].

Another difficulty is sampling. Biological membranes represent a highly dynamic environment with motions occurring on very different time scales (see Fig. 14.1). Some of these motions are slower than the time scales accessible to MD simulations. Therefore, even if the simulation was started close to equilibrium, it is very difficult to judge if all relevant conformations of the molecule under investigation have been sampled with the correct probability [51, 52]. This is particularly

true if a membrane protein e.g. a GPCR is simulated. Furthermore, the matter of reproducibility is a problem in MD simulations. Ideally, one would like to run multiple simulations such that the different trajectories can prove that the obtained results are reproducible. This is particularly true if a single molecule is observed or events that occur just once are reported. However, this is often also very limited by computational power.

All these inaccuracies and uncertainties can potentially lead to results that are not representative of the real system. This necessitates the MD simulations to be checked and validated by experimental results. In general, any experimental data that can also be obtained from MD simulations can be used as a benchmark and again data obtained by NMR is particularly useful. The reason is that it can be traced back to atomic details such as bond orientations that are easy to extract from MD simulations. One such quantity is the molecular order parameter that has been described above. In the case of ^{2}H NMR order parameters of fast rotating molecules such as lipids, their extraction from the MD simulation is very easy as one just has to create a time series of the angle β between the C-D bond and the membrane normal and then calculate the order parameter according to Eq. (14.1). If several identical molecules are present, in addition to a time averaging an ensemble averaging can also be applied for better sampling. In the case of C-H order parameters measured for instance in the DIPSHIFT experiment, their extraction from a trajectory is more complicated since the molecules (e.g. membrane proteins) usually do not rotate fast enough for complete rotational averaging. Henceforth these order parameters will be called C-H order parameters. For their calculation first, the dipolar interaction tensor has to be expressed in the laboratory (lab) frame. In the principal axis system (PAS), which is the coordinate system that is attached to the C-H bond of the molecule this tensor is diagonal and has the general matrix representation

$$\mathbf{D}^{\mathrm{PAS}} = \begin{pmatrix} D_{\mathrm{xx}} & 0 & 0 \\ 0 & D_{\mathrm{yy}} & 0 \\ 0 & 0 & D_{\mathrm{zz}} \end{pmatrix}, \tag{14.22}$$

where for a ^{13}C-^{1}H bond $D_{\mathrm{xx}} = D_{\mathrm{yy}} = -11.35$ kHz and $D_{\mathrm{zz}} = 22.7$ kHz. The coordinate transformation to the lab frame has to be conducted for all simulation frames using

$$\mathbf{D}^{\mathrm{lab}} = \mathbf{R}^{-1}(\alpha, \beta, \gamma)\mathbf{D}^{\mathrm{PAS}}\mathbf{R}(\alpha, \beta, \gamma), \tag{14.23}$$

where $\mathbf{R}(\alpha,\beta,\gamma)$ denotes the Euler rotation matrix with the Euler angles α, β, and γ [64, 65]. When determining the Euler angles one has to be careful to distinguish between passive and active rotations as α, β, γ, and $\mathbf{R}(\alpha,\beta,\gamma)$ are differently defined for the two cases. After the Euler angles have been determined for each frame, the interaction tensor in the lab frame $\mathbf{D}^{\mathrm{lab}}$ can be calculated for all frames. Subsequently, $\mathbf{D}^{\mathrm{lab}}$ is averaged over all time steps of the simulation. For this, one has to keep in mind that although the order parameter is a measure of the amplitude of

motion it is defined on a certain time scale. For ^{1}H-^{13}C order parameters, the upper limit of the correlation time is ~44 μs and any motion significantly slower than that will not contribute to the amplitude information contained in the order parameter. Consequently, often sampling issues remain in MD simulation as this time scale typically is not achieved by current MD simulations. Therefore, instead of averaging over the individual order parameters, at the end additional ensemble averaging can be applied for the calculation of the average tensor if various molecules exist in the simulation that are expected to exchange on this time scale. Lipids or small molecules in the same leaflet of a membrane can sometimes be expected to exchange on the NMR time scale while molecules in different leaflets are unlikely to exchange. This way, motions not completely sampled for a single molecule of the simulation (e.g. axial reorientation) can artificially be introduced and contribute to the reduction of the C-H order parameter. The average tensor is then diagonalized by calculation of the eigenvectors, assembling them into a rotation matrix $\mathbf{R}_2$ by using each eigenvector for one column and subsequent coordinate transformation using

$$\mathbf{D}^{\text{diagonal}} = \mathbf{R}_2^{-1} \langle \mathbf{D}^{\text{fixed}} \rangle \mathbf{R}_2. \tag{14.24}$$

The largest principal component of $\mathbf{D}^{\text{diagonal}}$ is then put into proportion with D_{zz} to yield the C-H order parameter as

$$S_{\text{C-H}} = \max\left(\left| D_{xx}^{\text{diagonal}} \right|, \left| D_{yy}^{\text{diagonal}} \right|, \left| D_{zz}^{\text{diagonal}} \right| \right) / D_{zz}. \tag{14.25}$$

Other experimental quantities that can be directly compared to MD simulations are relaxation rates. While the order parameter contains information on the amplitude of motion, a relaxation rate is also influenced by the correlation time of the motion. In general, various types of relaxation rates exist and depend on the type of experiment as well as the nucleus that is investigated (for examples see Sect. 14.2.2). However, when calculating relaxation rates, they mostly consist of spectral densities $J(\omega)$ that are sampled at different frequencies ω (e.g. see Eqs. 14.18, 14.19, and 14.20). Therefore, in the following, we will focus on the determination of the spectral density from the MD simulation. For the actual calculation of the relaxation rate, one will have to find the right expression for the investigated nucleus and type of relaxation rate in the literature. Their calculation will then be fairly straightforward from the spectral densities. Depending on the details either the spectral density $J(\omega)$ or some of its projections $J_0(\omega)$, $J_1(\omega)$, or $J_2(\omega)$ will be needed which can easily be converted using

$$J(\omega) = \frac{J_0(\omega) + 2J_1(\omega) + 2J_2(\omega)}{5}. \tag{14.26}$$

As before, the projections of the spectral densities $J_m(\omega)$ are the Fourier transforms of the correlation functions $G_m(t)$ and are defined as

$$J_m(\omega) = \mathrm{Re} \int_{-\infty}^{\infty} G_m(t) e^{-i\omega t} dt. \tag{14.27}$$

However, in MD simulations, the trajectory is discrete and therefore the time t is replaced by $n\Delta t$ where n is the running index and Δt is the distance between neighboring time points. The discrete spectral density can be calculated as

$$J_m(\omega_k) = 2 \sum_{n=0}^{l-1} G_m(n\Delta t) \cdot \cos(\omega_k \cdot n\Delta t)\Delta t, \tag{14.28}$$

where l is the number of points in the correlation function and k=0,...,l−1. The discrete frequencies ω_k are defined as

$$\omega_k = 2\pi \frac{k}{l\Delta t}. \tag{14.29}$$

The projections of the correlation function are defined as

$$G_{\mathrm{m}}(n\Delta t) = \frac{4\pi}{5} \left(\left\langle Y_{2\mathrm{m}}(o, \vartheta, \varphi) Y^*_{2\mathrm{m}}(o - n\Delta t, \vartheta, \varphi) \right\rangle_o - \left| \left\langle Y_{2\mathrm{m}}(p, \vartheta, \varphi) \right\rangle_p \right|^2 \right), \tag{14.30}$$

where averaging is performed over all possible indices o and p. In this equation, $Y_{2\mathrm{m}}(n\Delta t, \vartheta, \varphi)$ represent the well-known spherical harmonics, which are calculated using the spherical coordinates (ϑ, φ) of the bond vector at the time point $n\Delta t$ that can be directly extracted from the MD simulation. In commercially available mathematics packages, predefined functions with superior performance are often available to calculate the correlation functions and Fourier transforms. However, one has to be careful since they often use different prefactors. With these equations, it seems fairly straightforward to obtain correlation functions and spectral densities, which can then be used to calculate relaxation rates. However this formalism poses several technical problems. One problem is that the correlation function typically becomes very noisy at the end due to limited data for long correlation times. Upon Fourier transformation, this noise refolds into the spectral density. If the correlation function has not leveled off at this point, one possible solution is to fit a set of exponentials to it and replace the noisy long time tail by the fit. For this approach, one has to be careful to switch from the true correlation function to the fit in a point, where both are very close to each other since any discontinuity leads to artifacts in the spectral density. Another problem is that the spectral density calculated from MD simulations will be discrete. Since it needs to be sampled at certain frequencies for the calculation of the relaxation times this often leads to considerable errors as this frequency might be very different from the discrete frequencies available. This problem can be circumvented by cutting a few points at the end of the correlation

function. This changes the spacing of points in the spectral density after Fourier transformation since the distance between neighboring points is $2\pi/l\Delta t$.

14.4.3 Interpretation of NMR Data Using MD Simulations

While the calculation of order parameters, relaxation times, structures etc. can be used to validate MD simulations, a more detailed analysis of the simulation can yield significant insight into the mechanisms that lead to experimental observables. Given that the agreement to experimental data is good, such detailed analysis can greatly benefit the interpretation of the results. As described in Sect. 14.2.2, various models can be used to interpret experimental relaxation rates in terms of correlation time, order parameter, and sometimes additional quantities of the investigated system. However, these values are often model dependent and their interpretation is difficult. MD simulations can be very helpful to aid in this task. For instance, a correlation function obtained from a trajectory can be fitted by exponential functions to directly obtain correlation times and order parameters. Also, different motional models can be fitted to the correlation function for the assessment of their applicability to the investigated system. Furthermore, correlation functions can not just be calculated for bond vectors, but also for larger parts of the investigated molecule. Since their motions propagate to the motion of the bond this approach allows tracing the origin of an experimentally determined correlation time or order parameter.

Another example are ^{2}H NMR order parameters of molecules with more than one label. Experimentally, it is usually not known which Pake doublet and corresponding order parameter belongs to which labeled position. This is not a problem in MD simulations, which therefore can be used to assign the Pake doublets in the ^{2}H NMR spectrum. Further, if the molecules rotate around one axis (which is the case for most small molecules in liquid-crystalline membranes) ^{2}H NMR order parameters are not just dependent on the amplitude of the motion, but also on the average orientation of the bond. Therefore, in molecules, in which the average orientation is not known, it is often difficult to separate the influence of the two, which again is not difficult in MD simulations, where both quantities can easily be calculated. For instance, in the top segments of lipid acyl chains the C-H bonds deviate from the perpendicular orientation with respect to the membrane normal. This leads to a reduction in the order parameters of these positions that is not caused by larger amplitude motions. Furthermore, in experimentally obtained chain extension plots (see Fig. 14.3B) typically the position of the terminal methyl group is artificially placed at position 0. This is particularly important if chain extension plots of several components that reside in the same membrane (e.g. different lipid species) are compared because it implies that the terminal methyl groups of all components are at the same distance from the membrane center. Again from MD simulations this information is easily determined.

However, while the validation of MD simulations can be standardized for certain NMR experiments, more detailed analysis for interpretation of the results very much depends on the system and the questions under investigation. While some observations can be made by simply looking at the trajectory, many underlying structures, motions, etc. can only be assessed statistically and are not immediately obvious. In principle, the inherent detail of the simulation means that only the imagination of the researcher is the limit. In fact, a single simulated system can result in many different investigations depending on the researcher that is looking at it. For instance, one of the first microsecond timescale MD simulations of a GPCR (in this case rhodopsin) led to a number of publications by various authors that all investigated separate aspects [52, 66–72]. The simulation actually existed as a set of 26 trajectories of at least 100 ns length each and an additional 1600 ns trajectory of rhodopsin in the ground state that were made available to various research groups. Some articles investigated interactions between rhodopsin and polyunsaturated fatty acids [66–68] while others investigated the interactions with cholesterol [66, 71]. Another group was interested in the post-translational modifications of rhodopsin [72] while the structure and dynamics of the ligand retinal were also investigated [69]. Further, the trajectories also were used to investigate more technical aspects of membrane protein MD simulations such as sampling and convergence [52] as well as elastic network models [70].

In the following, we will illustrate how combinations of NMR and MD simulations have been used successfully and led to a very detailed understanding of the behavior of the membrane associated human N-Ras protein.

14.5 Examples

14.5.1 The Human N-Ras Protein

The human N-Ras protein is a peripheral membrane protein that belongs to the class of small GTPases. It has a molecular weight of ~21 kDa and consists of 189 amino acids. It acts as a molecular switch in a signal transduction cascade responsible for cell proliferation, differentiation, and apoptosis [73]. In its ground state, it binds GDP and upon exchange of GDP for GTP, N-Ras becomes activated. Deactivation is achieved via the GTPase activity of N-Ras that is further catalyzed by a GTPase activating protein (GAP). Mutations of N-Ras have been identified that disrupt its GTPase activity as well as the catalysis via GAP. This leads to the inability of N-Ras to become deactivated and results in uncontrolled cell growth and ultimately cancer [74]. Such mutated N-Ras proteins are found in up to 30% of all human tumors. Another possibility to deactivate N-Ras is the disruption of its membrane association as it has been shown that it is only active in the membrane bound state [75]. This membrane association is achieved via the C terminus that acts as a membrane anchor. In the case of N-Ras, the membrane binding is mediated mostly

by two post translational lipid modifications that are attached to cysteine 181 and cysteine 186. It has been shown that already removing just one of the two lipid modification results in almost complete loss of N-Ras function since a single lipid modification is not sufficient for permanent membrane anchoring [76]. Other members of the human Ras protein family are identical in the soluble part but vary drastically in the membrane anchor but all of them feature at least one lipid modification. The soluble part of Ras proteins was well understood and structures had been determined by X-ray diffraction [77] and NMR spectroscopy [78]. However, despite its importance for N-Ras function the membrane anchor was not resolved in the structures and only poorly understood due to the typical problems arising when studying membrane proteins. Therefore, a combination of various NMR methods and MD simulations has been used to investigate its structure and dynamics.

At first, small peptides consisting of seven amino acids were used as models for the membrane anchor. The two cysteines to which the lipid modifications are attached in the wildtype were modified by chemically stable hexadecyl hydrocarbon chains that closely mimic palmitoyl lipid modifications. This approach allowed the hexadecyl chains to be ^{2}H labeled and investigated by ^{2}H NMR spectroscopy [33]. In addition, unlabelled peptides were investigated in membranes consisting of deuterated lipids. This switching of the label between the individual molecular species allowed their separate investigation. A host of useful information was extracted for the membrane anchor as well as for the surrounding lipids that were used to setup the first 100 ns MD simulation of the system [79]. Particularly useful was the information that the hydrocarbon chains of the N-Ras membrane anchor are embedded in the membrane [80]. From the order parameter profiles, chain extension plots were calculated by use of the mean torque model, which resulted in the information that the chains fully extended to the membrane center [33]. Also, the peptide backbone was located inside the membrane-water interface. Furthermore, with the help of the mean torque model, the interfacial areas of the lipid acyl chains as well as the N-Ras peptide hydrocarbon chains were determined and used to define the size of the periodic boundary cell [33]. This resulted in a system that was much closer to equilibrium than previous simulations where just the ends of the peptide were inserted in the membrane and where the peptide first had to "find" the correct position which took about 20 ns [81]. The goal of the following study was to investigate the structure and dynamics of the lipid modifications in the membrane bound state. To this end, oriented samples were prepared that allowed the collection of angular dependent ^{2}H NMR spectra which are summarized in Fig. 14.6 [79]. A number of well resolved Pake doublets are observed that are labeled consecutively from peak 'a' with the highest order to peak 'm' with the lowest order. In addition, for all resolved carbon positions in the hexadecyl chains R_1 relaxation rates were determined in an angular dependent manner, which are summarized in Fig. 14.7 [79]. The orientation dependence of the relaxation rates was surprisingly low indicating large amplitude motions of the hexadecyl chains. The data was fitted with a complex composite membrane deformation model that included molecular motions as well as collective motions of the membrane. The obtained fit closely

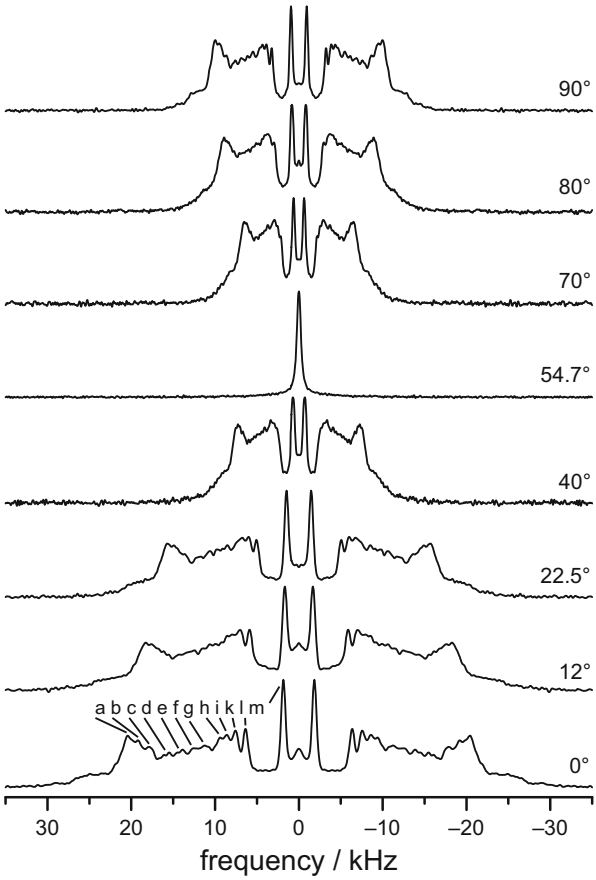

Fig. 14.6 Angular dependent spectra obtained for the hexadecyl chains of a N-Ras-d_{66} heptapeptide in DMPC bilayers (molar ratio 1:15). For the 0° orientation all resolved peak positions are identified. Reprinted from [79], Copyright (2007), with permission from Elsevier

resembled the experimental relaxation rates and various parameters of the dynamics of the hexadecyl modifications such as rotational diffusion constants parallel and perpendicular to the membrane normal were determined as $D_{\parallel} = 2.1 \times 10^9\ s^{-1}$ and $D_{\perp} = 4.5 \times 10^5\ s^{-1}$, respectively [79]. The MD simulation was validated against the experimental data by calculation of its angular dependent relaxation rates R_1.

This was achieved by calculation of spectral densities as described above and subsequent use of the following expression for spin-lattice relaxation of a deuterium nucleus that features a quadrupolar moment

$$R_1 = \frac{1}{T_1} = \frac{3}{4}\pi^2\chi_Q^2[J_1(\omega_D, \beta_{DL}) + 4J_2(2\omega_D, \beta_{DL})]. \tag{14.31}$$

Here ω_D is the Larmor frequency of the ^2H nucleus and χ_Q is the quadrupolar coupling constant, that has a value of 167 kHz for ^2H in an aliphatic C-^2H bond, while β_{DL} is the angle between the membrane normal and the external magnetic field.

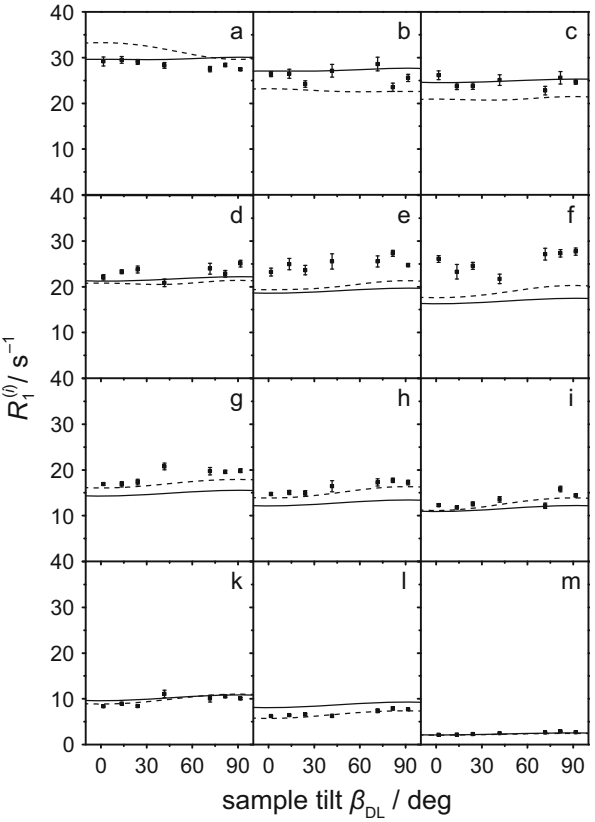

Fig. 14.7 Spin lattice relaxation rates $R^{(i)}{}_1$ obtained for the hexadecyl chains of a N-Ras-d_{66} heptapeptide in DMPC bilayers (molar ratio 1:15) obtained at a magnetic field strength of 17.6 T in dependence on the angle β_{DL} between the membrane normal and the external magnetic field. The individual panels correspond to all resolved peaks in the spectra as labeled in Fig. 14.6. The *solid lines* represent the simultaneous best fit of a composite membrane deformation model to the data while the *dashed lines* represent the relaxation rates extracted from the 100 ns MD simulation. Reprinted from [79], Copyright (2007), with permission from Elsevier

To save computation time spectral densities J_m were only calculated for an orientation of $\beta_{DL} = 0°$ and converted to the other angles using

$$\begin{aligned} J_m(\omega_D, \beta_{DL}) = {} & d^{(2)}_{0m}(\beta_{DL})^2 J_0(\omega_D, 0^\circ) \\ & + \left[d^{(2)}_{-1m}(\beta_{DL})^2 + d^{(2)}_{1m}(\beta_{DL})^2 \right] J_1(\omega_D, 0^\circ) \\ & + \left[d^{(2)}_{-2m}(\beta_{DL})^2 + d^{(2)}_{2m}(\beta_{DL})^2 \right] J_2(\omega_D, 0^\circ), \end{aligned} \tag{14.32}$$

where $d^{(2)}{}_{lm}(\beta_{DL})$ are the reduced Wigner rotation matrix elements. Note that this equation is only valid for axially symmetric molecules and an axially symmetric distribution about the director axis. The spectral densities at $\beta_{DL} = 0°$ were calculated from correlation functions of the orientation of the C-D bonds at the appropriate carbon position in the hydrocarbon chain. The obtained angular dependent relaxation rates are plotted in Fig. 14.7 and very good agreement between MD simulation and experiment was observed [79]. In particular, the fact that the slope of the relaxation rates with increasing angle β_{DL} changes its sign around peak position 'd' is well reproduced in the MD simulations. Therefore, further analysis of

the MD simulation could be conducted. This helped in the interpretation of the fact that experimentally significant differences were observed between the motions of the hexadecyl chains of the N-Ras peptide and the acyl chains of the surrounding DMPC matrix. In particular, the hexadecyl chains showed much lower order than the surrounding lipids and the relaxation rates indicated that they are more flexible than the surrounding DMPC acyl chains [33]. Analytical models already helped in the interpretation as they showed that this results in relatively short C16 hexadecyl chains that are almost identical in length to the C14 acyl chains of DMPC [33]. Later investigations extended this observation to membranes of varying thickness and showed that the hexadecyl chains are very malleable and adapt their chain length almost perfectly to the environment [82]. In fact from a DLPC matrix with C12 chains to a highly ordered C16 DPPC matrix in the presence of cholesterol the chain length of the N-Ras peptide hexadecyl chains almost doubled closely matching the matrix lipids in both cases. The MD simulation shed further light on this by calculation of the correlation function of both the hexadecyl and the DMPC chains. For this, the moment of inertia tensor of the chains was calculated and its smallest diagonal element taken as the chain axis. In Fig. 14.8, the correlation functions of these axes are shown for the hexadecyl chains of the N-Ras heptapeptide and the acyl chains of DMPC. They were fitted by a two component exponential decay

$$G(t) = \left(1 - S_{\mathrm{f}}^2\right)\exp\left(-\frac{t}{\tau_{\mathrm{f}}}\right) + \left(S_{\mathrm{f}}^2 - S^2\right)\exp\left(-\frac{t}{\tau_{\mathrm{s}}}\right) + S^2, \tag{14.33}$$

where τ_{f} and τ_{s} are the correlation times of the fast and slow motion respectively. The order parameters of the individual motions are S_{f} and S_{s} and are related to the order parameter S of the total motion via

$$S^2 = S_{\mathrm{f}}^2 S_{\mathrm{s}}^2. \tag{14.34}$$

From the total correlation function, it is immediately obvious that the N-Ras hydrocarbon chain has lower order overall because the plateau value, at which the correlation functions level off, corresponds to the square of the order parameter. When analyzing the individual components, it does become clear that the fast motions are very similar for the hydrocarbon chains of DMPC and N-Ras. Both have very similar order parameters S_{f} (0.69 vs. 0.71) and correlation times τ_{f} (0.81 vs. 0.72 ns). For the slow component however significant differences are observed. The order parameter S_{s} of DMPC is much higher (0.87 vs. 0.69) and its correlation time τ_{s} significantly longer (6.23 vs. 3.85 ns). Assuming that the hydrocarbon chains wobble inside a cylinder the opening semi-angle θ of this cylinder can be determined via [45]

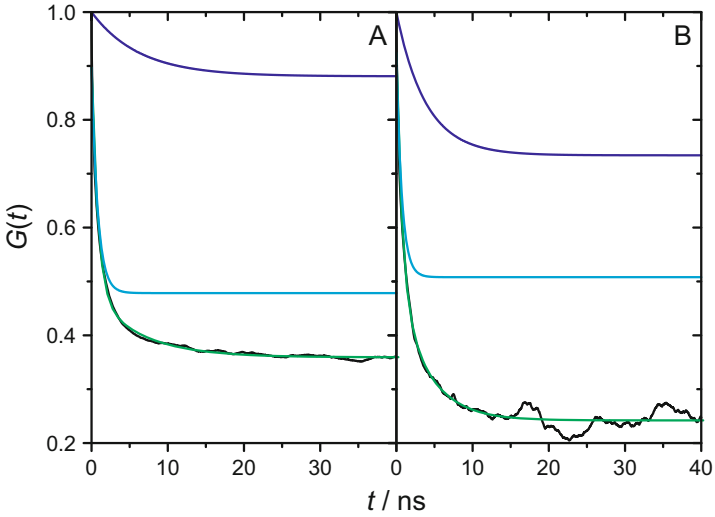

Fig. 14.8 Correlation functions of the hydrocarbon chains of DMPC (**A**) and N-Ras (**B**) are shown in *black*. Both were fitted by a two-component exponential decay shown in *green* whose two individual components are shown in *light blue* (fast component) and *dark blue* (slow component) which both were started at a value of 1 at $t = 0$ for clarity

$$S = \frac{1}{2}\cos\theta(1 + \cos\theta). \tag{14.35}$$

Using this equation the opening semi-angle of the slow motions of the hydrocarbon chains is 25° for DMPC while it is 39° for N-Ras. Therefore, the lipid-modifications of the N-Ras heptapeptide adapt to the surrounding DMPC bilayer by undergoing much larger amplitude motions on a timescale of a few ns.

In further experimental investigations, the full-length protein was used [83]. From the experiments, ^{13}C chemical shifts of all amino acids in the N-Ras membrane anchor were determined. Since these shifts are a direct result of the immediate environment of the investigated nucleus, they can be used to predict the secondary structure of the element in which the labeled amino acid resides in. Also, using the information of the amino acid sequence a database approach called TALOS based on known protein structures with known chemical shifts can be used to even predict the torsion angles Φ and Ψ of the amino acid [41]. Since the backbone structure of a protein solely is determined by these torsion angles, a full set can be used to calculate a structure. Although this approach is typically rather precise, the relationship between chemical shift and secondary structure is not always unambiguous. In this case, the result was unambiguous torsion angle pairs for all but one amino acid [83]. For methionine 182, however, three clusters of different torsion angle pairs were predicted, which resulted in three different structure families of the N-Ras anchoring domain that are summarized in

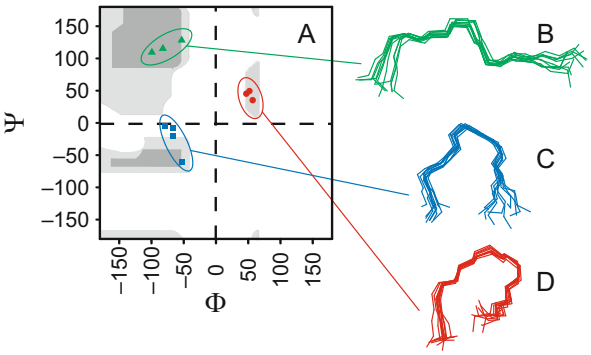

Fig. 14.9 A Ramachandran diagram of the torsion angles Φ and Ψ, in which the sterically allowed regions are marked *grey* (**A**). For methionine 182 of the human N-Ras membrane anchor three different clusters of torsion angle pairs were predicted by TALOS indicated by *green*, *blue*, and *red* symbols. This resulted in three different structure families (**B**–**D**) predicted for the membrane anchor. Reprinted from [64], Copyright (2010), with permission from Elsevier

Fig. 14.9 [64]. Based on other experimental evidence such as the information that both lipid modifications have to face the same side of the protein, the structure family shown in Fig. 14.9D was considered the most likely conformation [83].

This information was very valuable for the following MD simulations since most conformational changes are too slow to be completely sampled in all-atom MD simulations. Therefore, the backbone structure of cluster D was used to setup further MD simulations of the N-Ras membrane anchor in DMPC [64]. For the simulations, the soluble part of N-Ras was again omitted to reduce the size of the system. This allowed improving structural sampling via a replica exchange MD simulation with 34 replicas ranging from 303 to 514 K that was run for more than 90 ns. From the final 39 ns of the replica exchange MD simulation, histograms of all torsion angles in the N-Ras backbone at 303 K were calculated. The corresponding Ramachandran diagrams of each amino acid are shown in Fig. 14.10 along the torsion angles pairs predicted by TALOS [64]. The simulation results nicely agreed with the experiments as all torsion angles predicted by TALOS are close to maxima in the distribution obtained from the MD simulation. However from this it also is immediately obvious that the membrane anchor backbone is not fixed in a very rigid structure but rather samples many different structures. This is particularly true for methionine 182, for which all three torsion angle pair regions predicted by TALOS are found in the MD simulation. All other amino acids also show at least one torsion angle pair region with considerable probability that was not predicted by TALOS further highlighting the structural flexibility of the N-Ras membrane anchor.

This was somewhat surprising since it was known that the two lipid modifications attached to cysteine 181 and cysteine 186 were facing the same side of the peptide. Furthermore, it was believed that the hydrophobic side chains of methionine 182 and leucine 184 are facing the same side for membrane insertion [80]. These constraints should severely limit the number of possible structures.

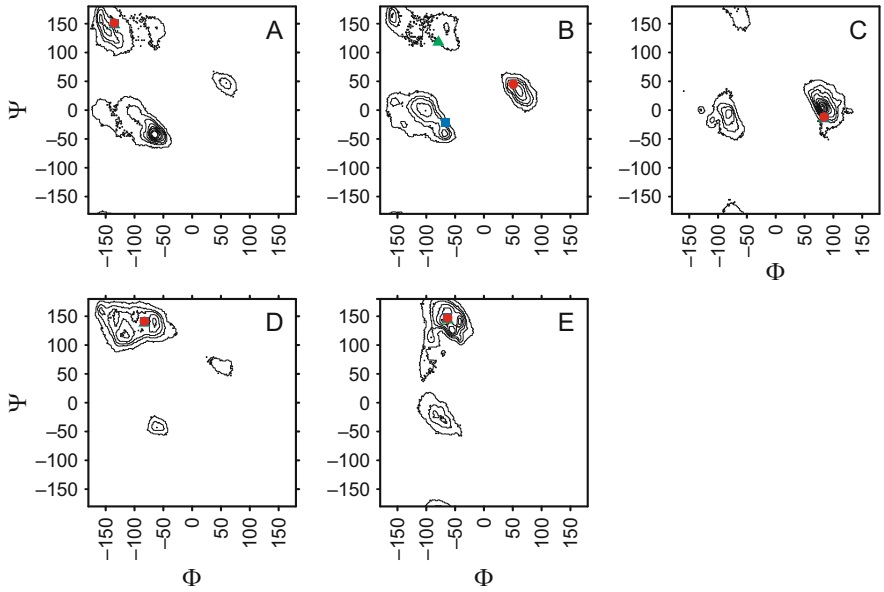

Fig. 14.10 Ramachandran diagrams of the five amino acids cysteine 181 (**A**), methionine 182 (**B**), glycine 183 (**C**), leucine 184 (**D**), and proline 185 (**E**) of the membrane anchor of the human N-Ras protein obtained at 303 K from the last 39 ns of more than 90 ns replica exchange MD simulation. The torsion angle pairs of the three different structures predicted by TALOS are shown as symbols for each amino acid where the colors are the same as in Fig. 14.9 (note that the structures only differ in the conformation of methionine 182). Reprinted from [64], Copyright (2010), with permission from Elsevier

Therefore, it was investigated if torsion angles from different amino acids are also correlated. For this correlation scores between all possible torsion angle pairs were calculated and the results are shown in Fig. 14.11 [64]. The torsion angles Φ and Ψ of the same amino acid are obviously strongly coupled and marked by black crosses. Interestingly, very strong correlation is also observed between the torsion angles of cysteine 181 and methionine 182. Further, the strongest long range correlation (where long range means amino acids not directly neighboring each other) is observed between leucine 184 and cysteine 181.

These correlations indicated that instead of random fluctuations a number of structures exist. Subsequently, all structures from the replica exchange MD simulation were clustered. The two largest clusters named cluster 1 and cluster 2 in the following represented about 34 and 26% of all structures, respectively, and all other clusters were below 10% probability [64]. Some of the minor cluster structures were very similar to the structures of clusters 1 and 2 and if these are interpreted as fluctuations of the two main clusters, they would in total represent about 77% of all structures. Comparison to the experimental structure showed very good agreement for cluster 2. The most prominent cluster 1, however, differed in the conformation of methionine 182 resulting in a kink at this position that led to a different

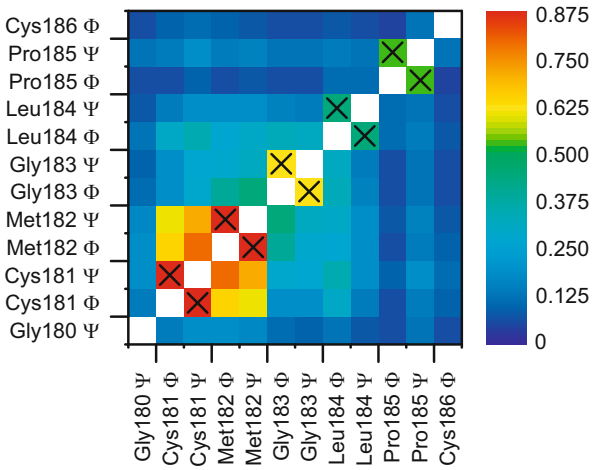

Fig. 14.11 Correlation matrix for the entire Ras backbone where the correlation score of each torsion angle pair is color coded. Torsion angle pairs within the same amino acid which naturally are highly correlated are labeled by a *black cross*. Reprinted from [64], Copyright (2010), with permission from Elsevier

conformation of the N-terminus of the membrane anchor. At the same time, cysteine 181 also shows a different conformation such that the lipid modification attached to this position is pointing in the same direction as the lipid modification on cysteine 186. The hydrophobic side chains of methionine 182 and leucine 184 also face the same side as the lipid modifications such that they can all be embedded in the membrane simultaneously.

While it had been established already that the lipid modifications of the human N-Ras membrane anchor are highly flexible the large degree of structural flexibility in the backbone posed the question if it was similarly flexible. To further study its dynamics, a uniformly $^{13}C/^{15}N$-labeled heptapeptide of the same amino acid sequence again modified by two hexadecyl modifications on the cysteines was investigated in a DMPC membrane. On these samples C-H order parameters were determined with the use of the DIPSHIFT experiment that are summarized in Fig. 14.12 [64].

These order parameters are indicative of the motions of the C_α-H bonds that are directly connected to the backbone and, therefore, also indicative of the backbone dynamics. Overall, very low order parameters are obtained supporting the observation of the large structural flexibility. Interestingly, apart from the termini of the peptide the inner five amino acids show monotonically rising order parameters towards the C-terminus. The two cysteines that could not be distinguished in the spectra as well as methionine 182, which are the amino acids that are most tightly correlated in their torsion angles show the largest amplitude motions. These order parameters were also extracted from the replica exchange MD simulations and are shown in Fig. 14.12. They are very low as well but with the exception of glycine 180 higher than the experimental values despite the use of a rapid sampling method. Nevertheless, this is not very surprising as C-H order parameters measured with the DIPSHIFT experiment are sensitive to motions on timescales that were not achieved by the MD simulations. Further, with exception of the termini the general

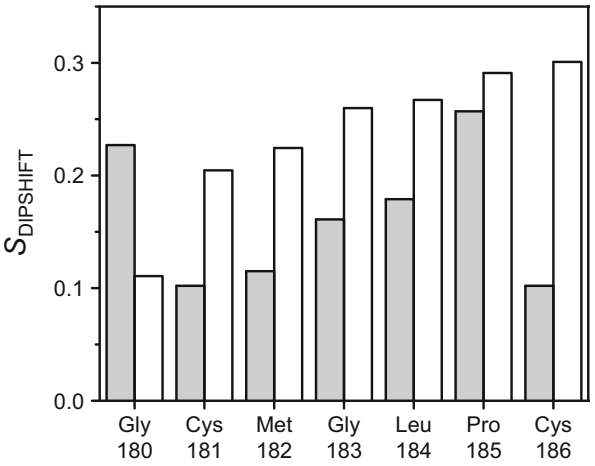

Fig. 14.12 C-H order parameters measured for all seven amino acids in the membrane anchor of the human N-Ras protein in a DMPC matrix. Values determined with the DIPSHIFT experiment are shown as *grey bars* while data obtained from the replica exchange MD simulations is shown as *white bars*. The experimental C-H order parameters for cysteine 181 and cysteine 186 are identical because they could not be distinguished in the NMR spectrum. All data was determined at 303 K. Reprinted from [64], Copyright (2010), with permission from Elsevier

trend of rising order parameters towards the C-terminus is also observed in the MD simulation. To obtain further information about the timescale of these motions T_1 and T_2 relaxation times were recorded in a temperature dependent manner which are summarized in Fig. 14.13 [64].

This data was fitted by a modified Lipari-Szabo model, in which it was assumed that the relaxation of the ^{13}C nuclei was governed by fast and slow anisotropic motions, while overall isotropic tumbling was assumed to be inhibited by the presence of the membrane. This resulted in the following spectral density [46]

$$J(\omega) = \frac{1}{5}\left[\frac{\left(1 - S_f^2\right)\tau_f}{1 + (\omega\tau_f)^2} + \frac{\left(S_f^2 - S^2\right)\tau_s}{1 + (\omega\tau_s)^2}\right], \tag{14.36}$$

where the overall order parameter S again is connected to the fast and slow order parameters S_f and S_s via Eq. (14.34). To reduce the number of fitting parameters by one, the C-H order parameters were used for the overall order parameter S. To model the temperature dependence of the correlation times, an Arrhenius approach with $\tau_0 = 10^{-15}$ s was used. The spectral densities were substituted into Eqs. (14.18) and (14.20) for the R_1 and R_2 relaxation rates of a ^{13}C nucleus in the presence of one or more bound ^{1}H. For each amino acid the T_1 and T_2 relaxation times were fitted simultaneously using these equations where correlation times of fast and slow motions were obtained as fitting parameters and the resulting fits are shown in Fig. 14.13 [64]. At 310 K the correlation time τ_f for the fast motions was on the order of 0.5–1.1 ns while τ_s for the slow motions was on the order of 100–650 ns for

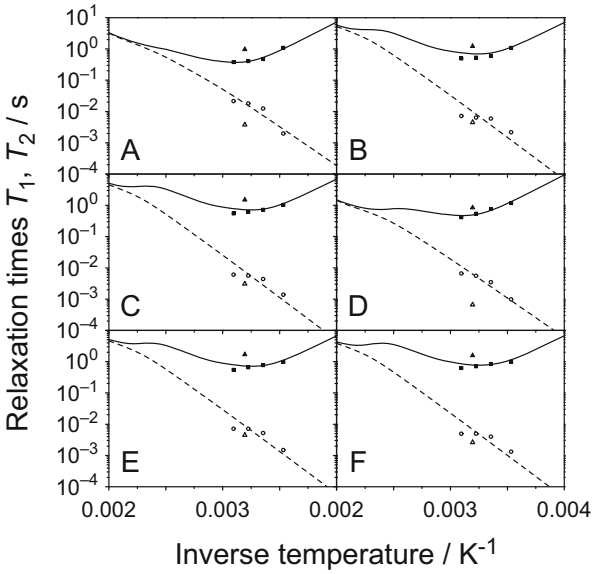

Fig. 14.13 Summary of the T_1 and T_2 relaxation times in dependence on the inverse temperature for glycine 180 (**A**), cysteine 181/186 (**B**), methionine 182 (**C**), glycine 183 (**D**), leucine 184 (**E**), and proline 185 (**F**) of the human N-Ras membrane anchor in a DMPC matrix. Experimental values are shown as *black squares* for T_1 and *white circles* for T_2 while the theoretical fits using the modified Lipari-Szabo approach are represented by *solid* and *dashed lines* respectively. The relaxation times obtained from the conventional MD simulations at 313 K are indicated by *black triangles* for T_1 and *white triangles* for T_2. Reprinted from [64], Copyright (2010), with permission from Elsevier

the individual amino acids. Since T_1 and T_2 relaxation times are not sensitive on the timescale of the slow motions the large values are very imprecise and simply indicate that the overall motions of the peptide are very slow.

To interpret these values, MD simulations were employed again. The replica exchange MD simulation could not be used for this as one of its disadvantages is that due to swaps of the replicas no continuous trajectory exists at any given temperature. Consequently, correlation functions and spectral densities can not be calculated, severely limiting the ability to analyze the timescale of the dynamics of the peptide. Therefore, snapshots were extracted at the end of the replica exchange MD simulation from two independent replicas at 313 K that were used as starting coordinates of two additional conventional 300 ns MD simulations [64]. These simulations were compared against the experimental data. Again, correlation functions and spectral densities were calculated but this time for the $^{13}C_{\alpha}$-^{1}H vectors. From this, T_1 and T_2 relaxation times were calculated using Eqs. (14.18) and (14.20), which are also shown in Fig. 14.13. Agreement to experimental data was good again and as before the correlation functions were fitted by Eq. (14.36). The correlation time τ_f for the fast motions was on the order of 1–20 ns while τ_s for the slow motions was on the order of 30–250 ns for the individual amino acids. These

values agree well to the experimentally obtained values given the fact that the Lipari-Szabo model is a relatively simple approach and that the correlation times for the slow motions are on the order of the MD simulation length. These values also show good agreement to the diffusion constants obtained for motions parallel and perpendicular to the membrane normal from the angular dependent ^{2}H NMR relaxation rates [79].

14.6 Conclusions

Experimental techniques along with MD simulations have largely advanced our understanding of biophysical systems, in particular with respect to membrane interactions. NMR spectroscopy provides structural and dynamical information with atomistic resolution, but as an ensemble technique, can often not resolve the impact of individual molecules in a large ensemble. MD simulations on the other hand are limited by the size of the ensemble as well as the simulation time, but provide atomistic resolution on the single molecule level. Both shortcomings can be at least partially overcome by the combination of the two methods. Thus, a comprehensive picture of the molecular details of biophysical processes emerges, that benefits from the synergies of the combination of the two methods. MD simulations greatly benefit from experimental parameters for the most perfect reflection of the natural system in the simulation. Furthermore, a number of experimental quantities such as structural and geometrical parameters, correlation times and amplitudes of motion, nuclear Overhauser effects etc. can be well determined from MD simulations and used for their validation and assessment if the system has reached equilibrium. In turn, MD simulations greatly aid in the interpretation of experimental parameters as they contain extremely detailed information on the whole simulated system and thereby often uncover the biophysical processes and mechanisms that led to the measured observable. It is rather clear that neither experimental nor computational methods will dominate the future in membrane biophysical research, rather, the combination of both methods will be most promising. Both NMR and MD techniques have continuously improved over the last decade such that larger systems can be investigated and the understanding of complex systems and machineries has much improved.

References

1. Raucher D, Stauffer T, Chen W, et al. Phosphatidylinositol 4,5-bisphoshate functions as a second messenger that regulates cytoskeleton-plasma membrane adhesion. Cell. 2000;100:221–8.
2. Czech MP. PIP2 and PIP3: complex roles at the cell surface. Cell. 2000;100:603–6.

3. Preiss J, Loomis CR, Bishop WR, et al. Quantitative measurement of sn-1,2-diacylglycerols present in platelets, hepatocytes, and Ras-transformed and Sis-transformed normal rat-kidney cells. J Biol Chem. 1986;261:8597–600.
4. Cherezov V, Rosenbaum DM, Hanson MA, et al. High-resolution crystal structure of an engineered human beta(2)-adrenergic G protein-coupled receptor. Science. 2007;318:1258–65.
5. Valiyaveetil FI, Zhou YF, Mackinnon R. Lipids in the structure, folding, and function of the KcsA K+ channel. Biochemistry. 2002;41:10771–7.
6. Singer SJ, Nicolson GL. Fluid mosaic model of structure of cell-membranes. Science. 1972;175:720–31.
7. Simons K, Ikonen E. Functional rafts in cell membranes. Nature. 1997;387:569–72.
8. Brown DA, London E. Structure and function of sphingolipid- and cholesterol-rich membrane rafts. J Biol Chem. 2000;275:17221–4.
9. Weise K, Triola G, Brunsveld L, et al. Influence of the lipidation motif on the partitioning and association of N-Ras in model membrane subdomains. J Am Chem Soc. 2009;131:1557–64.
10. Weise K, Kapoor S, Denter C, et al. Membrane-mediated induction and sorting of K-Ras microdomain signaling platforms. J Am Chem Soc. 2011;133:880–7.
11. White SH, Ladokhin AS, Jayasinghe S, et al. How membranes shape protein structure. J Biol Chem. 2001;276:32395–8.
12. Nagle JF, Tristram-Nagle S. Structure of lipid bilayers. Biochim Biophys Acta Rev Biomembr. 2000;1469:159–95.
13. Mihailescu M, Vaswani RG, Jardon-Valadez E, et al. Acyl-chain methyl distributions of liquid-ordered and -disordered membranes. Biophys J. 2011;100:1455–62.
14. Huster D, Gawrisch K. NOESY NMR crosspeaks between lipid headgroups and hydrocarbon chains: spin diffusion or molecular disorder? J Am Chem Soc. 1999;121:1992–3.
15. Brown MF, Seelig J, Haeberlen U. Structural dynamics in phospholipid-bilayers from deuterium spin-lattice relaxation-time measurements. J Chem Phys. 1979;70:5045–53.
16. Huster D, Arnold K, Gawrisch K. Investigation of lipid organization in biological membranes by two-dimensional nuclear Overhauser enhancement spectroscopy. J Phys Chem B. 1999;103:243–51.
17. Feller SE, Gawrisch K, MacKerell AD. Polyunsaturated fatty acids in lipid bilayers: intrinsic and environmental contributions to their unique physical properties. J Am Chem Soc. 2002;124:318–26.
18. Pastor RW. Molecular-dynamics and Monte-Carlo simulations of lipid bilayers. Curr Opin Struct Biol. 1994;4:486–92.
19. Reuther G, Tan KT, Vogel A, et al. The lipidated membrane anchor of full length N-Ras protein shows an extensive dynamics as revealed by solid-state NMR spectroscopy. J Am Chem Soc. 2006;128:13840–6.
20. Schmidt P, Thomas L, Muller P, et al. The G-protein-coupled neuropeptide Y receptor type 2 is highly dynamic in lipid membranes as revealed by solid-state NMR spectroscopy. Chem Eur J. 2014;20:4986–92.
21. Huster D. Investigations of the structure and dynamics of membrane-associated peptides by magic angle spinning NMR. Prog Nucl Magn Reson Spectrosc. 2005;46:79–107.
22. Serber Z, Selenko P, Hansel R, et al. Investigating macromolecules inside cultured and injected cells by in-cell NMR spectroscopy. Nat Protoc. 2006;1:2701–9.
23. Sakakibara D, Sasaki A, Ikeya T, et al. Protein structure determination in living cells by in-cell NMR spectroscopy. Nature. 2009;458:102–U10.
24. Kaplan M, Cukkemane A, van Zundert GCP, et al. Probing a cell-embedded megadalton protein complex by DNP-supported solid-state NMR. Nat Methods. 2015;12:649–52.
25. Seelig J. Deuterium magnetic-resonance – theory and application to lipid-membranes. Q Rev Biophys. 1977;10:353–418.
26. Davis JH. The description of membrane lipid conformation, order and dynamics by H-2-NMR. Biochim Biophys Acta. 1983;737:117–71.

27. Vogel A, Schroder T, Lange C, et al. Characterization of the myristoyl lipid modification of membrane-bound GCAP-2 by H-2 solid-state NMR spectroscopy. Biochim Biophys Acta. 2007;1768:3171–81.
28. Pake GE. Nuclear resonance absorption in hydrated crystals – fine structure of the proton line. J Chem Phys. 1948;16:327–36.
29. Huster D, Arnold K, Gawrisch K. Influence of docosahexaenoic acid and cholesterol on lateral lipid organization in phospholipid mixtures. Biochemistry. 1998;37:17299–308.
30. Petrache HI, Tu KC, Nagle JF. Analysis of simulated NMR order parameters for lipid bilayer structure determination. Biophys J. 1999;76:2479–87.
31. Petrache HI, Dodd SW, Brown MF. Area per lipid and acyl length distributions in fluid phosphatidylcholines determined by H-2 NMR spectroscopy. Biophys J. 2000;79:3172–92.
32. Brown MF. Theory of spin-lattice relaxation in lipid bilayers and biological-membranes – H-2 and N-14 quadrupolar relaxation. J Chem Phys. 1982;77:1576–99.
33. Vogel A, Katzka CP, Waldmann H, et al. Lipid modifications of a Ras peptide exhibit altered packing and mobility versus host membrane as detected by 2H solid-state NMR. J Am Chem Soc. 2005;127:12263–72.
34. Nevzorov AA, Trouard TP, Brown MF. Lipid bilayer dynamics from simultaneous analysis of orientation and frequency dependence of deuterium spin-lattice and quadrupolar order relaxation. Phys Rev E. 1998;58:2259–81.
35. Torchia DA, Szabo A. Spin-lattice relaxation in solids. J Magn Reson. 1982;49:107–21.
36. Schmidt-Rohr K, Spiess HW. Multidimensional solid-state NMR and polymers. London: Academic Press; 1994.
37. Marchetti A, Jehle S, Felletti M, et al. Backbone assignment of fully protonated solid proteins by 1H detection and ultrafast magic-angle-spinning NMR spectroscopy. Angew Chem Int Ed. 2012;51:10756–9.
38. Agarwal V, Penzel S, Szekely K, et al. De novo 3D structure determination from sub-milligram protein samples by solid-state 100 kHz MAS NMR spectroscopy. Angew Chem Int Ed. 2014;53:12253–6.
39. Bockmann A, Ernst M, Meier BH. Spinning proteins, the faster, the better? J Magn Reson. 2015;253:71–9.
40. Andronesi OC, Becker S, Seidel K, et al. Determination of membrane protein structure and dynamics by magic-angle-spinning solid-state NMR spectroscopy. J Am Chem Soc. 2005;127:12965–74.
41. Cornilescu G, Delaglio F, Bax A. Protein backbone angle restraints from searching a database for chemical shift and sequence homology. J Biomol NMR. 1999;13:289–302.
42. Shen Y, Delaglio F, Cornilescu G, et al. TALOS plus: a hybrid method for predicting protein backbone torsion angles from NMR chemical shifts. J Biomol NMR. 2009;44:213–23.
43. Munowitz MG, Griffin RG, Bodenhausen G, et al. Two-dimensional rotational spin-echo nuclear magnetic-resonance in solids – correlation of chemical-shift and dipolar interactions. J Am Chem Soc. 1981;103:2529–33.
44. Hong M, Gross JD, Griffin RG. Site-resolved determination of peptide torsion angle phi from the relative orientations of backbone N-H and C-H bonds by solid-state NMR. J Phys Chem B. 1997;101:5869–74.
45. Lipari G, Szabo A. Model-free approach to the interpretation of nuclear magnetic-resonance relaxation in macromolecules. 1. Theory and range of validity. J Am Chem Soc. 1982;104:4546–59.
46. Clore GM, Szabo A, Bax A, et al. Deviations from the simple two-parameter model-free approach to the interpretation of nitrogen-15 nuclear magnetic relaxation of proteins. J Am Chem Soc. 1990;112:4989–91.
47. Lipari G, Szabo A. Pade approximants to correlation-functions for restricted rotational diffusion. J Chem Phys. 1981;75:2971–6.
48. Alder BJ, Wainwright TE. Studies in molecular dynamics.1. General method. J Chem Phys. 1959;31:459–66.

49. Jo S, Kim T, Im W. Automated builder and database of protein/membrane complexes for molecular dynamics simulations. PLoS One. 2007;2:e880.
50. Liu C, Perilla JR, Ning JY, et al. Cyclophilin A stabilizes the HIV-1 capsid through a novel non-canonical binding site. Nat Commun. 2016;7:10714.
51. Vogel A, Feller SE. Headgroup conformations of phospholipids from molecular dynamics simulation: sampling challenges and comparison to experiment. J Membr Biol. 2012;245:23–8.
52. Grossfield A, Feller SE, Pitman MC. Convergence of molecular dynamics simulations of membrane proteins. Proteins Struct Funct Bioinf. 2007;67:31–40.
53. Kaufmann KW, Lemmon GH, Deluca SL, et al. Practically useful: what the ROSETTA protein modeling suite can do for you. Biochemistry. 2010;49:2987–98.
54. Biasini M, Bienert S, Waterhouse A, et al. SWISS-MODEL: modelling protein tertiary and quaternary structure using evolutionary information. Nucleic Acids Res. 2014;42:W252–8.
55. Klauda JB, Venable RM, Freites JA, et al. Update of the CHARMM all-atom additive force field for lipids: validation on six lipid types. J Phys Chem B. 2010;114:7830–43.
56. Essmann U, Perera L, Berkowitz ML, et al. A smooth particle mesh Ewald method. J Chem Phys. 1995;103:8577–93.
57. van Gunsteren WF, Berendsen HJC. Algorithms for macromolecular dynamics and constraint dynamics. Mol Phys. 1977;34:1311–27.
58. Sugita Y, Okamoto Y. Replica-exchange molecular dynamics method for protein folding. Chem Phys Lett. 1999;314:141–51.
59. Marrink SJ, Risselada HJ, Yefimov S, et al. The MARTINI force field: coarse grained model for biomolecular simulations. J Phys Chem B. 2007;111:7812–24.
60. Huster D, Yao XL, Hong M. Membrane protein topology probed by H-1 spin diffusion from lipids using solid-state NMR spectroscopy. J Am Chem Soc. 2002;124:874–83.
61. Vogel A, Scheidt HA, Huster D. The distribution of lipid attached spin probes in bilayers: application to membrane protein topology. Biophys J. 2003;85:1691–701.
62. Liang BY, Bushweller JH, Tamm LK. Site-directed parallel spin-labeling and paramagnetic relaxation enhancement in structure determination of membrane proteins by solution NMR spectroscopy. J Am Chem Soc. 2006;128:4389–97.
63. Buffy JJ, Hong T, Yamaguchi S, et al. Solid-state NMR investigation of the depth of insertion of protegrin-1 in lipid bilayers using paramagnetic Mn2+. Biophys J. 2003;85:2363–73.
64. Vogel A, Reuther G, Roark MB, et al. Backbone conformational flexibility of the lipid modified membrane anchorof the human N-Ras protein investigated by solid-state NMR and molecular dynamics simulation. Biochim Biophys Acta. 2010;1798:275–85.
65. Brown MF. Membrane structure and dynamics studied with NMR spectroscopy. In: Merz KM, Roux B, editors. Biological membranes. A molecular perspective from computation and experiment. Boston: Birkhäuser; 1996. p. 175–252.
66. Pitman MC, Grossfield A, Suits F, et al. Role of cholesterol and polyunsaturated chains in lipid-protein interactions: molecular dynamics simulation of rhodopsin in a realistic membrane environment. J Am Chem Soc. 2005;127:4576–7.
67. Grossfield A, Feller SE, Pitman MC. A role for direct interactions in the modulation of rhodopsin by omega-3 polyunsaturated lipids. Proc Natl Acad Sci U S A. 2006;103:4888–93.
68. Grossfield A, Feller SE, Pitman MC. Contribution of omega-3 fatty acids to the thermodynamics of membrane protein solvation. J Phys Chem B. 2006;110:8907–9.
69. Lau PW, Grossfield A, Feller SE, et al. Dynamic structure of retinylidene ligand of rhodopsin probed by molecular simulations. J Mol Biol. 2007;372:906–17.
70. Romo TD, Grossfield A. Validating and improving elastic network models with molecular dynamics simulations. Proteins Struct Funct Bioinformatics. 2011;79:23–34.
71. Khelashvili G, Grossfield A, Feller SE, et al. Structural and dynamic effects of cholesterol at preferred sites of interaction with rhodopsin identified from microsecond length molecular dynamics simulations. Proteins Struct Funct Bioinformatics. 2009;76:403–17.

72. Olausson BES, Grossfield A, Pitman MC, et al. Molecular dynamics simulations reveal specific interactions of post-translational palmitoyl modifications with Rhodopsin in membranes. J Am Chem Soc. 2012;134:4324–31.
73. Hall A. A biochemical function for ras – at last. Science. 1994;264:1413–4.
74. Wittinghofer A, Waldmann H. Ras – a molecular switch involved in tumor formation. Angew Chem Int Ed. 2000;39:4192–214.
75. Dudler T, Gelb MH. Palmitoylation of Ha-Ras facilitates membrane binding, activation of downstream effectors, and meiotic maturation in Xenopus oocytes. J Biol Chem. 1996;271:11541–7.
76. Peitzsch RM, McLaughlin S. Binding of acylated peptides and fatty acids to phospholipid vesicles: pertinence to myristoylated proteins. Biochemistry. 1993;32:10436–43.
77. Milburn MV, Tong L, deVos AM, et al. Molecular switch for signal transduction: structural differences between active and inactive forms of protooncogenic ras proteins. Science. 1990;247:939–45.
78. Pai EF, Kabsch W, Krengel U, et al. Structure of the guanine-nucleotide-binding domain of the HA-ras oncogene product p21 in the triphosphate conformation. Nature. 1989;341:209–14.
79. Vogel A, Tan KT, Waldmann H, et al. Flexibility of ras lipid modifications studied by H-2 solid-state NMR and molecular dynamics simulations. Biophys J. 2007;93:2697–712.
80. Huster D, Vogel A, Katzka C, et al. Membrane insertion of a lipidated Ras peptide studied by FTIR, solid-state NMR, and neutron diffraction spectroscopy. J Am Chem Soc. 2003;125:4070–9.
81. Gorfe AA, Pellarin R, Caflisch A. Membrane localization and flexibility of a lipidated ras peptide studied by molecular dynamics simulations. J Am Chem Soc. 2004;126:15277–86.
82. Vogel A, Reuther G, Weise K, et al. The lipid modifications of Ras that sense membrane environments and induce local enrichment. Angew Chem Int Ed. 2009;48:8784–7.
83. Reuther G, Tan KT, Kohler J, et al. Structural model of the membrane-bound C terminus of lipid-modified human N-ras protein. Angew Chem Int Ed. 2006;45:5387–90.

Chapter 15
Computer Simulations of Membrane Proteins

Christian Jorgensen, Victoria Oakes, and Carmen Domene

Abstract Developments in computational algorithms and structure-determination technologies have enabled molecular dynamics simulations to become a routine tool to investigate the structure and dynamics of biological membranes and membrane proteins in great detail. In this chapter, we provide an overview of atomistic molecular dynamics simulations and related methods, such as coarse-grain simulations and biased sampling methods, and illustrate using key examples how such methods have advanced our understanding in the field of membrane protein biophysics. We exemplify how MD simulations have provided insights into selective permeation mechanisms through lipid bilayers and ion channels, as well as conformational changes associated with transport in both G-protein coupled receptors and membrane transporters.

15.1 Introduction

Cell membranes are formed by a lipid bilayer, spanning two layers of fatty acid molecules, which regulate the passage of ions, small molecules and peptides into the cell interior. Embedded proteins, in particular, are crucial for the transmission of many of these species. Over the past half-century, our understanding of these assemblies has been greatly aided by experimental and computational techniques alike. Advancements in X-ray crystallography, NMR, and more recently, electron microscopy, have resulted in an exponential growth in the number of available membrane protein structures. Computational algorithms, such as molecular dynamics (MD) simulations, have become a powerful tool to complement structural information, providing insights into the dynamics of biological assemblies at an

C. Jorgensen • V. Oakes
Department of Chemistry, King's College London, Britannia House, 7 Trinity Street, London SE1 1DB, UK

C. Domene (✉)
Department of Chemistry, King's College London, Britannia House, 7 Trinity Street, London SE1 1DB, UK

Chemistry Research Laboratory, University of Oxford, Mansfield Road, Oxford OX1 3TA, UK
e-mail: carmen.domene@kcl.ac.uk

A. Chattopadhyay (ed.), *Membrane Organization and Dynamics*, Springer Series in Biophysics 20, DOI 10.1007/978-3-319-66601-3_15

atomistic level that cannot be obtained experimentally. The field of membrane protein MD simulations has matured alongside developments in computer technology, continuously reaching longer timescales and displaying increasing levels of agreement with experimental observations. The availability of coarse-grained approaches has significantly aided the timescales available for the study of complex systems. In addition, biased-sampling simulations can be used to sample rare-events that involve considerable energetic barriers unreachable in the time scales presently available to MD simulations. Thus a wide range of biological timescales, system sizes and phenomena are accessible, allowing us to fully probe the dynamics of biological systems. In this chapter, computational methods commonly used for the study of membrane proteins are reviewed, highlighting notable applications concerning permeability through biological membranes and associated proteins, namely ion channels, transporters and G-protein coupled receptors (GPCRs).

15.2 Molecular Dynamics Simulations

Computational chemistry is a branch of chemistry that supplements experimental data on the structure and properties of matter, by using mathematical formulations. Computational chemistry can be broadly categorized into Quantum Mechanics (QM) and Molecular Mechanics (MM) methods, depending on the sophistication, and hence accuracy, of the calculation. Ab initio QM methods are primarily concerned with the calculation of molecular electronic structure by solving the Schrödinger equation, whilst semi-empirical methods use approximations and are parameterized using experimental data or data obtained from quantum calculations. Quantum chemistry calculations are inherently computationally intensive, and therefore, the size of the system, in other words, the number of particles that can be studied, is limited. Accordingly, MM methods, which utilize classical physics and ignore electronic contributions, are usually used for the study of the dynamics of complex biological systems. In this respect, MD is a computational technique used to generate the time evolution of an N-atom system configuration by iteratively integrating Newton's equation of motion. Based on an initial set of coordinates, the potential energy of the system and the forces can be derived at each timestep to obtain new positions and produce a trajectory of the positions of all system particles as a function of time. In order to calculate the potential energy of a system at each timestep, ab initio or classical techniques are employed. In the latter case, particles are modelled as spherical objects with a particular charge and a particular radii, interconnected by elastic springs. An expression for the energy of the system, known as a force field (FF), is described as a sum of several components generally including: (i) bond stretching, (ii) angle bending, (iii) torsional terms, and (iv) non-bonded interactions [1, 2]. Many classical force-fields are widely available for the simulation of proteins, lipids, water and related molecules, among which the most popular are CHARMM [3], AMBER [4], GROMOS [5], and OPLS [6]. Force fields often differ in the functional form of the force field

described earlier and the procedure adopted for their parameterization. In some cases, parameters are obtained by fitting to ab initio QM data, and others rely on the reproduction of experimental data. These force fields are compatible with popular MD codes such as AMBER [7], NAMD [8], GROMACS [9, 10], LAMMPS [11], or DESMOND [12].

Due to the development of such FF's and MD codes, the applicability of MD simulations has expanded considerably since its outset when hard sphere simulations were undertaken by Alder and Wainwright in 1957, [13] followed by simulations of water performed by Rahman and Stillinger in 1971 [14], and by protein simulations shortly after. Simulation of the bovine pancreatic trypsin inhibitor (BPTI) in unfolded (Levitt and Warshel in 1975) [15] and folded (McCammon, Gelin and Karplus in 1977) [16] conformations illustrates a key early example, significantly contributing the field of in silico protein studies. In the context of this chapter, MD was not applied to membrane proteins until the early 1990s [17], once the first crystal structure of rhodopsin was unveiled [18]. Classical MD simulations are now routinely employed to investigate structure-function relationships in biological macromolecules in model environments.

To apply such methods to membrane proteins in particular, the protein structure, obtained from crystallographic data or by homology modeling, must be carefully prepared. Early simulations, such as those of rhodopsin, employed implicit solvent and membrane models [1]. However, due to expansions in classical FF's to include lipid molecules, and, the availability of computational power, simulations with an explicit environment are now attainable on biologically relevant timescales [8]. Proteins are typically embedded in a lipid bilayer, which is solvated and ionized to a biologically relevant concentration. This procedure can be undertaken manually or

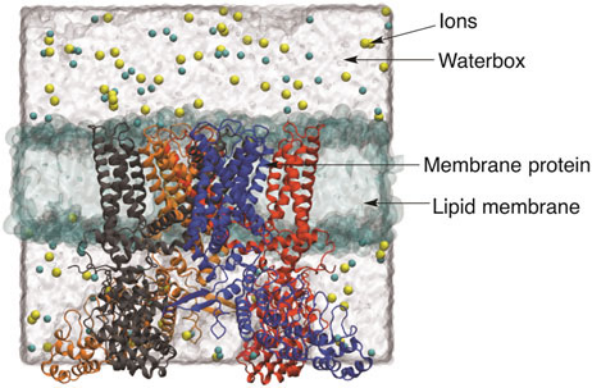

Fig. 15.1 Schematic illustration of a typical MD simulation setup of a membrane protein, showing the protein (TRPV1) embedded in a bilayer of 1-palmitoyl-2-oleoyl-sn-glycero-3-phosphocholine (POPC) and solvated with a background concentration of KCl. Colour code: TRPV1 domain A *blue*, domain B *red*, domain C *yellow*, domain D *gray*, POPC lipids *blue*

via automated online engines such as CHARMM-GUI [19]. An example of a simulation system set-up is given in Fig. 15.1 [2].

Overall, the tools to generate MD simulations of membrane proteins are now widely accessible and thus commonly used. It should be noted, however, that these methods are associated with various limitations. The use of classical forcefields prohibits the calculation of electronic properties, polarization is not explicitly included and charge transfer, or bond breaking and forming cannot be described. For some situations, a description of polarization is essential, and the development of polarizable forcefields has received considerable attention in recent years. Furthermore, all-atom MD simulations of large membrane protein systems are computationally expensive restricting the phenomena that can be sampled even if nanosecond timescale are now routine, with microsecond simulations currently attainable. D.E. Shaw and colleagues have been instrumental in enabling the performance of long-scale simulations, a millisecond in length, by the construction of the supercomputer Anton, and the development of the DESMOND [12] code. As these technologies are not widely available, many research groups have applied alternative methods to reach extended timescales.

Coarse-grained (CG) simulation is one alternative method to all-atom MD simulations. CG simulations use a reduced system representation whereby a collection of atoms is grouped into a single 'bead', reducing the number of degrees of system in the system and the computational expense. CG simulations have been used widely across membrane proteins, and the reader is referred to more detailed reviews on this subject [3]. The disadvantages of these methods should also be taken into consideration; the reduction of the all-atom system to simpler representations means that thermodynamic properties, such as diffusion constants, and ensemble quantities, such as free-energies, are less accurate in comparison with experiments and all-atom MD [3].

Biased simulations provide a further method to accelerate sampling, whilst retaining full detail. In addition, biased methods can be used to overcome high energetic barriers by speeding up sampling along selected low-dimensional collective variables (CV) representative of the desired transition. Popular methods include umbrella sampling [4] metadynamics [5], steered MD [6], or adaptive-biasing force (ABF) [20]. For example, in metadynamics, a Gaussian potential function bias is added to the chosen collective variables, in order to divert the trajectory away from energy minima and overcome barriers. The Potential of Mean Force (PMF) for the entire potential energy surface can be calculated after it has effectively been flattened, by summing the full list of bias potentials added during the simulation. In contrast, in umbrella sampling, the potential energy surface for a particular transition can be attained by discretizing the pathway into a set of windows, and imposing harmonic restraints ('umbrellas') in the form of a Hookean potential term to constrain the system around the centre of the bin and perform individual simulations, achieving full sampling when sufficient number of bins are employed. The PMF is obtained using an unbiasing procedure, such as the Weighted Histogram Analysis Method (WHAM) [21], to remove the presence of the umbrellas. In ABF, an adaptive on-the-fly average force is applied onto the Newtonian equations to provide a smooth energy landscape to obtain full sampling

of the collective variable [22, 23]. This force estimate is corrected during the simulation, and once the simulation converges the PMF is calculated from numerical integration of the free-energy gradient at each point in the simulation [20, 24–26]. Another of these techniques is steered MD, where the system is biased into sampling a specified transition by applying an external force onto the system using either constant-velocity of constant-force regimes. To obtain an estimate of the PMF from a constant-velocity steered MD simulation, the list of applied forces during the simulation is input into the Jarzynski identity [27, 28], while in a constant-force steered MD simulation, fitting procedures to obtain an unbiased free-energy PMF have been devised, such as that of Dudko, Hummer and Szabo [29, 30]. Biased sampling methods have greatly expanded the phenomena that can be sampled, with specialist versions of US, metadynamics and ABF that have also demonstrated notable successes when studying permeation [31–33], ligand binding, and conformational dynamics [34].

Finally, alternative methods to MD simulations include for example Brownian dynamics (BD) simulations [35, 36], in which the equation of motion is a simplified version of Langevin dynamics, and corresponds to the limit where no average acceleration takes place. This approximation can also be described as 'overdamped' Langevin dynamics, or as Langevin dynamics without inertia. In BD simulations the solvent molecules are not represented explicitly, but instead collectively as a random force. Alternatives to the free-energy methods listed above include the continuum electrostatic (Poisson-Boltzmann) methods [37], which can be used to obtain electrostatic potential surfaces of proteins, and calculate approximate ligand-protein binding free-energies [38, 39].

15.3 Small-Molecule Permeation Through Membranes

The permeation of small molecules across membrane involves the passage of a solute through a channel, transporter or receptor, or directly across the cell membrane. The transport of drug molecules across the cell membrane is crucial to reach intracellular targets. Hence, the study of these processes has important implications for drug discovery. MD simulations have been used to study permeability across a range of lipid bilayers [31–33], as well as multiscale approaches combining MD and QM calculations [40]. Examples cover a whole range of small molecule solutes, including anesthetics [41], drugs, hormones [42], and fullerenes [43].

Following the Overton rule on the proportionality of solute permeability to its partition in water/oil systems [44], Stouch et al. [45–47] used MD simulations to estimate the diffusion coefficient as the mean-squared displacement of the molecule in different regions of the hydrophobic membrane core. Concomitantly, theoretical and simulation estimates of the permeability coefficient of drugs through bilayers [33, 48] used reported drug diffusion constants [49–51] to obtain permeability values that were directly comparable to experimental estimates [52–55]. Simulations of anesthetic permeation in a DMPC bilayer for instance showed that diffusion is higher in the middle of the membrane than around the water-lipid interface [45]. The mean-squared

displacement was estimated for benzyl-alcohol [56], and halothane [57, 58], to show how the anesthetics affected the lipid bilayer structure. Pohorille et al. [59–61] extended this work to consider the free energies of permeation, calculated using methods including umbrella sampling. In general, the free energy of anesthetics permeating through the membrane was found to be at a minimum in the membrane core or at the polar interface, rather than in the water phase [62].

In a similar manner to anesthetics, simulations probed the permeability of other drugs, such as β-blockers alprenolol, atenolol, and pindolol, and steroid hormones, such as progesterone and testosterone, through lipid membranes. β-blockers were found to preferentially partition to the lipid headgroup region, while steroid hormones preferentially partition in the centre of the bilayer, with a larger partition coefficient of progesterone than testosterone estimated [42].

Finally, the permeability of systems such as fullerenes (C_{60}) or carbon-nanotubes (CNTs) across membranes has attracted great attention due to their potential applications in drug delivery [63–65]. Simulations found that fullerene molecules rapidly aggregate in bulk water [43], but do not associate in the membrane phase. Permeation of fullerene from the bulk into the lipophilic phase was found to be favoured from free-energy calculations occurring on the microsecond timescale. It was concluded that fullerene permeability through membranes does not cause mechanical damage of bilayers arising from high fullerene concentration. Therefore, this would be an unlikely mechanism for membrane disruption and fullerene toxicity [43]. Another study found that fullerenes are less likely to aggregate inside lipid bilayers compared to pure organic solvents, suggesting that fullerenes are interfacial permeants, which could be used to target tumor cells.

Even though some types of small molecules are able to permeate lipid bilayers, for many polar and charged species, such as water molecules and ions, the hydrophobic core imposes an energetic barrier to diffusion across the membrane. As a consequence, pore-forming membrane proteins facilitate the efficient and selective flux of small solutes across biological membranes. Aquaporins, for example, allow for the efficient permeation of water while excluding protons, thus preserving the electrochemical potential across the cell membrane. Aquaglyceroporins, a related class of membrane proteins, also allow the transport of water as well as other non-polar solutes, such as urea or glycerol, and gases, such as ammonia, carbon dioxide and nitric oxide. These assemblies have attracted great attention, being the subject of the 2003 Nobel Prize following the crystallization of the first crystal structure of an aquaporin in 2000 [66–68].

The first MD simulations of water permeation through human aquaporin-1 (AQP1) and the bacterial glycerol facilitator GlpF found the mechanism of permeability to consist of two stages. A conserved asparagine-proline-alanine motif was proposed to determine selectivity, with a second region comprised of aromatic or arginine residues functioning as a proton filter [69]. These simulations identified a single file line of seven to nine water molecules inside the AQP1 channel, with two conserved asparagine residues dictating the orientation of a central water molecule, so it can serve as a hydrogen bond donor to its neighboring water molecules

[66]. Comparison of the free energy profiles for permeation of small molecules, O_2, CO_2, NH_3, glycerol, urea, and water, through the permeation pathways of AQP1 and GlpF and lipophilic membrane permeation pathways provided key insights into transport energetics. An inverse correlation in AQP1 was observed between permeability and molecule hydrophobicity, paradoxical to what is observed in the membrane pathway, which favours hydrophobic solutes. AQP1 demonstrated selectivity for small polar solutes such as water. AQP1 selectivity for small polar molecules arises from the sterically-hindered filter that blocks the passage of larger molecules, and the polar nature of the filter which excludes hydrophobic molecules [70].

15.4 Ion Channels

Ion channels are a further class of membrane proteins, which are responsible for ion permeation across cell membranes. Ion channels facilitate passive diffusion of ions down electrochemical gradients, enabling cells to generate and transmit electrical signals, an integral process in the nervous system [71]. Ion channels exhibit very high transport rates of the order of 10^6–10^8 ions per second [71], and can be gated in response to different stimuli, such as ligand binding, transmembrane voltage, temperature, and mechanical stress. Ion channels can be non-selective, such as the transient receptor potential cation (TRP) channels, or highly selective for particular ions, such as chloride, sodium or potassium channels. Crystal structures of each of these channels are currently available, with representative examples given in Fig. 15.2.

Potassium channels play a crucial role in excitable cells affecting many neuronal, cardiac and immunological activities and are among the most studied by computational means. Multiple different families have been identified, including voltage-gated (Kv) channels, inward-rectifying (Kir) channels, two-pore

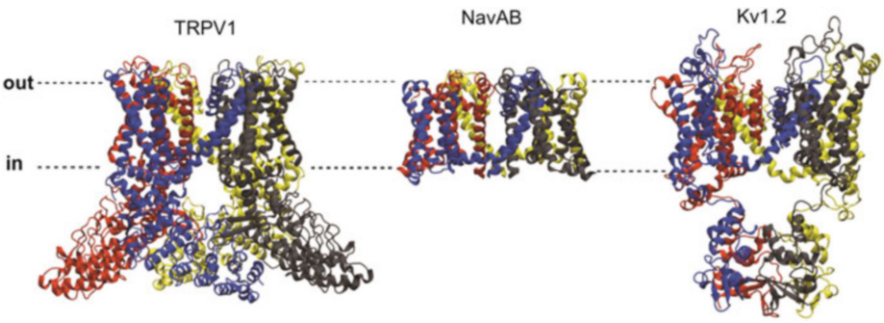

Fig. 15.2 Representative structures of ion channels: (**a**) TRPV1 (PDB id 3J5Q) [72], (**b**) NavAb (PDB id 3RVY) [73], (**c**) Kv1.2 (PDB id 3LUT; normal mode refinement of PDB id 2A79) [74, 75]

domain channels (K2P; leak channels) and calcium-activated channels (BKCa or SK), all of which are highly selective for K^+. A prototypical structure of a potassium channel consists of a transmembrane domain composed of four monomers, containing at least two pore-forming helices, with additional TM helices, intracellular or extracellular domains observed in many cases. The TM helices can rearrange in response to external stimuli to modulate conduction at the cytoplasmic entrance. Furthermore, a narrow ion selectivity filter, composed of specific amino acid residues, controls entrance from the extracellular side and determines ion selectivity. The mechanism of permeation and selectivity through the selectivity filter has been extensively studied using MD simulations, as detailed in recent reviews [76–80]. Ion conduction in K^+-channels is usually described in terms of a Hodgkin-Keynes knock-on mechanism [81–83], where K^+ ions progress in single file through a narrow pore in a concerted movement, driven by electrostatic repulsion with an incoming ion. MD simulations of K^+-channels permeation have confirmed the presence of five binding sites (S0–S4), proposed from the X-ray crystallographic data. Each site is formed by the backbone carbonyl groups from residues lining the selectivity filter. The first MD simulations of KcsA by Åqvist and Luzhkov [84], in combination with work by Bernèche and Roux [85], suggested that ion conduction involves transitions between two main states, in agreement with the Hodgkin-Keynes knock-on mechanism, with two or three K^+ ions occupying the selectivity filter and water molecules occupying vacant sites. The largest free-energy barrier was found to be of the order of 2–3 kcal mol^{-1}, suggesting that ion permeation is limited by diffusion in this case [85]. An alternative mechanism for KcsA conduction was proposed to involve site vacancies and ions occupying consecutive sites with direct ion-ion contact between two potassium ions in neighboring binding sites driving ion permeation, without the need for water to mediate the process [81].

Our understanding of the mechanism of ionic selectivity in potassium channels has also evolved significantly as a result of MD simulations, with two views emerging. Firstly, the thermodynamic origin of selectivity, that explains selectivity as arising from higher barriers for sodium conduction over potassium conduction. Secondly, the kinetic view, which proposes that potassium permeates with greater rates than sodium. Early MD simulations by Noskov et al. using KcsA showed that carbonyl groups coordinating the ion in the narrow pore are flexible and modulate ion selectivity [86]. Free-energy simulations underscored the thermodynamic view of selectivity, rendering energy barriers that are generally larger for Na^+ over K^+ [87]. Recent multi-ion free-energy MD simulations found evidence for selectivity arising from several potassium ions bound in the filter concomitantly [88].

As well as establishing selectivity in K^+ channels, it has been proposed that the selectivity filter is also capable of blocking ion conduction in a process known as C-type inactivation, whereby conformational changes at the selectivity filter are thought to obstruct ion passage. Simulations showed that KcsA can be gated by conformational changes at the selectivity filter in which the tetrameric symmetry of potassium channels is broken [89]. Global conformational changes are also responsible for impeding ionic current; in Kv channels the voltage-sensor domain (VSD) influences the conformational state of the pore-forming helices in response to

changes in transmembrane voltage. MD simulations of the Kv1.2 ion channel initially focused on the S4 helix in the VSD, which contains several positively charged residues, mainly arginines, located at every third position along the helix [90]. The VSD senses changes in the membrane potential across the channel, and simulations have probed the atomistic details of the VSD, finding that all four charged residues in the VSD interact with the bulk or polar headgroups, and none of them with the membrane hydrophobic interface [90]. Later work focused on describing the behaviour of the VSD in response to external currents or hyperpolarisation [91]. Additionally, continuum electrostatic Poisson-Boltzmann calculations [92] found that the transmembrane potential varies abruptly in the arginine-rich region of S4 voltage-sensor, which lead the authors to describe the membrane electric field as 'focused'. Overall, MD simulations have served as a powerful tool to study conformational dynamics [90, 93] and gating [94] in the pore-forming helices as well as agonist/antagonist druggability of these regions [95, 96]. For example, neuropeptides from spiders and scorpions have been shown to block the pore on the extracellular face [97–100], which is different from the known Kv inner-pore blockers including 4-AP, TEA [101], TBA [102], and correolide [103].

The emergence of the first high-resolution structures of voltage-gated sodium (Nav) channels from *Arcobacter butzleri* (NaVAb) [73], and from *Magnetococcus sp*. (NaVMs) [104], meant that similar MD methodologies were applied to the sodium channel family. Sodium ion channels initiate action potentials in nerve, muscle and other excitable cells, and are responsible for the fast depolarizing phase of the action potential in nerve and muscular cells [105], for which mechanistic understanding of the physiological basis of action potentials could lead to better therapies for a multitude of diseases and disorders. Sodium channels share similar pore architecture to potassium channels, expectantly differing in the selectivity filter region. In agreement with an experimental model of sodium selectivity involving an anionic coordination site [73], the crystal structures of the sodium channel identified a ring of four negatively charged glutamate side chains at the extracellular entrance which could accommodate partially dehydrated Na^+ ions. Two additional binding sites were also proposed deeper in the channel involving rings of carbonyl atoms. These sites were confirmed by MD simulations [106]. In stark contrast with K^+ channels, that exhibit significant distortions in the selectivity filter in the absence of K^+ [107–109], experimental observations from ion flux calculations [110] and patch clamp reversal potentials [111] suggested that the pore is stable independent of ion occupancy in Na^+-channels. These proposals were supported by early computational efforts using Brownian dynamics simulations [112] and classical MD simulations of NavAb [113], although the scientific community is at odds in this respect.

Analysis of ion occupancy of the selectivity filter of a bacterial sodium channel demonstrated the extracellular binding site to be a high occupancy site with ions approaching from the extracellular side and interacting with the charged E177 motif, before reaching additional sites, partially hydrated [106]. Chakrabarti et al. used unbiased MD simulations to identify a low-energy permeation pathway for Na^+ ion translocation through the selectivity filter of NavAb, reporting a rate of

translocation of $\sim 6 \times 10^6$ ions s^{-1}, and the NavAb pore occupied by two ions on average [114]. Several groups have recently employed MD simulations with umbrella sampling [115], metadynamics and bias-exchange metadynamics (BE-meta) [116–118] to study ion permeation in sodium channels. Single and multi-ion potential of mean force (PMF) calculations [119, 120], and unbiased MD simulations [114], have all identified the molecular basis of ion permeation in Na^+-channels as involving ion occupation of up to five sites, with multi-ion sites in the external region and the central cavity also thought to play a role [30–36]. Multi-ion PMF agrees with 1D PMF estimates of the energetic cost of permeation of <3 kcal mol^{-1}, finding that different conduction states are in equilibrium with each other, and that on average two ions occupy the filter [114, 121, 122].

Free-energy methods have also been used to uncover the mechanism of Na^+ selectivity in Na^+-channels. PMF calculations of Na^+ and K^+ ion permeation in NavAb found both ion types bind at similar sites but the free energy to traverse these sites is 2–3 kcal mol^{-1} higher for K^+ over Na^+ ions [79]. When considering a knock-on mechanism of sodium permeation in NavAb involving two solvated ions, selectivity for sodium over potassium was shown to arise using geometric arguments. Hydrated K^+ ions were unable to fit between the planes of glutamate residues at the central biding site in an optimal geometry, and thus passage was forbidden. It is worth noting other Nav channels have been studied using MD simulations. For example, simulations with NavMs [123] found ion binding sites that agree with those predicted for NavAb [124]. MD simulations of NavRh identified conformational rearrangements of certain residues that could lead to spontaneous opening of the selectivity filter [125]. In summary, simulations have enhanced our understanding of ion conduction in sodium channels elucidating the dynamics of the selectivity filter, potential conduction mechanisms and the origins of ion selectivity.

Understanding the lack of selectivity in some ion channels is another unique problem in which MD simulations have proven instrumental. The NaK channel is distinct from sodium and potassium channels by allowing non-selective conduction of monovalent ions K^+ and Na^+ [126, 127]. MD simulations under a strong applied potential were able to illustrate both Na^+ and K^+ permeation through NaK, obtaining faster conduction rates for K^+ ions [128]. By using free-energy simulations, comparison of the wild type and a mutated NaK channel, it was found that non-selective ionic conductance arose from a three ion-binding site selectivity filter [129] as opposed to the four-site selectivity filter in potassium-selective channels such as KcsA. Other MD simulations comparing NaK to KcsA proposed that NaK is non-selective due to differences in ion hydration in the selectivity filter of NaK, preventing discrimination of ions during permeation [130].

A second non-selective channel that has attracted great attention is the transient receptor potential Vannilloid-1 channel (TRPV1). TRPV1 is a known pain receptor, responsible for mediating nociception [131]. Recent cryo-EM structures of TRPV1 [2] show a similar tetrameric topology to those in voltage-gated ion channels. Due to the resolution of these EM structures, ion binding sites could not be resolved. However, MD simulation studies provided this information and three main ion binding sites where characterized. MD simulations of permeation of monovalent

(Na^+, K^+) and divalent (Ca^{2+}) ionic species in TRPV1 [132] observed multiple permeation events for monovalent ions, with different behaviour of the selectivity filter observed when sodium or calcium was present, compared to potassium. The availability of TRPV1 structures in complex with known agonists has also sparked interest in ligand binding to TRPV1. In particular, the properties of the activator capsaicin have been studied computationally. Capsaicin is thought to bind to a distinct intracellular vanilloid-binding site; docking studies and MD simulations confirmed the location and orientation of capsaicin in this position consistent with previous experimental studies [133]. Modelling refinement of the vanilloid-binding site of capsaicin and resiniferatoxin has predicted the pose of one hundred additional TRPV1 agonists, yielding five new TRPV1 mutants that bind capsaicin and resiniferatoxin [134]. These results provide a rational suggestion of TRPV1 ligand modifications that should improve binding affinity.

15.5 Transporters

As ion channels primarily endorse passive diffusion across the cell membrane, additional membrane assemblies exist that facilitate active transport when a concentration gradient is not present. Membrane transporters fulfill this role; using an external energy input, transporters undergo reversible conformational changes to deliver solutes across the cell membrane. The mechanism by which substrates are transported is called the alternating access model, where the transporter oscillates between cytoplasmic-open to extracellular-open states. There are currently 620 unique structures of membrane proteins reported (Stephen White laboratory; http://blanco.biomol.uci.edu/mpstruc/), of which almost 300 correspond to membrane transporters. The first simulations of a transporter embedded in explicit lipid membrane environment were those of the TonB-dependent transporter FhuA in 2003 [135], which examined conformational changes in the crystal structures of apo and holo states, with and without bound substrate [136, 137]. These simulations reported that substrate binding induces closure of the binding site. Since 2003, hundreds of publications on transporters [138–142] have addressed the mechanistic basis of substrate binding, the conformational changes required for alternating access and how this is coupled to external sources of energy.

In primary transporters, conformational changes are driven by exothermic reactions like the hydrolysis of ATP. ATP-binding cassette transporters provide a key example of this, using ATP to drive the active transport of substrates, such as ions, sugars, lipids, peptides, toxins, and small-molecule drugs across membranes. Conformational changes associated with the alternating access model are driven by cytoplasmic nucleotide-binding domains (NBDs), which interact with the transmembrane domains (TMDs) during an ATP hydrolytic cycle. MD simulations of primary transporters have studied the full ATP-hydrolytic cycle of binding and release of ADP in the maltose transporters MalK [143], and MalFGK-E (Fig. 15.3) as well as many others. Overall, MD simulations have suggested a common substrate access model, in which ATP-hydrolysis induces conformational changes

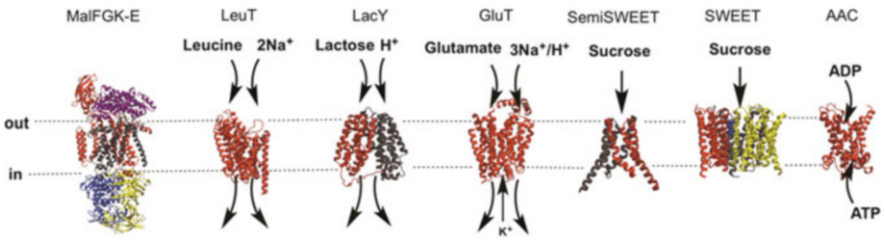

Fig. 15.3 Representative structures of transporters coloured by domain. Primary transporters MalFGK-E tetramer complex (PDB id 2R6G) [144], bound to the maltose-binding protein in purple. Secondary transporters LeuT (PDB id 2A65) [145], LacY (PDB id 1PV7) [146], GLUT (PDB id 4PYP) [147], bacterial SemiSWEET (PDB id 4X5N) [148], and eukaryotic SWEET (PDB id 5CTG) [149]. Finally, one transporter with non-primary or secondary substrate, the ADP/ATP transporter AAC (PDB id 1OKC) [150]. Monomer A is *red*, B is *black*, C is *yellow*.

in the helical sub-domain region, which are transferred to the TMD via the coupling helices [151]. The NBD dimer proposed to close upon ATP binding, with ADP release prompting opening suggesting that a single ATP binding event is needed to induce the opening of the NBD dimer [152]. MD simulations showed that in the absence of bound species, the NBD dimer dissociates to an intermediate signalling state, with subsequent opening dependent on the nature of the substrate. Proposals have since emerged of cooperative or allosteric coupling between the dimer active sites, mediated by intrasubunit conformational changes.

While primary ABC transporters utilize ATP to drive transport, secondary transport of substrates is driven by the co-transport of ions (e.g. Na^+, K^+ or H^+) down the ion concentration gradient. The alternative access model of facilitated diffusion has been studied extensively in secondary transporters, by both experimental and computational means. The recent publication of the structures of the secondary SemiSWEET transporter in intracellular-open, closed and extracellular-open states (Fig. 15.4) [148] has provided structural insights into this phenomenon. MD simulations have been crucial in elucidating dynamic processes that cannot be obtained from static structures, concerning the proposed mechanisms of alternating access [153]. The rocker-switch opening mechanism, in which a large conformational change in two protein domains is needed to transition between conformational states, a gated-pore mechanism, in which smaller, localized conformational gates control access, and, the elevator-like substrate model, in which the vertical motion of an interior domain allows for substrate access [154] have all been explored computationally.

For both lactose transport in LacY or leucine transport into LeuT [19, 155–158], substrate access occurs through small helix motions and side-chain rotations, consistent with the gated-pore hypothesis, and dismissing rocker-switch behaviour [159]. In GLUTPh, vertical motion of an interior domain is observed to allow substrate access suggesting an elevator-like substrate access [154]. Other studies have suggested that salt-bridge dynamics and the protonation of key residues could modulate transport. [159–163] Finally, certain transporters are proposed to function

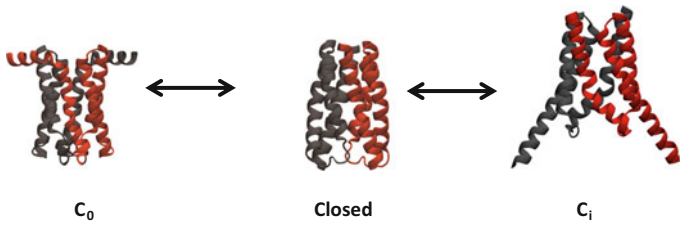

Fig. 15.4 Bacterial SemiSWEET transporter in outward-open (C_0) state (PDB id 4QND) [148], closed state (PDB id 4QNC) [148], and inward-open (C_i) state (PDB id 4X5N). Individual monomers are coloured black and red.

via an electrostatic funnel, like the mitochondrial ADP/ATP carrier (AAC) (Fig. 15.3) [164, 165].

15.6 G Protein-Coupled Receptors (GPCRs)

Another important class of membrane proteins, known as receptors, is responsible for signal transduction across the cell membrane. These proteins convert extracellular signals, such as chemical stimuli into an intracellular response. G protein-coupled receptors (GPCRs) are the largest family of membrane receptors, with the human genome encoding for over 1000 GPCR genes, and spanning 19% of the established drug-targeted portion of the human genome [166]. Their overall architecture consists of seven transmembrane (TM) helices, which rearrange on receipt of an extracellular signal to couple with intracellular entities, such as G-proteins. MD simulations have focused on three main aspects of GPCR dynamics; conformational changes between active and inactive signalling states of receptors, ligand binding mechanisms of GPCRs, and finally, protein-lipid interactions.

The first high-resolution structure of rhodopsin [167] gave insights into the organisation of these receptors, and was the subject of the first simulation of a GPCR in an explicit membrane bilayer [8], which probed the interconversion between two rhodopsin signalling states, a dark-state and a photoisomerized state. MD simulations demonstrated that this interconversion was mediated by conformational changes to the bound ligand (cis to trans), occurring via a concerted series of hydrogen-bond shifts. Several groups have studied how other GPCRs open and close via substrate binding, with a specific salt-bridge (denoted the ionic lock) crucial in this process. Microsecond MD simulation of the β2AR in the absence of agonists found the ionic lock to open and close on a nanosecond timescale, proposed to represent active and inactive functional states respectively [168]. Subsequent simulations by Dror et al. [169] revealed the inactive β2AR actually sampled two conformations, one with the lock broken and another with the lock formed. Finally,

both tryptophan and proline residues are also proposed to act as conformational switches in GPCR TMD domains [170]. Louet et al. [171] used MD simulations of the ghrelin GPCR A, to identify conformational movements of TM6 and TM7 required to induce opening of the G-protein binding pocket. The role of G-protein binding to the inactive GPCR state has also been studied in the β2Rs [172].

Ligand binding to GPCRs has received substantial attention from simulations. Microsecond MD simulations of retinal binding to rhodopsin has been studied by several groups (Lau et al. in 2007 [173]; Mertz et al. in 2012 [174]) have found that the bound state of rhodopsin spans an ensemble of states, with the substrate mobile in the binding pocket. Similar observations were also described in the A_{2A} adenosine receptor, showing that adenosine is highly dynamic when bound to A_{2A}, possessing more than one binding orientation, which is not apparent in the crystal structure [175]. MD simulations have further shown that agonist binding can break the ionic lock of GPCRs, such as in the binding of sn-2-arachidonylglycerol to the cannabinoid receptor [176]. Rosenbaum et al. reported β2AR to bind two different agonists [177], and further work described the transition between two conformational states predicted from the crystal structures of β2AR [178]. Other work on β-blockers and β-agonists, found that these drugs use the same pathway to bind to the β1AR and β2AR receptors, by interacting with the extracellular GPCR surface [172].

Besides manipulating the structure of GPCRs, simulations have also focused on the key interactions of GPCRs with their lipid environment. MD simulations of GPCR interactions with cholesterol have focused on the GPCR 'CRAC' (cholesterol recognition/interaction amino acid consensus) or 'CARC' [179–181] motifs, found in β2AR (Fig. 15.5) [184], with estimates reporting the CARC motifs accounting for 50 kcal mol^{-1} energy interaction on a single GPCR. Simulations found multiple cholesterol interaction sites (cholesterol hot spots) having a microsecond exchange timescale with bulk lipids [185]. Simulations suggest that the 5-HT_{1A} receptor is more compact in the presence of cholesterol [186]. Lipid regulation of other GPCRs has been studied, including the nAChR [187–189].

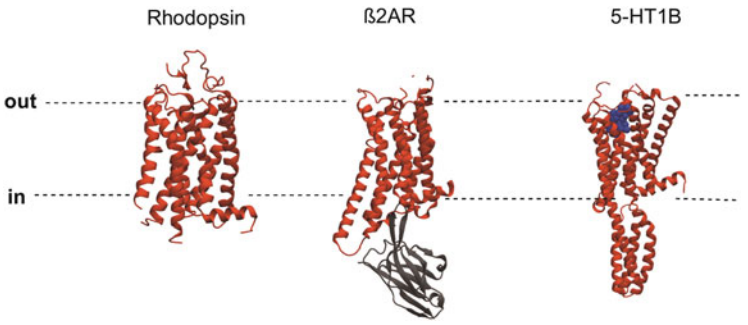

Fig. 15.5 Representative structures of GPCRs: Rhodosin monomer (PDB id 1F88) [167], β2-adrenergic receptor (β2AR) complexed with trypsin (PDB id 3VGA) [182], and 5-HT_{1B} receptor complexed with ergotamine ligand (*blue*; PDB id 4IAR) [183]. Monomers are represented in *red*, G-protein in *gray*, and the ligand substrate in *blue*

15.7 Conclusions

The key contributions of MD simulations and related methods to our understanding of transport across biological membranes have been reviewed. In the field of ion channels, computational work has provided insight into gating, ion permeation and selectivity. In the field of transporters, simulations have provided mechanisms of substrate access, and identified key residues involved in gating. Simulations have also mapped out the multiple conformational states of ligand-bound transporters. Finally, for GPCRs, simulations have advanced our understanding of the mechanisms linking distinct GPCR signaling states, and key insights into substrate and lipid binding.

The field of membrane proteins is expanding with the ever-increasing number of crystal structures. Therefore, MD simulations have come far in the aim of elucidating the conformational dynamics of membrane proteins, and in the process, have raised a great amount of new questions, whose answers are mainly limited by the amount of computing power available, as well as the number of structures solved. The continuous increase in the accessible timescales of routine MD simulation, as well as the development of smarter, more efficient biased sampling methodologies and sophisticated CG models and polarizable force fields will greatly aid this field in the future.

Acknowledgements C.J. thanks King's College London for a Graduate Teaching Assistant (GTA) studentship. V.O. acknowledges a BBSRC-CASE studentship, in association with Pfizer Neusentis. C.D. acknowledges use of ARCHER, the UK National Supercomputing Service, the National Service for Computational Chemistry Software (NSCCS) and the Hartree Center. Research in the Domene group is supported by the Engineer and Physical Sciences Research Council (EPSRC) and the Biotechnology and Biological Sciences Research Council (BBSRC).

References

1. Röhrig UF, Guidoni L, Rothlisberger U. Early steps of the intramolecular signal transduction in rhodopsin explored by molecular dynamics simulations. Biochemistry. 2002;41 (35):10799–809.
2. Liao M, Cao E, Julius D, Cheng Y. Structure of the TRPV1 ion channel determined by electron cryo-microscopy. Nature. 2013;504(7478):107–12.
3. Baaden M, Marrink SJ. Coarse-grain modelling of protein–protein interactions. Curr Opin Struct Biol. 2013;23(6):878–86.
4. Torrie GM, Valleau JP. Nonphysical sampling distributions in Monte Carlo free-energy estimation: umbrella sampling. J Comput Phys. 1977;23(2):187–99.
5. Laio A, Parrinello M. Escaping free-energy minima. PNAS. 2002;99(20):12562–6.
6. Evans E, Ritchie K. Dynamic strength of molecular adhesion bonds. Biophys J. 1997;72 (4):1541.
7. Pearlman DA, Case DA, Caldwell JW, Ross WS, Cheatham TE, DeBolt S, Ferguson D, Seibel G, Kollman P. AMBER, a package of computer programs for applying molecular mechanics, normal mode analysis, molecular dynamics and free energy calculations to simulate the structural and energetic properties of molecules. Comput Phys Commun. 1995;91(1–3):1–41.

8. Crozier PS, Stevens MJ, Forrest LR, Woolf TB. Molecular dynamics simulation of dark-adapted rhodopsin in an explicit membrane bilayer: coupling between local retinal and larger scale conformational change. J Mol Biol. 2003;333(3):493–514.
9. Berendsen HJC, van der Spoel D, van Drunen R. GROMACS: a message-passing parallel molecular dynamics implementation. Comput Phys Commun. 1995;91(1-3):43–56.
10. Van Der Spoel D, Lindahl E, Hess B, Groenhof G, Mark AE, Berendsen HJC. GROMACS: fast, flexible, and free. J Comput Chem. 2005;26(16):1701–18.
11. Plimpton S, Crozier P, Thompson A. LAMMPS-large-scale atomic/molecular massively parallel simulator. Sandia National Laboratories. 2007;18
12. Bowers K, Chow E, Xu H, Dror R, Eastwood M, Gregersen B, Klepeis J, Kolossvary I, Moraes M, Sacerdoti F, Salmon J, Shan Y, Shaw D. Scalable algorithms for molecular dynamics simulations on commodity clusters. SC '06: Proceedings of the 2006 ACM/IEEE Conference on Supercomputing. 2006. p. 43–43.
13. Alder B, Wainwright T. Phase transition for a hard sphere system. J Chem Phys. 1957;27 (5):1208.
14. Rahman A, Stillinger FH. Molecular dynamics study of liquid water. J Chem Phys. 1971;55 (7):3336–59.
15. Levitt M, Warshel A. Computer simulation of protein folding. Nature. 1975;253 (5494):694–8.
16. McCammon JA, Gelin BR, Karplus M. Dynamics of folded proteins. Nature. 1977;267 (5612):585–90.
17. Nonella M, Wlndemuth A, Schulten K. Structure of bacteriorhodopsin and in situ isomerization of retinal: a molecular dynamics study. Photochem Photobiol. 1991;54(6):937–48.
18. Dratz EA, Van Breemen JF, Kamps KP, Keegstra W, Van Bruggen EF. Two-dimensional crystallization of bovine rhodopsin. Biochim Biophys Acta Protein Struct Mol Enzymol. 1985;832(3):337–42.
19. Kniazeff J, Shi L, Loland CJ, Javitch JA, Weinstein H, Gether U. An intracellular interaction network regulates conformational transitions in the dopamine transporter. J Biol Chem. 2008;283(25):17691–701.
20. Darve E, Pohorille A. Calculating free energies using average force. J Chem Phys. 2001;115 (20):9169–83.
21. Grossfield A. WHAM: the weighted histogram analysis method. 2012.
22. den Otter WK. Thermodynamic integration of the free energy along a reaction coordinate in Cartesian coordinates. J Chem Phys. 2000;112(17):7283–92.
23. den Otter WK, Briels WJ. The calculation of free-energy differences by constrained molecular-dynamics simulations. J Chem Phys. 1998;109:4139–46.
24. Chipot C, Pohorille A. Free energy calculations. Berlin: Springer; 2007.
25. Darve E, Rodríguez-Gómez D, Pohorille A. Adaptive biasing force method for scalar and vector free energy calculations. J Chem Phys. 2008;128:144120.
26. Van Gunsteren WF. Methods for calculation of free energies and binding constants: successes and problems. In: van Gunsteren WF, Weiner PK, editors. Computer simulation of biomolecular systems: theoretical and experimental applications. Leiden: ESCOM; 1989. p. 27–59.
27. Jarzynski C. Equilibrium free-energy differences from nonequilibrium measurements: a master-equation approach. Phys Rev E. 1997;56(5):5018–35.
28. Jarzynski C. Nonequilibrium equality for free energy differences. Phys Rev Lett. 1997;78 (14):2690–3.
29. Dudko OK, Hummer G, Szabo A. Theory, analysis, and interpretation of single-molecule force spectroscopy experiments. PNAS. 2008;105(41):15755–60.
30. Dudko O, Hummer G, Szabo A. Intrinsic rates and activation free energies from single-molecule pulling experiments. Phys Rev Lett. 2006;96(10):108101.
31. Mathai JC, Tristram-Nagle S, Nagle JF, Zeidel ML. Structural determinants of water permeability through the lipid membrane. J Gen Physiol. 2008;131(1):69–76.

32. Bemporad D, Essex JW, Luttmann C. Permeation of small molecules through a lipid bilayer: a computer simulation study. J Phys Chem B. 2004;108(15):4875–84.
33. Marrink SJ, Berendsen HJ. Permeation process of small molecules across lipid membranes studied by molecular dynamics simulations. J Phys Chem. 1996;100(41):16729–38.
34. Domene C, Klein ML, Branduardi D, Gervasio FL, Parrinello M. Conformational changes and gating at the selectivity filter of potassium channels. J Am Chem Soc. 2008;130 (29):9474–80.
35. Gabdoulline RR, Wade RC. Brownian dynamics simulation of protein–protein diffusional encounter. Methods. 1998;14(3):329–41.
36. Mereghetti P, Gabdoulline RR, Wade RC. Brownian dynamics simulation of protein solutions: structural and dynamical properties. Biophys J. 2010;99(11):3782–91.
37. Im W, Beglov D, Roux B. Continuum solvation model: computation of electrostatic forces from numerical solutions to the Poisson-Boltzmann equation. Comput Phys Commun. 1998;111(1):59–75.
38. McCammon JA. Target flexibility in molecular recognition. Biochim Biophys Acta. 2005;1754(1):221–4.
39. Miller BR III, McGee TD Jr, Swails JM, Homeyer N, Gohlke H, Roitberg AE. MMPBSA. py: an efficient program for end-state free energy calculations. J Chem Theory Comput. 2012;8 (9):3314–21.
40. Orsi M, Sanderson WE, Essex JW. Permeability of small molecules through a lipid bilayer: a multiscale simulation study. J Phys Chem B. 2009;113(35):12019–29.
41. Arcario MJ, Mayne CG, Tajkhorshid E. Atomistic models of general anesthetics for use in in silico biological studies. J Phys Chem B. 2014;118(42):12075–86.
42. Orsi M, Essex JW. Permeability of drugs and hormones through a lipid bilayer: insights from dual-resolution molecular dynamics. Soft Matter. 2010;6(16):3797–808.
43. Wong-Ekkabut J, Baoukina S, Triampo W, Tang I-M, Tieleman DP, Monticelli L. Computer simulation study of fullerene translocation through lipid membranes. Nat Nanotechnol. 2008;3(6):363–8.
44. Overton CE. Über die osmotischen Eigenschaften der lebenden Pflanzen-und Tierzelle. Zürich: Fäsi & Beer; 1895.
45. Alper HE, Stouch TR. Orientation and diffusion of a drug analog in biomembranes: molecular dynamics simulations. J Phys Chem. 1995;99(15):5724–31.
46. Stouch TR, Alper HE, Bassolino D . In Simulations of drug diffusion in biomembranes, ACS Symposium Series, American Chemical Society. 1995; pp 127–138.
47. Bassolino-Klimas D, Alper HE, Stouch TR. Mechanism of solute diffusion through lipid bilayer membranes by molecular dynamics simulation. J Am Chem Soc. 1995;117 (14):4118–29.
48. Marrink S-J, Berendsen HJ. Simulation of water transport through a lipid membrane. J Phys Chem. 1994;98(15):4155–68.
49. Katz Y, Diamond JM. Thermodynamic constants for nonelectrolyte partition between dimyristoyl lecithin and water. J Membr Biol. 1974;17(1):101–20.
50. Wolosin J, Ginsburg H. The permeation of organic acids through lecithin bilayers resemblance to diffusion in polymers. Biochim Biophys Acta Biomembr. 1975;389(1):20–33.
51. Cohen BE. The permeability of liposomes to nonelectrolytes. J Membr Biol. 1975;20 (1):205–34.
52. Brunner J, Senn H, Richards F. 3-Trifluoromethyl-3-phenyldiazirine. A new carbene generating group for photolabeling reagents. J Biol Chem. 1980;255(8):3313–8.
53. Walter A, Gutknecht J. Permeability of small nonelectrolytes through lipid bilayer membranes. J Membr Biol. 1986;90(3):207–17.
54. Walter A, Gutknecht J. Monocarboxylic acid permeation through lipid bilayer membranes. J Membr Biol. 1984;77(3):255–64.
55. Bean RC, Shepherd WC, Chan H. Permeability of lipid bilayer membranes to organic solutes. J Gen Physiol. 1968;52(3):495–508.

56. Cascales JL, Cifre JH, de la Torre JG. Anaesthetic mechanism on a model biological membrane: a molecular dynamics simulation study. J Phys Chem B. 1998;102:625–31.
57. Koubi L, Tarek M, Klein ML, Scharf D. Distribution of halothane in a dipalmitoylphosphatidylcholine bilayer from molecular dynamics calculations. Biophys J. 2000;78(2):800–11.
58. Tu K, Tarek M, Klein ML, Scharf D. Effects of anesthetics on the structure of a phospholipid bilayer: molecular dynamics investigation of halothane in the hydrated liquid crystal phase of dipalmitoylphosphatidylcholine. Biophys J. 1998;75(5):2123–34.
59. Chipot C, Wilson MA, Pohorille A. Interactions of anesthetics with the water-hexane interface. A molecular dynamics study. J Phys Chem B. 1997;101(5):782–91.
60. Pohorille A, Cieplak P, Wilson MA. Interactions of anesthetics with the membrane-water interface. Chem Phys. 1996;204(2):337–45.
61. Pohorille A, Wilson MA, Chipot C. Interaction of alcohols and anesthetics with the water-hexane interface: a molecular dynamics study. J Phys Chem B. 1997;103:29–40.
62. Pratt LR, Pohorille A. Hydrophobic effects and modeling of biophysical aqueous solution interfaces. Chem Rev. 2002;102(8):2671–92.
63. Singh R, Lillard JW. Nanoparticle-based targeted drug delivery. Exp Mol Pathol. 2009;86 (3):215–23.
64. Montellano A, Da Ros T, Bianco A, Prato M. Fullerene C 60 as a multifunctional system for drug and gene delivery. Nanoscale. 2011;3(10):4035–41.
65. Faraji AH, Wipf P. Nanoparticles in cellular drug delivery. Bioorg Med Chem. 2009;17 (8):2950–62.
66. Tajkhorshid E, Nollert P, Jensen MØ, Miercke LJ, O'Connell J, Stroud RM, Schulten K. Control of the selectivity of the aquaporin water channel family by global orientational tuning. Science. 2002;296(5567):525–30.
67. Verkman A, Mitra AK. Structure and function of aquaporin water channels. Am J Physiol Ren Physiol. 2000;278(1):F13–28.
68. Murata K, Mitsuoka K, Hirai T, Walz T, Agre P, Heymann JB, Engel A, Fujiyoshi Y. Structural determinants of water permeation through aquaporin-1. Nature. 2000;407 (6804):599–605.
69. de Groot BL, Grubmüller H. Water permeation across biological membranes: mechanism and dynamics of aquaporin-1 and GlpF. Science. 2001;294(5550):2353–7.
70. Hub JS, De Groot BL. Mechanism of selectivity in aquaporins and aquaglyceroporins. PNAS. 2008;105(4):1198–203.
71. Hille B. Ion channels of excitable membranes, vol. 507. Sunderland, MA: Sinauer; 2001.
72. Cao E, Liao M, Cheng Y, Julius D. TRPV1 structures in distinct conformations reveal activation mechanisms. Nature. 2013;504(7478):113–8.
73. Payandeh J, Scheuer T, Zheng N, Catterall WA. The crystal structure of a voltage-gated sodium channel. Nature. 2011;475(7356):353–8.
74. Long SB. Voltage sensor of Kv1.2: structural basis of electromechanical coupling. Science. 2005;309(5736):903–8.
75. Chen X, Wang Q, Ni F, Ma J. Structure of the full-length Shaker potassium channel Kv1.2 by normal-mode-based X-ray crystallographic refinement. PNAS. 2010;107(25):11352–7.
76. Roux B. Perspectives on: molecular dynamics and computational methods. J Gen Physiol. 2010;135(6):547–8.
77. Dror RO, Jensen MØ, Borhani DW, Shaw DE. Exploring atomic resolution physiology on a femtosecond to millisecond timescale using molecular dynamics simulations. J Gen Physiol. 2010;135(6):555–62.
78. Eisenberg B. Interacting ions in biophysics: real is not ideal. Biophys J. 2013;104 (9):1849–66.
79. Furini S, Domene C. K+ and Na+ conduction in selective and nonselective ion channels via molecular dynamics simulations. Biophys J. 2013;105(8):1737–45.

80. Horn R, Roux B, Åqvist J. Permeation redux: thermodynamics and kinetics of ion movement through potassium channels. Biophys J. 2014;106(9):1859–63.
81. Furini S, Domene C. Atypical mechanism of conduction in potassium channels. PNAS. 2009;106(38):16074–7.
82. Hodgkin AL, Keynes RD. The potassium permeability of a giant nerve fibre. J Physiol. 1955;128(1):61–88.
83. Jensen MØ, Borhani DW, Lindorff-Larsen K, Maragakis P, Jogini V, Eastwood MP, Dror RO, Shaw DE. Principles of conduction and hydrophobic gating in K+ channels. PNAS. 2010;107 (13):5833–8.
84. Åqvist J, Luzhkov V. Ion permeation mechanism of the potassium channel. Nature. 2000;404 (6780):881–4.
85. Berneche S, Roux B. Energetics of ion conduction through the K+ channel. Nature. 2001;414 (6859):73–7.
86. Noskov SY, Berneche S, Roux B. Control of ion selectivity in potassium channels by electrostatic and dynamic properties of carbonyl ligands. Nature. 2004;431(7010):830–4.
87. Egwolf B, Roux B. Ion selectivity of the KcsA channel: a perspective from multi-ion free energy landscapes. J Mol Biol. 2010;401(5):831–42.
88. Medovoy D, Perozo E, Roux B. Multi-ion free energy landscapes underscore the microscopic mechanism of ion selectivity in the KcsA channel. Biochim Biophys Acta Biomembr. 2016;1858:1722–32.
89. Bernèche S, Roux B. A gate in the selectivity filter of potassium channels. Structure. 2005;13 (4):591–600.
90. Jogini V, Roux B. Dynamics of the Kv1.2 voltage-gated K+ channel in a membrane environment. Biophys J. 2007;93(9):3070–82.
91. Delemotte L, Tarek M, Klein ML, Amaral C, Treptow W. Intermediate states of the Kv1.2 voltage sensor from atomistic molecular dynamics simulations. PNAS. 2011;108 (15):6109–14.
92. Jogini V, Roux B. Dynamics of the Kv1. 2 voltage-gated K+ channel in a membrane environment. Biophys J. 2007;93(9):3070–82.
93. Jensen MO, Jogini V, Borhani DW, Leffler AE, Dror RO, Shaw DE. Mechanism of voltage gating in potassium channels. Science. 2012;336(6078):229–33.
94. Khalili-Araghi F, Jogini V, Yarov-Yarovoy V, Tajkhorshid E, Roux B, Schulten K. Calculation of the gating charge for the Kv1. 2 voltage-activated potassium channel. Biophys J. 2010;98 (10):2189–98.
95. Jorgensen C, Darré L, Vanommeslaeghe K, Omoto K, Pryde D, Domene C. In Silico Identification of PAP-1 Binding Sites in the Kv1. 2 potassium channel. Mol Pharm. 2015;12(4):1299–307.
96. Marzian S, Stansfeld PJ, Rapedius M, Rinné S, Nematian-Ardestani E, Abbruzzese JL, Steinmeyer K, Sansom MS, Sanguinetti MC, Baukrowitz T. Side pockets provide the basis for a new mechanism of Kv channel–specific inhibition. Nat Chem Biol. 2013;9(8):507–13.
97. Miller C. The charybdotoxin family of K+ channel-blocking peptides. Neuron. 1995;15 (1):5–10.
98. MacKinnon R, Heginbotham L, Abramson T. Mapping the receptor site for charybdotoxin, a pore-blocking potassium channel inhibitor. Neuron. 1990;5(6):767–71.
99. Gross A, Abramson T, MacKinnon R. Transfer of the scorpion toxin receptor to an insensitive potassium channel. Neuron. 1994;13(4):961–6.
100. Garcia-Calvo M, Leonard RJ, Novick J, Stevens SP, Schmalhofer W, Kaczorowski GJ, Garcia ML. Purification, characterization, and biosynthesis of margatoxin, a component of Centruroides margaritatus venom that selectively inhibits voltage-dependent potassium channels. J Biol Chem. 1993;268(25):18866–74.
101. Grissmer S, Nguyen AN, Aiyar J, Hanson DC, Mather RJ, Gutman GA, Karmilowicz MJ, Auperin DD, Chandy KG. Pharmacological characterization of five cloned voltage-gated K+ channels, types Kv1. 1, 1.2, 1.3, 1.5, and 3.1, stably expressed in mammalian cell lines. Mol Pharmacol. 1994;45(6):1227–34.

102. Zhou M, Morais-Cabral JH, Mann S, MacKinnon R. Potassium channel receptor site for the inactivation gate and quaternary amine inhibitors. Nature. 2001;411(6838):657–61.
103. Koo GC, Blake JT, Shah K, Staruch MJ, Dumont F, Wunderler D, Sanchez M, McManus OB, Sirotina-Meisher A, Fischer P, Boltz RC, Goetz MA, Baker R, Bao J, Kayser F, Rupprecht KM, Parsons WH, Tong X-C, Ita IE, Pivnichny J, Vincent S, Cunningham P, Hora D, Feeney W, Kaczorowski G, Springer MS. Correolide and derivatives are novel immunosuppressants blocking the lymphocyte Kv1.3 potassium channels. Cell Immunol. 1999;197(2):99–107.
104. McCusker EC, Bagneris C, Naylor CE, Cole AR, D'Avanzo N, Nichols CG, Wallace BA. Structure of a bacterial voltage-gated sodium channel pore reveals mechanisms of opening and closing. Nat Commun. 2012;3:1102.
105. Catterall WA. Voltage-gated sodium channels at 60: structure, function and pathophysiology. J Physiol. 2012;590(11):2577–89.
106. Carnevale V, Treptow W, Klein ML. Sodium ion binding sites and hydration in the lumen of a bacterial ion channel from molecular dynamics simulations. J Phys Chem Lett. 2011;2 (19):2504–8.
107. Domene C, Klein ML, Branduardi D, Gervasio FL, Parrinello M. Conformational changes and gating at the selectivity filter of potassium channels. J Am Chem Soc. 2008;130 (29):9474–80.
108. Zhou Y, Morais-Cabral JH, Kaufman A, MacKinnon R. Chemistry of ion coordination and hydration revealed by a K^+ channel-Fab complex at 2.0 Å resolution. Nature. 2001;414:43–8.
109. Domene C, Furini S. Dynamics, energetics, and selectivity of the low-K+ KcsA channel structure. J Mol Biol. 2009;389(3):637–45.
110. Benos DJ, Hyde BA, Latorre R. Sodium flux ratio through the amiloride-sensitive entry pathway in frog skin. J Gen Physiol. 1983;81(5):667–85.
111. Begenisich TB, Cahalan MD. Sodium channel permeation in squid axons. I: reversal potential experiments. J Physiol. 1980;307:217–42.
112. Vora T, Corry B, Chung SH. Brownian dynamics study of flux ratios in sodium channels. Eur Biophys J. 2008;38(1):45–52.
113. Qiu H, Shen R, Guo W. Ion solvation and structural stability in a sodium channel investigated by molecular dynamics calculations. Biochim Biophys Acta. 2012;1818(11):2529–35.
114. Chakrabarti N, Ing C, Payandeh J, Zheng N, Catterall WA, Pomès R. Catalysis of Na+ permeation in the bacterial sodium channel NaVAb. PNAS. 2013;110(28):11331–6.
115. Zhang Y, Voth GA. Combined metadynamics and umbrella sampling method for the calculation of ion permeation free energy profiles. J Chem Theory Comput. 2011;7 (7):2277–83.
116. Cossio P, Marinelli F, Laio A, Pietrucci F. Optimizing the performance of bias-exchange metadynamics: folding a 48-residue LysM domain using a coarse-grained model. J Phys Chem B. 2010;114(9):3259–65.
117. Todorova N, Marinelli F, Piana S, Yarovsky I. Exploring the folding free energy landscape of insulin using bias exchange metadynamics. J Phys Chem B. 2009;113(11):3556–64.
118. Domene C, Barbini P, Furini S. Bias-exchange metadynamics simulations: an efficient strategy for the analysis of conduction and selectivity in ion channels. J Chem Theory Comput. 2015;11(4):1896–906.
119. Corry B, Thomas M. Mechanism of ion permeation and selectivity in a voltage gated sodium channel. J Am Chem Soc. 2012;134(3):1840–6.
120. Furini S, Domene C. On conduction in a bacterial sodium channel. PLoS Comput Biol. 2012;8(4):e1002476.
121. Stock L, Delemotte L, Carnevale V, Treptow W, Klein ML. Conduction in a biological sodium selective channel. J Phys Chem B. 2013;117(14):3782–9.
122. Boiteux C, Vorobyov I, Allen TW. Ion conduction and conformational flexibility of a bacterial voltage-gated sodium channel. PNAS. 2014;111(9):3454–9.

123. Ke S, Timin EN, Stary-Weinzinger A. Different inward and outward conduction mechanisms in NaVMs suggested by molecular dynamics simulations. PLoS Comput Biol. 2014;10(7): e1003746.
124. McCusker EC, Bagneris C, Naylor CE, Cole AR, D'Avanzo N, Nichols CG, Wallace BA. Structure of a bacterial voltage-gated sodium channel pore reveals mechanisms of opening and closing. Nat Commun. 2012;3:1102.
125. Zhang X, Xia M, Li Y, Liu H, Jiang X, Ren W, Wu J, DeCaen P, Yu F, Huang S, He J, Clapham DE, Yan N, Gong H. Analysis of the selectivity filter of the voltage-gated sodium channel NavRh. Cell Res. 2013;23(3):409–22.
126. Alam A, Jiang Y. Structural analysis of ion selectivity in the NaK channel. Nat Struct Mol Biol. 2009;16(1):35–41.
127. Alam A, Jiang Y. High-resolution structure of the open NaK channel. Nat Struct Mol Biol. 2009;16(1):30–4.
128. Vora T, Bisset D, Chung S-H. Conduction of Na+ and K+ through the NaK channel: molecular and Brownian dynamics studies. Biophys J. 2008;95(4):1600–11.
129. Furini S, Domene C. Nonselective conduction in a mutated NaK channel with three cation-binding sites. Biophys J. 2012;103(10):2106–14.
130. Noskov SY, Roux B. Importance of hydration and dynamics on the selectivity of the KcsA and NaK channels. J Gen Physiol. 2007;129(2):135–43.
131. Venkatachalam K, Montell C. TRP channels. Annu Rev Biochem. 2007;76:387–417.
132. Darré L, Furini S, Domene C. Permeation and dynamics of an open-activated TRPV1 channel. J Mol Biol. 2015;108(2):37a.
133. Elokely KM, Palovack E, Delemotte L, Carnevale V, Klein ML. Understanding the molecular determinants of capsaicin mode of action. Biophys J. 2015;108(2):57a.
134. Elokely K, Velisetty P, Delemotte L, Palovcak E, Klein ML, Rohacs T, Carnevale V. Understanding TRPV1 activation by ligands: insights from the binding modes of capsaicin and resiniferatoxin. PNAS. 2016;113(2):E137–45.
135. Faraldo-Gómez JD, Smith GR, Sansom MS. Molecular dynamics simulations of the bacterial outer membrane protein FhuA: a comparative study of the ferrichrome-free and bound states. Biophys J. 2003;85(3):1406–20.
136. Locher KP, Rees B, Koebnik R, Mitschler A, Moulinier L, Rosenbusch JP, Moras D. Transmembrane signaling across the ligand-gated FhuA receptor: crystal structures of free and ferrichrome-bound states reveal allosteric changes. Cell. 1998;95(6):771–8.
137. Ferguson AD, Hofmann E, Coulton JW, Diederichs K, Welte W. Siderophore-mediated iron transport: crystal structure of FhuA with bound lipopolysaccharide. Science. 1998;282 (5397):2215–20.
138. Li J, Wen P-C, Moradi M, Tajkhorshid E. Computational characterization of structural dynamics underlying function in active membrane transporters. Curr Opin Struct Biol. 2015;31:96–105.
139. Pavlova A, Hwang H, Lundquist K, Balusek C, Gumbart JC. Living on the edge: simulations of bacterial outer-membrane proteins. Biochim Biophys Acta Biomembr. 2016;1858 (7):1753–9.
140. Yan N. Structural advances for the major facilitator superfamily (MFS) transporters. Trends Biochem Sci. 2013;38(3):151–9.
141. Dror RO, Dirks RM, Grossman J, Xu H, Shaw DE. Biomolecular simulation: a computational microscope for molecular biology. Annu Rev Biophys. 2012;41:429–52.
142. Khalili-Araghi F, Gumbart J, Wen P-C, Sotomayor M, Tajkhorshid E, Schulten K. Molecular dynamics simulations of membrane channels and transporters. Curr Opin Struct Biol. 2009;19(2):128–37.
143. Oloo EO, Fung EY, Tieleman DP. The dynamics of the MgATP-driven closure of MalK, the energy-transducing subunit of the maltose ABC transporter. J Biol Chem. 2006;281 (38):28397–407.

144. Oldham ML, Khare D, Quiocho FA, Davidson AL, Chen J. Crystal structure of a catalytic intermediate of the maltose transporter. Nature. 2007;450(7169):515–21.
145. Yamashita A, Singh SK, Kawate T, Jin Y, Gouaux E. Crystal structure of a bacterial homologue of Na+/Cl--dependent neurotransmitter transporters. Nature. 2005;437 (7056):215–23.
146. Abramson J, Smirnova I, Kasho V, Verner G, Kaback HR, Iwata S. Structure and mechanism of the lactose permease of Escherichia coli. Science. 2003;301(5633):610–5.
147. Deng D, Xu C, Sun P, Wu J, Yan C, Hu M, Yan N. Crystal structure of the human glucose transporter GLUT1. Nature. 2014;510(7503):121–5.
148. Xu Y, Tao Y, Cheung LS, Fan C, Chen L-Q, Xu S, Perry K, Frommer WB, Feng L. Structures of bacterial homologues of SWEET transporters in two distinct conformations. Nature. 2014;515(7527):448–52.
149. Tao Y, Cheung LS, Li S, Eom J-S, Chen L-Q, Xu Y, Perry K, Frommer WB, Feng L. Structure of a eukaryotic SWEET transporter in a homotrimeric complex. Nature. 2015;527 (7577):259–63.
150. Pebay-Peyroula E, Dahout-Gonzalez C, Kahn R, Trézéguet V, Lauquin GJ-M, Brandolin G. Structure of mitochondrial ADP/ATP carrier in complex with carboxyatractyloside. Nature. 2003;426(6962):39–44.
151. Oliveira ASF, Baptista AM, Soares CM. Inter-domain communication mechanisms in an ABC importer: a molecular dynamics study of the MalFGK 2 E complex. PLoS Comput Biol. 2011;7(8):e1002128.
152. Wen P-C, Tajkhorshid E. Dimer opening of the nucleotide binding domains of ABC transporters after ATP hydrolysis. Biophys J. 2008;95(11):5100–10.
153. Slotboom DJ. Structural and mechanistic insights into prokaryotic energy-coupling factor transporters. Nat Rev Microbiol. 2014;12(2):79–87.
154. Boudker O, Verdon G. Structural perspectives on secondary active transporters. Trends Pharmacol Sci. 2010;31(9):418–26.
155. Celik L, Schiøtt B, Tajkhorshid E. Substrate binding and formation of an occluded state in the leucine transporter. Biophys J. 2008;94(5):1600–12.
156. Huang X, Zhan C-G. How dopamine transporter interacts with dopamine: insights from molecular modeling and simulation. Biophys J. 2007;93(10):3627–39.
157. Shi L, Quick M, Zhao Y, Weinstein H, Javitch JA. The mechanism of a neurotransmitter: sodium symporter—inward release of Na+ and substrate is triggered by substrate in a second binding site. Mol Cell. 2008;30(6):667–77.
158. Noskov SY, Roux B. Control of ion selectivity in LeuT: two Na+ binding sites with two different mechanisms. J Mol Biol. 2008;377(3):804–18.
159. Jensen MØ, Yin Y, Tajkhorshid E, Schulten K. Sugar transport across lactose permease probed by steered molecular dynamics. Biophys J. 2007;93(1):92–102.
160. Law CJ, Almqvist J, Bernstein A, Goetz RM, Huang Y, Soudant C, Laaksonen A, Hovmöller S, Wang D-N. Salt-bridge dynamics control substrate-induced conformational change in the membrane transporter GlpT. J Mol Biol. 2008;378(4):828–39.
161. Klauda JB, Brooks BR. Sugar binding in lactose permease: anomeric state of a disaccharide influences binding structure. J Mol Biol. 2007;367(5):1523–34.
162. Holyoake J, Sansom MS. Conformational change in an MFS protein: MD simulations of LacY. Structure. 2007;15(7):873–84.
163. Yin Y, Jensen MØ, Tajkhorshid E, Schulten K. Sugar binding and protein conformational changes in lactose permease. Biophys J. 2006;91(11):3972–85.
164. Wang Y, Tajkhorshid E. Electrostatic funneling of substrate in mitochondrial inner membrane carriers. PNAS. 2008;105(28):9598–603.
165. Dehez F, Pebay-Peyroula E, Chipot C. Binding of ADP in the mitochondrial ADP/ATP carrier is driven by an electrostatic funnel. J Am Chem Soc. 2008;130(38):12725–33.
166. Rask-Andersen M, Almén MS, Schiöth HB. Trends in the exploitation of novel drug targets. Nat Rev Drug Discov. 2011;10(8):579–90.

167. Palczewski K, Kumasaka T, Hori T, Behnke CA, Motoshima H, Fox BA, Le Trong I, Teller DC, Okada T, Stenkamp RE. Crystal structure of rhodopsin: AG protein-coupled receptor. Science. 2000;289(5480):739–45.
168. Romo TD, Grossfield A, Pitman MC. Concerted interconversion between ionic lock substates of the β 2 adrenergic receptor revealed by microsecond timescale molecular dynamics. Biophys J. 2010;98(1):76–84.
169. Dror RO, Arlow DH, Borhani DW, Jensen MØ, Piana S, Shaw DE. Identification of two distinct inactive conformations of the β2-adrenergic receptor reconciles structural and biochemical observations. PNAS. 2009;106(12):4689–94.
170. Sansom MS, Weinstein H. Hinges, swivels and switches: the role of prolines in signalling via transmembrane α-helices. Trends Pharmacol Sci. 2000;21(11):445–51.
171. Louet M, Perahia D, Martinez J, Floquet N. A concerted mechanism for opening the GDP binding pocket and release of the nucleotide in hetero-trimeric G-proteins. J Mol Biol. 2011;411(1):298–312.
172. Dror RO, Pan AC, Arlow DH, Borhani DW, Maragakis P, Shan Y, Xu H, Shaw DE. Pathway and mechanism of drug binding to G-protein-coupled receptors. PNAS. 2011;108 (32):13118–23.
173. Lau P-W, Grossfield A, Feller SE, Pitman MC, Brown MF. Dynamic structure of retinylidene ligand of rhodopsin probed by molecular simulations. J Mol Biol. 2007;372(4):906–17.
174. Mertz B, Struts AV, Feller SE, Brown MF. Molecular simulations and solid-state NMR investigate dynamical structure in rhodopsin activation. Biochim Biophys Acta Biomembr. 2012;1818(2):241–51.
175. Lee JY, Lyman E. Agonist dynamics and conformational selection during microsecond simulations of the A 2A adenosine receptor. Biophys J. 2012;102(9):2114–20.
176. Hurst DP, Grossfield A, Lynch DL, Feller S, Romo TD, Gawrisch K, Pitman MC, Reggio PH. A lipid pathway for ligand binding is necessary for a cannabinoid G protein-coupled receptor. J Biol Chem. 2010;285(23):17954–64.
177. Rosenbaum DM, Zhang C, Lyons JA, Holl R, Aragao D, Arlow DH, Rasmussen SG, Choi H-J, DeVree BT, Sunahara RK. Structure and function of an irreversible agonist-[bgr] 2 adrenoceptor complex. Nature. 2011;469(7329):236–40.
178. Rasmussen SG, Choi H-J, Fung JJ, Pardon E, Casarosa P, Chae PS, DeVree BT, Rosenbaum DM, Thian FS, Kobilka TS. Structure of a nanobody-stabilized active state of the [bgr] 2 adrenoceptor. Nature. 2011;469(7329):175–80.
179. Cherezov V, Rosenbaum DM, Hanson MA, Rasmussen SG, Thian FS, Kobilka TS, Choi H-J, Kuhn P, Weis WI, Kobilka BK. High-resolution crystal structure of an engineered human β2-adrenergic G protein-coupled receptor. Science. 2007;318(5854):1258–65.
180. Hanson MA, Cherezov V, Griffith MT, Roth CB, Jaakola V-P, Chien EY, Velasquez J, Kuhn P, Stevens RC. A specific cholesterol binding site is established by the 2.8 Å structure of the human β 2-adrenergic receptor. Structure. 2008;16(6):897–905.
181. Liu W, Chun E, Thompson AA, Chubukov P, Xu F, Katritch V, Han GW, Roth CB, Heitman LH, IJzerman AP. Structural basis for allosteric regulation of GPCRs by sodium ions. Science. 2012;337(6091):232–6.
182. Hino T, Arakawa T, Iwanari H, Yurugi-Kobayashi T, Ikeda-Suno C, Nakada-Nakura Y, Kusano-Arai O, Weyand S, Shimamura T, Nomura N. G-protein-coupled receptor inactivation by an allosteric inverse-agonist antibody. Nature. 2012;482(7384):237–40.
183. Wang C, Jiang Y, Ma J, Wu H, Wacker D, Katritch V, Han GW, Liu W, Huang X-P, Vardy E. Structural basis for molecular recognition at serotonin receptors. Science. 2013;340 (6132):610–4.
184. Khelashvili G, Albornoz PBC, Johner N, Mondal S, Caffrey M, Weinstein H. Why GPCRs behave differently in cubic and lamellar lipidic mesophases. J Am Chem Soc. 2012;134 (38):15858–68.
185. Sengupta D, Chattopadhyay A. Molecular dynamics simulations of GPCR–cholesterol interaction: an emerging paradigm. Biochim Biophys Acta Biomembr. 2015;1848(9):1775–82.

186. Paila YD, Tiwari S, Sengupta D, Chattopadhyay A. Molecular modeling of the human serotonin 1A receptor: role of membrane cholesterol in ligand binding of the receptor. Mol Biosyst. 2011;7(1):224–34.
187. Addona GH, Sandermann H, Kloczewiak MA, Husain SS, Miller KW. Where does cholesterol act during activation of the nicotinic acetylcholine receptor? Biochim Biophys Acta Biomembr. 1998;1370(2):299–309.
188. Marsh D, Barrantes F. Immobilized lipid in acetylcholine receptor-rich membranes from Torpedo marmorata. PNAS. 1978;75(9):4329–33.
189. Lefkowitz RJ, Sun J-P, Shukla AK. A crystal clear view of the β2-adrenergic receptor. Nat Biotechnol. 2008;26(2):189–91.

Chapter 16
Hydrophobic Mismatch in Membranes: When the Tail Matters

Bhagyashree D. Rao, Sandeep Shrivastava, and Amitabha Chattopadhyay

Abstract Hydrophobic mismatch is a specific case of lipid-protein interaction that takes place when the hydrophobic thickness of the transmembrane region of a membrane protein does not match the hydrophobic thickness of the membrane in which it is localized. Depending on the type of mismatch (positive or negative), the responses of membrane lipids and proteins vary. Hydrophobic mismatch could lead to changes in membrane protein folding, conformation, oligomerization and activity due to adaptation (mismatch response) by lipids or proteins. Hydrophobic mismatch can be observed in peptides as well as in larger transmembrane proteins that traverse the membrane a number of times such as G protein-coupled receptors (GPCRs). We propose a model of GPCR activation *via* hydrophobic mismatch based on literature data. Hydrophobic mismatch could play a role in cellular sorting and trafficking due to the gradient of cholesterol present in cellular organelles which gives rise to a gradient of increasing bilayer thickness from the endoplasmic reticulum to Golgi to the plasma membrane. We envision that hydrophobic mismatch could be an important player in lipid-protein interactions in the complex cellular milieu.

B.D. Rao
Academy of Scientific and Innovative Research, New Delhi, India

CSIR-Indian Institute of Chemical Technology, Uppal Road, Hyderabad 500 007, India

S. Shrivastava
CSIR-Centre for Cellular and Molecular Biology, Uppal Road, Hyderabad 500 007, India

A. Chattopadhyay (✉)
Academy of Scientific and Innovative Research, New Delhi, India

CSIR-Centre for Cellular and Molecular Biology, Uppal Road, Hyderabad 500 007, India
e-mail: amit@ccmb.res.in

A. Chattopadhyay (ed.), *Membrane Organization and Dynamics*, Springer Series in Biophysics 20, DOI 10.1007/978-3-319-66601-3_16

16.1 Lipid-Protein Interaction

Biological membranes are organized molecular assemblies held together due to the hydrophobic effect [1] and display large variations in their lipid and protein compositions. They offer individual identity to the cell and its organelles, and are involved in cell-cell communication. Membrane proteins are crucial since they carry out a number of vital processes in cells and cell membranes help in maintaining an optimum environment for their function. Contrary to earlier models [2], cellular membranes are often crowded [3, 4] with a high protein density (typically ~25,000 proteins/μm^2; [5]). This is particularly true for biological membranes that carry out important cellular functions. A consequence of such crowding is that lipid-protein interactions play a crucial role in maintaining the structure and function of biological membranes [6, 7]. A major part of membrane proteins is immersed in the lipid bilayer and this offers a chance to membrane lipids to interact with the proteins for optimum functioning. Variations in cell membrane lipid composition due to stress or stimuli could therefore alter lipid-protein interactions.

In most cases of lipid-protein interactions, the interaction is mainly between various residues of the protein and the headgroup of the lipid (the hydroxyl group in case of cholesterol-protein interactions). However, there is a particular type of lipid-protein interaction, where the tail of the lipid is more important in terms of interaction with the membrane protein or peptide (and therefore 'the tail matters!').

16.2 Hydrophobic Mismatch

The hydrophobic thickness of the membrane is a fundamental property that has a profound effect on transmembrane protein structure and function [8, 9]. Hydrophobic mismatch is a specific case of lipid-protein interaction that takes place when the hydrophobic thickness of the transmembrane region of a membrane protein does not match the unperturbed hydrophobic thickness of the membrane in which it resides (see Fig. 16.1). Hydrophobic mismatch could lead to changes in membrane protein folding, conformation, and activity [10–12]. Such mismatch has obvious energetic consequences due to the juxtaposition of energetically unfavorable regions of the membrane lipids and the protein. While many lipid-protein interactions involve interaction of specific residues of membrane proteins with specific lipid headgroups (such as negatively charged lipids), hydrophobic mismatch is dependent on the hydrophobic thickness of the membrane bilayer, specifically of the annular lipids and the hydrophobic surface of the protein in contact with the membrane lipids. Mismatch is therefore an interaction that causes local perturbations in the membrane and may be linked to lateral heterogeneity in the membrane [13, 14].

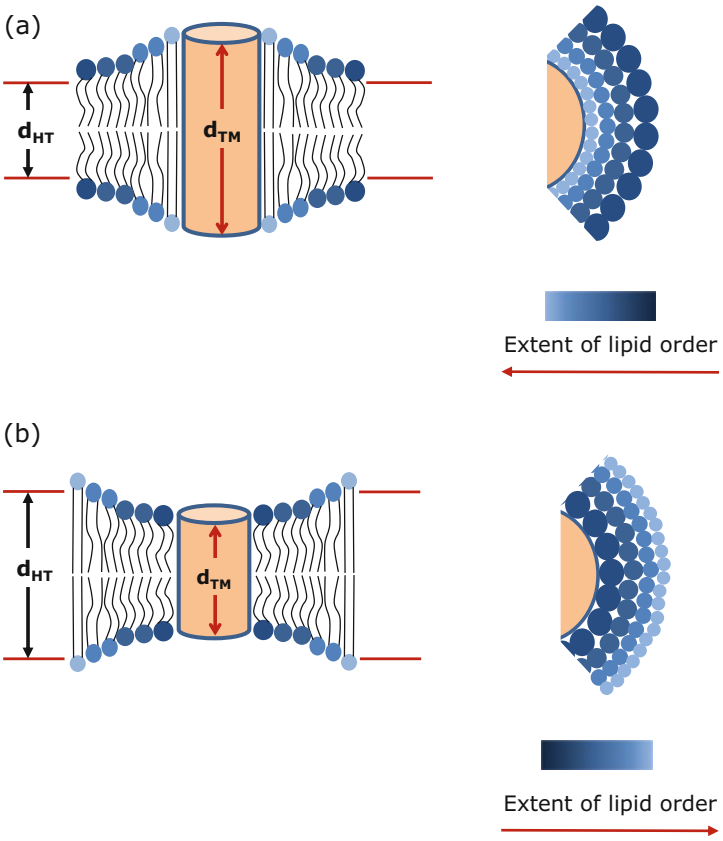

Fig. 16.1 A schematic representation of two types of hydrophobic mismatch and possible adaptations by membrane lipids. (**a**) A positive mismatch is induced when transmembrane domain length (d_{TM}) of the membrane protein is greater than the membrane bilayer hydrophobic thickness (d_{HT}). Under this condition ($d_{TM} > d_{HT}$), annular lipids surrounding the protein would get stretched to match the hydrophobic thickness of the transmembrane segment of the protein. This induces local ordering of lipid acyl chains in the vicinity of the protein and an increase in the phase transition temperature, leading to a reduction in the phospholipid headgroup area. The *top view* is shown at the *right*. (**b**) Negative mismatch results when the transmembrane domain length is shorter than the bilayer hydrophobic thickness (i.e., $d_{TM} < d_{HT}$). Negative mismatch induces local disorder in annular lipid chains, and a decrease in the phase transition temperature. This results in an increase in the phospholipid headgroup area. The *top view* is shown at the *right*

16.3 How to Determine Hydrophobic Thickness of Membranes and Membrane Proteins?

The extent of mismatch between the hydrophobic thickness of the membrane and the protein would determine the extent of the mismatch response [15]. A key concern is to experimentally estimate the hydrophobic thickness of membrane

proteins and the membrane bilayer. Determining membrane thickness is a non-trivial issue due to fluctuations of the membrane bilayer in addition to the inherent variations in available bilayer structural data [16]. One way to obtain hydrophobic thickness is from continuous X-ray scattering which measures the Gaussian distribution of the phosphate groups, and therefore the phosphate-to-phosphate distance [17]. The boundary of the hydrophobic thickness of the membrane is placed at the region where water ceases to be detected in the bilayer, i.e., at the *sn-2* carbonyl carbon [16, 18]. Hydrophobic thickness can therefore be obtained from the phosphate-to-phosphate distance by subtracting the thickness of the polar head group region, known from neutron diffraction of specifically deuterated samples to be 5.5 Å [19, 20]. Calculated this way, the hydrophobic thickness of pure fluid phase bilayers is found to vary linearly with acyl chain length [17]. This fluid phase thickness can be used to calculate the thickness of the gel phase by accounting for lipid tilt (∼30°) and increased thickness (∼30%) due to the all-*trans* acyl chain conformation in the gel phase [21]. However, such a calculation would give only approximate values for gel phase bilayers since average lipid tilt is known to be dependent on chain length [22].

The hydrophobic thickness of membrane proteins is more difficult to assess due to difficulty in obtaining high-resolution structures of membrane proteins. Hydrophobic thickness may be determined directly from crystal structures when the structure contains resolved lipid molecules that would mark the membrane interface [23]. In general, hydropathy profiles can provide an estimate of the number of residues in the transmembrane domain. The length of the hydrophobic (transmembrane) region can then be calculated assuming the transmembrane domain to be an α-helix, oriented parallel to the bilayer normal, with a vertical rise of 1.5 Å per residue. However, due to possible helical tilt, and contributions from the flanking residues, calculation of membrane protein thickness based on the length of the transmembrane domain may not always be straightforward. In addition, hydrophobic thickness of proteins has also been determined experimentally [24, 25].

16.4 Lipid and Protein Adaptation: Responses to Hydrophobic Mismatch

Lipids and proteins adapt to two different types of hydrophobic mismatch (positive and negative) in a number of ways. A positive mismatch occurs when the transmembrane domain length (d_{TM}) of the membrane protein is more than the membrane bilayer hydrophobic thickness (d_{HT}). When $d_{TM} > d_{HT}$, annular lipids surrounding the protein would get extended to match the hydrophobic thickness of the transmembrane domain of the protein (see Fig. 16.1a). This induces local ordering of annular lipid acyl chains resulting in an increase in the phase transition temperature, and a decrease in the phospholipid headgroup area (see Fig. 16.1a). The second kind of mismatch, i.e., negative mismatch, takes place when the

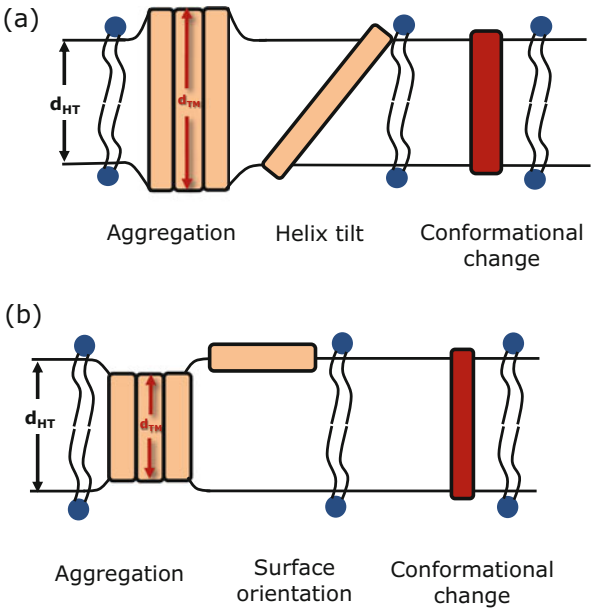

Fig. 16.2 A schematic representation of the possible adaptations of transmembrane proteins to hydrophobic mismatch. (**a**) Various adaptations of the protein upon positive mismatch (i.e., $d_{TM} > d_{HT}$). These include protein aggregation, tilting of transmembrane helices and conformational changes (shown in a different color) of the protein. (**b**) Under conditions of negative mismatch (i.e., $d_{TM} < d_{HT}$), the protein could adapt by aggregation, surface orientation and conformational change (shown in a different color)

transmembrane domain length is shorter relative to the bilayer hydrophobic thickness (i.e., $d_{TM} < d_{HT}$). Negative mismatch causes compression and local disordering of annular lipid acyl chains, a reduction in the phase transition temperature and a concomitant increase in the phospholipid headgroup area (see Fig. 16.1b). On the other hand, there could be several possible adaptations of the protein in case of positive mismatch (i.e., when $d_{TM} > d_{HT}$) which include protein aggregation, tilting of transmembrane helices and conformational changes (see Fig. 16.2a). In case of negative mismatch (i.e., when $d_{TM} < d_{HT}$), possible responses of the protein could be lateral aggregation, surface orientation and conformational change (see Fig. 16.2b). In addition, hydrophobic mismatch is believed to play an important role in membrane protein insertion and folding [26].

16.5 Hydrophobic Mismatch Models

Adaptation to hydrophobic mismatch has previously been described using a comprehensive thermodynamic model termed as the 'mattress model' [27]. The main idea underlying the mattress model is that any alteration of the sharp melting phase transition temperature (T_m) of lipid bilayers by the inclusion of proteins is a direct consequence of adaptation to hydrophobic mismatch that would occur on either side of the phase transition (since phase transition involves a large change (~30%) in the hydrophobic thickness of the membrane; [21]). In this model, adaptation to hydrophobic mismatch is modeled as a change in thickness of the annular lipid ring

as a result of compression or stretching of acyl chains, which leads to a shift (ΔT) in the phase transition temperature, relative to the T_m of a pure lipid bilayer. The magnitude of this shift is related to the extent of the mismatch. Therefore, long proteins in a short bilayer would cause stretching of annular lipids resulting in a shift toward a more gel-like (ordered) phase, and an increase in T_m (see Fig. 16.1a). Short proteins in a long bilayer would lead to compression of annular lipids, shift toward a more fluid phase and a decrease in T_m (see Fig. 16.1b).

In another model, Fattal and Ben-Shaul [28] characterized lipid-protein interactions and perturbations due to mismatch in terms of lipid deformation free energy change (ΔF), represented as a sum of hydrophobic core (lipid chain) and interfacial contributions. Importantly, this model assumes that protein-induced deformations persist in the membrane plane from the lipid-protein interface over typically a few molecular diameters (see Fig. 16.1). The lipid deformation free energy change (ΔF) accounts for changes in lipid chain order at the lipid-protein interface. When the hydrophobic lengths of the membrane and protein are equal, $\Delta F > 0$ due to the loss of conformational entropy experienced by the lipid chains at the protein interface. In mismatch situations, when the protein is longer than the membrane, ΔF further increases due to the enhanced stretching of the lipid chains. On the other hand, when the protein is shorter than the membrane, conformational entropy increases due to compression, but ΔF increases due to an increase in interfacial free energy. Therefore, ΔF is at a minimum when the hydrophobic lengths of the protein and membrane are equal but is always positive.

It should however be noted that theoretical models treat transmembrane proteins as smooth, rigid cylindrical impurities in the bilayer without vertical flexibility, characterized only by cross sectional area and hydrophobic thickness [15]. At the lipid-protein interface, the protein is assumed to be a nearly planar, smooth hydrophobic wall. In addition, these models are only valid for proteins at the infinite dilution limit and therefore do not account for any possible protein-protein interactions (e.g., lateral aggregation). Importantly, theoretical models highlight membrane deformation as a vital consequence of mismatch. Membrane deformation is related to the material properties of the membrane, and is therefore dependent on membrane composition, specifically cholesterol content ([29]; see later).

16.6 Hydrophobic Mismatch in Peptides

We will highlight representative examples of hydrophobic mismatch in peptides, which have been extensively studied. Gramicidin is a peptide which forms prototypical ion channels specific for monovalent ions and has been studied extensively to chararcterize lipid-protein interactions [30]. Previous experiments have shown that gramicidin adopts non-channel conformations under conditions of hydrophobic mismatch and aggregates in thicker gel phase membranes [31]. Simulation studies support the results obtained and revealed that in extremely negative mismatched condition, bilayer thinning occurs and is accompanied by conversion of gramicidin

from channel to non-channel form [32]. It has been previously shown that a mismatch between the length of gramicidin and the lipid acyl chains could induce non-bilayer phase (such as the hexagonal II phase) in model membranes [33]. In another study, the affinity of the pore-forming cholesterol-dependent peptide Perfringolysin O was found to increase for ordered lipid domains by hydrophobic matching between transmembrane hydrophobic thickness and bilayer hydrophobic thickness [34].

The WALP family of peptides [35], contains a stretch of alternating Leu-Ala residues that form the hydrophobic core of the peptide and two Trp residues at both ends that act as membrane interfacial anchors. Trp-flanked WALP peptides form rigid α-helices in the membrane [36] and have proved to be useful to understand basic characteristics of mismatch adaptation [37, 38]. Interestingly, synthetic WALP peptides illustrate the role of anchoring residues in mismatch adaptation, due to specific interactions of amino acid side chains with the membrane interface. The mismatch response of peptides of equal transmembrane thickness (i.e., with the same number of residues in the hydrophobic core) has been shown to be dependent on the nature of the anchoring residues [39–41]. Trp-flanked WALP peptides induce a larger lipid response (i.e., acyl chain ordering) in shorter bilayers as compared to equivalent Lys-flanked (KALP) or Arg-flanked (RALP) peptides [40, 42] due to the 'snorkeling' effect.

16.7 Hydrophobic Mismatch in GPCRs: A Model for GPCR Activation

G protein-coupled receptors (GPCRs) are important signaling hubs that serve as key drug targets in all clinical areas [43, 44]. Hydrophobic mismatch not only affects peptide orientation and function, but recent reports show that it plays a key role in maintaining the structure and function of GPCRs. For example, NMR measurements have shown that increasing bilayer thickness favors formation of metarhodopsin II (MII, active conformation) while oligomerization favors metarhodopsin I (MI, inactive conformation) [45].

Integral membrane proteins such as GPCRs utilize oligomerization as a response to hydrophobic mismatch since this helps to prevent the exposure of specific residues. The dimerization of β_2-adrenergic receptor has been studied at different cholesterol concentrations and a modulation of the dimer interface was observed by increasing cholesterol concentration [46]. Interestingly, in case of the β_2-adrenergic receptor, the hydrophobic mismatch was observed to be higher in presence of cholesterol [7, 46].

An elegant model of GPCR activation could be envisaged based on results of Alves et al. [47] on hydrophobic mismatch of human delta opioid receptor (see Fig. 16.3). This is based on active state dependent partitioning of the receptor, i.e., preferential partitioning of the agonist bound delta opioid receptor to

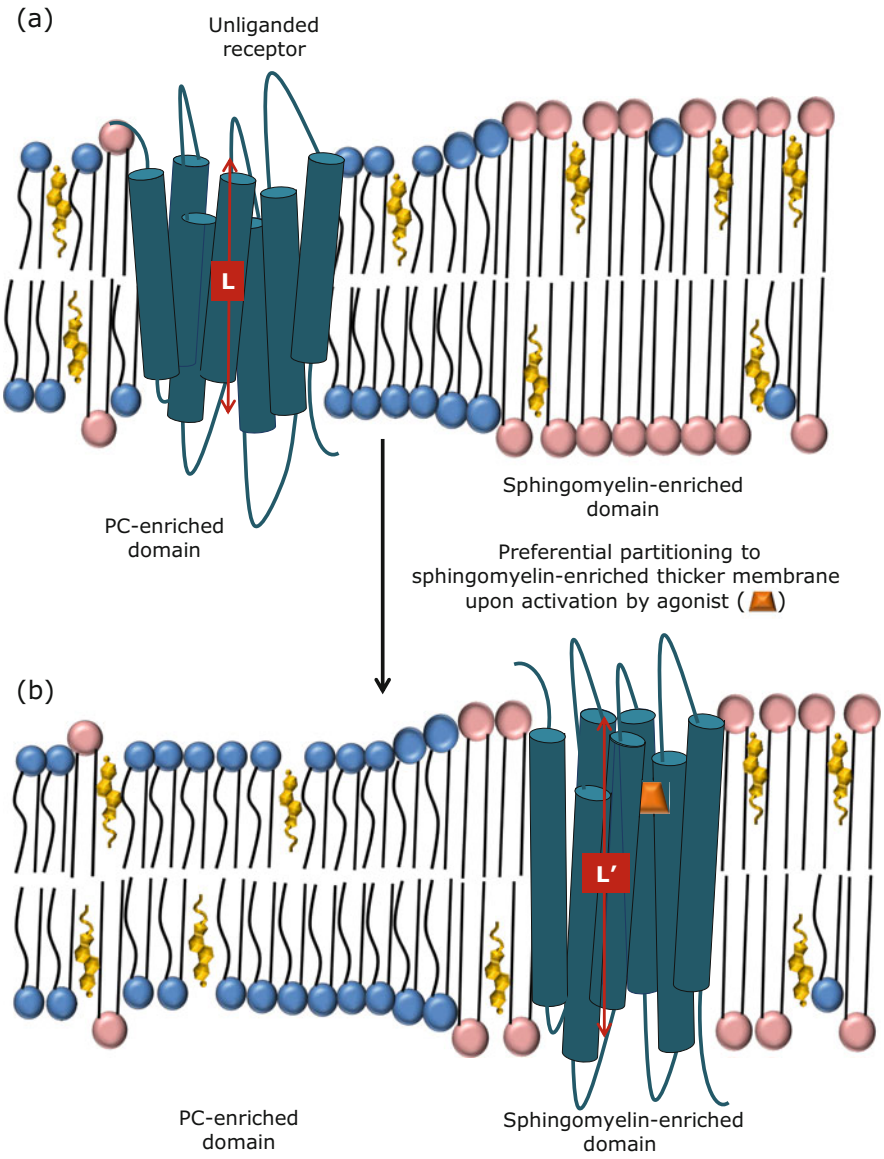

Fig. 16.3 Proposed model for activation of GPCR based on hydrophobic mismatch. (**a**) The receptor is localized in the shorter phosphatidylcholine (PC)-rich domain in the absence of ligand. (**b**) Upon activation by the agonist, the receptor undergoes conformational change such that the length of its transmembrane domain increases from L (unliganded state) to L′ (activated state). In response to the change in the transmembrane length of the receptor, the activated receptor is preferentially partitioned in the thicker sphingomyelin-rich domain due to favorable hydrophobic matching. This model is inspired from data reported in Alves et al. [47] on the human delta opioid receptor

sphingomyelin-rich thicker regions of the membrane due to elongation of its transmembrane domain upon activation by the ligand (see Fig. 16.3).

16.8 Is Hydrophobic Mismatch Relevant in Cell Membranes?

Cellular membranes display heterogeneity in thickness and composition due to the presence of a cholesterol gradient in various intracellular membranes. In eukaryotic cells, there is a gradient of increasing bilayer thickness from the endoplasmic reticulum to Golgi to the plasma membrane and all membrane proteins traverse this path. Hydrophobic mismatch has been proposed to play a crucial role in such sorting [48].

The endoplasmic reticulum is the site of cholesterol biosynthesis, yet interestingly has the lowest cholesterol content in membranes of the secretory pathway [48]. Cholesterol content increases gradually in the Golgi (along the *cis*-, *medial*-, and *trans*-Golgi stacks) with the plasma membrane having the highest concentration of cholesterol (∼90% of total cellular cholesterol). This cholesterol gradient could set up a possible thickness gradient along the biosynthetic pathway of membrane proteins since cholesterol is known to increase thickness of bilayers [49, 50]. This means that hydrophobic mismatch could occur if proteins specific to the Golgi, for example, gets mis-targeted to the plasma membrane. Interestingly, several studies have pointed out the importance of the transmembrane domain (TMD) in retention of proteins in the Golgi and ER [51–56]. Analysis from hydropathy plots showed that the average length of the TMD in Golgi proteins is ∼15 amino acids whereas the average length of the TMD in plasma membrane proteins is ∼20 amino acids [48, 51]. For example, replacing the TMD of a Golgi protein (sialyltransferase) by a hydrobhobic poly-Leu stretch of the same length results in its retention in the Golgi. However, when the length of the poly-Leu sequence was increased to ∼23 amino acids, the protein was expressed at the cell surface. This proves the significance of the length rather than sequence of the TMD to be the driving factor for sorting of proteins in cells [48, 51–53].

Long chain lipids and cholesterol often phase separate to form membrane domains of increased thickness in a complex membrane. Mismatched proteins could segregate to domains to relieve mismatch under such conditions. This type of membrane domains act as clustering hubs for mismatched proteins. Hydrophobic mismatch could lead to sorting of membrane proteins from cholesterol/sphingolipid rich domains of the Golgi to the plasma membrane. This hypothesis is further supported by the prediction that shorter proteins are efficiently excluded out of thicker cholesterol rich domains due to the high energetic penalty of deformation [57]. We should mention here that an alternate hypothesis, based on membrane thickness change along the exocytic pathway due to depletion of membrane proteins (rather than cholesterol content), has been reported [58].

16.9 Future Perspectives: What Lies Ahead

Biological membranes are complex, closely packed assemblies of lipids, proteins and carbohydrates. Work from a large number of groups over the years has shown the relevance of lipid-protein interactions in maintaining membrane structure and function. Most of these interactions involve the phospholipid headgroup with its various characteristics (size, shape, charge). In contrast, hydrophobic mismatch brings into focus the importance of the lipid acyl chains in lipid-protein interactions. In this review, we have highlighted the importance of hydrophobic mismatch in model and biological membranes with representative examples. Since membranes of eukaryotic cells contain thousands of diverse lipid types [59, 60], there could be further implications of hydrophobic mismatch that would encompass a broader area of cell biology. This will become apparent in years to come with advancements in lipidomics, proteomics and related approaches.

Acknowledgments A.C. gratefully acknowledges J.C. Bose Fellowship from the Department of Science and Technology, Govt. of India. B.D.R. thanks the University Grants Commission for the award of a Senior Research Fellowship. We thank Dr. Devaki A. Kelkar for help in the initial stages of this manuscript. A.C. is an Adjunct Professor of Tata Institute of Fundamental Research (Mumbai), RMIT University (Melbourne, Australia), Indian Institute of Technology (Kanpur), and Indian Institute of Science Education and Research (Mohali). We thank members of the Chattopadhyay laboratory for their comments and discussions.

References

1. Tanford C. The hydrophobic effect and the organization of living matter. Science. 1978;200: 1012–8.
2. Singer SJ, Nicolson GL. The fluid mosaic model of the structure of cell membranes. Science. 1972;175:720–31.
3. Goose JE, Sansom MSP. Reduced lateral mobility of lipids and proteins in crowded membranes. PLoS Comput Biol. 2013;9:e1003033.
4. Takamori S, Holt M, Stenius K, et al. Molecular anatomy of a trafficking organelle. Cell. 2006; 127:831–46.
5. Ramadurai S, Holt A, Krasnikov V, et al. Lateral diffusion of membrane proteins. J Am Chem Soc. 2009;131:12650–6.
6. Lee AG. Biological membranes: the importance of molecular detail. Trends Biochem Sci. 2011;36:493–500.
7. Sengupta D, Chattopadhyay A. Molecular dynamics simulations of GPCR-cholesterol interaction: an emerging paradigm. Biochim Biophys Acta. 2015;1848:1775–82.
8. Jensen MØ, Mouritsen OG. Lipids do influence protein function – the hydrophobic matching hypothesis revisited. Biochim Biophys Acta. 2004;1666:205–26.
9. Lee AG. How lipids affect the activities of integral membrane proteins. Biochim Biophys Acta. 2004;1666:62–87.
10. Dumas F, Tocanne J-F, Leblanc G, et al. Consequences of hydrophobic mismatch between lipids and melibiose permease on melibiose transport. Biochemistry. 2000;39:4846–54.

11. Kleinschmidt JH, Tamm LK. Secondary and tertiary structure formation of the β-barrel membrane protein OmpA is synchronized and depends on membrane thickness. J Mol Biol. 2002; 324:319–30.
12. Williamson IM, Alvis SJ, East JM, et al. Interactions of phospholipids with the potassium channel KcsA. Biophys J. 2002;83:2026–38.
13. Jacobson K, Sheets ED, Simson R. Revisiting the fluid mosaic model of membranes. Science. 1995;268:1441–2.
14. Vereb G, Szöllősi J, Matkó J, et al. Dynamic, yet structured: the cell membrane three decades after the Singer-Nicolson model. Proc Natl Acad Sci U S A. 2003;100:8053–8.
15. Mouritsen OG, Bloom M. Models of lipid-protein interactions in membranes. Annu Rev Biophys Biomol Struct. 1993;22:145–71.
16. Nagle JF, Tristam-Nagle S. Structure of lipid bilayers. Biochim Biophys Acta. 2000;1469: 159–95.
17. Lewis BA, Engelman DM. Lipid bilayer thickness varies linearly with acyl chain length in fluid phosphatidylcholine vesicles. J Mol Biol. 1983;166:211–7.
18. White SH, Wimley WC. Membrane protein folding and stability: physical principles. Annu Rev Biophys Biomol Struct. 1999;28:319–65.
19. Büldt G, Gally HU, Seelig J, et al. Neutron diffraction studies on phosphatidylcholine model membranes: I. Head group conformation. J Mol Biol. 1979;134:673–91.
20. Zaccai G, Büldt G, Seelig A, et al. Neutron diffraction studies on phosphatidylcholine model membranes: II. Chain conformation and segmental disorder. J Mol Biol. 1979;134:693–706.
21. Sperotto MM, Mouritsen OG. Dependence of lipid membrane phase transition temperature on the mismatch of protein and lipid hydrophobic thickness. Eur Biophys J. 1988;16:1–10.
22. Tristram-Nagle S, Zhang R, Suter RM, et al. Measurement of chain tilt angle in fully hydrated bilayers of gel phase lecithins. Biophys J. 1993;64:1097–109.
23. Lee AG. Lipid-protein interactions in biological membranes: a structural perspective. Biochim Biophys Acta. 2003;1612:1–40.
24. Dumas F, Lebrun MC, Tocanne J-F. Is the protein/lipid hydrophobic matching principle relevant to membrane organization and functions? FEBS Lett. 1999;458:271–7.
25. Powl AM, Wright JN, East JM, et al. Identification of the hydrophobic thickness of a membrane protein using fluorescence spectroscopy: studies with the mechanosensitive channel MscL. Biochemistry. 2005;44:5713–21.
26. Bowie JU. Solving the membrane protein folding problem. Nature. 2005;438:581–9.
27. Mouritsen OG, Bloom M. Mattress model of lipid-protein interactions in membranes. Biophys J. 1984;46:141–53.
28. Fattal DR, Ben-Shaul A. A molecular model for lipid-protein interaction in membranes: the role of hydrophobic mismatch. Biophys J. 1993;65:1795–809.
29. Needham D. Cohesion and permeability of lipid bilayer vesicles. In: Simon SA, Disalvo EA, editors. Permeability and stability of lipid bilayers. Boca Raton, Florida: CRC Press; 1995. p. 49–76.
30. Kelkar DA, Chattopadhyay A. The gramicidin ion channel: a model membrane protein. Biochim Biophys Acta. 2007;1768:2011–25.
31. Kelkar DA, Chattopadhyay A. Modulation of gramicidin channel conformation and organization by hydrophobic mismatch in saturated phosphatidylcholine bilayers. Biochim Biophys Acta. 2007;1768:1103–13.
32. Basu I, Chattopadhyay A, Mukhopadhyay C. Ion channel stability of gramicidin A in lipid bilayers: effect of hydrophobic mismatch. Biochim Biophys Acta. 2014;1838:328–38.
33. Killian JA, Prasad KU, Urry DW, et al. A mismatch between the length of gramicidin and the lipid acyl chains is a prerequisite of H_{II} phase formation in phosphatidylcholine model membranes. Biochim Biophys Acta. 1989;978:341–5.
34. Lin Q, London E. Altering hydrophobic sequence lengths shows that hydrophobic mismatch controls affinity for ordered lipid domains (rafts) in the multitransmembrane strand protein Perfringolysin O. J Biol Chem. 2013;288:1340–52.

35. Killian JA, Salemink I, de Planque MRR, et al. Induction of nonbilayer structures in diacylphosphatidylcholine model membranes by transmembrane α-helical peptides: importance of hydrophobic mismatch and proposed role of tryptophans. Biochemistry. 1996;35:1037–45.
36. de Planque MRR, Goormaghtigh E, Greathouse DV, et al. Sensitivity of single membrane-spanning α-helical peptides to hydrophobic mismatch with a lipid bilayer: effects on backbone structure, orientation, and extent of membrane incorporation. Biochemistry. 2001;40:5000–10.
37. Holt A, Killian JA. Orientation and dynamics of transmembrane peptides: the power of simple models. Eur Biophys J. 2010;39:609–21.
38. de Planque MRR, Killian JA. Protein-lipid interactions studied with designed transmembrane peptides: role of hydrophobic matching and interfacial anchoring. Mol Membr Biol. 2003;20: 271–84.
39. Mall S, Broadbridge R, Sharma RP, et al. Effects of aromatic residues at the ends of transmembrane α-helices on helix interactions with lipid bilayers. Biochemistry. 2000;39:2071–8.
40. de Planque MRR, Boots J-WP, Rijkers DTS, et al. The effects of hydrophobic mismatch between phosphatidylcholine bilayers and transmembrane α-helical peptides depend on the nature of interfacially exposed aromatic and charged residues. Biochemistry. 2002;41: 8396–404.
41. Strandberg E, Morein S, Rijkers DTS, et al. Lipid dependence of membrane anchoring properties and snorkeling behavior of aromatic and charged residues in transmembrane peptides. Biochemistry. 2002;41:7190–8.
42. de Planque MRR, Kruijtzer JAW, Liskamp RMJ, et al. Different membrane anchoring positions of tryptophan and lysine in synthetic transmembrane α-helical peptides. J Biol Chem. 1999;274:20839–46.
43. Chattopadhyay A. GPCRs: lipid-dependent membrane receptors that act as drug targets. Adv Biol. 2014;2014:143023.
44. Rosenbaum DM, Rasmussen SGF, Kobilka BK. The structure and function of G-protein-coupled receptors. Nature. 2009;459:356–63.
45. Soubias O, Teague WE, Hines KG, et al. Rhodopsin/lipid hydrophobic matching- rhodopsin oligomerization and function. Biophys J. 2015;108:1125–32.
46. Prasanna X, Chattopadhyay A, Sengupta D. Role of lipid-mediated effects in β_2-adrenergic receptor dimerization. Adv Exp Med Biol. 2015;842:247–61.
47. Alves ID, Salamon Z, Hruby VJ, et al. Ligand modulation of lateral segregation of a G-protein-coupled receptor into lipid microdomains in sphingomyelin/phosphatidylcholine solid-supported bilayers. Biochemistry. 2005;44:9168–78.
48. Bretscher MS, Munro S. Cholesterol and the Golgi apparatus. Science. 1993;261:1280–1.
49. Gallová J, Uhríková D, Islamov A, et al. Effect of cholesterol on the bilayer thickness in unilamellar extruded DLPC and DOPC liposomes: SANS contrast variation study. Gen Physiol Biophys. 2004;23:113–28.
50. Nezil FA, Bloom M. Combined influence of cholesterol and synthetic amphiphillic peptides upon bilayer thickness in model membranes. Biophys J. 1992;61:1176–83.
51. Masibay AS, Balaji PV, Boeggeman EE, et al. Mutational analysis of the Golgi retention signal of bovine β-1,4-galactosyltransferase. J Biol Chem. 1993;268:9908–16.
52. Munro S. Sequences within and adjacent to the transmembrane segment of α-2,6-sialyltransferase specify Golgi retention. EMBO J. 1991;10:3577–88.
53. Munro S. An investigation of the role of transmembrane domains in Golgi protein retention. EMBO J. 1995;14:4695–704.
54. Sharpe HJ, Stevens TJ, Munro S. A comprehensive comparison of transmembrane domains reveals organelle-specific properties. Cell. 2010;142:158–69.
55. Shi X, Lappin DF, Elliott RM. Mapping the Golgi targeting and retention signal of Bunyamwera virus glycoproteins. J Virol. 2004;78:10793–802.
56. Tang BL, Wong SH, Low SH, et al. The transmembrane domain of *N*- glucosaminyltransferase I contains a Golgi retention signal. J Biol Chem. 1992;267:10122–6.

57. Lundbaek JA, Andersen OS, Werge T, et al. Cholesterol-induced protein sorting: an analysis of energetic feasibility. Biophys J. 2003;84:2080–9.
58. Mitra K, Ubarretxena-Belandia I, Taguchi T, et al. Modulation of the bilayer thickness of exocytic pathway membranes by membrane proteins rather than cholesterol. Proc Natl Acad Sci U S A. 2004;101:4083–8.
59. van Meer G, de Kroon AIPM. Lipid map of the mammalian cell. J Cell Sci. 2011;124:5–8.
60. Sud M, Fahy E, Cotter D, et al. LMSD: LIPID MAPS structure database. Nucleic Acids Res. 2007;35:D527–32.